Titre: Title:	Development of a Thermodynamic Database for Nickel-Containing Oxide Systems for Simulation of Nickel Extraction from Laterite Ores
Auteur: Author:	Viktoria Prostakova
Date:	2013
Type:	Mémoire ou thèse / Dissertation or Thesis
Référence: Citation:	Prostakova, V. (2013). Development of a Thermodynamic Database for Nickel-Containing Oxide Systems for Simulation of Nickel Extraction from Laterite Ores [Thèse de doctorat, École Polytechnique de Montréal]. PolyPublie. https://publications.polymtl.ca/1247/

UNIVERSITÉ DE MONTRÉAL

DEVELOPMENT OF A THERMODYNAMIC DATABASE FOR NICKEL-CONTAINING OXIDE SYSTEMS FOR SIMULATION OF NICKEL EXTRACTION FROM LATERITE ORES

VIKTORIA PROSTAKOVA

DÉPARTEMENT DE GÉNIE CHIMIQUE

ÉCOLE POLYTECHNIQUE DE MONTRÉAL

THÈSE PRÉSENTÉE EN VUE DE L'OBTENTION

DU DIPLÔME DE PHILOSOPHIAE DOCTOR

(GÉNIE MÉTALLURGIQUE)

OCTOBRE 2013

UNIVERSITÉ DE MONTRÉAL

ÉCOLE POLYTECHNIQUE DE MONTRÉAL

Cette thèse intitulée:

DEVELOPMENT OF A THERMODYNAMIC DATABASE FOR NICKEL-CONTAINING OXIDE SYSTEMS FOR SIMULATION OF NICKEL EXTRACTION FROM LATERITE ORES

présentée par : PROSTAKOVA Viktoria

en vue de l'obtention du diplôme de : Philosophiae Doctor

a été dûment acceptée par le jury d'examen constitué de :

M. BALE Christopher, Ph.D., président

M. DECTEROV Sergei, Chercheur, membre et directeur de recherche

M. PELTON Arthur, Ph.D., membre et codirecteur de recherche

M. ROBELIN Christian, Chercheur, membre

M. MARIN Tanai L., Ph.D., membre

DEDICATION

“There is no way to peace; peace is the way.”

Mahatma Ghandi

"Self esteem is different from self importance. With Self esteem you become very humble, very loving."

Nirmala Srivastava

I would like to humbly dedicate this thesis to Mother.

ACKNOWLEDGEMENTS

I would like to thank all members of the jury for their time and essential corrections of this thesis.

I express deep gratitude to Dr. Sergei A. Decterov, whose guidance and advice were indispensable for the completion of this thesis. I am also grateful to him for the opportunity to participate in Calphad conferences, for his support and generosity he showed in unexpected circumstances.

I am also grateful to Prof. Arthur D. Pelton and Prof. Christopher W. Bale from CRCT for interesting and helpful courses.

I express gratitude to Prof. Eugene Jak and Dr. Jiang Chen from the Pyrometallurgy Research Centre for successful collaboration and financial support.

I would like to thank my husband Denis Shishin for his help in the process of working. Also, I would like to thank Evguenia Sokolenko for assistance with the literature, her kindness and sunny coffee breaks, Jacques Melançon for struggling with my computer and Christian Robelin for correction of the French language.

I thank all colleagues from the Centre for Research in Computational Thermochemistry. I appreciate their kindness.

I thank my family and friends, who are a constant source of inspiration to me. I am thankful to life for the opportunity to be with them and to learn from them. I am thankful to the source of life for the opportunity to grow and learn to love.

RÉSUMÉ

Un vaste programme de recherche collaborative s'est concentré sur le développement d'une base de données thermodynamiques auto-cohérente pour la simulation de l'extraction du nickel à partir de minerais latéritiques. Des systèmes chimiques pertinents pour le traitement de minerais latéritiques ont été étudiés expérimentalement et optimisés thermodynamiquement.

En général, les dépôts de minerais latéritiques sont constitués de mélanges hétérogènes d'oxydes de fer hydratés et de silicates de magnésium hydratés. La base des minerais latéritiques est l'olivine $(Fe, Mg)_2SiO_4$, qui contient souvent de faibles quantités de nickel à cause de la proximité des rayons ioniques de Fe^{2+}, Mg^{2+} et Ni^{2+}. Les technologies existantes produisant actuellement du nickel dans le monde entier utilisent seulement environ la moitié des gisements de latérites de nickel ; d'autres sources ne sont pas utilisées en raison de la minéralogie complexe. Pour créer des procédés de récupération de Ni à partir de minerais latéritiques qui soient rentables, respectueux de l'environnement et peu coûteux en énergie, il est important de pouvoir effectuer des calculs fiables d'équilibres de phases dans le système multi-composant Al–Ca–Cr–Fe–Mg–Ni–O–Si, où Fe, Al_2O_3, MgO, NiO et SiO_2 sont les principaux constituants des scories et des phases d'oxydes de la pyrométallurgie du nickel.

Le présent programme de recherche a relevé ce défi. Il visait à développer une base de données thermodynamiques pour les systèmes d'oxydes contenant **NiO** dans le système multi-composant Al_2O_3–CaO–FeO–Fe_2O_3–MgO–**NiO**–SiO_2 (Al–Ca–Fe–Mg–**Ni**–O–Si) à haute température d'intérêt pour les procédés pyrométallurgiques du nickel. Le projet a été réalisé grâce aux efforts conjoints de deux groupes de recherche. Le développement de la base de données a été effectué au Centre de Recherche en Calcul Thermochimique, Montréal, Canada par le biais de la modélisation thermodynamique, qui était étroitement liée aux études expérimentales d'équilibres de phases réalisées par nos collègues du Centre de Recherches Pyrométallurgiques (PyroSearch), Brisbane, Australie. Cette approche collaborative a considérablement augmenté l'efficacité de l'ensemble du programme en réduisant le nombre de travaux expérimentaux nécessaires et en fournissant des données expérimentales spécifiques pour la modélisation thermodynamique. Les évaluations thermodynamiques ont permis d'identifier les priorités pour les expériences et de planifier des mesures expérimentales pour fournir des données spécifiques pour la modélisation thermodynamique.

Un examen et une évaluation critique de la littérature publiée antérieurement sur la thermodynamique et les équilibres de phases dans les systèmes contenant NiO ont été réalisés. Les paramètres des modèles ont été optimisés pour reproduire une grande variété de données recueillies dans la littérature, incluant les données d'équilibres de phases, les propriétés thermodynamiques (capacité calorifique, entropie, enthalpie, énergie de Gibbs) et les données de distribution de cations. Cependant, pour plusieurs sous-systèmes d'ordre inférieur, les données manquaient dans la littérature parce que ces sous-systèmes n'ont pas d'importance directe pour les applications pratiques. Lorsqu'il n'y avait pas suffisamment de données pour contraindre les paramètres du modèle ou lorsque des divergences importantes ont été observées dans les données disponibles, un programme expérimental a été proposé à nos collègues du Centre PyroSearch. Un nombre limité de mesures expérimentales ont été prévues à des températures et à des compositions jugées les plus utiles pour la modélisation thermodynamique. De cette façon, la quantité de travail nécessaire pour obtenir une description thermodynamique précise d'un système multi-composant a été significativement réduite.

La procédure expérimentale a impliqué un équilibrage à haute température en atmosphère de gaz contrôlée et une trempe ultra rapide suivie par une microanalyse aux rayons X à l'aide d'une sonde électronique (EPMA) des échantillons trempés. Comme l'analyse a eu lieu après l'équilibrage, les changements de composition pendant l'équilibrage n'ont pas affecté la précision des résultats. Les conodes entre les phases liquides et solides à l'équilibre ont été mesurées directement, fournissant ainsi des données essentielles pour la modélisation thermodynamique ultérieure. L'ensemble des données expérimentales, incluant les nouveaux résultats expérimentaux et les données publiées antérieurement, a été pris en considération lors de la modélisation thermodynamique des phases d'oxydes du système multi-composant Al_2O_3–CaO–FeO–Fe_2O_3–MgO–**NiO**–SiO_2 (Al–Ca–Fe–Mg–**Ni**–O–Si) à une pression totale de 1 atm et pour une large gamme de températures et de pressions partielles d'oxygène. La modélisation thermodynamique a été réalisée à l'aide du logiciel thermochimique FactSage et de ses bases de données. Toutes les phases solides et liquides de

4 systèmes binaires: CaO-NiO, MgO-NiO, NiO-SiO_2, Al_2O_3-NiO,

7 systèmes ternaires: CaO-MgO-NiO, CaO-NiO-SiO_2, MgO-NiO-SiO_2, Al_2O_3-NiO-SiO_2, Al_2O_3-MgO-NiO, Al_2O_3-FeO-Fe_2O_3, FeO-Fe_2O_3-NiO,

5 systèmes quaternaires: CaO-MgO-NiO-SiO_2, Al_2O_3-FeO-Fe_2O_3-NiO, FeO-Fe_2O_3-MgO-NiO, FeO-Fe_2O_3-NiO-SiO_2, CaO-FeO-Fe_2O_3-NiO,

et **2 systèmes quinaires**, Fe-Mg-Ni-O-Si et Ca-Fe-Ni-O-Si, du système chimique multi-composant ont été optimisées dans la présente étude. Les optimisations sont auto-cohérentes et compatibles avec les bases de données existantes FToxid et FSstel du logiciel FactSage. Les modèles utilisés sont basés sur la structure de la solution considérée. Le Modèle Quasichimique Modifié, qui prend en compte l'ordre à courte distance entre les cations seconds voisins, a été utilisé pour la phase de scories (oxyde fondu). Des modèles basés sur le « Compound Energy Formalism » ont été développés pour les solutions solides d'olivine, de spinelle et de pyroxène. Un modèle de mélange aléatoire simple avec une expansion polynômiale de l'énergie de Gibbs en excès a été utilisé pour les solutions solides de monoxyde et de corindon. Un ensemble de fonctions d'énergie de Gibbs auto-cohérentes a été obtenu qui assure la meilleure description possible des propriétés thermodynamiques et des équilibres de phases dans le système chimique considéré. Les données de la littérature sont reproduites dans les limites de l'erreur expérimentale. En utilisant les paramètres du modèle optimisés, des prévisions très utiles des équilibres de phases dans les systèmes multi-composants ont été réalisées.

Les propriétés des solutions de spinelle, de monoxyde, d'olivine et de corindon dans les systèmes chimiques Al–Fe–Ni–O, Al–Mg–Ni–O, Fe–Mg–Ni–O, Ca–Fe–Ni–O et Fe–Mg–Ni–O–Si et de la phase de scories dans le système Ca–Fe–Ni–O–Si ont été prédites uniquement à partir des paramètres des modèles optimisés pour les solutions binaires (ternaires) correspondantes. La comparaison ultérieure avec les données thermodynamiques et d'équilibres de phases disponibles a montré que les modèles ayant un sens physique que nous avons appliqués ont une excellente capacité à prédire les relations de phases dans les systèmes multi-composants. De cette façon, nous avons démontré l'efficacité de l'approche appliquée consistant en un couplage entre les expériences et la modélisation.

La base de données actuelle a été incorporée dans les bases de données existantes de FactSage. Ainsi, la gamme d'applications des bases de données de FactSage a été élargie, et les bases de données existantes ont été mises à jour pour décrire les données expérimentales d'intérêt industriel les plus récentes et les plus précises.

La base de données obtenue couplée à un logiciel de minimisation de l'énergie de Gibbs permet de prédire les équilibres de phases de liquidus et de solidus ainsi que certaines propriétés thermodynamiques dans les conditions (gamme de compositions, de températures et de pressions partielles d'oxygène) les plus utiles pour les opérations métallurgiques et les pratiques d’ingénierie. La base de données est pertinente pour plusieurs types de procédés pyrométallurgiques pour les minérais lattéritiques comme le procédé de ‘’reduction roasting’’ ou le procédé de ‘’electric furnace smelting’’.

ABSTRACT

An extensive collaborative research program was focused on the development of a self-consistent thermodynamic database for simulation of nickel extraction from laterite ores. Chemical systems relevant to laterite ore processing were experimentally investigated and thermodynamically optimized.

In general, laterite ore deposits consist of heterogeneous mixtures of hydrated iron oxides and hydrous magnesium silicates. The basis of the laterite ore is olivine $(Fe,Mg)_2SiO_4$, which often contains small amounts of nickel due to the proximity of ionic radii of Fe^{2+}, Mg^{2+} and Ni^{2+}. Existing technologies that currently produce nickel worldwide utilize only about half of the nickel laterite deposits; other sources are not utilized due to complex mineralogy. For creation of cost-effective, environmentally-friendly and energy-efficient processes of Ni recovery from laterite ores, it is important to be able to perform reliable calculations of phase equilibria in the Al–Ca–Cr–Fe–Mg–Ni–O–Si system, where Fe, Al_2O_3, MgO, NiO and SiO_2 are the major components of slags and oxide phases in nickel pyrometallurgy.

The current research program met this challenge. It was aimed to develop a thermodynamic database for **NiO**-containing oxide systems in the Al_2O_3–CaO–FeO–Fe_2O_3–MgO–**NiO**–SiO_2 (Al–Ca–Fe–Mg–**Ni**–O–Si) multi-component system at high temperature of interest to nickel pyrometallurgical processes.

The project was accomplished by the joint efforts of two research groups. The database development was carried out at the Centre for Research in Computational Thermochemistry, Montreal, Canada by means of thermodynamic modeling, which was closely related to experimental study of phase equilibria performed by our colleagues from the Pyrometallurgy Research Centre (PyroSearch), Brisbane, Australia. This collaborative approach greatly increased the effectiveness of the overall program by reducing the amount of the required experimental work and providing specific experimental data for thermodynamic modeling. Thermodynamic assessments were applied to identify priorities for experiments and experimental measurements were planned to provide specific data for thermodynamic modeling.

A literature review and critical assessment of the previously published thermodynamic and phase equilibrium data on the NiO-containing systems were performed using thermodynamic modeling. The parameters of the models were optimized to fit a large variety of the literature data collected

from the literature, including phase equilibrium data, thermodynamic properties (heat capacity, entropy, enthalpy, Gibbs energy) and cation distribution data. However, for several low-order sub-systems, data were missing in the literature because they are of no direct importance for practical applications. In case there was not enough data to constrain the model parameters, or significant discrepancies in the available data were revealed, an experimental program was suggested to our colleagues from the PyroSearch Centre. A limited number of experimental measurements were planned for temperatures and compositions which were found to be most useful for thermodynamic modeling. In this way, the amount of the work required to obtain an accurate thermodynamic description of a multicomponent system was significantly reduced.

The experimental procedure involved the high-temperature equilibration in controlled gas atmospheres and ultra rapid quenching followed by electron probe X-ray microanalysis (EPMA) of quenched samples. Since the analysis took place after equilibration, the changes in composition during equilibration did not affect the accuracy of the results. Tie-lines between equilibrated liquid and solid phases were measured directly, providing essential data for subsequent thermodynamic modeling.

The whole set of experimental data, including the new experimental results and previously published data, was taken into consideration in thermodynamic modeling of oxide phases in the Al_2O_3–CaO–FeO–Fe_2O_3–MgO–NiO–SiO_2 (Al–Ca–Fe–Mg–Ni–O–Si) multi-component system at a total pressure of 1 atm and a wide range of temperatures and oxygen partial pressures. The thermodynamic modeling part was undertaken using the FactSage thermochemical software and its databases. All solid and liquid phases of

4 binary: CaO-NiO, MgO-NiO, NiO-SiO_2, Al_2O_3-NiO,

7 ternary: CaO-MgO-NiO, CaO-NiO-SiO_2, MgO-NiO-SiO_2, Al_2O_3-NiO-SiO_2, Al_2O_3-MgO-NiO, Al_2O_3-FeO-Fe_2O_3, FeO-Fe_2O_3-NiO,

5 quaternary: CaO-MgO-NiO-SiO_2, Al_2O_3-FeO-Fe_2O_3-NiO, FeO-Fe_2O_3-MgO-NiO, FeO-Fe_2O_3-NiO-SiO_2, CaO-FeO-Fe_2O_3-NiO,

and **2 quinary systems**, Fe-Mg-Ni-O-Si and Ca-Fe-Ni-O-Si, of the multi-component chemical system were optimized in the present study. The optimizations are self-consistent and consistent with existing FToxide and FSstel metallic databases of the FactSage software. The applied models are based on the structure of the corresponding solution. The Modified Quasichemical

Model, which takes into consideration second-nearest-neighbor short-range cation ordering, was used for the slag (molten oxide) phase. The models based on the Compound Energy Formalism have been developed for the olivine, spinel and pyroxene solid solutions. A simple random mixing model with a polynomial expansion of the excess Gibbs energy was used for the monoxide and corundum solid solutions. A set of self-consistent Gibbs energy functions was obtained that provides the best possible description of thermodynamic properties and phase equilibria in the chemical system. The literature data are reproduced within experimental error limits. Using optimized model parameters, valuable predictions of phase equilibria in the multicomponent systems have been made.

The properties of the spinel, monoxide, olivine and corundum solutions in the Al–Fe–Ni–O, Al–Mg–Ni–O, Fe–Mg–Ni–O, Ca–Fe–Ni–O and Fe–Mg–Ni–O–Si chemical systems and of slag in the Ca–Fe–Ni–O–Si system have been predicted solely from the optimized model parameters for the corresponding binary (ternary) solutions. The subsequent comparison with available thermodynamic and phase equilibrium data has shown that applied physically meaningful models have excellent ability to predict phase relations in multicomponent systems. In this way, the effectiveness of the applied coupled experimental/modeling approach has been demonstrated.

The current database has been incorporated into the existing FactSage databases. By this means, the range of applications of FactSage databases has been expanded, and the existing databases have been updated to describe the most recent and accurate experimental data of interest to industrial operations.

The obtained database along with software for Gibbs energy minimization allows the prediction of liquidus and solidus phase equilibria as well as thermodynamic properties under the conditions, such as range of compositions, temperatures and oxygen partial pressures, which are most useful for metallurgical operations and engineering practice. The database is relevant to various kinds of pyrometallurgical processes for laterite ores, such as reduction roasting as well as electric furnace smelting.

CONDENSÉ

Afin de développer une base de données thermodynamiques multicomposante auto-cohérente pour la simulation de l'extraction du nickel à partir de minerais latéritiques, un vaste programme de recherche a été entrepris, qui combine naturellement des études expérimentales et la modélisation thermodynamique assistée par ordinateur. Des systèmes chimiques pertinents pour le traitement de minerais latéritiques de nickel ont été étudiés expérimentalement et optimisés thermodynamiquement. La modélisation thermodynamique a été réalisée en utilisant le logiciel thermochimique FactSage et ses bases de données [1] développées au Centre de Recherche en Calcul Thermochimique de l'École Polytechnique de Montréal, Canada. Le programme expérimental a été effectué par nos collègues du Centre de Recherches Pyrométallurgiques, Brisbane, Australie [2].

Des expériences et la modélisation thermodynamique ont été étroitement intégrées afin d'accroître l'efficacité de l'ensemble du programme en termes de quantité de travail expérimental requise et la disponibilité des données spécifiques essentielles à la modélisation thermodynamique. Ceci a été réalisé en appliquant les évaluations thermodynamiques pour identifier les expériences prioritaires et en planifiant des mesures expérimentales de façon à fournir des données spécifiques pour la modélisation thermodynamique. Cette approche a augmenté la capacité de prédiction des modèles thermodynamiques appliqués et a permis de caractériser les relations de phases sur une large gamme de compositions, de températures et de pressions partielles d'oxygène ayant une importance directe pour les industries métallurgiques.

L'ensemble des données expérimentales, incluant les nouveaux résultats expérimentaux et les données publiées antérieurement, a été pris en considération lors de la modélisation thermodynamique des phases d'oxydes du système multi-composant Al_2O_3–CaO–FeO–Fe_2O_3–MgO–NiO–SiO_2 (Al–Ca–Fe–Mg–Ni–O–Si) à une pression totale de 1 atm et pour une large gamme de températures et de pressions partielles d'oxygène. Toutes les phases solides et liquides de 4 systèmes binaires, 7 systèmes ternaires, 5 systèmes quaternaires et 2 systèmes quinaires du système chimique multi-composant ont été optimisées dans la présente étude.

Les optimisations sont auto-cohérentes et compatibles avec les bases de données existantes FToxid et FSstel du logiciel FactSage. Les modèles utilisés sont basés sur la structure de la solution considérée. Le Modèle Quasichimique Modifié, qui prend en compte l'ordre à courte

distance entre les cations seconds voisins, a été utilisé pour la phase de scories (oxyde fondu). Des modèles basés sur le « Compound Energy Formalism » ont été développés pour les solutions solides d'olivine, de spinelle et de pyroxène. Un modèle de mélange aléatoire simple avec une expansion polynômiale de l'énergie de Gibbs en excès a été utilisé pour les solutions solides de monoxyde et de corindon. Un ensemble de fonctions d'énergie de Gibbs auto-cohérentes a été obtenu qui assure la meilleure description possible des propriétés thermodynamiques et des équilibres de phases dans le système chimique considéré. Les données de la littérature sont reproduites dans les limites de l'erreur expérimentale. En utilisant les paramètres du modèle optimisés, des prédictions très utiles des équilibres de phases dans les systèmes multi-composants ont été réalisées.

La méthodologie de la recherche a impliqué plusieurs étapes décrites en détail ci-dessous :

Revue de la littérature et évaluation critique. Nous avons tout d'abord réalisé un examen et une évaluation critique de la littérature publiée antérieurement sur la thermodynamique et les équilibres de phases dans les systèmes contenant NiO. Les données thermodynamiques disponibles dans la littérature pour les composants individuels (capacité calorifique, entropie, enthalpie, énergie de Gibbs), ainsi que les mesures d'équilibres de phases, la distribution des cations, etc., ont été analysées pour leur cohérence et leur précision.

Calculs de modèle initiaux. Les paramètres des modèles ont été optimisés afin de reproduire les données expérimentales recueillies dans la littérature. Les coefficients des modèles ont été déterminés à partir des données expérimentales par une méthode d'essais et d'erreurs.

Etude expérimentale utilisant équilibrage / trempe / EPMA (PyroSearch, Australia). Pour plusieurs sous-systèmes d'ordre inférieur, les données expérimentales manquaient dans la littérature parce que ces sous-systèmes n'ont pas d'importance directe pour les applications pratiques. Lorsqu'il n'y avait pas suffisamment de données pour contraindre les paramètres du modèle ou lorsque des divergences importantes ont été observées dans les données disponibles, un nombre limité de mesures expérimentales a été prévu pour les températures et les compositions considérées comme les plus utiles pour la modélisation thermodynamique.

Optimisation thermodynamique des systèmes d'ordre inférieur. Les nouvelles données expérimentales, en association avec les données disponibles dans la littérature, ont été utilisées pour obtenir les descriptions thermodynamiques des systèmes d'ordre inférieur. Pour chaque

phase, un modèle spécifique a été utilisé qui reflète la structure de la phase correspondante le plus adéquatement et les paramètres du modèle ont été optimisés. De cette façon, tous les systèmes d'ordre inférieur ont été optimisés.

Prédiction des relations de phases dans les systèmes multi-composants. Des propriétés thermodynamiques des phases présentes dans les systèmes multi-composants ont été essentiellement extrapolées à partir des paramètres optimisés dans les systèmes d'ordre inférieur, en utilisant la capacité des modèles à faire des extrapolations de manière thermodynamiquement correcte.

Vérification des modèles par rapport aux données expérimentales disponibles. La capacité de prédiction des modèles a été vérifiée par rapport aux équilibres de phases multi-composants étudiés expérimentalement.

En utilisant la méthodologie décrite ci-dessus, la quantité de travail nécessaire pour obtenir une description thermodynamique précise d'un système multi-composant a été considérablement réduite.

Les conclusions détaillées pour les systèmes optimisés sont résumées comme suit:

Systèmes CaO–NiO, MgO–NiO et NiO–SiO_2 (CHAPTER 5)

Les systèmes binaires (CaO–NiO, MgO–NiO et NiO–SiO_2) ont été optimisés, ainsi que les propriétés de NiO solide et liquide pur. Les fonctions thermodynamiques obtenues sont utilisées dans les optimisations des sous-systèmes ternaires et d'ordre supérieur du système Al–Ca–Fe–Mg–Ni–O–Si.

Les systèmes CaO–NiO et MgO–NiO ont été étudiés par un équilibrage et une trempe ultra rapide suivie d'une microanalyse aux rayons X à l'aide d'une sonde électronique (EPMA) des échantillons trempés pour résoudre les divergences entre les données expérimentales disponibles dans la littérature. La lacune de miscibilité dans la solution solide de monoxyde CaO–NiO a été mesurée entre 1200 et 1600 °C. Les équilibres de phases entre la solution de monoxyde MgO–NiO et Ni ont été étudiés à des pressions partielles d'oxygène fixes comprises entre $10^{-13.5}$ et $10^{-7.5}$ atm sur la gamme de températures 1000-1300 °C. Ces nouvelles mesures ont résolu les divergences observées entre les données expérimentales antérieures sur les diagrammes de phases, les activités et les chaleurs de mélange.

Les paramètres des modèles thermodynamiques pour les phases d'oxydes ont été optimisés pour reproduire simultanément les résultats expérimentaux de la présente étude et toutes les données de la littérature sur la thermodynamique et les diagrammes de phases pour les systèmes CaO–NiO, MgO–NiO et NiO–SiO_2. Un ensemble de fonctions d'énergie de Gibbs auto-cohérentes a été obtenu qui assure la meilleure description possible des propriétés thermodynamiques et des équilibres de phases dans ces systèmes. Toutes les données disponibles sont reproduites dans les limites de l'erreur expérimentale.

Système MgO–NiO–SiO_2 (CHAPTER 6)

Le système MgO–NiO–SiO_2 a été étudié en combinant l'évaluation critique des données expérimentales de la littérature, la modélisation thermodynamique et des mesures expérimentales des équilibres de phases à des compositions choisies. Ces mesures expérimentales, d'une part, peuvent être faites plus précisément et plus efficacement et, d'autre part, fournissent les données les plus importantes pour la modélisation thermodynamique.

En particulier, les conodes olivine / monoxyde, olivine / proto-pyroxène, liquide / olivine et liquide / cristobalite ont été mesurées afin de compléter les données de la littérature et résoudre certaines contradictions. L'étude expérimentale a été réalisée sur toute la gamme de températures 1400-1650 °C en utilisant une technique d'équilibrage et de trempe suivie d'EPMA.

Les paramètres des modèles thermodynamiques pour les phases d'oxydes ont été optimisés pour reproduire simultanément les résultats expérimentaux de la présente étude ainsi que les données thermodynamiques et les diagrammes de phases disponibles dans la littérature pour le système MgO–NiO–SiO_2. Un ensemble de fonctions d'énergie de Gibbs auto-cohérentes a été obtenu qui assure la meilleure description possible des propriétés thermodynamiques et des équilibres de phases dans ce système. Toutes les données disponibles sont reproduites à l’intérieur des incertitudes expérimentales.

Système CaO–MgO–NiO–SiO_2 et ses sous-systèmes ternaires CaO–NiO–SiO_2 et CaO–MgO–NiO (CHAPTER 7)

Le système quaternaire CaO–MgO–NiO–SiO_2 et ses sous-systèmes ternaires contenant NiO CaO–NiO–SiO_2 et CaO–MgO–NiO ont été optimisés à une pression totale de 1 atm.

Certains écarts dans les données de la littérature pour le système $CaO–NiO–SiO_2$ ont été mis en évidence. Pour résoudre les conflits dans les données de la littérature, une nouvelle étude expérimentale a été réalisée dans ce travail. La procédure expérimentale a impliqué un équilibrage et une trempe ultra rapide suivie d'une microanalyse aux rayons X à l'aide d'une sonde électronique (EPMA) des échantillons trempés.

Les conodes entre les oxydes liquides (scories) et les oxydes solides ont été mesurées sur les sections isothermes du diagramme de phases $CaO–NiO–SiO_2$ à des températures comprises entre 1330 et 1500 °C. Les nouvelles données expérimentales ont été comparées aux résultats publiés antérieurement et les divergences ont été clarifiées.

Une optimisation simultanée de toutes les données disponibles dans le système quaternaire $CaO–MgO–NiO–SiO_2$ et dans ses sous-systèmes ternaires $CaO–NiO–SiO_2$ et CaO–MgO–NiO a été effectuée. Les nouvelles données expérimentales et les résultats expérimentaux publiés antérieurement ont été pris en considération. Les paramètres des modèles optimisés pour les phases d'oxydes reproduisent toutes les données disponibles dans les limites de l'erreur expérimentale. Un ensemble de fonctions d'énergie de Gibbs auto-cohérentes des phases d'oxydes pour les systèmes chimiques a été dérivé.

Système Al–Fe–O (CHAPTER 8)

Une optimisation simultanée de toutes les données disponibles dans le système Al-Fe-O à une pression totale de 1 atm a été effectuée. Un ensemble de fonctions d'énergie de Gibbs auto-cohérentes des phases d'oxydes pour le système Al–Fe–O a été dérivé. La description des données de propriétés thermodynamiques et de relations de phases a été obtenue. Les paramètres des modèles optimisés pour les phases d'oxydes reproduisent toutes les données disponibles dans les limites de l'erreur expérimentale.

Système Al–Ni–O (CHAPTER 9)

Certains écarts dans les données de la littérature pour la section $Al_2O_3–NiO$ du système Al–Ni–O ont été mis en évidence. Pour aider à résoudre les conflits existant dans la littérature, une nouvelle étude expérimentale a été réalisée dans ce travail. La technique expérimentale améliorée inclut un équilibrage et une trempe ultra rapide suivie d'une microanalyse aux rayons X à l'aide d'une sonde électronique (EPMA) des échantillons trempés. La section $Al_2O_3–NiO$ du

diagramme de phases Al–Ni–O a été mesurée à 1500 et 1600 °C dans l'air. La solubilité de Al_2O_3 dans $NiAl_2O_4$ ainsi que les solubilités mutuelles de α-Al_2O_3 et NiO ont été mesurées. Ces mesures expérimentales ont fourni des données supplémentaires pour la modélisation thermodynamique ultérieure.

Une optimisation simultanée de toutes les données disponibles dans le système Al–Ni–O à une pression totale de 1 atm a été réalisée. Les nouvelles données expérimentales et les résultats expérimentaux publiés antérieurement ont été pris en considération. La meilleure description possible des données de propriétés thermodynamiques et de relations de phases a été obtenue. Les paramètres des modèles optimisés pour les phases d'oxydes reproduisent toutes les données disponibles dans les limites de l'erreur expérimentale. Un ensemble de fonctions d'énergie de Gibbs auto-cohérentes des phases d'oxydes dans le système Al–Ni–O a été dérivé.

Système Fe–Ni–O (CHAPTER 10)

Certains écarts dans les données de la littérature pour le système Fe–Ni–O ont été mis en évidence. Pour aider à résoudre les conflits existant dans la littérature, une nouvelle étude expérimentale a été réalisée dans ce travail. Les compositions de wüstite / alliage et spinelle / alliage à l'équilibre ont été mesurées à 1200 °C à des pressions partielles d'oxygène $\log_{10}[P(O_2), \text{atm}] = -9$ et -10. La technique expérimentale améliorée a inclus une microanalyse aux rayons X à l'aide d'une sonde électronique (EPMA). Ces mesures expérimentales ont fourni des données supplémentaires pour la modélisation thermodynamique ultérieure.

Une optimisation simultanée de toutes les données disponibles dans le système Fe–Ni–O à une pression totale de 1 atm a été effectuée. Les nouvelles données expérimentales et les résultats expérimentaux publiés antérieurement ont été pris en considération. La meilleure description possible des données de propriétés thermodynamiques et de relations de phases a été obtenue. Les paramètres des modèles optimisés pour les phases d'oxydes reproduisent toutes les données disponibles dans les limites de l'erreur expérimentale. Un ensemble de fonctions d'énergie de Gibbs auto-cohérentes des phases d'oxydes du système Fe–Ni–O a été dérivé.

Systèmes Al–Fe–Ni–O, Al–Mg–Ni–O et Fe–Mg–Ni–O (CHAPTER 11)

La base de données thermodynamiques, combinée aux bases de données obtenues antérieurement pour les systèmes Fe–Ni–O, Al–Ni–O, et Mg–Ni–O, s'est avérée être capable de prédire les

propriétés thermodynamiques et les équilibres de phases dans les systèmes chimiques Al–Fe–Ni–O, Al–Mg–Ni–O et Fe–Mg–Ni–O. Les données expérimentales disponibles sont en bon accord avec les prédictions du modèle. L'unique paramètre du modèle optimisé pour la phase liquide reproduit les données de liquidus disponibles pour le système Al–Fe–Ni–O dans les limites de l'erreur expérimentale.

Systèmes Al–Ni–O–Si et Fe–Ni–O–Si (CHAPTER 12)

Nous avons effectué une optimisation simultanée de toutes les données disponibles sur une large gamme de températures et de pressions partielles d'oxygène (de l'air jusqu'à la saturation en métal) dans les systèmes Al–Ni–O–Si et Fe–Ni–O–Si à une pression totale de 1 atm. Les équations de modèles optimisées pour les propriétés thermodynamiques de toutes les phases reproduisent toutes les données disponibles sur la thermodynamique et les équilibres de phases dans les limites de l'erreur expérimentale.

Système Fe–Mg–Ni–O–Si (CHAPTER 13)

En utilisant l'ensemble des paramètres de modèles optimisés, les prédictions des équilibres de phases dans le système Fe–Mg–Ni–O–Si ont été faites et les paramètres des modèles ont été vérifiés à partir des données disponibles dans la littérature.

Systèmes Ca–Fe–Ni–O et Ca–Fe–Ni–O–Si (CHAPTER 14)

En utilisant l'ensemble des paramètres de modèles optimisés, les prédictions des équilibres de phases dans les systèmes Ca–Fe–Ni–O et Ca–Fe–Ni–O–Si ont été faites et les paramètres des modèles ont été vérifiés à partir des données disponibles dans la littérature.

La base de données actuelle a été incorporée dans les bases de données existantes de FactSage. Ainsi, la gamme d'applications des bases de données de FactSage a été élargie et les bases de données existantes ont été mises à jour pour décrire les données expérimentales d'intérêt industriel les plus récentes et les plus précises.

La base de données obtenue couplée à un logiciel de minimisation de l'énergie de Gibbs permet de prédire les équilibres de phases de liquidus et de solidus ainsi que certaines propriétés thermodynamiques dans les conditions (gamme de compositions, de températures et de pressions partielles d'oxygène) les plus utiles pour les opérations métallurgiques.

En ce qui concerne les travaux futurs, Cr et Co pourraient être ajoutés dans la base de données ; Cr étant l'un des principaux composants des minerais latéritiques et Co étant l'une des principales impuretés dans le produit final de la transformation de ces minerais. De plus, la base de données pourrait être étendue pour inclure les sulfures afin de pouvoir calculer les équilibres matte/laitier/metal.

TABLE OF CONTENTS

LIST OF TABLES

LIST OF FIGURES

LIST OF SYMBOLS AND ABBREVIATIONS

LIST OF SYMBOLS

A	optimized proto-pyroxene model parameter
A^{2+}	divalent cation
a, b, c and d_n	n coefficients
B	optimized proto-pyroxene model parameter
B^{3+}	trivalent cation
$C_P(T)$	heat capacity function
$F_{Al^{+3}V}$	model parameter for spinel
$F_{Fe^{+2}Al^{+3}}$	1/7 part of Gibbs energy of hypothetical normal spinel $FeAl_2O_4$
$F_{Fe^{+2}Fe^{+3}}$	1/7 part of Gibbs energy of hypothetical normal spinel Fe_3O_4
$F_{Ni^{+2}Al^{+3}}$	1/7 part of Gibbs energy of hypothetical normal spinel $NiAl_2O_4$
$F_{Ni^{+2}Fe^{+3}}$	1/7 part of Gibbs energy of hypothetical normal spinel $NiFe_2O_4$
G	total Gibbs energy
G_m	molar Gibbs energy
G^o	weighted sum of the standard Gibbs energies of all components
G_1^o, G_2^o	Gibbs energies of pure components 1 and 2
G_A^o	standard Gibbs energies of component A
$G^o_{AlO_{1.5}}$	standard Gibbs energy of $AlO_{1.5}$ component of monoxide solution
$G_{[Al^{+3}Al_2^{+3}O_4]^{+1}}$	Gibbs energy of the $\left[Al^{+3}Al_2^{+3}O_4\right]^{+1}$ spinel end-member

$G_{[Al^{+3}Fe_2^{+2}O_4]^{-1}}$ Gibbs energy of $\left[Al^{+3}Fe_2^{+2}O_4\right]^{-1}$ spinel end-member

$G_{[Al^{+3}Fe_2^{+3}O_4]^{+1}}$ Gibbs energy of $\left[Al^{+3}Fe_2^{+3}O_4\right]^{+1}$ spinel end-member

$G_{[Al^{+3}Ni_2^{+2}O_4]^{-1}}$ Gibbs energy of $\left[Al^{+3}Ni_2^{+2}O_4\right]^{-1}$ spinel end-member

$G_{[Al^{+3}Va_2O_4]^{-5}}$ Gibbs energy of $\left[Al^{+3}Va_2O_4\right]^{-5}$ spinel end-member

G_B^0 standard Gibbs energies of component *B*

G_{CaMg} Gibbs energy of $\left(Ca^{2+}\right)^{M2}\left(Mg^{2+}\right)^{M1}SiO_4$ olivine (or $\left(Ca^{2+}\right)^{M2}\left(Mg^{2+}\right)^{M1}Si_2O_6$ pyroxene) end-member

G_{CaNi} Gibbs energy of $\left(Ca^{2+}\right)^{M2}\left(Ni^{2+}\right)^{M1}SiO_4$ olivine (or $\left(Ca^{2+}\right)^{M2}\left(Ni^{2+}\right)^{M1}Si_2O_6$ pyroxene) end-member

G^E excess Gibbs energy

G_{12}^E excess Gibbs energy

$G_{Fe^{+2}Al_2^{+3}O_4}$ Gibbs energy of hypothetical normal spinel $Fe^{+2}Al_2^{+3}O_4$

$G_{[Fe^{+3}Al_2^{+3}O_4]^{+1}}$ Gibbs energy of $\left[Fe^{+3}Al_2^{+3}O_4\right]^{+1}$ spinel end-member

$G_{[Fe^{+3}Ca_2^{+2}O_4]^{-1}}$ Gibbs energy of $\left[Fe^{+3}Ca_2^{+2}O_4\right]^{-1}$ spinel end-member

G_{FeFe} Gibbs energy of $\left(Fe^{2+}\right)^{M2}\left(Fe^{2+}\right)^{M1}SiO_4$ olivine end-member

$G_{[Fe^{+2}Fe_2^{+2}O_4]^{-2}}$ Gibbs energy of $\left[Fe^{+2}Fe_2^{+2}O_4\right]^{-2}$ spinel end-member

$G_{Fe^{+2}Fe_2^{+3}O_4}$ Gibbs energy of $Fe^{+2}Fe_2^{+3}O_4$ spinel end-member

$G_{[Fe^{+3}Fe_2^{+3}O_4]^{+1}}$ Gibbs energy of $\left[Fe^{+3}Fe_2^{+3}O_4\right]^{+1}$ spinel end-member

$G_{[Fe^{+3}Fe_2^{+2}O_4]^{-1}}$ Gibbs energy of $\left[Fe^{+3}Fe_2^{+2}O_4\right]^{-1}$ spinel end-member

G_{FeNi} Gibbs energy of $\left(Fe^{2+}\right)^{M2}\left(Ni^{2+}\right)^{M1}SiO_4$ olivine end-member

$G_{[Fe^{+2}Ni_2^{+2}O_4]^{-2}}$ Gibbs energy of $\left[Fe^{+2}Ni_2^{+2}O_4\right]^{-2}$ spinel end-member

$G_{[Fe^{+3}Ni_2^{+2}O_4]^{-1}}$ Gibbs energy of $\left[Fe^{+3}Ni_2^{+2}O_4\right]^{-1}$ spinel end-member

G^{o}_{FeO} standard Gibbs energy of FeO component of monoxide solution

$G^{o}_{FeO_{1.5}}$ standard Gibbs energy of $FeO_{1.5}$ component of monoxide solution

$G_{[Fe^{+3}Va_2O_4]^{-5}}$ Gibb energy of $\left[Fe^{+3}Va_2O_4\right]^{-5}$ spinel end-member

$G_{[Fe^{+2}Va_2O_4]^{-6}}$ Gibb energy of $\left[Fe^{+2}Va_2O_4\right]^{-6}$ spinel end-member

G_i Gibbs energy of phase *i*

G_i^{o} standard Gibbs energies of component *i*

G^{ideal} contribution to Gibbs energy of entropy of mixing of ideal solution

G_{ij} in Compound Energy Formalism, Gibbs energy of end-member *ij* of the solution in which the M2 sublattice is occupied only by cation *i* and the M1 sublattice is occupied only by cation *j*

G_m^E excess Gibbs energy

G_{MgMg} Gibbs energy of $\left(Mg^{2+}\right)^{M2}\left(Mg^{2+}\right)^{M1}SiO_4$ olivine (or $\left(Mg^{2+}\right)^{M2}\left(Mg^{2+}\right)^{M1}Si_2O_6$ pyroxene) end-member

G_{MgNi} Gibbs energy of $\left(Mg^{2+}\right)^{M2}\left(Ni^{2+}\right)^{M1}SiO_4$ olivine (or $\left(Mg^{2+}\right)^{M2}\left(Ni^{2+}\right)^{M1}Si_2O_6$ pyroxene) end-member

g^{o}_{MO} standard Gibbs energy of MO

$G_m(T_c, \beta_0, T, X)$ magnetic contribution of the Curie or Néel temperature T_c and the average magnetic moment per atom β_0

$G_{Ni^{+2}Al_2^{+3}O_4}$ Gibbs energy of hypothetical normal spinel $Ni^{+2}Al_2^{+3}O_4$

G_{NiCa} Gibbs energy of $\left(Ni^{2+}\right)^{M2}\left(Ca^{2+}\right)^{M1}SiO_4$ olivine (or $\left(Ni^{2+}\right)^{M2}\left(Ca^{2+}\right)^{M1}Si_2O_6$ pyroxene) end-member

$G_{[Ni^{+2}Ca_2^{2+}O_4]^{-2}}$ Gibbs energy of $\left[Ni^{+2}Ca_2^{+2}O_4\right]^{-2}$ spinel end-member

G_{NiFe} Gibbs energy of $\left(Ni^{2+}\right)^{M2}\left(Fe^{2+}\right)^{M1}SiO_4$ olivine end-member

$G_{[Ni^{+2}Fe_2^{+2}O_4]^{-2}}$ Gibbs energy of $\left[Ni^{+2}Fe_2^{+2}O_4\right]^{-2}$ spinel end-member

$G_{Ni^{+2}Fe_2^{+3}O_4}$ Gibbs energy of hypothetical normal spinel $Ni^{+2}Fe_2^{+3}O_4$

G_{NiMg} Gibbs energy of $\left(Ni^{2+}\right)^{M2}\left(Mg^{2+}\right)^{M1}SiO_4$ olivine (or $\left(Ni^{2+}\right)^{M2}\left(Mg^{2+}\right)^{M1}Si_2O_6$ pyroxene) end-member

G_{NiNi} Gibbs energy of $\left(Ni^{2+}\right)^{M2}\left(Ni^{2+}\right)^{M1}SiO_4$ olivine (or $\left(Ni^{2+}\right)^{M2}\left(Ni^{2+}\right)^{M1}Si_2O_6$ pyroxene) end-member

$G_{[Ni^{+2}Ni_2^{+2}O_4]^{-2}}$ Gibbs energy of $\left[Ni^{+2}Ni_2^{+2}O_4\right]^{-2}$ spinel end-member

$G(Ni_2SiO_4, olivine)$ Gibbs energy of Ni_2SiO_4 with olivine structure

$G_{[Ni^{+2}Va_2O_4]^{-6}}$ Gibbs energy of $\left[Ni^{+2}Va_2O_4\right]^{-6}$ spinel end-member

$G_P(p, T, X)$ contribution to Gibbs energy of pressure p

$g^{o}_{SiO_2}$ standard Gibbs energy of SiO_2

$G(SiO_2, tridymite)$ Gibbs energy of tridymite

$G_T(T, X)$ contribution to Gibbs energy by temperature T and composition

$G°(\gamma\text{-}Al_2O_3)$ Gibbs energy of $\gamma\text{-}Al_2O_3$

i inversion parameter i

$I_{Fe^{+2}Al^{+3}}$ degree of inversion of real simple spinel $FeAl_2O_4$

$I_{Fe^{+2}Fe^{+3}}$ degree of inversion of real simple spinel Fe_3O_4 spinel

$I_{Ni^{+2}Al^{+3}}$ degree of inversion of real simple spinel $NiAl_2O_4$

$I_{Ni^{+2}Fe^{+3}}$ degree of inversion of real simple spinel $NiFe_2O_4$

K equilibrium constant

K_{CaNi} change in Gibbs energy when Ca^{2+} and Ni^{2+} cations occupying M2 and M1 sites of olivine or pyroxene structure change places

K_{FeNi} change in Gibbs energy when Fe^{2+} and Ni^{2+} cations occupying M2 and M1 sites of olivine structure change places

K_{MgNi} change in Gibbs energy when Mg^{2+} and Ni^{2+} cations occupying M2 and M1 sites of olivine or pyroxene structure change places

${}^iL$ coefficients of excess Gibbs energy

$L_{ij:k}$, $L_{k:ij}$ interaction energies between cations *i* and *j* on the one sublattice when the other sublattice is occupied by *k*.

L_{ij}^{mn} and L_{ijk}^{lmn} interaction parameters, which can be temperature dependent; and the powers *l*, *m*, and *n* are ≥ 0

Log_{10} common logarithm

M^{2+} divalent metal

$M_{Al^{+3}:Fe^{+3}Al^{+3}}$, $M_{Fe^{+2}:Fe^{+3}Al^{+3}}$, $M_{Fe^{+3}:Fe^{+3}Al^{+3}}$, $M_{Al^{+3}:Al^{+3}Ni^{2+}}$, $M_{Ni^{+2}:Al^{+3}Ni^{2+}}$, etc. interaction energies in the spinel solution

mol %	mole per cent
n_i	number of moles of phase *i*
n_m	number of moles of component *m*
n_{MM} , n_{SiSi} and n_{MSi}	number of moles of MM, SiSi and MSi pairs
n_M , n_{Si}	number of moles of components M and Si
n_{MO} , n_{SiO_2}	number of moles of *MO* and *SiO2*
n'_{MO} , n'_{SiO_2}	number of moles of unassociated MO and SiO_2
n_{MSiO_3}	number of moles of associates
O	octahedral sublattice
p	structural constant
$P(O_2)$	partial pressure of oxygen
q_{i12}^{ij}	model parameters of excess Gibbs energy expression
q_{mn}^{ij}	empirical binary coefficient of (m-n) pair exchange reaction
$q_{mn(p)}$	ternary terms, which give the effect of the presence of component *p* upon the energy of pair exchange reaction Δg_{mn}
q_{MSi}	coefficient of Gibbs energy of reaction of formation of associate $MSiO_3$
R	gas constant
$r_{Ca^{2+}}$	cationic radius of Ca^{2+}
$r_{Mg^{2+}}$	cationic radius of Mg^{2+}
$r_{Ni^{2+}}$	cationic radius of Ni^{2+}

$S^{o}_{298.15}$	entropy of compound at 1 atm and 298.15 K
S_c	configurational entropy assuming random mixing on each sublattice
T	temperature
T	tetrahedral sublattice
T_C	critical temperature for magnetic ordering (Curie or Néel temperature)
Va	vacancy
$V_{Fe^{+3}}$	parameter of CEF, which describes the formation of vacancies in Fe_3O_4 spinel
wt.%	weight per cent
X_1, X_2	mole fractions of components 1 and 2
X_A, X_B	mole fractions of components *A* and *B*
$X_{AlO_{1.5}}$	mole fraction of $AlO_{1.5}$ component of monoxide solution
X_{FeO}	mole fraction of FeO component of monoxide solution
$X_{FeO_{1.5}}$	mole fraction of $FeO_{1.5}$ component of monoxide solution
X_i	mole fraction of the component *i*
X_{MM}, X_{SiSi} and X_{MSi}	pair fractions of MM, SiSi and MSi
X_M, X_{Si}	mole fractions of components *M* and *Si*
X_{MO}, X_{SiO_2}	mole fractions of *MO* and SiO_2
X'_{MO}, X'_{SiO_2}, X_{MSi}	mole fractions of unassociated *MO* and SiO_2 and associates
Y_A, Y_B	"coordination-equivalent" fractions of *A* and *B*
Y_M, Y_{Si}	"coordination-equivalent" fractions of *M* and *Si*

Y_i^{M2}, Y_j^{M1} site fractions of the constituents *i* and *j* on the M2 and M1 sublattices, respectively

Y_m "coordination-equivalent" fraction of the component *m*

Y_{MO}, Y_{SiO_2} "coordination-equivalent" fractions of *MO* and SiO_2

Y_n "coordination-equivalent" fraction of the component *n*

Z_m coordination number of the component *m*

Z_M, Z_{Si} second-nearest-neighbor coordination numbers of *M* and *Si*

β average magnetic moment per atom

$\Delta_{Al^{+3}Ni^{+2}Va}$ Compound Energy Formalism model parameter for spinel, which describes the formation of vacancies in Al-Ni spinel

$\Delta_{CaNi:MgMg}$ Gibbs energy of reaction among end-members of Ca-Mg-Ni pyroxene solution

$\Delta_{CaNi:NiCa}$ Gibbs energy of reciprocal reaction among end-members of Ca-Ni olivine or pyroxene solution

$\Delta_{CaNi:NiMg}$ Gibbs energy of reaction among end-members of Ca-Mg-Ni pyroxene solution

$\Delta_{Fe^{+2}Al^{+3}}$ Compound Energy Formalism model parameter for spinel, which describes the thermodynamic properties of real simple spinel $FeAl_2O_4$

$\Delta_{Fe^{+3}Al^{+3}}$ Compound Energy Formalism model parameter for spinel, which describes the thermodynamic properties of real simple spinel $FeAl_2O_4$

$\Delta_{Fe^{+2}Fe^{+3}}$ Compound Energy Formalism model parameter for spinel, which describes the thermodynamic properties of real simple spinel Fe_3O_4

$\Delta_{Fe^{+2}Fe^{+3}Al^{+3}}$ Compound Energy Formalism model parameter for spinel, which reproduces the thermodynamic properties of solution between Fe_3O_4 and $FeAl_2O_4$

$\Delta_{Fe^{+3}Fe^{+2}Va}$ Compound Energy Formalism model parameter, which describes the formation of vacancies of spinel in the Fe-O system

$\Delta_{Fe^{+2}Ni^{+2}Fe^{+3}}$ Compound Energy Formalism model parameter for spinel, which reproduces the thermodynamic properties of solution between Fe_3O_4 and $NiFe_2O_4$

$\Delta_{FeNi:NiFe}$ Gibbs energy of reaction among end-members of Fe-Ni olivine solution

$\Delta_{Fe^{+3}Ni^{+2}Ca^{+2}}$ Compound Energy Formalism model parameter for spinel, which reproduces Ca solubility in Fe-Ni spinel

ΔH_{melt} enthalpy of melting

Δg_{AB} Gibbs energy of reaction of formation of AB

$\Delta g_{Al,Fe}$ parameter of the Modified Quasichemical Model, which is the Gibbs energy of the corresponding pair exchange reaction: $(\text{Al-Al}) + (\text{Fe-Fe}) = 2(\text{Al-Fe})$

$\Delta g_{Al,Ni}$ parameter of the Modified Quasichemical Model, which is the Gibbs energy of the pair exchange reaction $(\text{Al-Al}) + (\text{Ni-Ni}) = 2(\text{Al-Ni})$

$\Delta g_{Ca,Ni}$ parameter of the Modified Quasichemical Model, which is the Gibbs energy of the pair exchange reaction $(\text{Ca-Ca}) + (\text{Ni-Ni}) = 2(\text{Ca-Ni})$

ΔG^{ex} excess Gibbs energy of mixing

$\Delta g_{Fe,Ni}$ parameter of the Modified Quasichemical Model, which is the Gibbs energy of the pair exchange reaction $(\text{Fe-Fe}) + (\text{Ni-Ni}) = 2(\text{Fe-Ni})$

$\Delta g_{Mg,Ni}$ parameter of the Modified Quasichemical Model, which is the Gibbs energy of the pair exchange reaction $(\text{Mg-Mg}) + (\text{Ni-Ni}) = 2(\text{Mg-Ni})$

Δg_{mn} Gibbs energy of (m-n) pair exchange reaction

Δg^{o}_{mn} empirical binary coefficient of (m-n) pair exchange reaction

Δg_{MSi} Gibbs energy of reaction of formation of associate $MSiO_3$

Δg^{o}_{MSi} standard Gibbs energy of reaction of formation of associate $MSiO_3$

$\Delta g_{\mathrm{Ni,Si}}$ parameter of the Modified Quasichemical Model, which is the Gibbs energy of the pair exchange reaction $\mathrm{(Ni\text{-}Ni) + (Si\text{-}Si) = 2(Ni\text{-}Si)}$

ΔH enthalpy

$\Delta H^{o}_{298.15}$ standard enthalpy of formation of compound at 1 atm and 298.15 K

$\Delta_{\mathrm{MgNi:NiMg}}$ Gibbs energy of reciprocal reaction among end-members of Mg-Ni olivine or proto-pyroxene solution

$\Delta_{\mathrm{Ni^{+2}Al^{+3}}}$ Compound Energy Formalism model parameter for spinel, which describes the thermodynamic properties of real simple spinel $NiAl_2O_4$

$\Delta_{\mathrm{Ni^{+2}Fe^{2+}Fe^{+3}}}$ Compound Energy Formalism model parameter for spinel, which reproduces the thermodynamic properties of a solution between Fe_3O_4 and $NiFe_2O_4$

ΔS^{config} configurational entropy

μ_n chemical potential of component *n*

LIST OF ABBREVIATIONS

AL Atmospheric Leaching

BNC Basic Nickel Carbonate

CALPHAD CALculation of PHAse Diagrams

CEF Compound Energy Formalism

Coru Corundum

Cpx Clino-pyroxene

Crist	Cristobalite
CRCT	Centre for Research in Computational Thermochemistry
DSC	Differential Scanning Calorimetry
EDS	Energy Dispersive Spectra
EMF	ElectroMotive Force
EPMA	Electron Probe x-ray MicroAnalysis
FNN	First-Nearest-Neighbour
Hem	Hematite
HL	Heap Leaching
HPAL	High-Pressure Acid Leaching
L	Liquid
Mono	Monoxide
MQM	Modified Quasichemical Model
Ppx	Proto-pyroxene
P-woll	Pseudo-wollastonite
PyroSearch	Pyrometallurgy Research Centre, Brisbane, Australia
Qz	Quartz
SEM	Scanning Electron Microscope
SGTE	Scientific Group Thermodata Europe
SNN	Second-Nearest-Neighbour
Sp	Spinel
SRO	Short-Range Ordering
Trid	Tridymite
XRD	X-Ray powder Diffraction analysis

Woll	Wollastonite
WDD	Wavelength Dispersive Detectors

INTRODUCTION

The present project deals with the development of a comprehensive thermodynamic database for simulation of nickel extraction from laterite ores. In fact, accurate modeling of an industrial process is a complex task since all kinds of transport phenomena, including various aspects of non-equilibrium fluid dynamics, should be considered. While thermodynamic databases serve to equilibrium state calculations and provide a thorough description of phase relations in various systems in a wide range of conditions, they also aim at being suitable for application to industrial process simulations. Taking into account the fact that the operating conditions of most smelters are not far from equilibrium [3], one can expect thermodynamic calculations to be rather accurate for being used in industrial practice.

In order to develop a self-consistent multi-component thermodynamic database for nickel extraction from laterite ores, a large scale research program was undertaken over the past several years, which naturally combined experimental investigation and computer-assisted thermodynamic modeling. Chemical systems relevant to nickel laterite ore processing were experimentally studied and optimized. The thermodynamic modeling part was performed using the FactSage thermochemical software and its databases [1] developed at the Centre for Research in Computational Thermochemistry, École Polytechnique de Montreal, Canada. The experimental program was carried out by our colleagues from the Pyrometallurgy Research Centre, Brisbane, Australia [2].

The experimental and thermodynamic modeling parts were closely integrated in order to enhance the effectiveness of the overall program in terms of quantity of the required experimental work and availability of specific data that are essential for thermodynamic modeling. This was achieved by applying thermodynamic assessments to identify priorities for experiments and planning experimental measurements to provide specific data for thermodynamic modeling. This approach increased the predictive ability of the applied thermodynamic models and enabled the characterization of phase relations over the wide range of compositions, temperatures and oxygen partial pressures of direct importance to metallurgical industries.

At present nickel metal is mostly extracted from high-grade sulphide ores; the rest is produced from low-grade laterite ores. The continued depletion of high grade nickel sulphide ores has led to greater efforts in recovering nickel from low-grade laterite ores, which are classified into two

groups: the high-magnesia ores (*saprolites or serpentines*) and the high-iron, low-magnesia hydroxides (*limonites*) [4]. Nickel is normally recovered from the high-magnesia ores by smelting under reducing conditions to produce ferronickel alloy, while *limonites* can be processed by selective reduction followed by leaching with an ammonia–ammonium carbonate solution [4]. General laterite processing technologies are discussed in detail in Section 1.1.

Rhamdhani *et al.* [5, 6] reported that the factors affecting the nickel recovery in the latter processes are quite complex. It was demonstrated that the chemical and physical characteristics of the ore played an important role in overall nickel recovery. Moreover, it was shown that thermodynamic factors also play a significant role and should be thoroughly studied for optimizing processing technologies.

The chemistry of laterite processing technologies can be presented by the Al–Ca–Cr–Fe–Mg–Ni–O–Si multi-component chemical system, where Fe, MgO, NiO and SiO_2 are the major components. Although S might be present in some processes for treating laterites ores, optimization of matte/slag/metal equilibria was out of the scope of the present study. Despite the importance of this multi-component chemical system, there is a lack of experimental information in its subsystems and phase relations are not well established, even in the lower-order systems. However, to optimize laterite ore processing metallurgy, accurate calculations of the distribution of nickel between various solid oxide phases and the metallic phase, or slag (liquid oxide) and metal, are essential. A thermodynamic database which correctly describes phase equilibria in this chemical system is important for improving Ni extraction, optimizing processing conditions (such as temperature, oxygen partial pressure), reducing operating costs and developing new environmentally-friendly and energy-efficient pyrometallurgical processes of Ni recovery from laterite ores.

In this study, the database for oxide systems of the Al–Ca–Fe–Mg–Ni–O–Si multi-component chemical system was created. This was accomplished by means of thermodynamic modeling which was combined with the experimental study of phase equilibria. The methodology of the research was the following. A preliminary thermodynamic modeling and critical assessment of all experimental data available in the literature were carried out to identify the areas where the model parameters could not be well constrained due to the shortage or contradiction of the experimental information. New experimental measurements were then planned over the composition and

temperature ranges where the experiments are most reliable and useful for thermodynamic modeling.

The experimental procedure developed by our colleagues from the Pyrometallurgy Research Centre, Australia [2] involved equilibration and ultra rapid quenching followed by accurate measurements of compositions of phases using electron probe X-ray microanalysis (EPMA) of quenched samples. Since the analysis took place after equilibration, the changes in composition during equilibration did not affect the accuracy of the results. Tie-lines between equilibrated phases were measured directly, providing essential data for subsequent thermodynamic modeling. The advantages of the applied experimental technique are highlighted in Section 3.2.4.

The obtained experimental data along with the previously published experimental results were used in a thermodynamic "optimization" of all oxide phases in 4 binary, 7 ternary, 5 quaternary and 2 quinary systems of the Al–Ca–Fe–Mg–Ni–O–Si multi-component chemical system. The results of optimizations are discussed in Sections 5.5, 6.5, 7.8, 8.4, 9.5, 10.4, 11.4, 12.3.2, 12.4.2, CHAPTER 13 and CHAPTER 14.

In a thermodynamic "optimization" of a system, all available thermodynamic and phase diagram data are evaluated simultaneously in order to obtain one set of model equations for the Gibbs energies of all phases as functions of temperature and composition. From these equations, all of the thermodynamic properties and the phase diagrams can be back-calculated. In this way, all the data are rendered self-consistent and consistent with thermodynamic principles. Thermodynamic property data, such as activity data, can aid in the evaluation of the phase diagram, and phase diagram measurements can be used to deduce thermodynamic properties. Discrepancies in the available data can often be resolved, and interpolations and extrapolations can be made in a thermodynamically correct manner. A small set of model parameters is obtained. This is ideal for computer storage and calculation of properties and phase diagrams. All calculations were carried out using the FactSage thermochemical software and databases [1].

The liquid oxide phase has been modeled by the Modified Quasichemical Model [7, 8], which takes into account the second-nearest neighbour short-range ordering of cations in the melt. Models developed for the spinel and pyroxene solid solutions were based on the Compound Energy Formalism [9], which takes into consideration the crystal structure and physical nature of each solution. Metallic, monoxide and corundum solutions have been described with a simple

Bragg-Williams model. The detailed description of models used in this study is presented in Section 4.5.

CHAPTER 1 OVERVIEW OF LATERITE ORES PROCESSING

Equation Chapter (Next) Section 1Increasing demand for stainless steels and other nickel alloys by growing economies is driving demand for nickel. As can be seen from Figure 1.1 and Figure 1.2 [10], Canada is one of the leading exporters of unwrought nickel, nickel mattes and other products of nickel metallurgy. Nickel basically occurs in two types of ores: magmatic sulphides and laterite ores. Laterite ores are found in two general regions and are referred to as wet or tropical laterites (from Cuba, Indonesia, New Caledonia, etc.) or dry laterites as found in Australia. Many years of exploitation led to depletion of sulphide ore bodies. Moreover, these ores are usually more expensive to mine due to their position at greater depths. However, worldwide, the majority of nickel is still produced from sulphide sources, although this is rapidly changing [11].

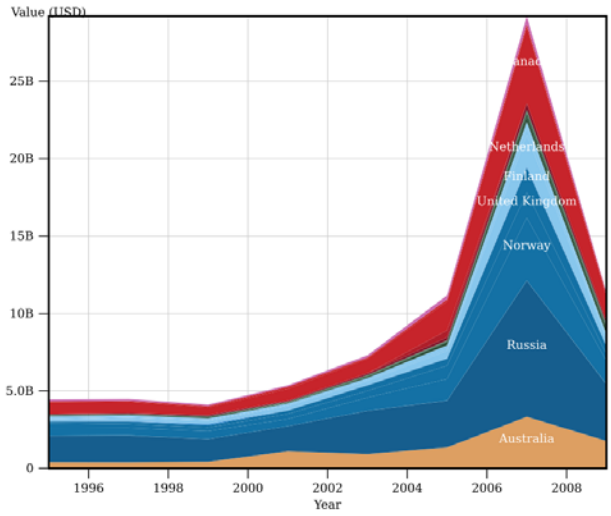

Figure 1.1 : World exporters of unwrought nickel [10]

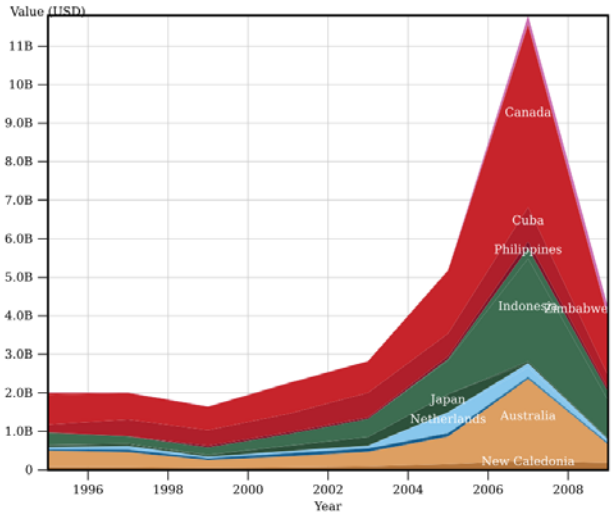

Figure 1.2 : World exporters of nickel mattes and other products of nickel metallurgy [10]

1.1 Laterite ore

Laterite ores are typically low grade deposits, averaging 1.5 to 2.5% Ni and 0.05 to 0.2% Co [12]. Provided that most of these deposits found usually in the tropics are close to the surface, mining is relatively low cost. On the other hand, because of their location, laterite ores contain a substantial amount of moisture.

Lateritic nickel deposits consist of heterogeneous mixtures of hydrated iron oxides and hydrous magnesium silicates [13]. The basis of the lateritic ore is olivine [$(Fe,Mg)_2SiO_4$]. This often contains small amounts of nickel due to the fact that the ionic radii of Fe^{2+}, Mg^{2+} and Ni^{2+} are very similar so that nickel can substitute either iron or magnesium in the olivine structure. Nickeliferous olivines are attacked and gradually dissolved by surface waters that have been made acidic by dissolved carbon dioxide and organic acids derived from decomposing vegetable matter. Iron is oxidized and is precipitated from solution near the surface as a hydrated iron oxide, goethite. Much of the cobalt and part of the dissolved nickel is co-precipitated with the iron in solid solution in the goethite lattice, resulting in an iron-rich, nickeliferous mineralization, which is usually described as *limonitic ore*. The remaining dissolved nickel, together with the magnesium and silica, is carried on down through the underlying basic rock. As it descends, the pH of ground water increases due to reactions with the bed rock and this causes the precipitation of hydrous nickel-magnesium silicates *(garnierites)*.

A typical lateritic nickel deposit can therefore usually be divided into three distinct zones, which occur at increasing depths from the surface [11, 13]:

1. ***Limonite zone***. This zone lies closest to the surface and consists primarily of *goethite*, α-**FeOOH**. Nickeliferous *limonite* is generally quite uniform in chemical and mineralogical composition and characteristically has a relatively low nickel content, poor crystallinity and very fine grain size.
2. ***Saprolite zone*.** At lower depths, just above the bed rock, lays the *saprolite* zone, which is mainly composed of *serpentines* or hydrous magnesium silicates $\mathbf{Mg_3Si_2O_5(OH)_4}$, with nickel replacing Mg to form hydrous magnesium silicates *garnierites* $\mathbf{(Mg, Ni)_3Si_2O_5(OH)_4}$. The *garnierite* zone usually contains ore with the highest concentrations of nickel, but it is extremely heterogeneous, both in chemical and mineralogical composition.
3. ***Transition zone*.** Between the limonitic and the garnieritic zones, a transition zone usually occurs, containing significant *garnierites* as well as some clays like *nontronite* $Na_{0.3}Fe_2(Si,Al)_4O_{10}(OH)_2 \cdot nH_2O$. The bulk of nickel is associated with the *nontronite*.

A profile of the variations in chemical composition of a typical nickel laterite deposit is shown in Figure 1.3 [11]. It is demonstrated by the figure that the average iron concentration steadily drops

with increasing depth, whereas the concentration of magnesium increases with depth. Nickel follows magnesium and silica and is found at highest concentrations in the *garnieritic zone*.

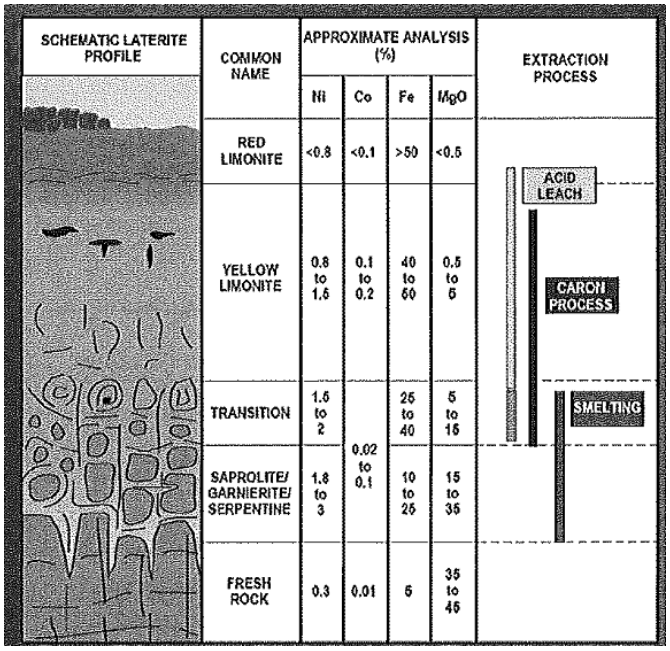

Figure 1.3: Typical tropical laterite profile, along with processing options [11]

The two principal types of the ore found in most laterite deposits, namely the iron-rich *limonitic ores* and the magnesium- and silica-rich *garnieritic ores* are so different mineralogically that, to date, each has been treated by different processes for the recovery of nickel [13]. The *garnieritic ores* are very heterogeneous in nature but are rich in nickel, containing up to 3% Ni, and conventionally these are treated by pyrometallurgical processes. Smelting to ferronickel in electric furnaces is a well known and proven technology. However, it requires high energy consumption and needs to be performed on a large scale to be cost-competitive [11]. The alternative is the production of nickel matte by mixing the ore with sulfur or pyrite and carrying out smelting.

The *limonitic ores*, on the other hand, are mineralogically very uniform, being composed principally of *goethite* [13]. They are too high in iron and too low in nickel to be economically smelted to ferronickel. They are instead treated by hydrometallurgical processes. A widely used process for treating limonitic ores is direct leaching of untreated limonitic ore with sulfuric acid at high temperatures and pressure (HPAL). HPAL is the process of choice for large scale developments; smaller scale developments are based on Atmospheric Leaching (AL) or Heap

Leaching (HL) technologies since these processes do not rely on autoclave technology and are therefore perceived to be less capital intensive and easier to operate [11]. HPAL has the advantage of high nickel recovery; however, it does suffer from significant waste disposal issues. Laterite ores low in magnesium and aluminum are amenable to acid leaching due to less acid consumption, however, ores high in iron and magnesium are best processed with ammonia-ammonium carbonate solutions (Caron process) [12]. Although the current study is concerned with the development of an extensive database appropriate for various ways of pyrometallurgical nickel production from laterite ores, the Caron process will be considered in detail since initially this study was performed in response to reduced nickel recovery from the ore at the BHP Billiton Yabulu refinery, where a modified Caron process is used.

1.2 Caron process

Developed in the 1940s, the Caron process is the oldest for processing *limonitic ores* [14]. The process, which utilizes atmospheric ammoniacal leaching of the pre-reduced ore, has two main advantages over the HPAL process: avoidance of high temperature and pressure and recycling of the leaching reagents. The process is applicable to high iron *limonitic laterite ores* or a mixture of *limonites* and *garnierites* and involves the following operations [13]:

1. ***Ore drying and grinding.*** The ore is first dried in direct-fire rotary kilns to about 2-3% moisture. Since the moisture content of the raw ore is usually in the range 30-50 wt. %, considerable energy is expended in the drying operation.

2. ***Reduction roasting.*** Reduction roasting is the most critical step in the process. The objective is to reduce selectively nickel and cobalt to the metallic state while minimizing the reduction of iron according to the reaction:

$$NiO + 2Fe_2O_3 + 3H_2 = FeNi + Fe_3O_4 + 3H_2O \tag{1.1}$$

   Nickel in *limonitic ores* is relatively loosely bonded to goethite (matrix of limonite composite) and is effectively reduced at ~700 °C. Efficient reduction of *garnieritic* nickel silicate is, however, more difficult since nickel and cobalt are locked in a silicate matrix and are difficult to reduce [15].

3. ***Leaching.*** The hot reduced ore leaving the roasters is first cooled to 150-200 °C under a reducing atmosphere and is then discharged into quench tanks containing ammoniacal ammonium carbonate leach solution. This solution, which is recycled from the leach residue washing circuit, contains about 6.5 wt.% NH_3, 3.5 wt.% CO_2, and 1 wt.% Ni. Leaching is carried out in a series of agitated tanks into which air is introduced in order to oxidize and dissolve the iron-nickel alloy. In spite of the high pH of the leach solution, which is about 10, hydrolysis of nickel and cobalt is prevented by their strong affinities for dissolved ammonia, which result in the formation of soluble nickel and cobalt complex ammine ions. Iron, on the other hand, although initially dissolving as ferrous ammine complexes, is rapidly oxidized to the ferric state, which hydrolyses and precipitates as ferric hydroxide, eventually leaving the process in the leach residues:

$$FeNi + O_2 + 8NH_3 + 2H_2O = Ni(NH_3)_6^{2+} + Fe(NH_3)_6^{2+} + 4OH^- \quad (1.2)$$

$$Fe(NH_3)_6^{2+} + O_2 + 8OH^- + 2H_2O = 4Fe(OH)_3 + 8NH_3 \quad (1.3)$$

   Following leaching, the pregnant leach liquor is separated from the undissolved barren solids by countercurrent decantation washing in a series of thickeners.

4. ***Metal recovery.*** The pregnant liquor is first filtered to remove suspended solids and then hydrogen sulphide gas or ammonium sulphide solution is mixed with the liquor to cause precipitation of cobalt sulphide. The cobalt-free solution then passes to the nickel precipitation stage. Ammonia is removed from solution by steam heating, causing precipitation of basic nickel carbonate (BNC), which is then roasted to recover CO_2. Ammonia and carbon dioxide are recovered for reuse in the leaching circuit by absorbing the gases in water and returning the ammonium carbonate solution to the countercurrent decantation washing circuit. Nickel metal is then obtained by various ways.

There are several advantages of the Caron-type processes [13]. First, there is almost no consumption of the leaching reagents, ammonia and carbon dioxide, in the process due to their recycling. In addition, the leaching reactions are selective for nickel and cobalt, with iron, the major component of the ore, remaining in the leach residue. However, the Caron process has not become a defining technology and there are only four Caron plants in operation [14]. The disadvantages of the process include increased energy requirements for drying and reduction

roasting, and reduced overall metal recovery, which is typically 75-80 % recovery of nickel and only 40-50 % recovery of cobalt [13]. Moreover, the process is mainly applicable to high iron *limonitic laterites*. The amount of silicate ore that can be accepted is limited due to losses of nickel caused by forsterite formation during roasting.

Although laterite ores due to their proximity to the surface are relatively attractive from the mining point of view, existing technologies that currently produce nickel worldwide utilize only about half of the nickel laterite deposits [16]. Other sources are not utilized due to complex mineralogy. So, the current laterite processing technologies require substantial modernization to make nickel extraction from laterite ores economically attractive.

1.3 Characterization of the ore from the BHP Billiton refinery

In order to understand factors which might help increase nickel recovery from the lateritic ores, several studies by Rhamdhani *et al.* [5, 6] were undertaken, which aimed at characterization of the lateritic ore at the BHP Billiton Yabulu refinery. These studies were performed in response to reduced nickel recovery from the ore at the refinery, where nickel and nickel oxide are produced from a mixture of *limonite and serpentine ores* (70 and 30 wt.%, respectively) through a modified Caron process. The process details are given as following.

Nickel lateritic ores are processed through reduction roasting in multiple hearth roasters to a maximum temperature of approximately 740^{o}C. The reducing conditions are achieved through partial combustion of fuel oil and supplementary hydrogen added to the hearths. Ammoniacal leaching is then performed. The resulting liquor is refined by solvent extraction and subsequently basic nickel carbonate (BNC) is precipitated to form an intermediate product. BNC is then partially reduced in a rotary kiln before final gaseous reduction to nickel metal compacts.

Rhamdhani *et al.* [5, 6] performed detailed microstructure and phase characterization of the processed nickel laterite ore using scanning electron microscope (SEM), electron probe X-ray microanalysis (EPMA) and synchrotron X-ray powder diffraction. EPMA was used to characterize the compositions of the phases in the ore feed (see results in Table 1.1), reduced ore and leached ore. The proportions of the phases were determined by estimating the area on the SEM micrographs.

Rhamdhani *et al.* [5, 6] found that the majority of the nickel in the ore feed is associated with fine-grained *goethite* (matrix of limonite composite), and in the *serpentine* particles; these phases transformed to magnetite and olivine, respectively, upon reduction roasting and partly to iron-nickel alloy. In the case of *serpentine*, it was not totally clear whether the process was limited by kinetics or equilibrium. However, in the case of the Fe-rich matrix, it appeared that the formation of iron-nickel alloy, which directly affected the nickel recovery upon leaching, from this mixture was limited by equilibrium. At the conditions of interest, all of the nickel extractable from the thermodynamic point of view was extracted from Fe-rich matrix. If thermodynamic approach is to be used, accurate reliable thermodynamic databases are indispensable. They can be effectively applied for improvement of existing industrial operations and searching novel approaches and processes with increased nickel recovery from laterite ores.

Table 1.1: Summary of major particle and phase average compositions, measured by EPMA, observed in the ore feed sample (wt.%)

	Approx. wt.% of total	**Particle**	**Phase Name**		**Approx. proportion in particles**	**MgO wt.%**	**SiO_2 wt.%**	**Fe_2O_3 wt.%**	**Al_2O_3 wt.%**	**NiO wt.%**
Limonite composite	60.0%	Limonite composite	Fe-rich matrix		70.0%	3.8	7.6	70.2	4.4	2.14
			Goethite (Fe.Ni)O(OH)		12.0%	0.6	2.2	79.6	3.9	1.42
			Magnetite $(Fe.Ni)O{\cdot}Fe_2O_3$		5.0%	0.4	0.8	91.4	3.4	0.47
			Chromite $(Fe,Mg)O{\cdot}(Cr, Al, Fe)_2O_3$		2.0%	9.8	0.1	21.3	17.7	0.08
			Serpentine $(Mg, Fe, Ni)_3Si_2O_5(OH)_4$		6.0%	27.5	32.9	22.6	1.1	2.26
			Olivine $(Mg,Fe,Ni)_2SiO_4$		1.0%	40.7	46.5	9.4	0.7	1.74
			Olivine-Serpentine Composite	Serpentine	1.0%	33.4	39.5	9.0	0.4	2.33
				Olivine	1.0%	43.2	47.4	5.5	1.3	1.64
			Quartz SiO_2		2.0%	0.2	97.8	1.6	0.1	0.07
Goethite	5.0%	Goethite	Goethite (Fe,Ni)O(OH)		100.0%	1.2	1.9	78.8	4.7	1.03

Table 1.1 (Continued): Summary of major particle and phase average compositions, measured by EPMA, observed in the ore feed sample (wt.%)

Spinel	2.0%	Magnetite	Magnetite $(Fe,Ni)O{\cdot}Fe_2O_3$	100.0%	0.3	0.8	90.9	3.6	0.34
	2.0%	Chromite	Chromite $(Fe,Mg)O{\cdot}(Cr,Al,Fe)_2O_3$	100.0%	9.1	0.1	26.1	13.3	0.09
Serpentine	24.0%	Serpentine	Serpentine $(Mg,Fe,Ni)_3Si_2O_5(OH)_4$	100.0%	32.1	39.6	10.0	2.2	2.65
	2.0%	Serpentine with magnetite inclusions	Serpentine $(Mg,Fe,Ni)_3Si_2O_5(OH)_4$	95.0%	35.8	39.4	9.2	0.5	1.68
			Magnetite $(Fe,Ni)O{\cdot}Fe_2O_3$	5.0%	1.1	1.4	92.8	1.7	0.41
Olivine	1.0%	Olivine	Olivine $(Mg,Fe,Ni)_2SiO_4$	100.0%	36.3	43.5	16.5	1.6	1.61
	1.0%	Olivine-serpentine composite	Serpentine $(Mg,Fe,Ni)_3Si_2O_5(OH)_4$	50.0%	34.3	42.9	6.8	0.1	2.65
			Olivine $(Mg,Fe,Ni)_2SiO_4$	50.0%	40.6	49.8	6.8	0.7	1.64
Quartz	3.0%	Quartz	Quartz SiO_2	100.0%	0.1	99.3	0.4	0.0	0.02

1.4 Goal of the present study

The current thesis was aimed at the development of a thermodynamic database to characterize NiO-containing oxide systems in the **Al_2O_3–CaO–FeO–Fe_2O_3–MgO–NiO–SiO_2** (Al–Ca–Fe–Mg–Ni–O–Si) multi-component system at high temperature of interest to nickel pyrometallurgical processes. All solid and liquid phases of 4 binary, 7 ternary, 5 quaternary and 2 quinary systems of the multi-component chemical system were optimized in the present study, using the FactSage thermochemical software and databases [1, 17].

The database development performed at the Centre for Research in Computational Thermochemistry, Montreal, Canada (CRCT) was carried out by means of thermodynamic modeling, which was closely related to experimental study of phase equilibria performed by our colleagues from the Pyrometallurgy Research Centre, Australia. This approach greatly increased

the effectiveness of the overall program by reducing the amount of the required experimental work and providing specific experimental data for thermodynamic modeling by applying thermodynamic assessments to identify priorities for experiments and planning experimental measurements to provide specific data for thermodynamic modeling. The methodology of the research is explained in detail in the next chapter.

CHAPTER 2 **METHODOLOGY**

Equation Chapter (Next) Section 1An overall research program applied in this thesis was basically a combination of experimental studies of phase equilibria and thermodynamic modeling, which were performed in an interactive way. This approach was successfully applied for chemical systems important to other industrial applications, including ferrous and non-ferrous smelting slags, coal ash fusion temperatures, ceramic systems, refractories and geological applications [18].

The methodology of the research involved a series of steps:

1. ***Literature review, critical assessment.*** First, a literature review and critical assessment of previously published thermodynamic and phase equilibrium data for the NiO-containing systems were performed using thermodynamic modeling. Available thermodynamic information on the individual components such as heat capacity, entropy, enthalpy, Gibbs energy, as well as phase equilibrium measurements, cation distribution, etc. were analyzed for their consistency and accuracy.

2. ***Initial model calculations.*** Parameters of models were obtained by optimization to fit the experimental data collected from the literature. The coefficients of the models were determined from the experimental data by a trial and error method.

3. ***Experimental investigation using Equilibration/quenching/EPMA technique (PyroSearch, Australia).*** For several lower-order subsystems, experimental data were missing in the literature because these systems are of no direct importance for practical applications. In case there was not enough data to constrain the model parameters, or significant discrepancies in the available data were revealed, a limited number of experimental measurements were planned for temperatures and compositions which were found to be most useful for thermodynamic modeling. The experimental investigation was carried out by our colleagues from the Pyrometallurgy Research Centre, Australia.

4. ***Thermodynamic optimization of lower-order systems.*** The new experimental data, in combination with the available literature data, were used to obtain the thermodynamic descriptions of the constituent lower-order systems. For each phase, a specific model was used which most adequately reflects the structure of the corresponding phase and the

model parameters were optimized. In this way, all the lower-order systems were optimized.

5. ***Prediction of phase relations in multicomponent systems.*** Thermodynamic properties of phases present in multicomponent systems were basically extrapolated from the parameters optimized in the lower-order systems, using the ability of the models to extrapolate in a thermodynamically correct manner.
6. ***Verification of models against available experimental data.*** The predictive ability of models was verified in regards to the experimentally studied multicomponent phase equilibria.

Using the above-described methodology, the amount of the work required to obtain an accurate thermodynamic description of a multicomponent system was significantly reduced.

CHAPTER 3 EXPERIMENTAL TECHNIQUE

3.1 General overview of experimental techniques in phase equilibria studies

Equation Chapter (Next) Section 1Experimental techniques used in phase equilibria studies can be divided into two major groups: dynamic and static methods. Dynamic techniques are based on measurement of property change which occurs as the system is undergoing phase transformation. The most widely used dynamic techniques are thermal, differential thermal (DTA) and thermogravimetric analyses (TGA). The common disadvantage of any dynamic type technique is the fact that the system is in a non-equilibrium condition. Metastability effects are common sources of inaccuracies, especially in systems with sluggish phase transformations. For this reason dynamic methods are not appropriate for the liquidus determination in the silica-containing systems and for most solid state phase equilibria studies.

Static methods are based on the in-situ measurement of a property or observation of a sample at an equilibrium state, for example high temperature X-ray diffraction, hot stage microscopy and solid electrolyte cell EMF measurement. There can be a variety of other methods based on the measurements of other properties of a system including electrical resistance, magnetic properties, etc.

An alternative to in-situ high-temperature investigations of phase equilibria is the quenching technique, which has advantages of the accuracy and convenience of measurements at room temperature of the phase equilibrium occurring at high temperatures [18]. The quenching technique involves the equilibration of the material at a specific temperature followed by rapid cooling. For systems where the phase assemblage which exists at high temperature can be preserved by rapid cooling to room temperature, the quenching technique is superior for phase equilibria studies. Solid solutions, solid state phase relations and liquidus phase equilibria, where liquids can be quenched to glass, can be investigated using quenching techniques.

3.2 Experimental technique (PyroSearch, Australia)

A new research methodology was developed by our colleagues from the Pyrometallurgy Research Centre (Australia), which takes advantage of improvements in the accuracy of EPMA with wave-length detectors and enables systematic study of phase relations in metallurgical systems [18, 19]. The experimental technique involves equilibration of samples at high temperatures, rapid quenching followed by measurement of phase compositions in the quenched samples using EPMA analysis. Each experiment provides information on both the liquidus composition and on the compositions of the solid phase formed, which greatly increases the productivity of the research. The technique was successfully applied for the investigation of various non-ferrous and ferrous slag systems.

The equilibration/quenching/EPMA experimental approach can be explained with reference to Figure 3.1 [20]. A small quantity of oxide mixture, with bulk composition X, is prepared from pure powders, pelletized, and equilibrated at temperature T_1 below the liquidus so that two phases (or more in higher order systems) are formed. The sample is cooled rapidly by drop quenching directly into water following equilibration. The result is that the phases present at temperature T_1 and their respective compositions are retained at room temperature. The compositions of the glass (liquid), point *a*, and solid phases, point *c*, are then measured using EPMA. So, EPMA measurement of glass and crystalline phase composition in the sample from only a single quench provides the liquidus and the solidus at that temperature. The same mixture can be used to obtain liquidus and solid solubility data sets at several other temperatures.

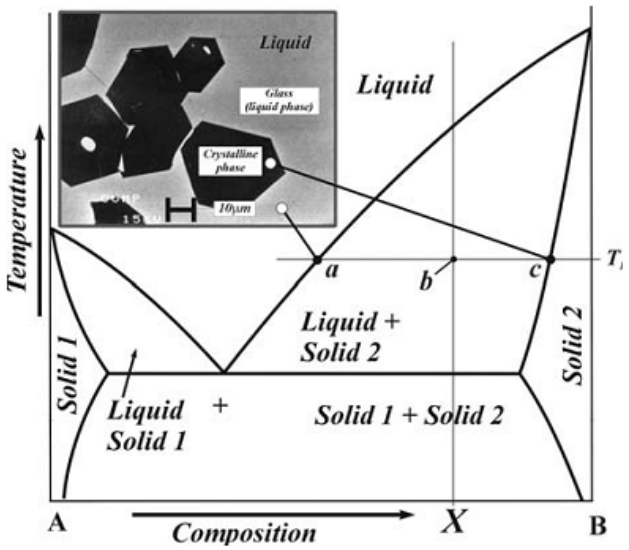

Figure 3.1: Schematic phase diagram illustrating use of the subsolidus equilibration technique [20]

3.2.1 Sample and crucible preparation

3.2.1.1 General sample and crucible preparation

The general sample and crucible preparation is demonstrated referring to the study [20]. Starting mixtures are prepared from pure oxides. The mixtures are accurately weighed and mixed in an agate mortar and pestle and then pelletized. The pellets are broken to the required shape and placed inside open platinum crucibles for insertion into the furnace. The platinum crucibles are folded. All crucibles are suspended by platinum wire within the furnaces. An illustration of the crucible design is shown in Figure 3.2.

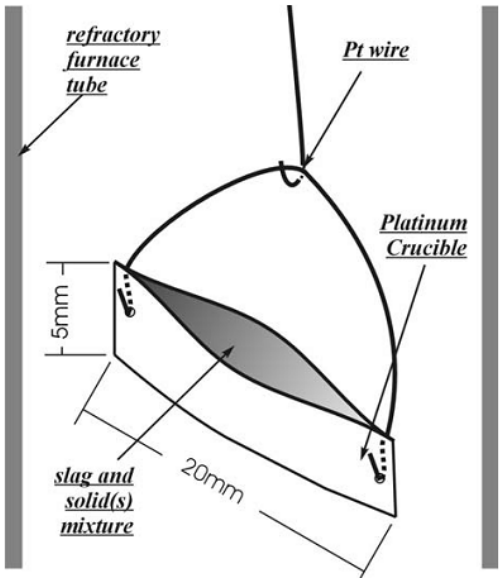

Figure 3.2 : Platinum crucible design and suspension [20]

3.2.1.2 Temperature and gas atmosphere control

The experiments are conducted in a vertical tube electrical resistance silicon carbide (SiC) heated furnaces (Figure 3.3) [20]. The furnace temperature is monitored with alumina shielded Pt/Pt-13 pct Rh thermocouple placed next to the samples with an overall temperature accuracy estimated to be ± 3 K. The atmosphere within these furnaces is held at a fixed oxygen partial pressure using either CO/CO_2 or H_2/CO_2 gas mixtures. Flow rates of gases to the furnace are controlled using glass capillary flow meters with the gas flowing from the bottom to the top of the furnace.

The oxygen partial pressures within the furnaces are verified with a DS-type oxygen probe, which measures electromotive force (EMF) between the furnace atmosphere and supplied reference air using a Y_2O_3-stabilized zirconia solid electrolyte cell. At oxygen partial pressures and temperatures of the present study, the accuracy of oxygen probe is defined at ± 0.1 log (pO_2) units.

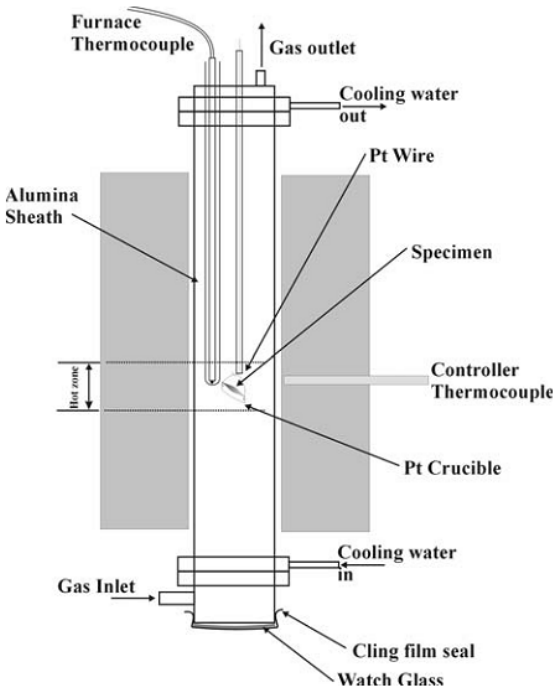

Figure 3.3: Furnace design used in equilibration experiments [20]

3.2.2 Equilibration

3.2.2.1 Phase equilibration procedure

Two methods of equilibration experiments can be used [21]:

a) Gas/oxide equilibrated in open systems at fixed oxygen partial pressure;
b) Oxide/alloy equilibrated in closed systems.

In the method (a) [20], the platinum crucibles holding specific oxide mixtures are first suspended by platinum wire in the cold zone at the base of the furnace. The base of the furnace is then covered with a borosilicate watch glass, which enables the samples to be viewed during equilibration, and finally sealed with polyethylene-wrap. The furnace is then flushed with argon gas for a period of 30 minutes, and then the relevant gas flow rates are established before the sample is raised into the hot zone of the furnace.

The samples are positioned adjacent to the Pt/Pt-13 pct Rh thermocouple in the furnace [22]. Sample weights are monitored before and after the experiments. Each experiment is carried out in 2 steps. The first step is to pre-melt a sample at temperatures higher than that of final

equilibration (1000 – 1400 ^{o}C) for half an hour to four hours depending on melt composition to ensure that the sample is homogeneous. The second step is to lower the furnace temperature and to equilibrate the sample at the desired final equilibration temperature. So, the crucibles, after being premelted, are air quenched (if applicable; otherwise, gas mixtures are appropriately adjusted to maintain the required oxygen partial pressure during cooling), weighed, equilibrated at predetermined final temperatures for times sufficient to achieve equilibrium (from a half an hour to few days) and then quenched into iced-water. On quenching, silica-containing liquid is readily retained as glass, so that the phase assemblage that exists at the equilibration temperature is frozen in the sample.

The temperatures and times for two-step equilibration are planned individually for each particular melt behavior. For instance, the peritectic reaction on cooling involves diffusion through solid, therefore, long times are required before the primary solid decomposes and the equilibrium phases are formed. To avoid this slow diffusion step through the solid phase, mixtures are heated during premelting to temperatures where they are completely liquid and then quenched to glass thus ensuring no primary phase precipitated. The low temperature equilibrium phase assemblage then crystallizes directly from metastable liquid. The opposite plan is used for melts having high viscosity and slow crystallization: premelting temperature is selected so as to leave some primary phase as heterogeneous nuclei.

In the method (b), the samples are placed in a closed-end 15-mm-diameter quartz tube [21]. The tube is then evacuated to approximately 0.001 atm using a rotary vacuum pump before sealing using an oxy-fuel torch. The sealed capsule is then suspended on a Pt wire in the furnace at the desired temperature to reach equilibrium.

3.2.2.2 Checking of equilibrium state

The achievement of equilibrium within the system can be directly tested by measuring compositional profiles across phases. Each reported phase composition is an average of a minimum of five to ten measurements within that phase, performed in various parts of the sample. At equilibrium each phase should have a uniform composition. If the composition of the glass phase is shown to vary with location within the sample, this indicates incomplete equilibration. The experiment is then repeated until this effect is eliminated. Attention is also given to the morphology, shape, and compositions of the solid crystallized phases: the presence

of crystals homogenous in composition, with well-developed facets, is taken as further indication of the attainment of equilibrium.

Attainment of equilibrium may be also checked by comparison of the samples equilibrated for different times. In this case, repeating experiments are conducted at extended equilibration times by doubling or tripling the equilibration times. The fact that no further change in composition occurs as the sintering time is increased indicates the achievement of equilibrium.

In order to confirm the achievement of equilibrium, the equilibration experiments can also be repeated starting from different phase compositions.

3.2.3 Sample examination

After final quenching samples are separated carefully from crucibles and mounted so that whole sections of melt from wall to wall and from top to bottom can be examined [22]. This enables any segregation of the phases during equilibration to be detected.

Microstructures are analyzed using optical as well as electron microscopy coupled with Energy Dispersive Spectra Analysis (EDS). Secondary and backscattered electron images and EDS are used for preliminary examination of the microstructures. EPMA measurements are carried out with a JEOL 8900L Electron Probe X-ray Microanalyser with wavelength dispersive detectors. An accelerating voltage of 15 KV and a probe current of 15 nAmps are used. The average accuracy of the EPMA measurements is within ± 1 per cent of element concentration in weight per cent. It is ensured by the appropriate selection standards. X-ray powder diffraction analysis (XRD) is used in some cases to confirm phase identification. The XRD measurements are carried out with a PHILIPS PW1130 X-ray diffractometer with a graphite monochromator using Cu K_{α} radiation.

It should be noted that the EPMA measurements provide information only on the total metal content in a given phase. This technique does not provide information on the proportion of cations of the same element with different valences, such as Fe^{2+} and Fe^{3+}.

3.2.4 Advantages

Major advantageous features of the equilibration/quenching/EPMA technique may be summarized as follows [18]:

1. The phase compositions are measured at the completion of the equilibration so that changes of bulk composition of samples during experiment that usually take place in high-temperature phase equilibria studies due to vaporization, reactions with containment material or reactions between phases do not affect the accuracy of final results.
2. Only a small sample size (down to 10-50 μm) is needed for EPMA measurements – this essential factor enables the use of small samples and therefore achievement of extremely rapid cooling rates within the liquid phase to be achieved (10^5-10^6 K/s), which is confirmed by the small grain size in the quenched sample using SEM micrographs.
3. The compositions of all phases in equilibrium are measured enabling for determination of not only liquid compositions, but, importantly, the compositions of solid solutions coexisting with these liquids.
4. The solid phases can be identified exactly from their compositions, accurately measured with EPMA.
5. The achievement of equilibrium within the system can be directly tested by measuring compositional profiles across phases; at equilibrium each phase should have a uniform composition.
6. The use of very small slag masses means that gas/slag equilibria are readily obtained.

CHAPTER 4 THERMODYNAMIC MODELING

4.1 Thermodynamic equilibrium modeling

Equation Chapter (Next) Section 1For the calculation of phase equilibria in a multicomponent system, it is necessary to minimize the total Gibbs energy, *G*, of all the phases that take part in this equilibrium [23]:

$$G = \sum_{i=1}^{p} n_i G_i = \text{minimum} \tag{4.1}$$

where n_i is the number of moles and G_i is the Gibbs energy of a phase *i*. A thermodynamic description of a system requires assignment of thermodynamic functions for each phase. The contributions to the Gibbs energy of a phase can be written:

$$G = G_T(T,X) + G_P(p,T,X) + G_m(T_c,\beta_o,T,X) \tag{4.2}$$

where $G_T(T,X)$ is the contribution to the Gibbs energy by the temperature T and the composition X, $G_P(p,T,X)$ is the contribution of the pressure p, and $G_m(T_c,\beta_o,T,X)$ is the magnetic contribution of the Curie or Néel temperature T_c and the average magnetic moment per atom β_o.

The temperature dependence of the concentration terms of G_T is usually expressed as a power series of T:

$$G = a + bT + cT\ln(T) + \sum d_n T^n \tag{4.3}$$

where a, b, c and d_n are *n* coefficients.

For multicomponent systems, it has proven useful to distinguish three contributions from the concentration dependence to the Gibbs energy of a phase:

$$G = G^{o} + G^{\text{ideal}} + \Delta G^{\text{ex}} \tag{4.4}$$

The first term G^{o} is simply the weighted sum of the unary standard Gibbs energies, the second G^{ideal} is the contribution to the Gibbs energy from the entropy of mixing of an ideal solution, and the third ΔG^{ex} is the excess Gibbs energy of mixing. The form of the excess Gibbs energy depends on the applied model.

Binary solution phases, such as liquid and disordered solid solutions, are often described as random mixtures of the components by a regular solution type model:

$$G = X_A G_A^o + X_B G_B^o + RT(X_A \ln X_A + X_B \ln X_B) + X_A X_B \sum_{i=0}^{n} {}^{i}L(X_A - X_B)^i \qquad (4.5)$$

where X_A and X_B are the mole fractions and G_A^o and G_B^o the standard Gibbs energies of components A and B, respectively, and ${}^{i}L$ are coefficients of the excess Gibbs energy. The sum of the terms $(X_A - X_B)^i$ is the so-called Redlich-Kister polynomial [24], which is the most commonly used polynomial in regular solution type descriptions.

From the condition that the Gibbs energy at thermodynamic equilibrium shows a minimum for given temperature, pressure and composition, Gibbs derived the well known equilibrium conditions where the chemical potential of each of n components, μ_n, is the same in all phases:

$$\mu_1' = \mu_1'' = ...;\ \mu_2' = \mu_2'' = ...;\ \mu_n' = \mu_n'' = ... \qquad (4.6)$$

This equation results in non-linear equations which can be used in numerical calculations.

4.2 CALPHAD method

In 1970 Kaufman and Bernstein [25] summarized the general features of the calculation of phase diagrams and listed computer programs for the calculation of binary and ternary phase diagrams, thus laying the foundation for the CALPHAD method (CALculation of PHAse Diagrams).

According to the CALPHAD method, the model description of a chemical system is obtained by combining available knowledge on the phase diagram and the thermodynamic properties of a system. Descriptions of lower-order systems are combined to make extrapolations to higher-order systems. For this purpose, the Gibbs energy of each phase is described by a suitable model containing a relatively small number of variable coefficients. These coefficients are optimized

using experimental information on phase equilibria such as melting temperatures, other transformation temperatures, solubilities and on thermodynamic properties such as heat capacities, enthalpies of formation, chemical potentials from EMF or pressure measurements.

4.3 Thermodynamic optimization

In this study, basics of CALPHAD modeling were employed in a thermodynamic optimization of chemical systems. All types of data, including thermodynamic and phase equilibria data, were evaluated simultaneously. As a result, one set of model equations for the Gibbs energies of all phases as functions of temperature and composition was obtained. The model equations along with Gibbs energy minimization software provide a self-consistent description of thermodynamic properties and phase diagrams. From these equations, all of the thermodynamic properties and the phase diagrams can be back-calculated. In this way, all the data are rendered self-consistent and consistent with thermodynamic principles. Thermodynamic property data, such as activity data, aid in the evaluation of the phase diagram, and phase diagram measurements can be used to deduce thermodynamic properties. Discrepancies in the available data can often be resolved, and interpolations and extrapolations can be made in a thermodynamically correct manner. Based on physically reasonable models, obtained set of parameters can give correct predictions of phase relations in multicomponent systems. A small set of model parameters is obtained. This is ideal for computer storage and calculation of properties and phase diagrams.

In this project, the FactSage thermochemical software served as Gibbs energy minimization software. FactSage was used in combination with its FactPS, FToxid and FSstel databases [1]. Even though the solubilities of minor elements in ferronickel are not well reproduced by the FSstel database, it was well suited for calculations of the present study, since it had no major effect on oxide phase equilibria.

4.4 FactSage software

FactSage™ package, which was introduced in 2001 [17] as a thermochemical software and database package, was developed jointly between Thermfact/CRCT (Montreal, Canada) and GTT-Technologies (Aachen, Germany). The package consists of a series of information, database, calculation and manipulation modules that enable to access and manipulate pure substances and solution databases. With the various models one can perform different

thermochemical calculations and generate tables, graphs and figures of interest to a wide variety of applications, such as chemical and physical metallurgy, chemical engineering, corrosion engineering, inorganic chemistry, ceramics, combustion, electrochemistry, geochemistry, environmental chemistry, etc.

FactSage is currently used worldwide as a research tool and educational aid at approximately 400 installations in universities, governmental and non-governmental research laboratories and industry [1]. The package is applied for the calculation of slag/solid/gas/matte/metal/salt equilibria in multicomponent systems of industrial interest. The main menu of FactSage incorporates various modules, which may be grouped into four categories [1, 17]:

1. ***Info*** is provided through the ***General*** module of the FactSage software, which incorporates presentations of all the modules as well as database documentation, information on the FactSage family of products and services, contact details, etc.

2. ***Databases.*** Compound and solution databases can be listed and manipulated through the ***Documentation, View Data***, ***Compound*** and ***Solution*** modules. The FactSage databases involve FactPS compound, solution (*FToxid, FTsalt, FTmisc, FThall, FTOxCN, FTfrtz, FThelg, FTpulp*) and alloy (*FScopp, FSlead, FSlite, FSstel, FSupsi, FSnobl*) databases as well as SGTE pure substances, intermetallic and solution databases. Other databases include aqueous databases and a thermodata nuclear database. These databases are the largest set of evaluated and optimized thermodynamic databases for inorganic systems in the world and have been under development for over 25 years. FactSage supports 11 different solution models including simple polynomial models (Redlich-Kister and Legendre polynomials) combined with different higher order extrapolations (Muggianu, Kohler, Toop), the Unified Interaction Parameter Model, Modified Quasichemical Models for short-range ordering in pair and quadruplet approximations, the Pitzer model (for concentrated aqueous solutions) and sublattice models such as the Compound Energy Formalism.

3. ***Calculate.*** It is possible to interact with the software and databases in a variety of ways and calculate and display thermochemical equilibria and phase diagrams in a multitude of formats through ***Reaction***, ***Predom***, ***EpH***, ***Equilib***, ***OptiSage*** and ***Phase Diagram*** modules. ***Viscosity*** module is available for oxide melts viscosity calculations.

4. ***Manipulate.*** It is possible to manipulate the results with the ***Results***, ***Mixtur***e, ***Figure*** and ***Fact-XML*** modules.

4.4.1 FToxid and FSstel databases

The current project was devoted to the expansion of the FToxid database of FactSage. The metallic solutions were described using the FSstel FactSage database.

FToxid is oxide database for slags, glasses, minerals, ceramics, refractories, etc. [1]. It contains data for stoichiometric oxides and oxide solutions of the following components: Al_2O_3, As_2O_3, B_2O_3, CaO, CoO, CrO, Cr_2O_3, Cu_2O, FeO, Fe_2O_3, GeO_2, K_2O, MgO, MnO, Na_2O, NiO, PbO, SiO_2, SnO, TiO_2, Ti_2O_3, ZnO, ZrO_2. Not all binary, ternary and higher-order sub-systems were evaluated and optimized, nor are all composition ranges covered. However, the system Al_2O_3-CaO-FeO-Fe_2O_3-MgO-SiO_2 was fully optimized from 25 °C to above the liquidus temperatures at all compositions and oxygen partial pressures. Components CoO, CrO, Cr_2O_3, Cu_2O, MnO, NiO, PbO, SnO, TiO_2, Ti_2O_3, ZnO and ZrO_2 were added to this core six-component system and the relevant subsystems were optimized over the composition ranges important for applications in ferrous and non-ferrous metallurgy, production of ceramics, refractories and paint pigments. B_2O_3, K_2O and Na_2O were added to the core six-component system for applications in the glass industry, combustion, coal gasification and waste management. The liquid/glass solution phase called FToxid-Slag includes all the oxide components mentioned above as well as dilute solutions of S, SO_4, PO_4, H_2O/OH, CO_3, F, Cl, I.

There are many oxide solid solutions in the database. Some of the most extensive solutions include:

1. **Spinel:** $(Al^{3+}, Co^{2+}, Co^{3+}, Cr^{2+}, Cr^{3+}, Fe^{2+}, Fe^{3+}, Mg^{2+}, Ni^{2+}, Zn^{2+})^{T}[Al^{3+}, Co^{2+}, Co^{3+}, Cr^{3+}, Fe^{2+}, Fe^{3+}, Mg^{2+}, Ni^{2+}, Zn^{2+}]_2{}^{O}O_4$;
2. **Pyroxene:** $(Ca^{2+}, Fe^{2+}, Mg)^{M2}\ (Al^{3+}, Fe^{2+}, Fe^{3+}, Mg^{2+})^{M1}(Al^{3+}, Fe^{3+}, Si)^{T1}Si^{T2}O_6$;
3. **Melilite:** $(Ca^{2+}, Pb^{2+})_2{}^{A}\ [Al^{3+}, Fe^{2+}, Fe^{3+}, Mg^{2+}, Zn^{2+}]^{T1}(Al^{3+}, Fe^{3+}, Si)_2{}^{T2}O_7$;
4. **Olivine:** $(Ca^{2+}, Co^{2+}, Fe^{2+}, Mg^{2+}, Mn^{2+}, Ni^{2+}, Zn^{2+})^{M2}\ [Ca^{2+}, Co^{2+}, Fe^{2+}, Mg^{2+}, Mn^{2+}, Ni^{2+}, Zn^{2+}]^{M1}SiO_4$.

FSstel is a steel database [1]. It contains data for 115 completely assessed binary alloy systems, 85 ternary and 17 quaternary systems that include the elements: Al, B, Bi, C, Ca, Ce, Co, Cr, Cu, Fe, La, Mg, Mn, Mo, N, O, Nb, Ni, P, Pb, S, Sb, Si, Sn, Ti, V, W, Zr. It provides a sound basis for calculations covering a wide range of steelmaking processes, e.g. reduction of oxygen and sulphur concentration levels through deoxidation and desulphurization of the melt; constitution of a wide range of steels, including austenitic, ferritic and duplex stainless steels and including carbide and nitride formation; conditions for heat treatment operations to produce a desired constitution; conditions for scrap remelting to maintain as low concentrations as possible of undesirable “tramp elements”; melt-crucible interactions, etc.

4.5 Thermodynamic phases and their modeling

The thermodynamic oxide solution phases present in the Al_2O_3–CaO–FeO–Fe_2O_3–MgO–**NiO**–SiO_2 (Al–Ca–Fe–Mg–Ni–O–Si) multi-component system include slag (molten oxide), monoxide (solid oxide), corundum, olivine, spinel and pyroxenes. They are shown in Table 4.1. Cations shown within a set of parentheses occupy the same sublattice.

Table 4.1: Stable oxide solutions present in the Al–Ca–Fe–Mg–Ni–O–Si multicomponent system at ambient pressure

Phase name	**Formula**	**Notation**
Slag	Al_2O_3–CaO–FeO–Fe_2O_3–MgO–NiO–SiO_2	L or Liquid
Monoxide	CaO–FeO–MgO–NiO–($FeO_{1.5}$–$AlO_{1.5}$)	Mono or Monoxide
Corundum	$AlO_{1.5}$–$FeO_{1.5}$–(NiO)	Coru or Corundum
Olivine	$(Ca^{2+}, Fe^{2+}, Mg^{2+}, Ni^{2+})^{M2}(Ca^{2+}, Fe^{2+}, Mg^{2+}, Ni^{2+})^{M1}SiO_4$	Olivine
Pyroxene	$(Ca^{2+}, Fe^{2+}, Mg^{2+}, Ni^{2+})^{M2}(Al^{3+}, Fe^{2+}, Fe^{3+}, Mg^{2+}, Ni^{2+})^{M1}(Al^{3+}, Fe^{3+}, Si)^{T1}Si^{T2}O_6$;	Ppx or Cpx
Spinel	$(Al^{3+}, Fe^{2+}, Fe^{3+}, Mg^{2+}, Ni^{2+})^{T}(Al^{3+}, Ca^{2+}, Fe^{2+}, Fe^{3+}, Mg^{2+}, Ni^{2+}, Va)_2^{O}O_4$*	Sp or Spinel

*T=tetrahedral sublattice, O=octahedral sublattice

The Modified Quasichemical Model [26, 27], which takes into account short-range ordering of second-nearest-neighbor cations in the ionic melt, was used for modeling the slag phase (molten oxide phase).

Monoxide solution was modeled as a simple random mixture of cations on cation sites with simple polynomial excess Gibbs energy terms [28]. The properties of the ternary, quaternary, etc. monoxide solution were calculated from the binary parameters using the symmetric "Kohler-like" or asymmetric "Toop-like" techniques, depending on the chemical system [28].

The models for olivine, spinel and pyroxene solutions were developed within the framework of the compound-energy formalism (CEF) [9].

4.5.1 Slag (liquid oxide) modeling

4.5.1.1 Slag structure

Slags and glasses are polymers in the form of chains, rings, etc., which are made up of SiO_4^{4-} tetrahedral units (see Figure 4.1). It is a solution of molten oxides, which include FeO, SiO_2 and other oxides (Al_2O_3, CaO, MgO, NiO) [29]. Silica SiO_2 and alumina Al_2O_3 form so-called acidic slags. When acidic oxides melt, they polymerize, forming long polyions. These polyions increase slag viscosity, making it difficult to work with. The acidic slag has low solubility for other acidic oxides (such as As_2O_3, Bi_2O_3, Sb_2O_3). This results in difficulty in metallurgical productions, because impurities which form acidic oxides will not be removed in slag and may remain in the metal and matte phases. Adding basic oxides, CaO or MgO, breaks the polyions into smaller structural units and lowers viscosity of the slag as well as the melting point of the slag.

In general, slags have the following characteristics [30]:

1. Each Si with a valence of 4 is surrounded tetrahedrally by four O^{2-} ions with a valence of 2 each connecting to two Si ions;
2. In silica, these SiO_4^{4-} polyhedra are connected in a three-dimensional polymerized structure (Figure 4.1) and the oxygens are predominantly bridging oxygens;
3. Cations such as Ca^{2+}, Mg^{2+}, etc., tend to break up the Si-O bonds and de-polymerize the melt by forming non-bridging oxygens and free oxygens i.e. oxygens not bound to Si at all but only to the cation;

4. Other cations such as Al^{3+}, P^{5+}, Ti^{4+} can fit into the Si polymeric chain but need to maintain charge balance e.g. if an Al^{3+} is incorporated into a Si^{4+} chain, it must have a Na^{+} (or one half of a Ca^{2+}) near the Al^{3+} to maintain local charge balance;
5. Smaller cations such as Mg^{2+} tend to give a wider distribution of chain lengths than larger cations such as Ba^{2+};
6. Cations such as Fe^{3+} in small concentrations can act as network breakers but in higher concentrations can be incorporated into the chain in a similar way to Al^{3+};
7. The degree of polymerization can be expressed in terms of the numbers of bridging, non-bridging and free oxygens;
8. The structure of melts (both slags and metals) can be represented using thermodynamic quantities (e.g. excess free energy) since thermodynamics provides a description of bond strengths;
9. Some metallurgical slags have a high basicity (e.g. $CaO/SiO_2>2$) and consequently the Si^{4+} ions are predominantly in the form of monomers i.e. completely de-polymerized.

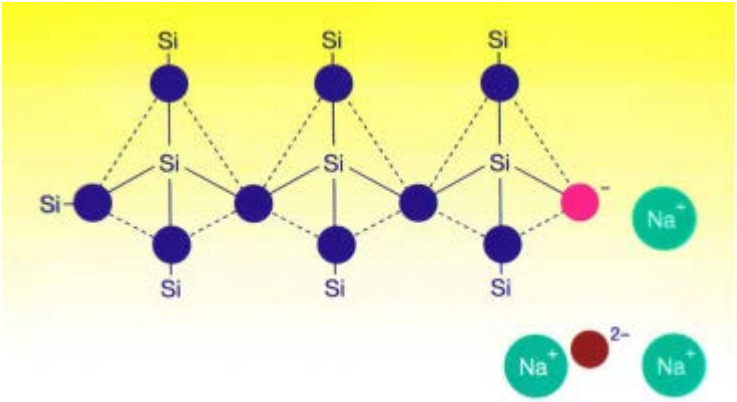

Figure 4.1 : Schematic representation of a silicate chain [30]

Dealing with systems involving silica is the main reason of difficulties of slag modeling [31]. Because silica is a relatively strong acid, the excess Gibbs energy of its interaction in solutions with alkaline-earth oxides cannot easily be represented using the polynomial expansion model. Furthermore, silica exhibits a miscibility gap with most of the oxides found in slags.

4.5.1.2 Development of thermodynamic slag modeling

The Gibbs energy of a solution phase has the following general form:

$$G = \sum X_i G_i + RT \sum X_i \ln X_i + \Delta G^{ex} \quad (4.7)$$

In this equation, the first term is simply the weighted sum of the unary data, the second is the sum of contributions from the configurational entropy to the Gibbs energy of mixing, and the third is the excess Gibbs energy. The form of the excess Gibbs energy depends on the applied model.

During the past decades, efforts have been made to develop thermodynamic models for multi-component oxide systems [31]. These models have been incorporated into computer programs, such as the MTDATA [32], Thermo-calc [33] and FactSage software packages [34], in order to cope with complex metallurgical problems. The most intensively applied models include the ionic liquid model [35], the associate model [36] and the Modified Quasichemical Model [7, 8], the latter used for modeling the slag in the present study. These models are based on phase equilibrium and thermodynamic data for various chemical systems available in the literature.

4.5.1.3 Two-sublattice ionic liquid model

In the two-sublattice ***ionic liquid model*** [35], it is assumed that there are two sublattices, one for cations and the other for anions and neutral constituents [31]. This model is implemented in Thermo-Calc, MTDATA and GEMINI2 [37]. The ratio of sites on the two sublattices is not fixed; instead, it changes to maintain charge balance. In the CaO-SiO_2 system, for instance, the cation sublattice carries only Ca^{2+} ions and the anion sublattice carries O^{2-}, SiO_4^{2-}, and SiO_2. The model has considerable flexibility because associates can be introduced, usually on the second sublattice. The main disadvantage of the ionic liquid model is problems with assigning data to charged end members of solution phases.

4.5.1.4 Associate Model

In the ***associate model*** [36], the sharp minimum in Gibbs energy of the liquid at specific composition can be achieved by assuming the associate composition [31].

Let us consider a simple case, i.e. the formation of the associate $MSiO_3$ in the MO-SiO_2 binary system by the following reaction, with the Gibbs energy Δg_{MSi}:

$$MO + SiO_2 = MSiO_3 \tag{4.8}$$

Let X_M and X_{Si} be mole fractions of components M and Si, n'_{MO} and n'_{SiO_2} – moles of unassociated MO and SiO_2 and n_{MSiO_3} – moles of associates. Then

$$X_M = n'_{MO} + n_{MSiO_3}; X_{Si} = n'_{SiO_2} + n_{MSiO_3} \tag{4.9}$$

$MSiO_3$ "associates" and unassociated MO and SiO_2 are randomly distributed over the lattice sites. The configurational entropy is given by

$$\Delta S^{config} = -R(n'_{MO} \ln X'_{MO} + n'_{SiO_2} \ln X'_{SiO_2} + n_{MSiO_3} \ln X_{MSi}) \tag{4.10},$$

where

$$X'_{MO} = n'_{MO}/(n'_{MO} + n'_{SiO_2} + n_{MSiO_3}), etc. \tag{4.11}$$

The enthalpy is given by

$$\Delta H = X_{MSi} \cdot \Delta g_{MSi} \tag{4.12}$$

The mole fraction of associate at equilibrium at any overall composition X_{Si} is determined by setting $\partial(G/\partial X_{MSi})_{n_M, n_{Si}} = 0$. This results in an equilibrium constant:

$$K = X_{MSi}/(X'_{MO}\, X'_{SiO_2}) = \exp(-\Delta g_{MSi}/RT) \tag{4.13}$$

In the case of an ideal solution, the configurational entropy in Equation (4.10) does not reduce to the ideal random mixing point approximation (Bragg-Williams model), because if $\Delta g_{MSi} = 0$ and $K = 1$, there is still a number of associate particles present.

The associate model is widely used in the MTDATA [32] software package, where, for instance, the liquid in the CaO–SiO_2 system can be considered as an example, where "associate species" involve $CaSiO_3$ and Ca_2SiO_4. The amounts of the associates vary with the composition of the system and are determined mainly by their Gibbs energies but also in part by their non-ideal interactions with CaO and SiO_2.

The main advantages of the associate model for the liquid include its conceptual simplicity, its ability to represent the data in binary systems and characteristic shape of the enthalpy and entropy

functions. However, even though liquid associate species can be usually selected from the congruent melting crystalline phases, they are fictive without considering the melt structure. There is no absolute basis to decide whether an associate should be used or not, nor is there a basis for choosing the formula to give to any associate.

As well as being physically unreasonable, the associate model has the disadvantage of failing to adequately predict the positive deviations observed in ternary solutions from optimized binary model parameters when the binary subsystems exhibit short-range ordering.

The significant drawbacks of the associate model can be overcome by employing the Modified Quasichemical Model.

4.5.1.5 Modified Quasichemical Model

The liquid oxide phase is an ionic melt where metal cations are always surrounded by oxygen anions. In other words, there is almost full first-nearest-neighbour short-range ordering (SRO) between cations and anions. Furthermore, there is a strong tendency for second-nearest-neighbour SRO of cations in melts. In particular, basic cations such as Mg form strong second-nearest-neighbour (SNN) pairs with acidic cations such as Si. This is taken into account by the ***Modified Quasichemical Model*** which is used in the present study for modeling the liquid oxide phase. The Modified Quasichemical model was first introduced by Pelton and Blander in a series of articles [26, 27]. In these articles, the classical Quasichemical model was modified to permit the composition of maximum short-range ordering in a binary system to be freely chosen and to extend the model to multicomponent systems. Several modifications to the model have been introduced recently [7, 8, 38, 39]. To provide greater flexibility and ease of fitting, the energy of pair formation has been expanded as a polynomial in the pair fraction rather than the component fractions. Furthermore, the coordination numbers are permitted to vary with composition.

In the binary MO–SiO_2 liquid solution, the short-range ordering is taken into account by considering the following SNN pair exchange reactions:

$$(\text{M-M}) + (\text{Si-Si}) = 2(\text{M-Si}); \quad \Delta g_{MSi} \qquad (4.14),$$

where (M-Si) represents a second-nearest-neighbour pair and Δg_{MSi} is the Gibbs energy of the corresponding pair exchange reaction. Let n_M and n_{Si} be the moles of components M and Si,

respectively, X_M and X_{Si} be its mole fractions and Z_M and Z_{Si} – its second-nearest-neighbor coordination numbers (Z_{Si}/Z_M is the valence ratio of Si and M cations). The "coordination-equivalent" fractions (Y_M and Y_{Si}) are then defined as

$$Y_M = Z_M X_M /(Z_M X_M + Z_{Si} X_{Si}) \tag{4.15}$$

$$Y_{Si} = Z_{Si} X_{Si} /(Z_M X_M + Z_{Si} X_{Si}) \tag{4.16}$$

"Coordination-equivalent" fractions may be equivalently presented through pair fractions X_{MM}, X_{SiSi} and X_{MSi} as

$$Y_M = X_{MM} + X_{MSi}/2 \tag{4.17}$$

$$Y_{Si} = X_{SiSi} + X_{MSi}/2 \tag{4.18}$$

The Gibbs energy of the solution is expressed as

$$G = (X_{MO} g^{o}_{MO} + X_{SiO_2} g^{o}_{SiO_2}) - T\Delta S^{config} + (n_{MSi}/2)\Delta g_{MSi} \tag{4.19},$$

where the configurational entropy is given by randomly distributing the pairs over imaginary pair sites:

$$\Delta S^{config} = -R(n_{MO} \ln X_{MO} + n_{SiO_2} \ln X_{SiO_2}) - R\left(n_{MM} \ln \frac{X_{MM}}{Y^2_{MO}} + n_{SiSi} \ln \frac{X_{SiSi}}{Y^2_{SiO_2}} + n_{MSi} \ln \frac{X_{MSi}}{2Y_{MO}Y_{SiO_2}} \right) \tag{4.20}$$

Since no exact expression is known for the entropy of this distribution in three dimensions, Equation (4.20) is only an approximate equation. However, this is exact for a one-dimensional lattice (Z=2). In case of ideal solution, $\Delta g_{MSi} = 0$ and M and Si should be randomly distributed over the quasi lattice sites. Thus,

$$X_{MM} = Y^2_M; X_{SiSi} = Y^2_{Si}; X_{MSi} = 2Y_M Y_{Si} \tag{4.21}$$

In this case, the configurational entropy correctly reduces to the random mixing point approximation (Bragg-Williams model).

The values of pair fractions at equilibrium at any overall composition X_{SiO_2} are determined by setting $\partial(G/\partial X_{MSi})_{n_M,n_{Si}} = 0$. This results in an equilibrium constant for reaction (4.14):

$$K = X_{MSi}^2/(X_{MM}X_{SiSi}) = 4\exp(-\Delta g_{MSi}/RT) \tag{4.22}$$

As Δg_{MSi} becomes progressively more negative, equilibrium in reaction (4.14) is shifted to the right, and the calculated enthalpy and configurational entropy of mixing show, respectively, the negative *V* and *m* shapes characteristic of short-range ordering with minima at $Y_A = Y_B = 0.5$, as shown in Figure 4.2.

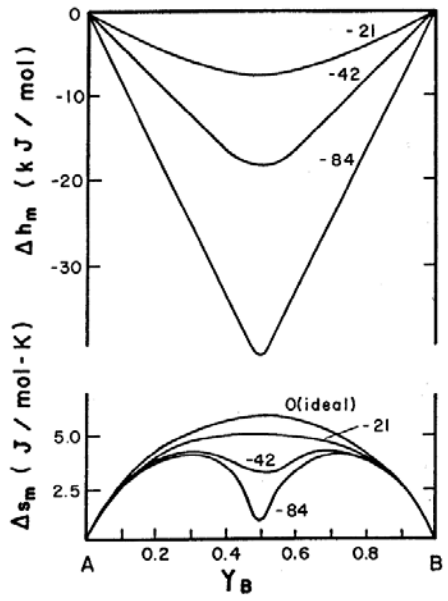

Figure 4.2 : Molar enthalpy and entropy of mixing for a system A-B calculated at 1000 °C with $Z_A = Z_B = 2$ from the Quasichemical model for short-range ordering with Δg_{AB}=constant=0,-21,-42, and -84 kJ

In order to describe the literature data in real oxide systems, Δg_{MSi} can be expanded as a polynomial in the "coordination-equivalent" fractions of the components

$$\Delta g_{MSi} = \Delta g^{o}_{MSi} + \sum_{(i+j)\geq 1} q^{ij}_{MSi} Y^i_M Y^j_{Si} \tag{4.23}$$

or in pair fractions

$$\Delta g_{MSi} = \Delta g^{o}_{MSi} + \sum_{i\geq 1} g^{i0}_{MSi} X^{i}_{MM} + \sum_{j\geq 1} g^{0j}_{MSi} X^{j}_{SiSi} \quad (4.24),$$

where Δg^{o}_{MSi} and q^{ij}_{MSi} are empirical binary coefficients which may be functions of temperature and pressure. They are optimized to describe all available thermodynamic and phase equilibria data in the binary systems.

The symmetric "Kohler-like" extrapolation [28] or the asymmetric "Toop-like" extrapolation [28] of binary terms into the ternary system is used in order to calculate the Gibbs energy of the ternary liquid, the latter if silica is present, with SiO_2 as the "asymmetric component". Except for the binary terms, the model can have ternary terms, $q_{mn(p)}$, which give the effect of the presence of component *p* upon the energy of pair exchange reaction Δg_{mn}. Ternary terms are also expanded as empirical polynomials containing model parameters. The formulae for ternary terms and for extrapolation of binary and ternary terms into a multicomponent system are discussed in detail elsewhere [28].

4.6 Compound Energy Formalism (CEF)

The models for the olivine, spinel and pyroxene solutions were developed within the framework of the Compound Energy Formalism (CEF) [9]. It is well suited to model solid solutions with two or more distinct sublattices. The Gibbs energy expression per formula unit is

$$G_m = \sum_i \sum_j Y_i^{M2} Y_j^{M1} G_{ij} - TS_c + \Delta G^{ex} \quad (4.25),$$

where Y_i^{M2} and Y_j^{M1} represent the site fractions of the constituents *i* and *j* on the M2 and M1 sublattices, respectively, G_{ij} is the Gibbs energy of an end-member *ij* of the solution in which the M2 sublattice is occupied only by cation *i* and the M1 sublattice is occupied only by cation *j*, S_c is the configurational entropy assuming random mixing on each sublattice

$$S_c = -R(n_{M2} \sum_i Y_i^{M2} \ln Y_i^{M2} + n_{M1} \sum_j Y_j^{M1} \ln Y_j^{M1}) \quad (4.26),$$

where n_{M1} and n_{M2} are the number of sites on the corresponding sublattices, and ΔG^{ex} is the excess Gibbs energy,

$$\Delta G^{ex} = \sum_i \sum_{j>i} \sum_k Y_i^{M2} Y_j^{M2} Y_k^{M1} L_{ij:k} + \sum_i \sum_{j>i} \sum_k Y_k^{M2} Y_i^{M1} Y_j^{M1} L_{k:ij} \quad (4.27)$$

where $L_{ij:k}$ and $L_{k:ij}$ are the interaction energies between cations *i* and *j* on the one sublattice when the other sublattice is occupied by *k*. The dependence of the interaction energies on the composition can be expressed by Redlich-Kister power series:

$$L_{ij:k} = \sum_m {}^m L_{ij:k} (Y_j^{M2} - Y_i^{M2})^m \quad (4.28)$$

$$L_{k:ij} = \sum_m {}^m L_{k:ij} (Y_j^{M1} - Y_i^{M1})^m \quad (4.29)$$

4.6.1 Spinel modeling

A general chemical formula of a simple 2-3 spinel is $A^{2+}B_2^{3+}O_4^{2-}$, where A^{2+} = Mg, Mn, Fe, Co, Ni, Cu, Zn and B^{3+} = Al, Cr, V, Mn, Fe, Co [40]. A cation arrangement in the spinel structure is particularly important when certain properties of spinel (e.g. magnetic) are considered. The oxygen atoms form nearly face-centred, cubic close-packed arrays. Metal ions A^{2+} and B^{3+} occupy one-eighth of the tetrahedral sites and one-half of the octahedral sites. These sites are crystallographically distinct and are often referred as tetrahedral (T) and octahedral (O) sublattices. Physical properties of any spinel are strongly dependent on the ordering of cations over these sublattices. The arrangement of metal ions A^{2+} and B^{3+} has two extreme cases: in "normal" spinel $(A^{2+})^T[B^{3+}]_2^O O_4^{2-}$, all divalent cations occupy only the tetrahedral sublattice, and in "inverse" spinel $(B^{3+})^T[A_{0.5}^{2+}, B_{0.5}^{3+}]_2^O O_4^{2-}$, divalent ions are placed only in the octahedral positions, while trivalent ions are equally distributed between the octahedral and tetrahedral sublattices.

Most spinels show distribution over the tetrahedral and octahedral sites, which is intermediate between inverse and normal and can be described using an inversion parameter *i*. The corresponding spinel formula is $(A_{1-i}^{2+}, B_i^{3+})^T[A_{i/2}^{2+}, B_{1-i/2}^{3+}]_2^O O_4^{2-}$. A fully disordered spinel would have i = 2/3. The inversion parameter for a certain spinel depends on the temperature and pressure of equilibration as well as cationic radii, cationic charge and crystal-field effects.

It is well known that the degree of inversion of a spinel is temperature-dependent. When the temperature goes to 0 K, and kinetics permits, either fully inverse or normal spinel is expected. When temperature is increased, the cation arrangement tends to random distribution (i = 2/3) due to the increasing entropy contribution to the free energy.

The model for the spinel solution has been developed within the framework of the Compound Energy Formalism (CEF):

$$(Al^{3+}, Fe^{2+}, Fe^{3+}, Mg^{2+}, Ni^{2+})^{T}(Al^{3+}, Ca^{2+}, Fe^{2+}, Fe^{3+}, Mg^{2+}, Ni^{2+}, Va)_2^{O}O_4 \qquad (4.30)$$

The formation of neutral vacancies on the octahedral sublattice describes the non-stoichiometry of the spinel towards excess oxygen.

The Gibbs energy expression and model parameters for a general spinel solution are explained in detail by Decterov et al. [41].

The model parameters for the Al-Fe-Mg-Ni spinel solution are as follows. These model parameters have physical meaning and are not to be confused with the formalism parameters, end-member Gibbs energies, which often do not.

Fe-O spinel:

$$F_{Fe^{+2}Fe^{+3}} = \frac{1}{7}G_{Fe^{+2}Fe_2^{+3}O_4} = \frac{1}{7}G_{[Fe^{+3}Fe_2^{+2}O_4]^{-1}} \qquad (4.31)$$

$$I_{Fe^{+2}Fe^{+3}} = G_{[Fe^{+3}Fe_2^{+3}O_4]^{+1}} + G_{[Fe^{+3}Fe_2^{+2}O_4]^{-1}} - 2G_{Fe^{+2}Fe_2^{+3}O_4} \qquad (4.32)$$

$$\Delta_{Fe^{+2}Fe^{+3}} = G_{[Fe^{+2}Fe_2^{+2}O_4]^{-2}} + G_{[Fe^{+3}Fe_2^{+3}O_4]^{+1}} - G_{[Fe^{+3}Fe_2^{+2}O_4]^{-1}} - G_{Fe^{+2}Fe_2^{+3}O_4} \qquad (4.33)$$

$$V_{Fe^{+3}} = G_{[Fe^{+3}Va_2O_4]^{-5}} - \frac{5}{7}G_{[Fe^{+3}Fe_2^{+2}O_4]^{-1}} \qquad (4.34)$$

$$\Delta_{Fe^{+3}Fe^{+2}Va} = G_{[Fe^{+2}Fe_2^{+2}O_4]^{-2}} + G_{[Fe^{+3}Va_2O_4]^{-5}} - G_{[Fe^{+3}Fe_2^{+2}O_4]^{-1}} - G_{[Fe^{+2}Va_2O_4]^{-6}} \qquad (4.35)$$

Mg-Fe spinel:

$$F_{Mg^{+2}Fe^{+3}} = \frac{1}{7}G_{Mg^{+2}Fe_2^{+3}O_4} \qquad (4.36)$$

$$I_{Mg^{+2}Fe^{+3}} = G_{[Fe^{+3}Fe_2^{+3}O_4]^{+1}} + G_{[Fe^{+3}Mg_2^{+2}O_4]^{-1}} - 2G_{Mg^{+2}Fe_2^{+3}O_4} \qquad (4.37)$$

$$\Delta_{Fe^{+2}Mg^{+2}Fe^{+3}} = G_{[Mg^{+2}Mg_2^{+2}O_4]^{-2}} + G_{Fe^{+2}Fe_2^{+3}O_4} - G_{[Fe^{+2}Mg_2^{+2}O_4]^{-2}} - G_{Mg^{+2}Fe_2^{+3}O_4} \qquad (4.38)$$

$$\Delta_{Mg^{+2}Fe^{+2}Fe^{+3}} = G_{[Fe^{+2}Fe_2^{+2}O_4]^{-2}} + G_{Mg^{+2}Fe_2^{+3}O_4} - G_{[Mg^{+2}Fe_2^{+2}O_4]^{-2}} - G_{Fe^{+2}Fe_2^{+3}O_4} \quad (4.39)$$

Mg-Al spinel:

$$F_{Mg^{+2}Al^{+3}} = \frac{1}{7} G_{Mg^{+2}Al_2^{+3}O_4} \quad (4.40)$$

$$I_{Mg^{+2}Al^{+3}} = G_{[Al^{+3}Al_2^{+3}O_4]^{+1}} + G_{[Al^{+3}Mg_2^{+2}O_4]^{-1}} - 2G_{Mg^{+2}Al_2^{+3}O_4} \quad (4.41)$$

$$\Delta_{Mg^{+2}Al^{+3}} = G_{[Mg^{+2}Mg_2^{+2}O_4]^{-2}} + G_{[Al^{+3}Al_2^{+3}O_4]^{+1}} - G_{[Al^{+3}Mg_2^{+2}O_4]^{-1}} - G_{Mg^{+2}Al_2^{+3}O_4} \quad (4.42)$$

$$\Delta_{Al^{+3}Mg^{+2}Va} = G_{[Mg^{+2}Mg_2^{+2}O_4]^{-2}} + G_{[Al^{+3}Va_2O_4]^{-5}} - G_{[Al^{+3}Mg_2^{+2}O_4]^{-1}} - G_{[Mg^{+2}Va_2O_4]^{-6}} \quad (4.43)$$

Fe-Al spinel:

$$F_{Fe^{+2}Al^{+3}} = \frac{1}{7} G_{Fe^{+2}Al_2^{+3}O_4} \quad (4.44)$$

$$I_{Fe^{+2}Al^{+3}} = G_{[Al^{+3}Al_2^{+3}O_4]^{+1}} + G_{[Al^{+3}Fe_2^{+2}O_4]^{-1}} - 2G_{Fe^{+2}Al_2^{+3}O_4} \quad (4.45)$$

$$\Delta_{Fe^{+2}Al^{+3}} = G_{[Fe^{+2}Fe_2^{+2}O_4]^{-2}} + G_{[Al^{+3}Al_2^{+3}O_4]^{+1}} - G_{[Al^{+3}Fe_2^{+2}O_4]^{-1}} - G_{Fe^{+2}Al_2^{+3}O_4} \quad (4.46)$$

$$\Delta_{Fe^{+3}Al^{+3}} = G_{[Fe^{+3}Fe_2^{+3}O_4]^{+1}} + G_{[Al^{+3}Al_2^{+3}O_4]^{+1}} - G_{[Al^{+3}Fe_2^{+3}O_4]^{+1}} - G_{[Fe^{+3}Al_2^{+3}O_4]^{+1}} \quad (4.47)$$

$$\Delta_{Fe^{+2}Fe^{+3}Al^{+3}} = G_{[Fe^{+3}Fe_2^{+3}O_4]^{+1}} + G_{Fe^{+2}Al_2^{+3}O_4} - G_{Fe^{+2}Fe_2^{+3}O_4} - G_{[Fe^{+3}Al_2^{+3}O_4]^{+1}} \quad (4.48)$$

Al-Ni spinel:

$$F_{Ni^{+2}Al^{+3}} = \frac{1}{7} G_{Ni^{+2}Al_2^{+3}O_4} \quad (4.49)$$

$$I_{Ni^{+2}Al^{+3}} = G_{[Al^{+3}Al_2^{+3}O_4]^{+1}} + G_{[Al^{+3}Ni_2^{+2}O_4]^{-1}} - 2G_{Ni^{+2}Al_2^{+3}O_4} \quad (4.50)$$

$$\Delta_{Ni^{+2}Al^{+3}} = G_{[Ni^{+2}Ni_2^{+2}O_4]^{-2}} + G_{[Al^{+3}Al_2^{+3}O_4]^{+1}} - G_{[Al^{+3}Ni_2^{+2}O_4]^{-1}} - G_{Ni^{+2}Al_2^{+3}O_4} \quad (4.51)$$

$$\Delta_{Al^{+3}Ni^{+2}Va} = G_{[Ni^{+2}Ni_2^{+2}O_4]^{-2}} + G_{[Al^{+3}Va_2O_4]^{-5}} - G_{[Al^{+3}Ni_2^{+2}O_4]^{-1}} - G_{[Ni^{+2}Va_2O_4]^{-6}} \quad (4.52)$$

Fe-Ni spinel:

$$F_{Ni^{+2}Fe^{+3}} = \frac{1}{7} G_{Ni^{+2}Fe_2^{+3}O_4} \quad (4.53)$$

$$I_{Ni^{+2}Fe^{+3}} = G_{[Fe^{+3}Fe_2^{+3}O_4]^{+1}} + G_{[Fe^{+3}Ni_2^{+2}O_4]^{-1}} - 2G_{Ni^{+2}Fe_2^{+3}O_4} \quad (4.54)$$

$$\Delta_{Fe^{+2}Ni^{+2}Fe^{+3}} = G_{[Ni^{+2}Ni_2^{+2}O_4]^{-2}} + G_{Fe^{+2}Fe_2^{+3}O_4} - G_{[Fe^{+2}Ni_2^{+2}O_4]^{-2}} - G_{Ni^{+2}Fe_2^{3+}O_4} \quad (4.55)$$

$$\Delta_{Ni^{+2}Fe^{2+}Fe^{+3}} = G_{[Fe^{2+}Fe_2^{+2}O_4]^{-2}} + G_{Ni^{+2}Fe_2^{+3}O_4} - G_{[Ni^{+2}Fe_2^{+2}O_4]^{-2}} - G_{Fe^{+2}Fe_2^{3+}O_4} \quad (4.56)$$

In general, *F* parameters in Equations are 1/7 parts of the Gibbs energy of the corresponding hypothetical normal spinels; *I* parameters describe the degree of inversion of these spinels; Δ parameters take into account the thermodynamic properties of real simple spinels and thermodynamics of mixing of these spinels. Vacancy parameters describe the formation of vacancies.

Model parameters in Equations (4.31)-(4.35), (4.36)-(4.39) and (4.40)-(4.43) for the Fe_3O_4, Fe-Mg and Mg-Al spinels, respectively, were optimized earlier [41-43]. Model parameters in Equations (4.44)-(4.48), (4.49)-(4.52), (4.53)-(4.56) have been optimized in this study to fit available thermodynamic and phase diagram data for the Al-Fe, Al-Ni, and Fe-Ni spinel solutions, correspondingly. The meaning of these model parameters and the procedure of their optimization are described in detail in Sections 8.2.2 and 8.4.1, 9.2.2 and 9.5.1, 10.2.2 and 10.4.1, respectively.

In addition to the model parameters given above, an $F_{Al^{+3}V}$ parameter defined as

$$F_{Al^{+3}V} \equiv \frac{1}{5}G°(\gamma\text{-}Al_2O_3) - \frac{1}{20}RT(5\ln 5 - 6\ln 6) \quad (4.57)$$

was optimized in order to simultaneously take into consideration the thermodynamic properties of γ-Al_2O_3 available from the literature and the solubility of Al_2O_3 in several spinel solutions. Also, where applicable, interaction energies introduced by Equation (4.27) were optimized.

The Gibbs energies of the end-members which take part in CEF equations can be derived from the model parameters. The model parameters are used to calculate the fractions of end-members using the Gibbs energy minimization procedure built into the FactSage software [1].

The phenomenological approach proposed by Hillert and Jarl [44] was used to describe the magnetic contribution to thermodynamic functions. The formulae are given in [41].

To introduce Ca into spinel solution, one parameter was added:

$$\Delta_{Fe^{+3}Ni^{+2}Ca^{+2}} = G_{[Ni^{+2}Ni_2^{+2}O_4]^{-2}} + G_{[Fe^{+3}Ca_2^{+2}O_4]^{-1}} - G_{[Fe^{+3}Ni_2^{+2}O_4]^{-1}} - G_{[Ni^{+2}Ca_2^{2+}O_4]^{-2}} \quad (4.58),$$

which describes Ca solubility in Fe-Ni spinel solution.

4.6.2 Olivine modeling

In natural olivines, $\mathbf{M}_2SiO_4$, Mg is one of the major elements along with Fe, while Ni is a minor component. Cations **M** occupy two distinct octahedral sites, called M1 and M2, where M2 sites are larger than M1. Ca^{2+}, Fe^{2+}, Mg^{2+} and Ni^{2+} cations can occupy both M2 and M1 sites (sublattices) in the olivine structure:

$$\left(Ca^{2+}, Fe^{2+}, Mg^{2+}, Ni^{2+}\right)^{M2}\left(Ca^{2+}, Fe^{2+}, Mg^{2+}, Ni^{2+}\right)^{M1} SiO_4 \qquad (4.59)$$

The Gibbs energy of the olivine solution is given by Equation (4.25) of the CEF. According to formula unit (4.59), the Ca-Fe-Mg-Ni olivine solution has 16 end-members, the Gibbs energies of which must be defined. Seven of these parameters (G_{NiNi}, G_{NiMg}, G_{MgNi}, G_{NiCa}, G_{CaNi}, G_{FeNi}, G_{NiFe}) were optimized in the present study, the rest were accepted from the previous optimizations [45-47].

The Gibbs energy of G_{NiNi} was set equal to the Gibbs energy of the corresponding stoichiometric compound Ni_2SiO_4, which is stable in the binary system and has the olivine structure. The end-members, $\left(Mg^{2+}\right)^{M2}\left(Ni^{2+}\right)^{M1} SiO_4$ and $\left(Ni^{2+}\right)^{M2}\left(Mg^{2+}\right)^{M1} SiO_4$, do not exist as real compounds. Two physically meaningful model parameters were introduced to define the Gibbs energies of these end-members. The first parameter, $K_{\mathrm{MgNi}} = G_{\mathrm{NiMg}} - G_{\mathrm{MgNi}}$, represents the change in the Gibbs energy when the Mg^{2+} and Ni^{2+} cations occupying M2 and M1 sites, respectively, change places. This parameter determines the cation distribution between M2 and M1 sites in olivine. The second parameter is the Gibbs energy of the reciprocal reaction among end-members: $\Delta_{\mathrm{MgNi:NiMg}} = G_{\mathrm{MgMg}} + G_{\mathrm{NiNi}} - G_{\mathrm{MgNi}} - G_{\mathrm{NiMg}}$. The parameters K_{MgNi} and $\Delta_{\mathrm{MgNi:NiMg}}$ were optimized to reproduce all experimental data on olivine, including the cation distribution, thermodynamic properties and phase equilibria. Clearly, G_{MgNi} and G_{NiMg} can be expressed as linear combinations of G_{MgMg}, G_{NiNi}, K_{MgNi} and $\Delta_{\mathrm{MgNi:NiMg}}$. In a similar way, end-member Gibbs energies, G_{NiFe} and G_{FeNi} were optimized.

G_{CaNi} was first estimated as half sum of the Gibbs energies of Ca_2SiO_4 and Ni_2SiO_4 olivines, with additional Gibbs energy parameter, which was optimized to describe some solubility data

available from the literature. Another parameter, $K_{\mathrm{CaNi}} = G_{\mathrm{NiCa}} - G_{\mathrm{CaNi}}$, was optimized to describe cation distribution of Ca-Ni olivine.

In addition, in the case of Ca-Ni olivine, the excess Gibbs energy parameters were introduced to take into account a big difference of cationic radii of Ca^{2+} and Ni^{2+}, $r_{Ca^{2+}} = 100\,\mathrm{pm}$ and $r_{Ni^{2+}} = 69\,\mathrm{pm}$ [48].

4.6.3 Pyroxene modeling

Like olivine, pyroxene has two distinct octahedral sublattices, M2 and M1, and tetrahedral sites occupied by Si [49]. The formula unit of pyroxene can be written as

$$(Ca^{2+}, Fe^{2+}, Mg^{2+}, Ni^{2+})^{M2}(Al^{3+}, Fe^{2+}, Fe^{3+}, Mg^{2+}, Ni^{2+})^{M1}(Al^{3+}, Fe^{3+}, Si)^{T1}Si^{T2}O_6 \qquad (4.60)$$

Only Ca-Mg-Ni pyroxenes were modeled in the present study, since no data were found in the literature on the solubility of Ni in pyroxenes in the systems with Al and Fe.

4.6.3.1 Proto-pyroxene

The Gibbs energy of the proto-pyroxene solution is given by Equation (4.25). In this study, Ca-Mg-Ni proto-pyroxene $\left(Ca^{2+}, Mg^{2+}, Ni^{2+}\right)^{M2}\left(Mg^{2+}, Ni^{2+}\right)^{M1} Si_2O_6$ was optimized. For the Ca-Mg-Ni proto-pyroxene, the Gibbs energies of six end-members must be defined. From the previous optimization [50], G_{MgMg} is equal to the Gibbs energy of the proto-pyroxene modification of the $Mg_2Si_2O_6$ stoichiometric compound, which is stable in the MgO-SiO_2 binary system above about 984 °C. G_{CaMg} was previously optimized by Jung *et al.* [45] for the Ca-Mg proto-pyroxene solution. Similar to $CaMgSi_2O_6$ end-member, G_{CaNi} was set equal to the Gibbs energy of the stoichiometric clino-$CaNiSi_2O_6$, with the enthalpy of transition of clino- to proto-$CaNiSi_2O_6$ equal to that of $CaMgSi_2O_6$.

The thermodynamic properties of the end-member $(Ni)(Ni)Si_2O_6$ were evaluated as

$$G_{\mathrm{NiNi}} = G(Ni_2SiO_4, olivine) + G(SiO_2, tridymite) + A + B \cdot T \qquad (4.61)$$

where an additional enthalpy term *A* and a small entropy term *B* are the optimized model parameters.

Similar to olivine, two more model parameters were introduced to define the Gibbs energies of the other two end-members. The parameter $K_{\mathrm{MgNi}} = G_{\mathrm{NiMg}} - G_{\mathrm{MgNi}}$ affects mainly the cation distribution between M2 and M1 sites in proto-pyroxene and the second parameter is the Gibbs energy of the reciprocal reaction among end-members: $\Delta_{\mathrm{CaNi:NiMg}} = G_{\mathrm{CaMg}} + G_{\mathrm{NiNi}} - G_{\mathrm{CaNi}} - G_{\mathrm{NiMg}} = 0$. Finally, one excess Gibbs energy parameter equal to that for the Ca-Mg proto-pyroxene solution [45] was introduced due to the big difference of cationic radii of Ca^{2+} and Ni^{2+}, as mentioned above (Section 4.6.2).

4.6.3.2 Clino-pyroxene

In this study, Ca-Mg-Ni clino-pyroxene solution $\left(\mathrm{Ca}^{2+},\ \mathrm{Mg}^{2+},\ \mathrm{Ni}^{2+}\right)^{\mathrm{M2}}\left(\mathrm{Mg}^{2+},\ \mathrm{Ni}^{2+}\right)^{\mathrm{M1}}\mathrm{Si_2O_6}$ was optimized. For clino-pyroxene, two of six end-member Gibbs energies, G_{CaMg} and G_{MgMg}, were previously optimized by Jung *et al.* [45] for the Ca-Mg clino-pyroxene solution. The rest were optimized in this study.

G_{CaNi} is the Gibbs energy of the stoichiometric clino-$CaNiSi_2O_6$. To define the Gibbs energies of the other three end-members, similar to olivine solution, the linear combinations of the parameters, K_{MgNi}, $\Delta_{\mathrm{CaNi:NiMg}}$, and $\Delta_{\mathrm{CaNi:MgMg}}$, were introduced as model parameters. The parameter $K_{\mathrm{MgNi}} = G_{\mathrm{NiMg}} - G_{\mathrm{MgNi}}$ affects mainly the cation distribution between M2 and M1 sites in the Mg-Ni clino-pyroxene, while the other two parameters are the Gibbs energies of the reciprocal reactions among end-members.

Finally, two excess Gibbs energy parameters equal to those for the Ca-Mg clino-pyroxene solution [45] were introduced due to the big difference of cationic radii of Ca^{2+} and Ni^{2+}, as mentioned above (Section 4.6.2).

4.6.4 Monoxide and corundum solutions

The Gibbs energy of monoxide and corundum solutions were represented by the polynomial model, in most cases with the “Kohler-like” extension of binary and ternary terms into multicomponent systems [28]:

$$G_m = \sum_i X_i G_i^o + RT \sum_i X_i \ln X_i + \Delta G^{ex} \qquad (4.62),$$

where

$$\Delta G^{ex} = \sum_i \sum_j X_i X_j \left(\frac{X_i}{X_i + X_j} \right)^m \left(\frac{X_i}{X_i + X_j} \right)^n L_{ij}^{mn} \tag{4.63}$$

In these expressions, X_i and G_i^o are the mole fraction and the Gibbs energy of the component *i*; L_{ij}^{mn} are interaction parameters, which can be temperature dependent; and the powers *m* and *n* are ≥0.

4.6.5 Other solutions and stoichiometric compounds

Metallic solutions and the majority of stoichiometric compounds were optimized previously within the scope of the FSstel and FToxide databases of FactSage software [1]. NiO (solid and liquid) was optimized by Prostakova et al. [51].

CHAPTER 5 ARTICLE 1: EXPERIMENTAL STUDY AND THERMODYNAMIC OPTIMIZATION OF THE CaO–NiO, MgO–NiO AND NiO–SiO_2 SYSTEMS

Equation Chapter (Next) Section 1Viktoria Prostakova, Jiang Chen, Evgueni Jak, Sergei A. Decterov, Calphad (2012) 1-10.

Abstract

A combination of thermodynamic modeling and experimental studies is used to characterize NiO-containing oxide systems at high temperature of interest to nickel pyrometallurgical processes. It is part of an on-going research project to develop a self-consistent multi-component thermodynamic database. A literature review and critical assessment of the previously published thermodynamic and phase equilibria data on the NiO-containing binary systems CaO–NiO, MgO–NiO and NiO–SiO_2 at a total pressure of 1 atm have been performed using thermodynamic modeling. Considerable discrepancies among previously available experimental data have been found for the CaO–NiO and MgO–NiO systems. To resolve the contradictions in the literature data, a new experimental investigation has been carried out using an equilibration and quenching technique followed by electron probe X-ray microanalysis (EPMA) by our colleagues from PyroSearch, Australia. The CaO–NiO phase diagram in air has been measured from 1200 to 1600 °C. The equilibrium between the MgO–NiO solid solution, metal alloy and gas phase has been studied over the temperature range from 1000 to 1300 °C, which enabled the activity of NiO to be calculated. The whole set of experimental data, including the new experimental results and previously published data, has been taken into consideration in thermodynamic modeling of oxide phases in the CaO–NiO, MgO–NiO and NiO–SiO_2 systems at a total pressure of 1 atm. The Modified Quasichemical Model has been used for modeling of the liquid phase. A simple random mixing model with a polynomial expansion of the excess Gibbs energy has been used for the monoxide solid solution. The optimized model parameters reproduce all available thermodynamic and phase diagram data within experimental error limits.

Keywords: Thermodynamic modeling; Phase diagram; Nickel extraction; Phase equilibrium measurements.

5.1 Introduction

The present study reports results of a research program that naturally combines an experimental investigation and thermodynamic modeling of the CaO–NiO, MgO–NiO and NiO–SiO_2 systems. It is part of an on-going research project to develop a self-consistent multi-component thermodynamic database for nickel extraction from laterite ores.

Laterite ores are an increasingly important source of nickel in view of the continual depletion of overall reserves of high grade nickel sulphide ores [52]. In general, laterite ores are processed using either pyrometallurgical or hydrometallurgical techniques [15]. The Caron process [53] involves the reduction of the ore into metallic form followed by roasting and leaching with an ammonia-ammonium carbonate solution [12].

Rhamdhani *et al.* [5, 6] reported that the factors affecting the nickel recovery in the Caron process are quite complex. The chemical and physical characteristics of the ore were found to be important for overall nickel recovery. It was demonstrated that thermodynamic factors also play a significant role and should be thoroughly studied with a view to increasing nickel recovery from the ore.

Most of the chemical processes occurring at the reduction stage of the Caron process may be considered within the scope of the Al–Ca–Cr–Fe–Mg–Ni–O–Si chemical system. A thermodynamic database which correctly describes phase equilibria in this chemical system is required for optimizing the process metallurgy. An initial stage of the development of this database is reported in the present study.

The database development is done by thermodynamic modeling which is combined with the experimental study of phase equilibria. Initially, parameters of thermodynamic models are optimized to fit the experimental data collected from the literature. When there is not enough data to constrain the model parameters, or significant discrepancies in the available data are revealed, experimental measurements are initiated for temperatures and compositions which are most useful for thermodynamic modeling by our colleagues from PyroSearch, Australia.

The experimental procedure involves equilibration and ultra rapid quenching followed by measurements of compositions of phases using electron probe X-ray microanalysis (EPMA) of quenched samples. Since the analysis takes place after equilibration, the changes in composition during equilibration do not affect the accuracy of the results. Tie-lines between equilibrated phases are measured directly, providing essential data for subsequent thermodynamic modeling.

A critical assessment of the previously published thermodynamic and phase equilibrium data for the CaO–NiO and MgO–NiO systems revealed substantial discrepancies between various sources. The monoxide solid solution exists in these binary systems. NiO and CaO have limited solubilities in each other forming a miscibility gap, whereas NiO and MgO are completely miscible at all studied temperatures. The experimental information on the CaO–NiO solid solution is limited and the data on the solubility limits and activities of the components are contradictory. Even though the MgO–NiO system has been studied by many authors, the reported activities and heats of mixing are widely scattered. To resolve the contradictions in the literature, an experimental investigation of the CaO–NiO and MgO–NiO systems was undertaken in the present study. The obtained experimental data along with the previously published experimental results were used in a thermodynamic "optimization" of the CaO–NiO, MgO–NiO and NiO–SiO_2 systems.

In a thermodynamic "optimization" of a system, all available thermodynamic and phase diagram data are evaluated simultaneously in order to obtain one set of model equations for the Gibbs energies of all phases as functions of temperature and composition. From these equations, all of the thermodynamic properties and the phase diagrams can be back-calculated. In this way, all the data are rendered self-consistent and consistent with thermodynamic principles. Thermodynamic property data, such as activity data, can aid in the evaluation of the phase diagram, and phase diagram measurements can be used to deduce thermodynamic properties. Discrepancies in the available data can often be resolved, and interpolations and extrapolations can be made in a thermodynamically correct manner. A small set of model parameters is obtained. This is ideal for computer storage and calculation of properties and phase diagrams. In the present study, all calculations were carried out using the FactSage thermochemical software and databases [1].

5.2 Experimental technique and procedure

Experimental procedures for phase equilibrium measurements have been developed by the Pyrometallurgy Research Centre at the University of Queensland [19, 20, 54]. The technique involves high temperature equilibration of a synthetic oxide sample in a controlled gas atmosphere. The sample is then rapidly quenched so that the phase assemblage present at high temperature remains unaltered. The quenched sample is mounted in epoxy resin, polished for metallographic examination and microanalysis, and the compositions of the crystalline solid phases are measured by electron probe X-ray microanalysis (EPMA) with wavelength dispersive detectors (WDD).

All equilibration experiments were conducted in a vertical reaction tube (impervious re-crystalized alumina, 30-mm i.d.) in electrical resistance silicon carbide (SiC) heated furnace. The furnace temperature was controlled within ± 1 °C by an alumina shielded Pt–Pt/13%Rh thermocouple placed immediately adjacent to the sample. The thermocouple was periodically calibrated against a standard thermocouple (supplied by National Measurement Institute of West Lindfield, NSW, Australia). The overall temperature accuracy was estimated to be within ± 5 °C. A flowing mixed gas stream with an accurately controlled CO/CO_2 ratio was used to maintain a designated oxygen potential within the reaction tube.

The starting mixtures were made from CaO (99.98 wt% purity), NiO (99.99 wt% purity), MgO (99.99 wt% purity) and Ni (99.8 wt% purity) supplied by Sigma-Aldrich Co. The powders for each sample were weighed, mixed with an agate mortar and pestle, and then pelletized. The pellets (0.2 g) were placed inside open platinum crucibles. All crucibles were suspended by platinum wire within the reaction tube in the furnace.

The oxygen partial pressure inside the vertical tube furnace was controlled by flowing mixtures of high purity CO (99.95%, Coregas, Australia) and CO_2 (99.995%, Coregas, Australia) in proportions calculated for a given temperature using the FactSage thermochemical software and databases [1]. The volumetric gas flow rates were controlled using pre-calibrated differential pressure manometers with precision necessary to ensure the required accuracy of the oxygen partial pressure. The total volumetric gas flow rates used in the study were around 300 ml/min. The oxygen partial pressures, $P(O_2)$, inside the furnace were verified with a DS-type oxygen probe supplied by Australian Oxygen Fabricators (AOF, Melbourne, VIC, Australia). At the experimental conditions, the accuracy was ± 0.1 in the $\log_{10}P(O_2)$ scale.

Special efforts were made to ensure that equilibrium is reached. In initial experiments, equilibration was carried out for different periods of time. The attainment of equilibrium in these samples was verified by repeating selected experiments at extended equilibration times, i.e. twice the equilibration time. If possible, equilibrium was approached from different directions, i.e. from oxygen-rich and metal-rich starting compositions. The attainment of equilibrium was also tested by checking the compositional homogeneity of phases in all samples using EPMA.

The compositions of various phases within a sample were measured by EPMA JEOL JXA 8200L (trademark of Japan Electron Optics Ltd., Tokyo). An acceleration voltage of 15 kV and a probe current of 15 nA were used. The Duncumb-Philibert ZAF correction procedure supplied with the

JEOL JXA 8200L probe was applied. The standards (Charles M. Taylor, Stanford, CA) used in the EPMA measurements were as follows: wollastonite ($CaSiO_3$) for Ca, magnesite (MgO) for Mg, Ni olivine (Ni_2SiO_4) for Ni in the oxide phases, and Ni metal for Ni in the alloy phase. The compositions were measured with an accuracy of 1 wt. %.

5.3 Experimental results

The experiments in the MgO–NiO system were conducted between 1000 and 1300 °C over the range of oxygen partial pressures from $10^{-13.5}$ to $10^{-7.5}$ atm. As can be seen from an isothermal section of the Mg–Ni–O phase diagram shown in Figure 5.1, the monoxide solid solution of various compositions is in equilibrium with the alloy of the composition close to pure solid Ni at these temperatures. The aim of this series of experiments was to determine the composition of the (Mg,Ni)O monoxide solid solution in equilibrium with metallic Ni at fixed oxygen partial pressures.

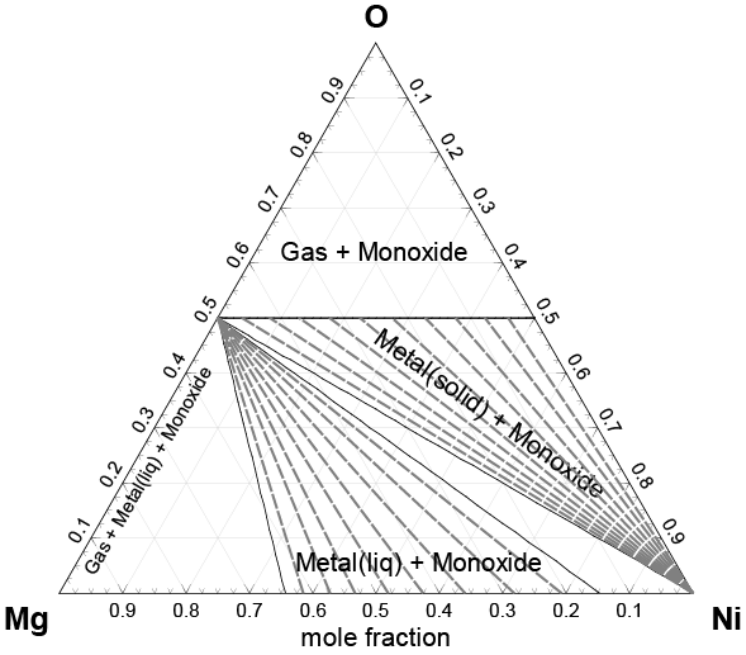

Figure 5.1: Calculated isothermal section of the Mg–Ni–O phase diagram at 1200 °C

The experiments in the CaO–NiO system were conducted between 1200 and 1600 °C in air, $P(O_2)$ = 0.21 atm, to obtain the solubility of CaO in bunsenite (NiO) and NiO in lime (CaO), i.e. the miscibility gap in the monoxide solid solution was measured.

Examples of typical microstructures of these samples after equilibration are shown in Figure 5.2.

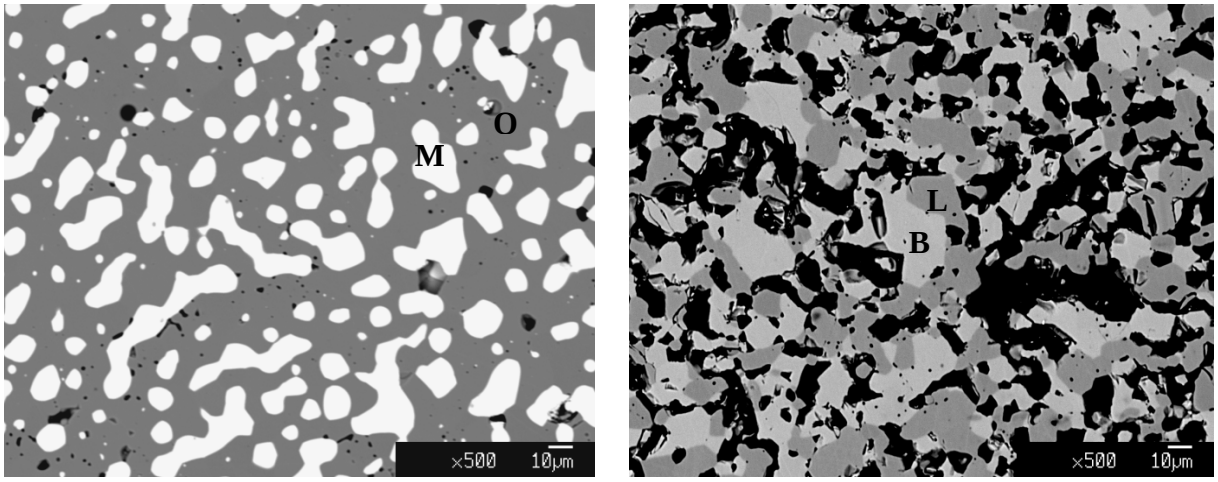

I II

Figure 5.2: Typical backscattered SEM micrographs of the equilibrated phases in the MgO–NiO (I) and CaO–NiO (II) systems. (I) Ni metal (M) and (Mg, Ni)O monoxide (O) at 1300 °C and $P(O_2)$ = 10^{-10} atm; (II) (Ni, Ca)O bunsenite (B) and (Ca, Ni)O lime (L) at 1600 °C in air

As can be seen from Figure 5.2(I), the solid metallic Ni phase and the monoxide phase, (Mg,Ni)O, form a dense microstructure. The fact that they are in good contact with each other is indicative of attained equilibrium which is also confirmed by uniform compositions measured by EPMA. Even though some porosity is observed in the microstructure of the CaO–NiO sample shown in Figure 5.2(II), the equilibrated oxide phases are interconnected and homogeneously distributed throughout the sample suggesting that equilibrium is reached. The composition of each phase was measured by EPMA in multiple locations across the sample and found to be uniform. No solubility of Mg in solid Ni was detected within the accuracy of EPMA microanalysis.

Particular attention was paid to attainment of equilibrium that was continuously re-confirmed by i) different equilibration times, ii) uniformity of phase compositions across the sample, iii) approaching equilibrium from opposite directions and iv) considering possible reactions taking place in the sample during equilibration.

The compositions of the monoxide solid solution measured by EPMA are given in Tables 1 and 2. Each reported composition represents an average of six measurements in different areas across the sample. Samples 4, 8, 12 and 16 in Table 5.1 demonstrate the accuracy of the composition measurements by EPMA and the fact that equilibrium was attained. Each pair of these samples, (a) and (b), corresponds to the same tie-line Ni + monoxide at the given T and $P(O_2)$, but equilibrium

was approached either from the oxygen-rich side, starting from the mixture of NiO and MgO for samples (a), or from the metal-rich side, starting from Ni and MgO for samples (b).

The oxygen partial pressures over the (Mg,Ni)O solid solution in equilibrium with solid Ni are also plotted in Figure 5.3 as a function of monoxide composition. The lines in this figure are calculated using the model parameters optimized in the present study.

Table 5.1: Compositions of the monoxide solid solution (Mg,Ni)O in equilibrium with solid Ni measured at fixed temperatures and oxygen partial pressures

Sample №	**Temperature, °C**	**$\log_{10}[P(O_2)$, atm]**	**Mol% NiO in monoxide**
1	1300	-10	3.7
2	1300	-9.5	5.5
3	1300	-9	8.7
4(a)	1300	-7.5	43.6
4(b)	1300	-7.5	44.3
5	1200	-11	4.2
6	1200	-10.5	6.4
7	1200	-10	10.3
8(a)	1200	-8.5	46.8
8(b)	1200	-8.5	45.9
9	1100	-12	5.6
10	1100	-11.5	8.7
11	1100	-11	14.2
12(a)	1100	-9.5	56.4
12(b)	1100	-9.5	54.9
13	1000	-13.5	6.2
14	1000	-13.0	9.7

Table 5.1 (Continued): Compositions of the monoxide solid solution (Mg,Ni)O in equilibrium with solid Ni measured at fixed temperatures and oxygen partial pressures

15	1000	-12.5	14.2
16(a)	1000	-11.0	53.0
16(b)	1000	-11.0	52.2

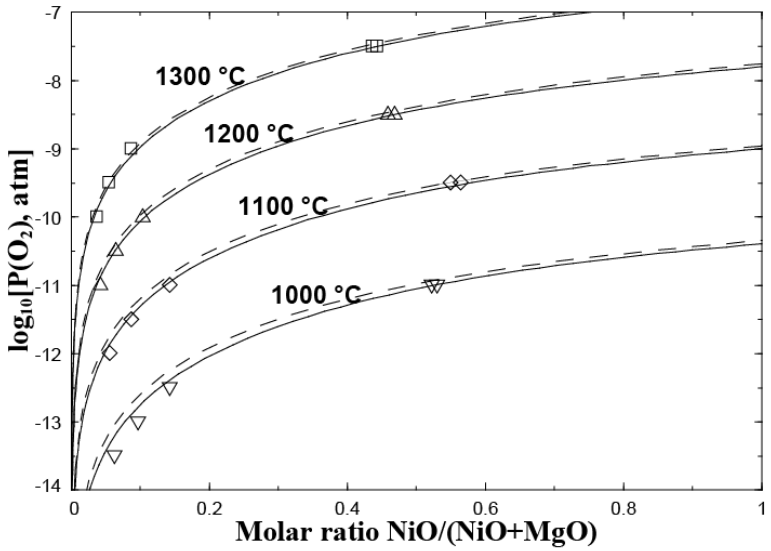

Figure 5.3: Equilibrium oxygen pressure over tie-lines between the monoxide (Mg,Ni)O solid solution and solid Ni as a function of mole fraction of NiO in monoxide. Points indicate the experimental data obtained in the present study. Solid and dashed lines are calculated from the model parameters optimized in the present study and by Woo *et al*. [55], respectively

Table 5.2: Measured miscibility gap in the (Ca,Ni)O monoxide solid solution in air

Temperature	Lime (CaO-rich side)	Bunsenite (NiO-rich side)
°C	Mol% NiO	Mol% NiO
1600	9.3	85.2
1400	5.5	90.7
1200	2.1	96.5

5.4 Phases and thermodynamic models

There are no intermediate compounds in the CaO–NiO and MgO–NiO systems. The only intermediate compound found in the NiO–SiO_2 system is Ni_2SiO_4 with olivine structure. It is modeled as a stoichiometric compound.

Two solution phases are present in the CaO–NiO, MgO–NiO and NiO–SiO_2 binary systems:

- Liquid oxide: CaO–MgO–NiO–SiO_2,
- Monoxide: CaO–MgO–NiO.

The optimized binary model parameters for solutions as well as optimized Gibbs energies of stoichiometric compounds are listed in Table 3.

5.4.1 Liquid oxide

The liquid oxide phase is an ionic melt where metal cations are always surrounded by oxygen anions. Furthermore, there is a strong tendency for short-range ordering (SRO) of second-nearest-neighbour cations in ionic melts. In particular, basic cations such as Ca form strong second-nearest-neighbour pairs with acidic cations such as Si. This is taken into account by the Modified Quasichemical Model [7, 8] which is used in the present study for modeling the liquid oxide phase. In the binary CaO–NiO, MgO–NiO and NiO–SiO_2 liquid solutions, the short-range ordering is taken into account by considering the following second-nearest-neighbour pair exchange reactions, respectively:

$$(\text{Ca-Ca}) + (\text{Ni-Ni}) = 2(\text{Ca-Ni}); \quad \Delta g_{\text{Ca,Ni}} \tag{5.1}$$

$$(\text{Mg-Mg}) + (\text{Ni-Ni}) = 2(\text{Mg-Ni}); \quad \Delta g_{\text{Mg,Ni}} \tag{5.2}$$

$$(\text{Ni-Ni}) + (\text{Si-Si}) = 2(\text{Ni-Si}); \quad \Delta g_{\text{Ni,Si}} \tag{5.3}$$

where (m-n) represents a second-nearest-neighbour pair and Δg_{mn} is the Gibbs energy of the corresponding pair exchange reaction. Let n_m and Z_m be the number of moles and the coordination number of component *m*, respectively. The "coordination-equivalent" fractions (Y_m) are then defined as

$$Y_m = Z_m n_m / \sum_i Z_i n_i \tag{5.4}$$

Δg_{mn} is expanded as a polynomial in the "coordination-equivalent" fractions of the components

$$\Delta g_{mn} = \Delta g^{o}_{mn} + \sum_{(i+j)\geq 1} q^{ij}_{mn} Y^{i}_{m} Y^{j}_{n} \tag{5.5}$$

where Δg^{o}_{mn} and q^{ij}_{mn} are empirical binary coefficients which may be functions of temperature and pressure. These binary coefficients are optimized to reproduce all available experimental data.

5.4.2 Monoxide

The monoxide solid solution exists in the CaO–NiO and MgO–NiO binary systems. CaO and NiO have limited solubilities in each other whereas MgO and NiO are completely miscible. The monoxide solid solution in both systems is modeled as a simple random mixture of Ca^{2+}, Mg^{2+} and Ni^{2+} ions on cation sites. The Gibbs energy per formula unit of a binary solution is

$$G = (G^{o}_{1} X_1 + G^{o}_{2} X_2) + RT(X_1 \ln X_1 + X_2 \ln X_2) + G^{E}_{12} \tag{5.6}$$

where G^{o}_{1} and G^{o}_{2} are the Gibbs energies of pure components 1 and 2, X_1 and X_2 are the mole fractions. G^{E}_{12} is the excess Gibbs energy which is expanded as a polynomial in the mole fractions of the components:

$$G^{E}_{12} = \sum_{i,j\geq 1} q^{ij}_{12} X^{i}_{1} X^{j}_{2} \tag{5.7}$$

where q^{ij}_{12} are the model parameters.

5.5 Critical evaluation of experimental data and optimization

The MgO–NiO and NiO–SiO_2 systems were previously optimized by Woo *et al.* [55]. These systems were reoptimized in the present study taking into account the new experimental data shown in Table 1 and using the revised thermodynamic properties of pure solid and liquid NiO which describe better available experimental data as discussed below.

The thermodynamic properties of stoichiometric oxides CaO, MgO and SiO_2 were taken from the FactSage database [1].

5.5.1 Solid and liquid NiO

A thermodynamic assessment of the Ni–O system was reported by Taylor and Dinsdale [56]. They accepted the thermodynamic properties of pure NiO assessed by J. Haas (quoted by Taylor and

Dinsdale as a private communication). These properties were later used in the optimizations of Woo *et al.* [55] who also used the heat capacity of liquid NiO estimated by Barin [57].

The thermodynamic properties of solid and liquid NiO were reviewed, analyzed, and optimized by Gurvich *et al.* [58, 59]. The following properties of NiO selected by Gurvich *et al.* were accepted in the present study without modification: entropy at 298.15 K ($S^{o}_{298.15}$), enthalpy of formation at 298.15 K ($\Delta H^{o}_{298.15}$), magnetic properties, melting temperature and heat capacity of liquid NiO.

The high-temperature heat capacity of solid NiO was optimized in the present study. Solid NiO exhibits a transition from the antiferromagnetic to paramagnetic state at Neel temperature, which causes a peak in its heat capacity function. The heat content of NiO was measured by Tomlinson *et al.* [60] (ice calorimeter, 0-835 °C) and King and Christensen [61] (drop calorimetry, 25-1537 °C). Their data are in agreement within 1%. Kapustinskii and Novosel'tsev [62] also measured the heat content (drop calorimetry, 100-1122 °C), but reported only the average heat capacity derived from these data. Their heat capacities are much higher than the ones consistent with the data of Tomlinson *et al.* [60] and King and Christensen [61]. Therefore, the results of Kapustinskii and Novosel'tsev [62] were not taken into account in the present optimization.

The heat capacity around the magnetic transition temperature was measured by Zhuze *et al.* [63] (impulse technique, 142-249 °C), Lewis and Saunders [64] (differential scanning calorimetry, 47-367 °C) and Massot *et al.* [65] (photopyroelectric calorimeter, 207-287 °C). All these data have been fitted simultaneously in the present study and joined smoothly with the low-temperature heat capacity measurements [66, 67]. The optimized parameters of the heat capacity function are given in Table 5.3. The experimental heat capacity and heat content data are compared with the optimized curves in Figure 5.4 and Figure 5.5.

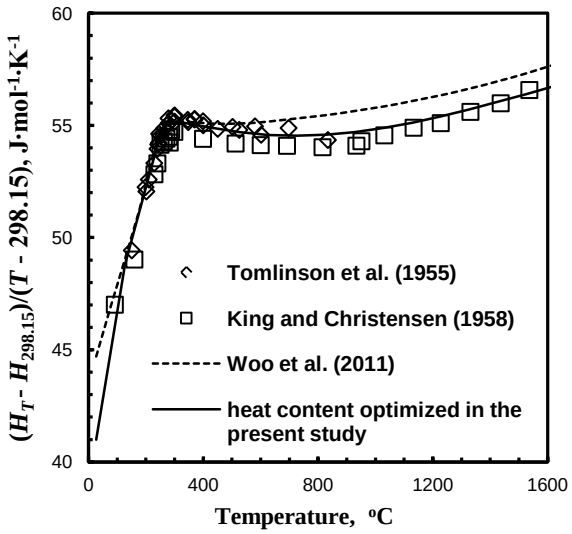

Figure 5.4: Heat content of solid NiO: experimental points [60, 61] and solid lines optimized in the present study. The dashed lines were used in the optimization of Woo *et al.* [55]

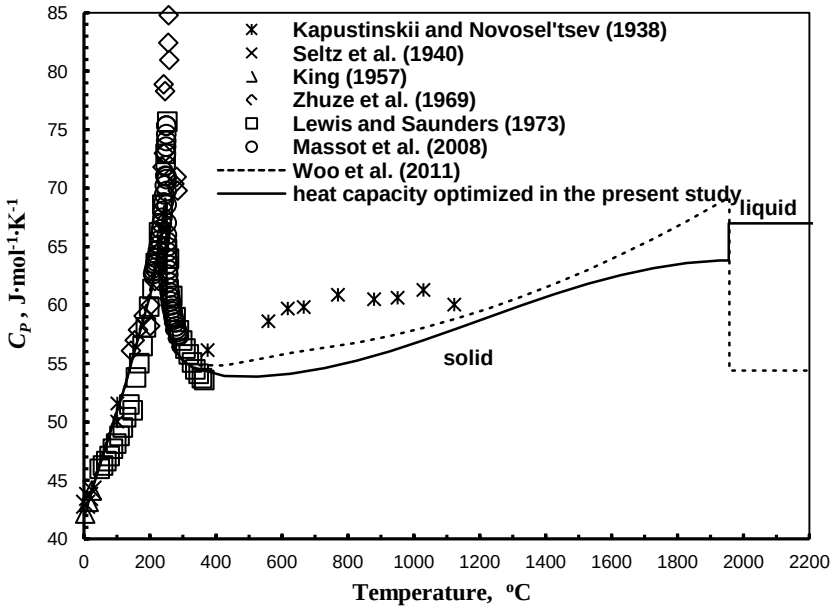

Figure 5.5: Heat capacity of NiO: experimental points [62-67] and solid lines optimized in the present study. The dashed lines were used in the optimization of Woo *et al.* [55]

There are no experimental data in the literature for the enthalpy of melting (ΔH_{melt}) of NiO. The selected value $\Delta H_{melt} = 58.25$ kJ/mol was estimated in the present study from a linear correlation between the enthalpies of melting and melting temperatures of halogenides and oxides with the rock salt structure. This value is also consistent with the limiting slopes of the liquidus and solidus curves

at the melting point of pure NiO in the binary system MgO–NiO reported by Wartenberg and Prophet [68] (see Figure 5.9 in Section 5.3). In their assessment, Woo *et al.* [55] used the value $\Delta H_{melt} = 50.66$ kJ/mol.

5.5.2 CaO–NiO system

The CaO–NiO phase diagram is shown in Figure 5.6. Pure CaO and NiO have the same rock-salt structure. Since the effective ionic radii of Ca^{2+} and Ni^{2+} are substantially different ($r_{Ca^{2+}} = 100\ pm$ and $r_{Ni^{2+}} = 69\ pm$ in octahedral coordination [48]), there is a large miscibility gap in the monoxide solid solution formed by these components.

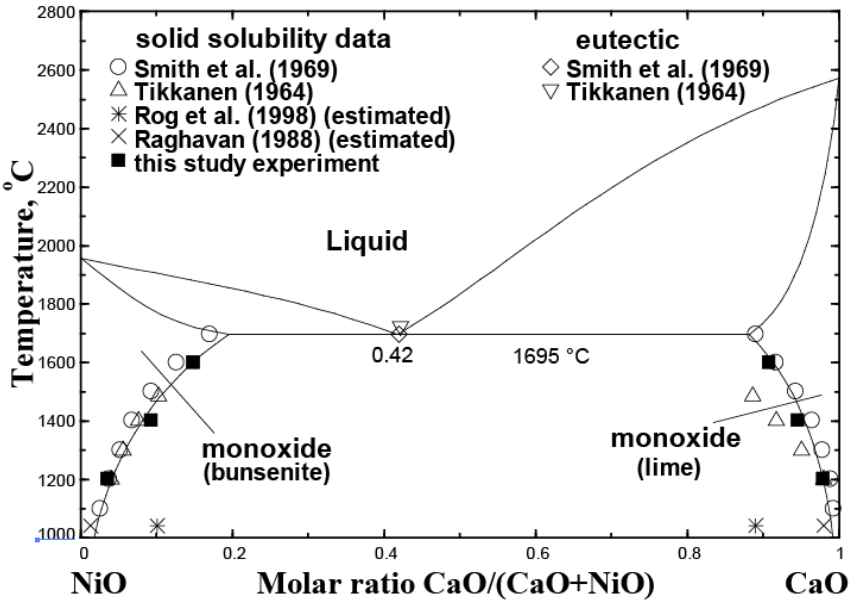

Figure 5.6: CaO–NiO phase diagram: experimental points [69-72] and calculated lines

The CaO–NiO phase diagram was studied by Tikkanen [69] (cited from Levin *et al.* [73], Fig. 230). He reported the diagram with a simple eutectic at 1720 °C and the CaO mole fraction *X*(CaO) = 0.42. Smith *et al.* [70] found the eutectic to be at the same composition and 1695 °C based on metallographic examination. Smith *et al.* also studied the solid solubility limits in the monoxide solution from 1100 °C to 1700 °C by quenching and X-ray diffraction and reported a wider miscibility gap than measured by Tikkanen, especially on the CaO-rich side.

To resolve this contradiction, the solid solubility limits have been measured in the present study over the temperature range from 1200 to 1600 °C by equilibration and quenching followed by EPMA analysis. The experimental results are given in Table 5.2 and shown in Figure 5.6.

The activities of components in the monoxide solid solution were obtained by EMF measurements [71, 72]. Raghavan [71] studied the activity of CaO at 1040 °C using a cell with CaF_2 solid electrolyte and found strong positive deviations from ideality. His data are shown in Figure 5.7. From the kinks in the activity curves he estimated the solid solubilities which are in good agreement with the results of Tikkanen [69] and Smith *et al.* [70].

Rog *et al.* [72] measured the activities of both CaO and NiO in the monoxide solid solution over the temperature range from 850 to 1040 °C, using Ca-β"-alumina electrolyte and Ni(II)- β"-alumina electrolyte, respectively. These data are shown in Figure 5.7-Figure 5.8. As can be seen from Figure 5.7, their activities of CaO are in disagreement with the results of Raghavan [71]. The solid solubilities estimated by Rog *et al.* [72] from the kinks in their activity curves are also inconsistent with the phase diagram data (see Figure 5.6), suggesting much larger solubility limits. Therefore, the results of Rog *et al.* [72] were deemed unreliable in the present optimization.

No experimental data on thermodynamic properties such as enthalpies of mixing, activities or others were found in the literature for the liquid phase in the CaO–NiO system.

The model parameters of the monoxide solid solution were optimized to reproduce simultaneously the solid solubility limits and the activity data of Raghavan [71]. Subsequently, the thermodynamic properties of the liquid phase were optimized to reproduce the eutectic point of Smith *et al.* [70]. Two parameters were introduced to fit both the temperature and the composition of the eutectic. The optimized model parameters are given in Table 5.3 and the calculated phase diagram and activities are shown in Figure 5.6-Figure 5.8. The agreement with the experimental data is believed to be within the experimental error limits.

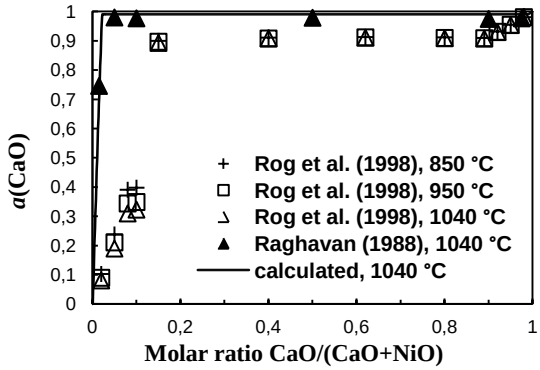

Figure 5.7: Activity of CaO in the monoxide solid solution: experimental points [71, 72] and calculated lines

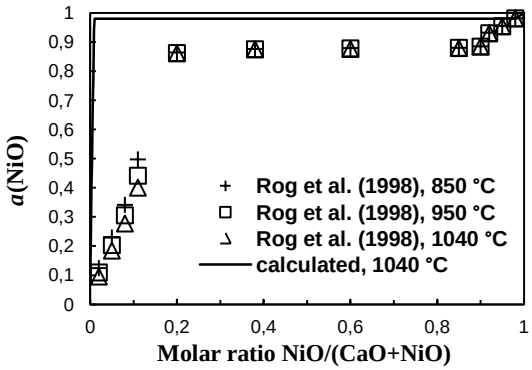

Figure 5.8: Activity of NiO in the monoxide solid solution: experimental points [72] and calculated lines

5.5.3 MgO–NiO system

The phase diagram of the MgO–NiO system is shown in Figure 5.9. Holgersson and Karlsson [74] reported that MgO and NiO are completely miscible in each other forming a continuous range of solid solutions. The only experimental study of the solidus and liquidus in this system was done by Wartenberg and Prophet [68].

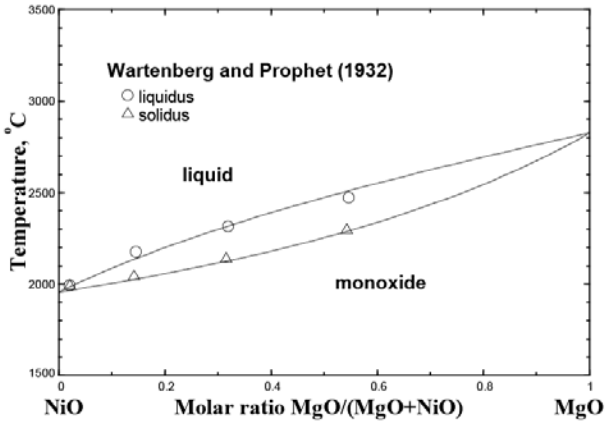

Figure 5.9: NiO–MgO phase diagram: experimental points [68] and calculated lines

Nuessler and Kubaschewski [75] measured the enthalpy of mixing of the monoxide solid solution using an adiabatic high-temperature calorimeter. They found the solution to be very close to ideal from 700 to 1300 °C. By contrast, Davies and Navrotsky [76] reported a negative asymmetric enthalpy of mixing at 713 °C based on oxide melt solution calorimetry. They interpreted the negative enthalpy of mixing in terms of a tendency towards ordering. The experimental data are shown in Figure 5.10.

The activity of NiO in the monoxide (Mg,Ni)O solid solution was studied by a gas-equilibration [77-79] and an EMF technique [80-87]. As can be seen from Figure 5.11, the results of these measurements are widely scattered. Hahn and Muan [77] performed gas equilibration measurements of the activity of NiO in the (Mg,Ni)O solid solution in the temperature interval 1100-1300 °C using CO_2/H_2 gas mixtures and reported ideal behaviour. In subsequent gas equilibration studies, Evans and Muan [78] observed small negative deviations from ideality at 1400 °C using CO_2/CO gas mixtures. Ariya *et al.* [79] reported fairly negative deviations from ideality at 900 and 1000 °C based on equilibration with H_2O/H_2 gas mixtures.

In all EMF studies [80-87], calcia-stabilized or yttria-stabilized zirconia was used as the solid electrolyte. Petot *et al.* [81] reported that the monoxide solid solution behaved almost ideally in the temperature range from 840 to 1200 °C. Paulsson [82] observed very small positive deviations from ideality from 727 to 1177 °C. Jakobsson *et al.* [85] and Kreidler and Park [86] also reported nearly ideal behaviour from 800 to 1200 °C and from 882 to 982 °C, respectively. The results of Seetharaman and Abraham [80] showed significantly positive deviations from ideality in the temperature range from 927 to 1077 °C, whereas Shirane *et al.* [83] and Kale [84] reported

considerable negative deviations from 800 °C to 1000 °C and at 1027 °C, respectively. Contrary to other authors, Shirane *et al.* [83] found a large temperature dependence of the activity of NiO. The most recent EMF study by Mukhopadhyay and Jacob [87] indicates that the (Mg,Ni)O solid solution exhibits slightly negative deviations from ideality, with a small temperature dependence.

In view of the discrepancies in the literature data, the activities of NiO in the monoxide solid solution were measured in the present study from 1000 to 1300 °C by equilibration and quenching followed by EPMA microanalysis. The activities of NiO shown in Figure 5.11 were derived from the experimental results given in Table 5.1. These data are believed to have lower uncertainties because special efforts were made to ensure equilibration and the composition of the monoxide solid solution in equilibrium with solid Ni was accurately measured by EPMA. The obtained activities show small negative deviations from ideality with a small temperature dependence. This is in excellent agreement with the most recent experiments of Jacob *et al.* [87] and in general agreement with the majority of activity measurements showing near ideal behaviour [75, 77, 81, 82, 85, 86] or small negative deviations from ideality [78, 87]. It should be noted that the large positive or large negative deviations from ideality reported in several studies [79, 80, 83, 84] are unlikely since the effective ionic radii of Mg^{2+} and Ni^{2+} are close ($r_{Mg^{2+}} = 72\ pm$ and $r_{Ni^{2+}} = 69\ pm$ in octahedral coordination [48]).

Three model parameters were optimized for the monoxide solid solution (Mg,Ni)O to fit both the enthalpy and the activity data. Preference was given to the activity data obtained in the present study. A small excess entropy term was needed to reproduce the small temperature dependence of the activities. The optimized model parameters are given in Table 5.3. The optimized enthalpy of mixing and activity of NiO for the monoxide solid solution are shown in Figure 5.10-Figure 5.11, respectively. The agreement with the experimental data is believed to be within the experimental error limits. The activities measured in the present study are in good agreement with the enthalpies of mixing reported by Davies and Navrotsky [76] since both sets of data show small negative deviations from ideality.

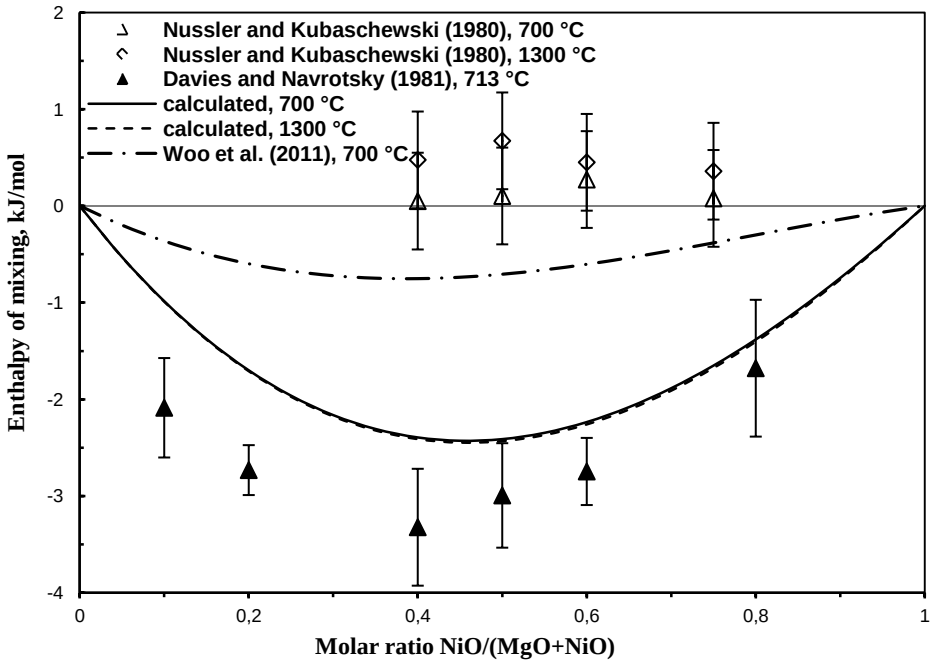

Figure 5.10: Enthalpy of mixing for the monoxide solid solution: experimental points [75, 76] and calculated lines. Error bars for the experimental points of Davies and Navrotsky [76] correspond to one standard deviation. The dash-dot line indicates the assessment of Woo *et al.* [55]

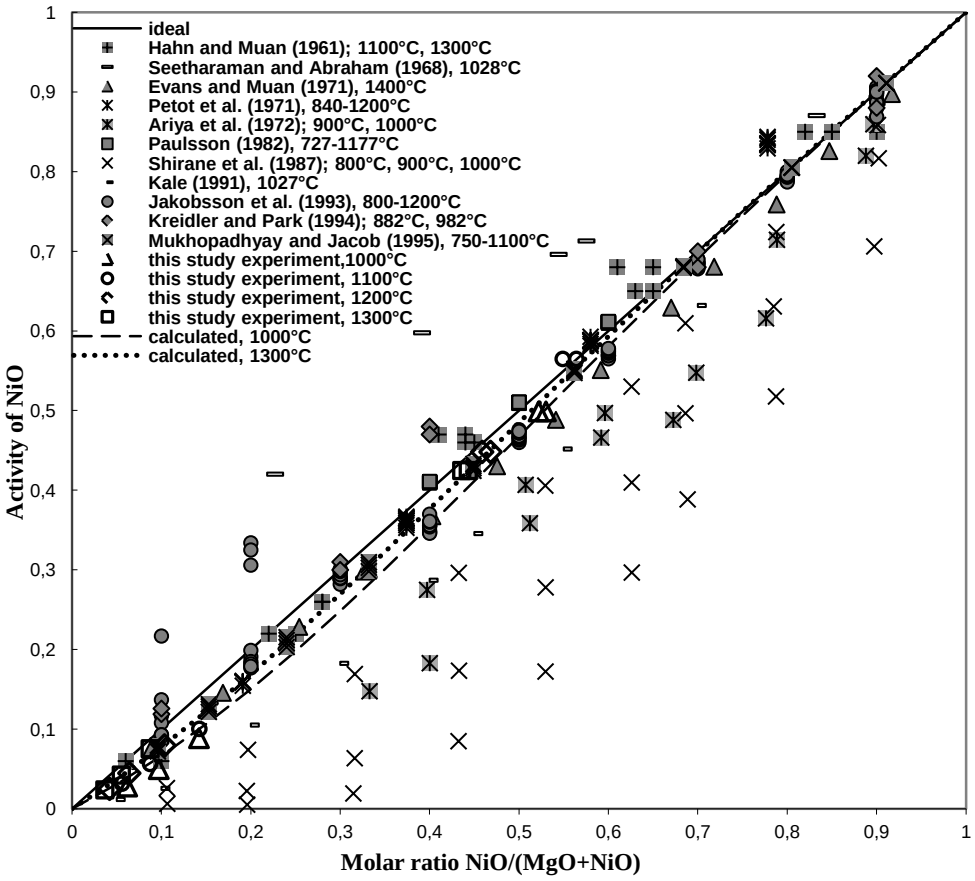

Figure 5.11: Activity of NiO in the monoxide (Mg,Ni)O solid solution: experimental points are from the present study and References [77-87]; calculated lines are based on the optimized model parameters

No experimental data on thermodynamic properties of the liquid phase in the MgO–NiO system were found in the literature. A good description of the experimental phase diagram [68] shown in Figure 5.9 was obtained assuming the liquid phase to be ideal and using the optimized model parameters for the monoxide solution. Woo *et al.* [55] had to introduce one model parameter for the liquid phase, $\Delta g^{o}_{Mg,Ni}$ = -8368 J/mol , to fit the phase diagram shown in Figure 5.9.

5.5.4 NiO–SiO_2 system

The NiO–SiO_2 phase diagram is shown in Figure 5.12. The only intermediate compound in this system is Ni_2SiO_4, which has the olivine structure. The phase diagram was studied by equilibration followed by quenching and phase identification by optical microscopy and X-ray diffraction [88-94].

Greig [88] found liquid immiscibility in the silica-rich region of the NiO–SiO_2 system slightly above 1700 °C. The compositions of both liquids at the monotectic temperature of 1700 °C were reported by Babayan [91] who also specified the temperature and composition of the critical point. The actual compositions of the studied samples and equilibration temperatures are not given in this article and the reported monotectic temperature is about 25 °C higher than measured by Phillips *et al*. [90].

Ringwood [89] observed incongruent melting of Ni_2SiO_4 to liquid and NiO at 1625 ± 20 °C. A relatively inaccurate method of temperature determination by optical pyrometer was used. Ringwood's observation was later refined by Phillips *et al*. [90] who performed a more systematic study of the NiO–SiO_2 phase diagram. He detected that Ni_2SiO_4 decomposed to NiO and SiO_2 (cristobalite) at 1545 ± 5 °C and that NiO and SiO_2 coexisted up to 1650 ± 10 °C. Above this temperature, NiO in equilibrium with liquid became stable at the Ni_2SiO_4 composition. The decomposition of Ni_2SiO_4 to NiO and SiO_2 was confirmed by O'Neill [92] and Grutzeck and Muan [93, 94] who reported the decomposition temperature of 1547 ± 5 °C.

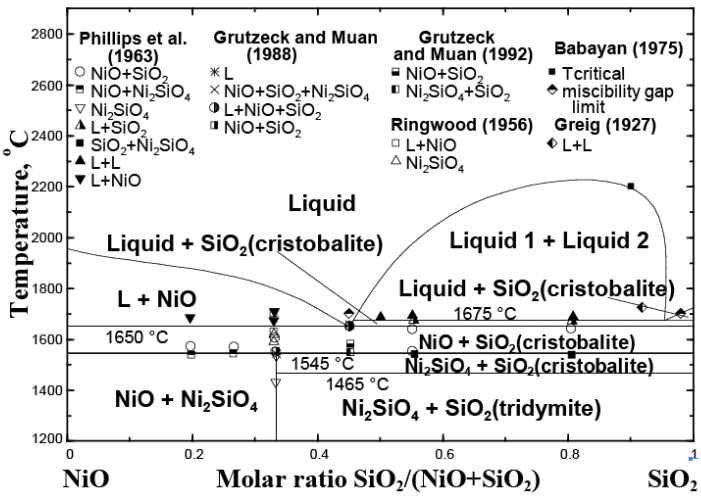

Figure 5.12: NiO–SiO_2 phase diagram: experimental points [88-94] and calculated lines

The thermodynamic properties of Ni_2SiO_4 have been studied repeatedly. Watanabe [95] determined the heat capacity of Ni_2SiO_4 in the temperature range of 77 to 427 °C by differential scanning calorimetry (DSC). Shortly after that, Robie *et al*. [96] studied both the low-temperature heat capacity by adiabatic calorimetry and the high-temperature heat capacity from 87 to 727 °C by DSC. The results of Watanabe are systematically 3-4% higher than the heat capacities of Robie *et al*. [96]. Hirschmann [97] refitted the heat capacity data of Robie *et al*. [96] to obtain a better extrapolation to

high temperatures. His function is reasonably close to the sum of heat capacities of pure solid oxides at all temperatures, with maximum deviations of about 5%.

The heat capacity data for Ni_2SiO_4 can be compared with the measurements of heat content by drop calorimetry [98, 99]. Navrotsky [98] reported the value H(713 °C) – H(24 °C) = 107.6 ± 1.8 kJ/mol in good agreement with 110.6 kJ/mol calculated from the heat capacities of Robie *et al*. [96]. Sugawara and Akaogi [99] measured the heat content H(1500 °C) – H(25 °C) both in air and in argon. The value obtained in air, 271.8 ± 11.3 kJ/mol, is substantially lower than the one obtained in Ar, 308.8 ± 22.3 kJ/mol, indicating some chemical reactions taking place in the samples. Sugawara and Akaogi [99] mentioned that Ni absorption into Pt capsules could have taken place during their experiments. Even the lower value in air is 6% higher than the heat content calculated from the heat capacity function of Hirschmann [97].

In the present study, the heat capacity function of Hirschmann [97] which is based on the data of Robie *et al*. [96] was accepted without modification along with the value of the standard entropy, $S^{o}_{298.15}$, calculated by Robie *et al*. [96] from their low-temperature heat capacities. The standard enthalpy of formation of Ni_2SiO_4, $\Delta H^{o}_{298.15}$, was obtained from the temperature of decomposition of Ni_2SiO_4 into NiO and SiO_2 reported in the phase diagram studies [90, 92-94]. The selected thermodynamic properties of Ni_2SiO_4 are given in Table 5.3. The enthalpies and Gibbs energies of Ni_2SiO_4 were then calculated at various temperatures and compared with the following three sets of experimental data.

Navrotsky [100] measured the enthalpy of formation of Ni_2SiO_4 from the component oxides NiO and SiO_2 (quartz), using solution calorimetry in a molten oxide solvent ($2PbO{\cdot}B_2O_3$). She reported the enthalpy of formation at 692°C to be -13.9 ± 1.9 kJ/mol (the error is one standard deviation), which is in good agreement with the value of -14.2 kJ/mol calculated from the selected thermodynamic functions of Ni_2SiO_4.

The Gibbs energy of the reaction $2NiO(s) + SiO_2(s) = Ni_2SiO_4(s)$ was obtained by EMF measurements on galvanic cells with different solid electrolytes: zirconia, doped with CaO and MgO [101], ThO_2 containing 15 mol% La_2O_3 [102], nickel-substituted sodium-*β"*-alumina [103], Y_2O_3-stabilized ZrO_2 [104] (Jacob *et al*. [104] also tried CaF_2 electrolyte, but the results were not reproducible), Y_2O_3-stabilized ZrO_2 [92] and composite electrolyte containing SiO_2 dispersed in CaF_2 matrix [105]. Jacob *et al*. [104] had silica in the form of quartz in their cells and pointed out

the uncertainty related to unspecified polymorph of silica used in the earlier studies. O'Neill [92] reported two sets of data using either SiO_2 (quartz) or SiO_2 (cristobalite). As can be seen from Figure 5.13, the Gibbs energy of formation of Ni_2SiO_4 from NiO(s) and SiO_2 (quartz) calculated from the thermodynamic functions selected in the present study is in excellent agreement with the majority of the EMF experiments. The data of Rog and Borchardt [103] are somewhat higher than the other measurements and the results of O'Neill [92] have a slightly different slope. The Gibbs energies of formation from quartz and from cristobalite do not differ much.

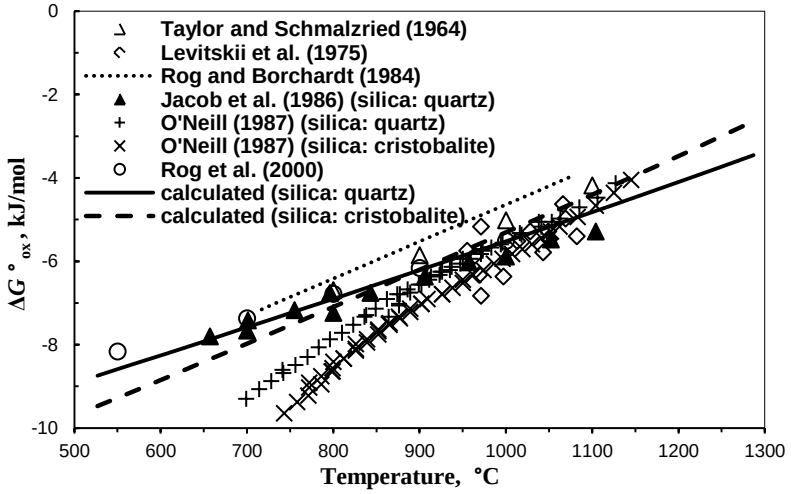

Figure 5.13: Gibbs energies of formation of Ni_2SiO_4 from pure oxides: results of EMF measurements [92, 101-105] and calculated lines

Several gas equilibration studies [106-108] reported the equilibrium oxygen partial pressure over the three-phase region Ni(s)+SiO_2(s)+Ni_2SiO_4(s), which gives the Gibbs energy of the reaction

$$2Ni(s) + SiO_2(s) + O_2(g) = Ni_2SiO_4(s) \qquad (5.8)$$

Oxygen potential was controlled either by CO_2/CO [106, 107] or by CO_2/H_2 gas mixtures [108]. Again, there is some uncertainty related to the crystal form of silica used in these measurements. In particular, Lebedev and Levitskii [106] used SiO_2 (quartz) crucibles and Campbell and Roeder [108] most likely used SiO_2 (cristobalite) over the temperature range where tridymite should be the stable form of silica. However, our calculations indicate that the resulted uncertainty in equilibrium $P(O_2)$ is negligible. As can be seen from Figure 5.14, the results of the gas equilibration studies are in excellent agreement with the line calculated from the thermodynamic functions of Ni_2SiO_4 selected in the present study, except for the data of Lebedev and Levitskii [106] which are lower than the oxygen potentials reported by the other authors. The Gibbs energies obtained from the EMF

measurements [92, 101-105] were also recalculated into $P(O_2)$ and plotted in Figure 5.14 to demonstrate that the gas equilibration and EMF results are in good agreement.

The properties of the liquid phase were optimized to reproduce the phase diagram data shown in Figure 5.12. The parameters of the Modified Quasichemical Model are given in Table 5.3.

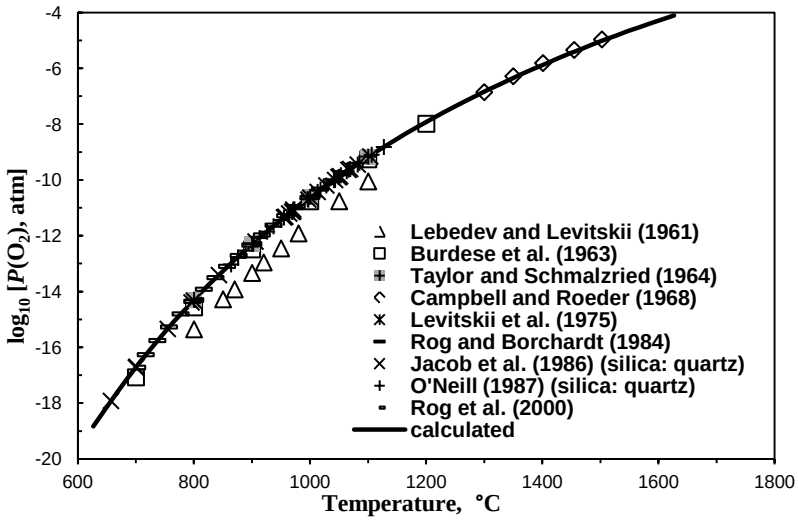

Figure 5.14: Equilibrium partial pressure of oxygen for the reaction $2Ni(s) + SiO_2(s) + O_2(g) = Ni_2SiO_4(s)$. Points show the results of gas equilibration [106-108] and EMF studies [92, 101-105]. The calculated line corresponds to SiO_2 in its stable state

5.6 Conclusions

The present study forms a basis for development of a thermodynamic database that can be used for simulation of nickel extraction from ores. The most important binary systems CaO–NiO, MgO–NiO and NiO–SiO_2 were optimized as well as the properties of pure solid and liquid NiO. The obtained thermodynamic functions are being used in optimizations of ternary and higher-order subsystems of the Al–Ca–Cr–Fe–Mg–Ni–O–Si system. In particular, critical assessment and optimization of the CaO–NiO–SiO_2, MgO–NiO–SiO_2, CaO–MgO–NiO, CaO–MgO–NiO–SiO_2 and Ni–Fe–Al–O systems is being done within the same on-going research project and will be reported elsewhere.

The approach employed in the present study is characterized by a combination of critical assessment of experimental data from the literature and thermodynamic modeling with experimental measurements of phase equilibria at a few selected compositions which, on the one hand, can be done most accurately and efficiently and, on the other hand, provide the most important data for thermodynamic modeling.

In particular, the CaO–NiO and MgO–NiO systems were studied by equilibration and quenching followed by electron probe X-ray microanalysis (EPMA) to resolve the discrepancies in the experimental data available in the literature. The miscibility gap in the CaO–NiO monoxide solid solution was measured from 1200 to 1600 °C. The phase equilibria between the MgO–NiO monoxide solution and Ni were studied at fixed oxygen partial pressures from $10^{-7.5}$ to $10^{-13.5}$ atm over the temperature range of 1000 to 1300 °C. These new measurements resolved the discrepancies in the earlier experimental data on phase diagrams, activities and heats of mixing.

The parameters of thermodynamic models for the oxide phases were optimized to reproduce simultaneously the experimental results from the present study and all thermodynamic and phase diagram data for the CaO–NiO, MgO–NiO and NiO–SiO_2 systems from the literature. A set of self-consistent Gibbs energy functions was obtained that provides the best possible description of thermodynamic properties and phase equilibria in these systems. All available data are reproduced within experimental error limits.

Table 5.3 : Optimized properties of stoichiometric compounds and model parameters for the liquid phase and monoxide solid solution in the CaO–NiO, MgO–NiO and NiO–SiO_2 systems ($J \cdot mol^{-1}$ and $J \cdot mol^{-1} \cdot K^{-1}$)

Compounds	**Temperature range (K)**	$\Delta H^{o}_{298.15}$	$S^{o}_{298.15}$	$C_P(T)$
NiO (solid)	298-2228	-239700.0	37.8900	$514.2700 + 0.397590T - 3.4982 \times 10^{-5} T^2 + 5035500T^{-2} - 68525T^{-1} - 24.001T^{0.5}$
		Magnetic properties of NiO		
		β (magnetic moment) = 0.933 [17]		
		T_N (Neel temperature) = 523 K [17]		
		P factor = 0.28 [17]		
NiO (liquid)	298-4000			67.000 [17]
		Transition NiO (solid) → NiO (liquid)		
		Enthalpy of melting $\Delta H_{melt} = 58252.2$		
		Melting temperature T_{melt} = 2228 K [17]		

Table 5.3 (Continued) : Optimized properties of stoichiometric compounds and model parameters for the liquid phase and monoxide solid solution in the CaO–NiO, MgO–NiO and NiO–SiO_2 systems ($J \cdot mol^{-1}$ and $J \cdot mol^{-1} \cdot K^{-1}$)

CaO (solid)	298-2845	-635090.0	37.7500	$58.7912 - 1147150T^{-2} - 133.904T^{-0.5} + 1.0298 \times 10^{8} T^{-3}$
	2845-3500			62.760
CaO (liquid)	298-2845	-555594.0	65.6908	$58.7912 - 1147150T^{-2} - 133.904T^{-0.5} + 1.0298 \times 10^{8} T^{-3}$
	2845-3500			62.760
MgO (solid)	298-3098	-601500.0	26.9514	$61.1097 - 621154T^{-2} - 296.199T^{-0.5} + 5844610T^{-3}$
	3098-3500			66.944
MgO (liquid)	298-3098	-545345.0	27.0040	$72.7956 - 0.003142\,2T + 522752T^{-2} - 296.199T^{-0.5} + 5844610T^{-3}$
	3098-3500			66.944
SiO_2 (low-quartz)	298-373	-910699.9	41.4600	$80.0120 - 3546680T^{-2} - 240.276T^{-0.5} + 4.9157 \times 10^{8} T^{-3}$
	373-848			$80.0120 + 8.4400 \times 10^{-3} T - 3546680T^{-2} - 4.52127 \times 10^{-5} T^{2}$ $+ 6.05504 \times 10^{-8} T^{3} - 240.276T^{-0.5} + 4.9157 \times 10^{8} T^{-3}$

Table 5.3 (Continued): Optimized properties of stoichiometric compounds and model parameters for the liquid phase and monoxide solid solution in the CaO–NiO, MgO–NiO and NiO–SiO_2 systems ($J \cdot mol^{-1}$ and $J \cdot mol^{-1} \cdot K^{-1}$)

SiO_2 (high-quartz)	298-1996	-908626.8	44.2068	$80.0120 - 3546680\,T^{-2} - 240.276\,T^{-0.5} + 4.9157 \times 10^{8}\,T^{-3}$
	1996-3000			85.7720
SiO_2 (high-tridymite)	298-1991	-907045.1	45.5237	$75.3727 - 5958100\,T^{-2} + 9.5825 \times 10^{8}\,T^{-3}$
	1991-3000			85.7720
SiO_2 (high-cristobalite)	298-1996	-906377.2	46.0288	$83.5136 - 2455360\,T^{-2} - 374.693\,T^{-0.5} + 2.8007 \times 10^{8}\,T^{-3}$
	1996-3000			85.7720
SiO_2 (liquid)	298-1996	-896795.9	50.8291	$83.5136 - 2455360\,T^{-2} - 374.693\,T^{-0.5} + 2.8007 \times 10^{8}\,T^{-3}$
	1996-3000			85.7720
Ni_2SiO_4 (solid)	298-1850	-1395090.0	128.1000	$214.9970 - 1030.750\,T^{-0.5} - 4944530\,T^{-2} + 6.2371 \times 10^{8}\,T^{-3}$

Table 5.3 (Continued): Optimized properties of stoichiometric compounds and model parameters for the liquid phase and monoxide solid solution in the CaO–NiO, MgO–NiO and NiO–SiO_2 systems ($J \cdot mol^{-1}$ and $J \cdot mol^{-1} \cdot K^{-1}$)

Slag (liquid oxide phase)

$Z_{Ca} = Z_{Mg} = Z_{Ni} = 1.37744375, \quad Z_{Si} = 2.75488750$

$\Delta g^{o}_{Ni,Ca} = -11715.2, \quad q^{01}_{Ni,Ca} = -32216.8$

$\Delta g^{o}_{Mg,Ni} = 0$

$\Delta g^{o}_{Ni,Si} = -1882.8 + 14.1838T, \quad q^{01}_{Ni,Si} = 5857.6, \quad q^{07}_{Ni,Si} = 803328.0 - 284.5120T$

Monoxide (solid oxide solution)

$q^{00}_{Ni,Ca} = 57739.2 - 10.8784T, \quad q^{01}_{Ni,Ca} = 7322.0, \quad q^{00}_{Mg,Ni} = -11310.2 + 4.1840T, \quad q^{01}_{Mg,Ni} = 3138.0$

The Gibbs energy of formation of a compound from elements in their standard state at a temperature of T(K) and a pressure of 1 atm is given by $\Delta G = \Delta H^{o}_{298.15} - T S^{o}_{298.15} + \int_{298.15}^{T} C_P(T) dT - T \int_{298.15}^{T} \frac{C_P(T)}{T} dT$, where $\Delta H^{o}_{298.15}$ is the enthalpy of formation of the compound at 1 atm and 298.15 K, $S^{o}_{298.15}$ is the entropy of the compound at 1 atm and 298.15 K, and $C_P(T)$ is the heat capacity at constant pressure.

CHAPTER 6 ARTICLE 2: EXPERIMENTAL STUDY AND THERMODYNAMIC MODELING OF THE MgO–NiO–SiO_2 SYSTEM

Equation Chapter (Next) Section 1 Viktoria Prostakova, Jiang Chen, Evgueni Jak, Sergei A. Decterov, J.Chem.Thermodyn. (2013) 43-55.

Some corrections were made to the original version of the article: description of the model for the Mg-Ni proto-pyroxene as well as minor corrections to phase equilibria including proto-pyroxene solution

Abstract

The MgO–NiO–SiO_2 system has been studied by a combination of thermodynamic modeling and experimental measurements of phase equilibria. A complete literature review, critical evaluation and thermodynamic modeling of phase diagrams and thermodynamic properties of all oxide phases in the MgO–NiO–SiO_2 system at 1 atm total pressure are presented. To resolve the contradictions in the literature data, a new experimental investigation has been carried out over the temperature range from 1400 to 1650 °C using an equilibration and quenching technique followed by electron probe X-ray microanalysis (EPMA) by our colleagues from PyroSearch, Australia. Tie-lines between olivine and monoxide, olivine and proto-pyroxene, liquid and olivine and liquid and cristobalite have been measured. The whole set of experimental data, including the new experimental results and previously published data, has been taken into consideration in thermodynamic modeling of oxide phases in the MgO–NiO–SiO_2 system. The Modified Quasichemical Model has been used for the liquid phase. A simple random mixing model with a polynomial expansion of the excess Gibbs energy has been used for the monoxide solid solution. The models for olivine and proto-pyroxene were developed within the framework of the Compound Energy Formalism. The optimized model parameters reproduce all available thermodynamic and phase diagram data within experimental error limits.

Keywords: Thermodynamic modeling; Nickel extraction; Phase equilibrium measurements; MgO–NiO–SiO_2 system.

6.1 Introduction

This study is part of an on-going research project to develop a self-consistent multicomponent thermodynamic database for nickel extraction from laterite ores. The database development involves experimental and thermodynamic modeling parts, which are closely integrated in order to enhance the effectiveness of the overall program in terms of quantity of the required experimental work and availability of specific data that are essential for thermodynamic modeling.

At present nickel metal is mostly extracted from high-grade sulphide ores; the rest is produced from low-grade laterite ores. The continued depletion of high grade nickel sulphide ores has led to greater efforts in recovering nickel from low grade laterite ores, which are normally classified into two groups: the high-magnesia ores (saprolites or serpentines) and the high-iron, low-magnesia hydroxides (limonites) [4]. Nickel is normally recovered from the high-magnesia ores by smelting under reducing conditions, while limonites can be processed by selective reduction followed by leaching with an ammonia–ammonium carbonate solution [4]. For creation of cost-effective, environmentally-friendly and energy-efficient processes of Ni recovery from laterite ores, it is important to have the ability to perform reliable calculations of phase equilibria in the Al–Ca–Cr–Fe–Mg–Ni–O–Si system, where Fe, MgO, NiO and SiO_2 are the major components.

A thermodynamic “optimization” of the MgO–NiO–SiO_2 system is reported in the present study. In a thermodynamic “optimization” of a system, all available thermodynamic and phase diagram data are evaluated simultaneously in order to obtain one set of model equations for the Gibbs energies of all phases as functions of temperature and composition. From these equations, all of the thermodynamic properties and the phase diagrams can be back-calculated. In this way, all the data are rendered self-consistent and consistent with thermodynamic principles. Thermodynamic property data, such as activity data, can aid in the evaluation of the phase diagram, and phase diagram measurements can be used to deduce thermodynamic properties. Discrepancies in the available data can often be resolved, and interpolations and extrapolations can be made in a thermodynamically correct manner. A small set of model parameters is obtained. This is ideal for computer storage and calculation of properties and phase diagrams. In the present study, all calculations were carried out using the FactSage thermochemical software and databases [1]. The binary NiO–MgO and NiO–SiO_2 systems were optimized earlier [51].

Initially, parameters of thermodynamic models for all oxide phases in the MgO–NiO–SiO_2 system were optimized to fit the experimental data collected from the literature. This revealed a shortage of

experimental information for subsolidus phase equilibria at high temperatures: even though the distributions of Ni between olivine and monoxide and between olivine and proto-pyroxene were measured at 1100 °C [87], there were no data to constrain the temperature dependence of these distributions. Furthermore, the solubility limits of Ni in proto-pyroxene reported in different studies were contradictory and some of the phase equilibrium measurements in the liquidus region [93] were difficult to rationalize.

Therefore, experimental measurements were made at temperatures and compositions which are most useful for thermodynamic modeling by our colleagues from PyroSearch, Australia. The experimental procedure involved equilibration and ultra rapid quenching followed by electron probe X-ray microanalysis (EPMA) of quenched samples. The tie-lines olivine/monoxide and olivine/proto-pyroxene were studied at 1400 and 1500 °C, and a number of tie-lines liquid/olivine and liquid/cristobalite were measured over the temperature range from 1566 to 1650 °C.

Finally, a self-consistent set of optimized model parameters for all oxide phases in the MgO-NiO-SiO_2 system was obtained by fitting all available data, including the new phase equilibrium measurements from the present study and the experimental results published earlier.

6.2 Experimental procedure

6.2.1 Preparation of oxide mixtures

The starting mixtures were made from NiO (99.99 wt.% purity), MgO (99.99 wt.% purity) and SiO_2 (99.98 wt.% purity) supplied by Sigma-Aldrich Co. Mixtures of selected bulk compositions were prepared by weighing the high purity powders and mixing them thoroughly using an agate mortar and pestle. The initial compositions of the mixtures were selected to have two or more phases in equilibrium. Each mixture was then compacted with pressure of 40 MPa to produce a pellet weighing less than 0.2 gram. 10 mm x 12 mm envelopes made from 0.025 mm-thick platinum foil supplied by AGR Metthey were used as sample containers. It was found that platinum was inert to the sample materials under the conditions of the investigation, so there was no contamination of the samples.

6.2.2 High temperature equilibration technique

All equilibration experiments were conducted in a vertical reaction tube (impervious re-crystalized alumina, 30-mm i.d.) in electrical resistance heated furnaces with silicon carbide (SiC) elements. Samples were introduced from the bottom of the vertical tube furnace and suspended by a sample holder made of Pt wire. The 30-mm i.d. re-crystallized alumina reaction tube was preconditioned at the target temperature for more than 5 minutes, and the specimen was then raised into the uniform temperature hot zone of the furnace.

For measurements of phase equilibria involving the liquid phase, pre-melting of the sample was carried out by increasing the temperature 25 °C above the target temperature. After 30 minutes of pre-melting, the temperature of the furnace was decreased back to the target temperature and the sample was equilibrated inside the furnace for at least 24 hours.

After the equilibration, the specimen was rapidly quenched by dropping it directly into iced water. The quenched sample was dried on a hot plate, crushed into smaller pieces, which were mounted in epoxy resin, polished using conventional metallographic polishing techniques and carbon coated for subsequent electron probe X-ray micro-analysis (EPMA).

6.2.3 Control of temperature

To monitor the actual temperature surrounding the sample, a working thermocouple was placed in a re-crystallised alumina thermocouple sheath immediately adjacent to the sample. The working thermocouple was calibrated against a standard thermocouple (supplied by the National Measurement Institute of Australia, NSW, Australia). The temperature of the experiment was continuously controlled within ± 1 °C of the target temperature. It is estimated that the overall temperature accuracy of the experiment is ± 4 °C or better.

6.2.4 Analysis technique and representation of systems

The rapid quenching technique successfully retained phase assemblages and phase compositions present at equilibration temperatures so that they could be subsequently measured at room temperature. The compositions of various phases were measured using JEOL 8200L EPMA with wavelength dispersive detectors (JEOL is a trademark of Japan Electron Optics Ltd., Tokyo). A 15-kV accelerating voltage and 15 nA probe current were selected for the micro-analyzer operation. The standards (Charles M. Taylor, Stanford, CA) used in the EPMA measurements were as follows:

wollastonite ($CaSiO_3$) for Ca and Si, magnesite (MgO) for Mg, and Ni olivine (Ni_2SiO_4) for Ni. The Duncumb–Philibert correction based on the atomic number, absorption, and fluorescence (ZAF correction, supplied by JEOL) was applied. The compositions were measured with an accuracy of 1 wt. %.

There are several advantages of the EPMA over the XRD technique which was largely adopted in early phase equilibria studies; these include the following.

(i) Increased accuracy: EPMA, including the measurements of phase compositions, is carried out after an equilibration experiment, circumventing uncertainties due to unavoidable losses of components or materials during the sample preparation and equilibration process, i.e. losses due to vaporization or reactions with containment materials.

(ii) Microanalysis capability: The quantitative analysis of the phase compositions can be carried out accurately in a small area 1 to 2 μm in lateral size, which can be used for evaluating a local equilibrium.

(iii) Imaging capability: The secondary and backscattered electron imaging provide additional information for evaluating the phases present and their morphology, and for evaluating other microstructural characteristics.

(iv) The EPMA technique can detect and measure small variations in the concentrations of metal cations and accurately determine the phase boundaries, XRD on the other hand cannot detect a phase present at low concentrations.

(v) By measuring the actual compositions of the phases, tie-lines between solid solutions can be determined.

(vi) Phase relations in a multicomponent system at fixed conditions can be determined.

One of the main advantages essential for a study of high temperature phase equilibria is the fact that the final results are not affected by changes in bulk composition during heat treatment (since the compositions of phases are measured directly after the experiment). The interaction with the containment material (crucible, substrate), vaporization of some elements during equilibration and uncertainties in the initial mixture composition do not introduce inaccuracy in final results.

6.2.5 Assessment of achievement of equilibrium

Particular attention was paid to achievement of equilibrium that was continuously re-confirmed by i) equilibration over different time intervals, ii) checking the uniformity of phase compositions across a sample, iii) approaching equilibrium from different directions and iv) considering possible reactions taking place in a sample during equilibration.

Selected experiments were carried out for increasingly long periods to determine the minimum time required to attain equilibrium. For example, the sample marked with * in Table 6.2 was equilibrated for 12, 24, 36 and 48 hours. The results are shown in Table 6.1.

Table 6.1: Measured phase compositions for samples equilibrated for different periods of time in air at 1570 °C

Time of equilibration	Phase at equilibrium	Composition, wt.%		
hours		SiO_2	NiO	MgO
12	Liquid	54.1	16.0	29.9
	Cristobalite	99.9	0.1	0.0
24	Liquid	59.5	12.1	28.4
	Cristobalite	99.7	0.3	0.0
36	Liquid	59.1	12.2	28.7
	Cristobalite	99.6	0.4	0.0
48	Liquid	59.6	11.9	28.5
	Cristobalite	99.6	0.4	0.0

As can be seen from Table 6.1, the composition of the liquid phase remains constant within the experimental uncertainty for equilibration times of 24 hours or greater. This indicates that 24 hours is the minimum time required for equilibration.

The homogeneity of phases in samples after experiments was checked by SEM back scattered imaging and by EPMA measurements of phase compositions in various parts of the sample. Figure

6.1 shows the microstructure of a non-equilibrium sample treated for 72 hours at 1400 °C in air. In this experiment SiO_2, MgO and NiO powders were mixed in a certain ratio in order to achieve a two-phase equilibrium between olivine and pyroxene. As can be seen from the micrograph, a number of tridymite particles (dark) are surrounded by a rim of pyroxene (grey) and isolated from monoxide particles (bright). This micrograph indicates that the reaction between tridymite and metal oxides is still taking place and equilibrium has not been achieved. Such traces of incomplete reactions were searched for in all samples to ensure that the final results correspond to equilibrium.

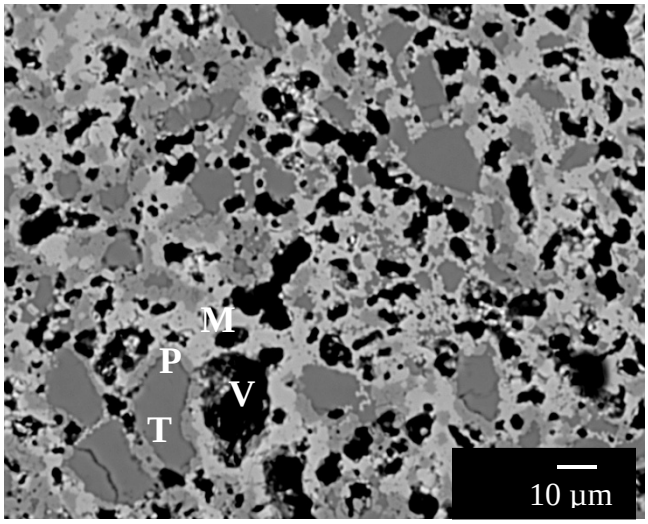

Figure 6.1: Microstructure of a sample in the MgO–NiO–SiO_2 system equilibrated for 72 hours at 1400 °C in air showing that equilibrium is not achieved. Monoxide (M), Pyroxene (P), Tridymite (T) and Voids (V)

Phase compositions across a sample were checked by EPMA. Six sampling points were selected for each phase. The samples were re-crushed and re-equilibrated if variations within any phase were found to be greater than 1 wt.%.

6.3 Experimental results

Experiments in the MgO–NiO–SiO_2 system were conducted in air from 1400 to 1650 °C. Examples of typical microstructures of these samples after equilibration are shown in Figure 6.2.

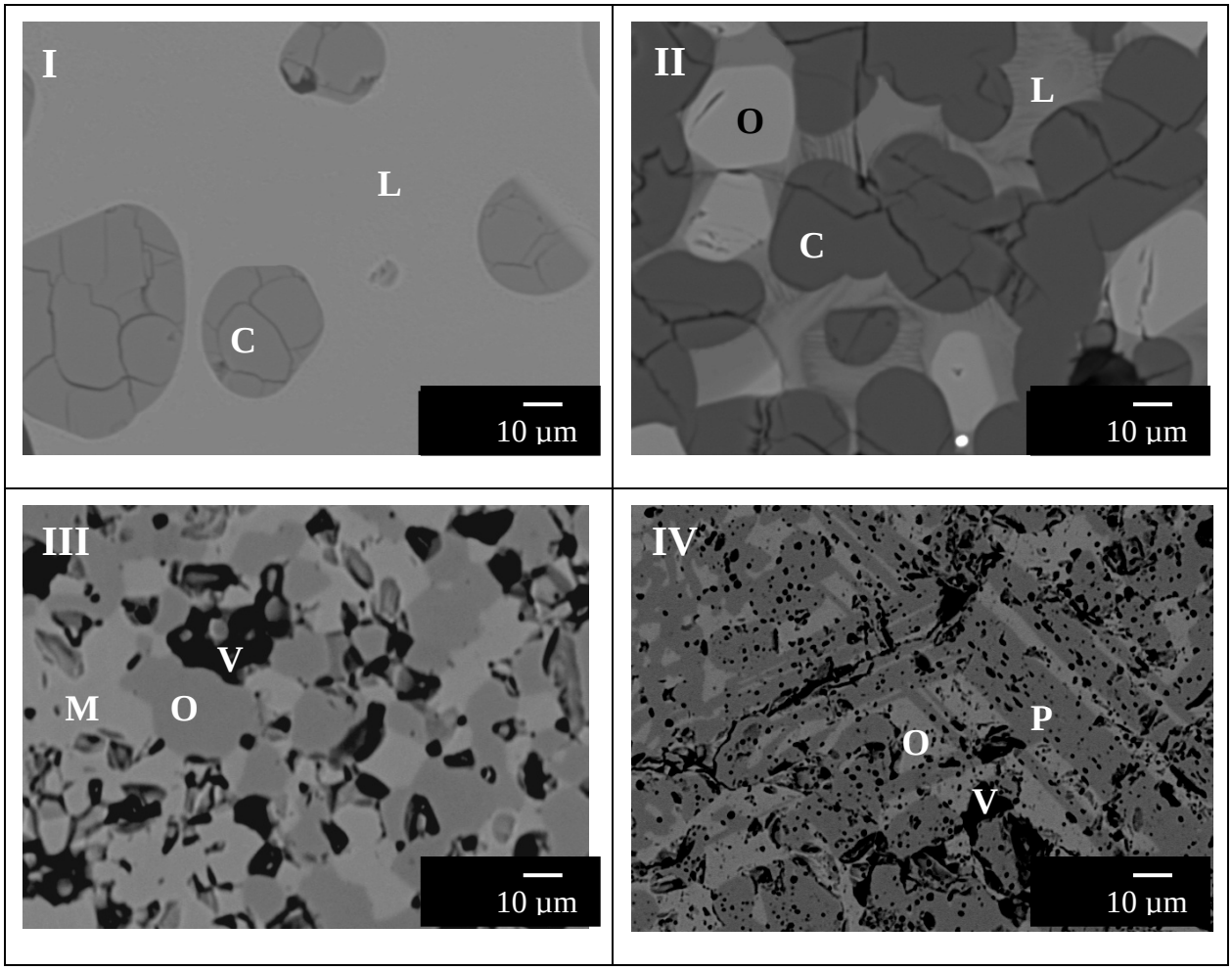

Figure 6.2: Typical backscattered SEM micrographs of samples in the MgO–NiO–SiO_2 system equilibrated in air: (I) Liquid (L) and Cristobalite (C) at 1570 °C; (II) Liquid (L), Olivine (O) and Cristobalite (C) at 1570 °C; (III) Monoxide (M), Olivine (O) and Voids (V) at 1400 °C; (IV) Pyroxene (P), Olivine (O) and Voids (V) at 1400 °C

Homogeneous glassy (liquid) phase can be seen in Figure 6.2-I and Figure 6.2-II, indicating that the liquid was well quenched and equilibrium was achieved.

When the liquid phase is absent, i.e. under subsolidus conditions, even though porosity is observed in the microstructure of the samples shown in Figure 6.2-III and Figure 6.2-IV, the equilibrated solid phases are interconnected and homogeneously distributed throughout the sample suggesting that equilibrium is reached. The composition of each phase was measured by EPMA in multiple locations across the sample and was found to be uniform within 1 wt.%.

The compositions of phases measured by EPMA in the samples equilibrated in air are presented in Table 6.2 and Table 6.3.

Table 6.2: Equilibrium phase compositions measured by EPMA in the liquidus region of the MgO–NiO–SiO_2 system for temperatures ranging between 1566 °C and 1650 °C

Temperature,°C	**Phases at equilibrium**	**Composition, mol%**		
		SiO_2	**NiO**	**MgO**
1566	Liquid	51.5	3.7	44.8
1570*	Liquid	53.3	8.7	38.0
	Cristobalite	99.8	0.2	0.0
1570	Liquid	51.2	4.2	44.6
	Olivine	33.1	10.3	56.6
1570	Liquid	48.6	18.5	32.9
	Olivine	33.5	28.3	38.2
	Cristobalite	99.2	0.8	0.0
1570	Liquid	48.5	18.4	33.1
	Olivine	32.3	24.2	43.5
	Cristobalite	99.4	0.6	0.0
1583	Liquid	50.4	8.0	41.6
	Cristobalite	100	0.0	0.0
1598	Liquid	54.9	11.1	34.0
1600	Liquid	56.3	9.4	34.3
	Cristobalite	99.7	0.3	0.0
1600	Liquid	49.5	20.2	30.3
	Cristobalite	99.1	0.9	0.0
1600	Liquid	49.5	4.7	45.8
	Olivine	32.8	9.5	57.7

Table 6.2 (Continued): Equilibrium phase compositions measured by EPMA in the liquidus region of the MgO–NiO–SiO_2 system for temperatures ranging between 1566 °C and 1650 °C

1600	Liquid	48.1	12.3	39.6
	Olivine	33.5	30.3	36.2
1650	Liquid	58.1	9.4	32.5
	Cristobalite	99.7	0.3	0.0
1650	Liquid	51.9	20.8	27.3
	Cristobalite	99.2	0.8	0.0
1650	Liquid	47.4	25.1	27.5
	Cristobalite	99.1	0.9	0.0

Table 6.3: Equilibrium phase compositions measured by EPMA in the subsolidus region of the MgO–NiO–SiO_2 system for temperatures ranging between 1400 °C and 1546 °C

Temperature, ^oC	**Phases at equilibrium**	**Composition, mol%**		
		SiO_2	**NiO**	**MgO**
1400	Olivine	33.1	0.5	66.4
	Monoxide	0.0	4.3	95.7
1400	Olivine	33.0	0.9	66.1
	Monoxide	0.0	7.6	92.4
1400	Olivine	33.0	1.4	65.6
	Monoxide	0.0	11.3	88.7
1400	Olivine	33.0	2.0	65.0
	Monoxide	0.0	15.2	84.8
1400	Olivine	33.1	2.4	64.5
	Monoxide	0.0	18.8	81.2

Table 6.3 (Continued): Equilibrium phase compositions measured by EPMA in the subsolidus region of the MgO–NiO–SiO_2 system for temperatures ranging between 1400 °C and 1546 °C

1400	Olivine	33.1	2.7	64.2
	Monoxide	0.0	22.9	77.1
1400	Olivine	32.9	10.2	56.9
	Monoxide	0.0	52.0	48.0
1400	Olivine	32.9	24.8	42.3
	Monoxide	0.0	77.9	22.1
1400	Olivine	33.0	50.8	16.2
	Monoxide	0.3	94.0	5.7
1400	Olivine	33.2	1.5	65.3
	Proto-pyroxene	50.2	0.5	49.3
1400	Olivine	33.5	2.9	63.6
	Proto-pyroxene	50.4	1.0	48.6
1400	Olivine	33.1	4.3	62.6
	Proto-pyroxene	50.3	1.6	48.1
1400	Olivine	33.3	5.4	61.3
	Proto-pyroxene	50.2	2.4	47.4
1400	Olivine	33.3	6.4	60.3
	Proto-pyroxene	50.3	3.0	46.7
1400	Olivine	33.2	10.7	56.1
	Proto-pyroxene	49.8	4.6	45.6
	Tridymite	99.9	0.0	0.1
1500	Olivine	33.1	0.5	66.4
	Monoxide	0.0	4.1	95.9

Table 6.3 (Continued): Equilibrium phase compositions measured by EPMA in the subsolidus region of the MgO–NiO–SiO_2 system for temperatures ranging between 1400 °C and 1546 °C

1500	Olivine	33.2	0.9	65.9
	Monoxide	0.0	7.5	92.5
1500	Olivine	33.1	1.4	65.5
	Monoxide	0.0	11.4	88.6
1500	Olivine	33.1	1.9	65.0
	Monoxide	0.0	15.0	85.0
1500	Olivine	33.2	2.4	64.4
	Monoxide	0.0	18.7	81.3
1500	Olivine	33.1	2.9	64.0
	Monoxide	0.1	22.5	77.4
1500	Olivine	33.1	10.9	56.0
	Monoxide	0.0	51.3	48.7
1500	Olivine	33.0	25.6	41.4
	Monoxide	0.2	76.0	23.8
1500	Olivine	33.2	50.1	16.7
	Monoxide	0.1	92.8	7.1
1500	Olivine	33.1	1.3	65.6
	Proto-pyroxene	50.2	0.7	49.1
1500	Olivine	33.2	2.7	64.1
	Proto-pyroxene	50.2	1.3	48.5
1500	Olivine	33.1	3.8	63.1
	Proto-pyroxene	50.1	1.8	48.1

Table 6.3 (Continued): Equilibrium phase compositions measured by EPMA in the subsolidus region of the MgO–NiO–SiO_2 system for temperatures ranging between 1400 °C and 1546 °C

1500	Olivine	33.2	4.8	62.0
	Proto-pyroxene	50.2	2.7	47.1
1500	Olivine	33.1	6.0	60.9
	Proto-pyroxene	50.2	3.4	46.4
1500	Olivine	32.8	10.9	56.3
	Proto-pyroxene	49.9	4.7	45.4
	Tridymite	99.9	0.1	0.0
1519	Olivine	33.2	12.6	54.2
	Cristobalite	99.9	0.1	0.0
1520	Proto-pyroxene	50.1	3.5	46.4
	Cristobalite	99.9	0.1	0.0
1520	Olivine	33.0	10.7	56.3
	Proto-pyroxene	49.9	4.7	45.4
	Cristobalite	99.9	0.1	0.0
1546	Olivine	33.1	10.8	56.1
	Proto-pyroxene	49.8	4.8	45.4
	Cristobalite	99.9	0.1	0.0

6.4 Phases and thermodynamic models

The stable oxide phases present in the MgO–NiO–SiO_2 pseudo-ternary system at ambient pressure are listed in Table 6.4. Cations shown within a set of parentheses occupy the same sublattice in the corresponding solution. The optimized thermodynamic properties of the monoxide solution and silica were reported earlier [51]. Slag, proto-pyroxene and olivine are discussed below.

Table 6.4: Stable oxide phases present in the MgO–NiO–SiO_2 system at ambient pressure

Phase name (space group)	**Formula**	**Notation used in the present study**
Solution phases:		
Slag (liquid oxide)	MgO–NiO–SiO_2	L or Liquid
Monoxide (Fm3m)	(Mg,Ni)O	Monoxide
Olivine (Pbnm)	$(Mg^{2+}, Ni^{2+})^{M2}(Mg^{2+}, Ni^{2+})^{M1}SiO_4$	Olivine
Proto-pyroxene (Pbcn)	$(Mg^{2+}, Ni^{2+})^{M2}(Mg^{2+}, Ni^{2+})^{M1}Si_2O_6$	Ppx
Stoichiometric compounds:		
Low-Quartz or α-Quartz	SiO_2	Qz(low)
High-Quartz or β-Quartz	SiO_2	Qz
High-Tridymite or β-Tridymite	SiO_2	Trid
High-Cristobalite or β-Cristobalite	SiO_2	Crist

6.4.1 Slag (liquid oxide)

The liquid oxide phase is an ionic melt where metal cations are always surrounded by oxygen anions. In other words, there is almost full first-nearest-neighbour short-range ordering (SRO) between cations and anions. Furthermore, there is a strong tendency for second-nearest-neighbour SRO of cations in melts. In particular, basic cations such as Mg form strong second-nearest-neighbour (SNN) pairs with acidic cations such as Si. This is taken into account by the Modified Quasichemical Model [7, 8] which is used in the present study for modeling of the liquid oxide phase. For example, in the binary MgO–NiO and NiO–SiO_2 liquid solutions, the short-range ordering is taken into account by considering the following SNN pair exchange reactions:

$$(\text{Mg-Mg}) + (\text{Ni-Ni}) = 2(\text{Mg-Ni}); \quad \Delta g_{\text{Mg,Ni}} \tag{6.1}$$

$$(\text{Ni-Ni}) + (\text{Si-Si}) = 2(\text{Ni-Si}); \quad \Delta g_{\text{Ni,Si}} \tag{6.2}$$

where (m-n) represents a second-nearest-neighbour pair and Δg_{mn} is the Gibbs energy of the corresponding pair exchange reaction. Let n_m and Z_m be the number of moles and the second-

nearest-neighbor coordination number of component *m*, respectively. The "coordination-equivalent" fractions (Y_m) are then defined as

$$Y_m = Z_m n_m / \sum_i Z_i n_i \tag{6.3}$$

Δg_{mn} is expanded as a polynomial in the "coordination-equivalent" fractions of the components

$$\Delta g_{mn} = \Delta g^{o}_{mn} + \sum_{(i+j)\geq 1} q^{ij}_{mn} Y^i_m Y^j_n \tag{6.4}$$

where Δg^{o}_{mn} and q^{ij}_{mn} are empirical binary coefficients which may be functions of temperature and pressure. These were optimized to describe all available thermodynamic and phase equilibria data in the binary systems [51].

The asymmetric "Toop-like" extrapolation [28] of binary terms into the ternary system is used in order to calculate the Gibbs energy of the ternary liquid, with SiO_2 as the "asymmetric component". Except for the binary terms, the model can have ternary terms, $q_{mn(p)}$, which give the effect of the presence of component *p* upon the energy of pair exchange reaction Δg_{mn}. Ternary terms are also expanded as empirical polynomials containing model parameters. The formulae for ternary terms and for extrapolation of binary and ternary terms into a multicomponent system are discussed in detail elsewhere [28]. In order to reproduce the liquidus data in the MgO–NiO–SiO_2 system, three optimized ternary model parameters were added in the present study.

6.4.2 Compound Energy Formalism (CEF)

The models for the olivine and pyroxene solutions were developed within the framework of the Compound Energy Formalism (CEF) [9]. It is well suited to model solid solutions with two or more distinct sublattices. The Gibbs energy expression per formula unit is

$$G_m = \sum_i \sum_j Y_i^{M2} Y_j^{M1} G_{ij} - TS_c + G_m^E \tag{6.5}$$

where Y_i^{M2} and Y_j^{M1} represent the site fractions of the constituents *i* and *j* on the M2 and M1 sublattices, respectively, G_{ij} is the Gibbs energy of an end-member *ij* of the solution in which the M2 sublattice is occupied only by cation *i* and the M1 sublattice is occupied only by cation *j*, S_c is the configurational entropy assuming random mixing on each sublattice

$$S_c = -R(\sum_i Y_i^{M2} \ln Y_i^{M2} + \sum_j Y_j^{M1} \ln Y_j^{M1}) \quad (6.6)$$

and G_m^E is the excess Gibbs energy,

$$G_m^E = \sum_i \sum_{j>i} \sum_k Y_i^{M2} Y_j^{M2} Y_k^{M1} L_{ij:k} + \sum_i \sum_{j>i} \sum_k Y_k^{M2} Y_i^{M1} Y_j^{M1} L_{k:ij} \quad (6.7)$$

where $L_{ij:k}$ and $L_{k:ij}$ are the interaction energies between cations *i* and *j* on the one sublattice when the other sublattice is occupied by *k*. The dependence of the interaction energies on the composition can be expressed by Redlich-Kister power series:

$$L_{ij:k} = \sum_m {}^m L_{ij:k} (Y_j^{M2} - Y_i^{M2})^m \quad (6.8)$$

$$L_{k:ij} = \sum_m {}^m L_{k:ij} (Y_j^{M1} - Y_i^{M1})^m \quad (6.9)$$

6.4.2.1 Olivine

A complete miscibility exists between the end-members Mg_2SiO_4 and Ni_2SiO_4 in the olivine solid solution.

In natural olivines, $\mathbf{M}_2SiO_4$, Mg is one of the major elements along with Fe, while Ni is a minor component. Cations **M** occupy two distinct octahedral sites, called M1 and M2, where M2 sites are larger than M1. Mg^{2+} and Ni^{2+} cations can occupy both M2 and M1 sites (sublattices) in the olivine structure:

$$\left(Mg^{2+}, Ni^{2+}\right)^{M2} \left(Mg^{2+}, Ni^{2+}\right)^{M1} SiO_4 \quad (6.10)$$

The Gibbs energy of the olivine solution is given by Equation (6.5). According to formula unit (6.10), the Mg-Ni olivine solution has four end-members, the Gibbs energies of which must be defined.

The Gibbs energies of two end-members, G_{MgMg} and G_{NiNi}, are equal to the Gibbs energies of the corresponding stoichiometric compounds, Mg_2SiO_4 and Ni_2SiO_4, which are stable in the binary systems and have the olivine structure. The remaining two end-members, $\left(Mg^{2+}\right)^{M2} \left(Ni^{2+}\right)^{M1} SiO_4$ and $\left(Ni^{2+}\right)^{M2} \left(Mg^{2+}\right)^{M1} SiO_4$, do not exist as real compounds. Two model parameters were introduced to define the Gibbs energies of these end-members. The first parameter,

$K_{\mathrm{MgNi}} = G_{\mathrm{NiMg}} - G_{\mathrm{MgNi}}$, represents the change in the Gibbs energy when the Mg^{2+} and Ni^{2+} cations occupying M2 and M1 sites, respectively, change places. This parameter has a major effect on the cation distribution between M2 and M1 sites in olivine. The second parameter is the Gibbs energy of the reciprocal reaction among end-members: $\Delta_{\mathrm{MgNi:NiMg}} = G_{\mathrm{MgMg}} + G_{\mathrm{NiNi}} - G_{\mathrm{MgNi}} - G_{\mathrm{NiMg}}$. The constant values of the parameters K_{MgNi} and $\Delta_{\mathrm{MgNi:NiMg}}$ were optimized to reproduce all experimental data on olivine, including the cation distribution, thermodynamic properties and phase equilibria. Clearly, G_{MgNi} and G_{NiMg} can be expressed as linear combinations of G_{MgMg}, G_{NiNi}, K_{MgNi} and $\Delta_{\mathrm{MgNi:NiMg}}$.

The effective ionic radii of Mg^{2+} and Ni^{2+} are similar: $r_{Mg^{2+}} = 0.72\,\text{Å}$ and $r_{Ni^{2+}} = 0.69\,\text{Å}$ in octahedral coordination [48]. Hence, the excess Gibbs energy for olivine is expected to be small, if any.

6.4.2.2 Pyroxene

The Gibbs energy of the proto-pyroxene solution is given by Equation (6.5). Mg-Ni proto-pyroxene was optimized within a wider Ca-Mg-Ni proto-pyroxene solution $\left(Ca^{2+}, Mg^{2+}, Ni^{2+}\right)^{M2}\left(Mg^{2+}, Ni^{2+}\right)^{M1}Si_2O_6$. For the Ca-Mg-Ni proto-pyroxene, the Gibbs energies of six end-members must be defined. From the previous optimization [50], G_{MgMg} is equal to the Gibbs energy of the proto-pyroxene modification of the $Mg_2Si_2O_6$ stoichiometric compound, which is stable in the MgO–SiO_2 binary system above about 984 °C. G_{CaMg} was previously optimized by Jung *et al.* [45] for the Ca-Mg proto-pyroxene solution. Similar to $CaMgSi_2O_6$ end-member, G_{CaNi} was set equal to the Gibbs energy of the stoichiometric clino-$CaNiSi_2O_6$, with the enthalpy of transition of clino- to proto-$CaNiSi_2O_6$ equal to that of $CaMgSi_2O_6$.

The thermodynamic properties of the end-member (Ni)(Ni)Si_2O_6 were evaluated as

$$G_{\mathrm{NiNi}} = G(\mathrm{Ni_2SiO_4}, \textit{olivine}) + G(\mathrm{SiO_2}, \textit{tridymite}) + A + B \cdot T \qquad (6.11)$$

where an additional enthalpy term *A* and a small entropy term *B* are the optimized model parameters.

Similar to olivine, two more model parameters were introduced to define the Gibbs energies of the other two end-members. The parameter $K_{\mathrm{MgNi}} = G_{\mathrm{NiMg}} - G_{\mathrm{MgNi}}$ affects mainly the cation distribution between M2 and M1 sites in proto-pyroxene and the second parameter is the Gibbs energy of the reciprocal reaction among end-members: $\Delta_{\mathrm{CaNi:NiMg}} = G_{\mathrm{CaMg}} + G_{\mathrm{NiNi}} - G_{\mathrm{CaNi}} - G_{\mathrm{NiMg}} = 0$. Finally, one excess Gibbs energy parameter equal to that for the Ca-Mg proto-pyroxene solution [45] was introduced due to a big difference of cationic radii of Ca^{2+} and Ni^{2+}, as mentioned above.

6.5 Critical evaluation of experimental data and optimization

The ternary MgO–NiO–SiO_2 system was recently optimized by Woo *et al.* [55]. However, since the time of their optimization the new experimental data appeared in the MgO–NiO–SiO_2 system and its binary subsystems. Some of these data are presented here and the rest – in our previous study [51]. To take into account the new data, reoptimization of the ternary MgO–NiO–SiO_2 system has been performed in this study.

6.5.1 Solid solutions and subsolidus phase equilibria

No ternary stoichiometric compounds were found in the MgO–NiO–SiO_2 system. As can be seen from Figure 6.3, there is an extensive olivine solid solution with complete miscibility between Mg_2SiO_4 and Ni_2SiO_4 that was first reported by Ringwood [89]. The proto-pyroxene solution was reported [109] to have limited solubility of $NiSiO_3$ in $MgSiO_3$.

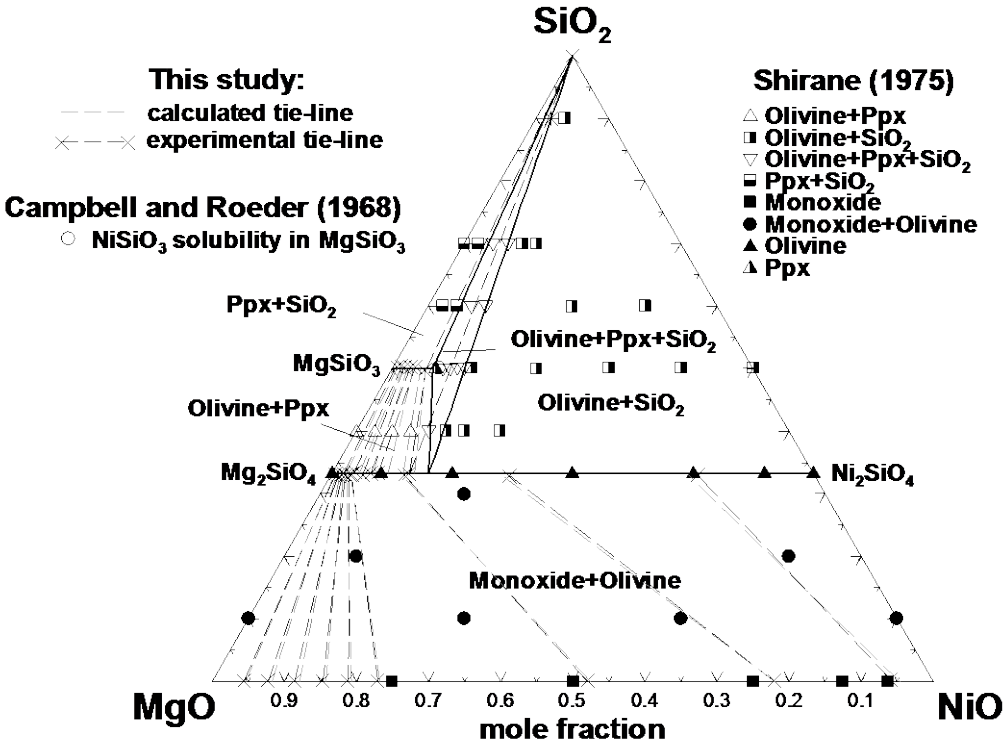

Figure 6.3: Isothermal section of the MgO–NiO–SiO_2 phase diagram at 1400 °C: experimental tie-lines measured in this study, literature data [108, 110], and calculated lines (see Table 6.4 for the phase names)

Experimental data for the MgO–NiO–SiO_2 system include structural [111-119] and thermodynamic data [108, 120, 121] for the olivine solution as well as some phase equilibrium data [87, 89, 93, 108, 110, 122].

The distribution of Mg and Ni between the M1 and M2 sites in olivine was studied repeatedly at temperatures ranging from 500 to 1400 °C [111-119]. Rajamani *et al.* [111] measured the cation occupancies in a synthetic Mg-Ni olivine sample quenched from 1280 °C by single-crystal X-ray analysis. Preferential ordering of Ni cations on the smaller M1 sites and Mg cations on the larger M2 sites was reported, which is shown in Figure 6.4.

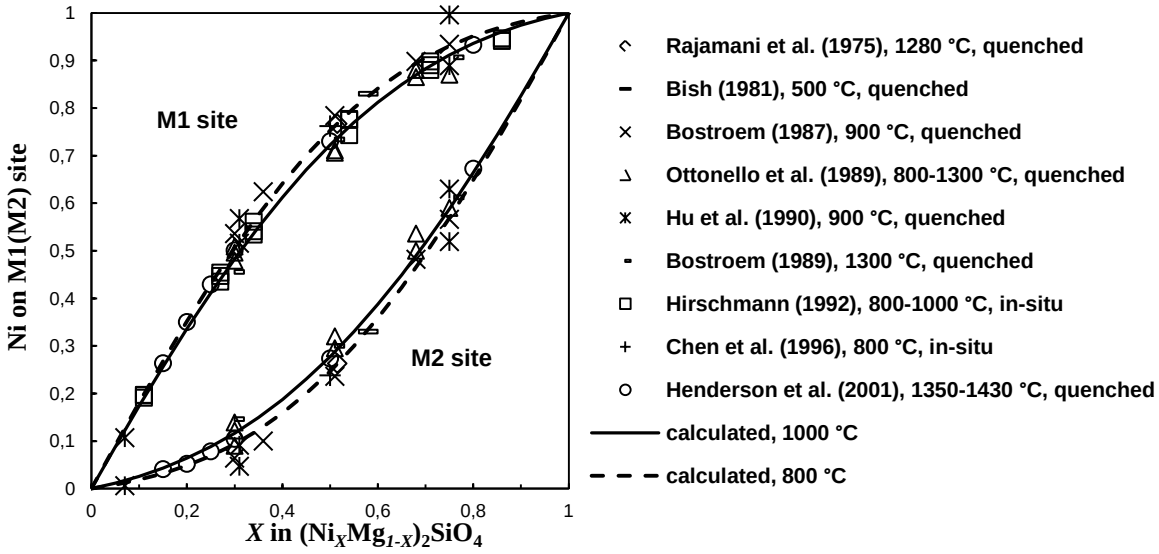

Figure 6.4: Composition dependence of cation ordering in Mg-Ni olivine: experimental points [111-119] and calculated lines

The strong tendency to the cation ordering in Mg-Ni olivine was confirmed in subsequent studies [112-119], where the cation ordering was measured on quenched [112-116] or *in situ* [117-119] samples as a function of composition at specified equilibration temperatures. *In situ* measurements were essential at higher temperatures, when equilibrium distribution of cations could not be retained by quenching.

In the majority of studies [112-115, 119], a single-crystal X-ray diffraction technique was used: Bish [112] studied the olivine solution at 500 °C, Bostroem [113, 114] at 900 and 1300 °C, Ottonello *et al.* [115] from 800 to 1300 °C and Hirschmann [119] at 800, 900, and 1000 °C. Some other techniques were also employed: Hu *et al.* [116] measured the cation ordering at 900 °C by polarized optical absorption spectroscopy and Chen *et al.* [117] used high-pressure powder X-ray diffraction analysis at 800 °C.

Henderson *et al.* [118] used a neutron powder diffraction technique and X-ray absorption spectroscopy to measure both the composition and temperature dependence of the cation ordering (see Figure 6.4 and Figure 6.5). In their *in-situ* experiments shown in Figure 6.5, the samples were initially annealed at high temperature and quenched. The cation distribution was frozen during quenching at about 800 °C. The *in-situ* neutron powder diffraction measurements were then performed on heating and re-ordering started to occur on the time-scale of the experiments at about

700 °C, showing an increase in order compared to the quenched sample. At higher temperature, a decrease in equilibrium order was observed towards a random state. As can be seen from Figure 6.5, most samples quenched from high temperatures show higher degree of order than measured *in-situ*, indicating that the equilibrium cation distribution at the annealing temperature was not quenched but rather it got frozen at about 1000 to 800 °C. Only Ottonello *et al.* [115] managed to quench the cation distribution from higher temperatures. They dropped sealed quartz capillaries containing very small samples in cold water, achieving the temperature drop from 1200 to 500 °C in about 0.5 seconds. Hence, the measurements shown in Figure 6.4 most likely correspond to equilibrium cation ordering at 1000 to 800 °C rather than at the annealing temperatures.

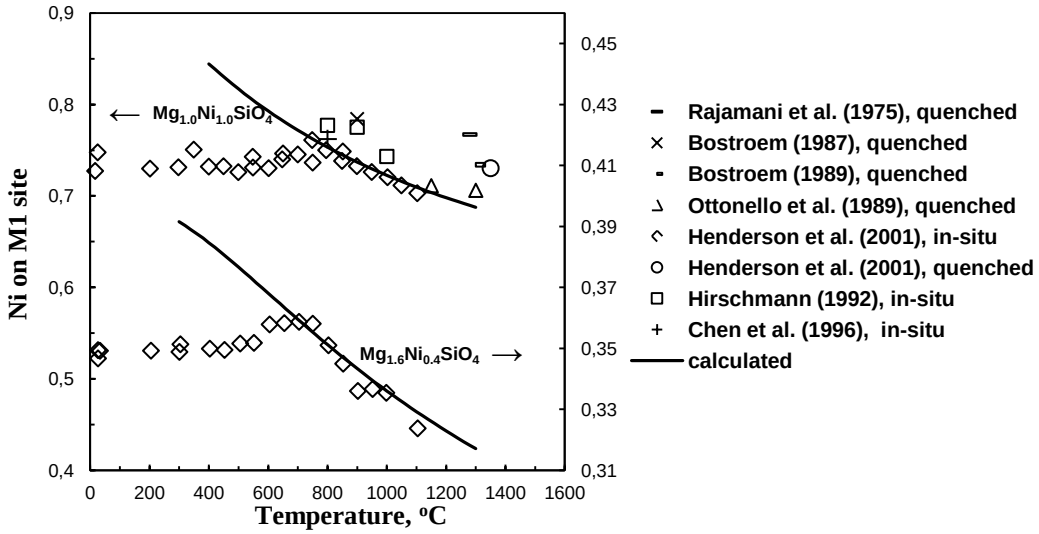

Figure 6.5: Temperature dependence of the cation ordering of Ni on M1 sites in the olivine solutions $Mg_{1.0}Ni_{1.0}SiO_4$ and $Mg_{1.6}Ni_{0.4}SiO_4$: experimental points [111, 113-115, 117-119] and calculated lines

The activity of Ni_2SiO_4 in Mg-Ni olivine was reported in several studies [108, 120, 121]. Essentially, the equilibrium oxygen partial pressure was measured in the three-phase olivine-Ni-SiO_2 region, which made it possible to calculate the activity of Ni_2SiO_4. The results of these studies are shown in Figure 6.6.

Campbell and Roeder [108] used a CO_2/H_2 gas equilibration method at 1400 °C and found the activity of Ni_2SiO_4 in the olivine solution to be nearly ideal. Silica was reported to be in the form of cristobalite, even though tridymite is the stable crystalline form of SiO_2 at this temperature.

Ottonello and Morlotti [120] and Bostroem and Rosen [121] used the EMF technique with calcia-stabilized zirconia electrolyte. The cell reaction in both studies was

$$2Ni(solid) + SiO_2(solid) + O_2 = Ni_2SiO_4(in\ solid\ solution) \quad (6.12)$$

Neither of these authors mentioned the form of silica in their studies. As shown in Figure 6.6, Bostroem and Rosen [121] measured much lower oxygen potentials for olivine in equilibrium with nickel and silica than Ottonello and Morlotti [120] and reported the activity of Ni_2SiO_4 in olivine having slightly negative deviations from ideality at 927 °C and slightly positive deviations at 1127 °C. On the contrary, Ottonello and Morlotti [120] observed large positive deviations from ideality in the temperature range of 716-1188 °C. Their results are inconsistent with the existence of a continuous range of solid solutions between Mg_2SiO_4 and Ni_2SiO_4. The most probable explanation for this inconsistency is the sluggishness of reaction (6.12) and the transport of oxygen through the electrolyte, which became more pronounced at low concentrations of Ni in olivine as the difference in the oxygen pressures on each side of the electrolyte increased [121]. Bostroem and Rosen [121] overcame this difficulty by replacing the Ni(solid) + NiO(solid) + O_2(gas) reference electrode with the CO_2(gas) + CO(gas) + O_2(gas) electrode where the CO/CO_2 ratio was adjusted until the EMF of the sample cell approached zero.

As can be seen from Figure 6.6, the calculated oxygen partial pressures in the olivine-Ni-SiO_2 region are in excellent agreement with the measurements of Campbell and Roeder [108] and Bostroem and Rosen [121]. Using different crystalline forms of SiO_2 in the calculation has a negligible effect on the results.

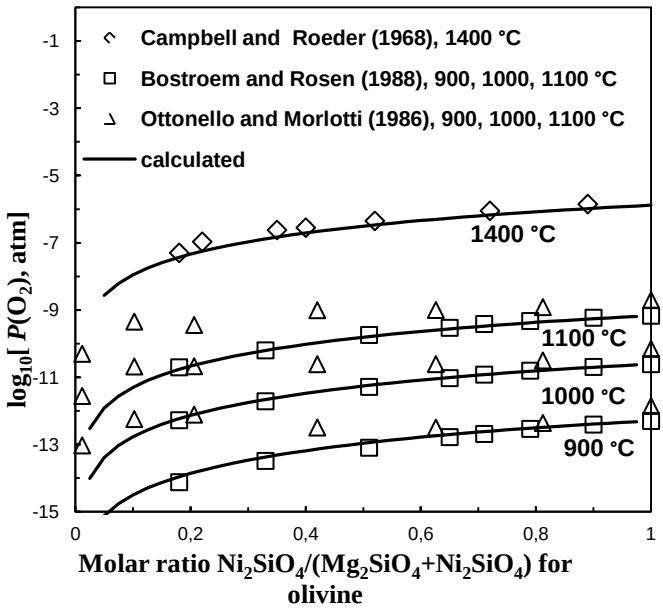

Figure 6.6: Partial pressures of oxygen for olivine in equilibrium with nickel and silica: experimental points [108, 120, 121] and calculated lines

There are no data in the literature on the thermodynamic properties of Mg-Ni proto-pyroxene and on the distribution of Mg and Ni between the M1 and M2 sites in this phase.

The tie-lines between olivine and monoxide and between olivine and proto-pyroxene were measured by Seifert and O'Neill [122], Mukhopadhyay and Jacob [87] and, at higher temperatures, in the present study. All these studies used the quenching method followed by EPMA. The results are shown in Figure 6.7 and Figure 6.8. The calculated lines reproduce well the temperature dependence of the experimental data. As can be seen from Figure 6.8, the calculated lines based on the optimization of Woo *et al.* [55] are almost independent of temperature over the range from 1100 to 1500 °C.

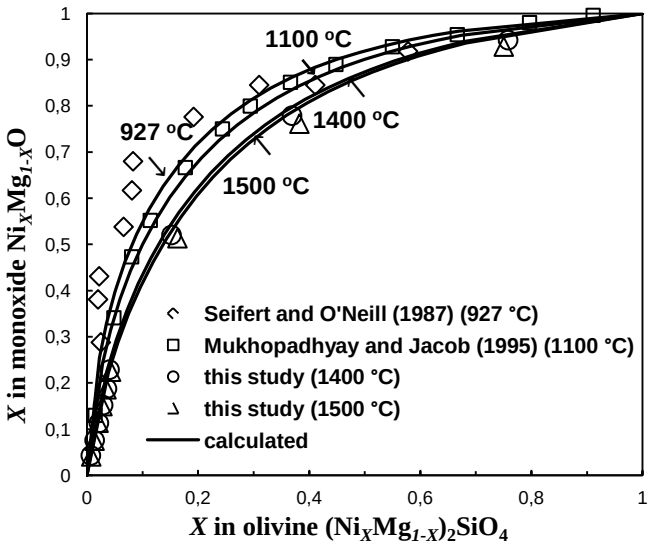

Figure 6.7: Distribution of Ni between $Ni_XMg_{1-X}O$ (monoxide) and $(Ni_XMg_{1-X})_2SiO_4$ (olivine) at several temperatures: experimental points [87, 122] and calculated lines

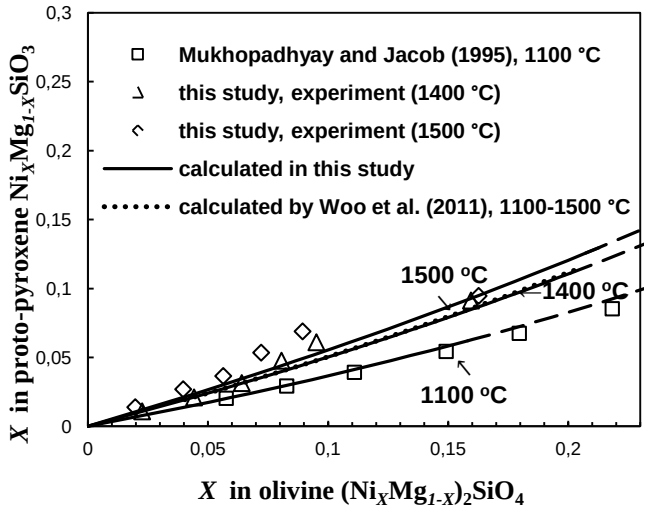

Figure 6.8: Distribution of Ni between $Ni_XMg_{1-X}SiO_3$ (proto-pyroxene) and $(Ni_XMg_{1-X})_2SiO_4$ (olivine) at several temperatures: experimental points [87] and calculated lines. Dashed lines are metastable extrapolations into the proto-pyroxene/olivine/SiO_2 three-phase region

The maximum solubility of $NiSiO_3$ in the proto-pyroxene solution was found to be 9.6 mol% at 1100 °C [87] and 12 mol% [110] or 13 mol% [108] at 1400 °C. This is in disagreement with the data of Grutzeck and Muan [93] that indicate the maximum solubility of less than 6.9 mol% at 1520 °C. To resolve this contradiction, the composition of proto-pyroxene in equilibrium with olivine and SiO_2 was measured by EPMA in the present study (see Table 6.3). The corresponding solubility limit of $NiSiO_3$ in $MgSiO_3$ was obtained to be 9.2 mol% at 1400 °C, 9.4 mol% at 1500 °C and 9.6

mol% at 1546 °C. The maximum solubility of $NiSiO_3$ calculated using the model parameters optimized in the present study is 6.3 mol% at 1100 °C, 11.3 mol% at 1400 °C and 13.0 mol% at 1500 °C, which is lower than reported in studies [87, 108, 110], but a little higher than our EPMA measurements.

Campbell and Roeder [108] measured the oxygen partial pressure at 1400 °C in the equilibrium mixture of four phases: olivine, proto-pyroxene, SiO_2 (cristobalite) and metallic nickel. The experimental value of $10^{-7.45}$ atm is in excellent agreement with $P(O_2) = 10^{-7.33}$ atm calculated from the optimized model parameters.

6.5.2 Phase equilibria with liquid

Phase equilibria involving the liquid phase were reported by Ringwood [89] and Grutzeck and Muan [93], who used a quenching technique in combination with phase identification by optical microscopy and X-ray diffraction. The calculated isothermal sections of the $MgO–NiO–SiO_2$ phase diagram are compared with the results of Grutzeck and Muan [93] and EPMA measurements from the present study in Figure 6.9-Figure 6.12. Only the experimental points that are within ± 5 degrees from the temperature of the calculated isothermal sections are shown in the figures. The reported [93] experimental temperatures are given in brackets.

As can be seen from Figure 6.9 and Figure 6.10, the experimental points [93] corresponding to the cristobalite + olivine and liquid + cristobalite + olivine phase fields suggest somewhat smaller liquid region than the EPMA results from the present study, i.e. the liquid + cristobalite + olivine triangle entirely consistent with the data of Grutzeck and Muan [93] would be shifted to the left from the calculated one. This would be hard to reconcile with the empty circle in Figure 6.10 corresponding to single-phase liquid and suggesting a larger liquid region. Our EPMA measurements show that this particular point is located in the liquid + olivine field.

The liquid + cristobalite point in Figure 6.11 is contradictory to the liquid + cristobalite + olivine and cristobalite + olivine points. Similarly, the liquid + cristobalite + olivine and monoxide + cristobalite + olivine points in Figure 6.12 are inconsistent with the data of the same authors for the binary eutectic in the $NiO–SiO_2$ system, which was reported to be at 1650 °C [93]. The liquid phase field should then expand all the way from the $MgO–SiO_2$ to $NiO–SiO_2$ system, making the liquid + cristobalite + olivine and monoxide + cristobalite + olivine equilibria impossible.

Overall, the phase diagrams calculated using the model parameters optimized in the present study reproduce all available experimental data on solid-liquid phase equilibria within experimental uncertainty. The earlier optimization of Woo *et al.* [55] was based solely on the results of Grutzeck and Muan [93]. Therefore, it gives a smaller liquid region at 1570, 1600 and 1620 °C and is not consistent with our EPMA measurements. It should be noted that it also does not reproduce the liquid + cristobalite + olivine and cristobalite + olivine points of Grutzeck and Muan [93] at 1620 °C. In the present study, the model parameters were optimized with the preference given to the EPMA data because this technique is believed to be more accurate and it provides not only the equilibrium phase assemblage at a particular overall composition, but also the compositions of all phases.

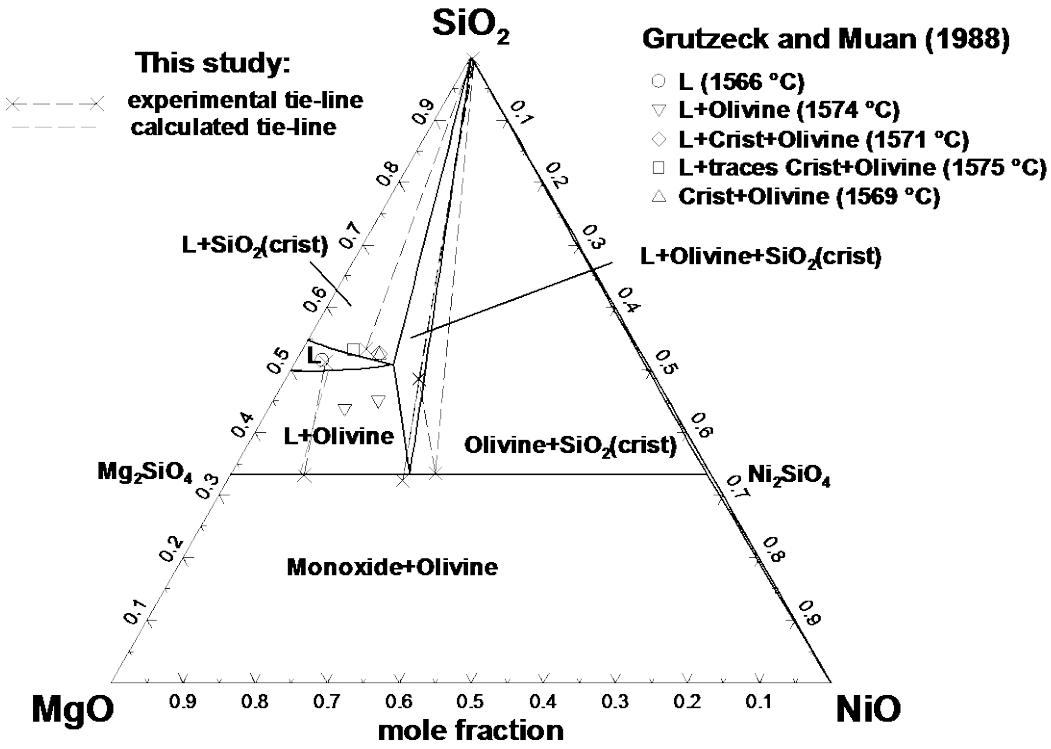

Figure 6.9: Isothermal section of the MgO–NiO–SiO_2 phase diagram at 1570 °C: tie-lines measured in the present study, experimental points [93], and calculated lines (see Table 6.4 for the phase names). Temperatures in brackets are the actual temperatures at which experiments of Grutzeck and Muan [93] were made

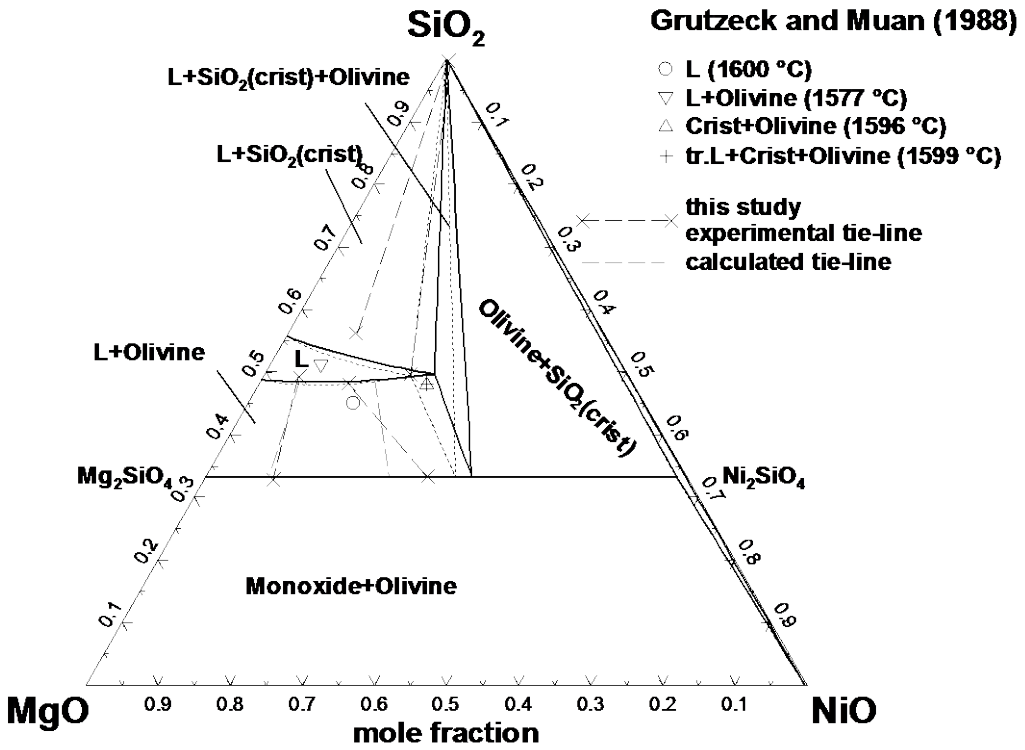

Figure 6.10: Isothermal section of the MgO–NiO–SiO_2 phase diagram at 1600 °C: tie-lines measured in the present study, experimental points [93], and calculated lines (see Table 6.4 for the phase names). Temperatures in brackets are the actual temperatures at which experiments of Grutzeck and Muan [93] were made. Phase boundaries calculated using the optimization of Woo *et al.* [55] are shown by short-dashed lines

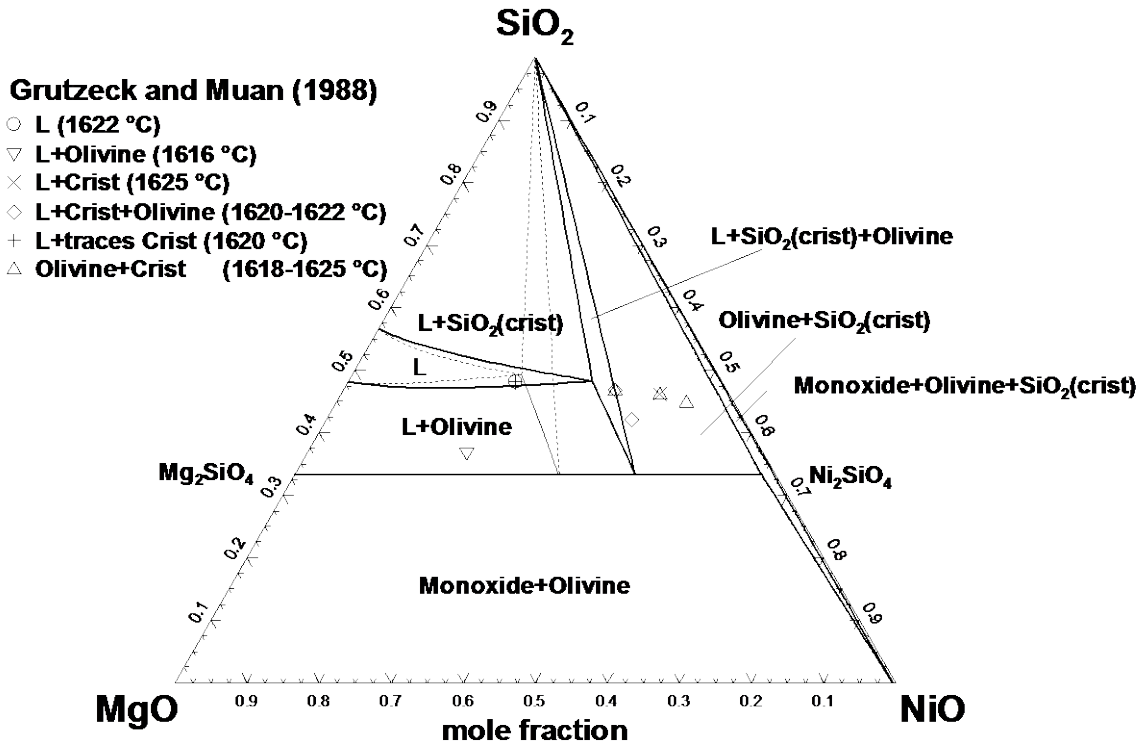

Figure 6.11: Isothermal section of the MgO–NiO–SiO_2 phase diagram at 1620 °C: experimental points [93] and calculated lines (see Table 6.4 for the phase names). Temperatures in brackets are the actual temperatures at which experiments of Grutzeck and Muan [93] were made. Phase boundaries calculated using the optimization of Woo *et al.* [55] are shown by short-dashed lines

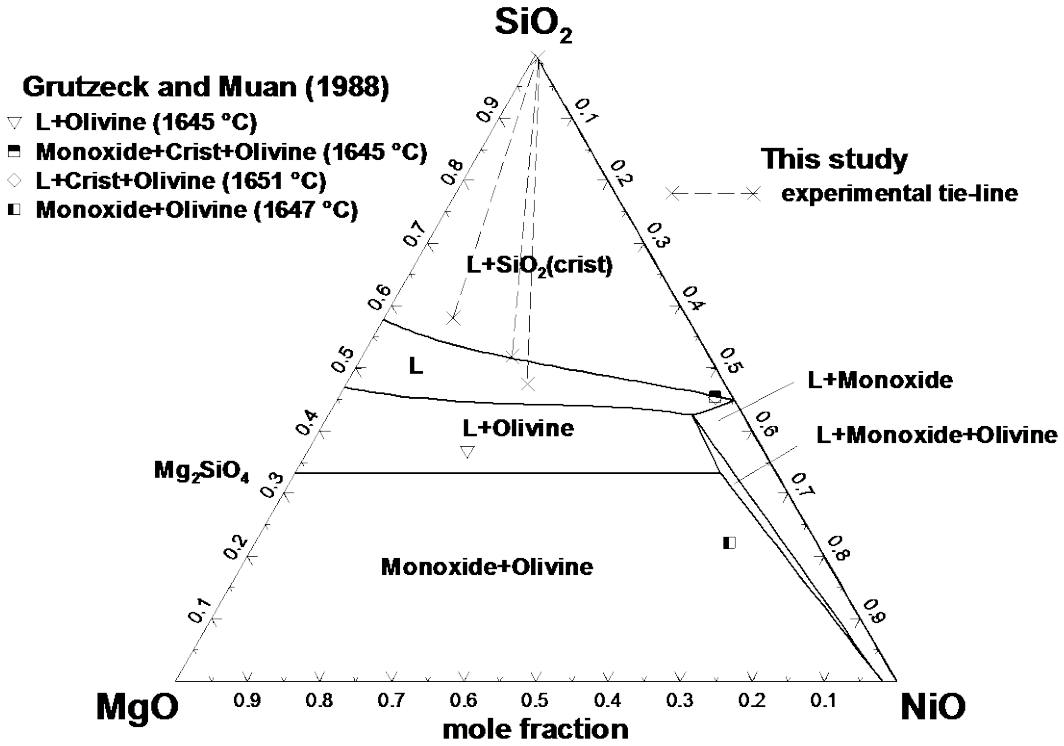

Figure 6.12: Isothermal section of the MgO–NiO–SiO_2 phase diagram at 1650 °C: tie-lines measured in the present study, experimental points [93], and calculated lines (see Table 6.4 for the phase names). Temperatures in brackets are the actual temperatures at which experiments of Grutzeck and Muan [93] were made

Two eutectic points deduced by Grutzeck and Muan [93] from their quenching experiments are compared with the calculated eutectics in Table 6.5.

Table 6.5: Experimental and calculated eutectic points in the MgO–NiO–SiO_2 system

Invariant equilibria		**Temperature, °C**	**Mole fractions**		
			SiO_2	**MgO**	**NiO**
L→ppx+olivine+crist	Experimental [93]	1547	0.526	0.418	0.056
	Calculated	1540	0.517	0.412	0.071
L→monoxide+olivine+crist	Experimental [93]	1633	0.450	0.017	0.534
	Calculated	1636	0.450	0.021	0.529

Ringwood [89] studied phase equilibria along the orthosilicate Mg_2SiO_4-Ni_2SiO_4 section of the MgO–NiO–SiO_2 phase diagram. His data are compared with the calculated phase diagram in Figure

6.13. The agreement is within experimental accuracy, considering that temperature was measured by an optical pyrometer with the precision not better than ± 20 degrees and that Ringwood mentioned some difficulties with quenching and distinguishing between devitrified liquid and crystals of equilibrium solid phases. Furthermore, the decomposition temperature of pure Ni_2SiO_4 shown in the calculated phase diagram is in agreement with the results of several studies as discussed earlier [51], whereas Ringwood [89] reported that Ni_2SiO_4 is still stable about 80 degrees above this temperature.

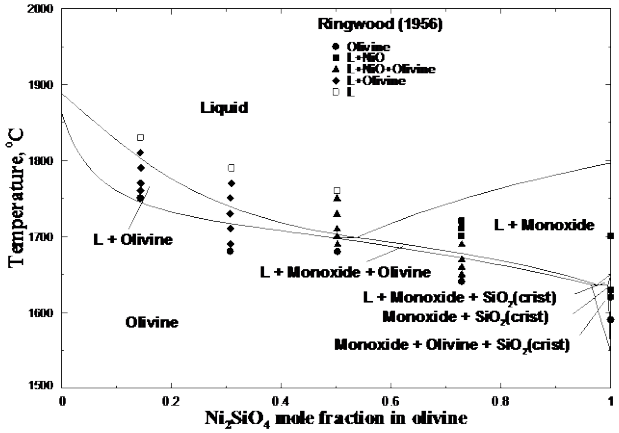

Figure 6.13: Phase diagram of the Mg_2SiO_4–Ni_2SiO_4 orthosilicate section: experimental points [89] and calculated lines

6.5.3 Optimization

Parameters of the models described in Section 6.4 were optimized to reproduce all available experimental data. All optimized parameters are given in Table 6.6.

Table 6.6: Optimized model parameters for the slag, olivine and proto-pyroxene phases in the MgO–NiO–SiO_2 system ($J \cdot mol^{-1}$)*

Slag (liquid oxide) MgO-NiO-SiO_2

$Z_{Mg} = Z_{Ni} = 1.3774,\ Z_{Si} = 2.7549$

$q^{001}_{Ni,\,Si\,(Mg)} = -39748, \quad q^{001}_{Mg,\,Si\,(Ni)} = 16736, \quad q^{001}_{Mg,\,Ni\,(Si)} = -58576$

The following parameters are taken from study [50]:

$\Delta g^{\circ}_{Mg,Si} = -86089,\ q^{01}_{Mg,Si} = -48972 + 37.6558 \cdot T,\ q^{07}_{Mg,Si} = 328105 - 125.519 \cdot T$

The asymmetric "Toop-like" extrapolation [28] of binary terms into the ternary system was used (silica – asymmetric component).

Olivine (orthosilicate solution) $(Mg^{2+}, Ni^{2+})^{M2}(Mg^{2+}, Ni^{2+})^{M1}SiO_4$

$G_{NiNi} = G(Ni_2SiO_4)$ [51]

$K_{MgNi} = G_{NiMg} - G_{MgNi} = 22677.3$

$\Delta_{MgNi:NiMg} = G_{MgMg} + G_{NiNi} - G_{MgNi} - G_{NiMg} = -5439.2$

$G_{MgMg} = G(Mg_2SiO_4,\ forsterite)$ is taken from [50].

Proto-pyroxene $(Ca^{2+}, Mg^{2+}, Ni^{2+})^{M2}(Mg^{2+}, Ni^{2+})^{M1}Si_2O_6$

$G_{NiNi} = G(Ni_2Si_2O_6) = G(Ni_2SiO_4, olivine) + G(SiO_2, tridymite) + 14112.6 - 4.184 \cdot T$

$G_{CaNi} = G^{o}(CaNiSi_2O_6,\ proto\text{-}) = G^{o}(CaNiSi_2O_6, clino\text{-}) + 17071.2;$

G_{CaMg} is taken from [45];

$K_{MgNi} = G_{NiMg} - G_{MgNi} = -25104;$

$\Delta_{CaNi:NiMg} = G_{CaMg} + G_{NiNi} - G_{CaNi} - G_{NiMg} = 0.$

The enthalpy of transition of $CaNiSi_2O_6$ from proto- to clino-structure was set equal to that for $CaMgSi_2O_6$ [45].

*The optimized thermodynamic properties of NiO, other stoichiometric compounds and the monoxide and liquid solutions in the MgO-NiO and NiO-SiO_2 binary systems were reported in our previous study [51].

First, the thermodynamic properties of the olivine solid solution were described using two model parameters. The distribution of cations between M1 and M2 sites shown in Figure 6.4 and Figure 6.5

is affected mainly by the K_{MgNi} parameter. The first approximation for the $\Delta_{\mathrm{MgNi:NiMg}}$ parameter was zero, but in the final optimization a small negative value was optimized to reproduce better the experimental data shown in Figure 6.6 and Figure 6.7.

Then, the thermodynamic properties of the proto-pyroxene solution were optimized. The distribution of cations between M1 and M2 sites in proto-pyroxene has to be estimated because of the lack of experimental data. Woo *et al.* [55] assumed that the cations are randomly distributed between M1 and M2 sites, i.e. there is no preferential ordering of Mg or Ni to a particular octahedral sublattice. In the present study, it was assumed that the distribution of Ni between M1 and M2 sites in the Mg-Ni proto-pyroxene solution is similar to that of Fe in the Mg-Fe ortho-pyroxene solution. The latter was optimized by Jung *et al.* [46] using available experimental data (see Figure 8 of their study). The composition dependence of the cation distributions in both pyroxenes is shown in Figure 6.14. For Mg-Ni proto-pyroxene, the model parameter K_{MgNi} was optimized to describe the estimated cation distribution. Parameters *A* and *B* in the Gibbs energy expression for the end-member $(\mathrm{Ni})(\mathrm{Ni})\mathrm{Si_2O_6}$ were optimized to fit subsolidus phase equilibria, in particular the ones shown in Figure 6.3 and Figure 6.8. The Gibbs energy of the reciprocal reaction among the proto-pyroxene end-members, $\Delta_{\mathrm{CaNi:NiMg}} = G_{\mathrm{CaMg}} + G_{\mathrm{NiNi}} - G_{\mathrm{CaNi}} - G_{\mathrm{NiMg}} = 0$, was assumed to be equal to zero.

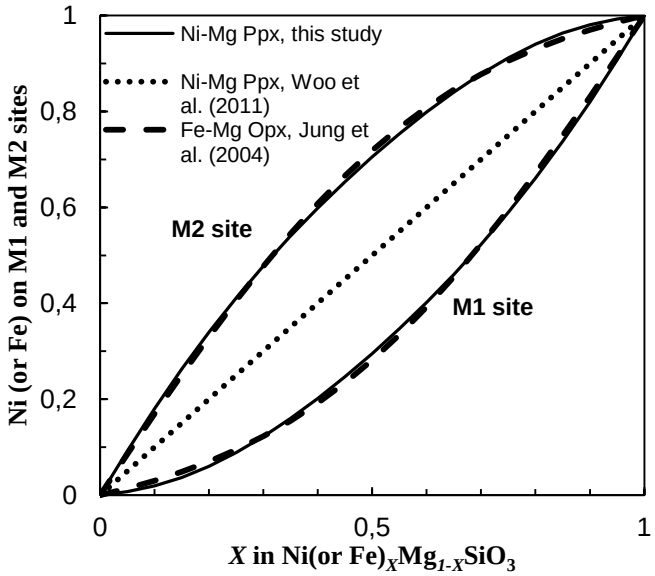

Figure 6.14 : Composition dependence of the cation ordering in Mg-Ni proto-pyroxene and Mg-Fe ortho-pyroxene (Opx) at 800 °C

Finally, three ternary model parameters for the liquid phase were optimized to reproduce the liquidus data of Ringwood [89], Grutzeck and Muan [93], and those obtained in the present study. The most representative experimental data are shown in Figure 6.9-Figure 6.13 and the calculated liquidus projection is given in Figure 6.15.

As can be seen from Figure 6.3-Figure 6.13, the experimental data are reproduced within experimental error limits. All other available experimental points that are not shown in the figures are described equally well.

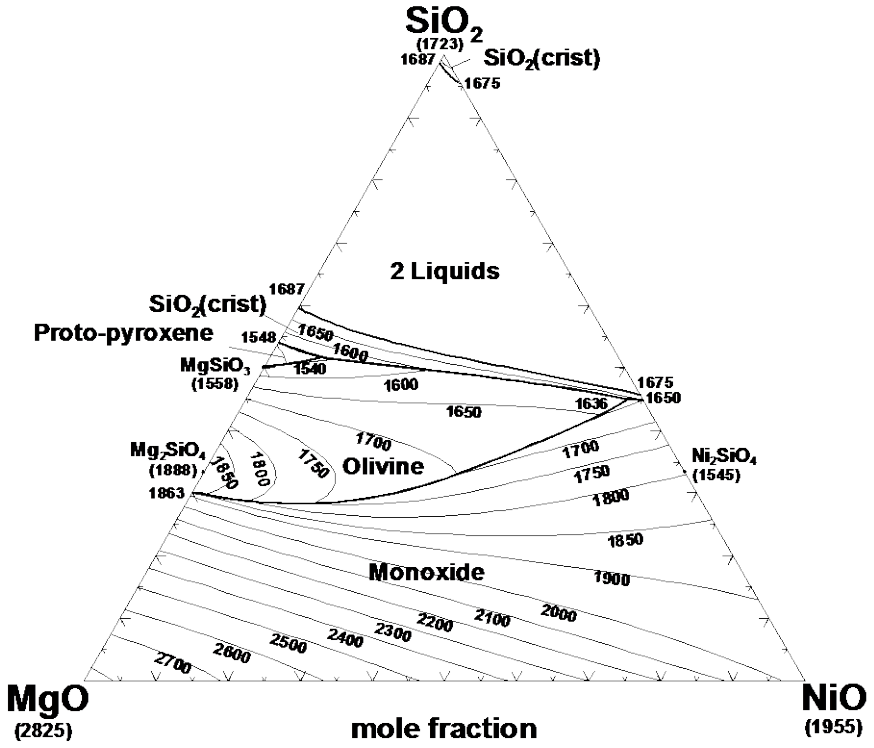

Figure 6.15 : Calculated liquidus projection of the MgO–NiO–SiO_2 phase diagram. Temperatures are in °C, phase names are given in Table 6.4

6.6 Conclusion

The present study forms a basis for development of a thermodynamic database that can be used for simulation of nickel extraction from ores. The MgO–NiO–SiO_2 system has been studied by a combination of critical assessment of the experimental data from the literature, thermodynamic modeling and experimental measurements of phase equilibria at selected compositions which, on the

one hand, can be done most accurately and efficiently and, on the other hand, provide the most important data for thermodynamic modeling.

In particular, tie-lines olivine/monoxide, olivine/proto-pyroxene, liquid/olivine and liquid/cristobalite have been measured to complement the literature data and to resolve some contradictions. The experimental investigation has been carried out over the temperature range from 1400 to 1650 °C using an equilibration and quenching technique followed by EPMA.

The parameters of thermodynamic models for the oxide phases were optimized to reproduce simultaneously the experimental results from the present study and all thermodynamic and phase diagram data for the MgO–NiO–SiO_2 system from the literature. A set of self-consistent Gibbs energy functions was obtained that provides the best possible description of thermodynamic properties and phase equilibria in this system. All available data are reproduced within experimental uncertainties.

CHAPTER 7 THERMODYNAMIC OPTIMIZATION OF THE QUATERNARY CaO–MgO–NiO–SiO_2 OXIDE SYSTEM AND ITS TERNARY SUBSYSTEMS CaO–NiO–SiO_2 AND CaO–MgO–NiO

Equation Chapter (Next) Section 1A combination of experimental investigation and thermodynamic modeling was applied to investigate the quaternary CaO–MgO–NiO–SiO_2 system and its ternary subsystems CaO–MgO–NiO and CaO–NiO–SiO_2. A complete literature review, critical evaluation and thermodynamic modeling of phase diagrams and thermodynamic properties of all oxide phases in these chemical systems at 1 atm total pressure are presented. The literature review and initial model calculations revealed contradictions in the available phase equilibrium data for the CaO–NiO–SiO_2 system. To resolve them, the experimental measurements were carried out by our colleagues from PyroSearch, Australia, including the high temperature equilibration in controlled gas atmospheres, rapid quenching and direct measurement of quenched samples with electron probe X-ray microanalysis (EPMA). The liquid oxide – solid oxides (i.e. wollastonite, silica, olivine, pyroxene) tie-lines have been measured over the temperatures from 1330 to 1500 °C. The newly obtained data in combination with previously available data were taken into consideration in the final stage of thermodynamic modeling. The Modified Quasichemical Model was used for modeling of the slag phase. The models based on the Compound Energy Formalism were developed for olivine, melilite and pyroxene solid solutions. Using the obtained self-consistent set of model parameters, significant predictions of phase equilibria in the CaO–MgO–NiO–SiO_2 system were made.

7.1 Background

This study is part of a broader research project to develop a thermodynamic database for simulation of nickel extraction from laterite ores by the joint effort of experimental measurements and thermodynamic modeling. This approach greatly increases the effectiveness of the overall program by reducing the amount of the required experimental work and providing specific experimental data for thermodynamic modeling.

Laterite ore deposits consist of heterogeneous mixtures of hydrated iron oxides and hydrous magnesium silicates [13]. The basis of the laterite ore is olivine $(Fe,Mg)_2SiO_4$, which often contains small amounts of nickel due to the proximity of ionic radii of Fe^{2+}, Mg^{2+} and Ni^{2+}. The nickel

recovery from laterite ores can be significantly increased if reliable thermodynamic calculations in the Al–Ca–Cr–Fe–Mg–Ni–O–Si system can be performed.

In the course of this project, initially, the binary systems NiO–CaO, NiO–MgO and NiO–SiO_2 were optimized [51]. Further, the optimization of the MgO–NiO–SiO_2 system was made by the present authors [123] that provided a basis for the current study.

Initially, the parameters of the models for all oxide phases were optimized to fit available experimental data collected from the literature. The initial calculations revealed shortage of experimental data in the liquidus region of the CaO–NiO–SiO_2 system: although this region was investigated by several authors [124, 125], it was difficult to constrain the temperature dependence of model parameters for the liquid phase. Therefore, experimental measurements were carried out to provide specific data for thermodynamic modeling by our colleagues from PyroSearch, Australia. The experimental technique involved equilibration and ultra rapid quenching followed by electron probe X-ray microanalysis (EPMA) of quenched samples. The experimental results of the present study, along with the literature data, were taken into account in the subsequent optimization of all oxide phases in the CaO–MgO–NiO–SiO_2 system and its ternary subsystems CaO–NiO–SiO_2 and CaO–MgO–NiO at 1 atm total pressure.

In a thermodynamic “optimization” of a system, all available thermodynamic and phase diagram data are evaluated simultaneously in order to obtain one set of model equations for the Gibbs energies of all phases as functions of temperature and composition. From these equations, all of the thermodynamic properties and the phase diagrams can be back-calculated. In this way, all the data are rendered self-consistent and consistent with thermodynamic principles. Thermodynamic property data, such as activity data, can aid in the evaluation of the phase diagram, and phase diagram measurements can be used to deduce thermodynamic properties. Discrepancies in the available data can often be resolved, and interpolations and extrapolations can be made in a thermodynamically correct manner. A small set of model parameters is obtained. This is ideal for computer storage and calculation of properties and phase diagrams. In the present study, all calculations were carried out using the FactSage thermochemical software and databases [1].

7.2 Experimental

7.2.1 Preparation of oxide mixtures

The starting mixtures were made from CaO (99.98 wt% purity), NiO (99.99 wt% purity), SiO_2 (99.98 wt% purity) supplied by Sigma-Aldrich Co. Mixtures of selected bulk compositions were prepared by weighing the high purity powders and mixing them thoroughly using an agate mortar and pestle. The initial compositions of the mixtures were selected to have two or more phases in equilibrium. Each mixture was then compacted with pressure of 40 MPa to produce a pellet weighing less than 0.2 gram. 10 mm x 12 mm envelopes made from 0.025 mm-thick platinum foil supplied by AGR Metthey were used as sample containers. It was found that platinum was inert to the sample materials under the conditions of the investigation so there was no contamination of the samples.

7.2.2 High temperature equilibration technique

All equilibration experiments were conducted in a vertical reaction tube (impervious re-crystalized alumina, 30-mm i.d.) in electrical resistance heated furnaces with silicon carbide (SiC) elements. The sample was introduced from the bottom of the vertical tube furnace and suspended by a sample holder constructed using Pt wire. The 30-mm i.d. re-crystallized alumina reaction tube was preconditioned at the target temperature for more than 5 minutes, and the specimen was then raised into the uniform temperature hot zone of the furnace.

For measurements of phase equilibria involving the liquid phase, pre-melting of the sample was carried out by increasing the temperature 25 °C above the target temperature. After 30 minutes of pre-melting, the temperature of the furnace was decreased back to the target temperature and the sample was equilibrated inside the furnace for at least 24 hours.

After the equilibration, the specimen was rapidly quenched by dropping it directly into iced water. The quenched sample was dried on a hot plate, crushed into smaller pieces, which were mounted in epoxy resin, polished using conventional metallographic polishing techniques and carbon coated for subsequent electron probe X-ray micro-analysis (EPMA).

7.2.3 Control of temperature

To monitor the actual temperature surrounding the sample, a working thermocouple was placed in a re-crystallised alumina thermocouple sheath immediately adjacent to the sample. The working thermocouple was calibrated against a standard thermocouple (supplied by the National Measurement Institute of Australia, NSW, Australia). The temperature of the experiment was continuously controlled within ± 1 °C of the target temperature. It is estimated that the overall absolute temperature accuracy of the experiment is ± 5 °C.

7.2.4 Analysis technique and representation of systems

The rapid quenching technique successfully retained the liquid slag as a homogenous glassy phase. The compositions of various phases were measured using JEOL 8200L EPMA with wavelength dispersive detectors (JEOL is a trademark of Japan Electron Optics Ltd., Tokyo). A 15-kV accelerating voltage and 15 nA probe current were selected for the micro-analyzer operation. The standards (Charles M. Taylor, Stanford, CA) used in the EPMA measurements were as follows: wollastonite ($CaSiO_3$) for Ca and Si and Ni olivine (Ni_2SiO_4) for Ni. The Duncumb–Philibert correction based on atomic number, absorption, and fluorescence (ZAF correction, supplied by JEOL) was applied. The compositions were measured with an accuracy of 1 wt. %.

The fact that compositions of phases are measured after rather than before the experiment make the accuracy of results independent from the changes of bulk composition during the experiment provided the achievement of equilibrium between phases is confirmed. The results therefore are not affected by interaction with the containment material (crucible, substrate), vaporization of some elements during equilibration and uncertainties in the initial mixture composition. Moreover, this independence from the changes in bulk composition enables the extension of the technique to the gas/metal (or matte)/slag/solid(s) systems as well as to the use of the substrate or levitation techniques. The small size of the liquid slag phase used in the suspension technique (down to the several micron liquid film) enhances achievement of a) equilibrium of condensed phases as well as b) high quenching rates (as the liquid contacts quenching media first without crucible interference), thus extending the applications to the systems where these factors are the limitations for research, such as Ca-ferrite slag and slag/matte systems.

The compositions of all phases at equilibrium are measured, enabling the determination not only of liquid compositions, but, importantly, the compositions of solid solutions coexisting with these liquids. The crystal phases are reliably identified from their compositions.

7.2.5 Assessment of achievement of equilibrium

Confirmation of the achievement of equilibria has always been one of the most important questions in experimental phase equilibrium studies. The key tests to ensure the achievement equilibrium include:

1. Changing the equilibration time to confirm that no further changes take place as the time is increased.

2. Confirming the chemical homogeneity of each of the phases.

3. Approaching equilibrium from different directions followed by analysis of the results.

4. Analyzing possible reactions taking place during equilibration, application of the available analytical techniques looking for possible signs of incomplete reaction pathways during equilibration. SEM imaging and EPMA analysis of the trends of the compositions across the phases used in the present series of studies are particularly effective in this analysis.

In the present study, selected experiments were carried out at different times to determine the minimum time required to attain equilibrium.

The uniformity of phase compositions across sample was checked by EPMA. Six sampling points were selected for each phase. The samples were re-crushed and re-equilibrated if variations within one single phase were found greater than 1 wt. %.

7.3 Experimental results

Experiments in the CaO–NiO–SiO_2 system were conducted in air at $P(O_2)$ = 0.21 atm from 1330 to 1500 °C. Examples of typical microstructures of these samples after equilibration are shown in Figure 7.1.

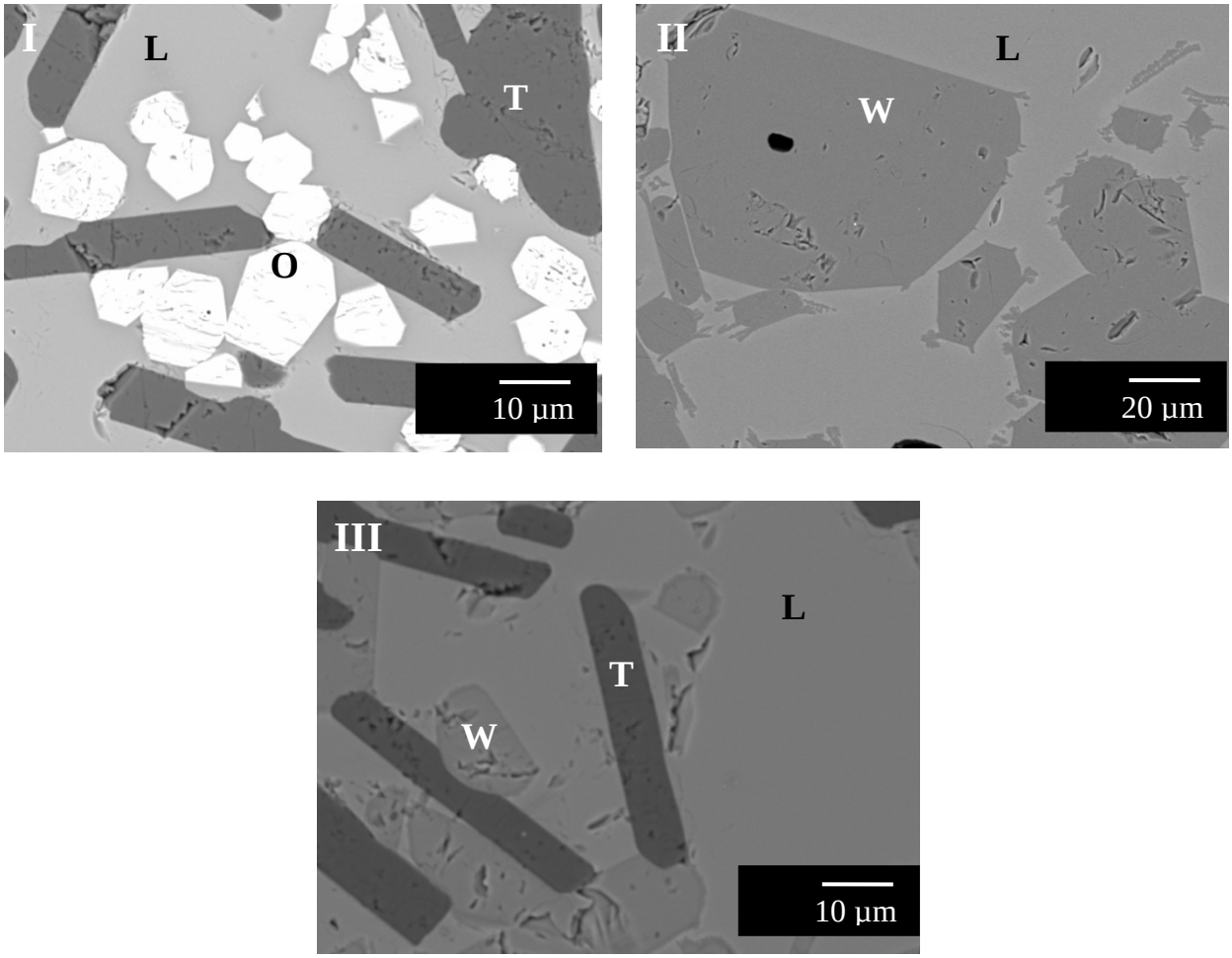

Figure 7.1: Backscattered SEM micrographs typical of the equilibrated CaO–NiO–SiO_2 system (I) Liquid (L), Olivine (O) and Tridymite (T) at 1370 °C in air; (II) Liquid (L) and wollastonite (W) at 1400 °C in air; (III) Liquid (L), Tridymite (T) and Wollastonite (W) at 1390 °C in air

The equilibrated phases were found to have good contact with each other and a dense structure was obtained which suggested a well equilibrated process. A homogenous glassy (liquid) phase was obtained indicating the liquid was well quenched; the composition of each phase was found to be uniform and within standard deviation of 1wt.% measured by EPMA.

The compositions of the phases in the equilibrated samples, as measured by EPMA, are presented in Table 7.1.

Table 7.1: Equilibrium phase compositions measured by EPMA in the system CaO–NiO–SiO_2 in air for temperatures ranging from 1330 to 1500 °C

Temperature, °C	**Phase at equilibrium**	**Composition, mol%**		
		SiO_2	**CaO**	**NiO**
1330	Olivine	33.6	0.2	66.2
	Tridymite	99.0	0.1	0.9
	Pyroxene	50.4	25.0	24.6
1350	Olivine	33.6	0.3	66.1
	Tridymite	99.2	0.1	0.7
	Pyroxene	50.5	24.6	24.9
1370	Liquid	56.2	26.7	17.1
	Olivine	33.7	0.6	65.7
	Tridymite	99.3	0.1	0.6
1360	Liquid	59.3	31.3	9.4
	Wollastonite	49.8	50.0	0.2
	Tridymite	99.4	0.3	0.4
1390	Liquid	58.4	35.4	6.2
	Wollastonite	49.9	50.0	0.1
	Tridymite	99.8	0.1	0.1
1360	Liquid	52.3	33.2	14.5
	Wollastonite	50.1	49.8	0.1
1390	Liquid	53.6	34.0	12.4
	Wollastonite	49.9	50.1	0.0
1400	Liquid	49.8	37.6	12.6
	Wollastonite	49.8	50.1	0.1

Table 7.1 (Continued): Equilibrium phase compositions measured by EPMA in the system CaO–NiO–SiO_2 in air for temperatures ranging from 1330 to 1500 °C

1450	Liquid	50.3	41.2	8.5
	Wollastonite	49.7	50.2	0.1
1500	Liquid	50.4	45.0	4.6
	Wollastonite	50.0	49.9	0.1

7.4 Phases and thermodynamic models

The stable oxide phases present in the CaO–MgO–NiO–SiO_2 quaternary system are listed in Table 7.2, along with the corresponding formulas and notations used in the article. Cations shown within a set of parentheses occupy the same sublattice in the corresponding solution. The thermodynamic properties of wollastonite, α-Ca_2SiO_4 and α'-Ca_2SiO_4 solution phases as well as stoichiometric compounds were optimized earlier by Jung *et al.* [45]. Slag, monoxide, olivine, melilite and pyroxenes are discussed below.

Table 7.2: Solution phases and stoichiometric compounds present in the CaO–MgO–NiO–SiO_2 system

Phase name	**Formula**	**Notation used in this study**
Solution phases:		
Slag (liquid oxide)	CaO–MgO–NiO–SiO_2	L or Liquid
Monoxide (solid oxide)	CaO–MgO–NiO	Monoxide
Olivine	$(Ca^{2+}, Mg^{2+}, Ni^{2+})^{M2}(Ca^{2+}, Mg^{2+}, Ni^{2+})^{M1}SiO_4$	Olivine
Clino-pyroxene (C2/c, monoclinic)	$(Ca^{2+}, Mg^{2+}, Ni^{2+})^{M2}(Mg^{2+}, Ni^{2+})^{M1}Si_2O_6$	Cpx
Proto-pyroxene (Pbcn, orthorhombic)	$(Ca^{2+}, Mg^{2+}, Ni^{2+})^{M2}(Mg^{2+}, Ni^{2+})^{M1}Si_2O_6$	Ppx
Wollastonite	$(Ca^{2+}, Mg^{2+})SiO_3$	Woll
α-Ca_2SiO_4	$(Ca^{2+}, Mg^{2+})_2SiO_4$	a-Ca_2SiO_4
α'-Ca_2SiO_4	$(Ca^{2+}, Mg^{2+})_2SiO_4$	a'-Ca_2SiO_4

Table 7.2 (Continued): Solution phases and stoichiometric compounds present in the CaO–MgO–NiO–SiO_2 system

Melilite	$Ca_2(Mg^{2+}, Ni^{2+})Si_2O_7$	
Stoichiometric compounds:		
Akermanite	$Ca_2MgSi_2O_7$	
Merwinite	$Ca_3MgSi_2O_8$	
Pseudo-wollastonite	$CaSiO_3$	P-woll
Hatrurite	Ca_3SiO_5	
Rankinite	$Ca_3Si_2O_7$	
Silica (quartz, tridymite, cristobalite)	SiO_2	qz, trid, crist

7.5 Slag (liquid oxide)

The liquid oxide phase is an ionic melt where metal cations are always surrounded by oxygen anions. In other words, there is almost full first-nearest-neighbour short-range ordering (SRO) between cations and anions. Furthermore, there is a strong tendency for second-nearest-neighbour SRO of cations in melts. In particular, basic cations such as Mg form strong second-nearest-neighbour (SNN) pairs with acidic cations such as Si. This is taken into account by the Modified Quasichemical Model [7, 8], which is used in the present study for modeling of the liquid oxide phase. In the binary CaO–NiO, MgO–NiO and NiO–SiO_2 liquid solutions, the short-range ordering is modeled by considering the following SNN pair exchange reactions, respectively:

$$(\text{Ca-Ca}) + (\text{Ni-Ni}) = 2(\text{Ca-Ni}); \quad \Delta g_{\text{Ca,Ni}} \tag{7.1}$$

$$(\text{Mg-Mg}) + (\text{Ni-Ni}) = 2(\text{Mg-Ni}); \quad \Delta g_{\text{Mg,Ni}} \tag{7.2}$$

$$(\text{Ni-Ni}) + (\text{Si-Si}) = 2(\text{Ni-Si}); \quad \Delta g_{\text{Ni,Si}} \tag{7.3}$$

where (m-n) represents a second-nearest-neighbour pair and Δg_{mn} is the Gibbs energy of the corresponding pair exchange reaction. Let n_m and Z_m be the number of moles and the coordination number of component *m*, respectively. The "coordination-equivalent" fractions (Y_m) are then defined as

$$Y_m = Z_m n_m / \sum_i Z_i n_i \tag{7.4}$$

Δg_{mn} is expanded as a polynomial in the "coordination-equivalent" fractions of the components

$$\Delta g_{mn} = \Delta g^{o}_{mn} + \sum_{(i+j)\geq 1} q^{ij}_{mn} Y^i_m Y^j_n \tag{7.5}$$

where Δg^{o}_{mn} and q^{ij}_{mn} are empirical binary coefficients which may be functions of temperature and pressure. These were previously optimized to take into account all available thermodynamic and phase equilibrium data in the binary systems [50, 51, 126, 127].

Extrapolation of binary parameters into the ternary systems CaO–MgO–NiO and CaO–NiO–SiO_2 is done by a grouping method [28]. The components are divided into two groups: basic components (CaO, MgO and NiO) and an acidic component (SiO_2). The symmetric "Kohler-like" extrapolation is applied in the case of the CaO–MgO–NiO system, where all three components belong to the first group; the asymmetric "Toop-like" extrapolation is used in the case of the CaO–NiO–SiO_2 system, with SiO_2 as an asymmetric component.

Except for the binary terms, the model can have ternary terms, $q_{mn(p)}$, which give the effect of the presence of component *p* upon the energy of pair exchange reaction Δg_{mn}. Ternary terms are also expanded as empirical polynomials containing model parameters. The formulae for ternary terms and for extrapolation of binary and ternary terms into a multicomponent system are discussed in detail elsewhere [28].

In order to reproduce the liquidus data for the CaO–NiO–SiO_2 system, three optimized ternary model parameters were introduced in the present study. The properties of the CaO–MgO–NiO ternary slag were predicted solely from the corresponding binaries. No adjustable ternary parameters were introduced.

7.6 Monoxide (solid oxide)

The monoxide phase exists in the CaO–MgO–NiO ternary system and its binary subsystems. MgO and NiO are continuously miscible in each other, while CaO has limited solubility in both NiO and MgO.

The Gibbs energy of the monoxide solution is represented by the polynomial model with the "Kohler-like" extension of binary and ternary terms into multicomponent systems [28]:

$$G_m = \sum_i X_i G_i^{\circ} + RT \sum_i X_i \ln X_i + G^E \qquad (7.6)$$, where

$$G^E = \sum_i \sum_j X_i X_j \left(\frac{X_i}{X_i + X_j}\right)^m \left(\frac{X_i}{X_i + X_j}\right)^n q_{ij}^{mn} + \sum_i \sum_j \sum_k X_i X_j X_k \left(\frac{X_i}{X_i + X_j + X_k}\right)^l \left(\frac{X_j}{X_i + X_j + X_k}\right)^m \left(\frac{X_k}{X_i + X_j + X_k}\right)^n q_{ijk}^{lmn} \qquad (7.7)$$

In these expressions, X_i and G_i^0 are the mole fraction and the Gibbs energy of component *i*; q_{ij}^{mn} and q_{ijk}^{lmn} are interaction parameters, which can be temperature dependent; and the powers *l*, *m*, and *n* are ≥ 0.

The binary terms were optimized previously to take into account available data in the binary systems [51, 126]. The properties of the ternary CaO–MgO–NiO monoxide solution were extrapolated from the binary parameters using the symmetric "Kohler-like" technique [28]. No ternary terms were introduced.

7.7 Compound energy formalism (CEF)

The models for the olivine, pyroxene and melilite solutions were developed within the framework of the compound-energy formalism (CEF) [9]. It is well suited to model solid solutions with two or more distinct sublattices. The Gibbs energy expression per formula unit is

$$G_m = \sum_i \sum_j Y_i^{M2} Y_j^{M1} G_{ij} - TS_c + G_m^E \qquad (7.8)$$

where Y_i^{M2} and Y_j^{M1} represent the site fractions of the constituents *i* and *j* on the M2 and M1 sublattices, respectively, G_{ij} is the Gibbs energy of an end-member *ij* of the solution in which the M2 sublattice is occupied only by cation *i* and the M1 sublattice is occupied only by cation *j*, G_m^E is the excess Gibbs energy and S_c is the configurational entropy assuming random mixing on each sublattice,

$$S_c = -R\left(\sum_i Y_i^{M2} \ln Y_i^{M2} + \sum_j Y_j^{M1} \ln Y_j^{M1}\right) \qquad (7.9)$$

and G_m^E is the excess Gibbs energy,

$$G_m^E = \sum_i \sum_j \sum_k Y_i^{M2} Y_j^{M2} Y_k^{M1} L_{ij:k} + \sum_i \sum_j \sum_k Y_k^{M2} Y_i^{M1} Y_j^{M1} L_{k:ij} \qquad (7.10)$$

where $L_{ij:k}$ and $L_{k:ij}$ are the interaction energies between cations *i* and *j* on the one sublattice when the other sublattice is occupied by *k*. The dependence of the interaction energies on the composition can be expressed by Redlich-Kister power series:

$$L_{ij:k} = \sum_m {}^m L_{ij:k} (Y_j^{\mathrm{M2}} - Y_i^{\mathrm{M2}})^m \tag{7.11}$$

$$L_{ij:k} = \sum_m {}^m L_{k:ij} (Y_j^{\mathrm{M1}} - Y_i^{\mathrm{M1}})^m \tag{7.12}$$

7.7.1 Olivine

A complete miscibility exists between the end-members Mg_2SiO_4 and Ni_2SiO_4 of the olivine solution. The solubility of Ca_2SiO_4 in Mg_2SiO_4 is limited; the small solubility of Ca_2SiO_4 in Ni_2SiO_4 was reported in the literature.

In natural olivines, $\mathbf{M}_2SiO_4$, Fe and Mg are major elements, while Ni and Ca are minor components. Cations **M** occupy two non-equivalent octahedral sites: a smaller M1 site and a larger M2 site. All three cations Ca^{2+}, Mg^{2+} and Ni^{2+} can occupy both M2 and M1 sites (sublattices) in the olivine structure:

$$\left(\mathrm{Ca}^{2+},\ \mathrm{Mg}^{2+},\ \mathrm{Ni}^{2+}\right)^{\mathrm{M2}} \left(\mathrm{Ca}^{2+},\ \mathrm{Mg}^{2+},\ \mathrm{Ni}^{2+}\right)^{\mathrm{M1}} \mathrm{SiO}_4 \tag{7.13}$$

The Gibbs energy of the solution is expressed by Equation (8). According to formula unit (13), the Ca-Mg-Ni olivine solution has nine end-members, Gibbs energies of which should be defined. Only two end-member Gibbs energies, G_{NiCa} and G_{CaNi}, were optimized in this study: the rest were accepted from the previous studies by Jung *et al.* [45] for the Ca-Mg olivine solution and by Prostakova *et al.* [123] for the Mg-Ni olivine. In those studies, the Gibbs energies of the end-members, G_{CaCa}, G_{MgMg} and G_{NiNi}, were set equal to the Gibbs energies of the corresponding stoichiometric compounds, Ca_2SiO_4, Mg_2SiO_4 and Ni_2SiO_4, which are stable in the binary systems and have the olivine structure [45, 123]. In addition to the end-member Gibbs energies, several excess Gibbs energy parameters were optimized in the studies [45, 123] and accepted in the present work.

$\left(\mathrm{Ca}^{2+}\right)^{\mathrm{M2}} \left(\mathrm{Ni}^{2+}\right)^{\mathrm{M1}} \mathrm{SiO}_4$ and $\left(\mathrm{Ni}^{2+}\right)^{\mathrm{M2}} \left(\mathrm{Ca}^{2+}\right)^{\mathrm{M1}} \mathrm{SiO}_4$ end-members do not exist as real compounds. Two model parameters were introduced to define the Gibbs energies of these end-members. G_{CaNi}

was first estimated as half sum of the Gibbs energies of Ca_2SiO_4 and Ni_2SiO_4 olivines, with additional Gibbs energy parameter, which was optimized to describe some solubility data available from the literature. Another parameter, $K_{\mathrm{CaNi}} = G_{\mathrm{NiCa}} - G_{\mathrm{CaNi}}$, represents the change in the Gibbs energy when the Ca^{2+} and Ni^{2+} cations occupying M2 and M1 sites, respectively, change places. This parameter has a major effect on the cation distribution between M2 and M1 sites in olivine and was optimized to describe cation distribution of Ca-Ni olivine. It was assumed that the distribution of Ca between M1 and M2 sites in the Ca-Ni olivine solution is similar to that of Ca in the Ca-Mg olivine solution that was previously optimized by Jung *et al.* [45]. Clearly, G_{CaNi} and G_{NiCa} can be expressed as linear combinations of G_{CaCa}, G_{NiNi}, K_{CaNi} and G_{CaNi}.

Finally, the excess Gibbs energy parameters were introduced to take into account a big difference of cationic radii of Ca^{2+} and Ni^{2+}, $r_{\mathrm{Ca}^{2+}} = 100\,\mathrm{pm}$ and $r_{\mathrm{Ni}^{2+}} = 69\,\mathrm{pm}$ [48] (see Table 7.7).

7.7.2 Pyroxenes

There exist two regions of pyroxene solution in the CaO–MgO–NiO–SiO_2 system: a limited region of the Mg-Ni proto-pyroxene solution, with $NiSiO_3$ showing limited solubility in $MgSiO_3$, and a complete clino-pyroxene solution between the end-members $CaMgSi_2O_6$ and $CaNiSi_2O_6$. The other pyroxenes (ortho- and low clino-) are not stable at ambient pressure.

Like olivine, pyroxene has two distinct octahedral sublattices, M2 and M1, and tetrahedral sites occupied by Si [49]. Mg and Ni can be present on both octahedral sublattices, while Ca occupies only the larger M2 site. So, a formula unit of the pyroxene solution is the following:

$$\left(\mathrm{Ca}^{2+},\ \mathrm{Mg}^{2+},\ \mathrm{Ni}^{2+}\right)^{\mathrm{M2}}\left(\mathrm{Mg}^{2+},\ \mathrm{Ni}^{2+}\right)^{\mathrm{M1}}\mathrm{Si}_2\mathrm{O}_6 \qquad (7.14)$$

The Gibbs energy of pyroxene is given by Equation (8) of the CEF.

According to formula unit (14), the Gibbs energies of six end-members must be defined. A set of model parameters for Mg-Ni proto-pyroxene solution was optimized in our previous study [123]. G_{CaMg} was previously optimized by Jung *et al.* [45] for the Ca-Mg proto-pyroxene solution. Similar to $CaMgSi_2O_6$ end-member, G_{CaNi} was set equal to the Gibbs energy of the stoichiometric clino-$CaNiSi_2O_6$, with the enthalpy of transition of clino- to proto-$CaNiSi_2O_6$ equal to that of $CaMgSi_2O_6$.

For clino-pyroxene, two of six end-member Gibbs energies, G_{CaMg} and G_{MgMg}, were previously optimized by Jung *et al.* [45] for the Ca-Mg clino-pyroxene solution. The rest were optimized in this study.

G_{CaNi} is the Gibbs energy of the stoichiometric clino-$CaNiSi_2O_6$. To define the Gibbs energies of the other three end-members, similar to the olivine solution, the linear combinations of the parameters, K_{MgNi}, $\Delta_{CaNi:NiMg}$, and $\Delta_{CaNi:MgMg}$, were introduced as model parameters. The parameter $K_{MgNi} = G_{NiMg} - G_{MgNi}$ affects mainly the cation distribution between M2 and M1 sites in the Mg-Ni clino-pyroxene, while the other two parameters are the Gibbs energies of the reciprocal reaction among end-members.

Finally, two excess Gibbs energy parameters equal to those for the Ca-Mg clino-pyroxene solution [45] were introduced due to a big difference of cationic radii of Ca^{2+} and Ni^{2+}, as mentioned above (see Table 7.7).

7.7.3 Melilite

$Ca_2(Mg^{2+}, Ni^{2+})Si_2O_7$ melilite solution has 2 end-members. G_{CaMg} was set equal to the Gibbs energy of the stoichiometric akermanite $Ca_2MgSi_2O_7$ compound with melilite structure, which was previously optimized by Jung *et al.* [45]. G_{CaNi} was estimated as a sum of the Gibbs energies of niopside $CaNiSi_2O_6$ with clino-pyroxene structure and solid CaO, with additional Gibbs energy parameter, which was optimized to describe the solubility of Ni in $Ca_2MgSi_2O_7$ available in the literature.

7.8 Critical evaluation of experimental data and optimization

The ternary CaO–NiO–SiO_2 and CaO–MgO–NiO systems, and the quaternary CaO–MgO–NiO–SiO_2 system were recently optimized by Woo *et al.* [55]. However, since the time of their optimization new experimental data appeared in the CaO–NiO–SiO_2 and MgO–NiO–SiO_2 ternary systems and its binary subsystems CaO–NiO and MgO–NiO. Some of these data are presented here in Table 7.1, and the rest in our previous studies [51, 123]. To take into account the new data, reoptimization of the quaternary CaO–MgO–NiO–SiO_2 system and its ternary subsystems CaO–NiO–SiO_2 and CaO–MgO–NiO has been performed in this study.

7.8.1 CaO-NiO-SiO_2 system

7.8.1.1 Summary of experimental data

7.8.1.1.1 Thermodynamic properties

The only ternary compound $CaNiSi_2O_6$, which was first synthesized by Gjessing [128] and has the clino-pyroxene structure, is present in the CaO–NiO–SiO_2 system. It is called niopside due to proximity of its structure to diopside $CaMgSi_2O_6$. Since there were no reports on non-stoichiometry of niopside in the literature, it was assumed to be stoichiometric in the present study. No ternary solid solutions were reported in the CaO–NiO–SiO_2 system.

Thermodynamic data for niopside $CaNiSi_2O_6$ include the enthalpy of formation [129] and the Gibbs energy data [124, 130]. The enthalpy of formation of $CaNiSi_2O_6$ from the corresponding oxides CaO, NiO and SiO_2 (quartz) was measured by Navrotsky and Coons [129] as -113.4 ± 2.1 $kJ \cdot mol^{-1}$ (one standard deviation) at 713 °C by means of oxide melt solution calorimetry. The calculated value of the present study is -115.9 kJ/mol, which will be discussed later. In addition, partial pressures of oxygen for the phase assemblage $CaNiSi_2O_6$ + SiO_2 + $CaSiO_3$ + Ni were measured in a couple of studies [124, 130]. Pretorius and Muan [124] measured them by employing gas equilibration technique in the range of temperatures 1200-1350 °C. In their study, oxygen pressures were fixed by the flow of CO_2/H_2 gas mixture, $CaSiO_3$ was stated to be in the form of pseudo-wollastonite, in agreement with the accepted temperature of transition of wollastonite to pseudo-wollastonite at 1125 °C, while the crystal modification of silica was not mentioned. In the subsequent study, Mukhopadhyay and Jacob [130] measured the oxygen pressures for the $CaNiSi_2O_6$ + SiO_2 + $CaSiO_3$ + Ni phase assemblage in the temperature range 727-1127 °C by the electromotive force measurements (EMF). The crystal modifications of reagents were quartz for silica and wollastonite for $CaSiO_3$. The slope of the curve for the Gibbs energy of formation of $CaNiSi_2O_6$ obtained by Mukhopadhyay and Jacob [130] significantly differs from that of Pretorius and Muan [124], as can be seen in Figure 7.2. Using pseudo-wollastonite and cristobalite in calculations changes the slope in the right direction, but not sufficiently to describe the data of Pretorius and Muan [124]. Between the two sets of data, the latter results of Mukhopadhyay and Jacob [130] were chosen for further optimizations, since they were in better agreement with the enthalpy data of Navrotsky and Coons [129]. In Figure 7.2, the calculated line of Woo *et al.* [55] is also presented. In their study, the literature data of Mukhopadhyay and Jacob [130] were represented

incorrectly on the partial pressures of oxygen for the $CaNiSi_2O_6 + SiO_2 + CaSiO_3 + Ni$ assemblage versus temperature curve. The resultant Gibbs energy function lays ≈ 2-6 kJ higher than it should be.

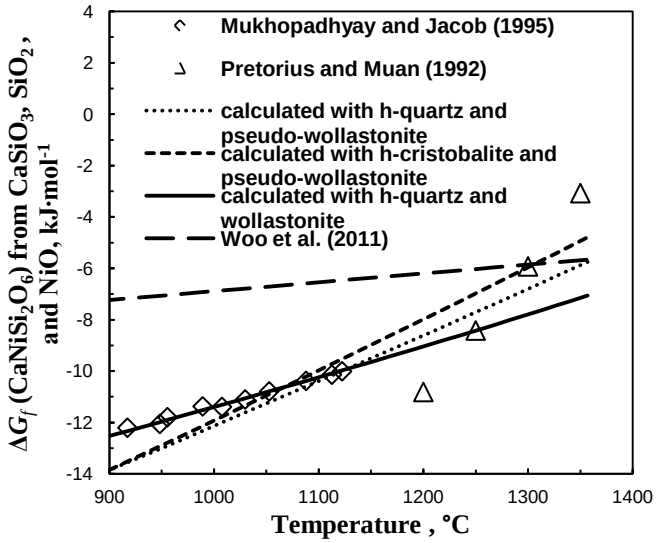

Figure 7.2: Temperature dependence of the Gibbs energy of formation of niopside $CaNiSi_2O_6$ from NiO, SiO_2 and $CaSiO_3$: literature data [124, 130] and calculated lines

The thermodynamic properties of the liquid solution were studied by Pretorius and Muan [131] who measured the activity of NiO in the CaO–NiO–SiO_2 slag at 1435 °C by equilibrating it with metallic nickel at oxygen pressure fixed by CO_2/H_2 mixture. Their results are given in Table 7.3.

7.8.1.1.2 Phase equilibria

The phase equilibria in the CaO–NiO–SiO_2 system were studied by several authors [124, 125, 130]. Phase relations in the subsolidus region of the CaO–NiO–SiO_2 ternary system were studied by Mukhopadhyay and Jacob [130] at 1100 °C by means of quenching technique and identifying the phases by X-ray diffraction and energy dispersive X-ray analysis. Their data are shown in Figure 7.3.

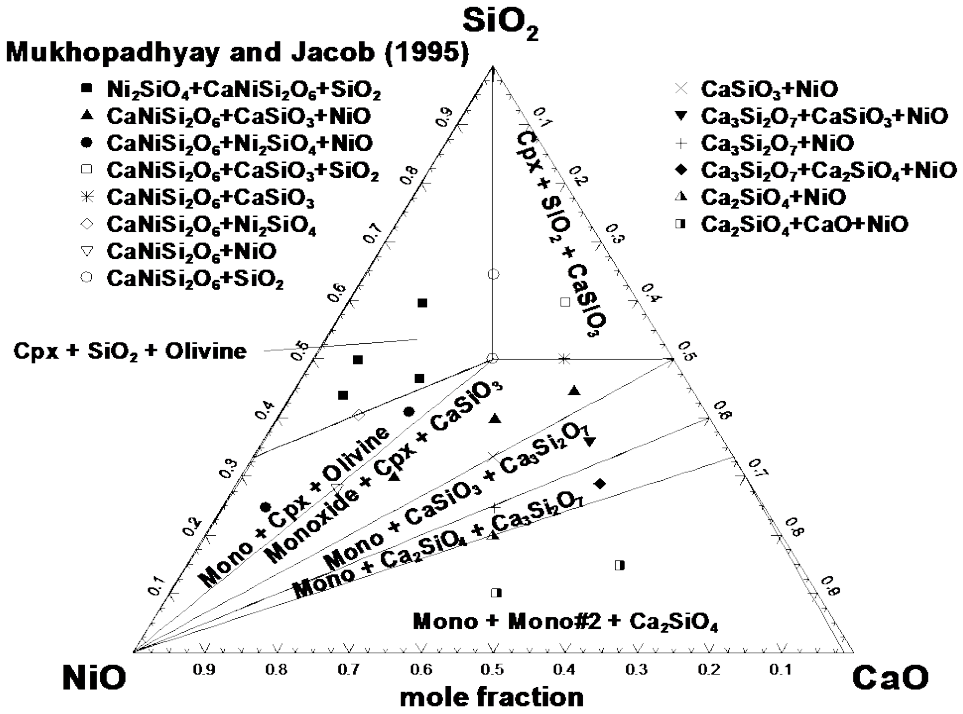

Figure 7.3: Isothermal section of the CaO–NiO–SiO_2 phase diagram at 1100 °C: literature data [130] and calculated lines

Phase relations in the liquidus region of the CaO–NiO–SiO_2 ternary system were investigated from 1360 to 1550 °C by Biggar [125] who employed the equilibration/quenching technique followed by microscopic and X-ray diffraction phase analyses. Biggar [125] observed nickel orthosilicate 5 °C above its melting temperature of 1545 °C, which is demonstrated in Figure 7.7. As an explanation, he suggested the existence of a crystalline solution of Ni_2SiO_4 containing small amount of Ca. Our calculations also suggest a small solubility of Ca in Ni_2SiO_4. However, it was problematic to reproduce other experimental points of Biggar [125], particularly, L + $CaSiO_3$ and L + $CaSiO_3$ + SiO_2 points at 1390 °C (see Figure 7.5). To check contradictory points, the CaO–NiO–SiO_2 ternary phase diagram has been re-investigated experimentally at 1360 and 1390 °C by the EPMA of quenched samples. The new experimental results, which are given in Table 7.1 and shown in Figure 7.4 and Figure 7.5, showed that L + $CaSiO_3$ + SiO_2 data point of Biggar [125] was erroneous.

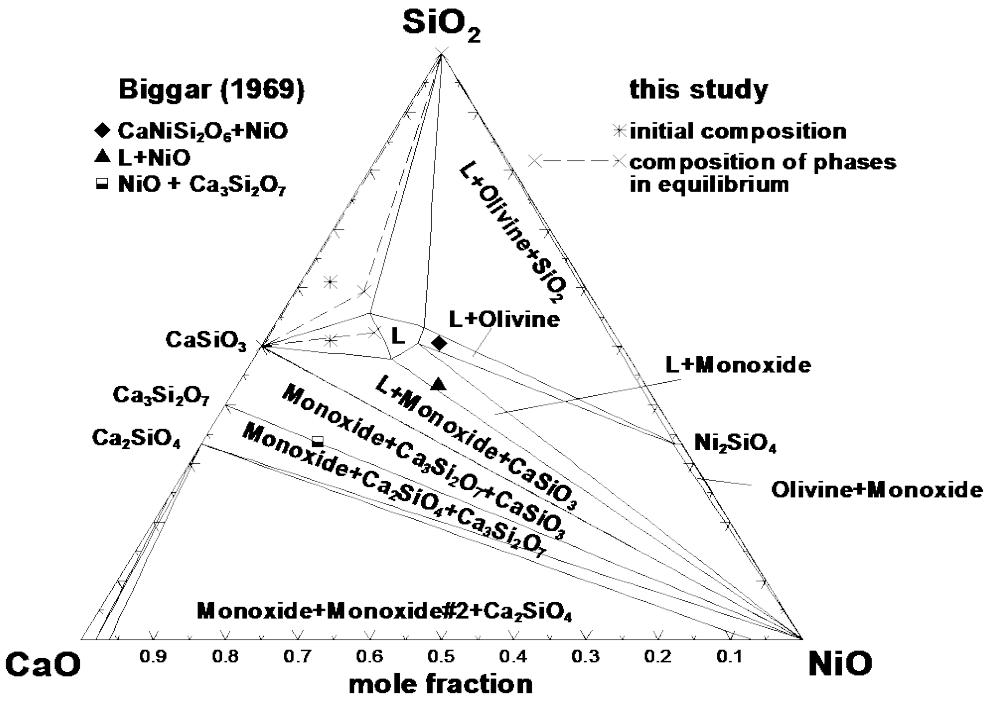

Figure 7.4: Isothermal section of the CaO–NiO–SiO_2 phase diagram at 1360 °C: literature data [125], this study experimental results and calculated lines

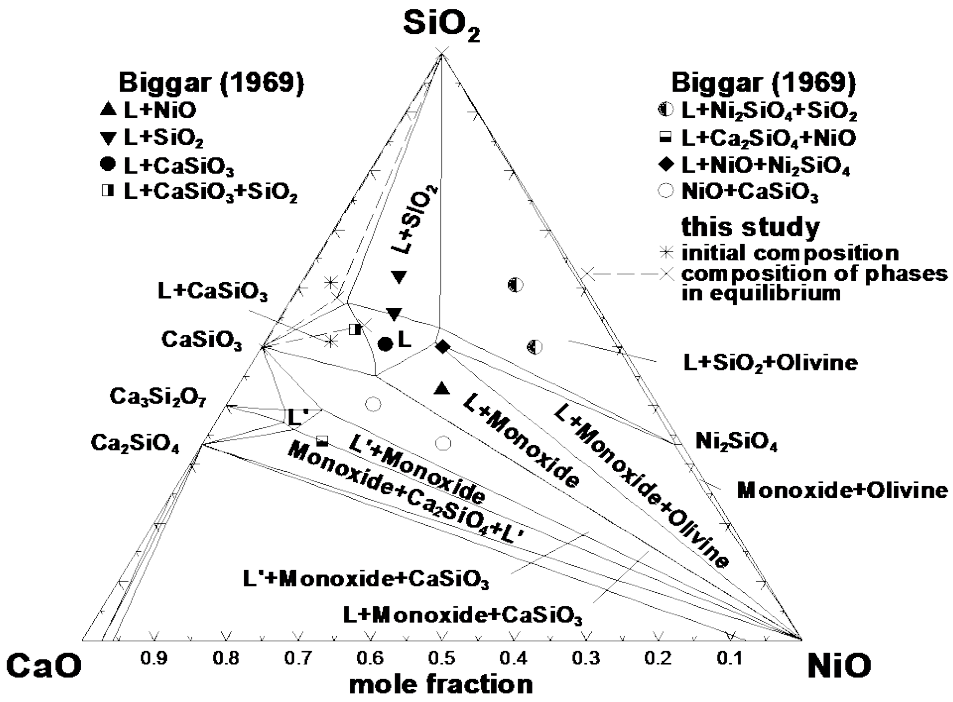

Figure 7.5: Isothermal section of the CaO–NiO–SiO_2 phase diagram at 1390 °C: literature data [125], this study experimental results and calculated lines

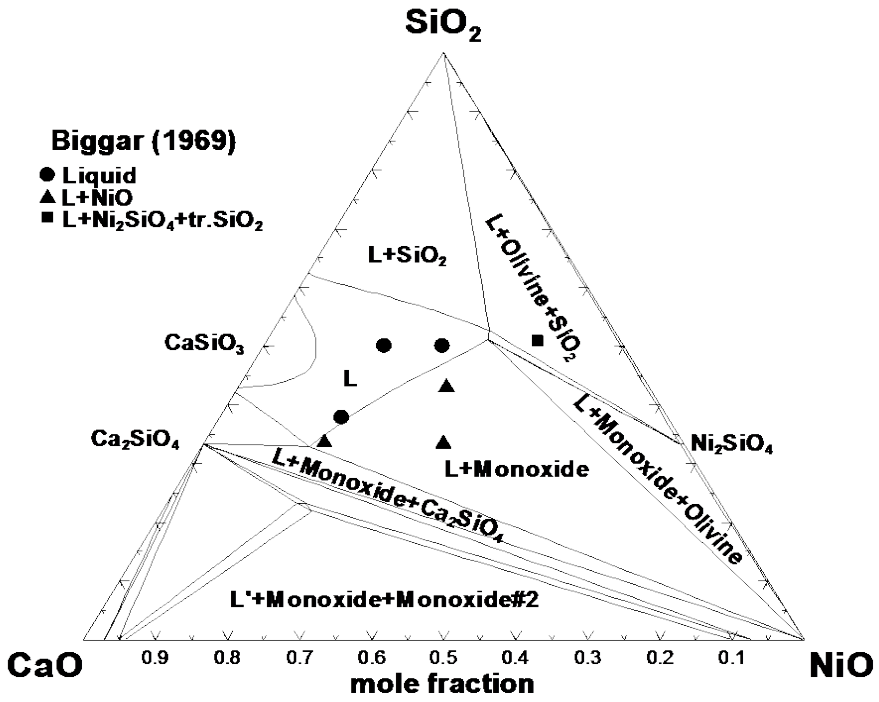

Figure 7.6: Isothermal section of the CaO–NiO–SiO_2 phase diagram at 1475 °C: literature data [125] and calculated lines

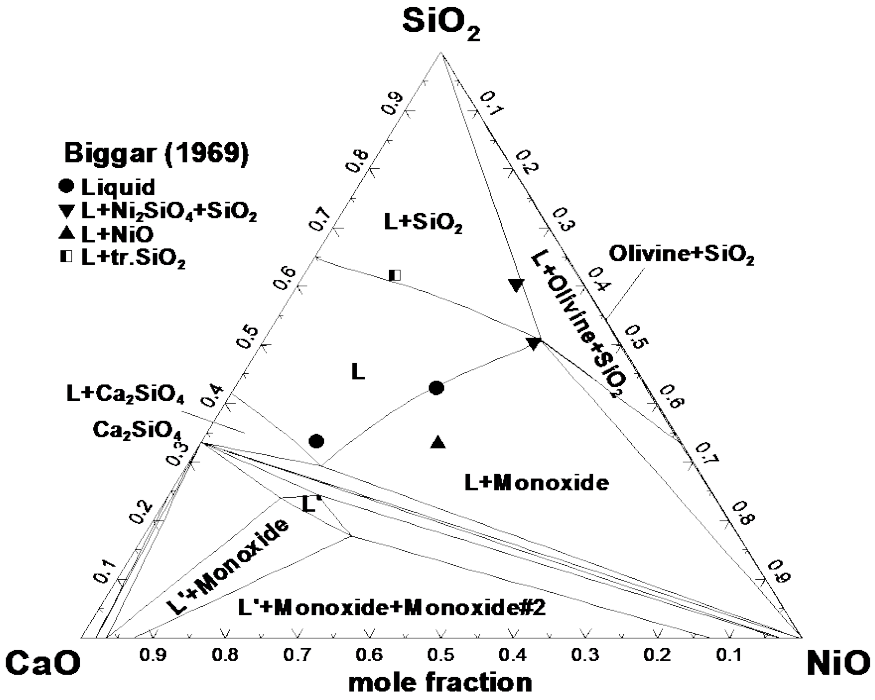

Figure 7.7: Isothermal section of the CaO–NiO–SiO_2 phase diagram at 1550 °C: literature data [125] and calculated lines

Several authors investigated the $CaSiO_3$–$NiSiO_3$ section of the CaO–NiO–SiO_2 phase diagram, which is shown in Figure 7.8. Biggar [125] observed incongruent melting of niopside at about 1340 °C, which was later confirmed by Pretorius and Muan [124] by quenching with optical microscopic observation. Pretorius and Muan [124] reported a temperature at which incongruent melting occurred as 1338 °C and a liquidus temperature above the niopside composition as 1420 °C. They also reported the temperatures of the invariant equilibria in the CaO–NiO–SiO_2 system involving niopside, which are given in Table 7.4.

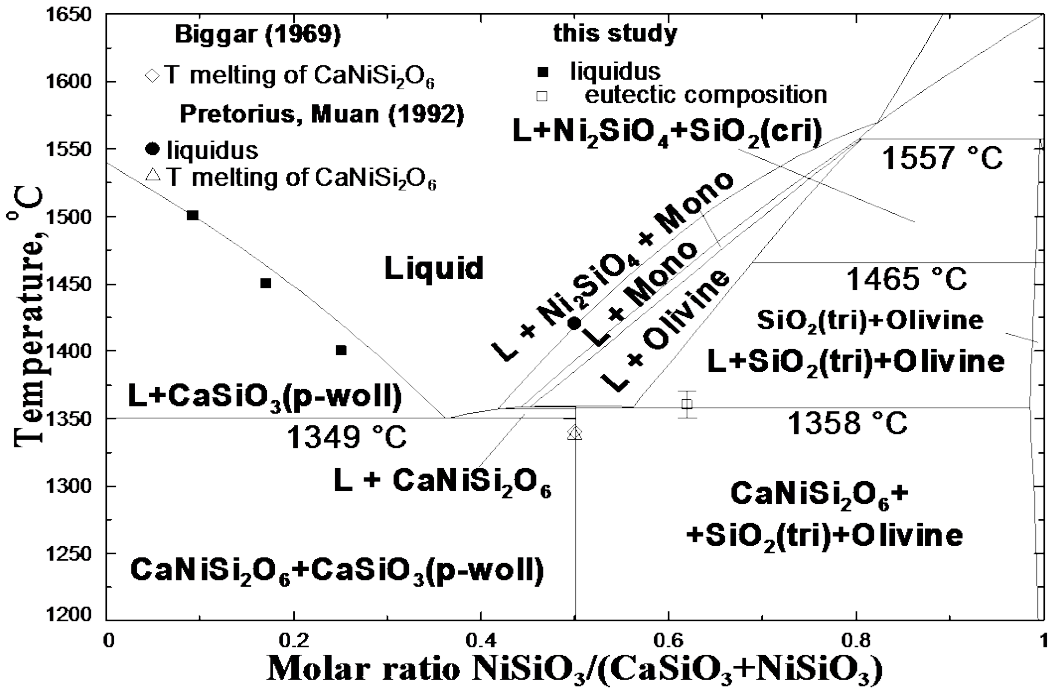

Figure 7.8: $CaSiO_3$–$NiSiO_3$ section of the CaO–NiO–SiO_2 phase diagram: literature data [124, 125], this study experimental results and calculated lines (see Table 7.2 for notations)

Although Biggar [125] reported incongruent melting of niopside at 1340 °C, he observed a phase, which he called primary niopside, above this temperature. He admitted that either niopside could be a crystalline solution, which was not confirmed experimentally in the literature, or the starting composition could be not exact. If the composition deviated from stoichiometric $CaNiSi_2O_6$, he could observe the formation of a liquid phase in the eutectic (see Figure 7.9). Thus, the melting temperature of niopside could have been measured erroneously. In particular, the liquid phase could have been observed in the $CaNiSi_2O_6$ + $CaSiO_3$ + SiO_2 + liquid eutectic at the temperature as low as 1342 °C, according to calculations.

To resolve the conflicting interpretations, the melting temperature of niopside was checked in this study using EPMA of quenched samples. However, it was not measured directly in order not to be faced with the experimental difficulties encountered in previous studies. Instead, a few critical experiments have been performed to determine the $CaNiSi_2O_6$ + Ni_2SiO_4 + SiO_2 + liquid eutectic temperature, as shown in Figure 7.8. In addition, the liquidus points on the $CaSiO_3$–$NiSiO_3$ section of the CaO–NiO–SiO_2 phase diagram on the $CaSiO_3$-side have been measured at 1400, 1450 and 1500 °C. The experimental results are given in Table 7.1.

7.8.1.2 Optimization

In the optimization of all available data in the CaO–NiO–SiO_2 system, first, the thermodynamic properties of niopside $CaNiSi_2O_6$ were optimized using the enthalpy and Gibbs energy data. Then, the Modified Quasichemical Model parameters of the liquid phase were optimized to reproduce available activity (Table 7.3) and phase diagram data (Figure 7.4-Figure 7.8, Table 7.4).

Figure 7.2 shows the calculated Gibbs energy of formation of niopside from NiO, SiO_2 (quartz) and $CaSiO_3$ (wollastonite) along with the literature data [124, 130]. As discussed above, priority in the optimization was given to the data of Mukhopadhyay and Jacob [130]. The enthalpy of formation of $CaNiSi_2O_6$ from the oxides CaO, NiO and SiO_2 (quartz) at 713 °C is calculated as -115.9 kJ/mol, which is in good agreement with -113.4 ± 2.1 kJ/mol by Navrotsky and Coons [129]. The subsolidus phase equilibria by Mukhopadhyay and Jacob [130] shown in Figure 7.3 are also very well described. The optimized thermodynamic properties of niopside $CaNiSi_2O_6$ are listed in Table 7.7.

The calculated activities of NiO in the CaO–NiO–SiO_2 liquid slag at 1435 °C given in Table 7.3 agree well with the values measured by Pretorius and Muan [131]. To describe this series of data along with the data of Biggar [125] and experimental tie-lines obtained in this study and shown on a series of isothermal sections in Figure 7.3-Figure 7.6, it was necessary to have a temperature-dependent parameter for the liquid phase. The calculated temperatures of invariant equilibria involving niopside given in Table 7.4 and shown in Figure 7.9 are in reasonable agreement with the data of Pretorius and Muan [124]. The calculated liquidus projection of the CaO–NiO–SiO_2 phase diagram is shown in Figure 7.9. The optimized parameters of the liquid phase are listed in Table 7.7.

Table 7.3: Measured [131] and calculated activities of NiO in the CaO–NiO–SiO_2 liquid slag at 1435 °C

Mol % NiO	**Mol % CaO**	**Mol % SiO_2**	**Measured activity of NiO [131] (st. state – solid NiO)**	**Calculated activity of NiO (st. state – solid NiO)**
8.39	32.45	59.16	0.34	0.34
9.98	31.93	58.09	0.39	0.40
8.01	38	53.99	0.37	0.38
8.65	40.2	51.15	0.41	0.44

Table 7.4: Calculated temperatures of invariant equilibria involving niopside compared to the experimental data of Pretorius and Muan [124]

Number in Figure 7.9	**Invariant equilibria involving niopside initial composition: 0.6 $CaNiSi_2O_6$ + 0.2 $CaSiO_3$(or Ni_2SiO_4) + 0.2 SiO_2(or NiO)**	**Experimental temperature, °C**	**Calculated temperature, °C**
1	$CaNiSi_2O_6$+$CaSiO_3$+SiO_2+liquid	1338	1342
2	$CaNiSi_2O_6$+Ni_2SiO_4+SiO_2+liquid	1380	1358
3	$CaNiSi_2O_6$+Ni_2SiO_4+NiO+liquid	1375	1359
4	$CaNiSi_2O_6$+$CaSiO_3$+NiO+liquid	1348	1349

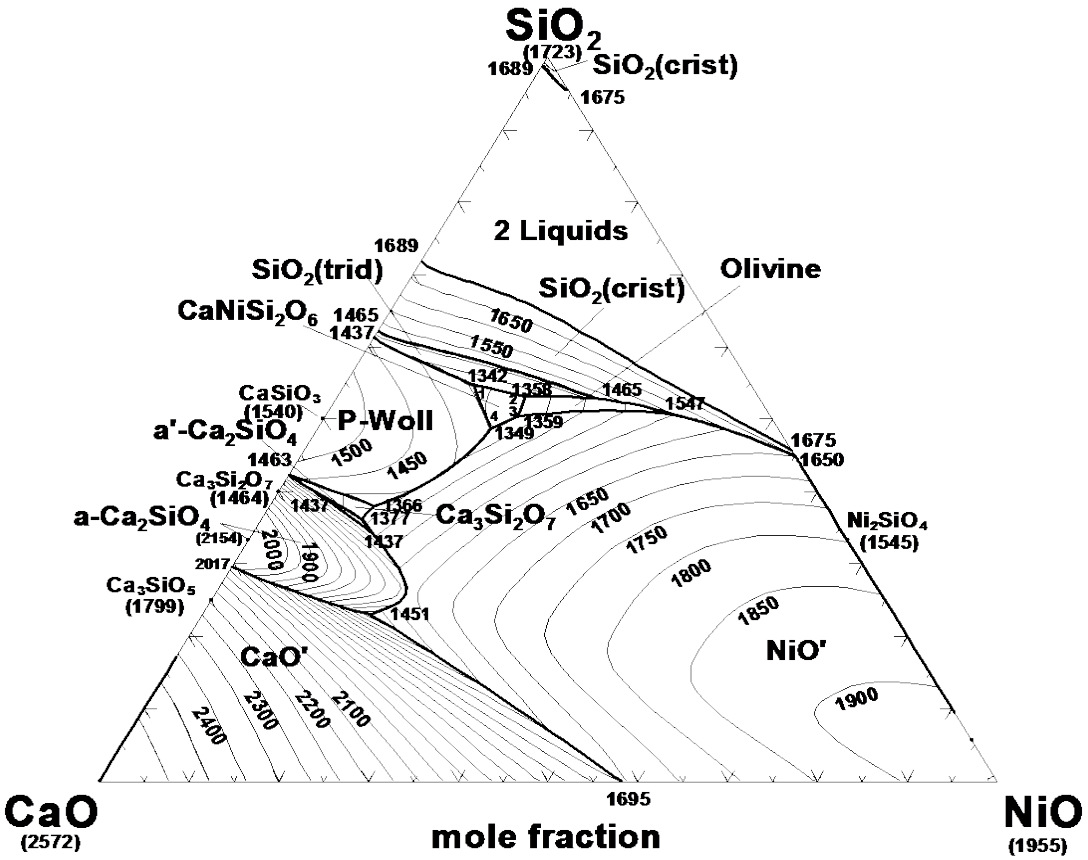

Figure 7.9: Calculated liquidus projection of the CaO–NiO–SiO_2 system (temperature in °C), where CaO' = monoxide rich in CaO, NiO' = monoxide rich in NiO (other notations are given in Table 7.2). Numbers 1-4 correspond to the phase equilibria given in Table 7.4

7.8.2 CaO–MgO–NiO system

7.8.2.1 Optimization

No literature data for the CaO–MgO–NiO ternary system were found. The properties of liquid slag and solid monoxide solutions originating from binary subsystems were predicted solely from the corresponding binary parameters using the symmetric "Kohler-like" technique [28]. No ternary parameters were introduced. The calculated liquidus projection of the CaO–MgO–NiO system is shown in Figure 7.10.

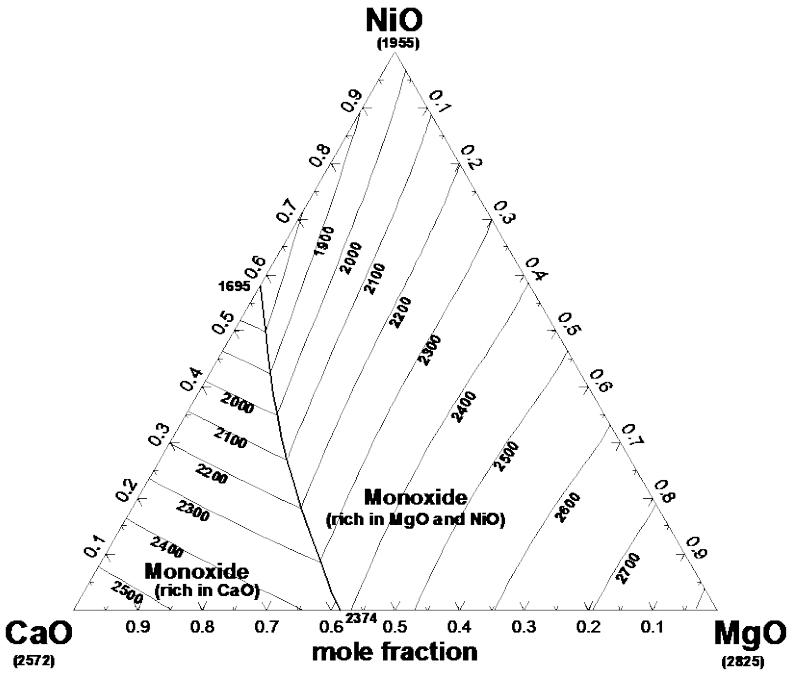

Figure 7.10: Calculated liquidus projection of the CaO–MgO–NiO phase diagram (temperatures in °C)

7.8.3 CaO–MgO–NiO–SiO_2 quaternary system

7.8.3.1 Summary of experimental data

The only quaternary solid phase in the system is a complete clino-pyroxene solution between the $CaMgSi_2O_6$ and $CaNiSi_2O_6$ end-members, which was first reported by White *et al.* [132].

The properties of the clino-pyroxene solution were studied by a limited number of authors [124, 133]. Wright and Navrotsky [133] determined the enthalpy of mixing of 0.5 mol $CaMgSi_2O_6$ and 0.5 mol $CaNiSi_2O_6$ at 702 °C as -3.05 ± 0.71 kJ/mol by high-temperature solution calorimetry. Pretorius and Muan [124] measured partial pressures of oxygen for the clino-pyroxene, $CaSiO_3$, silica and metallic Ni phase assemblage at 1350 °C using CO_2/H_2 gas mixtures. Their results are shown in Figure 7.12.

The $CaMgSi_2O_6$–$CaNiSi_2O_6$ section of the CaO–MgO–NiO–SiO_2 phase diagram was investigated as well [124] (see Figure 7.11). Solidus and liquidus temperatures on this section were obtained by employing a quenching technique with optical phase determination (see Table 7.5).

However, the initial data were not given by the authors. In Figure 7.11, phases that are present in very low quantities are given in brackets. Their formation is caused by slightly non-stoichiometric compositions of the clino-pyroxene solution. However, it is very difficult to observe the presence of these phases in the experiment due to their low quantities. In the case the liquid phase was not observed by Pretorius and Muan [124] in the clino-pyroxene + (L) phase field, the agreement between the experimental and calculated solidus temperatures is good. The liquidus temperatures are though higher than the calculated ones, especially on the Mg-side due to unknown reason.

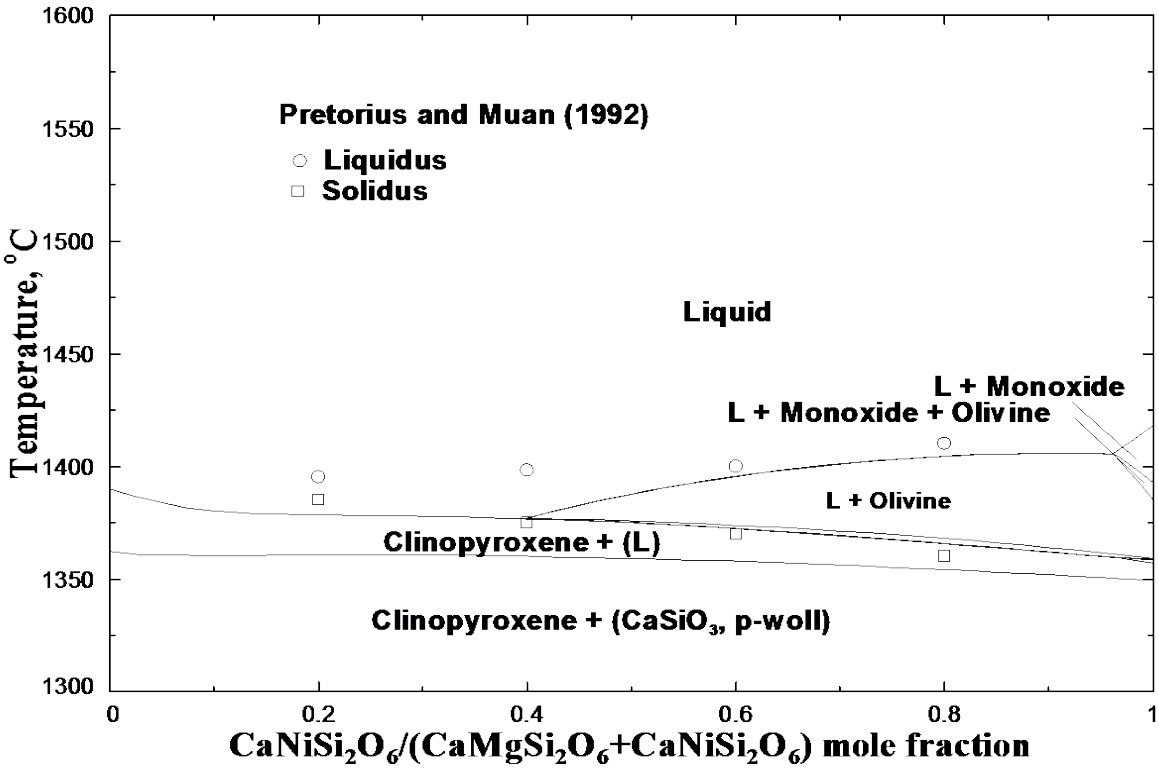

Figure 7.11: $CaMgSi_2O_6$–$CaNiSi_2O_6$ section of the CaO–MgO–NiO–SiO_2 phase diagram: experimental data [124] and calculated lines (notations are given in Table 7.2)

The percentage substitution of nickel for Mg in akermanite ($Ca_2MgSi_2O_7$, melilite solution end-member) and monticellite ($CaMgSiO_4$, olivine solution end-member) phases was determined as 20 and 57 %, respectively. However, the corresponding temperatures were not provided [124].

Pretorius and Muan [131] investigated the thermodynamic properties of the quaternary slag by measuring the activity of NiO in the liquid slag while equilibrating molten slag with metallic Ni and CO_2/H_2 mixture at about 1400 °C. Their results are shown in Table 7.6.

7.8.3.2 Optimization

Model parameters required for the description of the CaO–MgO–NiO–SiO_2 system were obtained as follows. First, three parameters of the clino-pyroxene model were optimized (see Section 7.7.2). Since no cation distribution data for the clino-pyroxene solution are available in the literature, K_{MgNi} was set equal to the similar parameter for the proto-pyroxene solution. The model parameters $\Delta_{\mathrm{CaNi:NiMg}}$, and $\Delta_{\mathrm{CaNi:MgMg}}$ were then optimized to describe thermodynamic data available for the clino-pyroxene solution.

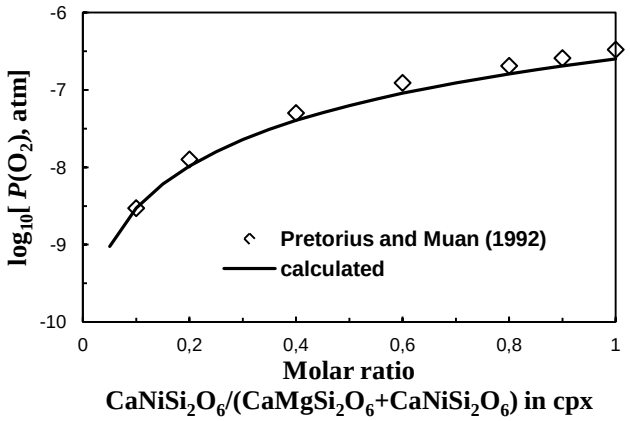

Figure 7.12: Partial pressures of oxygen for clino-pyroxene (cpx) in equilibrium with $CaSiO_3$, SiO_2 and Ni at 1350 °C: experimental data [124] and a calculated line

The calculated partial pressures of oxygen for clino-pyroxene in equilibrium with $CaSiO_3$, SiO_2 and Ni at 1350 °C are shown in Figure 7.12, along with the experimental data [124]. The enthalpy of mixing of 0.5 mol $CaMgSi_2O_6$ and 0.5 mol $CaNiSi_2O_6$ at 702 °C is calculated as zero value, a little bit higher than the value of -3.05 ± 0.71 kJ/mol by Wright and Navrotsky [133].

The properties of the liquid phase were predicted solely from the ternary parameters. The extension of ternary terms to multicomponent systems is described in [28]. The measured [131] and calculated activities of NiO in the CaO–MgO–NiO–SiO_2 liquid slag at 1400 °C are given in Table 7.6. There is a good agreement between the experimental and calculated results.

The calculated solidus and liquidus for several compositions on the $CaMgSi_2O_6$–$CaNiSi_2O_6$ section of the CaO–MgO–NiO–SiO_2 phase diagram shown in Figure 7.11 are compared to the experimental points by Pretorius and Muan [124] in Table 7.5. The data are in agreement within 25 °C.

Table 7.5: Experimental [124] and calculated solidus and liquidus temperatures for several compositions on the $CaMgSi_2O_6$–$CaNiSi_2O_6$ section of the CaO–MgO–NiO–SiO_2 phase diagram

X in $CaMg_{1-X}Ni_XSi_2O_6$	**Experimental [124]**		**Calculated**	
	Solidus, °C	**Liquidus, °C**	**Solidus, °C**	**Liquidus, °C**
0.2	1385	1395	1360	1378
0.4	1375	1398	1360	1377
0.6	1370	1400	1358	1396
0.8	1360	1410	1354	1404

A significant substitution of Ni for Mg in $CaMgSiO_4$ olivine measured by Pretorius and Muan [124] was modeled by introducing the G_{CaNi} parameter of the olivine solution and applying the same parameter to describe a low solubility of Ca in Ni_2SiO_4 olivine. The calculated substitution of Ni for Mg in monticellite is around 30 % at 1200 °C, 51 % at 1300 °C and 56 % at 1400 °C, compared to 57 % obtained by Pretorius and Muan [124] for an unspecified high temperature. The parameter K_{CaNi} was optimized to describe the cation distribution of Ca-Ni olivine, as it was explained before in Section 7.7.1.

A substitution of Ni for Mg in akermanite $Ca_2MgSi_2O_7$ (melilite solution end-member) was modeled by introducing the G_{CaNi} parameter, as described in Section 7.7.3. The calculated substitution of Ni for Mg in melilite is around 20 % at 1300 °C. The same percentage was obtained by Pretorius and Muan [124] at an unspecified high temperature.

Table 7.6: Measured [131] and calculated activities of NiO in the CaO–MgO–NiO–SiO_2 liquid slag at 1400 °C

Mol % NiO	**Mol % CaO**	**Mol % MgO**	**Mol % SiO_2**	**Measured activity of NiO [131] (st. state – solid NiO)**	**Calculated activity of NiO (st. state – solid NiO)**
1.89	36.5	16.68	44.93	0.17	0.15
1.9	40.7	13.25	44.15	0.17	0.16
1.94	39.94	13.18	44.94	0.17	0.16
3.06	19.03	20.91	57.01	0.17	0.17
3.09	17.87	22.12	56.92	0.17	0.17
4.91	22.83	19.76	52.5	0.27	0.27
4.78	27.39	19.86	47.97	0.36	0.30
2.47	28.03	20.43	49.07	0.17	0.16
4.33	32.64	20.04	42.98	0.44	0.32
1.99	32.22	20.69	45.1	0.17	0.15
5.56	26.6	14.63	53.2	0.30	0.30
3.08	26.94	14.76	55.22	0.17	0.18
5.62	23.01	15.69	55.69	0.29	0.29
4.93	23.34	16.19	55.54	0.26	0.26
2.35	22.08	25.07	50.5	0.17	0.14
2.75	23.59	22.13	51.53	0.17	0.16
1.3	17.98	23.55	57.17	0.07	0.08
2.95	17.05	23.59	56.4	0.16	0.16
1.29	19.08	23.44	56.2	0.07	0.08

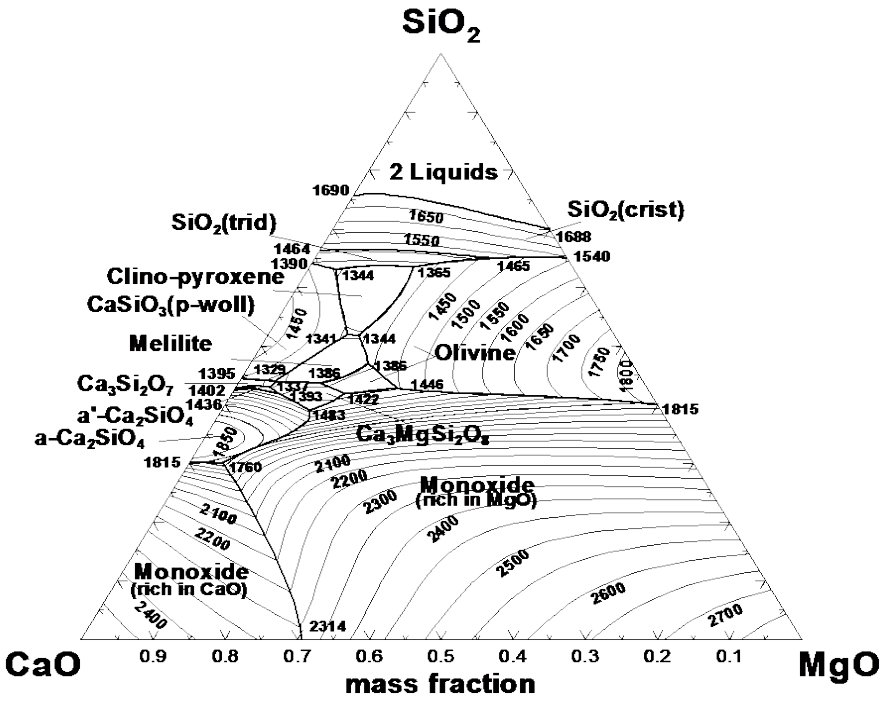

Figure 7.13: Calculated liquidus projection of the CaO–MgO–NiO–SiO_2 phase diagram at 10 wt.% NiO (temperatures in °C; notations are given in Table 7.2)

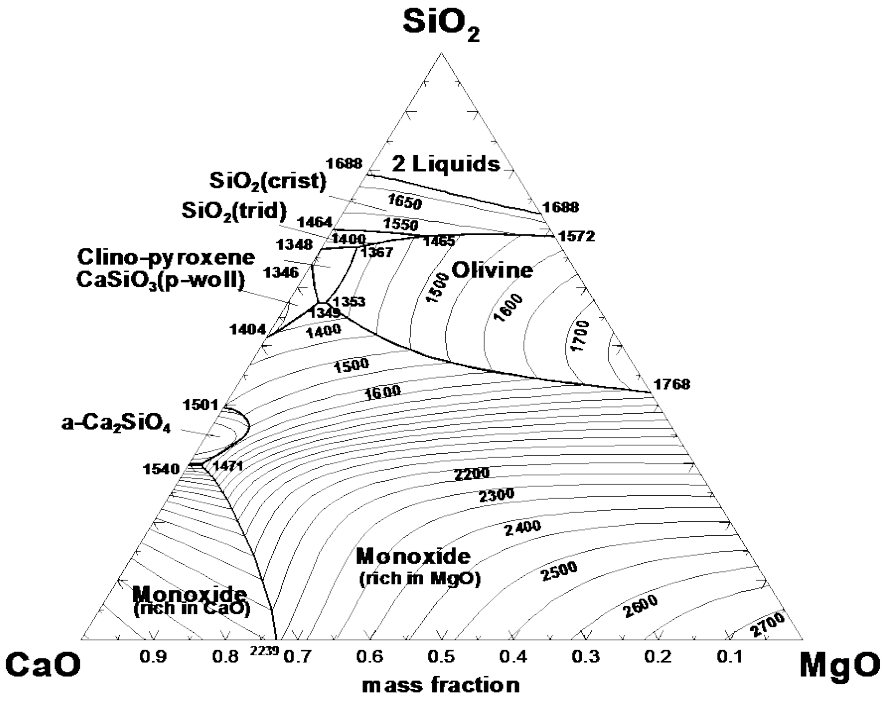

Figure 7.14: Calculated liquidus projection of the CaO–MgO–NiO–SiO_2 phase diagram at 20 wt.% NiO (temperatures in °C; notations are given in Table 7.2)

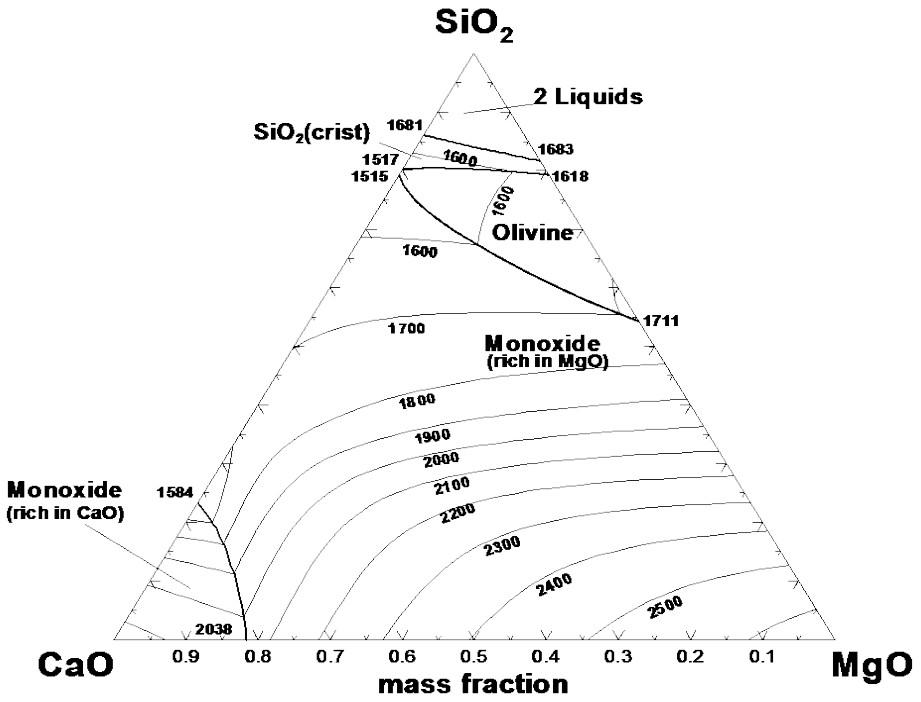

Figure 7.15: Calculated liquidus projection of the CaO–MgO–NiO–SiO_2 phase diagram at 40 wt.% NiO (temperatures in °C; notations are given in Table 7.2)

The optimized model parameters for the clino-pyroxene and liquid solutions in the CaO–MgO–NiO–SiO_2 system are given in Table 7.7.

The liquidus projections of the CaO–MgO–NiO–SiO_2 phase diagram at constant NiO contents (10, 20 and 40 weight% NiO) predicted from the optimized model parameters are given in Figure 7.13-Figure 7.15.

7.9 Summary of results

The present study characterizes oxide systems with a view to developing of a thermodynamic database that can be used for simulation of nickel extraction from ores. The quaternary system CaO–MgO–NiO–SiO_2 and its ternary NiO-containing subsystems CaO–NiO–SiO_2 and CaO–MgO–NiO have been optimized at a total pressure of 1 atm.

Some discrepancies in the literature data for the CaO–NiO–SiO_2 system have been demonstrated. To resolve the conflicts in the literature data, new experimental investigation has been carried out in this study. The experimental procedure involved equilibration and ultra rapid quenching followed by electron probe X-ray microanalysis (EPMA) of the quenched samples.

The liquid oxide (slag) – solid oxide tie-lines were measured on the isothermal sections of the CaO–NiO–SiO_2 phase diagram at temperatures from 1330 to 1500 °C. The new experimental data were compared with the previously published results and discrepancies were clarified.

A simultaneous optimization of all available data in the quaternary CaO–MgO–NiO–SiO_2 system and its ternary subsystems CaO–NiO–SiO_2 and CaO–MgO–NiO has been performed. New experimental data and previously published experimental results were taken into consideration. The optimized model parameters for oxide phases reproduce all available data within experimental error limits. A set of self-consistent Gibbs energy functions of the oxide phases in the chemical systems was derived.

Table 7.7 : Optimized model parameters for the slag, olivine and pyroxene phases in the CaO–MgO–NiO–SiO_2 system and its subsystems CaO–NiO–SiO_2 and CaO–MgO–NiO ($J \cdot mol^{-1}$ and $J \cdot mol^{-1} \cdot K^{-1}$)

Slag (liquid oxide) CaO–MgO–NiO–SiO_2

$$Z_{Ca} = Z_{Mg} = Z_{Ni} = 1.3774, \; Z_{Si} = 2.7549;$$

$$q^{001}_{Ni,\,Si\,(Mg)} = -39748, \quad q^{001}_{Mg,\,Si\,(Ni)} = 16736, \quad q^{001}_{Mg,\,Ni\,(Si)} = -58576;$$

$$q^{001}_{Ni,\,Si\,(Ca)} = -8368, \quad q^{001}_{Ca,\,Si\,(Ni)} = 12552 - 17.9912T.$$

The optimized parameters for the CaO-NiO, MgO-NiO and NiO-SiO_2 binary slags can be found in the previous study by Prostakova *et al*. [51]. The parameters for other binary slags can be found in previous optimizations [50, 126, 127]. The parameters for the ternary CaO-MgO-SiO_2 slag were optimized by Jung *et al.* [45], for MgO-NiO-SiO_2 – by Prostakova *et al.* [123].

The symmetric "Kohler-like" extrapolation of binary terms was applied for the CaO–MgO–NiO slag, the asymmetric "Toop-like" extrapolation was used for the CaO–NiO–SiO_2 slag, with SiO_2 as an asymmetric component [28]. The extension of ternary terms to multicomponent systems is also described in [28].

Olivine (orthosilicate solution) $(Ca^{2+}, Mg^{2+}, Ni^{2+})^{M2}(Ca^{2+}, Mg^{2+}, Ni^{2+})^{M1}SiO_4$

$$K = G_{NiCa} - G_{CaNi} = 121336,$$

$$G_{CaNi} = G^{o}(CaNiSiO_4) = 0.5\,G^{o}(Ni_2SiO_4, olivine) + 0.5\,G^{o}(Ca_2SiO_4, olivine) - 6903.6;$$

$${}^{0}L_{CaNi:M} = {}^{0}L_{CaMg:M} = 32235.5;$$

$${}^{1}L_{CaNi:M} = {}^{1}L_{CaMg:M} = 4279.9;$$

$${}^{0}L_{M:CaNi} = {}^{0}L_{M:CaMg} = 28032.8 - 12.5500T, \text{ where } M = Ca, Mg, Ni.$$

The model parameters for the Ca-Mg olivine solution were optimized by Jung *et al.* [45], for Ni-Mg olivine – by Prostakova *et al.* [123]. The excess Gibbs energy parameters were set equal to those for the Ca-Mg olivine solution.

Melilite $(Ca^{2+})_2(Mg^{2+}, Ni^{2+})Si_2O_7$

$$G_{CaMg} = G^{o}\,(Ca_2MgSi_2O_7, akermanite);$$

$$G_{CaNi} = G^{o}\,(CaNiSi_2O_6, clino\text{-}) + G^{o}(CaO) - 60668;$$

Akermanite was optimized by Jung *et al.* [45].

Table 7.7 (Continued): Optimized model parameters for the slag, olivine and pyroxene phases in the CaO–MgO–NiO–SiO_2 system and its subsystems CaO–NiO–SiO_2 and CaO–MgO–NiO ($J \cdot mol^{-1}$ and $J \cdot mol^{-1} \cdot K^{-1}$)

Clino-pyroxene (Ca^{2+}, Mg^{2+}, Ni^{2+})^{M2}(Mg^{2+}, Ni^{2+})^{M1}Si_2O_6

$G_{\mathrm{CaNi}} = G^{\mathrm{o}}$ ($CaNiSi_2O_6$, *clino*-), where

$\Delta H^{\mathrm{o}}_{298.15} = -2802600, \quad S^{\mathrm{o}}_{298.15} = 161.8\ , \ \Delta S^{\mathrm{ox}}_{f,298.15} = 3.3\ ;$

$C_P(T) = C_P(\mathrm{Ni_2SiO_4(solid)} + \mathrm{CaO(solid)} + \mathrm{SiO_2(quartz)\text{-}NiO(solid)});$

298.15-1000 K:

$C_P(T) = 307.7610 - 0.0186291T + 7.7455\times10^{-6}T^2 - 8.8725\times10^{6}T^{-2} - 1404.930T^{-0.5} + 12.183\times10^{8}T^{-3};$

1000-1800 K:

$C_P(T) = 297.4395 + 0.0050821T - 4.8709\times10^{-6}T^2 - 9.6358\times10^{6}T^{-2} - 1404.930T^{-0.5} + 12.183\times10^{8}T^{-3};$

1800-1850 K:

$C_P(T) = 298.0426 + 0.0044049T - 4.6806\times10^{-6}T^2 - 9.6384\times10^{6}T^{-2} - 1404.930T^{-0.5} + 12.183\times10^{8}T^{-3};$

$K_{\mathrm{MgNi}} = G_{\mathrm{NiMg}} - G_{\mathrm{MgNi}} = -16736;$

$\Delta_{\mathrm{CaNi:NiMg}} = G_{\mathrm{CaMg}} + G_{\mathrm{NiNi}} - G_{\mathrm{CaNi}} - G_{\mathrm{NiMg}} = 0;$

$\Delta_{\mathrm{CaNi:MgMg}} = G_{\mathrm{CaMg}} + G_{\mathrm{MgNi}} - G_{\mathrm{CaNi}} - G_{\mathrm{MgMg}} = 41840;$

${}^0L_{\mathrm{CaMg:Ni}} = {}^0L_{\mathrm{CaMg:Mg}} = 25304 + 2.358T;$

${}^1L_{\mathrm{CaMg:Ni}} = {}^1L_{\mathrm{CaMg:Mg}} = 3018.6.$

The parameters for the Ca-Mg clino-pyroxene solution were optimized by Jung *et al.* [45]. The excess Gibbs energy parameters were set equal to those for the Ca-Mg clino-pyroxene solution.

Table 7.7 (Continued): Optimized model parameters for the slag, olivine and pyroxene phases in the CaO–MgO–NiO–SiO_2 system and its subsystems CaO–NiO–SiO_2 and CaO–MgO–NiO ($J \cdot mol^{-1}$ and $J \cdot mol^{-1} \cdot K^{-1}$)

Proto-pyroxene (Ca^{2+}, Mg^{2+}, Ni^{2+})^{M2}(Mg^{2+}, Ni^{2+})^{M1}Si_2O_6

$$G_{\mathrm{CaNi}} = G^{\mathrm{o}}(\mathrm{CaNiSi_2O_6},\ \textit{proto-}) = G^{\mathrm{o}}(\mathrm{CaNiSi_2O_6},\ \textit{clino-}) + 17071.2;$$

G_{MgMg} and G_{CaMg} is taken from [45]

$$G_{\mathrm{NiNi}} = G^{\mathrm{o}}(\mathrm{Ni_2Si_2O_6}) = G^{\mathrm{o}}(\mathrm{Ni_2SiO_4}, \textit{olivine}) + G^{\mathrm{o}}(\mathrm{SiO_2}, \textit{tridymite}) + 14112.6 - 4.184 \cdot T;$$

$$K_{\mathrm{MgNi}} = G_{\mathrm{NiMg}} - G_{\mathrm{MgNi}} = -25104;$$

$$\Delta_{\mathrm{CaNi:NiMg}} = G_{\mathrm{CaMg}} + G_{\mathrm{NiNi}} - G_{\mathrm{CaNi}} - G_{\mathrm{NiMg}} = 0;$$

$${}^{0}L_{\mathrm{CaMg:Ni}} = {}^{0}L_{\mathrm{CaMg:Mg}} = 25304 + 2.358T.$$

The enthalpy of transition of $CaNiSi_2O_6$ from proto- to clino-structure was set equal to that for $CaMgSi_2O_6$ [45]. The excess Gibbs energy parameter ${}^{0}L_{\mathrm{CaMg:Ni}}$ was set equal to analogical parameter ${}^{0}L_{\mathrm{CaMg:Mg}}$ for the Ca-Mg proto-pyroxene solution [45].

The thermodynamic properties of other solutions and stoichiometric compounds can be found in [51] and [45].

The Gibbs energy of formation of a compound from elements at a temperature of T(K) and a pressure of 1 atm is given by $G = \Delta H^{\mathrm{o}}_{298.15} - TS^{\mathrm{o}}_{298.15} + \int_{298.15}^{T} C_P(T)dT - T\int_{298.15}^{T} \frac{C_P(T)}{T}dT$, where $\Delta H^{\mathrm{o}}_{298.15}$ is the enthalpy of formation of the compound at 1 atm and 298.15 K, $S^{\mathrm{o}}_{298.15}$ is the entropy of the compound at 1 atm and 298.15 K, and $C_P(T)$ is the heat capacity at constant pressure.

CHAPTER 8 Al–Fe–O THERMODYNAMIC MODELING

Equation Chapter (Next) Section 1A critical evaluation of literature data and optimization of the Al–Fe–O chemical system in a wide range of temperatures and oxygen partial pressures are reported in this Chapter. A literature review was carried out for the system and a large variety of the literature data, including phase equilibrium data, thermodynamic properties (heat capacity, entropy, enthalpy, Gibbs energy) and cation distribution data, were used in a subsequent thermodynamic modeling. The Modified Quasichemical Model was used for modeling of the slag phase (liquid oxide phase). The model based on the Compound Energy Formalism was developed for the spinel solid solution. Metallic and monoxide solutions were described with a simple Bragg-Williams model. These physically meaningful models are based on the structure of the corresponding solutions and, therefore, have good ability to predict the properties of multicomponent systems.

8.1 Background

The Al and Fe elements are major components of laterite ores. The Al–Fe–O system has complex phase relations, partly due to the presence of both ferrous and ferric oxides at equilibrium, ratio of which depends on the temperature as well as on the oxygen partial pressure [134]. Metallurgical industries require reliable predictions of phase equilibria in the Al–Fe–O system in order to improve the effectiveness of nickel extraction processes, decrease attendant expenses and make the processes more environmentally friendly. So, it was essential to optimize all available literature data on the thermodynamics of the Al–Fe–O system in the range of oxygen partial pressures varying from those of metal saturation to those of pure oxygen and in the range of temperatures – from 25°C to liquidus temperatures.

All available literature data were reviewed, analyzed and taken into consideration in the optimization of all oxide phases in the Al–Fe–O system at 1 atm total pressure.

8.2 Phases and thermodynamic models

A list of solution phases and stoichiometric compounds present in the Al–Fe–O system along with notations used in this Chapter is given in Table 8.1. In oxide phases in the range of oxygen partial pressures from that of metallic saturation up to 1 atm, iron exists in two oxidation states: Fe^{2+} and Fe^{3+}, while aluminum – only as Al^{3+}. For the spinel solid solution, cations shown within a set of parentheses occupy the same sublattice, which is explained in more details in Section 4.6.1. Metallic

solutions and stoichiometric compounds, Al_5Fe_2 and $Al_{61}Fe_{31}$, were optimized previously as part of the FSstel database of FactSage thermochemical software [1]. Model parameters for the liquid and solid oxide solutions as well as the stoichiometric compound $FeAlO_3$ were optimized in the present study. They are listed in Table 8.2.

Table 8.1: Solution phases and stoichiometric compounds present in the Al–Fe–O system

Phase name	**Formula**	**Notation used in this study**
Solution phases:		
Oxide solutions:		
Slag (liquid oxide)	Al_2O_3–FeO–Fe_2O_3	L or Liquid
Monoxide	$AlO_{1.5}$–FeO–$FeO_{1.5}$	Mono or Monoxide
Corundum	$AlO_{1.5}$–$FeO_{1.5}$	Coru or Corundum
Spinel	$(Fe^{2+}, Fe^{3+}, Al^{3+})^{T}[Fe^{2+}, Fe^{3+}, Al^{3+}, Va]_2^{O}O_4^{2-}$ *	Sp or Spinel
Metallic solutions :		
Fcc	Al–Fe	
Bcc_A2	Al–Fe	
Bcc_B2	Al–Fe	
$Al_{13}Fe_4$	Al–Fe	
Al_5Fe_4	Al–Fe	
Liquid metal	Al–Fe–O	L metal or Liquid metal
Stoichiometric compounds:		
Al_5Fe_2	Al_5Fe_2	
$Al_{61}Fe_{31}$	$Al_{61}Fe_{31}$	
$FeAlO_3$	$FeAlO_3$	

*T = tetrahedral sublattice, O = octahedral sublattice

8.2.1 Slag (liquid oxide)

The liquid oxide phase is an ionic melt where metal cations are predominantly surrounded by oxygen anions. In other words, they exhibit almost full first-nearest-neighbour (FNN) short-range ordering (SRO). Furthermore, there is a strong tendency for second-nearest-neighbour SRO of some cations in melts. In particular, basic cations such as Mg form strong second-nearest-neighbour (SNN) pairs with acidic cations such as Si^{4+}. The effects of both FNN and SNN are described by the Modified Quasichemical Model [7, 8]. Though, in the Al_2O_3-FeO-Fe_2O_3 system, SNN pairs ordering is not strong, the same model is used in a view of developing of a broader database for calculations in multicomponent systems. The most significant parameter of the MQM model is the Gibbs energy of the corresponding pair exchange reaction:

$$(\text{Al-Al}) + (\text{Fe-Fe}) = 2(\text{Al-Fe}); \quad \Delta g_{\text{Al,Fe}} \tag{8.1},$$

where (m-n) represents a second-nearest-neighbour pair. Let n_m and Z_m be the number of moles and the coordination number of the component *m*, respectively. The "coordination-equivalent" fractions (Y_m) are then defined as

$$Y_m = Z_m n_m / \sum_i Z_i n_i \tag{8.2}$$

Δg_{mn} is expanded as a polynomial in the "coordination-equivalent" fractions of the components

$$\Delta g_{mn} = \Delta g^{\circ}_{mn} + \sum_{(i+j)\geq 1} q^{ij}_{mn} Y^i_m Y^j_n \tag{8.3},$$

where Δg°_{mn} and q^{ij}_{mn} are empirical binary coefficients which may be functions of temperature and pressure. They were optimized to take into account available thermodynamic and phase equilibrium data.

The symmetric "Kohler-like" extrapolation [28] of binary terms into the ternary system was used in order to calculate the Gibbs energy of the ternary liquid. The liquidus data in the Al_2O_3–FeO–Fe_2O_3 system were described only with binary terms; no ternary terms were introduced.

8.2.2 Spinel

$FeAl_2O_4$, which naturally occurs as a mineral hercynite, is nearly a normal spinel. It has a small degree of inversion, which is demonstrated in Figure 8.1, which shows that Fe ions prefer tetrahedral

sites. It was first reported to be a normal cubic spinel by Barth and Posnjak [135]. The experimental details for the data shown in Figure 8.1 are given in Section 8.3.1.3. The calculated line corresponds to equilibrium cation distribution.

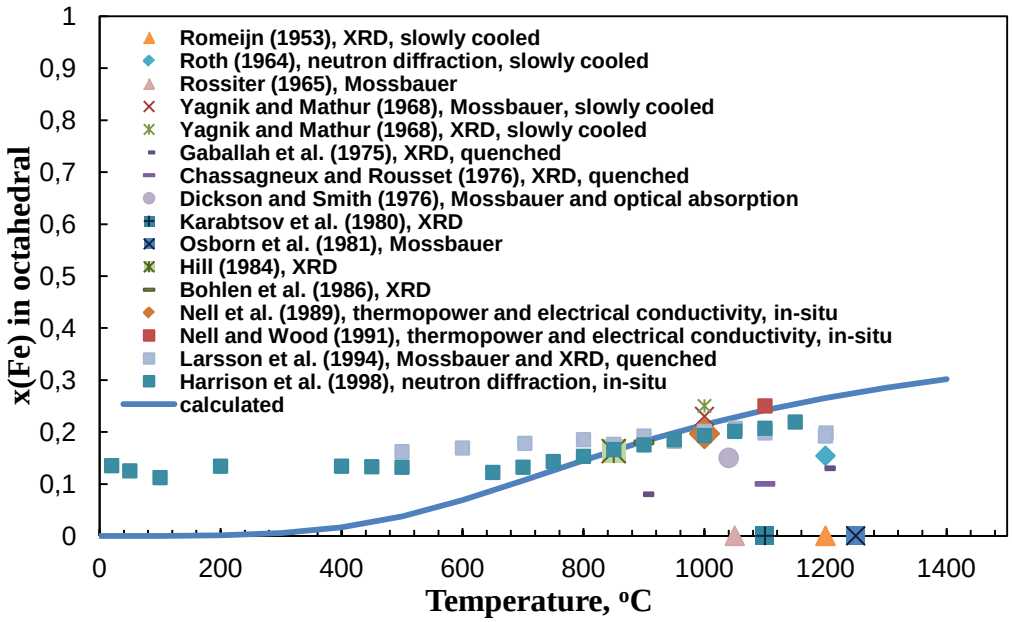

Figure 8.1: Cation distribution in stoichiometric $FeAl_2O_4$: literature data [136-150] and a calculated line

The stoichiometric hercynite $FeAl_2O_4$ and magnetite Fe_3O_4, both with the cubic spinel structure, are completely soluble in each other at temperatures above 860 °C [151]. The cation distribution of Fe^{2+}, $Fe^{3+}$and Al^{3+} in the $FeAl_2O_4$–Fe_3O_4 spinel solution is demonstrated in Figure 8.2, (a)-(c).

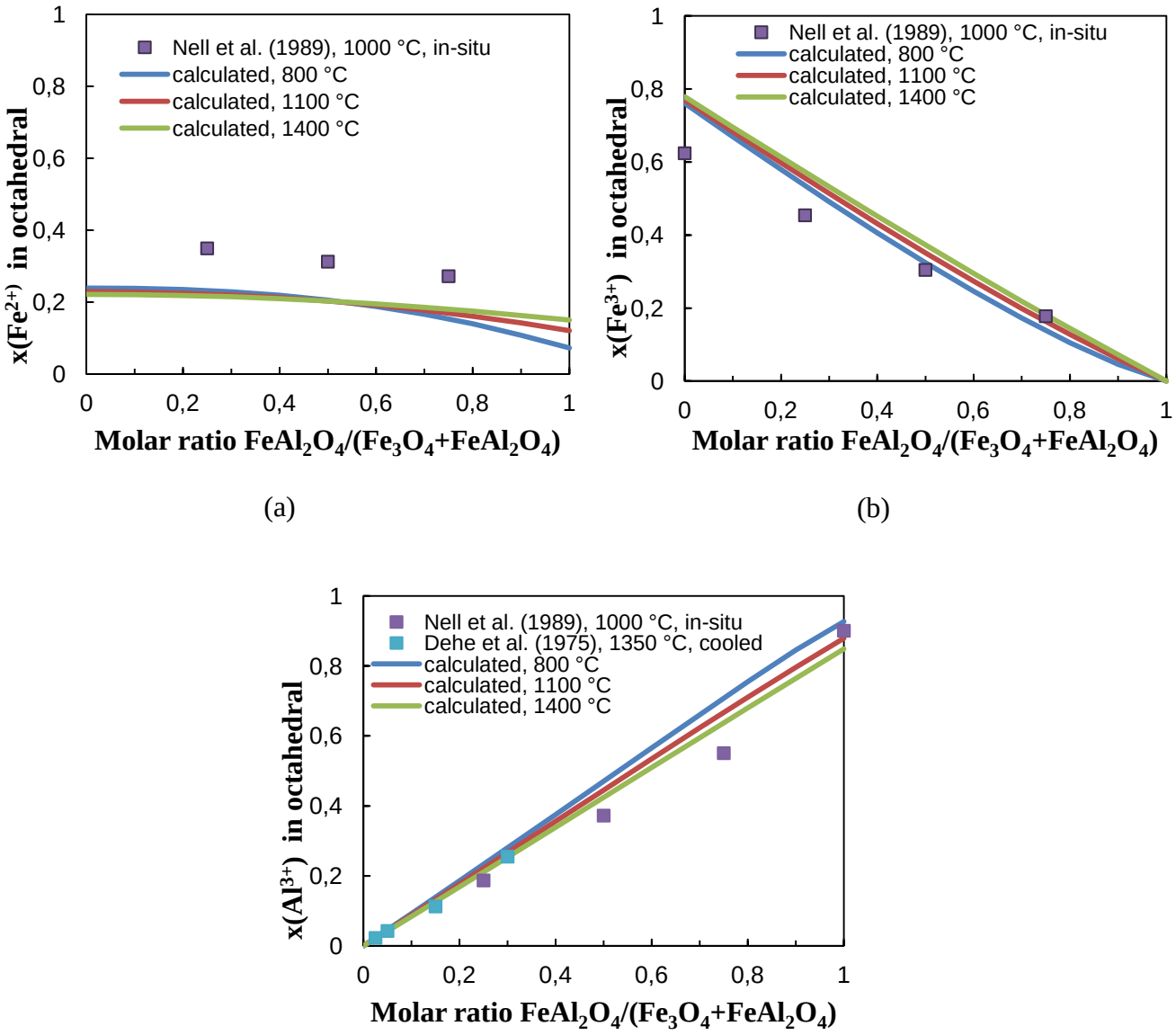

Figure 8.2: Cation distribution in $FeAl_2O_4$–Fe_3O_4 solid solution: literature data [147, 152] and calculated lines

The model for the Al-Fe spinel was developed within the framework of the Compound Energy Formalism (CEF):

$$(Fe^{2+}, Fe^{3+}, Al^{3+})^{T}[Fe^{2+}, Fe^{3+}, Al^{3+}, Va]_2^{O}O_4^{2-} \qquad (8.4)$$

The formation of neutral vacancies on the octahedral sublattice describes the non-stoichiometry of the Al-Fe spinel towards excess oxygen.

The Gibbs energy expression and model parameters for a general spinel solution are explained in detail by Decterov et al. [41]. In brief, the Gibbs-energy expression in the CEF per formula unit is the following:

$$G_m = \sum_i \sum_j Y_i^{\mathrm{T}} Y_j^{\mathrm{O}} G_{ij} - TS_c + \Delta G^{ex} \tag{8.5}$$

where Y_i^{T} and Y_j^{O} represent the site fractions of the constituents *i* and *j* on the tetrahedral (T) and octahedral (O) sublattices, respectively, G_{ij} is the Gibbs energy of a pseudo-component $(i)[j]_2O_4$, ΔG^{ex} is the excess Gibbs energy and S_c is the configurational entropy assuming random mixing on each sublattice,

$$S_c = -R(\sum_i Y_i^{\mathrm{T}} \ln Y_i^{\mathrm{T}} + 2\sum_j Y_j^{\mathrm{O}} \ln Y_j^{\mathrm{O}}) \tag{8.6}$$

$$\Delta G^{ex} = \sum_i \sum_{j>i} \sum_k Y_i^{\mathrm{T}} Y_j^{\mathrm{T}} Y_k^{\mathrm{O}} L_{ij:k} + \sum_i \sum_{j>i} \sum_k Y_k^{\mathrm{T}} Y_i^{\mathrm{O}} Y_j^{\mathrm{O}} L_{k:ij} \tag{8.7},$$

where $L_{ij:k}$ and $L_{k:ij}$ are the interaction energies between cations *i* and *j* on the one sublattice when the other sublattice is occupied by *k*.

The model parameters, which were applied for the Fe_3O_4–$FeAl_2O_4$ spinel solution, are given below:

$$F_{Fe^{+2}Fe^{+3}} = \frac{1}{7} G_{Fe^{+2}Fe_2^{+3}O_4} = \frac{1}{7} G_{[Fe^{+3}Fe_2^{+2}O_4]^{-1}} \tag{8.8}$$

$$I_{Fe^{+2}Fe^{+3}} = G_{[Fe^{+3}Fe_2^{+3}O_4]^{+1}} + G_{[Fe^{+3}Fe_2^{+2}O_4]^{-1}} - 2G_{Fe^{+2}Fe_2^{+3}O_4} \tag{8.9}$$

$$\Delta_{Fe^{+2}Fe^{+3}} = G_{[Fe^{+2}Fe_2^{+2}O_4]^{-2}} + G_{[Fe^{+3}Fe_2^{+3}O_4]^{+1}} - G_{[Fe^{+3}Fe_2^{+2}O_4]^{-1}} - G_{Fe^{+2}Fe_2^{+3}O_4} \tag{8.10}$$

$$V_{Fe^{+3}} = G_{[Fe^{+3}Va_2O_4]^{-5}} - \frac{5}{7} G_{[Fe^{+3}Fe_2^{+2}O_4]^{-1}} \tag{8.11}$$

$$\Delta_{Fe^{+3}Fe^{+2}Va} = G_{[Fe^{+2}Fe_2^{+2}O_4]^{-2}} + G_{[Fe^{+3}Va_2O_4]^{-5}} - G_{[Fe^{+3}Fe_2^{+2}O_4]^{-1}} - G_{[Fe^{+2}Va_2O_4]^{-6}} \tag{8.12}$$

$$F_{Fe^{+2}Al^{+3}} = \frac{1}{7} G_{Fe^{+2}Al_2^{+3}O_4} \tag{8.13}$$

$$I_{Fe^{+2}Al^{+3}} = G_{[Al^{+3}Al_2^{+3}O_4]^{+1}} + G_{[Al^{+3}Fe_2^{+2}O_4]^{-1}} - 2G_{Fe^{+2}Al_2^{+3}O_4} \tag{8.14}$$

$$\Delta_{Fe^{+2}Al^{+3}} = G_{[Fe^{+2}Fe_2^{+2}O_4]^{-2}} + G_{[Al^{+3}Al_2^{+3}O_4]^{+1}} - G_{[Al^{+3}Fe_2^{+2}O_4]^{-1}} - G_{Fe^{+2}Al_2^{+3}O_4} \tag{8.15}$$

$$\Delta_{Fe^{+3}Al^{+3}} = G_{[Fe^{+3}Fe_2^{+3}O_4]^{+1}} + G_{[Al^{+3}Al_2^{+3}O_4]^{+1}} - G_{[Al^{+3}Fe_2^{+3}O_4]^{+1}} - G_{[Fe^{+3}Al_2^{+3}O_4]^{+1}} \tag{8.16}$$

$$\Delta_{Fe^{+2}Fe^{+3}Al^{+3}} = G_{[Fe^{+3}Fe_2^{+3}O_4]^{+1}} + G_{[Fe^{+2}Al_2^{+3}O_4]} - G_{[Fe^{+2}Fe_2^{+3}O_4]} - G_{[Fe^{+3}Al_2^{+3}O_4]^{+1}} \tag{8.17}$$

F parameters in Equations (8.8) and (8.13) are 1/7 parts of the Gibbs energy of hypothetical normal spinels $FeAl_2O_4$ and Fe_3O_4; *I* parameters in Equations (8.9) and (8.14) describe the degree of inversion of these spinels; Δ parameters in Equations (8.10), (8.15) and (8.16) take into account the thermodynamic properties of real simple spinels $FeAl_2O_4$ and Fe_3O_4. The formation of vacancies is described by introducing the parameters *V* and Δ in Equations (8.11) and (8.12). Δ parameter in Equation (8.17) is used to reproduce the thermodynamic properties of a solution between Fe_3O_4 and $FeAl_2O_4$. The Gibbs energies of the end members, which take part in CEF equation (8.5), can be derived from the model parameters. Model parameters are used to calculate the fractions of end-members using the Gibbs energy minimization procedure built in the FactSage software [1].

Fe_3O_4 (magnetite) and $FeAl_2O_4$ (hercynite) undergo magnetic transitions: magnetite – a ferromagnetic ordering at around 850 K [153] and hercynite – an antiferromagnetic ordering at around 8 K [137]. This has an impact on the thermodynamic properties of the spinel. The phenomenological approach proposed by Hillert and Jarl [44] was used to describe the magnetic contribution to thermodynamic functions. The formulae are given in reference [41]. The main parameters are: T_C – the critical temperature for magnetic ordering (Curie or Néel temperature), β – the average magnetic moment per atom and p – the structural constant. The linear change of T_C and β between the Fe_3O_4 and $FeAl_2O_4$ was applied in this study, as it was suggested in [41].

8.2.3 Monoxide – $AlO_{1.5}$–FeO–$FeO_{1.5}$

Wüstite Fe_xO has a range of non-stoichiometry towards oxygen and a partial solubility for α-Al_2O_3. The Bragg-Williams random mixing model (FeO, $FeO_{1.5}$, $AlO_{1.5}$) was used, with the following Gibbs energy expression:

$$\begin{aligned} G &= (X_{\mathrm{FeO}} G^{o}_{\mathrm{FeO}} + X_{\mathrm{FeO_{1.5}}} G^{o}_{\mathrm{FeO_{1.5}}} + X_{\mathrm{AlO_{1.5}}} G^{o}_{\mathrm{AlO_{1.5}}}) \\ &+ RT(X_{\mathrm{FeO}} \ln X_{\mathrm{FeO}} + X_{\mathrm{FeO_{1.5}}} \ln X_{\mathrm{FeO_{1.5}}} + X_{\mathrm{AlO_{1.5}}} \ln X_{\mathrm{AlO_{1.5}}}) + \Delta G^{ex} \end{aligned} \tag{8.18}$$

The excess Gibbs energy ΔG^{ex} is a polynomial with Toop-like extension of binary terms into multicomponent systems, with FeO as an asymmetric component [28].

8.2.4 Corundum – $AlO_{1.5}$–$FeO_{1.5}$

α-Fe_2O_3 and α-Al_2O_3, both end-members of corundum solution, are partially soluble in each other. The model used for the corundum solution was the same as for the monoxide solution, but without the FeO component.

8.2.5 Metallic solutions and stoichiometric compounds

The Al-Fe metallic solutions and stoichiometric compounds Al_5Fe_2 and $Al_{61}Fe_{31}$ were optimized previously within the scope of the FSstel database of FactSage software [1]. The optimized parameters were applied in this study. The Al-Fe phase diagram is shown in Figure 8.3.

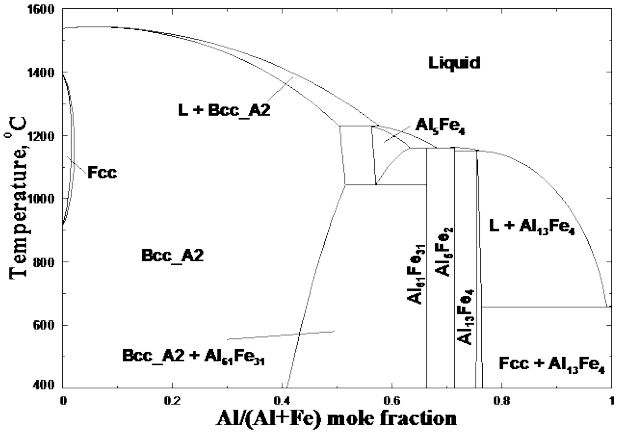

Figure 8.3: Al–Fe phase diagram (see Table 8.1 for notations)

8.3 Literature review of experimental data

Literature surveys for the Al–Fe–O system were reported recently by Team and Martienssen [134] and Raghavan [154]. The isothermal section of the Al–Fe–O phase diagram at 1000 °C is demonstrated in Figure 8.4. The Al–Fe–O system consists of the following solution phases: spinel $FeAl_2O_4$–Fe_3O_4, monoxide Fe_xO–($AlO_{1.5}$–$FeO_{1.5}$), corundum $AlO_{1.5}$–$FeO_{1.5}$, Al–Fe alloys, stoichiometric compounds Al_5Fe_2, $Al_{61}Fe_{31}$ and non-stoichiometric $FeAlO_3$. Liquid phases, metal and slag, form at higher temperatures. Magnetite Fe_3O_4 forms a continuous solid spinel solution with hercynite $FeAl_2O_4$, at temperatures above 860 °C [151]. Monoxide is a wüstite Fe_xO-based solution with limited solubility of α-Fe_2O_3 and α-Al_2O_3. Hematite α-Fe_2O_3 and corundum α-Al_2O_3 are partially soluble in each other.

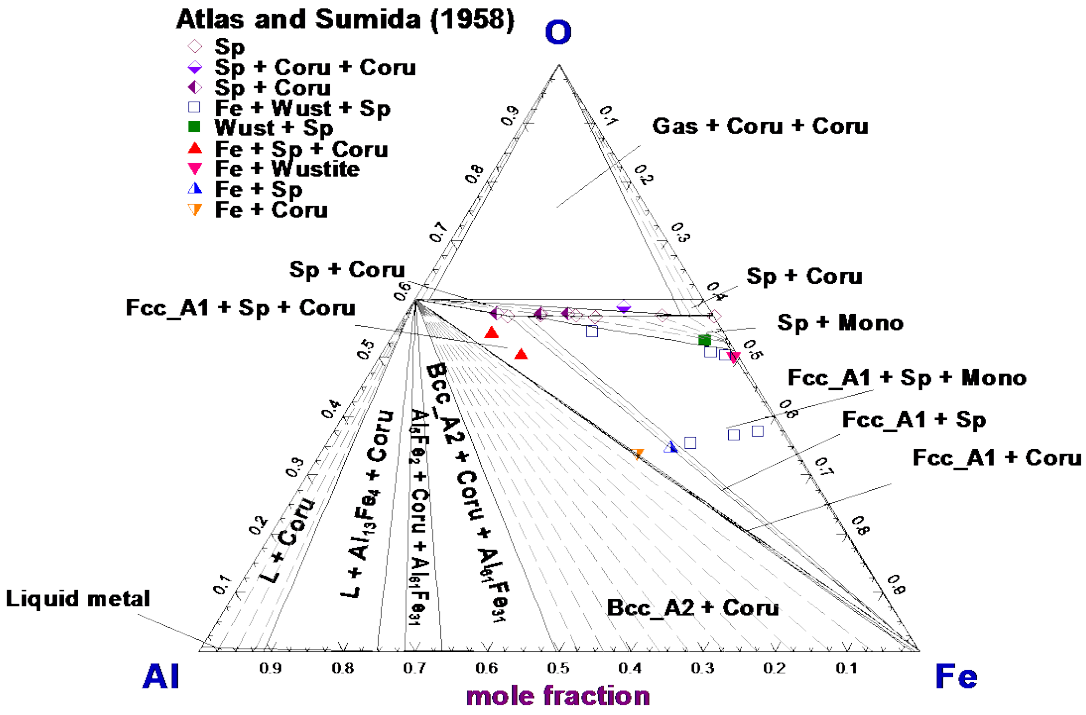

Figure 8.4: Isothermal section of the Al–Fe–O phase diagram in air at 1000 °C and P = 1 atm: literature data [155] and calculated lines. Dashed lines are calculated tie-lines (see Table 8.1 for notations)

8.3.1 $FeAl_2O_4$

The thermodynamics of $FeAl_2O_4$ was intensively investigated: the experimental data include the cation distribution [136-150, 152], heat capacity [156, 157] and Gibbs energy measurements [158-165].

8.3.1.1 Heat capacity and entropy

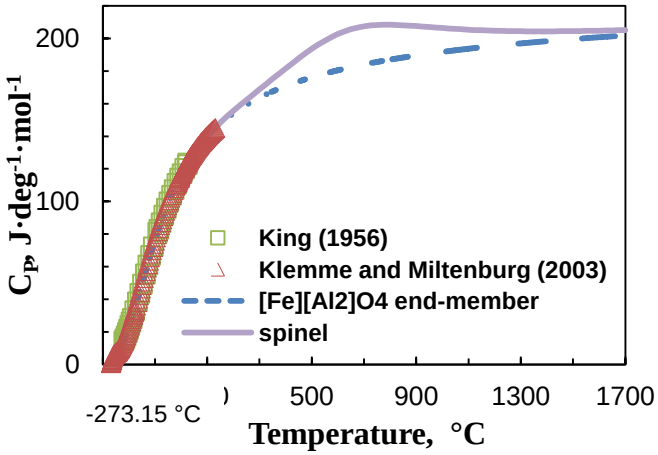

Figure 8.5: Heat capacity of $FeAl_2O_4$ spinel: literature data [156, 157] and calculated lines

The heat capacity of $FeAl_2O_4$ (see Figure 8.5) was measured by means of calorimetry by King [156] – from 53 to 298.15 K (-219 to 25 °C) and by Klemme and Miltenburg [157] – from 3 to 400 K (-270 to 127 °C). From their data, the standard entropy at 298 K $S^{o}_{298.15}$ was calculated as 106.3 ± 0.8 and 113.9 ± 0.2 J·mol^{-1}·K^{-1}, respectively. Klemme and Miltenburg [157] observed a small lambda-shaped anomaly peak on the heat capacity curve at around 13 K (-260 °C), which gave a contribution to the calculated entropy. This was not considered in the earlier study of King [156]. According to Klemme and Miltenburg [157], this transition was previously observed in early magnetic susceptibility measurements by Roth [137] and is probably due to a paramagnetic to antiferromagnetic transition [137, 166].

8.3.1.2 Stability of hercynite

The stability of hercynite was investigated by two different methods in the temperature range 800-1700 °C. The EMF technique was used to measure the oxygen chemical potential over the mixture $FeAl_2O_4$ + α-Al_2O_3 + Fe [161, 162, 164]. The method of heterogeneous equilibria was employed to measure partial pressures of oxygen for the $FeAl_2O_4$ + α-Al_2O_3 + Fe assemblage using H_2/H_2O or CO/CO_2 gas mixtures [158-160, 163, 165]. Both data series are shown in Figure 8.6. Both methods are useful to estimate the Gibbs energy of formation of hercynite $FeAl_2O_4$ from the oxides.

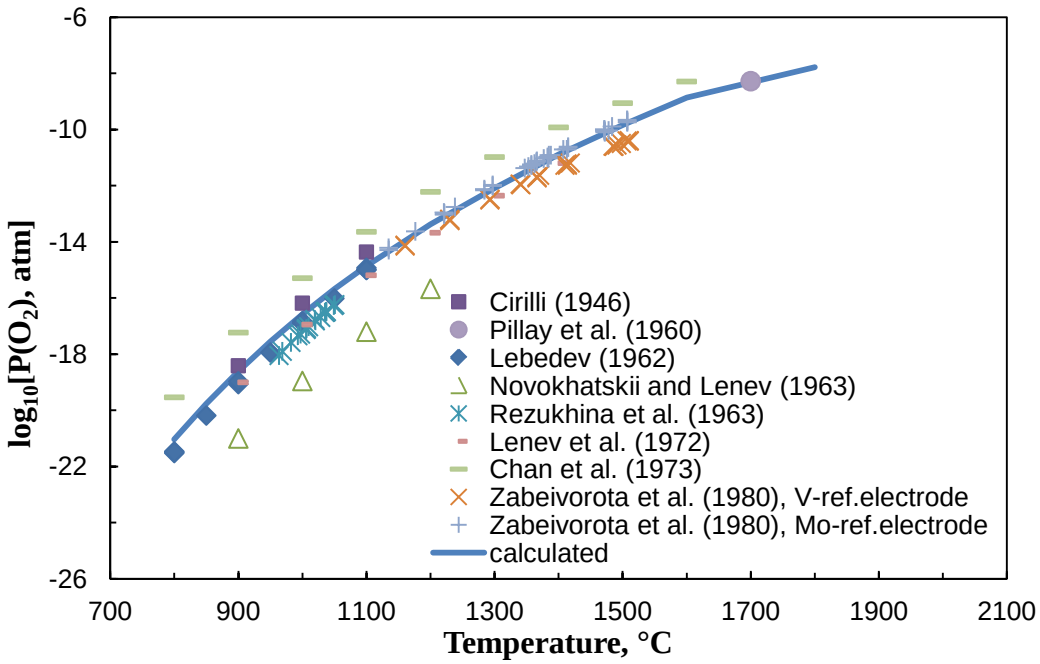

Figure 8.6: Partial pressures of oxygen for the $FeAl_2O_4$ + α-Al_2O_3 + Fe(s,l) assemblage: literature data [158-165] and a calculated line

8.3.1.3 Cation distribution

The cation distribution data for the stoichiometric $FeAl_2O_4$ spinel are shown in Figure 8.1. The samples were either slowly cooled, or quenched, or measured *in-situ*, which is pointed out in the figure; no information was given for some experimental points. The cation arrangement was studied using several different techniques: *Mössbauer spectroscopy* [138, 144], *neutron diffraction* [137, 150], *X-ray diffraction* [136, 140, 141, 143, 145], *Mössbauer spectroscopy and X-ray diffraction* [139, 146, 149], *Mössbauer spectroscopy and optical absorption* [142], *thermopower and electrical conductivity measurements* [147, 148].

Additionally, the cation distribution in the Fe_3O_4-$FeAl_2O_4$ solid spinel solutions was determined by Nell et al. [147] using *in situ* thermopower and electrical conductivity measurements at 1000 °C and by Dehe et al. [167] using *Mössbauer spectroscopy* for samples cooled from 1350 °C. Cation distribution data for the Fe_3O_4-$FeAl_2O_4$ solid spinel solutions are shown in Figure 8.2 (a)-(c).

As can be seen from Figure 8.1, published high-temperature cation distribution data in $FeAl_2O_4$ are scattered. The origin of contradictions was suggested by Harrison et al. [150]: 1) possible re-distribution of cations while quenching from high temperatures 2) possible deviation from ideal stoichiometry 3) poor resolution of Mössbauer spectra. The most recent and comprehensive

investigations by Larsson et al. [149] and Harisson et al. [150] show the degree of inversion increases smoothly with increasing temperature, which is in agreement with the general theory of randomization of cation distribution with increasing temperature.

8.3.2 $FeAlO_3$ phase

8.3.2.1 Heat capacity, entropy, enthalpy, Gibbs energy

The only ternary non-stoichiometric compound, stable between 1318 and about 1500 °C, depending on the oxygen pressure, was reported in the Al–Fe–O system [168, 169]. The thermodynamic properties of $FeAlO_3$ phase were determined by Majzlan et al. [170]: heat capacity shown in Figure 8.7 was measured between 298 and 1550 K using differential scanning calorimetric measurements. No detectable anomaly between 240 and 1550 K was found on the heat capacity curve. The enthalpy of formation of $FeAlO_3$ from the oxides, hematite and corundum, at 298 K was given as 27.9 ± 1.8 kJ/mol, obtained by means of high-temperature oxide-melt calorimetry. In addition, Majzlan et al. [170] estimated the standard entropy of $FeAlO_3$ as 98.9 J/mol K as the sum of various contributions.

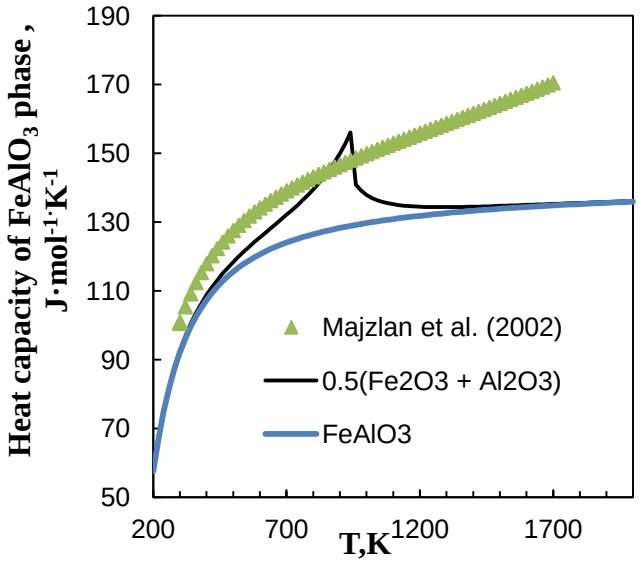

Figure 8.7: Heat capacity of $FeAlO_3$ phase: literature data of Majzlan et al. [170] and calculated lines (black – ½ sum of oxides, blue – current database)

8.3.3 Hematite-corundum solid solution

8.3.3.1 Enthalpy

Several studies indicated restricted mutual solubility between hematite and corundum [155, 168, 171-177]. The enthalpy of mixing in the hematite – corundum solid solution was investigated by Majzlan et al. [170] at 702 and 802 °C by means of high-temperature oxide-melt drop calorimetry. The samples for measurements at 802 °C were prepared by mixing ferric and aluminium nitrate nonanhydrate, annealing at high temperature (1350 °C for hematite-rich samples and 1400 °C for corundum-rich samples) for 2 days and quenching into water. They are referred as high-temperature samples. Enthalpy of mixing for these samples was given only for 25 °C and is shown in Figure 8.8. Another set of Al-hematite samples referred as low-temperature samples was prepared by thermal decomposition of Al-goethite at 702 °C overnight. Enthalpy of mixing for these samples was given for both 25 °C and 702 °C and is shown in Figure 8.8.

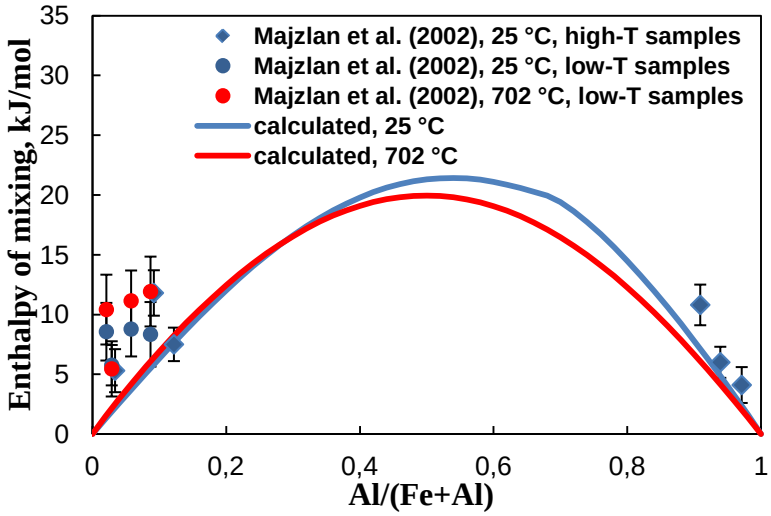

Figure 8.8: Enthalpy of mixing of hematite-corundum solid solution at 25 °C and 702 °C: literature data of Majzlan et al. [170] for differently prepared samples and calculated lines

8.3.4 Phase diagram data

Below 860 °C, a miscibility gap occurs between $FeAl_2O_4$ and Fe_3O_4, as reported by Turnock and Eugster [151]. They used a buffered hydrothermal technique to equilibrate samples of magnetite-hercynite compositions between 500 and 860 ± 15 °C (see Figure 8.9). A buffer controlled oxygen partial pressures in the range 10^{-14}-10^{-28} atm. The compositions of phases were determined by XRD analysis using calibration curves. Their data for measured spinel compositions from both sides of the

miscibility gap are shown in Figure 8.9. Later, Cremer [178] confirmed the formation of the miscibility gap by means of microscopy and X-ray diffraction, using Vegard's law to obtain phase compositions. He performed the experiments by mixing $FeAl_2O_4$ and Fe_3O_4 in quartz ampoules. However, partial pressures of oxygen were not specified. A miscibility gap suggested by this author is shown in Figure 8.9. As can be seen from the figure, both authors observed spinel at lower temperatures, where, according to calculations, it is metastable at oxygen partial pressure of 10^{-14} atm and stable at monoxide saturation, which corresponds to even lower $P(O_2)$. In fact, the calculated spinel miscibility gap for $P(O_2) = 10^{-14}$ and for monoxide saturation almost coincide, the form of the curve remains the same, but spinel + corundum phase field goes to higher temperatures at higher $P(O_2)$.

The temperature for decomposition of the spinel phase was also measured as 811 °C by Lykasov and Kimyashev [179] by considering the kinks in the EMF curves, which will be discussed later in this section.

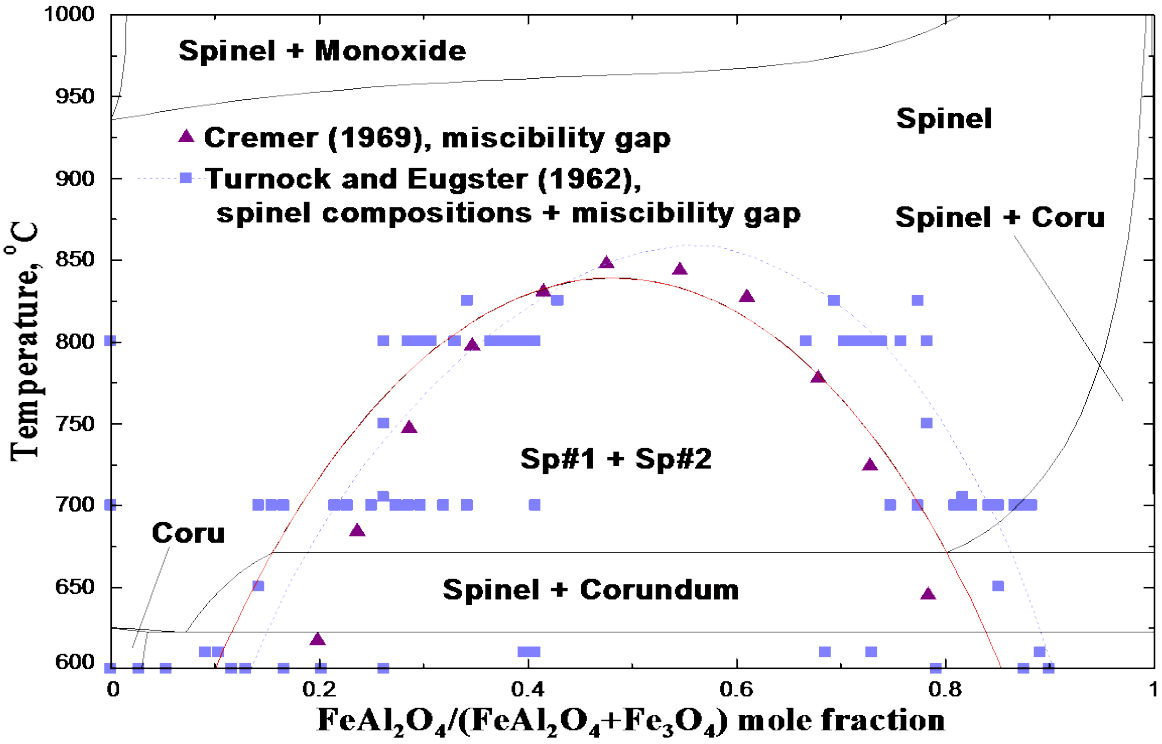

Figure 8.9: Fe_3O_4–$FeAl_2O_4$ section: experimental data [151, 178] indicating spinel miscibility gap at $P(O_2) = 10^{-14}$-10^{-28} atm and unspecified partial pressures of oxygen, respectively, and calculated

lines (see Table 8.1 for notations): black solid line – partial pressure of oxygen of 10^{-14} atm, red solid line – monoxide saturation.

The non-stoichiometry of the spinel solid solution $(Fe_{1-y}Al_y)_{3-\delta}O_4$ was investigated by Horn and Zacharias [180] at 1400 °C using the thermo-gravimetric measurement at partial pressures of oxygen in logarithmic scale varying from -0.7 to -2.9 and is shown in Figure 8.10.

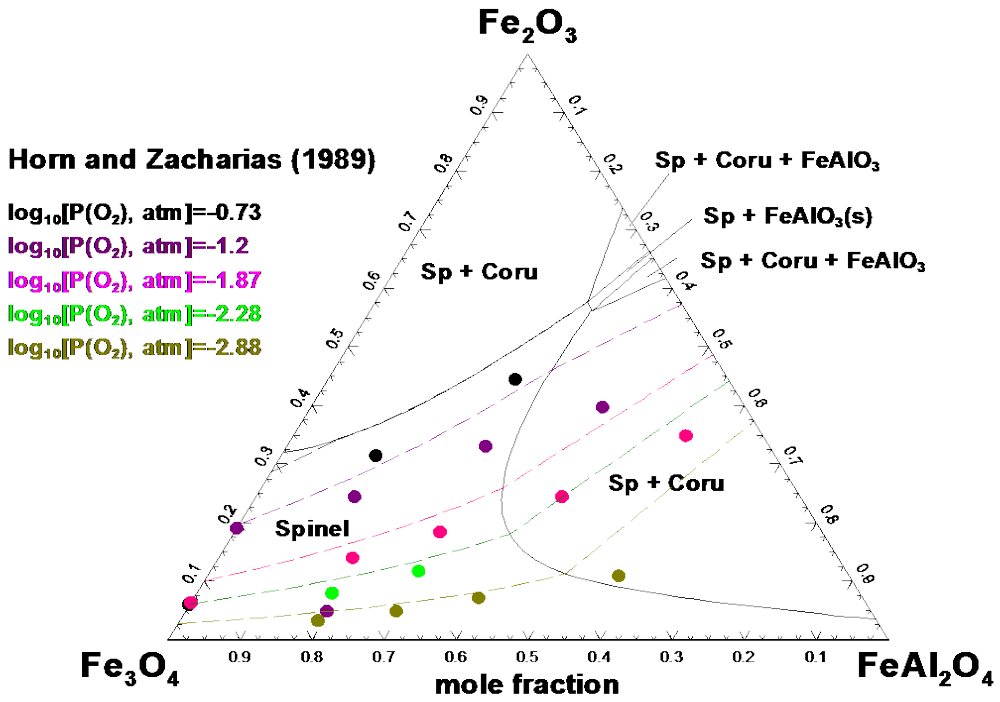

Figure 8.10: Non-stoichiometry of spinel at various oxygen partial pressures at 1400 °C: experimental isobars [180], solid lines – calculated diagram at 1 atm total pressure, dashed lines – calculated isobars (see Table 8.1 for notations)

The $FeAl_2O_4$–Fe_3O_4 section was further investigated by Lykasov and Kimyashev [179], who studied the equilibrium between the Fe_3O_4–$FeAl_2O_4$ spinel and wüstite solutions by the EMF method in the temperature range between 850 and 1000 °C. The EMF was measured for the following cell: $Pt,Fe,FeO|ZrO_2+Y_2O_3|Fe_{1-c}Al_cOy$, where y = 1.33 and c = 0.1-0.6. The critical temperature for decomposition of the spinel phase was found to be around 811 °C in their study by considering the kinks in the EMF curves. The results of their study are shown in Figure 8.11. In this figure, the data for the Fe–O system [181] are also given for comparison.

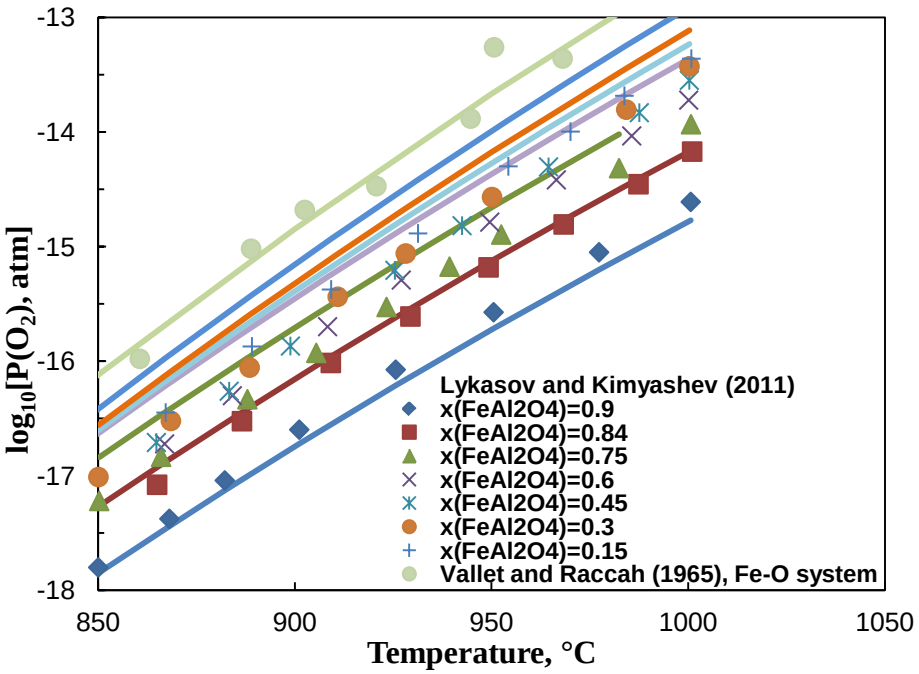

Figure 8.11: Partial pressures of oxygen for $FeAl_2O_4$–Fe_3O_4 + Wüstite assemblage for different compositions of the spinel phase: literature data of Lykasov and Kimyashev [179] and Valleh and Raccah [181] and calculated lines

The properties of the $FeAl_2O_4$–Fe_3O_4 spinel solution were further investigated by Petric et al. [182] at 1300 °C by employing gas equilibration technique. The spinel samples from pure Fe_3O_4 to mole fraction $x(FeAl_2O_4) = 0.9$ were equilibrated with Pt foils under controlled CO + CO_2 gas streams. The equilibrium iron mole fraction in the foil was measured in the range 0.2-0.4 by chemical analysis. The activity-composition relation for iron in the foil was derived from the runs with pure Fe_3O_4 by varying oxygen partial pressures. The results of Petric et al. [182] are recalculated to activity of Fe_3O_4 in the spinel solution and are shown in Figure 8.12. The agreement with calculation is reasonably good.

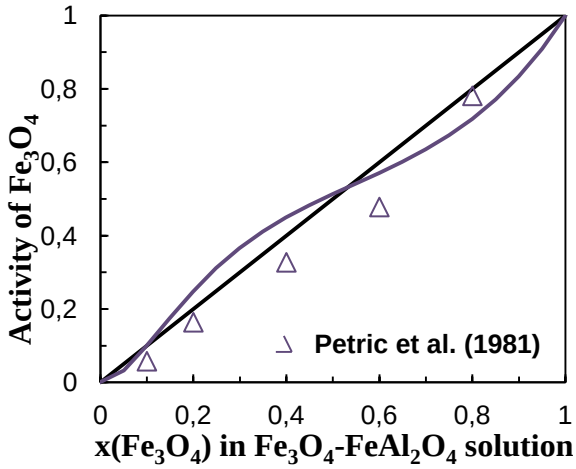

Figure 8.12: Activity of Fe_3O_4 in the $FeAl_2O_4$–Fe_3O_4 solution versus its compositions at 1300 °C: the experimental data of Petric et al. [182] and a calculated line

The FeO–Al_2O_3 section at metallic saturation shown in Figure 8.13 was intensively studied [151, 155, 183-190]. The solidus and liquidus on this section were investigated by Fischer and Hoffmann [183] using thermal, microscopic and XRD analysis by the kinks on the lattice parameter-composition curve. They reported a solubility limit of alumina in wüstite of 2 mol % Al_2O_3 at 1332 °C and of wüstite in alumina as 90.5 mol % Al_2O_3 at 1753 °C and 98 mol % Al_2O_3 at 1500 °C. The composition of spinel in equilibrium with alumina at 1753 °C was reported as 55.6 mol % Al_2O_3. Their results indicated that only at temperatures >1600 °C $FeAl_2O_4$ can deviate from stoichiometry, dissolving some Al_2O_3. They also measured two eutectic points: between wüstite and hercynite at about 5% wt.% (3.6 mol %) Al_2O_3 at 1332 °C and between the spinel and alumina at 65% wt.% (56.7 mol %) Al_2O_3 and 1753 °C. The spinel phase was reported to melt congruently at about 1783 °C.

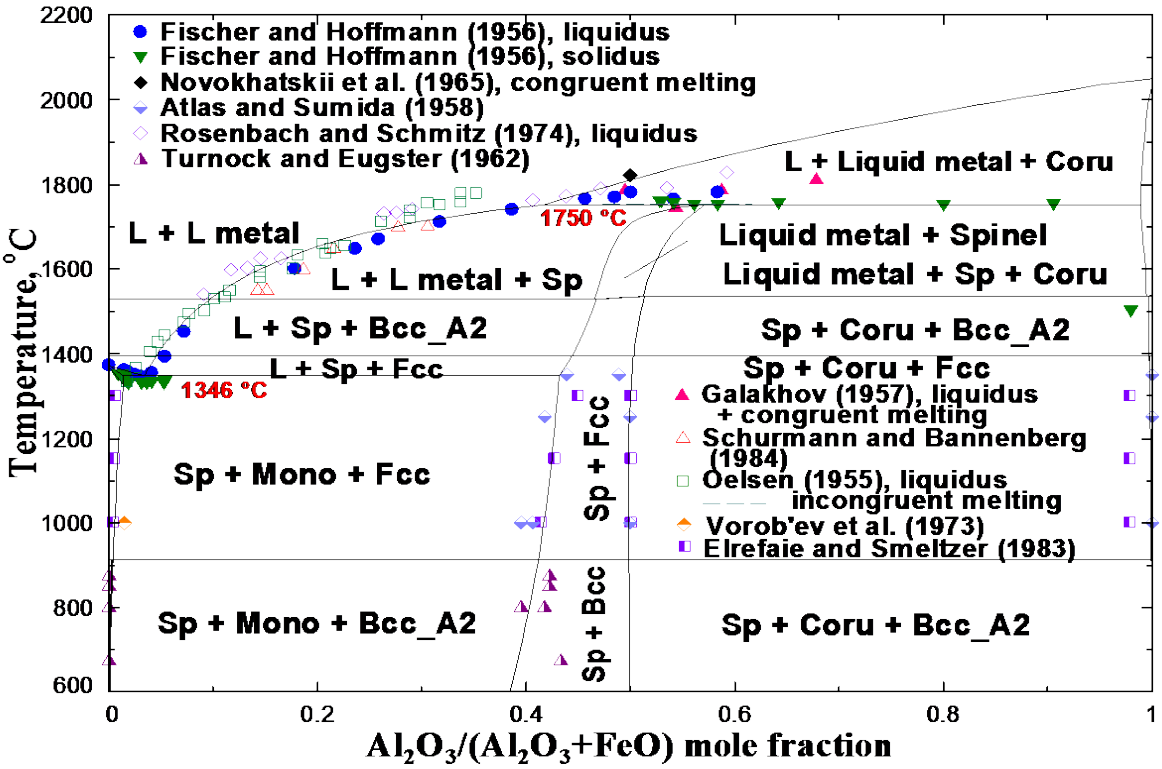

Figure 8.13: Al_2O_3–FeO section at metallic saturation: experimental data [151, 155, 183-190] and calculated lines (see Table 8.1 for notations)

Turnock and Eugster [151] also investigated the Al_2O_3–FeO section at metallic saturation by XRD analysis with calibration curves. They found the Al content of wüstite to be less than 1 wt.% at 1330 °C. In addition, they investigated oxygen partial pressures and compositions for the univariant assemblages in the Al–Fe–O system: 1) hematite + corundum + magnetite 2) corundum + magnetite + hercynite 3) hercynite + wüstite + metal. The oxygen partial pressures corresponding to a number of three-phase equilibria along with the literature data [151, 158-165, 169, 187] are given as a function of temperature in Figure 8.14.

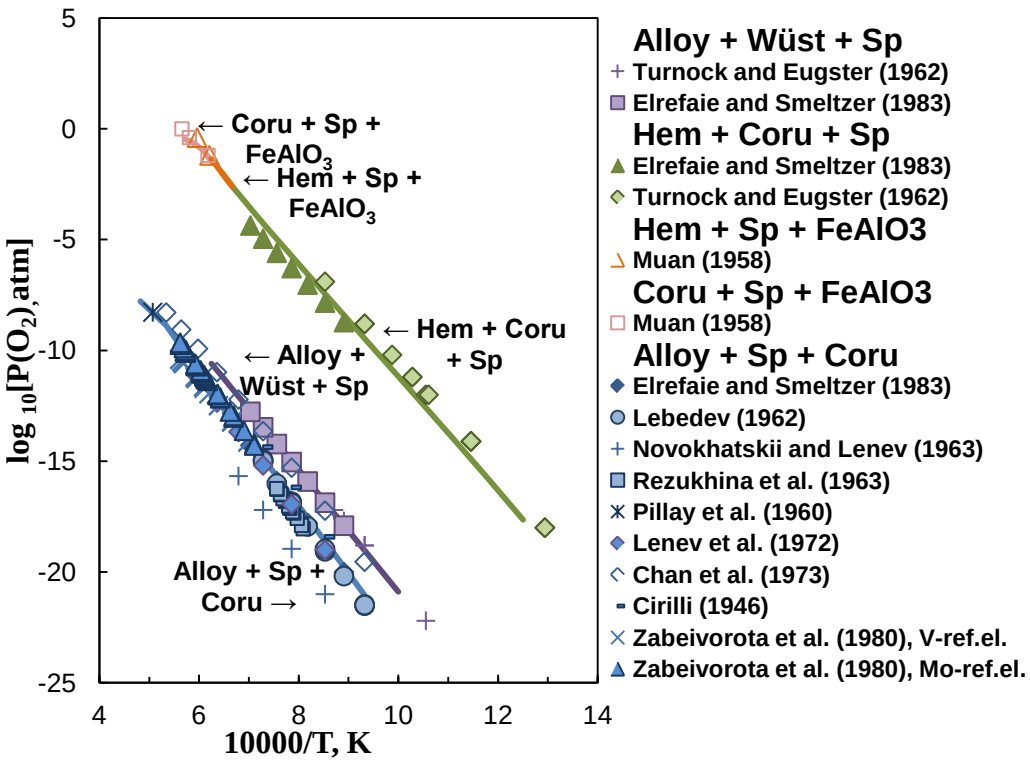

Figure 8.14: Partial pressures of oxygen as a function of temperature over phase triangles in the Al–Fe–O system: literature data [151, 158-165, 169, 187] and calculated lines (see Table 8.1 for notations)

Elrefaie and Smeltzer [187] investigated the Al_2O_3–FeO section at metallic saturation by XRD and EPMA. They also measured equilibrium oxygen pressures of the univariant ternary assemblages hematite + spinel + alumina, alloy + wüstite + spinel, and alloy + spinel + alumina in the range of temperatures between 850 and 1150 °C by employing the EMF method.

Atlas and Sumida [155] found small solubility of wüstite and alumina in each other using equilibration, quenching, XRD and chemical analysis. In addition, they studied subsolidus phase equilibria in the Al–Fe–O system at 1000, 1250, and 1350 °C. Their results are shown in Figure 8.4, Figure 8.13, Figure 8.15 and Figure 8.16.

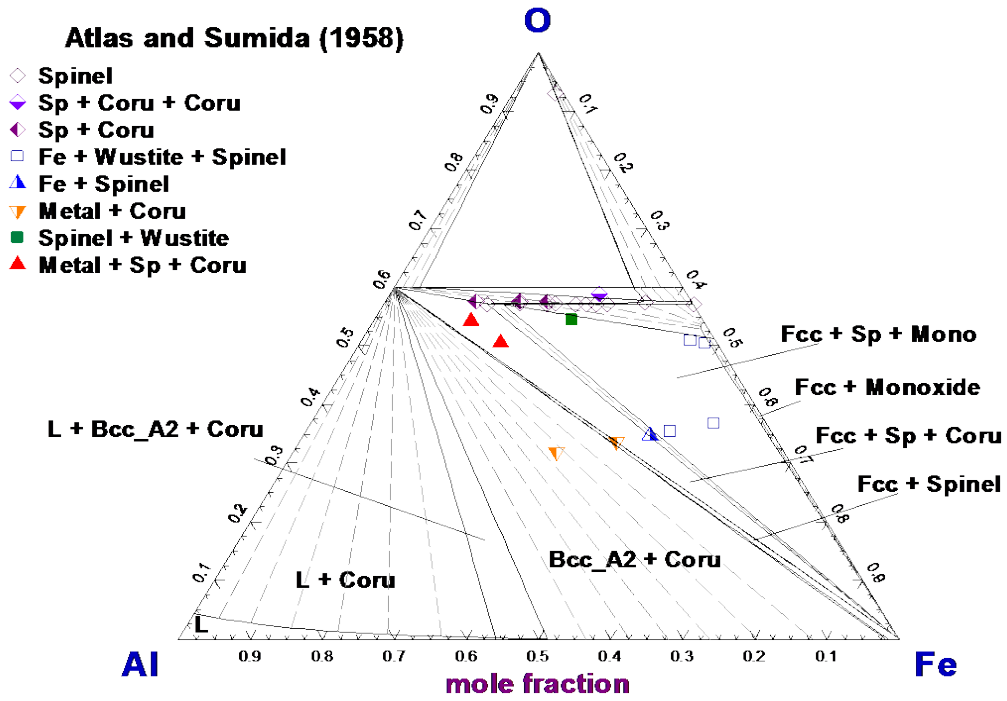

Figure 8.15: Isothermal section of the Al–Fe–O phase diagram at 1250 °C: experimental data [155] and calculated lines. Dashed lines are calculated tie-lines (see Table 8.1 for notations)

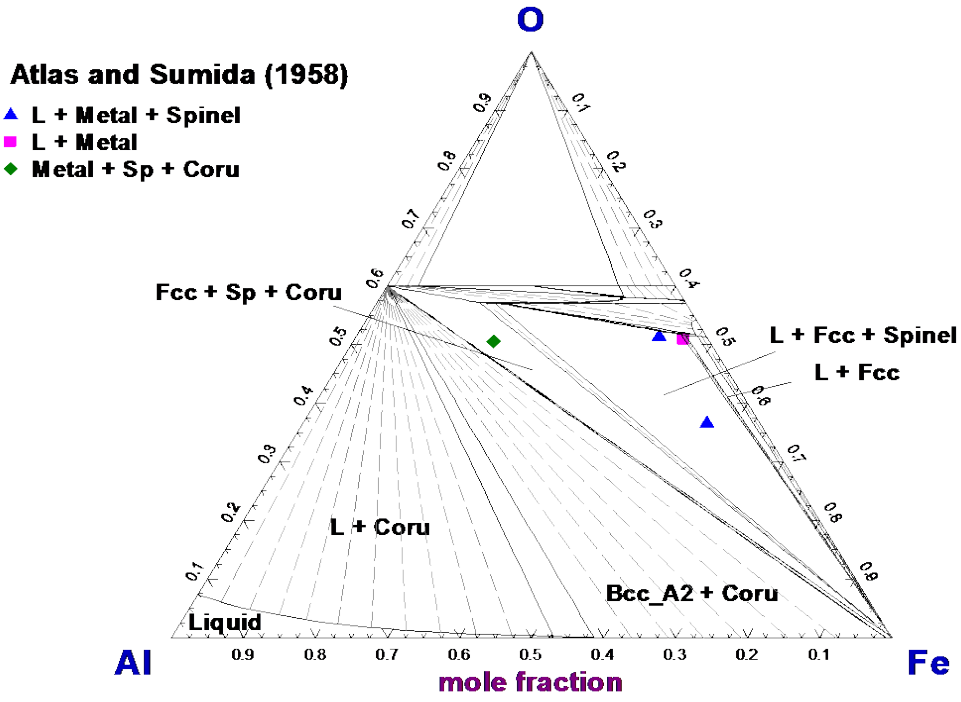

Figure 8.16: Isothermal section of the Al–Fe–O phase diagram at 1350 °C: experimental data [155] and calculated lines. Dashed lines are calculated tie-lines (see Table 8.1 for notations)

Novokhatskii et al. [184] investigated the FeO–Al_2O_3 section at metallic saturation by X-ray diffraction and Vegards' law for phase composition determination and microscopic analysis. It was reported that $FeAl_2O_4$ melts congruently at 1820 ± 15 °C; a eutectic reaction occurs at 4 mol % (5.6 wt.%) Al_2O_3 and 1310 ± 10 °C, which yields FeO dissolving 2 mol% (2.8 wt.%) of Al_2O_3 and $FeAl_2O_4$. Another eutectic reaction between $FeAl_2O_4$ and Al_2O_3 was reported to be at 1750 ± 15 °C and at 56 mol % (64.4 wt.%) Al_2O_3. The negligible miscibility between $FeAl_2O_4$ and Al_2O_3 in the solid phase was found. This result is in agreement with the data of Atlas and Sumida [155] and Elrefaie and Smeltzer [187], who also reported a small solubility of Al_2O_3 in $FeAl_2O_4$ at temperatures below 1400 °C.

Vorob'ev et al. [186] measured the solubility limit of Al_2O_3 in wüstite at 1000 °C as 1.4-1.5 mol% by equilibration, quenching and XRD technique by the kinks on the lattice parameter vs. composition curves.

Further, the Al_2O_3–FeO section was measured in the liquidus region by Oelsen and Heynert [190] by thermal analysis, who reported an eutectic temperature of 1327 °C and a peritectic decomposition of spinel at 1753 °C. Galakhov [185] investigated the $FeAl_2O_4$–Al_2O_3 region of the section by

equilibration in an argon atmosphere, quenching and microscopic analysis. The congruent melting point of $FeAl_2O_4$ was reported as 1800 °C and the eutectic point between hercynite and corundum – as 64 wt.% Al_2O_3 and 1750 °C. Later, Rosenbach and Schmitz [188], using equilibration, quenching and chemical analysis, and Schurmann and Bannenberg [189] reported liquidus temperatures on the same section. Schurmann and Bannenberg [189] did not explicitly reported the experimental method applied in their study.

Roiter [191] investigated the boundaries of the spinel region as a function of oxygen partial pressures ranging from $4 \cdot 10^{-7}$ to $7 \cdot 10^{-10}$ atm obtained by mixing CO and CO_2 at 1500 °C by XRD and lattice parameter measurements. Meyers et al. [192] performed similar investigation at 1280, 1370, and 1500 °C. Both studies showed that as aluminum is added to magnetite, the phase field shifts to lower oxygen pressures and is narrowed, as shown in Figure 8.17-Figure 8.19. The low $P(O_2)$ limit corresponds to the compound hercynite.

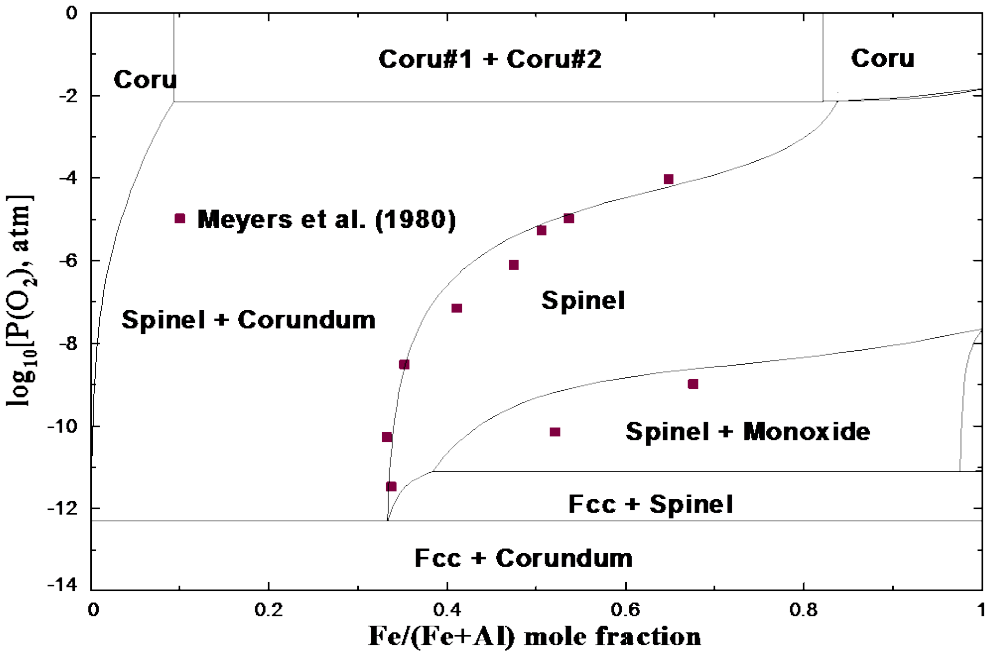

Figure 8.17: $P(O_2)$-x phase diagram at 1280 °C (see Table 8.1 for notations)

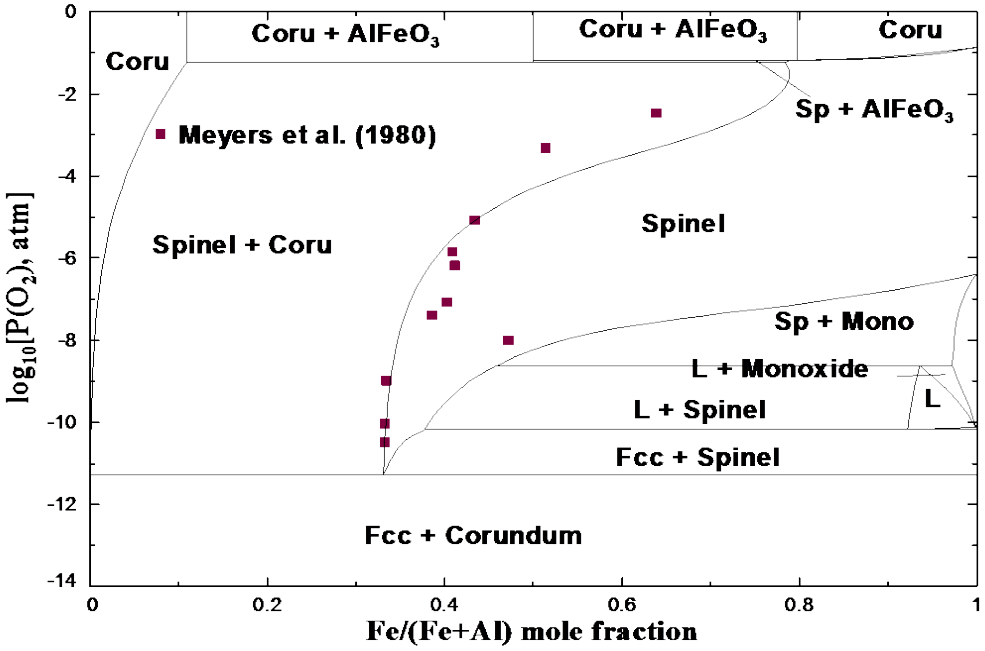

Figure 8.18: $P(O_2)$-x phase diagram at 1370 °C (see Table 8.1 for notations)

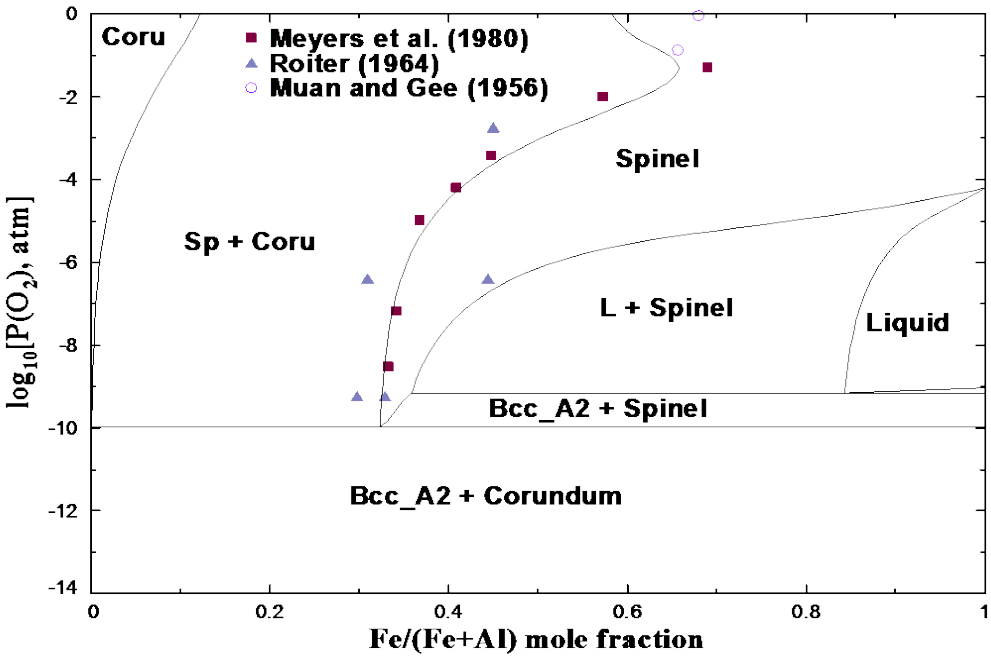

Figure 8.19: $P(O_2)$-x phase diagram at 1500 °C (see Table 8.1 for notations)

The Al_2O_3–Fe_2O_3 pseudo-binary section in air shown in Figure 8.20 was intensively investigated in the literature [151, 155, 168, 169, 171-177]. This section below 1000°C was studied by Turnock and Eugster [151] by XRD analysis in combination with calibration curves.

The Al_2O_3–Fe_2O_3 sections in air and at partial pressure of oxygen of 1 atm were investigated by Muan and Gee [168] in the temperature range between 1085 and 1725° C by employing equilibration and quenching. Microscopy and XRD analysis were used for phase identification. XRD in combination with lattice parameter measurements and comparison with standards of known compositions and chemical analysis were used to determine phase compositions. They found the $FeAlO_3$ phase to be stable between 1318 and 1410 °C in air and up to 1490 °C in oxygen, where it decomposes to spinel and corundum solid solution. The $FeAlO_3$ phase was reported as non-stoichiometric toward both Fe_2O_3 and Al_2O_3. Below 1318 °C, however, equilibrium relationships were uncertain in their study because of the sluggishness of the reactions. Fe_2O_3 dissolved a maximum of about 14 wt.% Al_2O_3 (20.3 mol %), and Al_2O_3 dissolved up to about 19 wt.% Fe_2O_3 (13.0 mol %). The liquid phase and corundum reacted peritectically at ~ 1700°C to yield spinel. The increase in O_2 pressure from that of air to 1 atm had only a minor effect on liquidus temperatures.

Atlas and Sumida [155] confirmed the result of Muan and Gee [168], showing that the $FeAlO_3$ phase is not stable below 1320 °C by applying the XRD analysis by constructing lattice constant-composition curves and chemical analysis. Later, Willshee and White [171] investigated the Al_2O_3–Fe_2O_3 section in air up to 1750 °C by means of a thermobalance following weight changes at equilibrium with temperature.

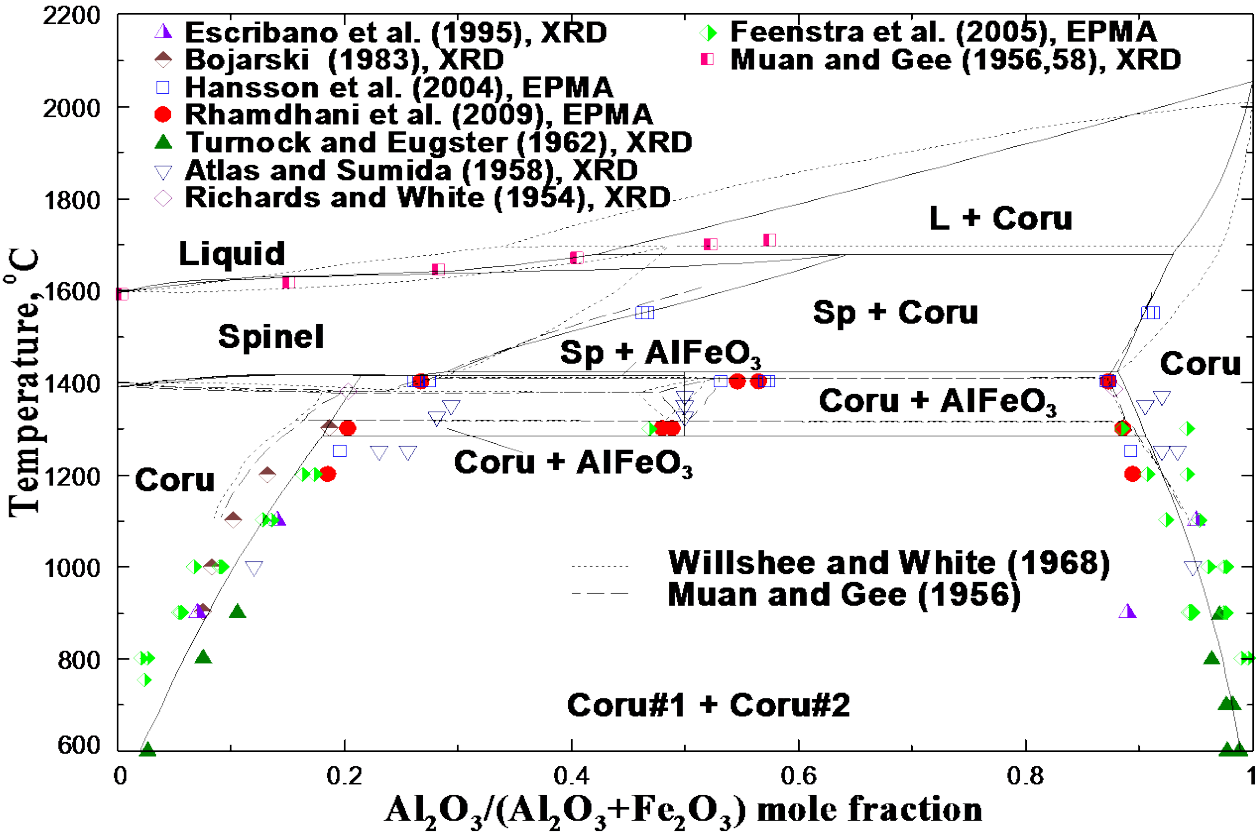

Figure 8.20: Al_2O_3–Fe_2O_3 section of the Al–Fe–O phase diagram in air: experimental data [151, 155, 168, 169, 171-177], where dashed lines are smoothed data, and calculated lines (see Table 8.1 for notations)

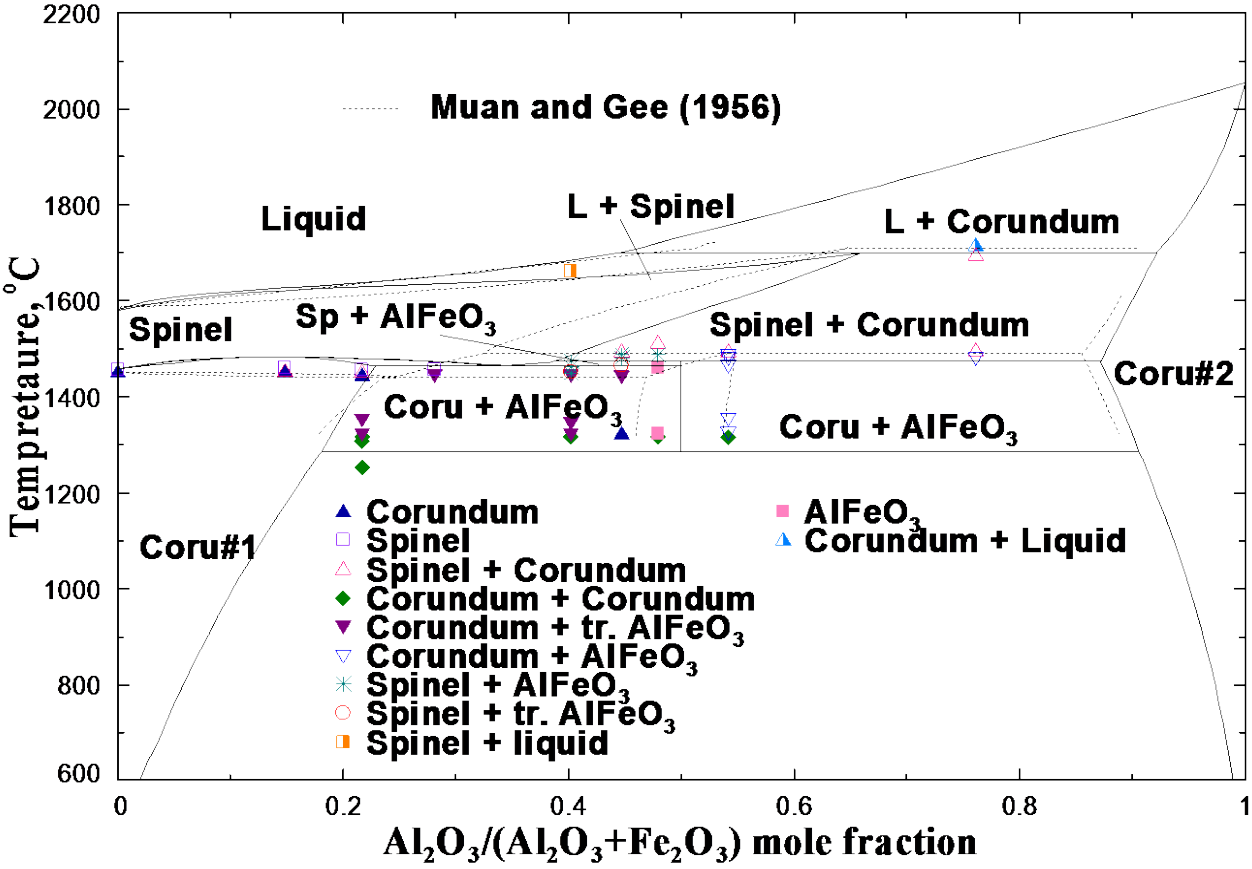

Figure 8.21: Al_2O_3–Fe_2O_3 section of the Al–Fe–O phase diagram at partial pressure of oxygen of 1 atm: experimental data of Muan and Gee [168] (dashed lines and points, where dashed lines are smoothed data) and calculated lines (see Table 8.1 for notations)

Earlier, Richards and White [172] investigated the solid solubility limits of hematite and corundum in each other in air by microscopic analysis and XRD. It was also reported that at higher temperatures, Fe_2O_3 solid solutions dissociate with the release of oxygen and the formation of a spinel phase. The dissociation temperature in air was about 1385 °C. Solubilities of alumina and hematite in each other were further studied by Atlas and Sumida [155], who found that Fe_2O_3 dissolves up to 31 mol % (22 wt.%) of Al_2O_3 and Al_2O_3 dissolves up to 8 mol % (12.5 wt.%) of Fe_2O_3, by Bojarski and Isakow [173], who determined the solubility of Al_2O_3 in Fe_2O_3 varying from 5.6 mol % (3.6 wt.%) at 900 °C to 14 mol % (9.4 wt.%) at 1300 °C, by Feenstra et al. [174] who used electron microprobe and XRD analysis in the temperature range 800-1300 °C and by Escribano et al. [175] at 900 and 1100 °C by XRD.

Recently, Hansson et al. [176] and Rhamdhani et al. [177] investigated the same section by equilibration, quenching and electron probe microanalysis. Hansson et al. [176] measured the extents of solid solutions in the corundum, hematite, spinel and $FeAlO_3$. The limiting compositions of $FeAlO_3$ phase were found to be slightly non-stoichiometric. The results of Hansson et al. [176] and Rhamdhani et al. [177] indicate a larger solubility of Al_2O_3 in hematite and $FeAlO_3$ phase than found by Muan and Gee [168]. Moreover, Rhamdhani et al. [177] observed the $FeAlO_3$ phase at the lower temperature of 1300 °C in the composition range between 54.6 and 56.5 mol% of Al.

Equilibria between the liquid Fe_xO–Al_2O_3 slags contained in solid iron crucibles and H_2-H_2O gas mixtures were measured at 1400 °C by Ban-Ya et al. [193]. Their results are shown in Figure 8.22.

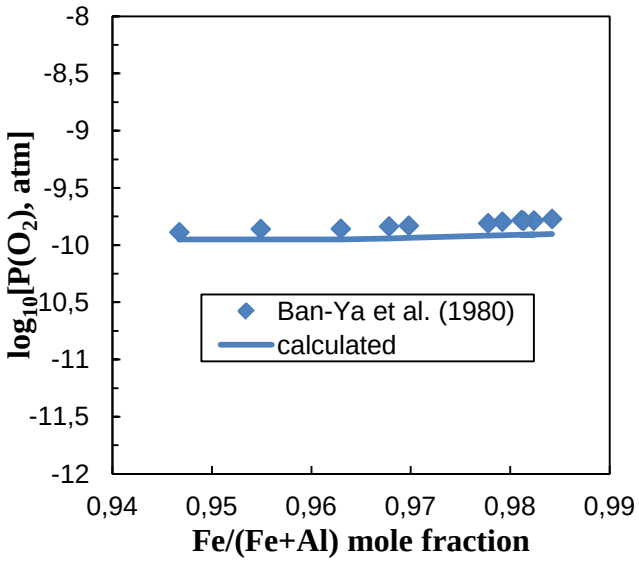

Figure 8.22: Equilibrium pressures of oxygen over Fe_xO–Al_2O_3 slag-metal tie-lines at 1400 °C

8.4 Optimization

The parameters of the models described in Section 8.2 were obtained in the following order. First, the model parameters for corundum (see Figure 8.4, Figure 8.13-Figure 8.21), monoxide (see Figure 8.4, Figure 8.11, Figure 8.13-Figure 8.15, Figure 8.17) and spinel solutions (see Figure 8.1-Figure 8.2, Figure 8.4-Figure 8.6, Figure 8.9-Figure 8.21) were optimized to describe available thermodynamic properties and sub-solidus phase equilibrium data. Afterwards, the parameters of the slag phase were optimized using available liquid-state equilibrium data (see Figure 8.13, Figure 8.20-Figure 8.22).

8.4.1 Spinel

The scheme of optimization of the spinel solution applied in this study was the following. First, the thermodynamic properties of the stoichiometric spinel $FeAl_2O_4$ were fixed. Then, all remaining parameters for the $FeAl_2O_4$–Fe_3O_4 spinel solution were optimized.

The thermodynamic functions of the stoichiometric iron aluminate $FeAl_2O_4$ were calculated with consideration of 3 contributions: lattice (mainly vibrational), magnetic and configurational. A magnetic contribution takes into account the magnetic ordering at around 8 K [137] on the thermodynamic functions of hercynite. It was calculated, as explained in Section 8.2.2. A configurational contribution to the entropy function may be calculated using Equation (8.6). A configurational contribution to the heat capacity function originates from heat of changes of the cation distribution between tetrahedral and octahedral sublattices in $FeAl_2O_4$ with temperature (see Figure 8.1).

A solid line in Figure 8.5 shows the optimized heat capacity C_P of stoichiometric $FeAl_2O_4$. As a first approximation, it was generally assumed that the lattice and magnetic contributions to C_P are independent of the cation distribution of a spinel end-member. As can be seen from Figure 8.5, the experiments on the heat capacity of $FeAl_2O_4$ were made at temperatures up to 200 °C, where the cation distribution was frozen. As a result, a configurational contribution to C_P was not present in these measurements. The sum of lattice and magnetic contributions of the heat capacity of the hypothetical normal spinel $(Fe^{2+})^{T}[Al^{3+}]_2^{O}O_4^{2-}$ was optimized to fit the heat capacity data [156, 157]. The calculated heat capacity of the $(Fe^{2+})^{T}[Al^{3+}]_2^{O}O_4^{2-}$ end-member is shown in Figure 8.5 by the dashed line. The heat effect of changes in the cation distribution and thus the configurational part of the C_P came from the optimization of all phase equilibria at high temperatures involving the spinel phase. The heat capacity of $FeAl_2O_4$ shown by solid line in Figure 8.5 was calculated at all temperatures taking into account the hypothetical equilibrium cation distribution.

The entropy of $FeAl_2O_4$ is well constrained by the oxygen partial pressure data shown in Figure 8.6 and the experimental high-temperature phase equilibria. The entropy of $FeAl_2O_4$ at 900 °C obtained by the optimization of these high-temperature data is 329.3 $J \cdot mol^{-1}K^{-1}$, which is in agreement within 4% with the value of 344.9 $J \cdot mol^{-1}K^{-1}$ calculated by the integration of the C_P shown by the solid line in Figure 8.5 from -273.15 to 900 °C.

The measured enthalpy of formation of spinel should depend upon the cation distribution between the sublattices in the studied samples. The enthalpy of $FeAl_2O_4$ was optimized to take into consideration the Gibbs energy data in studies [158-165]. Since the cation distribution of samples in these studies is not known and most of the data were obtained at temperatures higher than 900 °C, it was assumed to be close to equilibrium.

The parameter *I* was optimized to describe the cation distribution data [136-150, 152] in Figure 8.1 and Figure 8.2. The calculated lines are believed to be in accordance with the experimental data within experimental error limits.

The remaining parameters, $\Delta_{Fe^{+2}Al^{3+}}$, $\Delta_{Fe^{+3}Al^{3+}}$ and $\Delta_{Fe^{+2}Fe^{+3}Al^{3+}}$ and interaction energies $M_{Al^{+3}:Fe^{+3}Al^{+3}}$, $M_{Fe^{+2}:Fe^{+3}Al^{+3}}$, and $M_{Fe^{+3}:Fe^{+3}Al^{+3}}$ were optimized to describe the phase equilibrium data involving the spinel solution (see Figure 8.4, Figure 8.9-Figure 8.21). From available phase diagram data, the experimental data obtained earlier by Hansson et al. [176] and Rhamdhani et al. [177] were considered to be more accurate, which is achieved by applying carefully planned equilibration procedures followed by electron probe X-ray microanalysis.

The optimized model parameters for the spinel phase are given in Table 8.2.

8.4.2 Monoxide, corundum

The parameters of the monoxide phase were optimized to describe the data for phase equilibria involving monoxide (see Figure 8.4, Figure 8.11, Figure 8.13-Figure 8.15, Figure 8.17). Model parameters for corundum are defined by the enthalpy data of Majzlan et al. [170] (see Figure 8.8) and phase equilibria involving corundum from the literature (see Figure 8.4, Figure 8.13-Figure 8.21). However, there was a disagreement. The large positive enthalpy of mixing of the corundum solution at 25 and 702 °C suggested by Majzlan et al. [170] resulted in a wider miscibility gap between Fe_2O_3 and Al_2O_3 than reported by Turnock and Eugster [151] and the most recent data of Rhamdhani et al. [177] and Hansson et al. [176], both of which indicate higher solubility of hematite-based and alumina-based corundum solutions in each other. Majzlan et al. [170] suggested that the excess entropy of mixing in corundum may increase the mutual solubility of corundum-based solutions in each other, while the enthalpy of mixing remains large. Our calculations showed that the excess entropy required to describe the experimental miscibility gap in corundum would have resulted in higher stability of corundum at higher temperatures and unreasonably round shape of the miscibility gap. The only way to describe all experimental data on corundum was to make the

enthalpy of mixing less positive. So, the current optimization is a compromise between the enthalpy data and phase diagram data.

The optimized parameters of the monoxide and corundum solutions are given in Table 8.2. The calculated lines are believed to be in agreement with literature data within experimental error limits.

8.4.3 Liquid

The parameters of the Modified Quasichemical Model were optimized to describe the phase equilibrium data (see Figure 8.13, Figure 8.20-Figure 8.22) and are given in Table 8.2. The calculated lines are in good agreement with the experimental results.

8.4.4 $FeAlO_3$ phase

$FeAlO_3$ is a complex phase with the orthorhombic structure (*Pna*2_1), four distinct cation sublattices and non-stoichiometry towards excess Al_2O_3 and Fe_2O_3. However, there is little knowledge on its thermodynamic properties and cation distribution. Majzlan et al. [170] measured the heat capacity and enthalpy of formation from oxides, estimated the entropy, but could not resolve the cation distribution. Due to uncertainties in the structural and non-stoichiometry data, $FeAlO_3$ was modeled as a stoichiometric compound.

The $FeAlO_3$ phase is stable in a very narrow range in air, as reported by Muan and Gee [168], Atlas and Sumida [155], Feenstra et al. [174], Hansson et al. [176] and Rhamdhani et al. [177]. These authors agreed that in air this phase is stable between 1300 ± 20 and 1410 ± 20 °C. Given this temperature interval and fixed properties of spinel and corundum, the thermodynamic properties of $FeAlO_3$ are very well constrained. In fact, if the heat capacity is defined, the entropy and enthalpy of formation are fixed.

The heat capacity measured by Majzlan et al. [170] is much higher than that of the sum of oxides. With the heat capacity suggested by Majzlan et al. [170], $FeAlO_3$ appeared to be stable at temperatures below 700 °C with respect to oxides. It is the change of properties of corundum that could resolve this problem. But it was not possible to assign large excess entropy to corundum, as it was explained before. The introduction of the excess heat capacity was not possible as well since Majzlan et al. [170] reported themselves that the enthalpy of formation for corundum was independent of temperature. So, it was not possible to use the heat capacity suggested by Majzlan et al. [170] for the $FeAlO_3$ phase. Instead, the lattice part of sum of oxides was used. As a result, the

enthalpy of formation from the oxides and entropy were obtained to describe the interval of $FeAlO_3$ stability: $\Delta H^{o}_{298.15}$ = 19 kJ·mol^{-1} and $S^{o}_{298.15}$ = 87.6 J·mol^{-1}·K^{-1}. Majzlan et al. [170] measured 28 kJ·mol^{-1} for the enthalpy of formation – a somewhat higher value. The value optimized in the present study is close to the calculated enthalpy of mixing of corundum at 298 K at the composition of 0.5 Al_2O_3 and 0.5 Fe_2O_3, which is 21 kJ·mol^{-1}.

As soon as more experimental studies on the cation distribution and non-stoichiometry of the $FeAlO_3$ phase are available, a complex thermodynamic model may be developed and possibly resolve discrepancies in heat capacity and enthalpy of formation of this phase.

8.5 Summary of results

A simultaneous optimization of all available data in the system Al–Fe–O at 1 atm total pressure has been performed. A set of self-consistent Gibbs energy functions of the oxide phases in the Al–Fe–O system was derived. The description of thermodynamic properties data and phase relations were obtained. The optimized model parameters for oxide phases reproduce all available data within experimental error limits. By this means, the next part of the thermodynamic database for the multi-component Al–Ca–Fe–Mg–Ni–O–Si chemical system involved in the process of nickel extraction from the laterite ores was created.

Table 8.2: Optimized properties of stoichiometric compounds and model parameters for oxide phases in the Al–Fe–O system ($J \cdot mol^{-1}$ and $J \cdot mol^{-1} \cdot K^{-1}$)

Compounds	**Temperature range (K)**	$\Delta H^{o}_{298.15}$	$S^{o}_{298.15}$	$C_P(T)$
Al_2O_3 (alpha)	298-2327	-1675700	50.8200	$155.0188 - 3.8613\times10^{6}T^{-2} - 828.387T^{-0.5} + 4.091\times10^{8}T^{-3}$
	2327-3000			192.464
Al_2O_3 (kappa)	298-1100	-1662302	53.5550	$103.9399 + 0.0138795T - 9.1424\times10^{6}T^{-2} + 559.745T^{-0.5} + 1.1426\times10^{9}T^{-3}$
	1100-2327			$-452.6767 + 0.0437540T + 1.598064\times10^{8}T^{-2} + 42202.724T^{-0.5} - 9.576569\times10^{5}T^{-1}$
	2327-3000			192.464
Al_2O_3 (gamma)	298-1200	-1656864	52.3000	$-15.7333 + 0.0299485T + 4.9953\times10^{6}T^{-2} + 7068.351T^{-0.5} - 1.121094\times10^{5}T^{-1}$
	1200-2327			$-787.5153 + 0.0658774T + 2.638163\times10^{8}T^{-2} + 66885.728T^{-0.5} - 1.5255274\times10^{6}T^{-1}$
	2327-3000			192.464
$FeAlO_3$	298-2327	-1232099	87.6000	$146.0139 - 3.3845\times10^{6}T^{-2} + 2.045\times10^{8}T^{-3} - 414.193T^{-0.5}$

Table 8.2 (Continued): Optimized properties of stoichiometric compounds and model parameters for oxide phases in the Al–Fe–O system ($J \cdot mol^{-1}$ and $J \cdot mol^{-1} \cdot K^{-1}$)

	2327-2500			$164.7365 - 1.4538 \times 10^{6} T^{-2}$
	2500-3000			164.5039
$FeAl_2O_4$ (hercynite)	298-360	-1978919.7	94.0235	$-53.6258 + 0.8872765T - 1.0149943 \times 10^{-3} T^{2} + 1084.281 T^{-1}$
	360-2503			$240.0239 - 2.5968 \times 10^{6} T^{-2} - 1669.933 T^{-0.5} + 2.513 \times 10^{8} T^{-3}$

Slag (liquid oxide phase): $AlO_{1.5}$–FeO–$FeO_{1.5}$

$Z_{Al} = 2.06616563;\ Z_{Fe^{+2}} = 1.37744375,\ Z_{Fe^{+3}} = 2.06616563;$

$\Delta g^{o}_{Fe^{+2},Al} = 10041.6, \quad \Delta g^{o}_{Fe^{+3},Al} = 0, \quad q^{10}_{Fe^{+3},Al} = 28308.94, \quad q^{01}_{Fe^{+3},Al} = 9347.$

FeO-$FeO_{1.5}$ liquid oxide was optimized by Decterov et al. [41];

The symmetric “Kohler-like” extrapolation [28] of binary terms into the ternary system was used.

Monoxide (solid oxide): $AlO_{1.5}$–FeO–$FeO_{1.5}$

$q^{00}_{Al,Fe^{+3}} = 0, \quad q^{00}_{Al,Fe^{+2}} = 0.$

FeO-$FeO_{1.5}$ monoxide was optimized by Decterov et al. [41];

The Toop-like extension of binary terms into the ternary system was used, with FeO as an asymmetric component [28].

Corundum: $AlO_{1.5}$–$FeO_{1.5}$

Table 8.2 (Continued): Optimized properties of stoichiometric compounds and model parameters for oxide phases in the Al–Fe–O system ($J\cdot mol^{-1}$ and $J\cdot mol^{-1}\cdot K^{-1}$)

$G^{o}_{Al_2O_3}(coru) = G^{o}_{\alpha\text{-}Al_2O_3}, \quad G^{o}_{Fe_2O_3}(coru) = G^{o}_{\alpha\text{-}Fe_2O_3};$

$q^{00}_{Al,Fe^{+3}} = 41840 - 3.054T, \quad q^{02}_{Al,Fe^{+3}} = -14225.6, \quad q^{20}_{Al,Fe^{+3}} = -11296.8 + 5.0208T.$

Spinel: $(Al^{3+}, Fe^{2+}, Fe^{3+})^{T}(Al^{3+}, Fe^{2+}, Fe^{3+}, Va)_2^{O}O_4$

298-360 K : $7\cdot F_{Fe^{+2}Al^{+3}} = -1998494.2 - 237.3960\cdot T + 53.62583\cdot T\ln T - 0.4436382\cdot T^2 + 1.691657\times 10^{-4}\cdot T^3 + 1084.28\cdot \ln T;$

360-2503 K : $7\cdot F_{Fe^{+2}Al^{+3}} = -2000074.3 + 1718.3200\cdot T - 240.02389\cdot T\ln T - 41882431\cdot T^{-2} - 6679.7317\cdot T^{0.5} + 1298403.4\cdot T^{-1};$

$I_{Fe^{+2}Al^{+3}} = 56132;$

$\Delta_{Fe^{+2}Al^{+3}} = 89267.3 - 133.0617\cdot T + 7.03665\cdot T\ln(T), \quad \Delta_{Fe^{+3}Al^{+3}} = -28451.2, \quad \Delta_{Fe^{+2}Fe^{+3}Al^{+3}} = -25443;$

$M_{Al^{+3}:Fe^{+3}Al^{+3}} = M_{Fe^{+2}:Fe^{+3}Al^{+3}} = M_{Fe^{+3}:Fe^{+3}Al^{+3}} = M_{M_i:Fe^{+3}Al^{+3}} = 38492.8;$

Magnetic properties : $T_{Fe^{+2}Al^{+3}} = T^{i}_{Fe^{+2}Al^{+3}}$ =-24 K (T_{Neel} =8K) [137],

$\beta_{Fe^{+2}Al^{+3}} = \beta^{i}_{Fe^{+2}Al^{+3}}$ =-3.699, P=0.28.

All parameters for Fe_3O_4 spinel, including magnetic properties, were optimized by Decterov et al. [41].

The Gibbs energy of formation of a compound from elements in their standard state at a temperature of T(K) and a pressure of 1 atm is given by $\Delta G = \Delta H^{o}_{298.15} - TS^{o}_{298.15} + \int_{298.15}^{T} C_P(T)dT - T\int_{298.15}^{T}\frac{C_P(T)}{T}dT$, where $\Delta H^{o}_{298.15}$ is the enthalpy of formation of the compound at 1 atm and 298.15 K, $S^{o}_{298.15}$ is the entropy of the compound at 1 atm and 298.15 K, and $C_P(T)$ is the heat capacity at constant pressure.

CHAPTER 9 Al–Ni–O THERMODYNAMIC MODELING

Equation Chapter (Next) Section 1A thermodynamic optimization of the Al–Ni–O system is reported in this Chapter. A complete literature review of thermodynamic and phase equilibrium data in the Al–Ni–O system is provided. Contradictions in the literature data for spinel-corundum equilibria in air were uncovered and resolved with the use of new experimental measurements made by our colleagues from PyroSearch, Australia. The experimental procedure involved high temperature equilibration in controlled gas atmospheres, rapid quenching and direct measurement of quenched samples with electron probe X-ray microanalysis (EPMA). The Al_2O_3–NiO section of the Al–Ni–O phase diagram was measured at 1500 and 1600 °C in air. The solubility of Al_2O_3 in $NiAl_2O_4$ as well as the solubilities of α-Al_2O_3 and NiO in each other were studied. The experimental measurements provided additional data for a subsequent thermodynamic modeling. The thermodynamic modeling was undertaken using the computer package FactSage. The Modified Quasichemical Model was used for modeling of the slag phase (liquid oxide phase). The model based on the Compound Energy Formalism (CEF) was developed for the spinel solid solution. The solubilities of α-Al_2O_3 and NiO in each other as well as metallic solutions were described with a simple Bragg-Williams model. These physically meaningful models are based on the structure of the corresponding solutions and, therefore, have good ability to predict the properties of multicomponent systems.

9.1 Background

The Al–Ni–O system was optimized in the range of oxygen partial pressures varied from those of metal saturation to that of air, and temperatures – from 25°C to temperatures higher than liquidus.

The methodology of the research was as follows. Initially, available literature data for the Al–Ni–O system were reviewed and analyzed. Contradictions in the literature data for the Al_2O_3–NiO section of the Al–Ni–O phase diagram in air were found. To resolve the conflicts in the literature, this section was experimentally studied at 1500 and 1600 °C in air using equilibration and quenching technique by our colleagues from PyroSearch, Australia. The compositions of the quenched samples were determined by the electron-probe microanalysis (EPMA). Further, a set of all available data involving the earlier reported and newly obtained data was taken into consideration in the optimization of oxide phases in the Al–Ni–O system at a total pressure of 1 atm. The optimizations of metallic solutions were not performed in this study; the optimized model parameters for these solutions are available from Ansara et al. [194].

9.2 Phases and thermodynamic models

A list of possible phases in the Al–Ni–O system along with notations used the study is given in Table 9.1. They were modeled as stoichiometric compounds or as solutions as described below. For the spinel solution, cations shown within a set of parentheses occupy the same sublattice. The Al–Ni metallic solutions and stoichiometric compounds (Al_3Ni and Al_3Ni_5) were optimized previously by Ansara et al. [194]. Liquid and solid oxide solutions were optimized in the present study. The optimized model parameters are presented in Table 9.2.

Table 9.1: Solution phases and stoichiometric compounds present in the Al–Ni–O system

Phase name	**Formula**	**Notation used in this study**
Solution phases:		
Slag (liquid oxide)	Al_2O_3–NiO	L or Liquid
Monoxide (solid oxide)	NiO–$AlO_{1.5}$	Mono or Monoxide
Corundum	$AlO_{1.5}$–NiO	Coru or Corundum
Spinel	$(Al^{3+}, Ni^{2+})^{T}[Al^{3+}, Ni^{2+}, Va]_2^{O}O_4^{2-}$ *	Sp or Spinel
Fcc	Al–Ni	
L12-Fcc	Al–Ni	
AlNi	Al–Ni	
Al_3Ni_2	Al–Ni	
Liquid metal	Al–Ni–O	L or Liquid
Stoichiometric compounds:		
Al_3Ni	Al_3Ni	
Al_3Ni_5	Al_3Ni_5	

*T=tetrahedral sublattice, O=octahedral sublattice

9.2.1 Slag (liquid oxide)

The liquid oxide phase is an ionic melt where metal cations are always surrounded by oxygen anions. In other words, they exhibit almost full first-nearest-neighbour (FNN) short-range ordering

(SRO). Furthermore, there is a strong tendency for SRO of some cations in melts. In particular, basic cations such as Ca form strong second-nearest-neighbour (SNN) pairs with acidic cations such as Si. The effects of both FNN and SNN in slags are proven to be well described by the Modified Quasichemical Model (MQM) [7, 8]. Though, in the Al_2O_3–NiO system, the SNN ordering is apparently not strong, the same model is used in a view of the development of a broader database for calculations in multicomponent systems. The most important parameter of the Modified Quasichemical Model is the Gibbs energy of the corresponding pair exchange reaction:

$$(\text{Al-Al}) + (\text{Ni-Ni}) = 2(\text{Al-Ni}); \quad \Delta g_{\text{Al,Ni}} \tag{9.1}$$

where (m-n) represents a second-nearest-neighbour pair. Let n_m and Z_m be the number of moles and the coordination number of component *m*, respectively. The "coordination-equivalent" fractions (Y_m) are then defined as

$$Y_m = Z_m n_m / \sum_i Z_i n_i \tag{9.2}$$

Δg_{mn} is expanded as a polynomial in the "coordination-equivalent" fractions of the components

$$\Delta g_{mn} = \Delta g^{\circ}_{mn} + \sum_{(i+j)\geq 1} q^{ij}_{mn} Y^i_m Y^j_n \tag{9.3}$$

where Δg°_{mn} and q^{ij}_{mn} are empirical binary coefficients which may be functions of temperature and pressure. They are optimized to take into account available thermodynamic and phase equilibrium data. Full expressions for entropy and Gibbs energy of MQM solution are given elsewhere [7, 8].

9.2.2 Spinel

A spinel phase is often present in oxide systems of alumina. A large number of different bivalent cations may enter a spinel structure: M^{2+} = Ni, Mg, Zn, etc. The spinel field may extend from a stoichiometric composition of MAl_2O_4 to non-stoichiometric spinels due to solubility of Al_2O_3 [90, 195, 196].

Generally, cations in the spinel structure occupy two distinct kinds of crystallographic sites: tetrahedrally-coordinated and octahedrally-coordinated by the oxygen anions. A normal spinel is the one in which M^{2+}-cations occupy only the tetrahedral sites in the cubic closed packing of oxygen ions, and Al^{3+}-cations – only the octahedral sites. In this case, the distribution corresponds to the formula $(M^{2+})^{T}[Al^{3+}]^{O}_2 O^{2-}_4$, where T and O denote the tetrahedral and octahedral sites, respectively.

The cation arrangement of an inverse spinel corresponds to the formula $(Al^{3+})^{T}[M^{2+}_{0.5}Al^{3+}_{0.5}]^{O}_{2}O^{2-}_{4}$, so that M^{2+}-ion is placed in the octahedral position and Al^{3+}-ions are equally distributed between the octahedral and tetrahedral positions. The cation arrangement in real $NiAl_2O_4$ spinel is intermediate between these two extreme cases. It may be described as $(Ni^{2+}_{1-x}, Al^{3+}_{x})^{T}[Ni^{2+}_{x}, Al^{3+}_{1-x}, Al^{3+}]^{O}O^{2-}_{4}$, where x is the degree of inversion. Accordingly, in the case of normal spinel, $x = 0$, for an inverse spinel, $x = 1$, and intermediate cases are for $0 < x < 1$.

The stoichiometric $NiAl_2O_4$ spinel tends to be inverse at low temperatures, which is demonstrated by Figure 9.1. The details of the experimental data are given in Section 9.4.4. The cation arrangement tends to random distribution when temperature is increased. However, according to O'Neill et al. [197], above 1250 °C the cation re-distribution becomes so fast that it becomes difficult to quench properly. Contrariwise, below 800 °C the rate of cation diffusion becomes so slow that a complete internal equilibrium is hardly attained.

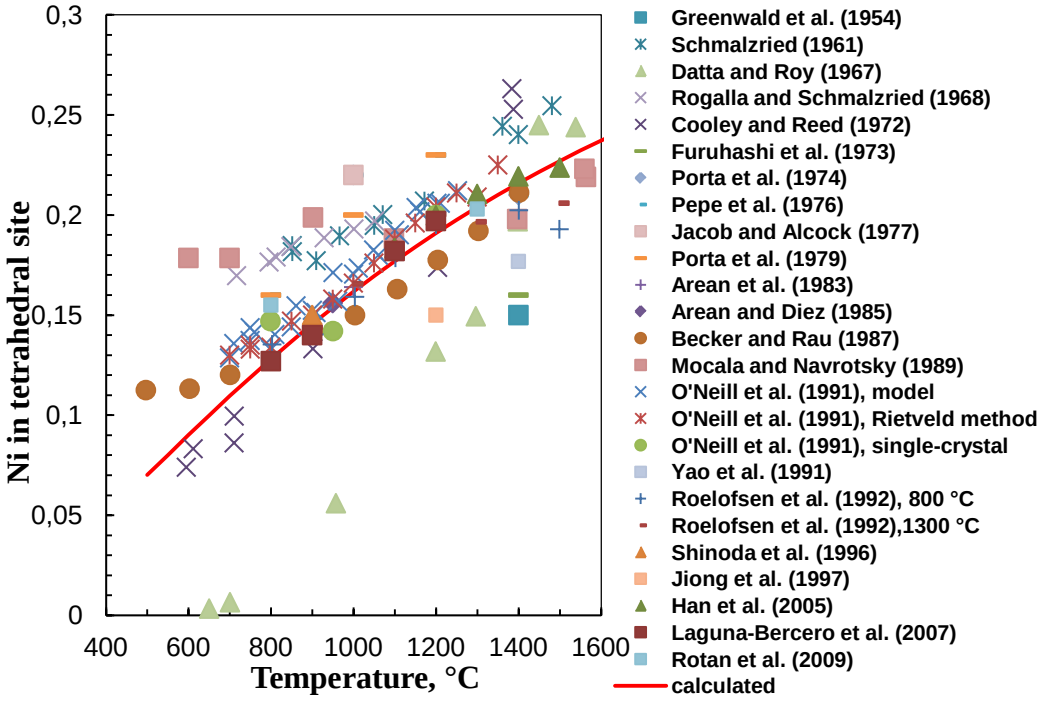

Figure 9.1: Cation distribution in stoichiometric $NiAl_2O_4$: literature data [197-219] and a calculated line

The non-stoichiometric Al–Ni spinel with high alumina content was found to be close to inverse spinel by Rotan et al. [218]. The dependence of inversion parameter on the overall composition is demonstrated in Figure 9.2.

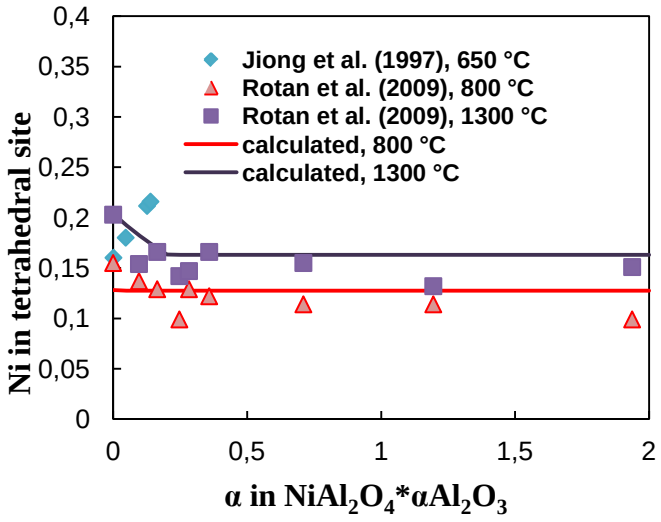

Figure 9.2: Cation distribution in $NiAl_2O_4$–α-Al_2O_3 solid solution: literature data [215, 218] and calculated lines

The model for the Al–Ni spinel was developed within the framework of the Compound Energy Formalism (CEF):

$$(Al^{3+}, Ni^{2+})^{T}[Al^{3+}, Ni^{2+}, Va]^{O}_{2}O^{2-}_{4} \tag{9.4}$$

The formation of neutral vacancies on the octahedral sublattice describes the non-stoichiometry of Al-Ni spinel towards excess alumina.

The Gibbs energy expression and model parameters for a general spinel solution are explained in detail by Decterov et al. [41]. In brief, the Gibbs-energy expression in the Compound Energy Formalism (CEF) per formula unit is the following:

$$G_m = \sum_i \sum_j Y_i^{T} Y_j^{O} G_{ij} - TS_c + \Delta G^{ex} \tag{9.5}$$

where Y_i^{T} and Y_j^{O} represent the site fractions of the constituents *i* and *j* on the tetrahedral (T) and octahedral (O) sublattices, respectively, G_{ij} is the Gibbs energy of a pseudo-component $(i)[j]_2O_4$, ΔG^{ex} is the excess Gibbs energy and S_c is the configurational entropy assuming random mixing on each sublattice,

$$S_c = -R(\sum_i Y_i^{T} \ln Y_i^{T} + 2\sum_j Y_j^{O} \ln Y_j^{O}) \tag{9.6}$$

$$\Delta G^{ex} = \sum_i \sum_{j>i} \sum_k Y_i^{\mathrm{T}} Y_j^{\mathrm{T}} Y_k^{\mathrm{O}} L_{ij:k} + \sum_i \sum_{j>i} \sum_k Y_k^{\mathrm{T}} Y_i^{\mathrm{O}} Y_j^{\mathrm{O}} L_{k:ij} \quad (9.7),$$

where $L_{ij:k}$ and $L_{k:ij}$ are the interaction energies between cations *i* and *j* on the one sublattice when the other sublattice is occupied by *k*.

The dependence of the interaction energies on the composition can be expressed by Redlich-Kister power series:

$$L_{ij:k} = \sum_m {}^m L_{ij:k} (Y_j^{\mathrm{M2}} - Y_i^{\mathrm{M2}})^m \quad (9.8)$$

$$L_{k:ij} = \sum_m {}^m L_{k:ij} (Y_j^{\mathrm{M1}} - Y_i^{\mathrm{M1}})^m \quad (9.9)$$

The model parameters applied for the Al–Ni spinel solution are the following:

$$F_{\mathrm{Ni^{+2}Al^{+3}}} = \frac{1}{7} \mathrm{G}_{\mathrm{Ni^{+2}Al_2^{+3}O_4}} \quad (9.10)$$

$$I_{\mathrm{Ni^{+2}Al^{+3}}} = \mathrm{G}_{\mathrm{[Al^{+3}Al_2^{+3}O_4]^{+1}}} + \mathrm{G}_{\mathrm{[Al^{+3}Ni_2^{+2}O_4]^{-1}}} - 2\mathrm{G}_{\mathrm{Ni^{+2}Al_2^{+3}O_4}} \quad (9.11)$$

$$\Delta_{\mathrm{Ni^{+2}Al^{+3}}} = \mathrm{G}_{\mathrm{[Ni^{+2}Ni_2^{+2}O_4]^{-2}}} + \mathrm{G}_{\mathrm{[Al^{+3}Al_2^{+3}O_4]^{+1}}} - \mathrm{G}_{\mathrm{[Al^{+3}Ni_2^{+2}O_4]^{-1}}} - \mathrm{G}_{\mathrm{Ni^{+2}Al_2^{+3}O_4}} \quad (9.12)$$

$$\Delta_{\mathrm{Al^{+3}Ni^{+2}Va}} = \mathrm{G}_{\mathrm{[Ni^{+2}Ni_2^{+2}O_4]^{-2}}} + \mathrm{G}_{\mathrm{[Al^{+3}Va_2O_4]^{-5}}} - \mathrm{G}_{\mathrm{[Al^{+3}Ni_2^{+2}O_4]^{-1}}} - \mathrm{G}_{\mathrm{[Ni^{+2}Va_2O_4]^{-6}}} \quad (9.13)$$

F parameter in Equation (9.10) is 1/7 part of the Gibbs energy of a hypothetical normal spinel $NiAl_2O_4$; *I* and Δ parameters in Equations (9.11) and (9.12) describe the degree of inversion and thermodynamic parameters of a real simple spinel $NiAl_2O_4$. The formation of vacancies is described by the parameter Δ in Equation (9.13).

The Gibbs energies of the end-members which take part in CEF equations can be derived from the model parameters. The model parameters are used to calculate the fractions of end-members using the Gibbs energy minimization procedure built in the FactSage software [1].

To correctly describe the solubility of Al_2O_3 in the Al-Ni spinel solution, in addition to the model parameters described above, the parameter $F_{\mathrm{Al^{+3}V}}$ was optimized.

Generally speaking, the spinel solution can be considered as a solution between $NiAl_2O_4$ and γ-Al_2O_3, which has the spinel structure. The formula of γ-Al_2O_3 can be written as $(Al^{3+})^{\mathrm{T}}[Al_{5/6}^{3+}, Va_{1/6}]_2^{\mathrm{O}}O_4^{2-}$. Assuming a random mixture of Al^{3+} and vacancies on the octahedral sites, the Gibbs energy of γ-Al_2O_3 is given by

$$8G°(\gamma\text{-}Al_2O_3) = G_{[Al^{+3}Va_2O_4]^{-5}} + 5G_{[Al^{+3}Al_2^{+3}O_4]^{+1}} + 2RT(5\ln 5 - 6\ln 6) \quad (9.14),$$

where $F_{Al^{+3}V}$ parameter defined as

$$F_{Al^{+3}V} \equiv \frac{1}{5}G°(\gamma\text{-}Al_2O_3) - \frac{1}{20}RT(5\ln 5 - 6\ln 6) \quad (9.15),$$

was optimized in order to simultaneously take into consideration the thermodynamic properties of γ-Al_2O_3 available in the literature and the solubility of Al_2O_3 in several spinel solutions.

The optimized $F_{Al^{+3}V}$ parameter correctly describes both the thermodynamic properties of γ-Al_2O_3, which is demonstrated by Figure 9.3 and Figure 9.4, as well as the solubility of alumina in Al-Ni spinel, which is demonstrated by Figure 9.11 and will be discussed in detail later in the thesis.

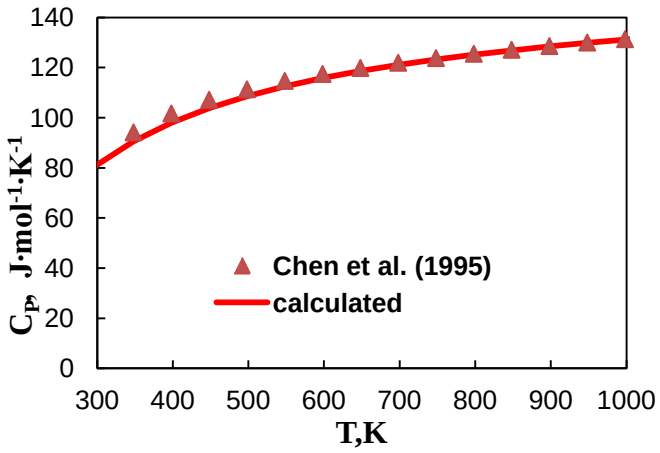

Figure 9.3: Heat capacity of γ-alumina: literature data [220] and a calculated line

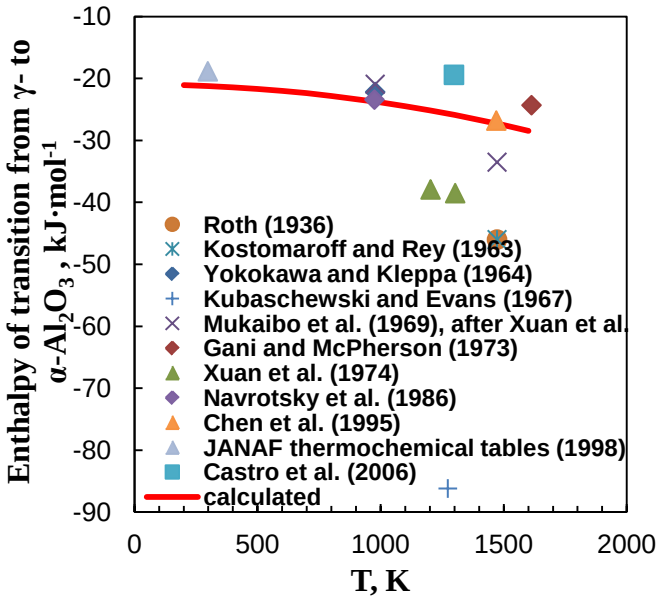

Figure 9.4: Enthalpy of transition of γ- to α-alumina: literature data [220-229] and a calculated line

9.2.3 Monoxide – $NiO(AlO_{1.5})$

NiO has a limited solubility of α-Al_2O_3. The Bragg-Williams random mixing model (NiO, $AlO_{1.5}$) was used, with the following Gibbs energy expression:

$$G = (X_{\mathrm{NiO}} G^{\circ}_{\mathrm{NiO}} + X_{\mathrm{AlO_{1.5}}} G^{\circ}_{\mathrm{AlO_{1.5}}}) + RT(X_{\mathrm{NiO}} \ln X_{\mathrm{NiO}} + X_{\mathrm{AlO_{1.5}}} \ln X_{\mathrm{AlO_{1.5}}}) + \Delta G^{ex} \qquad (9.16)$$

In these expressions, X_i and G_i° are the mole fraction and the Gibbs energy of the component *i*. The excess Gibbs energy ΔG^{ex} is a polynomial with Toop-like extension of binary terms into multicomponent systems, with Al_2O_3 as an asymmetric component [28].

It is assumed that vacancies remain associated with Al^{3+} ions and so do not contribute to the configurational entropy.

9.2.4 Corundum – $AlO_{1.5}(NiO)$

Corundum is α-Al_2O_3-based solution with a limited solubility of NiO. The model used for the corundum solution was the same as for the monoxide solution.

9.2.5 Other solutions and stoichiometric compounds

The Al–Ni metallic solutions and stoichiometric compounds (Al_3Ni and Al_3Ni_5) were optimized previously by Ansara et al. [194]. The optimized parameters were applied in the current study. The phase diagram of the Al–Ni system is shown in Figure 9.5.

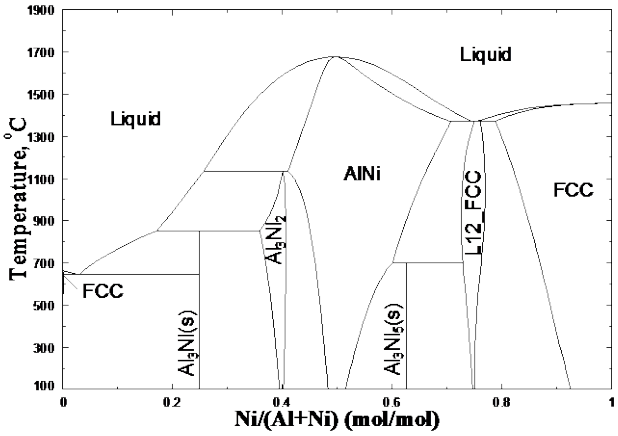

Figure 9.5: Al–Ni phase diagram [194]

9.3 Literature review of experimental data and evaluation

The evaluated isothermal section of the Al–Ni–O phase diagram at 1100 °C is shown in Figure 9.6.

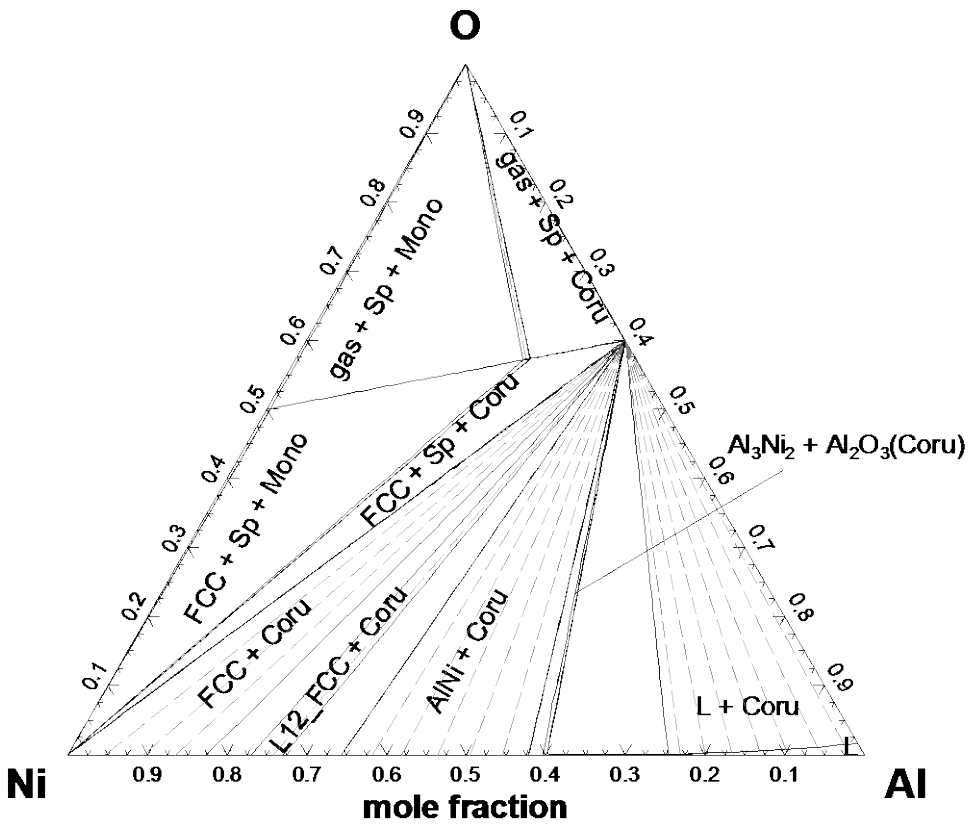

Figure 9.6: Calculated isothermal section of the Al–Ni–O phase diagram at 1100 °C

9.4 $NiAl_2O_4$

$NiAl_2O_4$ with a cubic spinel structure is the only ternary compound in the Al–Ni–O system. The thermodynamic properties of $NiAl_2O_4$ are relatively well-studied: the literature data include the heat capacity [230-232], enthalpy [233-236], cation distribution [197-218] and Gibbs energy data [163, 237-247].

9.4.1 Heat capacity and entropy

The heat capacity of $NiAl_2O_4$ was studied in both low-temperature and high-temperature regions, as shown in Figure 9.7.

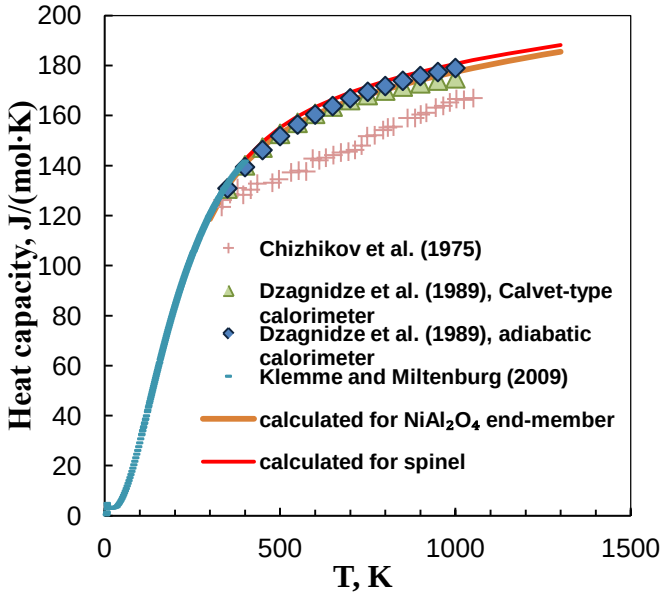

Figure 9.7: Heat capacity of $NiAl_2O_4$: literature data [230-232] and calculated lines

The low-temperature heat capacity of $NiAl_2O_4$ was recently measured between 4 and 400 K (-269-127°C) by Klemme and Miltenburg [232], using adiabatic calorimetry. A sharp anomaly on the heat capacity curve was observed at low temperature of 7.5 K and the authors supposed that it could be related to the cubic-tetragonal transition in spinels. From their data, the entropy of $NiAl_2O_4$ at T=298 K was calculated as 97.1 J/(mol·K).

The high-temperature heat capacity of $NiAl_2O_4$ was measured by Chizhikov et al. [230] in the temperature range 300-1100 K (27-827 °C), using adiabatic calorimetry, and later on by Dzagnidze et al. [231] in the range of 300-1000 K (27-727 °C), using adiabatic calorimetry and differential microcalorimeter of Calvet type.

Although the experimental results of Dzagnidze et al. [231] obtained by two distinct techniques are slightly different, they are compatible with each other and are in agreement with the recent data of Klemme and Miltenburg [232]. Contrariwise, the data of Chizhikov et al. [230] are inconsistent with the other data, therefore, they are probably erroneous.

9.4.2 Enthalpy of formation

The enthalpy of formation of $NiAl_2O_4$ spinel at 700 °C from the oxides NiO and α-Al_2O_3 was measured by solution calorimetry in borate solvents in four studies: Navrotsky and Kleppa [233], Akaogi and Navrotsky [234], Navrotsky [235], and in the most recent study by Lilova et al. [236]. The following results were obtained: -3.1 ± 1.0 kJ/mol (the samples were prepared from oxides by

heating at 1300 °C for 48 h with several cycles of grinding, repelletizing, heating and, finally, XRD analysis; no information whether the samples were quenched or cooled), -19.7 ± 1.3 kJ/mol (the samples were prepared from oxides by heating at 1400 °C for 47 hours and confirmation of phases by XRD and microscopic analysis; no information whether the samples were quenched or cooled), -0.3 ± 1.5 kJ/mol (the samples were prepared from oxides by heating at 1200 °C for 2-4 days, quenching and confirmation of phases by XRD and microscopic analysis), and -1.9 ± 2.5 kJ/mol (the samples were prepared from oxides by sintering at 1400 °C for 24h, annealing at 800 °C for 24h and quenching), respectively.

Navrotsky [235] also measured the enthalpies associated with the re-equilibration of cation distribution in $NiAl_2O_4$ for samples quenched from high temperatures of 1000-1400 °C to 700 °C as varying from -2.7 to -4.8 kJ/mol by drop calorimetry. A sample was quenched from high temperature, encapsulated in Pt foil and dropped from room temperature into the calorimeter at 700 °C (with no solvent present). The capsule was retrieved and then dropped a second time. The first drop gave the heat content H_{973}-H_{298} of the Pt and of the spinel and any heat released when the cation distribution relaxed. Subsequent drops gave the heat-content terms only. The Pt capsule contributed less than 30% of the total heat effect. The measured heat contents were in the range of 100-125 kJ/mol. The difference between the first and subsequent drops gave the enthalpy difference associated with the change in cation distribution. Based on the reproducibility of the results, it was supposed that when a spinel sample is dropped into a calorimeter at 700 °C, it re-equilibrates its cation distribution to or near the 973 K value during the course of the 30-60-min calorimetric experiment. However, this assumption seems to be questionable since re-equilibration at such low temperatures would require much longer times. According to calculations, the enthalpies associated with the re-equilibration of cation distribution in $NiAl_2O_4$ for spinel quenched from high temperatures of 1000-1400 °C to 700 °C are between -1 and -2 kJ/mol.

However, even if it is supposed that the re-distribution of cations from high temperatures to the temperature of calorimetric experiment can contribute several kJoules to the results, this effect cannot explain a large negative value for the enthalpy of formation of Akaogi and Navrotsky [234], which is apparently inconsistent with the rest of the data. Since no proper explanations were given by the authors and all these data were obtained in the same experimental group by the same method, the discrepancy in the experimental results shows the real experimental error of the applied experimental technique.

9.4.3 Gibbs energy

9.4.3.1 Ni-alloy(s,l) + spinel + Al_2O_3 assemblage

The partial pressures of oxygen for the Ni-alloy(s,l) + spinel + Al_2O_3 assemblage (FCC + Sp + Coru in Figure 9.6) are directly related to the Gibbs energy of formation of alumina-saturated spinel from α-Al_2O_3, Ni-alloy, and O_2. They were measured using 2 different types of techniques: EMF [237-243] and gas equilibration with CO/CO_2 mixtures [163, 244-246]. The results are summarized in Figure 9.8. The crystal modification of alumina was α-Al_2O_3 everywhere, except for the study of Fricke and Weitbrecht [244], where Al_2O_3 was claimed to be in the form of γ-Al_2O_3. Most of the experiments were conducted at temperatures low enough for Ni-alloy to be in the solid state, except for the studies of Jacob [242] and Majumdar et al. [243], who conducted their experiments in the temperature ranges 1730-1975 K (1457-1702 °C) and 1733-1873 K (1460-1600 °C), respectively, where the metal phase was liquid. Although some authors mentioned possible non-stoichiometry of the spinel phase in equilibrium with α-Al_2O_3 and Ni-alloy, in most cases experimental data on the composition of spinel were not provided. The only mention was made by Elrefaie and Smeltzer [241], Jacob [242], and Timucin and Muan [246]. Elrefaie and Smeltzer [241] measured the solubility of Al_2O_3 in $NiAl_2O_4$ as 56 mol % at 1273 K (1000 °C) by EPMA analysis, Jacob [242] – as 58.7 and 62.4 mol % at 1773 K (1500 °C) and 1973 K (1700 °C), respectively, by energy dispersive X-ray analysis, Timucin and Muan [246] – as 56 mol % Al_2O_3 in the range of temperatures 1573-1673 K (1300-1400 °C) by X-ray d-spacing measurement.

The experimental results for the spinel + Al_2O_3 + Ni-alloy(s,l) + O_2 assemblage are in general agreement.

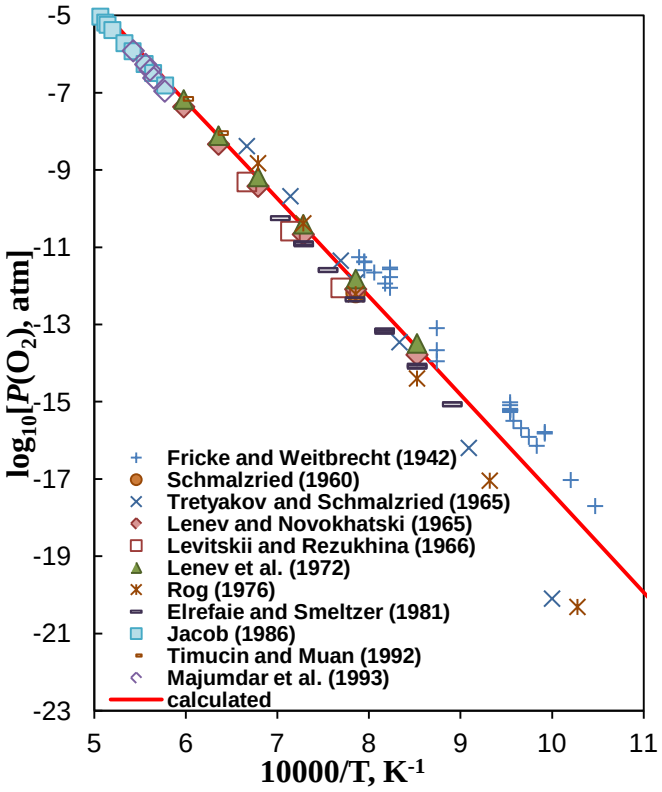

Figure 9.8: Partial pressures of oxygen for the Ni-alloy(s,l) + spinel + Al_2O_3 assemblage: literature data [163, 237-246] and a calculated line

In addition, Timucin and Muan [246] measured the partial pressures over spinel-Ni-alloy binary equilibria. The data are shown in Figure 9.9.

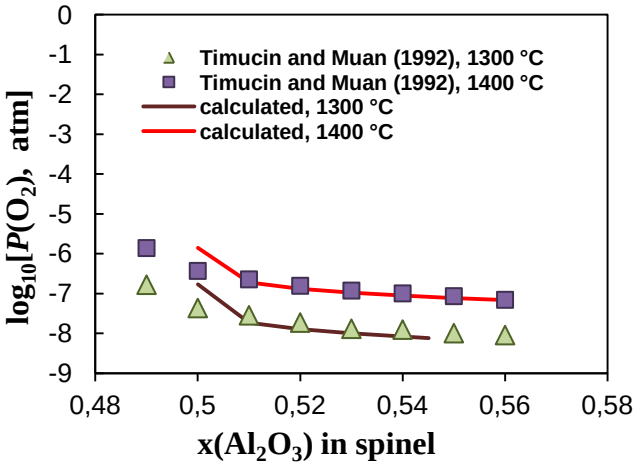

Figure 9.9: Partial pressures of oxygen for the spinel-Ni-alloy equilibria: literature data [246] and calculated lines

9.4.3.2 Ni-alloy(s,l) + $NiAl_2O_4$ + NiO-based monoxide assemblage

The partial pressures of oxygen for the Ni-alloy(s,l) + $NiAl_2O_4$ + NiO-based monoxide assemblage (FCC + Sp + Mono in Figure 9.6) are directly related to the Gibbs energy of formation of $NiAl_2O_4$. The experimental data of this kind are shown in Figure 9.10.

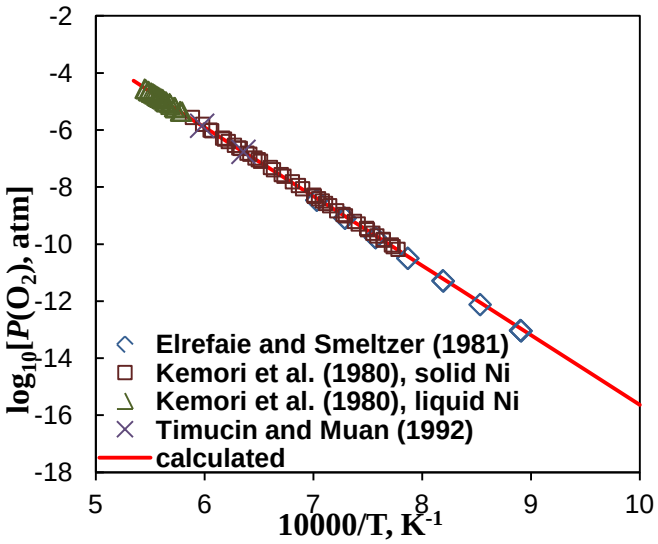

Figure 9.10: Partial pressures of oxygen for the $NiAl_2O_4$(spinel) + NiO-based monoxide + Ni-alloy(s,l) assemblage: literature data [241, 246, 247] and a calculated line

Elrefaie and Smeltzer [241] measured the EMF data for the cell: Ni(solid), NiO, $NiAl_2O_4$/ ZrO_2 /Ni, NiO between 1123-1423 K (850-1150 °C). The EPMA analysis of the phases at 1273 K (1000 °C) showed that the following phases were in equilibrium: stoichiometric $NiAl_2O_4$, NiO (with 1 mol % of dissolved Al_2O_3), and pure Ni.

Kemori et al. [247] measured the EMF data for the cell: Ni (solid or liquid), NiO, $NiAl_2O_4$/ ZrO_2 /air in the temperature range 1285-1835K (1012-1562 °C). The solubility of Al_2O_3 in NiO was reported to be negligibly small below 1573K (1300 °C).

Timucin and Muan [246] used a gas equilibration technique to study the same equilibrium at 1573 and 1673 K (1300 and 1400 °C).

The results of Elrefaie and Smeltzer [241], Timucin and Muan [246], and Kemori et al. [247] are in agreement.

9.4.4 Cation distribution

The cation distribution in the stoichiometric $NiAl_2O_4$ spinel is shown in Figure 9.1. The cation arrangement was measured mainly by the XRD analysis [197-200, 202-205, 207-209, 211, 213-218] in the range of temperatures 400-1560 °C. The samples of Roelofsen et al. [213] were divided into 2 groups (see Figure 9.1) by the temperature at which they were initially annealed, 800 or 1300 °C. Further, the samples were annealed at temperatures from 800 to 1500 °C and quenched. The measurements of O'Neill et al. [197] were divided into 3 groups (as shown in Figure 9.2): 1) powder-diffraction experiments with isotropic thermal motion model used as a refinement technique 2) powder-diffraction experiments with Rietveld method and 3) single-crystal experiments.

Some other experimental techniques were also applied: optical absorption [201] (720-1050 °C), magnetic measurements [204] (1000-1400 °C), optical transmission [210] (400-1400 °C), neutron diffraction [219] (25 °C), and X-ray absorption fine-structure spectroscopy (EXAFS, 1400 °C) [212]. Jacob and Alcock [206] calculated the cation distribution in $NiAl_2O_4$ at 1000 °C from site preference energies.

Furthermore, Rotan et al. [218] investigated the cation distribution in the $NiAl_2O_4$–αAl_2O_3 solid solution (see Figure 9.2). The samples were either slowly cooled to ambient temperature from 800 °C or quenched from 1300 °C.

Although most of the authors agree that the $NiAl_2O_4$ spinel is largely inverse, the literature data on the cation distribution are quite scattered. According to O'Neill et al. [197], inaccuracy of data may occur due to several reasons: 1) deviations from ideal stoichiometry 2) improper sample equilibration (insufficient equilibration time at low temperatures, slow quench rate at high temperatures, etc.) 3) low quality of the XRD measurements and the inadequacy of the XRD model used to reduce these measurements to structural information.

9.4.5 Phase diagram data

The Al_2O_3–NiO section of the Al–Ni–O phase diagram in air (see Figure 9.11) was studied by several authors [90, 177, 196, 199, 218, 246, 248-252]. The only ternary compound is $NiAl_2O_4$, with a spinel structure.

Figure 9.11 shows literature data obtained both in air and metallic saturation, which were described above. In general, for ternary systems of the kind 2 metals + oxygen, the T-x section of the phase diagram depends on the oxygen partial pressure $P(O_2)$. For instance, the oxide diagrams studied at

metal saturation, in air and $P(O_2)$ = 1 atm should look differently. However, in the Al–Ni–O system, both Al and Ni exhibit the only oxidation state, which is +3 and +2, respectively. This means that metal to oxygen ratio in solid and liquid oxides Al_2O_3 and NiO remains almost constant and does not depend on $P(O_2)$. For this reason the data at metallic saturation and in air are shown on the same diagram. The Al_2O_3–NiO section calculated in this study for air and metallic saturation and shown in Figure 9.11 also coincide.

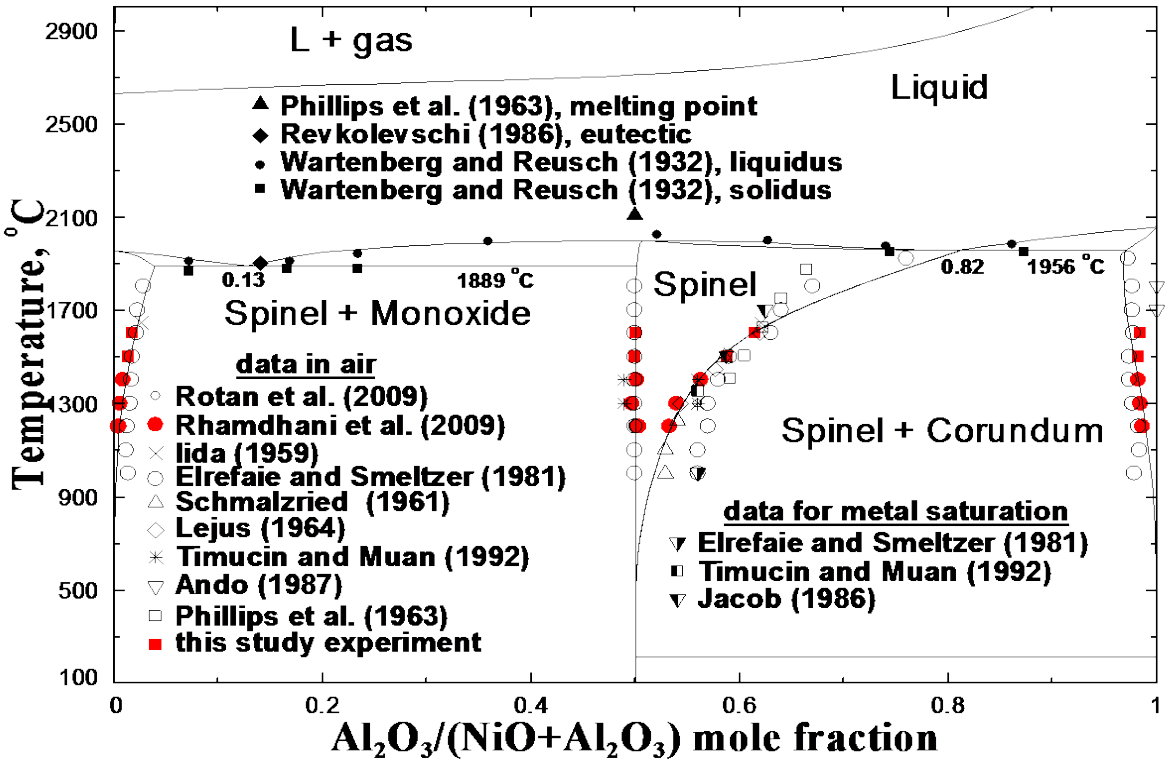

Figure 9.11: Calculated Al_2O_3–NiO section of the Al–Ni–O phase diagram: literature data [90, 177, 196, 199, 218, 246, 248-252] in air, at metallic saturation [241, 242, 246] and results of this study

In the subsolidus region, Al_2O_3–NiO section was investigated by Iida [249] – quenching and XRD at 1650 °C, Schmalzried [199] – XRD (1000-1500 °C), Lejus and Collonongues [250] – XRD (1300-1600 °C), Phillips et al. [90] – quenching and direct observational technique (from 1360 °C up to liquidus temperatures), Elrefaie and Smeltzer [196] – XRD and EPMA (1000-1920 °C), Ando [251] – EPMA of annealed samples at 1700 and 1800 °C, Timucin and Muan [246] – XRD of quenched samples at 1300 and 1400 °C, Rhamdhani et al. [177] – equilibration and quenching techniques

followed by EPMA from 1200 to 1400 °C, Rotan et al. [218] – XRD of quenched samples at 1300 °C. Basic features of the Al_2O_3–NiO section were the same in the majority of studies: 1) alumina content of the spinel increased with increasing temperature; 2) the binary oxides α-Al_2O_3 and NiO exhibited limited solubilities in each other; 3) the spinel equilibrated with NiO-based solid solution occurred at its stoichiometric composition, $NiAl_2O_4$. However, there was a controversy in the literature data on the spinel phase composition when in equilibrium with the corundum phase (α-Al_2O_3-based solution). To resolve contradictions, spinel/corundum and spinel/monoxide equilibria were re-measured in this study. It was mentioned before that the Al_2O_3–NiO section of the Al–Ni–O phase diagram was recently measured from 1200 to 1400 °C by Rhamdhani et al. from the Pyrometallurgy Research Centre (Brisbane, Australia) [177]. In this study, the same section was re-measured at higher temperatures 1500 and 1600 °C, using the same technique as before.

The liquidus region of the Al–Ni–O system was studied by several investigators [90, 248, 252]. Wartenberg and Reusch [248] studied liquidus on the Al_2O_3–NiO section of the Al–Ni–O phase diagram in air by optical microscopy. The melting point of $NiAl_2O_4$ composition was measured in air as 2020 ± 20 °C. Phillips et al. [90] investigated the melting point of the stoichiometric $NiAl_2O_4$ composition by quenching and direct observational technique. The melting point was found to be near 2110 ± 30 °C, higher than that reported by Wartenberg and Reusch [248]. Finally, Revkolevchi [252] found an eutectic between $NiAl_2O_4$ and NiO-based solid solution near 1900 °C and 14 mol% Al_2O_3 by XRD.

9.5 Optimization

9.5.1 Spinel

First, the thermodynamic properties of stoichiometric hypothetically normal $NiAl_2O_4$ were optimized. The high-temperature heat capacity was set by optimizing the data of Klemme and Miltenburg [232] and Dzagnidze et al. [231] (Figure 9.7). The data of Chizhikov et al. [230] were not taken into account due to their doubtfulness. For the entropy $S^{o}_{298.15}$, the value of 97.1 J/(mol·K) by Klemme and Miltenburg [232] was accepted.

According to the model described in Section 9.2.2, the thermodynamic properties of hypothetically normal $NiAl_2O_4$ were used for one of the end-members of the spinel solution. This is justified because i) in the temperature range of the experiments of Klemme and Miltenburg [232] and of

Dzagnidze et al. [231], the cation distribution in spinel is kinetically frozen and the measurements give only the lattice part of the heat capacity and entropy ii) in the model applied for the spinel solution, it is generally assumed that the lattice part of the heat capacity is independent of cation distribution of an end-member.

For kinetically unrestricted (unfrozen) spinel, the contribution of the cation arrangement (configurational part) to S is given by Equation (9.6). At 298 K the sum of lattice and configurational entropies for $NiAl_2O_4$ is calculated as 108.7 J/(mol·K). The change in the cation distribution with increasing temperature also affects the heat capacity of unfrozen spinel (see Figure 9.1).

The enthalpy of the hypothetical normal spinel $(Ni)(Al)_2O_4$ was optimized to take into consideration available enthalpy [233-236] as well as Gibbs energy data [163, 237-247] (Figure 9.8, Figure 9.9 and Figure 9.10). The molar enthalpy of formation of stoichiometric spinel $NiAl_2O_4$ from the oxides NiO and α-Al_2O_3 with the equilibrium cation distribution is calculated as -10.8 kJ/mol at 700 °C, between the extreme limits obtained experimentally by Akaogi and Navrotsky [234] and Navrotsky [235]: -19.7 ± 1.3 kJ/mol and -0.3 ± 1.5 kJ/mol, respectively.

The parameter *I* was optimized to describe the cation distribution data [197-219] in Figure 9.1 and Figure 9.2. The calculated lines are believed to be in accordance with the experimental data within experimental error limits.

The delta parameters $\Delta_{Ni^{+2}Al^{+3}}$, $\Delta_{Al^{+3}Ni^{+2}Va}$ and excess parameters $M_{Al^{+3}:Al^{+3}Ni^{2+}}$ and $M_{Ni^{+2}:Al^{+3}Ni^{2+}}$ were optimized to describe the phase diagram data [90, 177, 196, 199, 218, 246, 248-252] and the experimental results of this study (Figure 9.11). From the available phase diagram data, experimental data obtained in this study were given preference in the optimization due to their believed high accuracy, which is achieved by applying the improved experimental technique involving carefully planned equilibration procedures followed by electron probe X-ray microanalysis.

The optimized model parameters for the spinel phase are given in Table 9.2.

9.5.2 Corundum and monoxide

The parameters of the corundum phase were optimized to describe the phase diagram data [177, 196, 251] and the experimental results of this study (Figure 9.11). The parameters of the monoxide

solution were optimized to describe the literature data in Figure 9.10 and Figure 9.11 and the experimental results of this study in Figure 9.11. The calculated lines are in good agreement with the experimental results. The optimized parameters are given in Table 9.2.

9.5.3 Liquid

The parameters of the Modified Quasichemical Model were optimized to describe the phase diagram data [90, 248, 252] (Figure 9.11) and are given in Table 9.2.

9.6 Summary of results

Some discrepancies in the literature data for the Al_2O_3–NiO section of the Al–Ni–O system have been demonstrated. To help resolve the conflicts existing in the literature, a new experimental investigation was carried out in this study. The improved experimental technique included equilibration and quenching followed by electron probe X-ray microanalysis (EPMA). The Al_2O_3–NiO section of the Al–Ni–O phase diagram has been measured at 1500 and 1600 °C in air. The solubility of Al_2O_3 in $NiAl_2O_4$ as well as the solubilities of α-Al_2O_3 and NiO in each other have been measured. The experimental measurements provided additional data for a subsequent thermodynamic modeling.

A simultaneous optimization of all available data in the Ni-containing system Al–Ni–O at 1 atm total pressure was performed. New experimental data and previously published experimental results were taken into consideration. The best possible description of thermodynamic properties data and phase relations was obtained. The optimized model parameters for oxide phases reproduce all available data within experimental error limits. A set of self-consistent Gibbs energy functions of the oxide phases in the Al–Ni–O system was derived.

Table 9.2: Optimized properties of stoichiometric compounds and model parameters for oxide phases in the Al–Ni–O system (J·mol^{-1} and J·mol^{-1}·K^{-1})

Compounds	**Temperature range (K)**	$\Delta H^{o}_{298.15}$	$S^{o}_{298.15}$	$C_P(T)$
The thermodynamic properties of solid and liquid NiO are given in [51]				
Al_2O_3 (alpha)	298-2327	-1675700	50.8200	$155.0188 - 3.8613\times10^{6}T^{-2} - 828.387T^{-0.5} + 4.091\times10^{8}T^{-3}$
	2327-3000			192.464
Al_2O_3 (kappa)	298-1100	-1662302	53.5550	$103.9399 + 0.0138795T - 9.1424\times10^{6}T^{-2} + 559.745T^{-0.5} + 1.1426\times10^{9}T^{-3}$
	1100-2327			$-452.6767 + 0.0437540T + 1.598064\times10^{8}T^{-2} + 42202.724T^{-0.5} - 9.576569\times10^{5}T^{-1}$
	2327-3000			192.464
Al_2O_3 (gamma)	298-1200	-1656864	52.3000	$-15.7333 + 0.0299485T + 4.9953\times10^{6}T^{-2} + 7068.351T^{-0.5} - 1.121094\times10^{5}T^{-1}$
	1200-2327			$-787.5153 + 0.0658774T + 2.638163\times10^{8}T^{-2} + 66885.728T^{-0.5} - 1.5255274\times10^{6}T^{-1}$
	2327-3000			192.464

Table 9.2 (Continued): Optimized properties of stoichiometric compounds and model parameters for oxide phases in the Al–Ni–O system ($J \cdot mol^{-1}$ and $J \cdot mol^{-1} \cdot K^{-1}$)

Al_2O_3 (liquid)	298-2327	-1596353.2	43.5690	$179.3654 - 0.0091922T + 9.753\times10^{5}T^{-2} - 828.387T^{-0.5} + 4.091\times10^{8}T^{-1}$
	2327-3000			

Slag (liquid oxide phase): $AlO_{1.5}$-NiO

$Z_{Ni} = 1.37744375, \quad Z_{Al} = 2.06616563;$

$\Delta g^{o}_{Al,Ni} = 33472, \quad q^{01}_{Al,Ni} = -8368;$

$q^{05}_{Ni,Al} = -41840.$

Monoxide (solid oxide): NiO($AlO_{1.5}$)

$q^{00}_{Ni,Al} = 30224.4 - 15.69T,$

$G^{o}_{Al_2O_3}(\text{mono}) = G^{o}_{\alpha\text{-}Al_2O_3} + 77404, \quad G^{o}_{NiO}(\text{mono}) = G^{o}_{NiO}.$

Corundum: $AlO_{1.5}$(NiO)

$G^{o}_{Al_2O_3}(\text{coru}) = G^{o}_{\alpha\text{-}Al_2O_3}, \quad G^{o}_{NiO}(\text{coru}) = G^{o}_{NiO} + 40584.8.$

Table 9.2 (Continued): Optimized properties of stoichiometric compounds and model parameters for oxide phases in the Al–Ni–O system ($J \cdot mol^{-1}$ and $J \cdot mol^{-1} \cdot K^{-1}$)

Spinel: $(Al^{3+}, Ni^{2+})^{T}(Al^{3+}, Ni^{2+}, Va)_2^{O}O_4$

$$7 \cdot F_{Ni^{+2}Al^{+3}} = -1964026.7 + 969.9016 \cdot T - 154.66239 \cdot T \ln T - 0.0143781 \cdot T^2 + 2.0071 \times 10^6 \cdot T^{-1} + 1.601 \times 10^{-10} \cdot T^4;$$

$$I_{Ni^{+2}Al^{+3}} = -17154.4;$$

$$\Delta_{Ni^{+2}Al^{+3}} = 14896, \quad \Delta_{Al^{+3}Ni^{+2}Va} = 420387.4 - 317.984T;$$

$$M_{Al^{+3}:Al^{+3}Ni^{2+}} = M_{Ni^{+2}:Al^{+3}Ni^{2+}} = M_{M_i:Al^{+3}Ni^{2+}} = -46793.9 + 33.4720 \cdot T;$$

$$F_{Al^{+3}V} = -336603.1 + 220.8396 \cdot T - 5.858 \times 10^{-4} \cdot T^2 - 662.71 \cdot T^{0.5} - 1.36 \times 10^7 \cdot T^{-2} - 31.00344 \cdot T \ln T + 3.861 \times 10^5 \cdot T^{-1}.$$

The Gibbs energy of formation of a compound from elements in their standard state at a temperature of T(K) and a pressure of 1 atm is given by $\Delta G = \Delta H^{o}_{298.15} - T S^{o}_{298.15} + \int_{298.15}^{T} C_P(T) dT - T \int_{298.15}^{T} \frac{C_P(T)}{T} dT$, where $\Delta H^{o}_{298.15}$ is the enthalpy of formation of the compound at 1 atm and 298.15 K, $S^{o}_{298.15}$ is the entropy of the compound at 1 atm and 298.15 K, and $C_P(T)$ is the heat capacity at constant pressure.

CHAPTER 10 **Fe–Ni–O MODELING**

Equation Chapter (Next) Section 1This chapter is concerned with the thermodynamic optimization of the Fe–Ni–O chemical system over a wide range of temperatures and oxygen partial pressures. A literature review for this chemical system was performed, and the derived literature data were used in preliminary calculations. For the Fe–Ni–O phase diagram, discrepancies in the available data were revealed at low oxygen pressures in the spinel/metallic alloy and wüstite/metallic alloy regions. Therefore, experiments were performed in the regions of interest by our colleagues from PyroSearch, Australia. The experimental procedure involved high-temperature equilibration and rapid quenching followed by the electron probe X-ray microanalysis (EPMA) of quenched samples. The compositions of wüstite/metallic alloy and spinel/metallic alloy in equilibrium have been measured at 1200 °C at partial pressures of oxygen $\log_{10}[P(O_2), \text{atm}] = -9$ and -10. This provided additional data for a subsequent thermodynamic modeling. The Modified Quasichemical Model (MQM) was used for modeling of the liquid oxide phase, or slag. The model based on the Compound Energy Formalism has been developed for the spinel solid solution. Metallic solutions and mutual solubility of wüstite (Fe_xO-based solid oxide solution) and bunsenite (NiO-based solid oxide solution) were described with a simple Bragg-Williams model. These physically meaningful models are based on the structure of the corresponding solutions and, therefore, have good ability to predict the properties of multicomponent systems.

10.1 Background

This part of the project was aimed at optimizing the Fe–Ni–O system in the range of oxygen partial pressures varied from those at metal saturation to those of pure oxygen and temperatures – from 25°C to liquidus temperatures and above.

Initially, available literature data were reviewed and analyzed. Contradictions in the literature data for wüstite/alloy and spinel/alloy equilibria at low oxygen pressures were found. To resolve contradictions in the literature, the compositions of phases in equilibrium were measured at 1200 °C at partial pressures of oxygen $\log_{10}[P(O_2), \text{atm}] = -9$ and -10 by the electron-probe microanalysis (EPMA). Further, the whole set of available data, reported earlier and newly obtained, were taken into consideration in the thermodynamic optimization of oxide phases in the Fe–Ni–O system.

The assessment of the Fe–Ni–O system was performed earlier by Luoma [253], using the ionic two-sublattice model for the liquid phase, Compound Energy Formalism (CEF) for solid oxide phases

and Redlich-Kister polynomials for solid metal phases. The spinel phase was further reassessed by Kjellqvist et al. [254].

10.2 Phases and thermodynamic models

A list of phases in the Fe–Ni–O system along with notations used in this study is given in Table 10.1. Phases were modeled as stoichiometric compounds or as solutions as described below. For the spinel solution model, cations shown within a set of parentheses occupy the same sublattice. Metallic solutions were optimized previously by Dinsdale and Chart [255]. Liquid and solid oxide solutions have been optimized in the present study. The optimized model parameters are listed in Table 10.2.

In the range of oxygen partial pressures considered in the present study, which varied from low oxygen pressures up to that of air, iron is present in oxide phases in two oxidation states: Fe^{2+} and Fe^{3+}, while nickel – only as Ni^{2+}. Trivalent nickel reaches significant concentration in oxide phases at high temperatures only at oxygen partial pressures considerably higher than that in air.

Table 10.1: Solution phases and stoichiometric compounds present in the Fe–Ni–O system

Phase name	**Formula**	**Notation used in this study**
Slag (liquid oxide)	$FeO–Fe_2O_3–NiO$	L or Liquid
Monoxide (encompassing wüstite Fe_xO and bunsenite NiO)	$NiO–FeO–FeO_{1.5}$	Mono or Monoxide
Corundum (encompassing hematite α-Fe_2O_3)	$FeO_{1.5}–NiO$	Corundum (Coru) or Hematite (Hem)
Spinel	$(Fe^{2+}, Fe^{3+}, Ni^{2+})^{T}[Fe^{2+}, Fe^{3+}, Ni^{2+}, Va]^{O}_{2}O^{2-}_{4}$ *	Sp or Spinel
Fcc	Fe–Ni	
L12-Fcc	Fe–Ni	
Bcc	Fe–Ni	
Liquid metal	Fe–Ni–O	L metal or Liquid metal

*T=tetrahedral sublattice, O=octahedral sublattice

10.2.1 Slag (liquid oxide)

The liquid oxide phase is an ionic melt where metal cations are always surrounded by oxygen anions. In other words, they exhibit almost full first-nearest-neighbour (FNN) short-range ordering (SRO). Furthermore, there is a strong tendency for SRO of some cations in melts. In particular, basic cations such as Ca form strong second-nearest-neighbour (SNN) pairs with acidic cations such as Si. The effects of both FNN and SNN are described by the Modified Quasichemical Model [7, 8]. Though, in the $FeO–Fe_2O_3–NiO$ system, the second-nearest-neighbour pairs ordering is apparently not strong, the same model is used in view of developing of a broader database for calculations in multicomponent systems. The most significant parameter of the MQM model is the Gibbs energy of the corresponding pair exchange reaction:

$$(\text{Fe-Fe}) + (\text{Ni-Ni}) = 2(\text{Fe-Ni}); \quad \Delta g_{\text{Fe,Ni}} \tag{10.1},$$

where (m-n) represents a second-nearest-neighbour pair. Let n_m and Z_m be the number of moles and the coordination number of the component *m*, respectively. The "coordination-equivalent" fractions (Y_m) are then defined as

$$Y_m = Z_m n_m / \sum_i Z_i n_i \tag{10.2}$$

Δg_{mn} is expanded as a polynomial in the "coordination-equivalent" fractions of the components

$$\Delta g_{mn} = \Delta g^{\circ}_{mn} + \sum_{(i+j)\geq 1} q^{ij}_{mn} Y^i_m Y^j_n \tag{10.3},$$

where Δg°_{mn} and q^{ij}_{mn} are empirical binary coefficients which may be functions of temperature and pressure. They are optimized to take into account available thermodynamic and phase equilibrium data.

10.2.2 Spinel

Ferrites $A^{2+}B^{3+}{}_2O_4$ have a basic spinel structure. The characteristic feature of ferrite spinels is their ferromagnetism.

Ni ferrite $NiFe_2O_4$ is a typical inverse spinel, where Ni ions prefer octahedral sites to tetrahedral sites, which is demonstrated in Figure 10.1. Crystal field stabilization, oxidation state and ionic radii effects result in the preference of Ni^{2+} for the octahedral site. Figure 10.1 shows that the cation distribution of stoichiometric $NiFe_2O_4$ is almost independent of temperature.

The determination of the cation distribution in nickel ferrite using conventional X-ray sources is complicated due to the X-ray scattering amplitude of Ni close to that of Fe. So, some other methods such as neutron diffraction are commonly applied. The experimental details for the data in Figure 10.1 are given in Section 10.3.1.4.

Ni ferrite occurs in the nature as a mineral trevorite $NiFe_2O_4$.

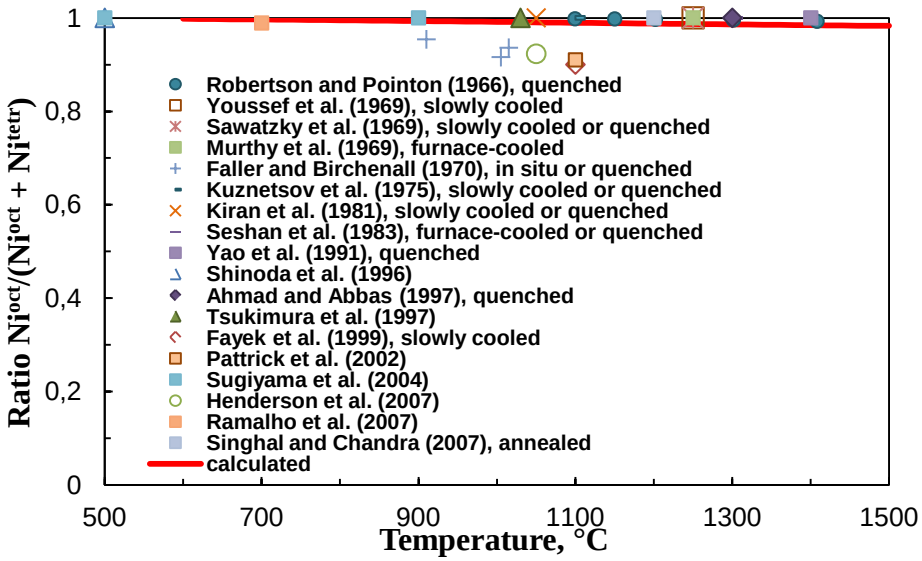

Figure 10.1: Cation distribution in stoichiometric $NiFe_2O_4$: literature data [40, 153, 212, 214, 256-269] and a calculated line

The stoichiometric nickel ferrite $NiFe_2O_4$ and magnetite Fe_3O_4, both with the cubic spinel structure, are completely soluble in each other. The distribution of Ni remains constant for the whole range of solid solutions between $NiFe_2O_4$ and Fe_3O_4 end-members, which is demonstrated in Figure 10.2.

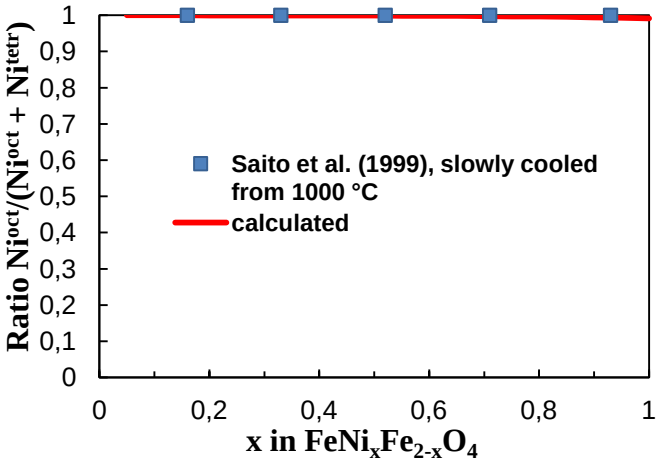

Figure 10.2: Cation distribution in $NiFe_2O_4$–αFe_2O_3 solid solution: literature data [270] and a calculated line

The model for the Fe-Ni spinel has been developed within the framework of the Compound Energy Formalism (CEF):

$$(Fe^{2+}, Fe^{3+}, Ni^{2+})^{T}[Fe^{2+}, Fe^{3+}, Ni^{2+}, Va]_2^{O}O_4^{2-}{}^{*} \qquad (10.4)$$

The formation of neutral vacancies on the octahedral sublattice describes the non-stoichiometry of the Fe-Ni spinel towards excess oxygen.

The Gibbs energy expression and model parameters for a general spinel solution are explained in detail by Decterov et al. [41]. In brief, the Gibbs-energy expression of the CEF per formula unit is the following:

$$G_m = \sum_i \sum_j Y_i^{T} Y_j^{O} G_{ij} - TS_c + \Delta G^{ex} \qquad (10.5)$$

where Y_i^{T} and Y_j^{O} represent the site fractions of the constituents *i* and *j* on the tetrahedral (T) and octahedral (O) sublattices, respectively, G_{ij} are the Gibbs energies of end-members – pseudo-components $(i)(j)_2O_4$, ΔG^{ex} is the excess Gibbs energy and S_c is the configurational entropy assuming random mixing on each sublattice,

$$S_c = -R\left(\sum_i Y_i^{T} \ln Y_i^{T} + 2\sum_j Y_j^{O} \ln Y_j^{O}\right) \qquad (10.6)$$

Excess Gibbs energy parameters were set to zero in this study.

The model parameters, which were applied for the Fe_3O_4–$NiFe_2O_4$ spinel solution, are shown below:

$$F_{Fe^{+2}Fe^{+3}} = \frac{1}{7} G_{Fe^{+2}Fe_2^{+3}O_4} = \frac{1}{7} G_{[Fe^{+3}Fe_2^{+2}O_4]^{-1}} \quad (10.7)$$

$$I_{Fe^{+2}Fe^{+3}} = G_{[Fe^{+3}Fe_2^{+3}O_4]^{+1}} + G_{[Fe^{+3}Fe_2^{+2}O_4]^{-1}} - 2G_{Fe^{+2}Fe_2^{+3}O_4} \quad (10.8)$$

$$\Delta_{Fe^{+2}Fe^{+3}} = G_{[Fe^{+2}Fe_2^{+2}O_4]^{-2}} + G_{[Fe^{+3}Fe_2^{+3}O_4]^{+1}} - G_{[Fe^{+3}Fe_2^{+2}O_4]^{-1}} - G_{Fe^{+2}Fe_2^{+3}O_4} \quad (10.9)$$

$$V_{Fe^{+3}} = G_{[Fe^{+3}Va_2O_4]^{-5}} - \frac{5}{7} G_{[Fe^{+3}Fe_2^{+2}O_4]^{-1}} \quad (10.10)$$

$$\Delta_{Fe^{+3}Fe^{+2}Va} = G_{[Fe^{+2}Fe_2^{+2}O_4]^{-2}} + G_{[Fe^{+3}Va_2O_4]^{-5}} - G_{[Fe^{+3}Fe_2^{+2}O_4]^{-1}} - G_{[Fe^{+2}Va_2O_4]^{-6}} \quad (10.11)$$

$$F_{Ni^{+2}Fe^{+3}} = \frac{1}{7} G_{Ni^{+2}Fe_2^{+3}O_4} \quad (10.12)$$

$$I_{Ni^{+2}Fe^{+3}} = G_{[Fe^{+3}Fe_2^{+3}O_4]^{+1}} + G_{[Fe^{+3}Ni_2^{+2}O_4]^{-1}} - 2G_{Ni^{+2}Fe_2^{+3}O_4} \quad (10.13)$$

$$\Delta_{Fe^{+2}Ni^{+2}Fe^{+3}} = G_{[Ni^{+2}Ni_2^{+2}O_4]^{-2}} + G_{[Fe^{+2}Fe_2^{+3}O_4]} - G_{[Fe^{+2}Ni_2^{+2}O_4]^{-2}} - G_{[Ni^{+2}Fe_2^{3+}O_4]} \quad (10.14)$$

$$\Delta_{Ni^{+2}Fe^{2+}Fe^{+3}} = G_{[Fe^{2+}Fe_2^{+2}O_4]^{-2}} + G_{[Ni^{+2}Fe_2^{+3}O_4]} - G_{[Ni^{+2}Fe_2^{+2}O_4]^{-2}} - G_{[Fe^{+2}Fe_2^{3+}O_4]} \quad (10.15)$$

F parameters in Equations (10.7) and (10.12) are 1/7 of the Gibbs energy of hypothetical normal spinels $NiFe_2O_4$ and Fe_3O_4; *I* parameters in Equations (10.8) and (10.13) describe the degree of inversion of these spinels; Δ parameter in Equation (10.9) describes the thermodynamic properties of a real simple spinel Fe_3O_4. The formation of vacancies is described by introducing the parameters *V* and Δ in Equations (10.10) and (10.11). All other delta parameters describe the thermodynamics of mixing between $NiFe_2O_4$ and Fe_3O_4. The Gibbs energies of the end members in (10.5) can be derived from the model parameters. They are used to calculate the fractions of end-members by application of the Gibbs energy minimization procedure built in the FactSage software [1].

Fe_3O_4 and $NiFe_2O_4$ undergo ferromagnetic orderings at T= 848 and 859 K [153], respectively. This has an impact on the thermodynamic properties of the spinel. The phenomenological approach proposed by Hillert and Jarl [44] was used to describe the magnetic contribution to the thermodynamic functions. The formulae are given in [41]. The main parameters are: T_C – the critical temperature for magnetic ordering (Curie temperature), β – the average magnetic moment per atom and p – the structural constant. The linear change of T_C and β between the Fe_3O_4 and $NiFe_2O_4$ was used in this study, as it was suggested in [41].

10.2.3 Monoxide – NiO–FeO–$FeO_{1.5}$

Wüstite Fe_xO has a range of non-stoichiometry towards oxygen, which was modeled by mixing FeO and $FeO_{1.5}$ oxides in the current study. Wüstite Fe_xO and bunsenite NiO are partially soluble in each other. At a certain temperature, these two solutions become a complete monoxide solution.

The monoxide solution was modeled using the Bragg-Williams random mixing model (FeO, $FeO_{1.5}$, NiO). The Gibbs energy expression is

$$\begin{aligned} G = & (X_{\mathrm{FeO}} g^{\mathrm{o}}_{\mathrm{FeO}} + X_{\mathrm{FeO_{1.5}}} g^{\mathrm{o}}_{\mathrm{FeO_{1.5}}} + X_{\mathrm{NiO}} g^{\mathrm{o}}_{\mathrm{NiO}}) \\ & + RT(X_{\mathrm{FeO}} \ln X_{\mathrm{FeO}} + X_{\mathrm{FeO_{1.5}}} \ln X_{\mathrm{FeO_{1.5}}} + X_{\mathrm{NiO}} \ln X_{\mathrm{NiO}}) + \Delta G^{ex} \end{aligned} \tag{10.16}$$

The excess Gibbs energy ΔG^{ex} is a polynomial with the Kohler-like extension of binary terms into multicomponent systems [28].

10.2.4 Corundum – $FeO_{1.5}$(NiO)

Corundum is α-Fe_2O_3(hematite)-based solution with a very small solubility of NiO. The model used for the corundum solution was similar to the monoxide solution ($FeO_{1.5}$, NiO).

10.2.5 Other solutions and stoichiometric compounds

The Fe–Ni metallic solutions were optimized previously by Dinsdale and Chart [255]. The optimized parameters were applied in this study.

10.3 Literature review of experimental data

The literature surveys for the Fe–Ni–O system were reported by Raghavan [271, 272] and Luoma [253].

The isothermal section of the Fe–Ni–O phase diagram at 1000 °C is demonstrated in Figure 10.3. The phases in the Fe–Ni–O system include the spinel solid solution $NiFe_2O_4$–Fe_3O_4, monoxide Fe_xO–NiO, corundum and Fe–Ni alloys. Also, liquid phases (slag and liquid metal) are present at higher temperatures. Hematite α-Fe_2O_3 has a negligible solubility of nickel. Magnetite Fe_3O_4 forms a continuous solid spinel solution with nickel ferrite, $NiFe_2O_4$. There is a miscibility gap in the monoxide solution between wüstite Fe_xO-based and bunsenite NiO-based solid solutions.

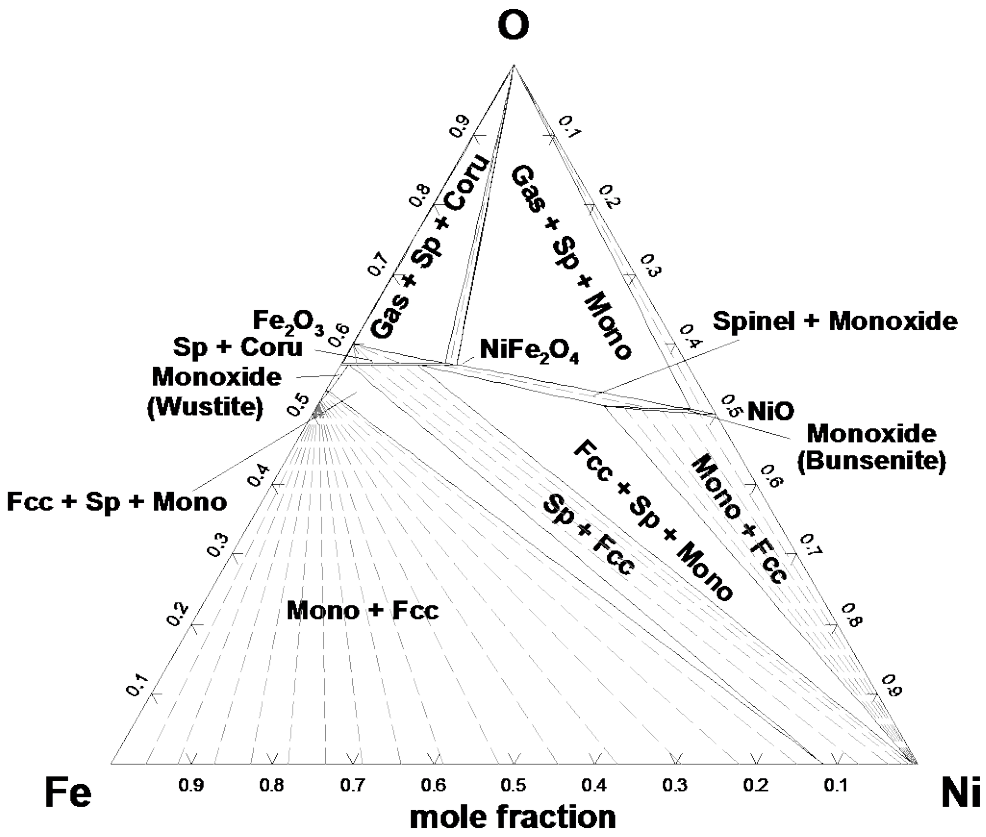

Figure 10.3: Isothermal section of the Fe–Ni–O phase diagram in air at 1273 K (1000 °C) and 1 atm

10.3.1 $NiFe_2O_4$

$NiFe_2O_4$ spinel is the only ternary compound in the Fe–Ni–O system. The thermodynamics of $NiFe_2O_4$ is relatively well-studied: the experimental data include the cation distribution [40, 153, 212, 214, 256-269], heat content [273, 274], heat capacity [156, 275-279], enthalpy of formation [233, 236] and Gibbs energy measurements [238, 240, 280, 281].

10.3.1.1 Heat capacity and entropy

The heat capacity of $NiFe_2O_4$ was measured in both low- and high-temperature regions, as shown in Figure 10.4.

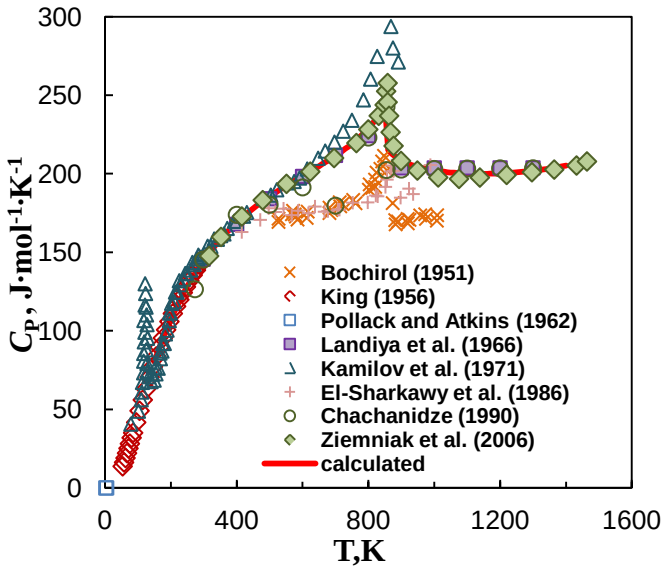

Figure 10.4: Heat capacity of $NiFe_2O_4$ spinel: literature data [156, 275-279] and a calculated line

The low-temperature heat capacity of $NiFe_2O_4$ was measured by calorimetry by several authors: Pollack and Atkins – from 2 to 5 K (-271 to -268 °C), King [156] – from 54 K to 298.15 K (-219 to 0 °C), and Kamilov et al. [277] – from 78 to 891 K (-195 to 618 °C). Kamilov et al. [277] observed 2 peaks on the heat capacity curve: a peak at the lower temperature was attributed to common orthorhombic to cubic transition in spinels, at the higher temperature – to magnetic transition. Contrariwise, King [156] did not observe any low-temperature maximum. X-ray measurement showed that his sample had a cubic structure in the whole range of temperatures. It is likely that the sample of King [156] did not undergo the cubic to orthorhombic transition during cooling due to kinetic reasons. From his low-temperature data, the standard entropy at 298 K was calculated as $S^{o}_{298.15}$ = 125.9±0.8 J·mol^{-1}·K^{-1}. Later, it was revised by King and Kelley [282] as 131.8 J·mol^{-1}·K^{-1}.

The high-temperature heat capacity of $NiFe_2O_4$ was determined in several studies: by Bochirol [275] – from 473 to 973 K (200 to 700 °C) by electrical measurement, El-Sharkawy et al. [276] – from 400 to 1000 K (127 to 727 °C) from thermal properties, and most recently by Ziemniak et al. [279] – from 323 to 1473 K (50 to 1200 °C) by a differential scanning calorimetry. Though Bochirol [275], actually, measured heat content, only heat capacity data were given in his study. Ziemniak et al. [279] observed a Curie temperature at 858 K (585 °C), El-Sharkawy et al. [276] – at 870 K (597 °C).

The heat content of $NiFe_2O_4$ was determined using adiabatic calorimetry by Landiya et al. [274] from 673 to 1272 K (400-999 °C) and Chachanidze [273] – from 400 to 1300 K (127 to 1027 °C),

who observed ferromagnetic transformation at 855 K. The heat content data are shown in Figure 10.5.

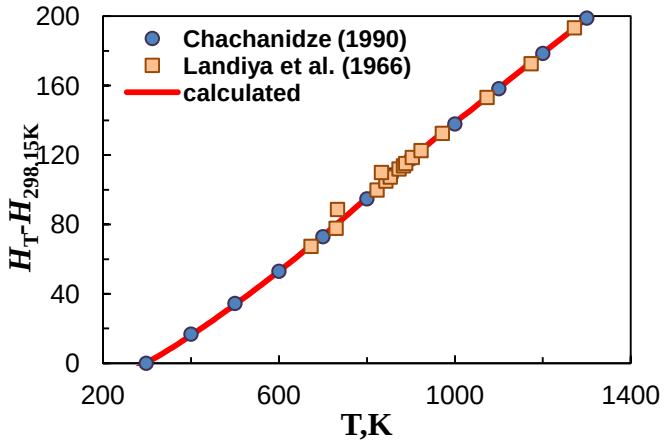

Figure 10.5: Heat content for $NiFe_2O_4$: literature data [273, 274] and a calculated line

In general, the heat content and heat capacity data are in agreement, except for the data of Bochirol [275] and El-Sharkawy et al. [276]. Since their data are in disagreement with other heat content and heat capacity data, including the recent data of Ziemniak et al. [279], they are probably erroneous.

10.3.1.2 Enthalpy

The enthalpy of formation of nickel ferrite $NiFe_2O_4$ from oxides NiO and α-Fe_2O_3 was measured using high temperature oxide melt solution calorimetry by Navrotsky and Kleppa [233] (in molten $9PbO{\cdot}3CdO{\cdot}4B_2O_3$) and Lilova et al. [236] (in molten $2PbO{\cdot}B_2O_3$) at 970 and 973 K (697 and 700 °C) as -5.1 ± 0.9 (one standard deviation) and -2.8 ± 2.6 (two standard deviations) kJ/mol, correspondingly. The measured values of these authors are in fair agreement.

10.3.1.3 Gibbs energy

The standard Gibbs energy of formation of nickel ferrite $NiFe_2O_4$ from oxides NiO and α-Fe_2O_3 was studied by employing the EMF technique [238, 240]. Tretyakov and Schmalzried [238] conducted their experiments in the temperature range 1000-1500 K (727-1227 °C), Rog [240] – in the range 973-1473 K (700-1200 °C). In both studies, $NiFe_2O_4$-Fe_2O_3-Ni assemblage was reported to be present in the EMF cells. However, this assemblage is not stable in the range of temperatures from 700 to 1227 °C, which is demonstrated in Figure 10.3. So, it is obscure to which equilibrium the data of Rog [240] and Tretyakov and Schmalzried [238], actually, correspond. Moreover, the slope of the Gibbs energy curves of these authors (Figure 10.6) is in disagreement with the enthalpy data

[233, 236]. Consequently, although the data of these authors are in agreement, they were given low weight in the subsequent optimization.

Trinel-Dufour [281] calculated the standard Gibbs energy of formation of nickel ferrite $NiFe_2O_4$ from oxides NiO and α-Fe_2O_3 from its gas equilibration measurements for spinel-alloy equilibria. Their data are also shown in Figure 10.6.

Also, the standard Gibbs energy of the formation of $NiFe_2O_4$ in the following reaction, $Ni + 2/3Fe_3O_4 + 2/3O_2 = NiFe_2O_4$, was measured by Terayama et al. [280] by the EMF method at 1273 K (1000 °C) as -120 kJ/mol. However, as in the case of Rog [240] and Tretyakov and Schmalzried [238], the assemblage is not stable at the given temperature.

Since there were no reliable Gibbs energy data for nickel ferrite $NiFe_2O_4$, to fix its Gibbs energy, phase equilibrium data [21, 283-289] shown in Figure 10.7 and described in detail later in the text were used.

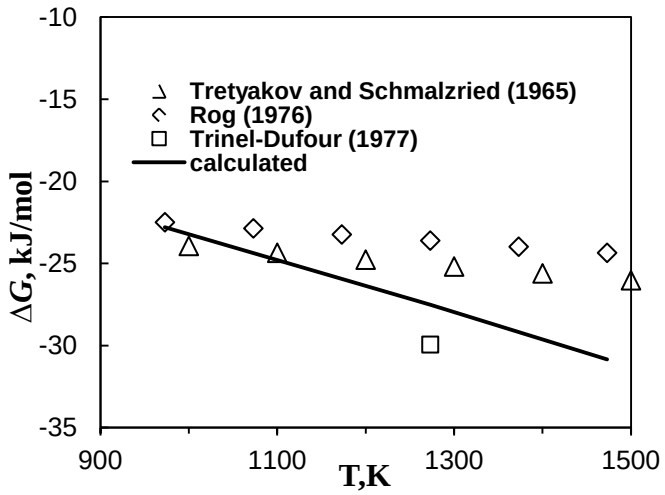

Figure 10.6: Gibbs energy of formation of nickel ferrite $NiFe_2O_4$ from oxides NiO and α-Fe_2O_3: literature data [238, 240] and a calculated line

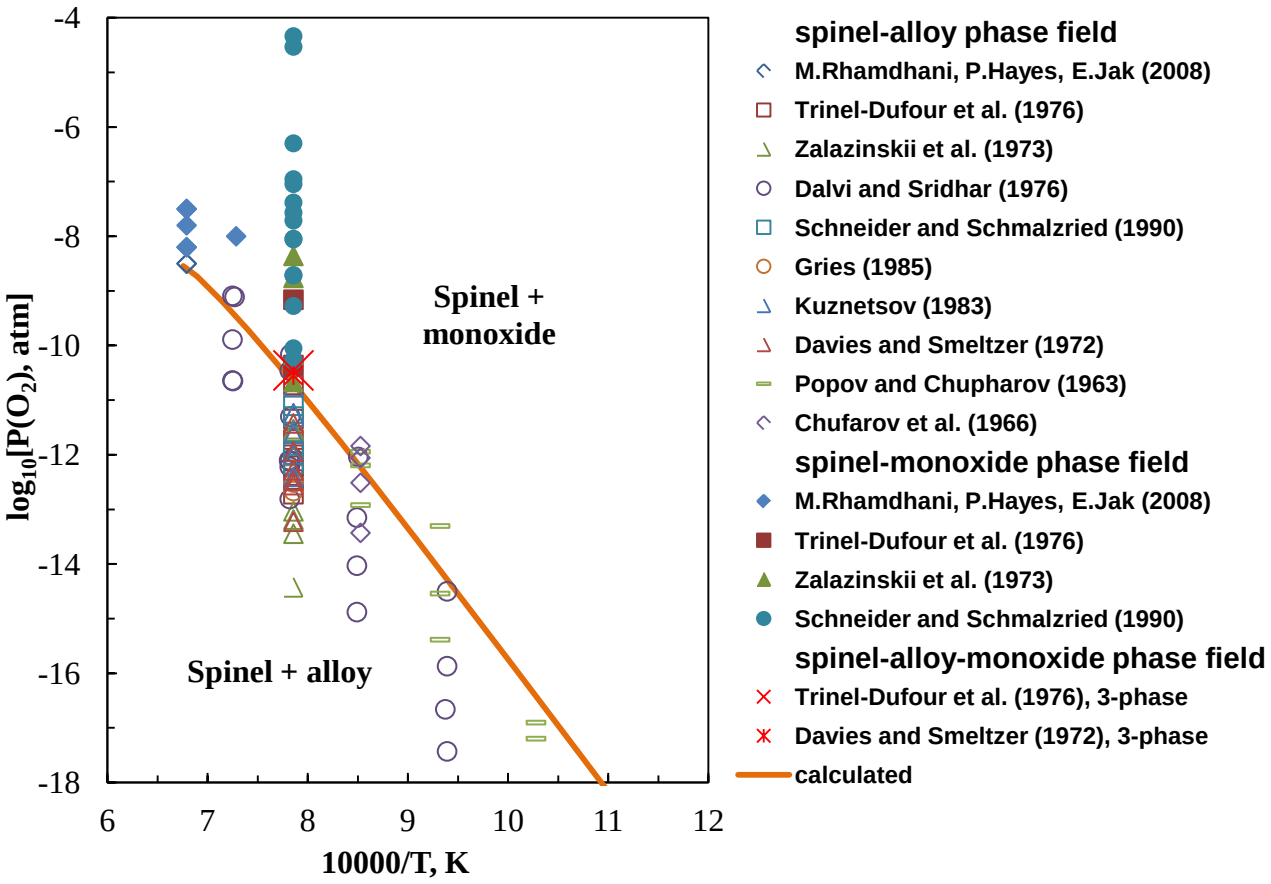

Figure 10.7: Calculated partial pressure of oxygen for the spinel-monoxide(NiO-rich)-alloy equilibria as function of temperature, along with the experimental data [21, 283-289]. The results of Gries and Kuznetsov are taken from Schneider and Schmalzried [286]

10.3.1.4 Cation distribution

The cation distribution data for the stoichiometric $NiFe_2O_4$ spinel are shown in Figure 10.1. The samples were either slowly cooled or quenched, which is pointed out in the figure; otherwise, no information was given in the article. The cation arrangement was studied using several techniques: *Mössbauer spectroscopy* – by Sawatzky et al. [257] in the temperature range 1250-1400 °C, Kuznetsov et al. [260] at 1100 °C, Seshan et al. [262] at 1302 °C, and Fayek et al. [265] in the range 1000-1200 °C; *magnetic measurements* – by Roberston and Pointon [153] in the temperature range 1100-1400 °C; *from magnetization data* – by Kiran et al. [261] at 1050 °C; *neutron diffraction* – by Youssef et al. [256] at 1250 °C and Murthy et al. [258] at 1250 °C; *X-ray diffraction* – by Faller and Birchenall [259] in the temperature range 910-1015 °C, Ahmad and Abbas [263] at 1300 °C and Tsukimura et al. [264] at 1030 °C; *anomalous X-ray scattering method* – by Shinoda et al. [214] at

500 °C and Sugiyama et al. [267] up to 900 °C; *X-ray magnetic circular dichroism* – by Pattrick et al. [266] at 1100 °C; *X-ray absorption spectroscopy* – by Yao et al. [212] at 1400°C and Henderson et al. [40] at 1050 °C. Ramalho et al. [268] used both *Mössbauer spectroscopy* and *X-ray diffraction* methods at 700 and 1100 °C, respectively. Singhal and Chandra [269] used magnetic spectra additionally to these 2 methods at 1200 °C.

The cation distribution in Ni ferrite solutions $FeNi_xFe_{2-x}O_4$, where x = 0.16, 0.33, 0.52, 0.71 and 0.93, was studied by Saito et al. [270] using *X-ray magnetic circular dichroism*. Their data are shown in Figure 10.2.

The majority of cation distribution studies (Figure 10.1) report more than 99% of Ni in octahedral position. Nevertheless, a group of authors [40, 259, 265, 266] state the lower site occupancy, around 90% of Ni in octahedral position. However, some of their data are less reliable. For instance, Pattrick et al. [266] used *X-ray magnetic circular dichroism* – the method, which was not developed enough to give quantitative results. In the study of Faller and Birchenall [259], *X-ray method* was used, which, as it was explained above, gives inexplicit results for Fe and Ni due to their similar scattering properties. Therefore, these data were not taken into account in the subsequent optimization.

10.3.2 Phase diagram data

10.3.2.1 Solid-state equilibria

The subsolidus phase equilibria of the Fe–Ni–O system were largely investigated over a wide range of temperatures and oxygen partial pressures [21, 283-298]. The results of these studies are demonstrated in Figure 10.7-Figure 10.20. Most of the studies concentrated on phase relations in the regions where Fe–Ni alloy is in equilibrium with solid oxide phases and where equilibrium oxygen pressures are low.

The following studies [290, 292, 293, 295] are limited to the wüstite-alloy two-phase region. Roeder and Smeltzer [293] used the dimethyl-glyoxime analytical method to measure the nickel contents of wüstite at 900 and 1000 °C and the EMF method – to determine the corresponding oxygen pressures. There was no information in the article on the method of measuring the alloy composition. The composition-oxygen pressure relationship for the wüstite-alloy phase field was further investigated by Gatellier et al. [295] by the EMF method for certain alloy compositions and Ono et al. [290] – by thermogravimetry and X-ray analysis in the temperature ranges 900-1100 and

757-1050 °C, respectively. In addition, Ono et al. [299] performed the EMF measurements over the temperature range 750-1150 °C. Viktorovich et al. [292] measured the distribution of nickel between the wüstite and alloy phases by means of XRD analysis, reaching the wüstite-alloy-spinel equilibrium. However, the corresponding oxygen pressures were not reported. The wüstite-alloy field expanded with increase in temperature from 700 to 1100 °C in accordance with the rise in the nickel boundary concentration of the alloy from 65 to 84.5 wt.%.

Popov and Chupharov [288] and Chufarov et al. [289] investigated the spinel-alloy equilibria in the temperature range 700-900 °C by the reduction of nickel ferrite followed by the XRD analysis and measuring the partial pressure of H_2 in the equilibrated H_2/H_2O gas mixtures.

Another group of authors [285, 287, 291] investigated both the wüstite/alloy and spinel/alloy regions of the system. Davies and Smeltzer [287] used the EMF technique to determine the oxygen pressures for Fe–Ni alloys in equilibrium with their oxides at 1000 and 1050 °C, and the electron probe microanalysis – to measure the compositions of the coexisting phases. The oxygen partial pressure was measured as $5.5 \cdot 10^{-14}$ atm for the invariant three-phase field of wüstite, spinel and alloy and $2.5 \cdot 10^{-11}$ atm - for spinel, bunsenite and alloy. Further, Dalvi and Sridhar [285] measured the equilibrium oxygen potentials and compositions in the temperature range of 1065 to 1380 K (792-1107 °C) by gas equilibration in the CO/CO_2 gas mixtures, identifying the phases in the quenched samples by the XRD method and metallography, and analyzing the phases by the EPMA method. Viktorovich and Lisovskii [291] measured nickel solubility in wüstite in the temperature range 900-1100 °C using the XRD method and chemical analysis. The corresponding oxygen pressures were not reported.

Schmalzried and Tretjakow [296] measured the oxygen partial pressures of spinel in equilibrium with coexisting oxides in the temperature range 900-1200 °C by the EMF method for the initial compositions of spinel.

Zalazinskii et al. [284] studied wüstite-alloy, spinel-alloy and spinel-bunsenite equilibria at 1000 °C by the reduction of nickel ferrite, employing the XRD analysis. No details were given for the method of measuring oxygen partial pressures.

Katayama et al. [297] studied spinel-hematite equilibria in the temperature range 1200-1350 K (927-1077 °C), using the EMF technique. The equilibrium compositions of spinel were not measured, only the initial compositions were given in the article.

Dalvi and Smeltzer [294] studied the isothermal section of the Fe–Ni–O system at 1000 °C by employing the equilibration and quenching technique, measuring the compositions by EPMA. In addition, X-ray and electron back-scatter pictures were used for phase identification and for qualitative analysis of the metal compositions in coexisting phases. According to their results, wüstite coexists with Fe–Ni alloys containing up to 79.6 mol % Ni. The three-phase field wüstite-spinel-alloy consists of wüstite containing 0.51 mol % Ni, spinel containing 0.6 mol % Ni, and an alloy containing 79.6 mol % Ni. The other three-phase field, spinel-bunsenite-alloy, consists of nickel ferrite, bunsenite containing 6.5 mol % Fe and an alloy containing 99.5 mol % Ni. However, corresponding oxygen partial pressures were not provided. Furthermore, Trinel-Dufour et al. [283] used CO/CO_2 gas equilibration for determination of iso-pressure tie-lines at the isothermal section of the Fe–Ni–O system at 1000 °C; radiocrystallographic technique, the reactions of transport of oxygen and solid electrolyte technique were used to determine limits of 2-phase equilibrium domains and compositions of 3 phases in equilibrium.

Schneider and Schmalzried [286] investigated phase equilibria in the Fe–Ni–O system, using the high temperature in-situ method of coulometric titration, with a solid oxygen ion electrolyte. The boundaries of the wüstite field and the spinel field were determined at 1000-1360 °C. They also measured the non-stoichiometry δ of the Ni-rich monoxide phase $(Ni, Fe)_{1-\delta}O$ in the temperature range 1173-1303 K (900-1030 °C) and in the log of oxygen potential range -12.4...-0.67 (see Figure 10.12). The experimental curves are starting from arbitrarily chosen reference potentials and compositions.

The non-stoichiometry of spinel region (see Figure 10.8-Figure 10.11) was investigated by O'Bryan et al. [300] at 1300 °C for oxygen partial pressures from $10^{-3.6}$ to 1 atm, using thermogravimetry, metallographic examination and X-ray lattice constant measurements, and by Shafer [301] – at 1400, 1500 and 1600 °C for oxygen partial pressures of 1, $10^{-0.7}$ and 10^{-2} atm by means of thermogravimetry and quenching with microscopic examination and chemical analysis.

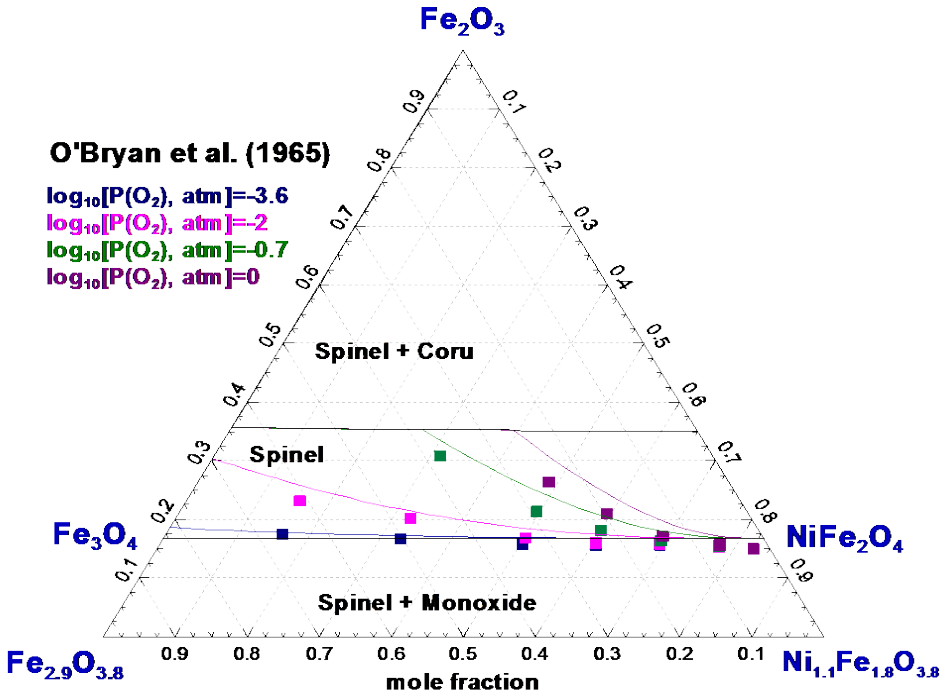

Figure 10.8 : Non-stoichiometry of spinel at various oxygen partial pressures at 1300 °C : experimental isobars of O'Bryan et al. [300] and calculated isobars. Black lines – the calculated isothermal section at 1 atm total pressure (See notations in Table 10.1)

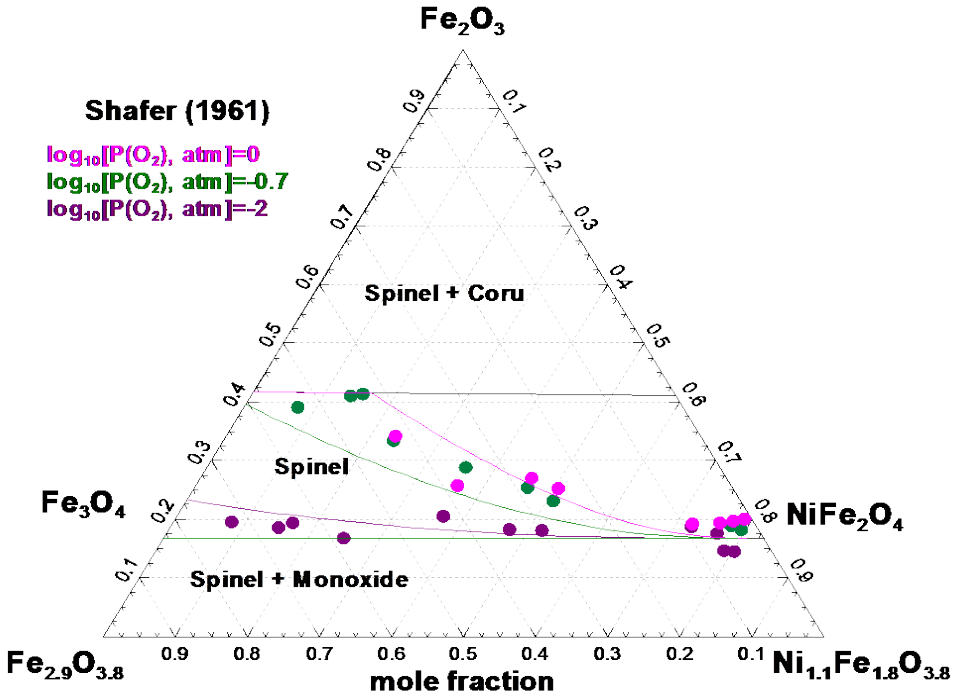

Figure 10.9 : Non-stoichiometry of spinel at various oxygen partial pressures at 1400 °C : experimental isobars of Shafer [301] and calculated isobars. Black lines – the calculated isothermal section at 1 atm total pressure (See notations in Table 10.1)

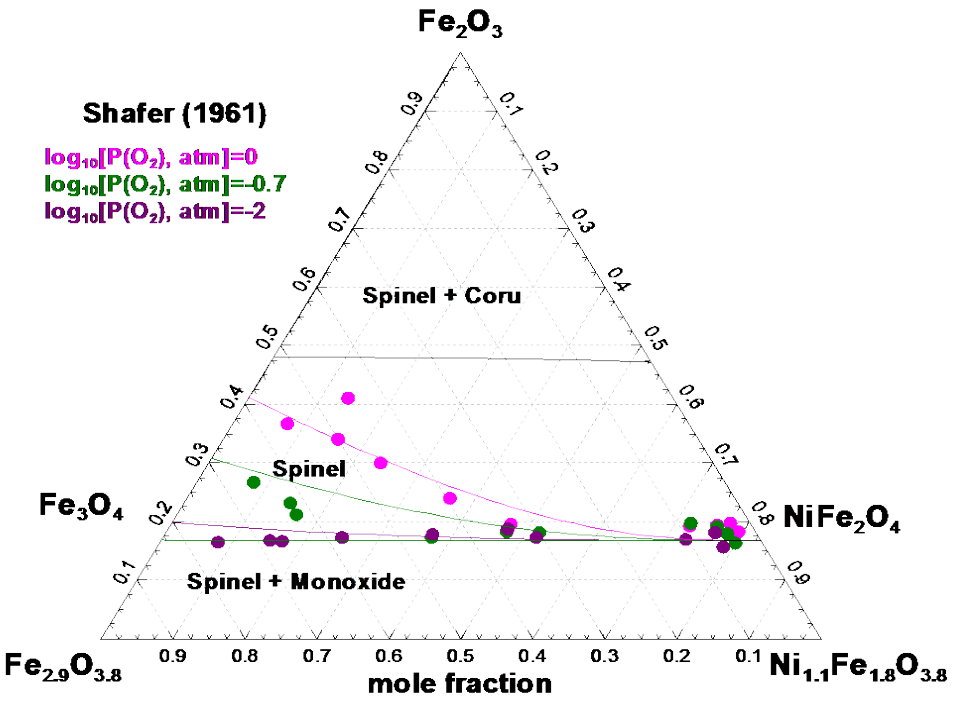

Figure 10.10 : Non-stoichiometry of spinel at various oxygen partial pressures at 1500 °C : experimental isobars of Shafer [301] and calculated isobars. Black lines – the calculated isothermal section at 1 atm total pressure (See notations in Table 10.1)

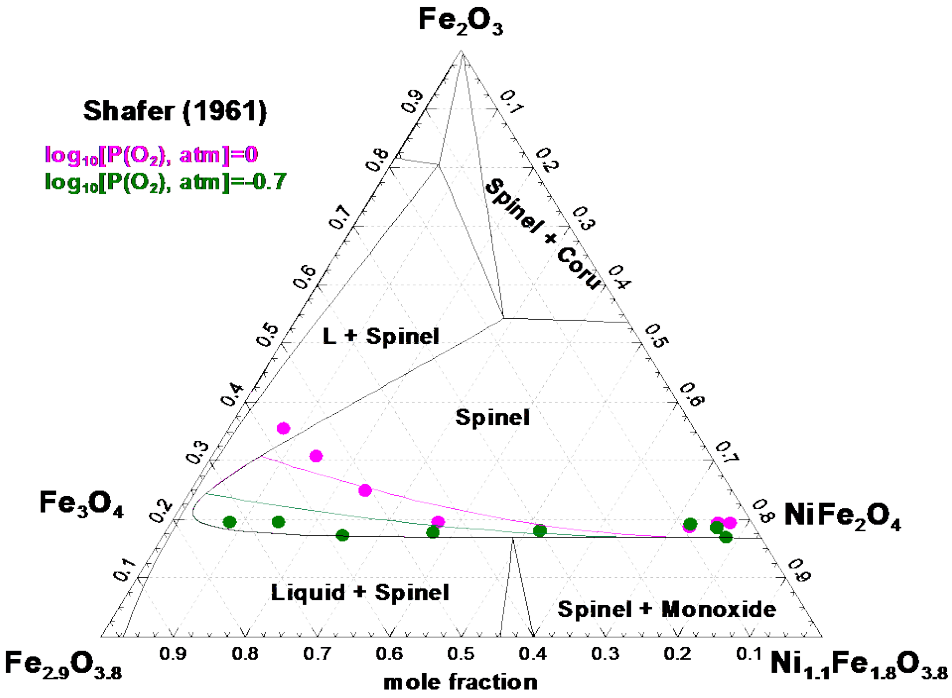

Figure 10.11 : Non-stoichiometry of spinel at various oxygen partial pressures at 1600 °C : experimental isobars of Shafer [301] and calculated isobars. Black lines – the calculated isothermal section at 1 atm (See notations in Table 10.1)

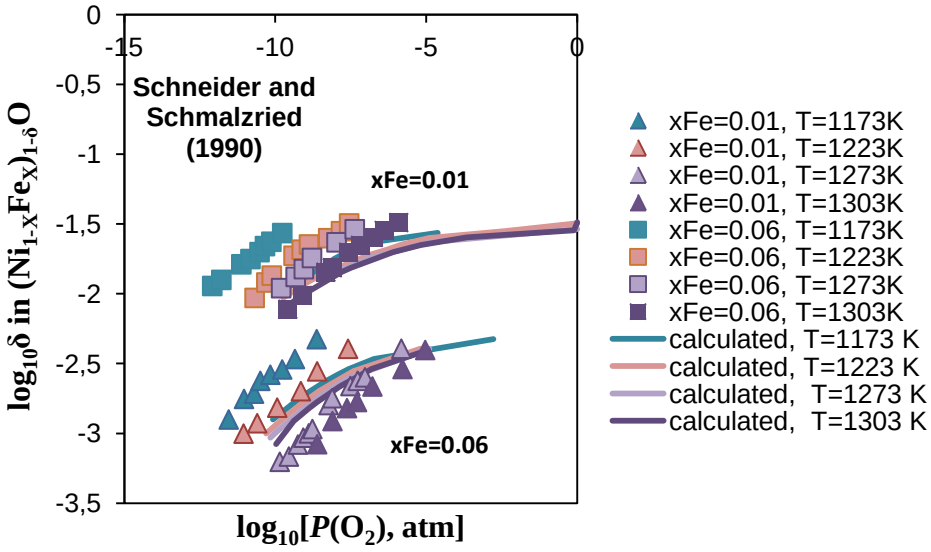

Figure 10.12 : Non-stoichiometry δ of the Ni-rich monoxide phase $(Ni, Fe)_{1-\delta}O$ in the temperature range 1173-1303 K (900-1030 °C): literature data of Schneider and Schmalzried [286] and calculated lines

The solubility of NiO in α-Fe_2O_3 in air was examined by Rajendran et al. [298] in the temperature range 300-1300 °C by XRD. The maximum solubility was found to be 2 mol % at 550 °C.

Recently, phase equilibria in the temperature range between 800 and 1600 °C at low oxygen pressures up to the partial pressure of oxygen of 0.21 atm in air were studied by Rhamdhani et al. [21], using the equilibration and quenching techniques followed by the electron-probe X-ray microanalysis. Two methods of equilibration were used in their study: (a) gas/oxide equilibrated in open systems at fixed oxygen partial pressures, and (b) oxide/alloy equilibrated in closed systems. In general, their data are in fair agreement with the results of other investigators, except for the bunsenite-spinel equilibria. The maximum solubility of iron in bunsenite was found to be 66.2 mol % metal at 1200 °C, which is significantly higher than that reported by Schneider and Schmalzried [286]. However, Schneider and Schmalzried [286] used equilibration times of the order of 2 days (48 hours) for their experiments compared to much longer equilibration times up to 194 hours used by Rhamdhani et al. [21]. Probably, the true equilibrium conditions were not achieved in the study of Schneider and Schmalzried [286], especially in the region where largely non-stoichiometric monoxide phase was involved. Moreover, Schneider and Schmalzried [286] did not provide microstructures nor detailed microanalysis of the phases in the equilibrated samples, which prevented further evaluation of the attainment of equilibrium.

The compositions of phases in the three-phase equilibrium between alloy, spinel, and bunsenite at 1000 °C were determined by Rhamdhani et al. [21] as $n_{Ni} = 0.956$ (for alloy), $n_{Ni} = 0.253$ (for spinel), and $n_{Ni} = 0.742$ (for bunsenite), where $n_{Ni} = n_{Ni}/(n_{Ni}+n_{Fe})$, which is in good agreement with previous studies. It should be mentioned that the partial pressures of oxygen for the corresponding three-phase equilibria were not measured by Rhamdhani et al. [21], but calculated by them using the earlier version of FactSage software and its databases [1]. As it can be suggested, in this series of experiments, oxide/alloy were equilibrated in closed systems and only the compositions were measured in the experiment. The calculated oxygen partial pressures given in the article of Rhamdhani et al. [21] were used to put three-phase equilibrium data of Rhamdhani et al. [21] on the $Log_{10}[P(O_2), atm]$-X plots in Figure 10.15-Figure 10.17.

Figure 10.14-Figure 10.17 show that there are some discrepancies in the available data at low oxygen pressures in the spinel/alloy and wüstite/alloy regions, especially from the Ni-rich side. However, the origin of discrepancies was not clear.

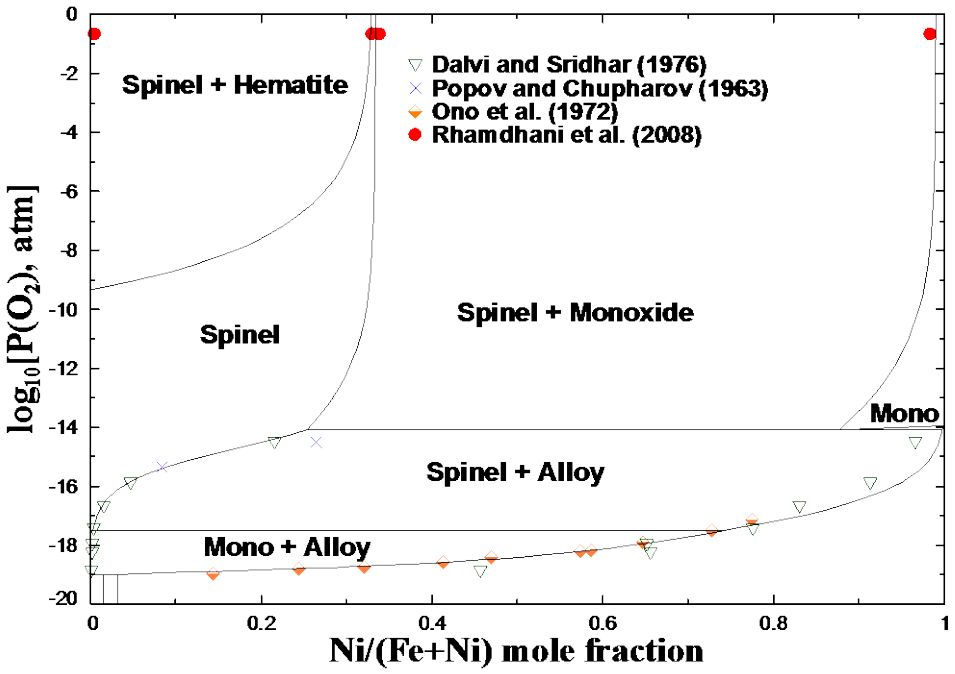

Figure 10.13: $Log_{10}[P(O_2)$, atm]-X phase diagram of the Fe–Ni–O system at 800 °C: literature data [21, 285, 288, 299] and calculated lines. See notations in Table 10.1

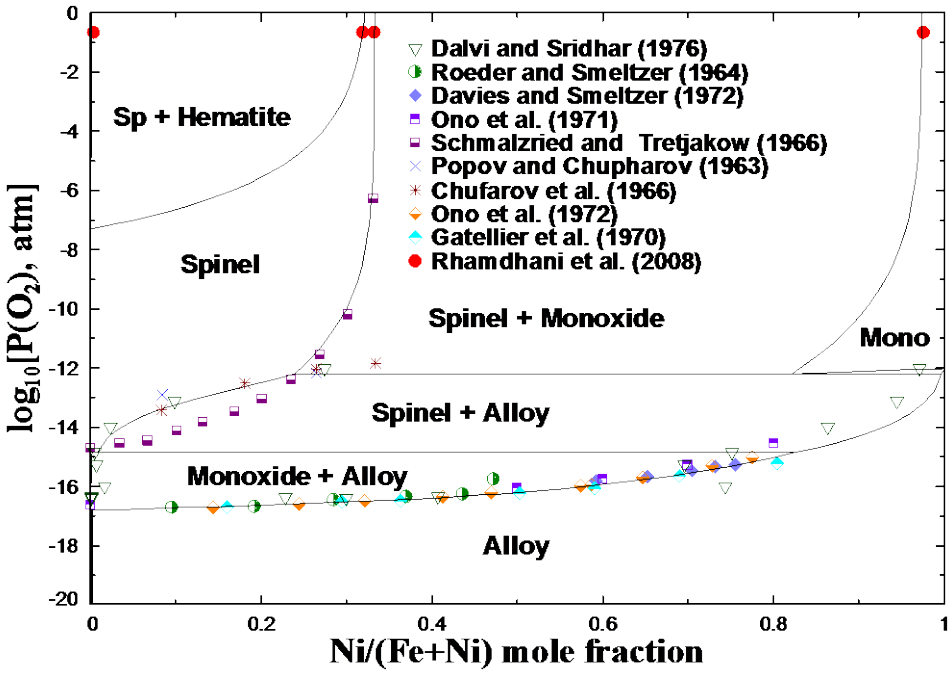

Figure 10.14: $Log_{10}[P(O_2), atm]$-X phase diagram of the Fe–Ni–O system at 900 °C: literature data [21, 285, 287-290, 293, 295, 296, 299] and calculated lines. See notations in Table 10.1

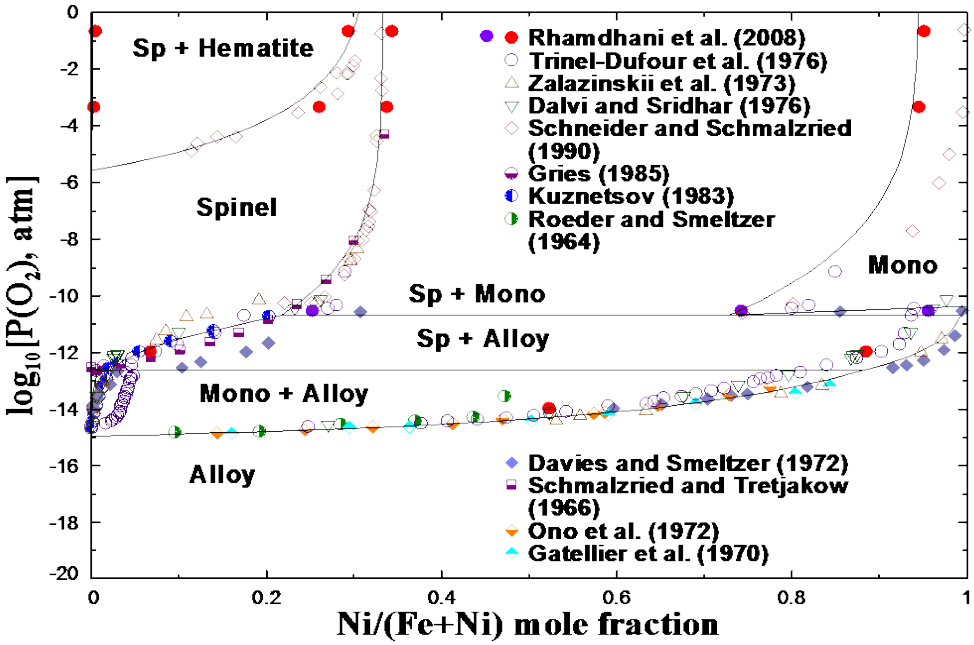

Figure 10.15: $Log_{10}[P(O_2)$, atm]-X phase diagram of the Fe–Ni–O system at 1000 °C: literature data [21, 283-287, 293, 295, 296, 299] and calculated lines. The results of Gries and Kuznetsov are taken from Schneider and Schmalzried [286]. See notations in Table 10.1. The partial pressure of oxygen for the spinel–(NiO-rich) monoxide–alloy equilibrium was estimated by Rhamdhani et al. [21] using the earlier version of the FactSage software. These data are shown by solid violet circles

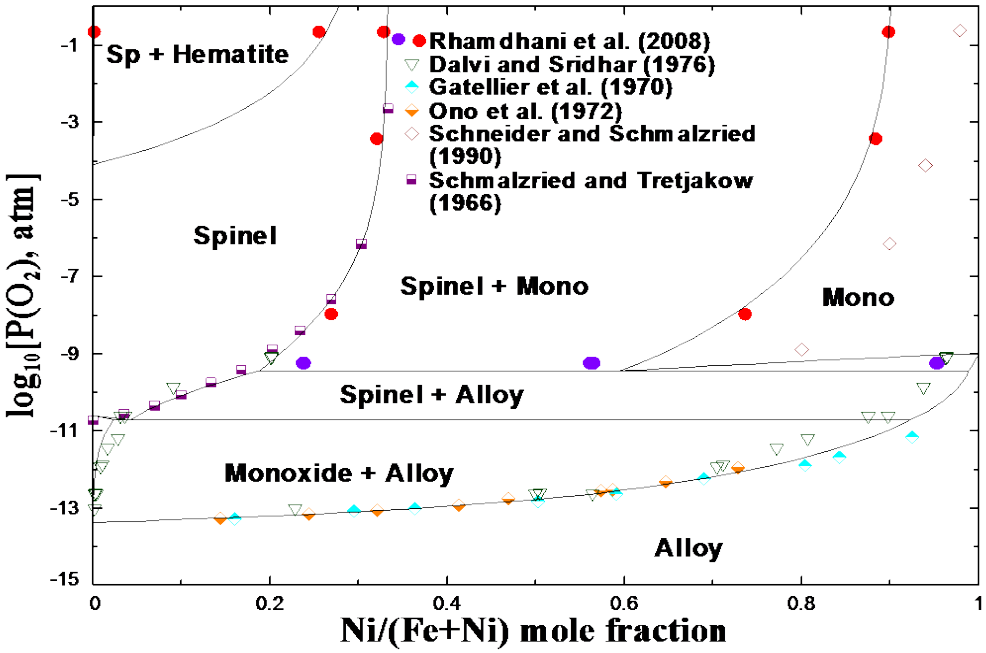

Figure 10.16: $Log_{10}[P(O_2)$, atm]-X phase diagram of the Fe–Ni–O system at 1100 °C: literature data [21, 285, 286, 293, 295, 296] and calculated lines. See notations in Table 10.1. The partial pressure of oxygen for the spinel–(NiO-rich) monoxide–alloy equilibrium was estimated by Rhamdhani et al. [21] using the earlier version of the FactSage software. These data are shown by solid violet circles

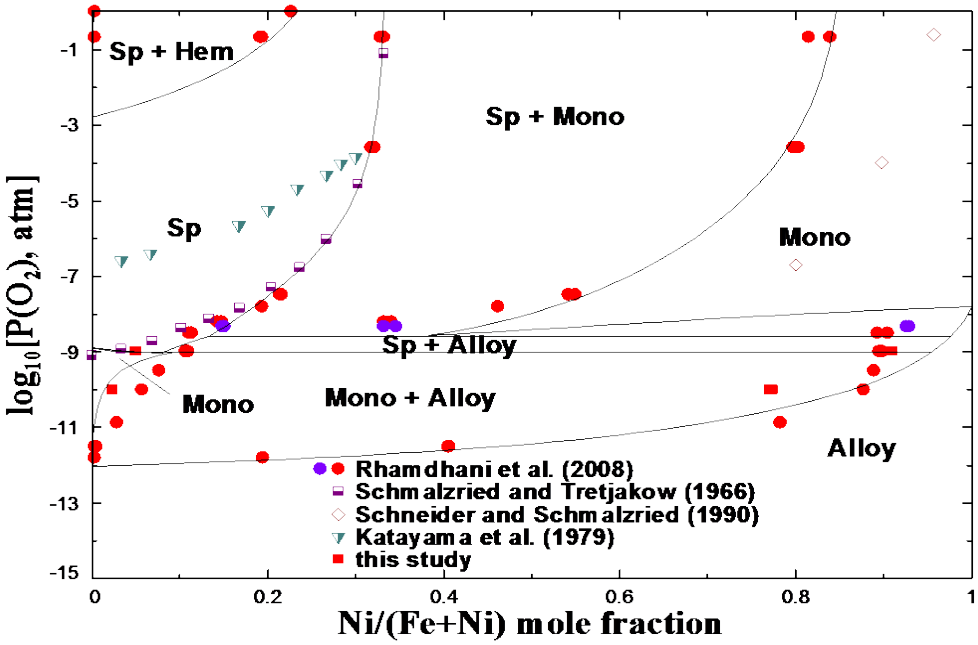

Figure 10.17: $Log_{10}[P(O_2)$, atm]- X phase diagram of the Fe–Ni–O system at 1200 °C: literature data [21, 286, 296, 297], experimental results of this study and calculated lines. See notations in Table 10.1. The partial pressure of oxygen for the spinel–(NiO-rich) monoxide–alloy equilibrium was estimated by Rhamdhani et al. [21] using the earlier version of the FactSage software. These data are shown by solid violet circles

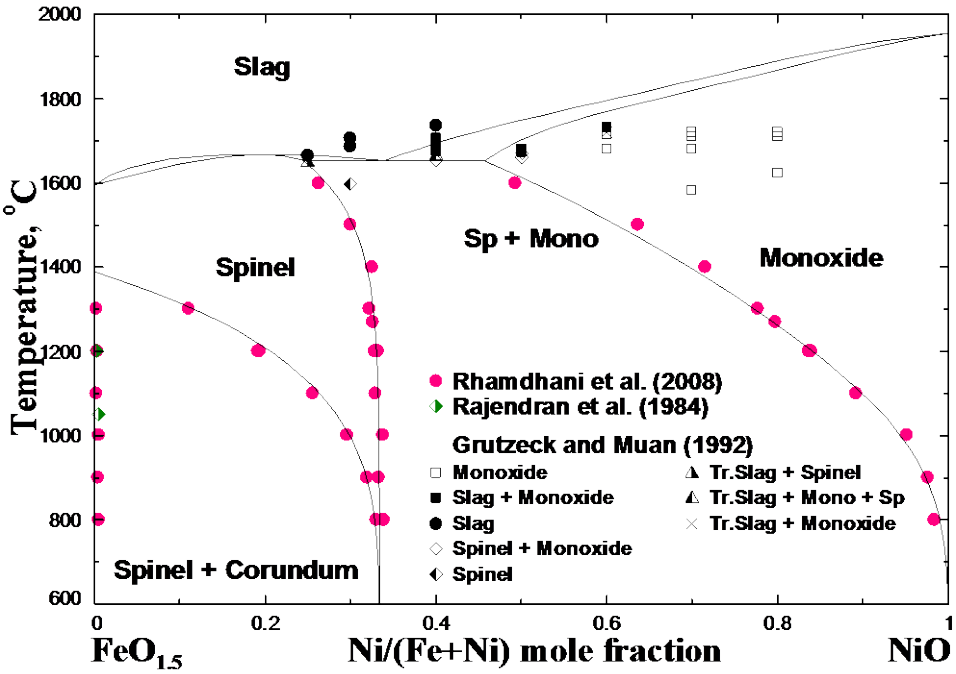

Figure 10.18: 0.5'Fe_2O_3'-NiO section of the Fe–Ni–O phase diagram in air: literature data [21, 298, 302] and calculated lines. See notations in Table 10.1

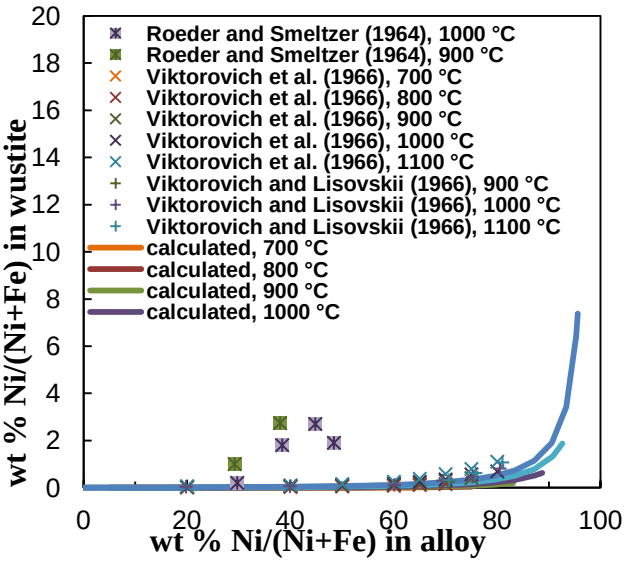

Figure 10.19: Distribution of nickel between wüstite and alloy in the temperature range 700-1200 °C: literature data [291-293] and calculated lines

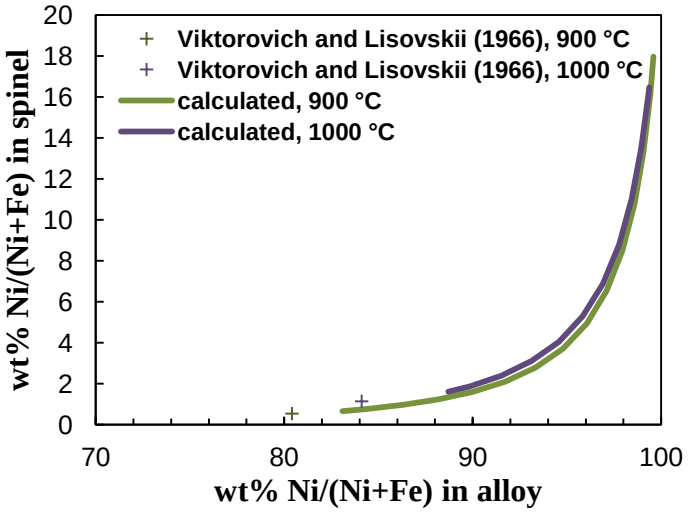

Figure 10.20: Distribution of nickel between spinel and alloy in the temperature range 900-1000 °C: literature data [291] and calculated lines

10.3.2.2 Liquid-state equilibria

The distribution of nickel between liquid slag and metal phases was examined by several authors [303-306]. Their data are shown in Figure 10.21 and Figure 10.22. Gran' and Tseidler [303] investigated it by the oxidation of the metal phase by air, sampling slag and metal followed by chemical analysis of phases at 1500-1525 °C (no other experimental details), Tsemekhman and Vaisburd [304] – by the method of equilibrium fusion in an atmosphere of purified argon at 1500-1600 °C (no other experimental details), von Bohlen Halbach and Leitgebel [305] – by the oxidation of the metal and thermogravimetry in the temperature range 1500-1750 °C in MgO crucibles supposing no solubility of MgO in slag, Kuxmann and Koch [306] – by quenching and chemical analysis at temperatures of 1540, 1600 and 1660 °C in quartz crucibles and at 1540 °C in lime and corundum crucibles supposing saturation with the crucible material. Since it is not clear from the latter article, it may be supposed that slag and metal formed easily separated layers, slag turned into solid phases on quenching and the total composition of iron and nickel in these solid phases was determined by the chemical analysis.

Tsemekhman and Vaisburd [304] also investigated the Fe^{III}/Fe^{II} ratio in the slag as a function of the composition of the equilibrium metallic phase. It was shown that the concentration of trivalent iron in slag increased as the nickel content in the metal was raised from 0 to 70 wt.% and then fell sharply. The maximum content of Fe_2O_3 in the slag was about 36 wt.%. However, Rhamdhani et al. [21] in their recent paper showed that to date there exists no reliable analytical method to determine

the Fe^{III}/Fe^{II} ratio in the phase in the presence of nickel, so the results obtained by Tsemekhman and Vaisburd [304] are questionable.

Schenck et al. [307] established the 'FeO'–NiO section of the Fe–Ni–O diagram, shown in Figure 10.23, by means of differential thermal analysis. The experiments were made in the flow of nitrogen to ensure low oxygen pressures. In such conditions, most of the iron was apparently divalent. The results of two series of experiments were provided by Schenck et al. [307], one of which was made at metallic saturation (metal was added to the sample).

Grutzeck and Muan [302] investigated the 0.5'Fe_2O_3'–NiO section of the Fe–Ni–O diagram in air, shown in Figure 10.18, by quenching followed by metallographic and polarizing microscopic techniques, and X-ray diffraction analysis. Spinel and monoxide were the only crystalline phases present. The temperature at which these two phases coexisted with the liquid phase was determined as 1665 ± 10 °C. The compositions of the liquid, spinel, and monoxide at this invariant temperature were measured as follows: liquid (26 wt.% NiO, 75 wt.% Fe_3O_4), spinel (32 wt.% NiO, 68 wt.% Fe_3O_4) and monoxide (53 wt.% NiO, 47 wt.% Fe_3O_4).

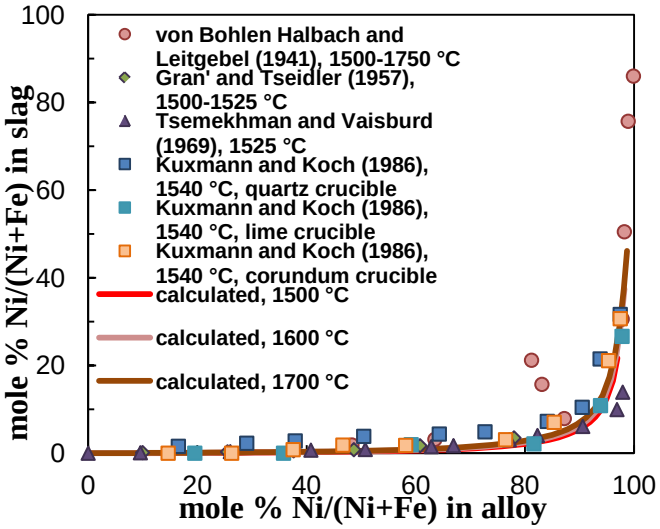

Figure 10.21: Distribution of Ni between alloy and slag phases of the Fe–Ni–O system in the temperature range 1500-1750 °C: literature data [303-306] and calculated lines

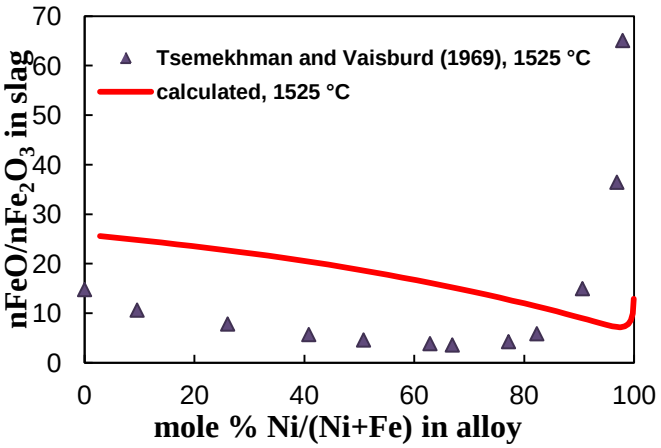

Figure 10.22: Fe^{III}/Fe^{II} ratio in the slag as a function of the composition of the equilibrium metallic phase: literature data [304] and a calculated line

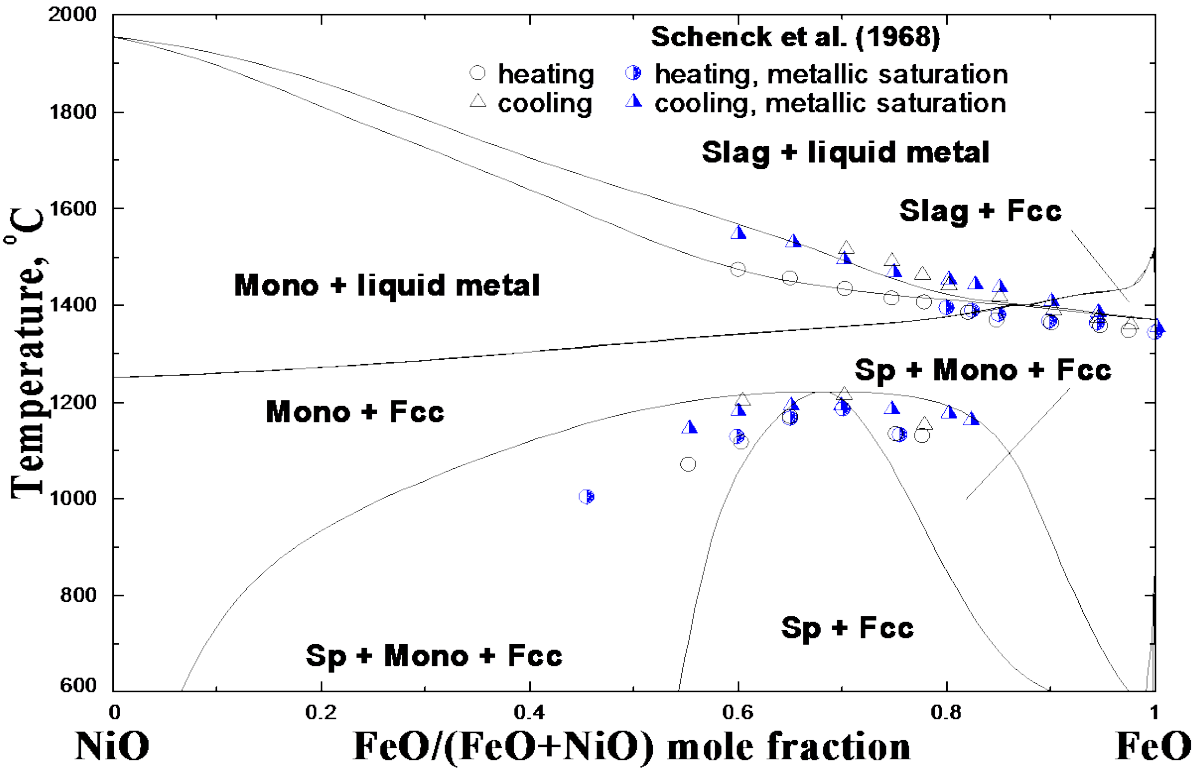

Figure 10.23: 'FeO'–NiO section of the Fe–Ni–O system at metal saturation along with the literature data of Schenck et al. [307]. See notations in Table 10.1

10.4 Optimization

The parameters of the models described in Section 10.2 were obtained in the following order. First, the model parameters for monoxide and spinel solutions were optimized to describe available thermodynamic properties and subsolidus phase equilibria data. Afterwards, the parameters of the slag phase were optimized using available liquid-state equilibria data.

10.4.1 Spinel

The scheme of optimization of the spinel solution applied in this study was the following. First of all, the thermodynamic properties of the stoichiometric spinel $NiFe_2O_4$ were fixed. All parameters for Fe_3O_4 spinel, including magnetic properties, were taken from the study by Decterov et al. [41]. Then, all remaining parameters for the $NiFe_2O_4$–Fe_3O_4 spinel solution were optimized.

The thermodynamic functions of stoichiometric nickel ferrite $NiFe_2O_4$ were calculated with consideration of 3 contributions: lattice (mainly vibrational), magnetic and configurational. A magnetic contribution takes into account the effect of ferromagnetic transformation at 859 K on thermodynamic functions of nickel ferrite. A configurational contribution to the entropy may be calculated using Equation (10.6). A configurational contribution to the heat capacity function originates from heat of changes of the cation distribution between tetrahedral and octahedral sublattices in $NiFe_2O_4$ with temperature (see Figure 10.1).

Figure 10.4 shows the optimized high-temperature heat capacity C_P of *cubic* stoichiometric $NiFe_2O_4$. As a first approximation, it was assumed that the lattice and magnetic contributions to C_P are independent of the cation distribution. As can be seen from Figure 10.4, most of the experiments on the heat capacity of $NiFe_2O_4$ were made at temperatures below 800 °C, where the cation distribution is believed to be frozen. As a result, a configurational contribution to C_P was not present in these measurements. The sum of lattice and magnetic contributions of the heat capacity of the hypothetical normal spinel $(Ni^{2+})^T[Fe^{3+}]_2^O O_4^{2-}$ was optimized to fit the heat capacity [156, 275-279] and heat content [273, 274] data. The heat effect of changes in the cation distribution and thus the configurational part of the C_P came from the optimization of all phase equilibria at high temperatures involving the spinel phase. The heat capacity curve shown in Figure 10.4 was calculated at all temperatures taking into account the hypothetical equilibrium cation distribution. High-temperature data of Ziemniak et al. [279] and Landiya et al. [274] seem to be not far from

equilibrium distribution, probably because cation distribution of $NiFe_2O_4$ does not change much with temperature, as shown in Figure 10.1.

The entropy of *cubic* $NiFe_2O_4$ is constrained by the data shown in Figure 10.7. The entropy of $NiFe_2O_4$ at 900 °C obtained by the optimization of these high-temperature data is 405 $J \cdot mol^{-1}K^{-1}$, which is in agreement within 2% with the value of 396.2 $J \cdot mol^{-1}K^{-1}$ calculated by the integration of the C_P shown by the solid line in Figure 10.4 from -273.15 to 900 °C, assuming that the residual entropy at -273.15 °C is the configurational entropy of the completely inverse spinel.

The measured enthalpy of formation of spinel should depend upon the cation distribution between the sublattices in the studied samples. The degree of inversion for the samples used in the calorimetric measurements of Navrotsky and Kleppa [233] and Lilova et al. [236] probably corresponds to a temperature between 700 and 950 °C and hence is very close to inverse spinel. The enthalpy of *cubic* $NiFe_2O_4$ was optimized to fit available enthalpy [233, 236] as well as Gibbs energy data [238, 240, 280, 281]. The molar enthalpy of formation of stoichiometric spinel $NiFe_2O_4$ from oxides NiO and α-Fe_2O_3 with the equilibrium cation distribution is calculated as -7.48 kJ/mol at 700 °C, compared to -5.1 ± 0.9 kJ/mol (one standard deviation) and -2.8 ± 2.6 kJ/mol of Navrotsky and Kleppa [233] and Lilova et al. [236], correspondingly. The Gibbs energy of formation of $NiFe_2O_4$ from oxides NiO and α-Fe_2O_3 at 1000 °C is then calculated as -27.5 kJ/mol, which is in between -29.9 kJ/mol of Trinel-Dufour [281] and -23.6 kJ/mol of Rog [240] (see Figure 10.6). The standard Gibbs energy of the formation of $NiFe_2O_4$ in the following reaction, $Ni + 2/3Fe_3O_4 + 2/3O_2 = NiFe_2O_4$, is calculated at 1000 °C as -177.6 kJ/mol, compared to -120 kJ/mol of Terayama et al. [280]. The reason for this inconsistency is explained above.

The parameter *I* was optimized to describe the cation distribution data [40, 153, 212, 214, 256-269] in Figure 10.1 and Figure 10.2. The calculated lines are believed to be in accordance with the experimental data within experimental error limits.

The remaining parameters $\Delta_{Fe^{+3}Fe^{+2}Ni^{2+}}$ and $\Delta_{Fe^{+3}Ni^{+2}Fe^{2+}}$ were optimized to describe the phase diagram data involving the spinel solution [21, 284-289, 291, 294, 296, 297, 300, 301, 307] and the experimental results of this study (see Figure 10.7-Figure 10.18, Figure 10.20, Figure 10.23). From the available phase diagram data, the experimental data obtained in this study and those obtained by Rhamdhani et al. [21] were given preference in the optimization due to their believed high accuracy, which is achieved by applying carefully planned equilibration procedures followed by electron probe X-ray microanalysis.

The optimized model parameters for the spinel phase are given in Table 10.2.

10.4.2 Monoxide, corundum

The parameters of the monoxide phase were optimized to describe the phase equilibria data including monoxide [21, 284-287, 290-296, 307] and the experimental results of this study (Figure 10.7-Figure 10.19, Figure 10.23). For the monoxide-spinel equilibria, the results of Rhamdhani et al. [21] were preferred to the results of Schneider and Schmalzried [286] due to the reasons explained above. The calculated lines are in good agreement with the experimental results.

The parameters of the corundum solid solution were optimized to describe the solubility limit of NiO in α-Fe_2O_3 in air measured by Rajendran et al. [298] shown in Figure 10.18. The optimized parameters of the monoxide and corundum solutions are given in Table 10.2.

10.4.3 Liquid

The parameters of the Modified Quasichemical Model were optimized to describe the phase equilibria data [303-306] (Figure 10.18, Figure 10.21, Figure 10.22 and Figure 10.23) and are given in Table 10.2. The calculated lines are in good agreement with the experimental results.

10.5 Summary of results

Some discrepancies in the literature data for the Fe–Ni–O system were demonstrated. To help resolve the conflicts existing in the literature, a new experimental investigation has been carried out in this study. The compositions of wüstite/alloy and spinel/alloy in equilibrium have been measured at 1200 °C at partial pressures of oxygen $\log_{10}[P(O_2), \text{atm}] = -9$ and -10. The improved experimental technique included equilibration and quenching followed by electron probe X-ray microanalysis (EPMA). The experimental measurements provided additional data for a subsequent thermodynamic modeling.

A simultaneous optimization of all available data in the Ni-containing system Fe–Ni–O at 1 atm total pressure has been performed. New experimental data and previously published experimental results were taken into consideration. The best possible description of thermodynamic properties data and phase relations has been obtained. The optimized model parameters for oxide phases reproduce all available data within experimental error limits. A set of self-consistent Gibbs energy functions of the oxide phases in the Fe–Ni–O system has been derived. By this means, the next part

of the thermodynamic database for the multi-component Al–Ca–Fe–Mg–Ni–O–Si chemical system involved in the process of nickel extraction from the laterite ores was created.

Table 10.2: Optimized properties of stoichiometric compounds and model parameters for oxide phases in the Fe–Ni–O system (J·mol^{-1} and J·mol^{-1}·K^{-1})

Compounds	**Temperature range (K)**	$\Delta H^{o}_{298.15}$	$S^{o}_{298.15}$	$C_P(T)$
The thermodynamic properties of solid and liquid NiO are given in [51]				
Fe_2O_3 (alpha)	298-2500	-825787.0	87.7285	$137.0089 - 2.9076\times10^{6}\,T^{-2}$
Slag (liquid oxide phase): FeO–$FeO_{1.5}$–NiO				
$Z_{Ni} = 1.37744375,\quad Z_{Fe^{+2}} = 1.37744375,\ Z_{Fe^{+3}} = 2.06616563;$ $\Delta g^{o}_{Ni,Fe^{+3}} = -8368,\quad q^{10}_{Ni,Fe^{+3}} = -29288;$ $q^{20}_{Ni,Fe^{+2}} = -33472.$ FeO-$FeO_{1.5}$ liquid oxide was optimized by Decterov et al. [41]; The Kohler-like extension of binary terms into the ternary system [28] was used.				
Monoxide (solid oxide): FeO–$FeO_{1.5}$–NiO				
$q^{00}_{Ni,Fe^{+2}} = -4184,\ q^{01}_{Ni,Fe^{+2}} = 29288,\ q^{00}_{Ni,Fe^{+3}} = 71571.5 - 62.7851T.$ FeO-$FeO_{1.5}$ monoxide was optimized by Decterov et al. [41]; The Kohler-like extension of binary terms into the ternary system [28] was used.				

Table 10.2 (Continued): Optimized properties of stoichiometric compounds and model parameters for oxide phases in the Fe–Ni–O system ($J \cdot mol^{-1}$ and $J \cdot mol^{-1} \cdot K^{-1}$)

Corundum: $FeO_{1.5}(NiO)$

$$G^{o}_{Fe_2O_3}(\text{coru}) = G^{o}_{\alpha\text{-}Fe_2O_3}, \quad G^{o}_{NiO}(\text{coru}) = G^{o}_{NiO} + 40584.8.$$

Spinel: $(Fe^{2+}, Fe^{3+}, Ni^{2+})^{T}(Fe^{2+}, Fe^{3+}, Ni^{2+}, Va)_2^{O}O_4$

$$7 \cdot F_{Ni^{+2}Fe^{+3}} = -1002734.4 - 1170.1398 \cdot T + 329.72000 \cdot T \ln T + 0.5163500 \cdot T^2 - 2.97983 \times 10^{-5} \cdot T^3 - 57.92533 \cdot T^{1.5} + 4313.60 \ln T;$$

$$\text{Magnetic properties}: T_{Ni^{+2}Fe^{+3}} = T^{i}_{Ni^{+2}Fe^{+3}} = 859 \text{ K [153]},$$

$$\beta_{Ni^{+2}Fe^{+3}} = \beta^{i}_{Ni^{+2}Fe^{+3}} = 6.159, \text{ P}=0.28;$$

$$I_{Ni^{+2}Fe^{+3}} = -168615.2;$$

$$\Delta_{Fe^{+2}Ni^{+2}Fe^{+3}} = -75312, \quad \Delta_{Ni^{+2}Fe^{+2}Fe^{+3}} = 0;$$

All parameters for Fe_3O_4 spinel, including magnetic properties, were optimized earlier by Decterov et al. [41].

The Gibbs energy of formation of a compound from elements in their standard state at a temperature of T(K) and a pressure of 1 atm is given by $\Delta G = \Delta H^{o}_{298.15} - T S^{o}_{298.15} + \int_{298.15}^{T} C_P(T) dT - T \int_{298.15}^{T} \frac{C_P(T)}{T} dT$, where $\Delta H^{o}_{298.15}$ is the enthalpy of formation of the compound at 1 atm and 298.15 K, $S^{o}_{298.15}$ is the entropy of the compound at 1 atm and 298.15 K, and $C_p(T)$ is the heat capacity at constant pressure.

CHAPTER 11 THERMODYNAMIC OPTIMIZATION AND PREDICTION OF PHASE EQUILIBRIA IN THE Al–Fe–Ni–O, Al–Mg–Ni–O AND Fe–Mg–Ni–O SYSTEMS

Equation Chapter (Next) Section 1This chapter is concerned with the optimization of thermodynamic and phase equilibrium data for the Al–Fe–Ni–O, Al–Mg–Ni–O and Fe–Mg–Ni–O chemical systems over a wide range of temperatures and oxygen partial pressures. A literature review for these chemical systems was performed. The literature review and critical analysis of data was followed by thermodynamic modeling of oxide phases. The Modified Quasichemical Model (MQM) was used for modeling of the slag phase (liquid oxide phase), the model based on the Compound Energy Formalism – for the spinel solid solution. The monoxide and corundum solutions were described using a simple Bragg-Williams model. The parameters of the MQM model were optimized in case there were available literature data for the slag phase in the corresponding quaternary systems. The properties of the spinel, monoxide and corundum solutions were predicted from the model parameters for the corresponding binary and ternary solutions, optimized earlier. The subsequent comparison with available thermodynamic and phase equilibrium data showed that these physically meaningful models have rather good ability to predict phase equilibria in multicomponent systems.

11.1 Background

This part of the study is aimed to optimize the Al–Fe–Ni–O, Al–Mg–Ni–O and Fe–Mg–Ni–O systems. In order to achieve that, initially, all available literature data were reviewed and analyzed.

11.2 Phases and thermodynamic models

A list of solution phases in the Al–Fe–Ni–O, Al–Mg–Ni–O and Fe–Mg–Ni–O systems along with notations used in this study is given in Table 11.1.

Metallic solutions were optimized previously: Al–Ni – by Ansara et al. [194], Fe–Ni – by Dinsdale and Chart [255], and Al–Fe and Al–Fe–Ni(O) – as part of the FSstel FactSage database of FactSage software [1]. The properties of the Al–Fe–Ni–O slag phase have been optimized in the present study. The resulting model parameters are listed in Table 11.2. The properties of solid oxide solutions and other slags were predicted from the optimized model parameters of the corresponding

binary and ternary solutions: the Mg–Ni–O system – by Prostakova et al. [51], the Al–Mg–O and Fe–Mg–O systems – by Jung et al. [42, 43]. For the optimizations of the Al–Fe–O, Al–Ni–O and Fe–Ni–O systems – see CHAPTER 5, CHAPTER 9 and CHAPTER 10.

For the spinel solution model, cations shown within a set of parentheses occupy the same sublattice.

Table 11.1: Solution phases and stoichiometric compounds in the Al–Fe–Ni–O, Al–Mg–Ni–O and Fe–Mg–Ni–O systems

Phase name	**Formula**	**Notation used in this study**
Solutions :		
Slag (liquid oxide)	$AlO_{1.5}$–FeO–$FeO_{1.5}$–MgO–NiO	L or Liquid
Monoxide	FeO–MgO–NiO–($FeO_{1.5}$–$AlO_{1.5}$)	Mono or Monoxide
Corundum	$AlO_{1.5}$–$FeO_{1.5}$– (NiO)	Coru or Corundum
Spinel	$(Al^{3+}, Fe^{2+}, Fe^{3+}, Mg^{2+}, Ni^{2+})^{T}(Al^{3+}, Fe^{2+}, Fe^{3+}, Mg^{2+}, Ni^{2+}, Va)_2{}^{O}O_4{}^{*}$	Sp or Spinel
Fcc	Al–Fe–Mg–Ni	
Bcc_A2	Al–Fe–Mg–Ni	
Bcc_B2	Al–Fe–Ni	
$Al_{13}Fe_4$	Al–Fe	
Al_5Fe_4	Al–Fe	
L12-Fcc	Al–Fe–Ni	
AlNi	Al–Ni	
Al_3Ni_2	Al–Ni	
Liquid metal	Al–Fe–Ni–O	L metal or Liquid metal

Table 11.1 (Continued): Solution phases and stoichiometric compounds in the Al–Fe–Ni–O, Al–Mg–Ni–O and Fe–Mg–Ni–O systems

Stoichiometric compounds:	
Al_5Fe_2	Al_5Fe_2
$Al_{61}Fe_{31}$	$Al_{61}Fe_{31}$
$FeAlO_3$	$FeAlO_3$
Al_3Ni	Al_3Ni
Al_3Ni_5	Al_3Ni_5

*T=tetrahedral sublattice, O=octahedral sublattice

11.2.1 Slag (liquid oxide)

The liquid oxide phase is an ionic melt where metal cations are always surrounded by oxygen anions. In other words, they exhibit almost full first-nearest-neighbour (FNN) short-range ordering (SRO). Furthermore, there is a strong tendency for SRO of some cations in melts. In particular, basic cations such as Ca form strong second-nearest-neighbour (SNN) pairs with acidic cations such as Si. The effects of both FNN and SNN are described by the Modified Quasichemical Model [7, 8]. Though, in the Al_2O_3–FeO–Fe_2O_3–MgO–NiO system, the second-nearest-neighbour pairs ordering is apparently not strong, the same model is used in view of developing of a broader database for calculations in multicomponent systems. The most significant parameter of the MQM model is the Gibbs energy of the corresponding pair exchange reaction:

$$(\text{m-m}) + (\text{n-n}) = 2(\text{m-n}); \quad \Delta g_{\text{m, n}} \tag{11.1}$$

where (m-n) represents a second-nearest-neighbour pair. Let n_m and Z_m be the number of moles and the coordination number of the component *m*, respectively. The "coordination-equivalent" fractions (Y_m) are then defined as

$$Y_m = Z_m n_m / \sum_i Z_i n_i \tag{11.2}$$

Δg_{mn} is expanded as a polynomial in the "coordination-equivalent" fractions of the components

$$\Delta g_{mn} = \Delta g^{\circ}_{mn} + \sum_{(i+j)\geq 1} q^{ij}_{mn} Y^i_m Y^j_n \tag{11.3}$$

where Δg^{o}_{mn} and q^{ij}_{mn} are empirical binary coefficients which may be functions of temperature and pressure. They are optimized to take into account available thermodynamic and phase equilibrium data.

The binary parameters are then extrapolated into ternary systems. The properties of the FeO–MgO–NiO and Al_2O_3–Fe_2O_3–NiO slags were calculated using the symmetric "Kohler-like" model [28]. The properties of the Al_2O_3–FeO–NiO, Al_2O_3–MgO–NiO and Fe_2O_3–MgO–NiO ternary slags were calculated from the corresponding binary parameters by means of the asymmetric "Toop-like" approximation [28], since one component (either Al_2O_3 or Fe_2O_3) in these systems is chemically different from others. For the Al_2O_3–FeO–NiO system, furthermore, an additional ternary model parameter was introduced to better describe available phase diagram data.

The optimization of the Al_2O_3-FeO-Fe_2O_3, FeO-Fe_2O_3-NiO and FeO-Fe_2O_3-MgO ternary slags is described in Sections 8.4.3 and 10.4.3 of the thesis and in the study [42], respectively.

The extension of ternary terms to multicomponent systems is described in [28].

11.2.2 Spinel, monoxide, corundum

The models for these solutions were described in detail earlier in the thesis. The properties of the Al_2O_3–MgO–NiO and Fe_2O_3–MgO–NiO monoxide solutions, as in the case of the slag solutions, were extrapolated from the binary parameters by means of the asymmetric "Toop-like" approximation [28], with Al_2O_3 or Fe_2O_3 as asymmetric components. For the remaining ternary monoxides, FeO–MgO–NiO, Al_2O_3–Fe_2O_3–NiO and Al_2O_3–FeO–NiO, the symmetric "Kohler-like" model [28] was employed.

The optimization of the Al_2O_3-FeO-Fe_2O_3, FeO-Fe_2O_3-NiO and FeO-Fe_2O_3-MgO ternary monoxide solutions is described in Sections 8.4.2 and 10.4.2 and in the study [42], respectively.

The properties of the Al_2O_3–FeO–NiO and Al_2O_3–Fe_2O_3–NiO corundum solutions were calculated from the corresponding binary parameters using the symmetric "Kohler-like" model [28].

The extension of ternary terms to multicomponent systems is described in [28].

11.2.3 Other solutions and stoichiometric compounds

Metallic solutions and stoichiometric compounds were optimized previously as part of the following systems: Al–Ni – by Ansara et al. [194], Fe–Ni – by Dinsdale and Chart [255], and Al–Fe – as part

of the FSstel FactSage database of FactSage software [1]. The $FeAlO_3$ compound was optimized, as described in Section 8.4.4.

11.3 Literature review of experimental data

11.3.1 Al–Fe–Ni–O system

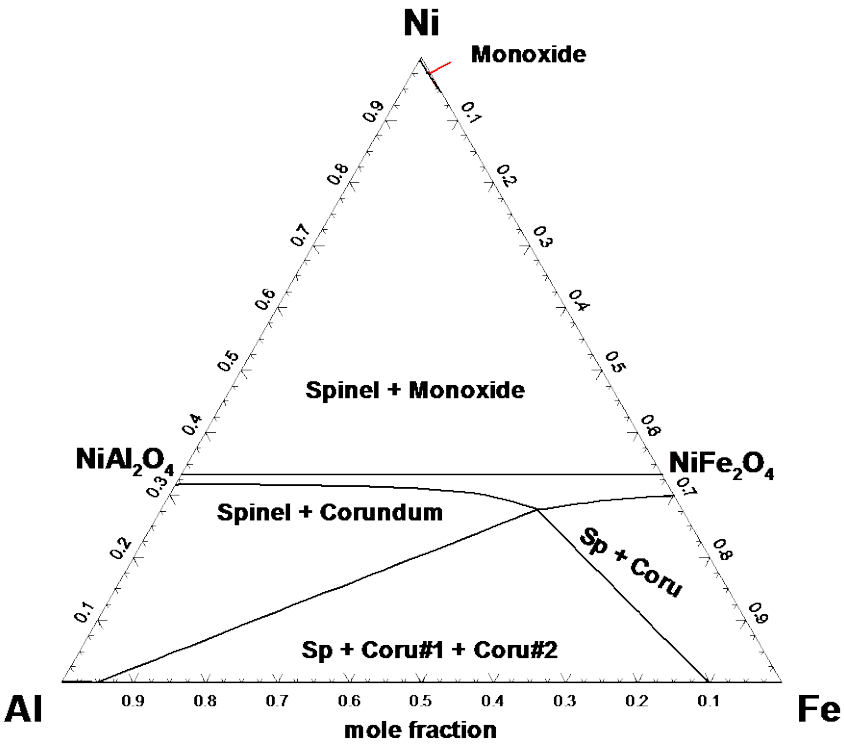

Figure 11.1: Ternary Al–Fe–Ni–O section in air at 1000 °C. See notations in Table 11.1

The projection of phase equilibria in the Al–Fe–Ni–O system in air at 1000 °C onto the Al–Fe–Ni plane through the oxygen corner is shown in Figure 11.1. The main solid solution phases are spinel, which is a continuous solid solution between the $NiAl_2O_4$ and $NiFe_2O_4$ spinel end-members, corundum, and monoxide.

11.3.1.1 Cation distribution in spinel

The cation distribution in the nickel aluminate-ferrite solution $NiAl_xFe_{2-x}O_4$ is well studied [198, 212, 219, 236, 265, 308-311]. The distribution of nickel, iron and aluminium between the tetrahedral and octahedral sites of the spinel structure is shown in Figure 11.2-Figure 11.4. The spinel solution series was studied by: Greenwald et al. [198] at 1400 °C by employing X-ray diffraction, Niziol [309] – using neutron diffraction and magnetic measurement, Chebotaev et al. [310] at 1250 °C – by

X-ray diffraction, Bara et al. [219] – by neutron diffraction and Mössbauer spectroscopy, Kulshreshtha [311] – using Mössbauer spectroscopy, Yao et al. [212] at 1400 °C – by means of EXAFS analysis, Fayek [265] at 1000-1200 °C – using X-ray diffraction and Mössbauer spectroscopy and Lilova et al. [236] at 800 °C – using X-ray absorption near edge structure (XANES) measurements and Mössbauer spectroscopy. Most of these studies are in agreement, as shown in Figure 11.2-Figure 11.4. The results show that the ratio of tetrahedral sites occupied by Ni^{2+} ions decreases with increasing iron content. The calculated lines for octahedral and tetrahedral sublattices correspond to 1000 °C. The calculations made at 1300 °C give almost the same results as for 1000 °C and, therefore, are not shown in the figures for better visibility. The results of Fayek [265] are also not shown in the figures since they are way out from other results and obviously erroneous.

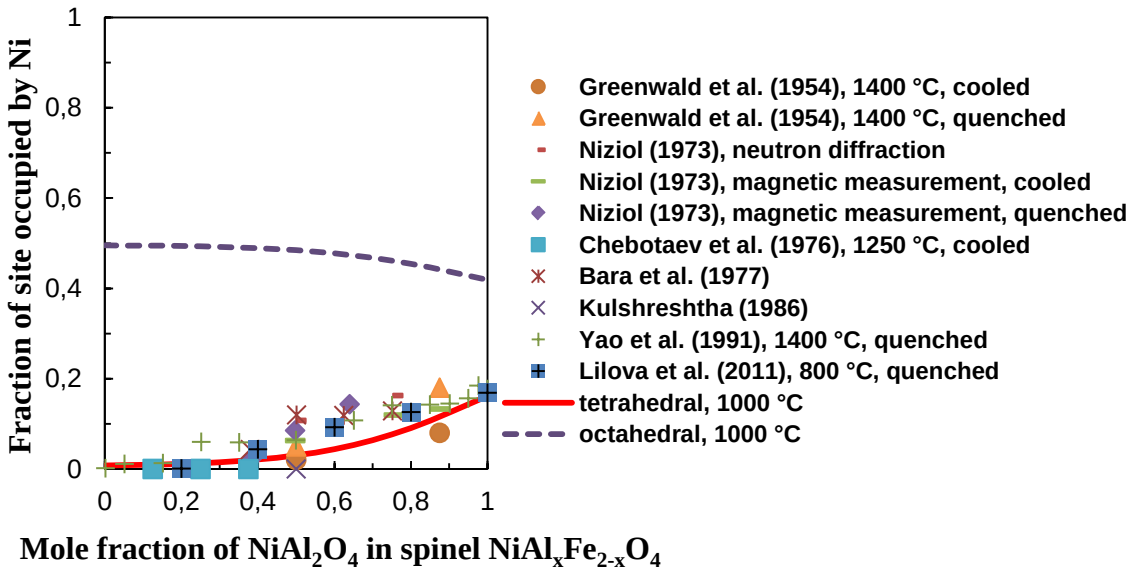

Figure 11.2: Composition dependence of Ni distribution between the tetrahedral and octahedral sublattices in the $NiAl_xFe_{2-x}O_4$ spinel: experimental data [198, 212, 219, 236, 265, 309-311] for the tetrahedral sublattice and calculated lines

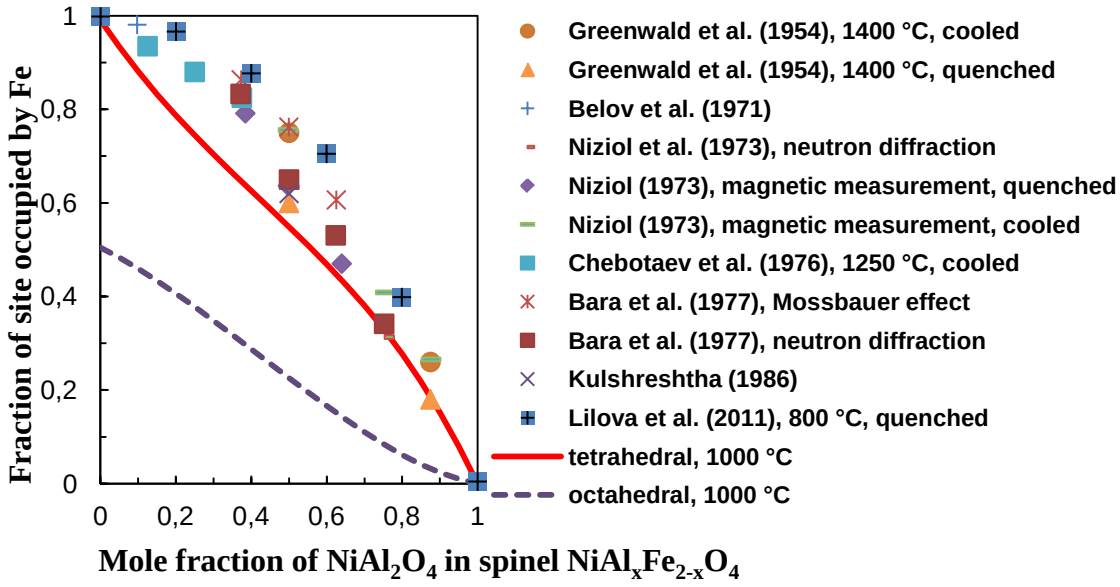

Figure 11.3: Composition dependence of Fe distribution between the tetrahedral and octahedral sublattices in the $NiAl_xFe_{2-x}O_4$ spinel: experimental data [198, 212, 219, 236, 265, 308-311] for the tetrahedral sublattice and calculated lines

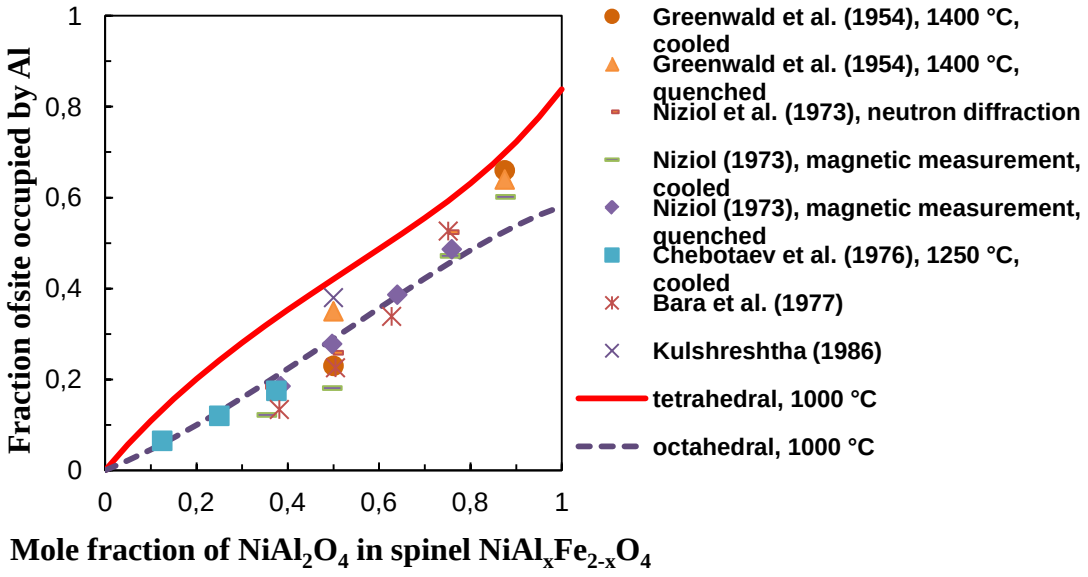

Figure 11.4: Composition dependence of Al distribution between the tetrahedral and octahedral sublattices in the $NiAl_xFe_{2-x}O_4$ spinel: experimental data [198, 212, 219, 265, 309-311] for the tetrahedral sublattice and calculated lines

11.3.1.2 Enthalpy

Enthalpy of mixing for the solid solutions $Ni(Fe_xAl_{1-x})_2O_4$ was investigated by Lilova et al. [236] at 700 °C, using high temperature oxide melt solution calorimetry in molten $2PbO{\cdot}B_2O_3$. Their results are shown in Figure 11.5.

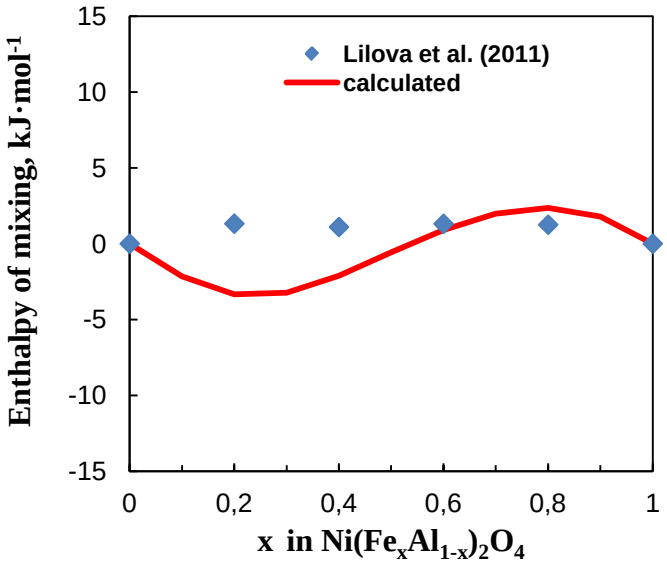

Figure 11.5: Enthalpy of mixing for the mixed nickel aluminate-ferrite spinel $Ni(Fe_xAl_{1-x})_2O_4$ at 700 °C: the experimental data of Lilova et al. [236] and a calculated line

11.3.1.3 Phase equilibria

Iron is generally present in oxide phases in two oxidation states: Fe^{2+} and Fe^{3+}, the ratio of which is dependent on oxygen partial pressure. Phase equilibria in the subsolidus region of the Al–Fe–Ni–O system were experimentally studied by Rhamdhani et al. [177] in the temperature range of 1200-1400 °C in air, using equilibration and quenching techniques followed by EPMA. Their tie-lines are projected onto the Al–Fe–Ni plane through the oxygen corner, as shown in Figure 11.6 (a-c).

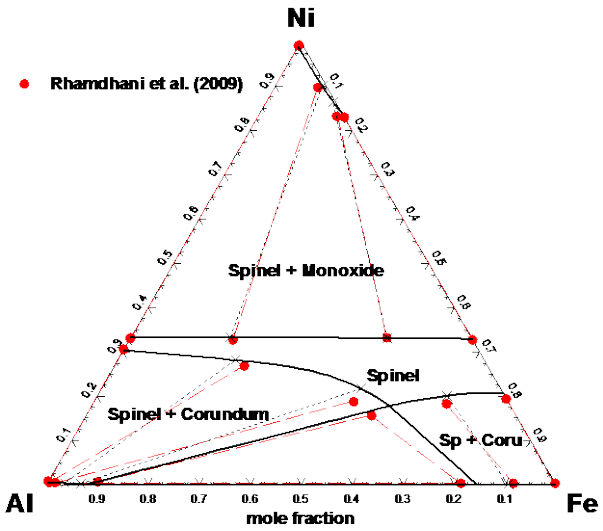

(a)

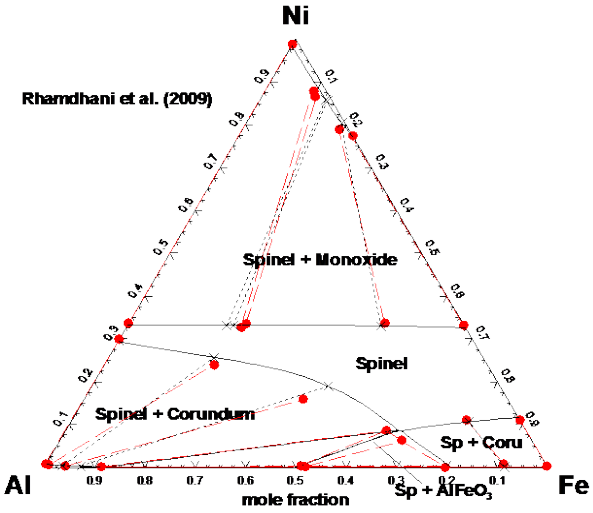

(b)

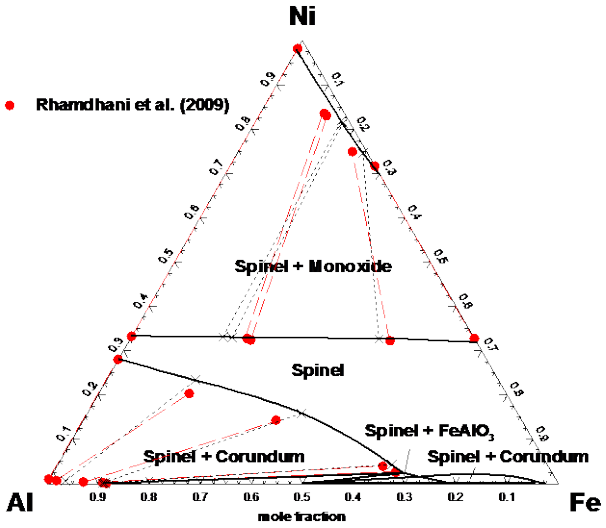

(c)

Figure 11.6: Ternary Al–Fe–Ni–O sections in air: (a) 1200 °C; (b) 1300 °C (c) 1400 °C. Solid lines are calculated phase boundaries, black short-dashed lines are calculated tie-lines, red dashed lines are tie-lines of Rhamdhani et al. [177]. See notations in Table 11.1

Phase equilibria with the metallic liquid, where oxygen pressure is low, were studied by two sets of authors [307, 312]. Jacob et al. [312] measured three-phase equilibrium between the liquid Fe–Ni alloy, spinel and corundum solutions at 1550 °C. The composition of the spinel solid solution was determined by the EPMA method. The nickel content of the alloy was determined by chemical

analysis. The corresponding oxygen pressures were measured using the EMF method. Their data are demonstrated in Figure 11.7 and Figure 11.8.

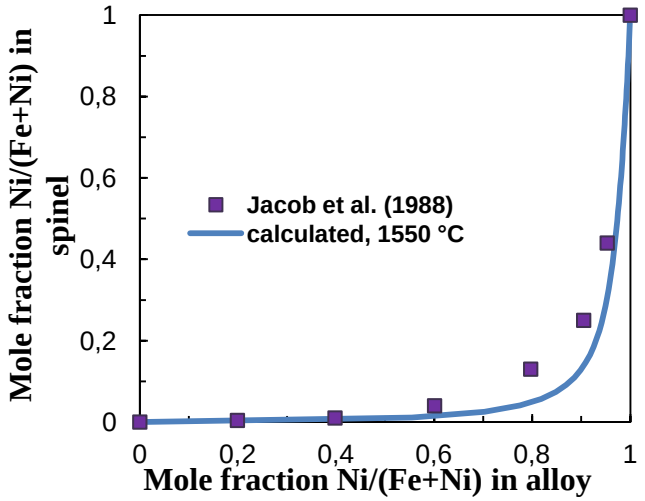

Figure 11.7: Distribution of Ni between alloy and spinel phases in the three-phase equilibrium between the liquid alloy, spinel and corundum solutions at 1550 °C: the literature data of Jacob et al. [312] and the calculated line

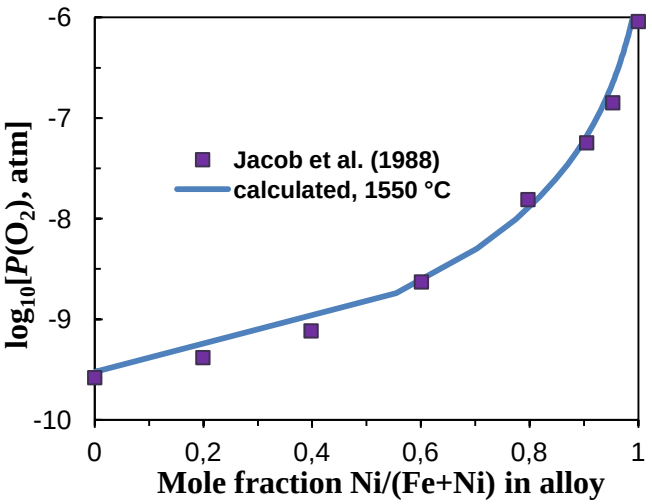

Figure 11.8: Oxygen partial pressure for the three-phase equilibrium between the liquid alloy, spinel and corundum solutions at 1550 °C: the literature data of Jacob et al. [312] and the calculated line

Equilibria between the slag phase and liquid metal at spinel saturation were established by Schenck et al. [307] in the temperature range 1560-1640 °C by equilibration and quenching techniques. The oxygen content in metal was determined by means of the vacuum hot extraction, the iron content – photometrically. The Al, Fe and Ni contents of the slag were determined by X-ray fluorescence

analysis, the Fe^{3+} content – by titration. The data of Schenck et al. [307] are shown in Figure 11.9(a-c) and Figure 11.10.

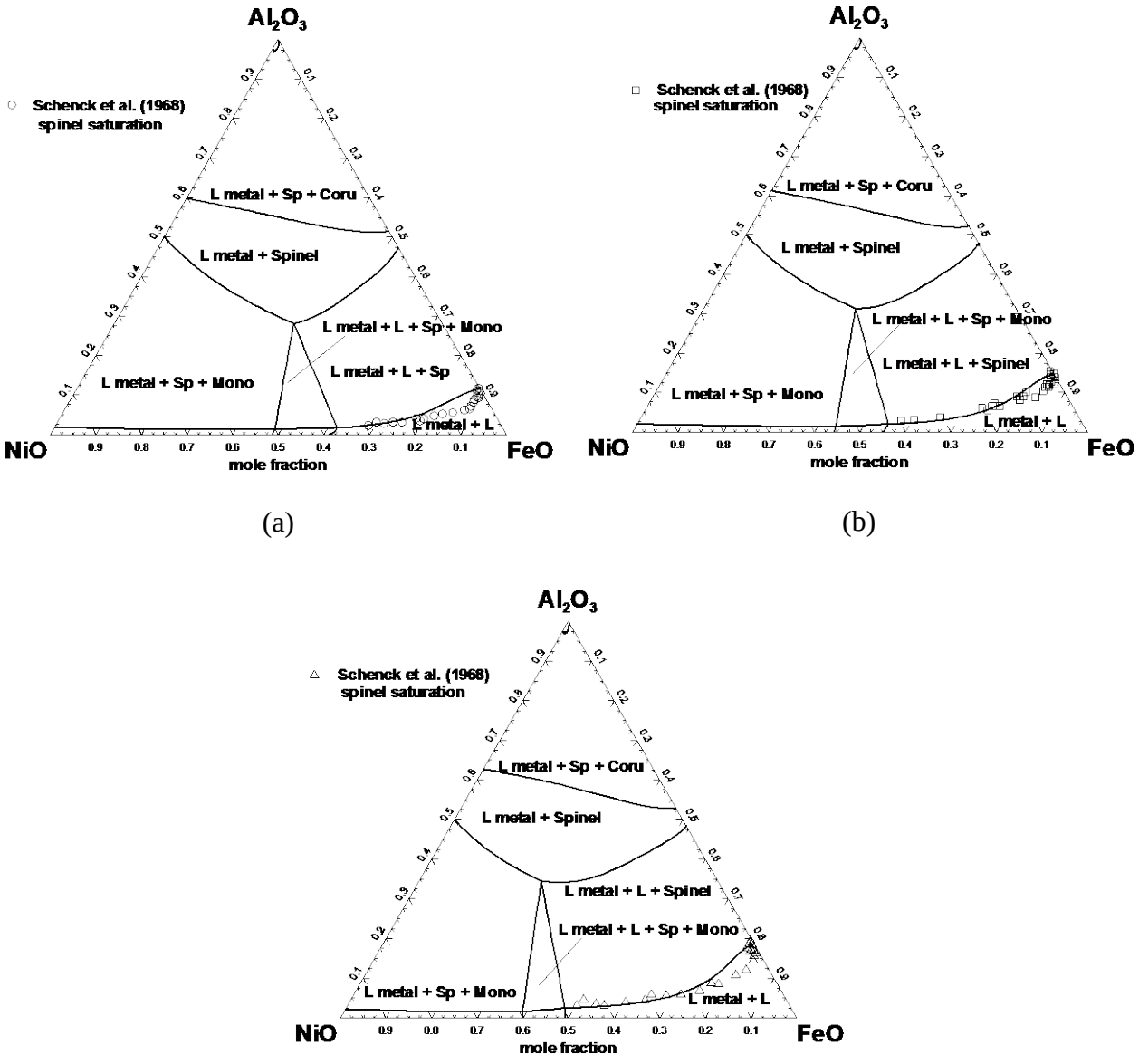

Figure 11.9: Ternary Al–Fe–Ni–O sections at metallic saturation along with the literature data of Schenck et al. [307]: (a) 1560 °C; (b) 1600 °C (c) 1640 °C. See notations in Table 11.1

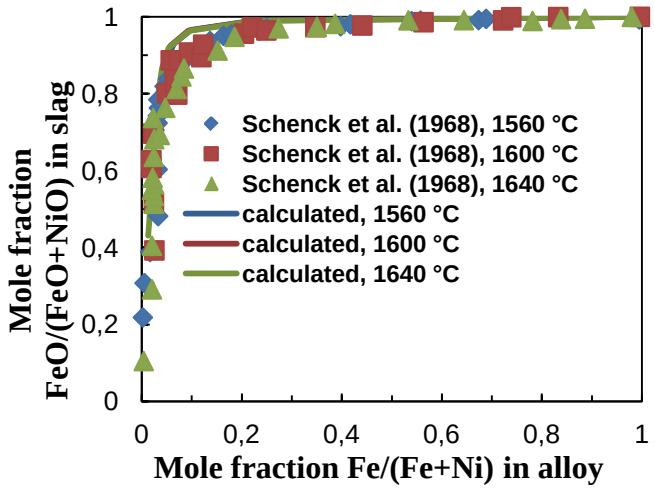

Figure 11.10: Distribution of Fe between the slag and alloy phases in equilibrium with spinel in the temperature range 1560-1640 °C: the literature data of Schenck et al. [307] and calculated lines

11.3.2 Al–Mg–Ni–O system

Magnesium aluminate, $MgAl_2O_4$, exhibits complete solid solubility in nickel aluminate, $NiAl_2O_4$, at high temperatures [204], as shown in Figure 11.11.

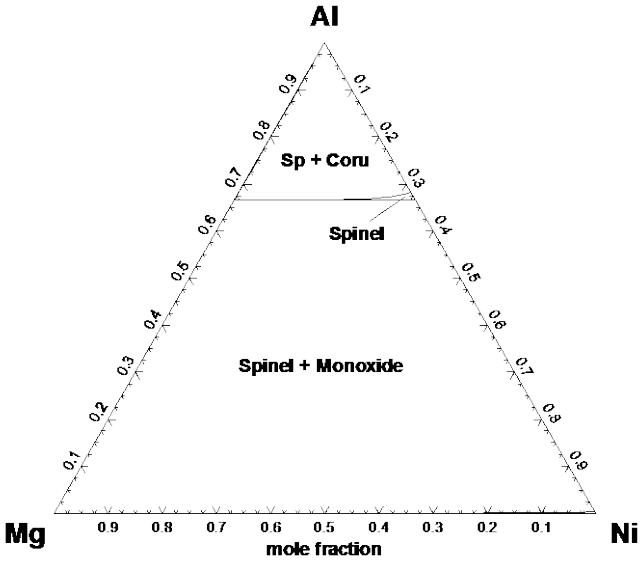

Figure 11.11: Ternary Al–Mg–Ni–O section in air at 1000 °C. See notations in Table 11.1

11.3.2.1 Cation distribution in spinel

The distribution of Ni between the tetrahedral and octahedral sites in the solid $Ni_xMg_{1-x}Al_2O_4$ solutions was studied by Porta et al. [204] and Pepe et al. [205] at 1000 and 1400 °C for quenched

samples by means of the X-ray analysis, magnetic susceptibility and reflectance spectroscopy. Their results, shown in Figure 11.12, demonstrate that in solid solutions nickel ions have a preference for octahedral sublattice and that there is a small change towards a random distribution with increasing temperature. There were no reports on the cation distribution of Mg or Al in nickel magnesium aluminate solutions in the literature. The calculated composition dependence of Al and Mg distribution over the tetrahedral and octahedral sites in the nickel magnesium aluminate spinel solution $Ni_xMg_{1-x}Al_2O_4$ is shown in Figure 11.13 and Figure 11.14.

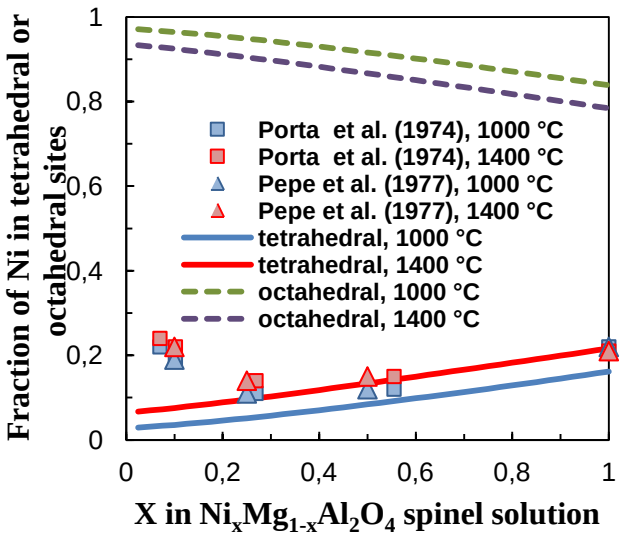

Figure 11.12: Composition dependence of Ni distribution between the tetrahedral and octahedral sublattices in the nickel magnesium aluminate $Ni_xMg_{1-x}Al_2O_4$ spinel solution: literature data [204, 205] for the tetrahedral site and calculated lines

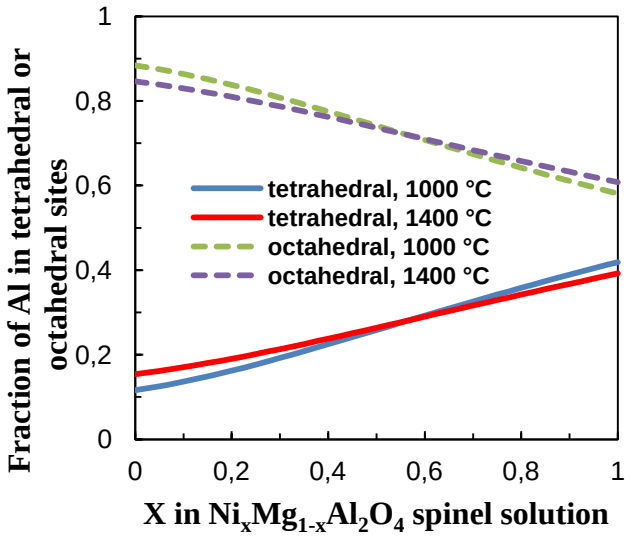

Figure 11.13: Calculated composition dependence of Al distribution between the tetrahedral and octahedral sublattices in the nickel magnesium aluminate $Ni_xMg_{1-x}Al_2O_4$ spinel solution

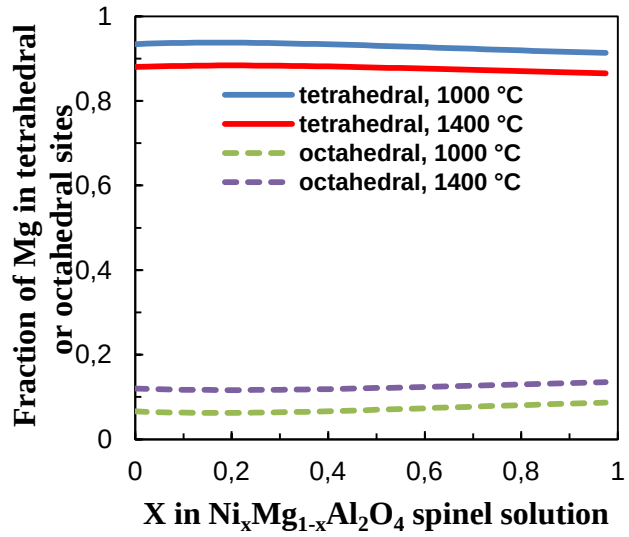

Figure 11.14: Calculated composition dependence of Mg distribution between the tetrahedral and octahedral sublattices in the nickel magnesium aluminate $Ni_xMg_{1-x}Al_2O_4$ spinel solution

11.3.2.2 Phase equilibria

The partial pressures of oxygen for the Ni-alloy-spinel-corundum assemblage were studied using the EMF method by Jacob and Alcock [206] in the temperature range 750-1150 °C and by Kozlowska-Rog and Rog [313] – in the temperature range 1000-1200 °C. In both studies, CaO-stabilized zirconia was used as a solid electrolyte. The results of these studies are shown in Figure 11.15.

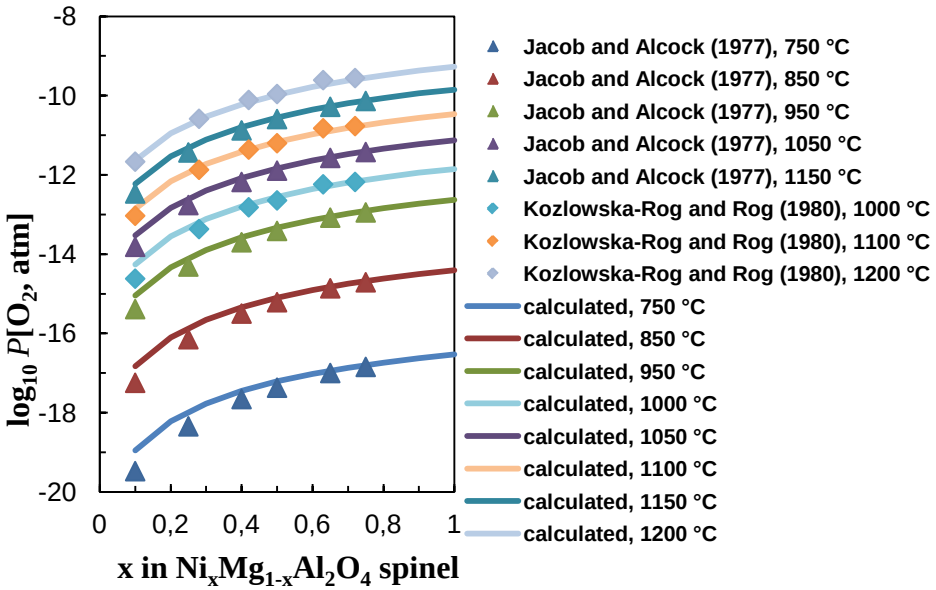

Figure 11.15: Partial pressures of oxygen for the Ni-alloy-spinel-corundum equilibrium in the temperature range 750-1200 °C: experimental data [206, 313] and calculated lines

11.3.3 Mg–Fe–Ni–O system

11.3.3.1 Cation distribution in spinel

The cation distribution in the $Ni_xMg_{1-x}Fe_2O_4$ spinel solutions is well studied [40, 262, 266, 314-319]. The distribution of nickel, iron and magnesium between the tetrahedral and octahedral sites of the spinel structure is shown in Figure 11.16-Figure 11.18. It was studied by: Sheshan et al. [319] at 1300 °C using magnetic measurements, Seshan et al. [314] at 1300 °C – by means of magnetization measurements, Seshan et al. [315] at 1302 °C – by ferromagnetic resonance measurements, Seshan et al. [262] at 1302 °C – by Mössbauer spectroscopy, Amer and El Hiti [320] – using X-ray diffraction and Mössbauer spectroscopy, Pattrick et al. [266] at 1100 °C – by X-ray magnetic circular dichroism, Mittal et al. [317] at 1200 °C – by X-ray photoelectron spectroscopy (XPS), Mittal et al. [318] at 1000 °C – by XPS and Mössbauer spectroscopy, and Henderson et al. [40] at 1250 °C – by K-edge x-ray absorption spectroscopy (EXAFS). The samples in all the studies were either cooled or quenched, which is pointed out in Figure 11.16-Figure 11.18; otherwise, no information was given by the authors. The results showed the incomplete inversion for all the compositions of the spinel solution and demonstrated the affinity of Ni and Mg for the octahedral sites. They are in fair agreement.

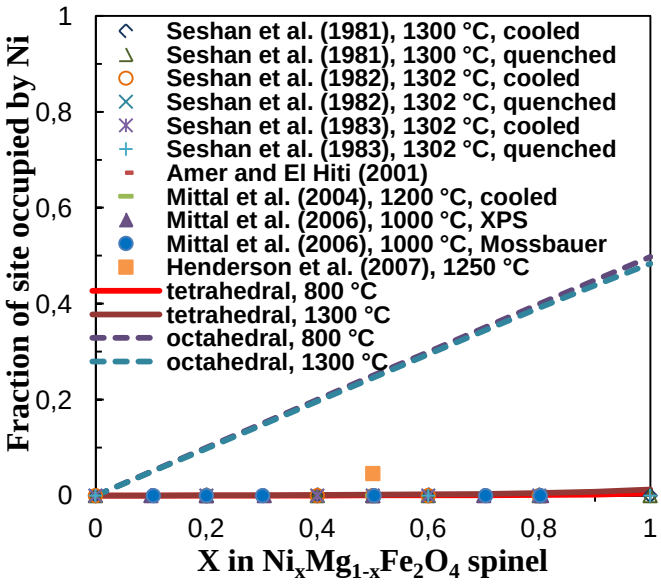

Figure 11.16: Composition dependence of Ni distribution between the tetrahedral and octahedral sublattices in the nickel-magnesium ferrite $Ni_xMg_{1-x}Fe_2O_4$ spinel solution: experimental data [40, 262, 314-318] for the tetrahedral sublattice and calculated lines

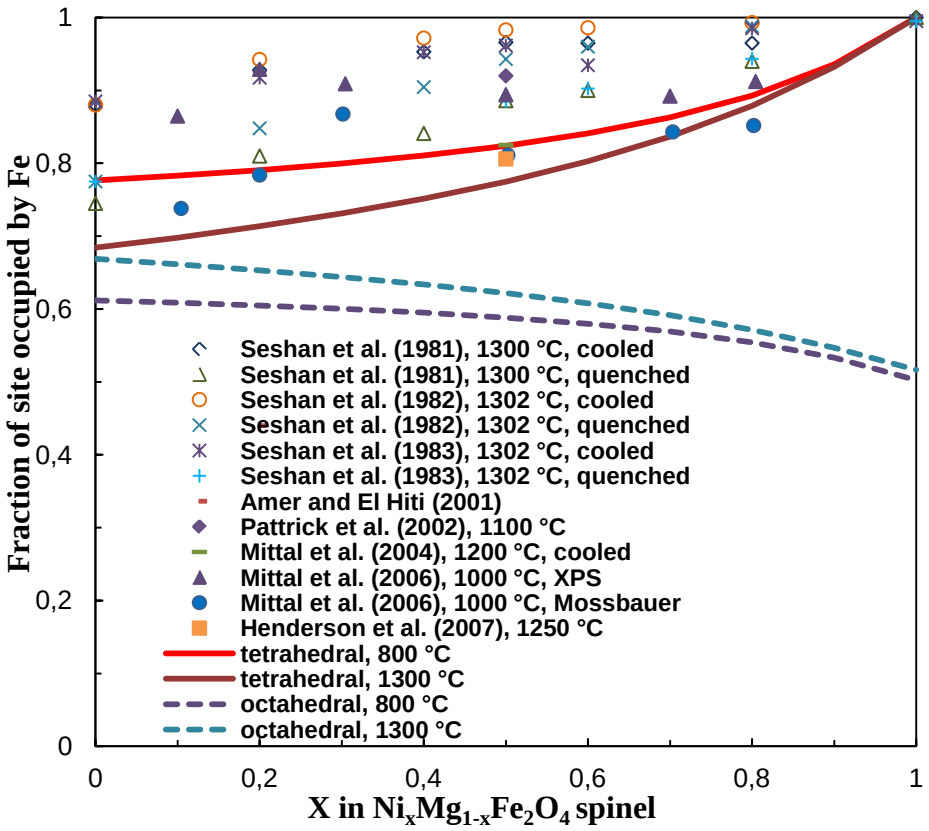

Figure 11.17: Composition dependence of Fe distribution between the tetrahedral and octahedral sublattices in the nickel-magnesium ferrite $Ni_xMg_{1-x}Fe_2O_4$ spinel solution: experimental data [40, 262, 266, 314-318] for the tetrahedral sublattice and calculated lines

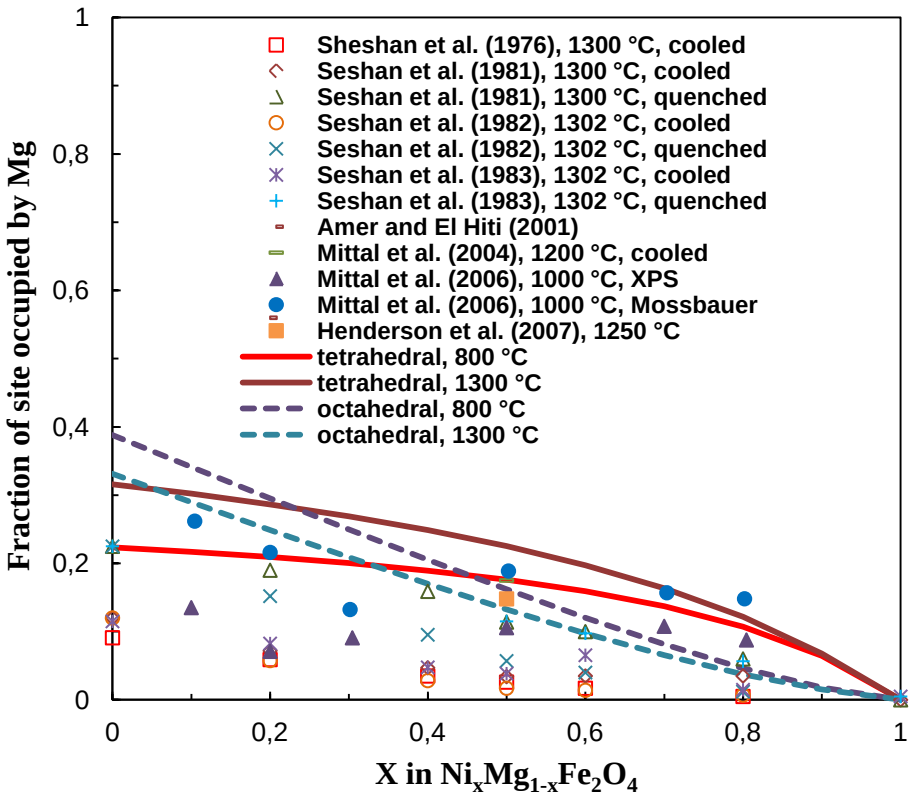

Figure 11.18: Composition dependence of Mg distribution between the tetrahedral and octahedral sublattices in the nickel-magnesium ferrite $Ni_xMg_{1-x}Fe_2O_4$ spinel solution: experimental data [40, 262, 314-319] for the tetrahedral sublattice and calculated lines

11.3.3.2 Phase equilibria

Phase equilibria between the spinel and monoxide solutions in air were studied by: Bashkirov and Bashkirova [321] in the temperature range 1040-1280 °C by quenching and X-ray analysis, Trinel-Dufour et al. [322] – at 1000 °C by measurement of cristalline parameters, Rhamdhani et al. [177] – in the temperature range 1200-1600 °C, using equilibration and quenching techniques followed by electron-probe X-ray microanalysis. Their data are shown in Figure 11.19. Bashkirov and Bashkirova [321] measured zero iron content in monoxide, this can explain discrepancy between their data and the recent results of Rhamdhani et al. [177].

In Figure 11.20, the data of Rhamdhani et al. [177] are projected onto the Fe–Mg–Ni plane.

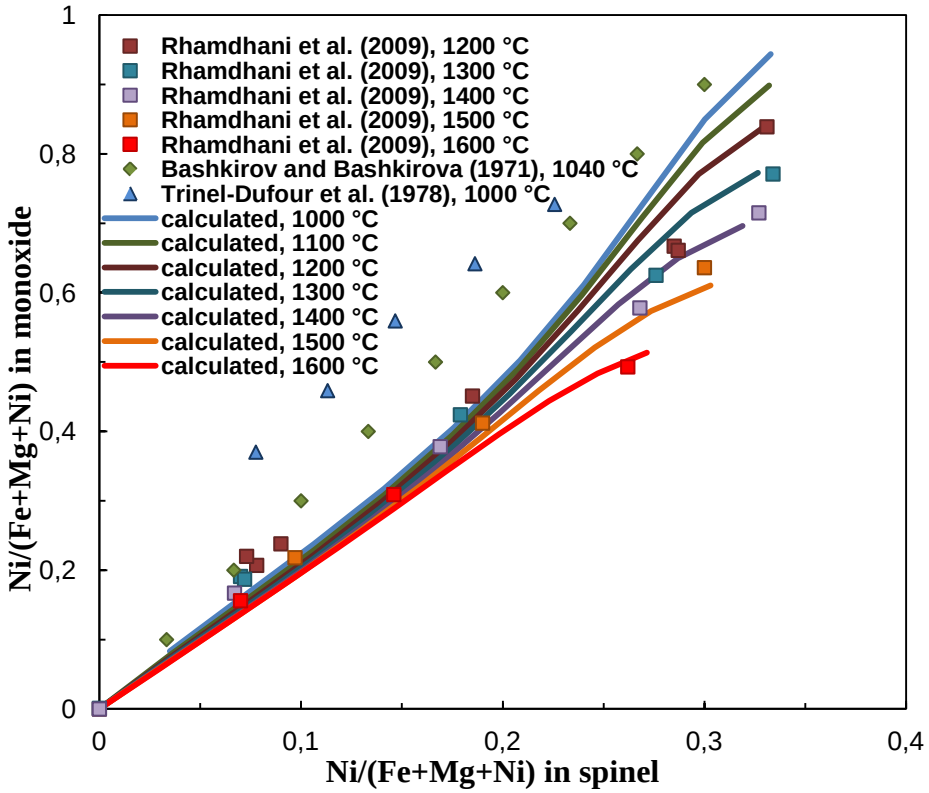

Figure 11.19: Distribution of nickel between spinel and monoxide solutions in air in the temperature range 1000-1600 °C: literature data [177, 321, 322] and calculated lines

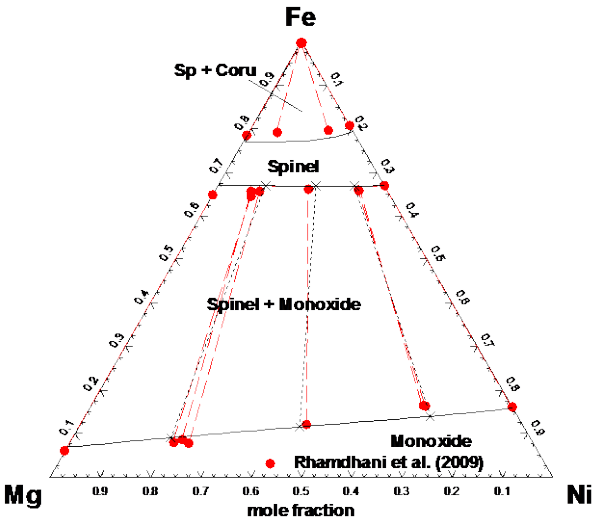
Fe
Sp + Coru
Spinel
Spinel + Monoxide
Monoxide
Rhamdhani et al. (2009)
Mg
Ni
mole fraction

(a)

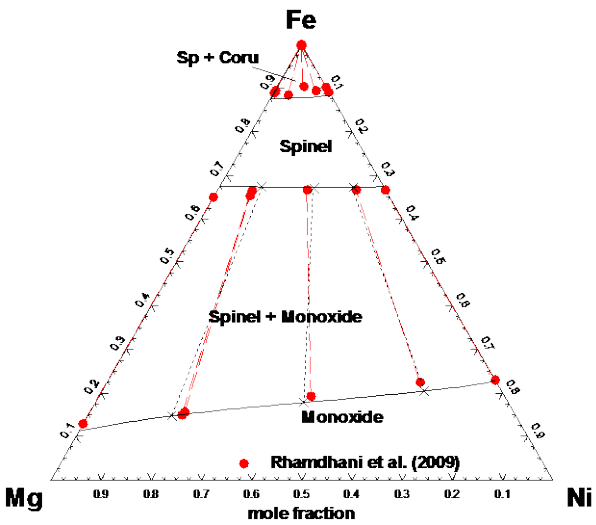
Fe
Sp + Coru
Spinel
Spinel + Monoxide
Monoxide
Rhamdhani et al. (2009)
Mg
Ni
mole fraction

(b)

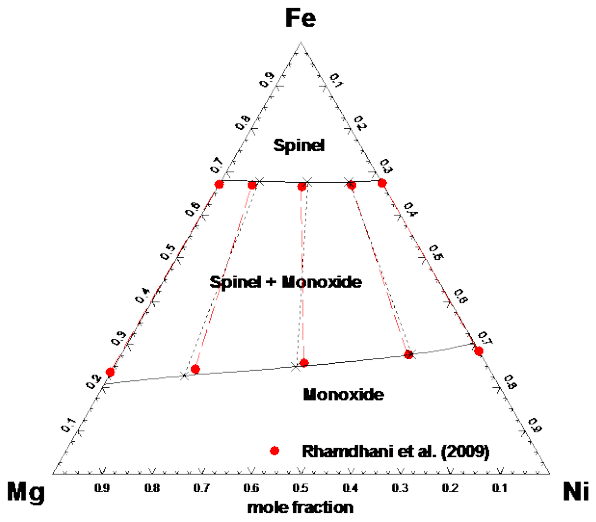
Fe
Spinel
Spinel + Monoxide
Monoxide
Rhamdhani et al. (2009)
Mg
Ni
mole fraction

(c)

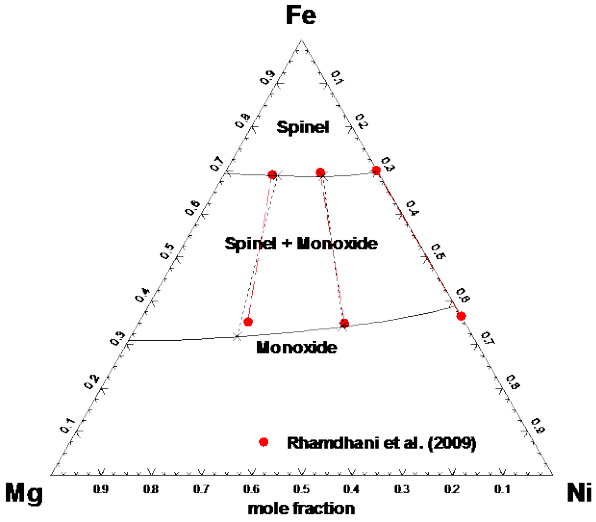
Fe
Spinel
Spinel + Monoxide
Monoxide
Rhamdhani et al. (2009)
Mg
Ni
mole fraction

(d)

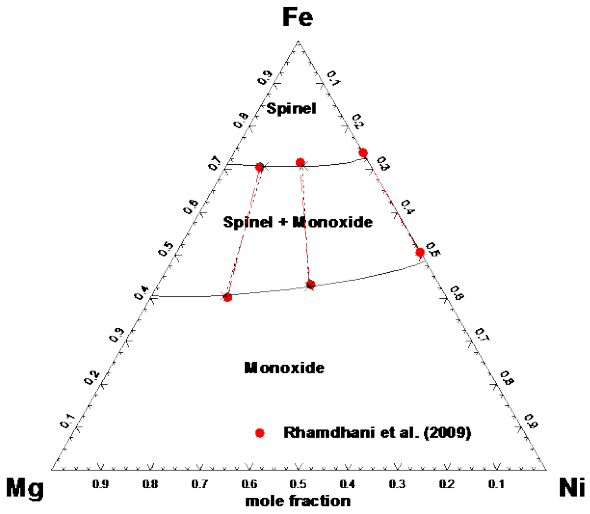

(e)

Figure 11.20: Ternary Fe–Mg–Ni–O sections in air: (a) 1200 °C; (b) 1300 °C; (c) 1400 °C; (d) 1500 °C; (e) 1600 °C. Solid lines are calculated phase boundaries, black short-dashed lines are calculated tie-lines, red dashed lines are tie-lines of Rhamdhani et al. [177]. See notations in Table 11.1

11.4 Optimization

The only parameter optimized was that of the Modified Quasichemical Model, to describe the phase equilibria data of Schenck et al. [307] for the Al–Fe–Ni–O system (see Table 11.2), shown in Figure 11.9.

The agreement between the calculated and experimental results is believed to be within experimental error limits.

11.5 Summary of results

The thermodynamic database, combined from the earlier obtained Fe–Ni–O, Al–Ni–O, and Mg–Ni–O databases, proved to be capable of predicting thermodynamic properties and phase equilibria in the Al–Fe–Ni–O, Al–Mg–Ni–O and Fe–Mg–Ni–O chemical systems. The available experimental data are in good agreement with model predictions. The only optimized model parameter for the liquid phase reproduces available liquidus data for the Al–Fe–Ni–O system within experimental error limits.

Table 11.2 : Optimized model parameters for the liquid phase in the Al–Fe–Ni–O system ($J \cdot mol^{-1}$)

Slag (liquid oxide phase): $AlO_{1.5}$–FeO–$FeO_{1.5}$–MgO–NiO

$q^{001}_{Fe^{+2},Al(Ni)} = 83680;$

FeO-$FeO_{1.5}$ liquid oxide was optimized by Decterov et al. [41];

MgO-NiO liquid oxide was optimized by Prostakova et al. [51]; the optimization of the $AlO_{1.5}$-FeO-$FeO_{1.5}$, $AlO_{1.5}$-NiO, FeO-$FeO_{1.5}$-NiO slags is described in Sections 8.4.3, 9.5.3, and 10.4.3, respectively;

$AlO_{1.5}$-MgO and FeO-$FeO_{1.5}$-MgO liquid oxide was optimized by Jung et al. [42, 43];

The properties of the FeO–MgO–NiO and $AlO_{1.5}$–$FeO_{1.5}$–NiO slags were calculated from the corresponding binary parameters using the symmetric "Kohler-like" model [28]. The properties of the $AlO_{1.5}$–FeO–NiO, $AlO_{1.5}$–MgO–NiO and $FeO_{1.5}$–MgO–NiO ternary slags were calculated by means of the asymmetric "Toop-like" approximation [28], with one component (either $AlO_{1.5}$ or $FeO_{1.5}$) as asymmetric. The extension of ternary terms to multicomponent systems is described in [28].

Monoxide (solid oxide): FeO–MgO–NiO–($FeO_{1.5}$–$AlO_{1.5}$)

FeO-$FeO_{1.5}$ monoxide oxide was optimized by Decterov et al. [41];

MgO-NiO monoxide was optimized by Prostakova et al. [51]; the optimization of the $AlO_{1.5}$-FeO-$FeO_{1.5}$, $AlO_{1.5}$-NiO, and FeO-$FeO_{1.5}$-NiO monoxide solutions is described in Sections 8.4.2, 9.5.2, and 10.4.2, respectively;

$AlO_{1.5}$-MgO and FeO-$FeO_{1.5}$-MgO monoxide was optimized by Jung et al. [42, 43];

The properties of the $AlO_{1.5}$–MgO–NiO and $FeO_{1.5}$–MgO–NiO monoxide solutions were extrapolated from the binary parameters by means of the asymmetric "Toop-like" approximation [28], with $AlO_{1.5}$ or $FeO_{1.5}$ as asymmetric components. For the remaining ternary monoxides, the symmetric "Kohler-like" model [28] was employed. The extension of ternary terms to multicomponent systems is described in [28].

Corundum: $AlO_{1.5}$–$FeO_{1.5}$– (NiO)

The optimization of the $AlO_{1.5}$-$FeO_{1.5}$, $AlO_{1.5}$-NiO, and $FeO_{1.5}$-NiO corundum solutions is described in Sections 8.4.2, 9.5.2, and 10.4.2, respectively.

The properties of the $AlO_{1.5}$–FeO–NiO and $AlO_{1.5}$–$FeO_{1.5}$–NiO corundum solutions were calculated from the corresponding binary parameters using the symmetric "Kohler-like" model [28].

Spinel: $(Al^{3+}, Fe^{2+}, Fe^{3+}, Mg^{2+}, Ni^{2+})^{T}(Al^{3+},Fe^{2+}, Fe^{3+}, Mg^{2+},Ni^{2+},Va)_2{}^{O}O_4$

$M_{Ni^{+2}:Fe^{+3}Al^{+3}} = 38492.8;\ M_{Fe^{+3}:Al^{+3}Ni^{2+}} = M_{Fe^{+2}:Al^{+3}Ni^{2+}} = -46793.9 + 33.4720 \cdot T;$

All parameters for the Fe_3O_4 spinel, including magnetic properties, were optimized by Decterov et al. [41];

Al-Mg and Fe-Mg spinel was optimized by Jung et al. [42, 43];

The optimization of the Al-Fe, Al-Ni and Fe-Ni spinels is described in Sections 8.4.1, 9.5.1, and 10.4.1, respectively.

CHAPTER 12 THERMODYNAMIC OPTIMIZATION OF THE Al–Ni–O–Si AND Fe–Ni–O–Si SYSTEMS

Equation Chapter (Next) Section 1This chapter deals with the optimization of thermodynamic and phase equilibrium data for the Al–Ni–O–Si and Fe–Ni–O–Si chemical systems over a wide range of conditions. A literature review for these chemical systems was performed. The literature review and critical analysis of data was followed by thermodynamic modeling of oxide phases. The Modified Quasichemical Model (MQM) was used for modeling of the slag phase (liquid oxide phase), the model based on the Compound Energy Formalism – for the olivine and spinel solid solutions. The monoxide and corundum solutions were described using a simple Bragg-Williams model. The parameters of the MQM model and the CEF model for olivine were optimized using available literature data for the slag and olivine phases. Optimized model equations for the thermodynamic properties of all phases reproduce all available thermodynamic and phase-equilibrium data within experimental error limits.

12.1 Background

This part of the study is aimed to optimize the Al–Ni–O–Si and Fe–Ni–O–Si systems. In order to achieve that, initially, all available literature data were reviewed and analyzed.

Ramirez et al. [323] optimized the Fe–Ni–O–Si system using the structural model for the liquid phase developed by Lin and Pelton [324], which accounts for two- and three-dimensional silicate network structure.

12.2 Phases and thermodynamic models

A list of optimized oxide phases in the Al–Ni–O–Si and Fe–Ni–O–Si systems along with notations used in this study is given in Table 12.1.

Metallic solutions were optimized previously: Al–Ni – by Ansara et al. [194], Fe–Ni – by Dinsdale and Chart [255], Al–Si – by Grobner et al. [325], and Fe–Si – by Lacaze and Sundman [326] and Al–Ni–Si and Fe–Ni–Si – as part of the FSstel FactSage database of FactSage software [1]. Properties of the Al–Ni–O–Si and Fe–Ni–O–Si liquids as well as Fe–Ni olivine were optimized using available literature data for the slag and olivine phases. Properties of the rest of

solutions were predicted from the previously optimized model parameters of the corresponding binary and ternary solutions: Ni–O–Si – by Prostakova et al. [51], Fe–O–Si – by Hidayat et al. [327], Al–O–Si – within FToxide FactSage database [1]. For the optimizations of the Al–Ni–O and Fe–Ni–O systems – see CHAPTER 9 and CHAPTER 10. For the spinel solution model, cations shown within a set of parentheses occupy the same sublattice.

Table 12.1: Oxide solution phases and stoichiometric compounds in the Al–Ni–O–Si and Fe–Ni–O–Si systems

Phase name	**Formula**	**Notation used in this study**
Solutions :		
Slag (liquid oxide)	$AlO_{1.5}$–FeO–$FeO_{1.5}$–NiO–SiO_2	L or Liquid
Monoxide	FeO–NiO–($FeO_{1.5}$–$AlO_{1.5}$)	Mono or Monoxide
Corundum	$AlO_{1.5}$–$FeO_{1.5}$–(NiO)	Coru or Corundum
Olivine	$(Fe^{2+}, Ni^{2+})^{M2}(Fe^{2+}, Ni^{2+})^{M1}SiO_4$	Olivine
Spinel	$(Al^{3+}, Fe^{2+}, Fe^{3+}, Ni^{2+})^{T}(Al^{3+}, Fe^{2+}, Fe^{3+}, Ni^{2+}, Va)_2{}^{O}O_4{}^{*}$	Sp or Spinel
Mullite	$(Al^{3+})_2(Al^{3+}, Si)(O, Va)_5$	Mullite
Stoichiometric compounds:		
SiO_2 (Quartz, tridymite, cristobalite)	SiO_2	Quartz, trid, crist
$Al_2Si_2O_7$	$Al_2Si_2O_7$	

*T=tetrahedral sublattice, O=octahedral sublattice

12.2.1 Slag (liquid oxide)

The liquid oxide phase is an ionic melt where metal cations are always surrounded by oxygen anions. In other words, they exhibit almost full first-nearest-neighbour (FNN) short-range ordering (SRO). Furthermore, there is a strong tendency for SRO of some cations in melts. In particular, basic cations such as Ca form strong second-nearest-neighbour (SNN) pairs with acidic cations such as Si. The effects of both FNN and SNN are described by the Modified Quasichemical Model [7, 8]. The most significant parameter of the MQM model is the Gibbs energy of the corresponding pair exchange reaction:

$$(\text{m-m}) + (\text{n-n}) = 2(\text{m-n}); \quad \Delta g_{\text{m, n}} \tag{12.1},$$

where (m-n) represents a second-nearest-neighbour pair. Let n_m and Z_m be the number of moles and the coordination number of the component m, respectively. The "coordination-equivalent" fractions (Y_m) are then defined as

$$Y_m = Z_m n_m / \sum_i Z_i n_i \tag{12.2}$$

Δg_{mn} is expanded as a polynomial in the "coordination-equivalent" fractions of the components

$$\Delta g_{mn} = \Delta g^{o}_{mn} + \sum_{(i+j)\geq 1} q^{ij}_{mn} Y^i_m Y^j_n \tag{12.3},$$

where Δg^{o}_{mn} and q^{ij}_{mn} are empirical binary coefficients which may be functions of temperature and pressure. They are optimized to take into account available thermodynamic and phase equilibrium data.

The binary parameters are then extrapolated into ternary systems. The properties of the Al_2O_3–NiO–SiO_2, Fe_2O_3–NiO–SiO_2 and FeO–NiO–SiO_2 slags were calculated from the corresponding binary parameters using the asymmetric "Toop-like" model [28], with silica as the asymmetric component. Furthermore, small additional ternary model parameters for the Al_2O_3–NiO–SiO_2 and FeO–NiO–SiO_2 slags were introduced to better describe available phase diagram data.

12.2.2 Spinel, Monoxide, Corundum

The models for these solutions were described in detail earlier in the thesis.

12.2.3 Olivine

The model for Fe-Ni olivine was developed within the framework of the Compound Energy Formalism.

In natural olivines, $\mathbf{M}_2SiO_4$, Fe is a major element, while Ni is a minor component. Cations **M** occupy two distinct octahedral sites, called M1 and M2, where M2 sites are larger than M1. Fe^{2+} and Ni^{2+} cations can occupy both M2 and M1 sites (sublattices) in the olivine structure:

$$\left(Fe^{2+},\ Ni^{2+}\right)^{M2}\left(Fe^{2+},\ Ni^{2+}\right)^{M1} SiO_4 \qquad (12.4)$$

The Gibbs energy of the olivine solution is given by Equation (10.5). According to formula unit (12.4), the Fe-Ni olivine solution has four end-members, the Gibbs energies of which must be defined.

The Gibbs energies of two end-members, G_{FeFe} and G_{NiNi}, are equal to the Gibbs energies of the corresponding stoichiometric compounds, Fe_2SiO_4 and Ni_2SiO_4, which are stable in the binary systems and have the olivine structure. The remaining two end-members, $\left(Fe^{2+}\right)^{M2}\left(Ni^{2+}\right)^{M1} SiO_4$ and $\left(Ni^{2+}\right)^{M2}\left(Fe^{2+}\right)^{M1} SiO_4$, do not exist as real compounds. Two model parameters were introduced to define the Gibbs energies of these end-members. The first parameter, $K_{FeNi} = G_{NiFe} - G_{FeNi}$, represents the change in the Gibbs energy when the Fe^{2+} and Ni^{2+} cations occupying M2 and M1 sites, respectively, change places. This parameter has a major effect on the cation distribution between M2 and M1 sites in olivine. The second parameter is the Gibbs energy of the reciprocal reaction among end-members: $\Delta_{FeNi:NiFe} = G_{FeFe} + G_{NiNi} - G_{FeNi} - G_{NiFe}$. The constant values of the parameters K_{FeNi} and $\Delta_{FeNi:NiFe}$ were optimized to reproduce experimental data on olivine, including its cation distribution. Clearly, G_{FeNi} and G_{NiFe} can be expressed as linear combinations of G_{FeFe}, G_{NiNi}, K_{FeNi} and $\Delta_{FeNi:NiFe}$.

12.2.4 Mullite

Mullite was modeled as a non-stoichiometric compound $(Al^{3+})_2(Al^{3+}, Si)(O, Va)_5$ as part of the FToxide FactSage database [1].

12.2.5 Other solutions and stoichiometric compounds

Metallic solutions and stoichiometric compounds were optimized previously as part of the following systems: Al–Ni – by Ansara et al. [194], Fe–Ni – by Dinsdale and Chart [255], and Al–Fe – as part of the FSstel FactSage database of FactSage software [1]. The $FeAlO_3$ compound was optimized, as described in Section 8.4.4.

12.3 Fe–Ni–O–Si system

12.3.1 Literature review

12.3.1.1 Cation distribution in olivine

A continuous range of solid solutions exists between the Ni_2SiO_4 and Fe_2SiO_4 end-members of the olivine solution, as was first reported by Riboud and Muan [328] for the temperature range 1170-1280 °C. The cation distribution in Fe-Ni olivines was studied by several authors: Annersten et al. [329] at 1000 °C – by means of Mössbauer spectroscopy for quenched samples, Ovchinnikov et al. [330] – by Mössbauer spectroscopy for samples quenched from 800-900 °C, and Wissmann et al. [331] – by *in-situ* Mössbauer study at temperatures up to 1200 °C. A strong tendency towards ordering of Ni on M1 sites was observed in all studies. However, only Annersten et al. [329] and Ovchinnikov et al. [330] provided experimental data, which are shown in Figure 12.1.

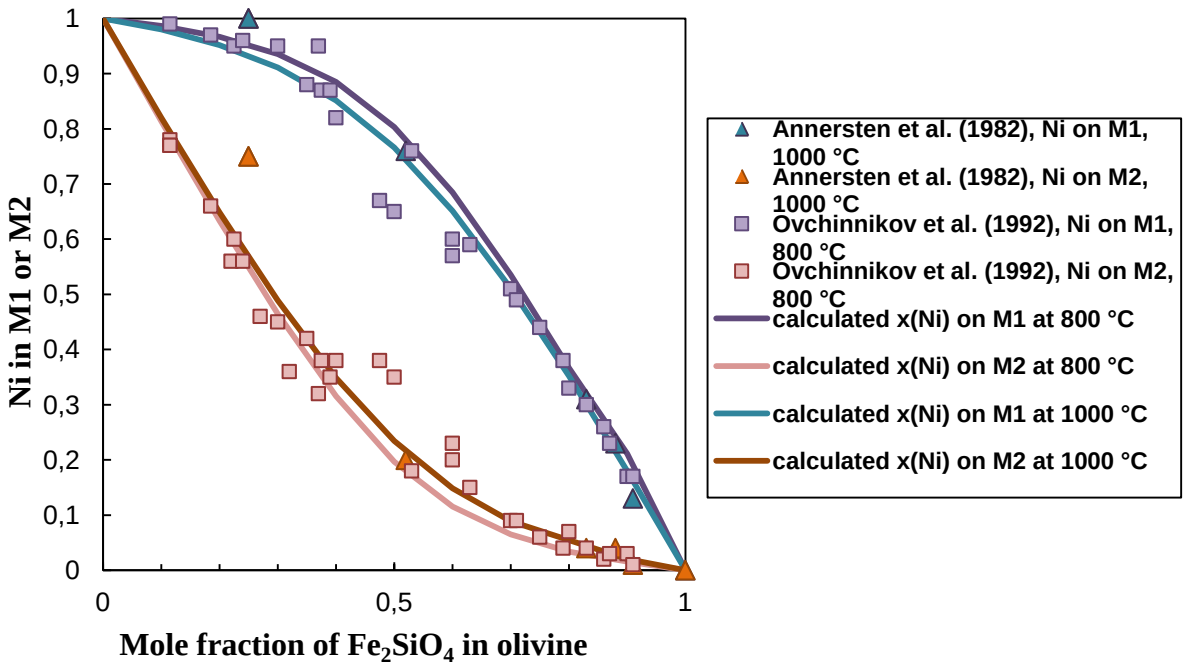

Figure 12.1: Cation distribution in Fe-Ni olivine solution: literature data of Annersten et al. [329] (quenched from 1000 °C) and Ovchinnikov et al. [330] (quenched from 800-900 °C) and calculated lines

12.3.1.2 Phase equilibria involving liquid

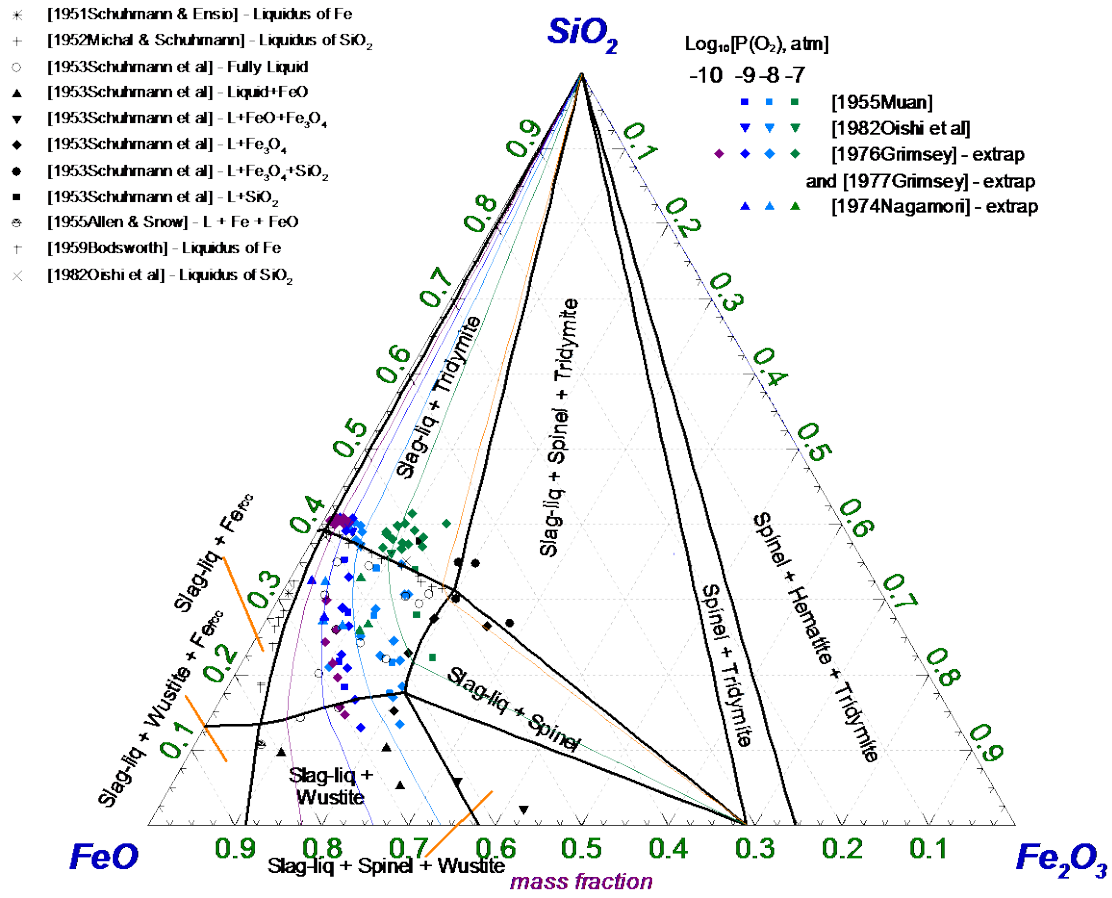

Figure 12.2 : Isothermal section of the oxide part of the Fe–O–Si system at 1300 °C and P = 1 atm. Black lines – phase boundaries, colored lines – oxygen isobars. The colors of lines correspond to oxygen partial pressures shown in the legend. Experimental data are from the Fe–O–Si system [332-338] and extrapolated data are from the Ni–Fe–O–Si system [339-341].

The solubility of nickel in liquid slag is governed by the reaction

$$\mathrm{Ni\ (liq)} + \frac{1}{2}\mathrm{O_2} = \mathrm{NiO\ (in\ slag)},\ \Delta G^\circ = -RT\ln\frac{a\mathrm{NiO}}{a\mathrm{Ni(liq)}\cdot[P(\mathrm{O_2})]^{1/2}}, \qquad (12.5)$$

$$a\mathrm{NiO} = \gamma(\mathrm{NiO})\cdot X(\mathrm{NiO})$$

where ΔG° is the standard Gibbs energy of the reaction (12.5); $a\mathrm{NiO}$, $\gamma(\mathrm{NiO})$ and $X(\mathrm{NiO})$ are activity with respect to pure liquid oxide, activity coefficient and mole fraction of NiO in slag, respectively; $a\mathrm{Ni(liq)}$ is activity of Ni with respect to pure liquid nickel. In general, $\gamma(\mathrm{NiO})$ is a function of slag composition, but its effect is smaller compared to the effect of ΔG°. The

thermodynamics of the solubility of NiO in Fe–O–Si slags is complicated by the fact that iron exhibits two oxidation states. Partial pressure of oxygen will have an effect not only on the reaction (12.5), but also on the Fe^{2+}/Fe^{3+} ratio in slag, which, in turn, changes $\gamma(\mathrm{NiO})$. The FeO–Fe_2O_3–SiO_2 part of the Fe–O–Si phase diagram at 1300 °C along with the oxygen isobars is shown in Figure 12.2 [327].

According to the Gibbs phase rule, 6 degrees of freedom must be fixed in order to study the Fe–Ni–O–Si system experimentally. Usually they are: temperature, total pressure of 1 atm, the presence of the slag phase, fixed partial pressure of oxygen $P(O_2)$, fixed SiO_2/Fe ratio in slag or silica saturation and the last is either saturation with the Fe-Ni metallic phase or fixed $a\mathrm{Ni(liq)}$.

Equilibrium of slag with the Fe-Ni metallic phase was studied by Grimsey and Biswas (1977) [340] at 1300 °C, by Nagamori (1974) [341] – at 1200 °C and 1300 °C, and by Ramirez et al. (2008) [323] – at 1300 °C and 1400 °C. The SiO_2/Fe ratio in slag was set by mixing the iron oxides (ferrous and ferric) and SiO_2 in initial slag in certain proportions. In all studies, $P(O_2)$ was controlled by the flow of CO/CO_2 gas of a certain composition. Slags were equilibrated with the flow of CO/CO_2 gas in Ni crucibles, which provided the saturation with the metallic phase. During the equilibration, some of iron from slag dissolved in the Ni metal. Only in the study of Grimsey and Biswas [340], this effect was properly taken into account. In addition to the Ni crucible, they introduced a thin Ni foil in the slag phase and analyzed the compositions of crucible and foil after attaining the equilibrium. The total content of iron in the crucible was around 90% of that in the foil, falling from the surface to inside the wall. It was assumed that the composition of the foil corresponds to the true equilibrium between the slag, metal and gaseous phases and a pseudo-equilibrium was reached with the surface of the crucible. Crucibles in the experiments of Nagamori [341] and of Ramirez et al. [323] were not analyzed. After attaining the equilibrium, samples were quenched. The slag phase was separated and analyzed by conventional wet chemical techniques for total Ni, total Fe, Fe^{2+} and SiO_2 content [323, 340]. In the study of Nagamori [341], the total Fe content was obtained by difference. The results on nickel solubility as a function of SiO_2/Fe ratio in slag are plotted in Figure 12.3 at different $P(O_2)$. Authors also recalculated the results of analysis to the FeO–Fe_2O_3–NiO–SiO_2 basis. The FeO/Fe_2O_3 ratios in slag are demonstrated in Figure 12.2 as oxygen isobars. For this purpose, slag composition is

represented in the $FeO–Fe_2O_3–SiO_2$ basis ($FeO + Fe_2O_3 + SiO_2 = 100\%$). The results may be compared with the Ni-free system.

The solubility data of Grimsey and Biswas [340] and of Nagamori [341] at $P(O_2) = 10^{-10}$, 10^{-9} and 10^{-8} atm are in reasonable agreement. Ramirez et al. [323] obtained much higher solubilities. Some of their points were approached from the high NiO content: the slag was prepared with the excess of NiO (12 wt.%). The idea was that excess NiO will be reduced and will precipitate as metallic nickel. Apparently, some Ni metal remained suspended in slag, which could result in the higher measured solubility of NiO in slag. The points that were approached from the zero NiO content also demonstrated higher Ni solubility comparing to the data of Grimsey and Biswas [340] and of Nagamori [341]. The possible reason is that the crucible material did not dissolve enough Fe and the pseudo-equilibrium activity of Ni in the system was higher. As reported by Grimsey and Biswas [340] at $P(O_2) = 10^{-10}$ atm, the equilibrium content of Fe in the metal phase should be between 25 and 45 wt.%.

There is a large scatter in the Ni solubility data at $P(O_2) = 10^{-7}$ atm. Our calculations showed that at this partial pressure of oxygen slag reaches saturation with the Ni_2SiO_4-Fe_2SiO_4 olivine phase rather than with the Fe-Ni metal phase. Under these conditions, it is not possible to determine the Ni solubility in slag using the Ni crucible. Most likely, the experimental results correspond to some non-equilibrium conditions.

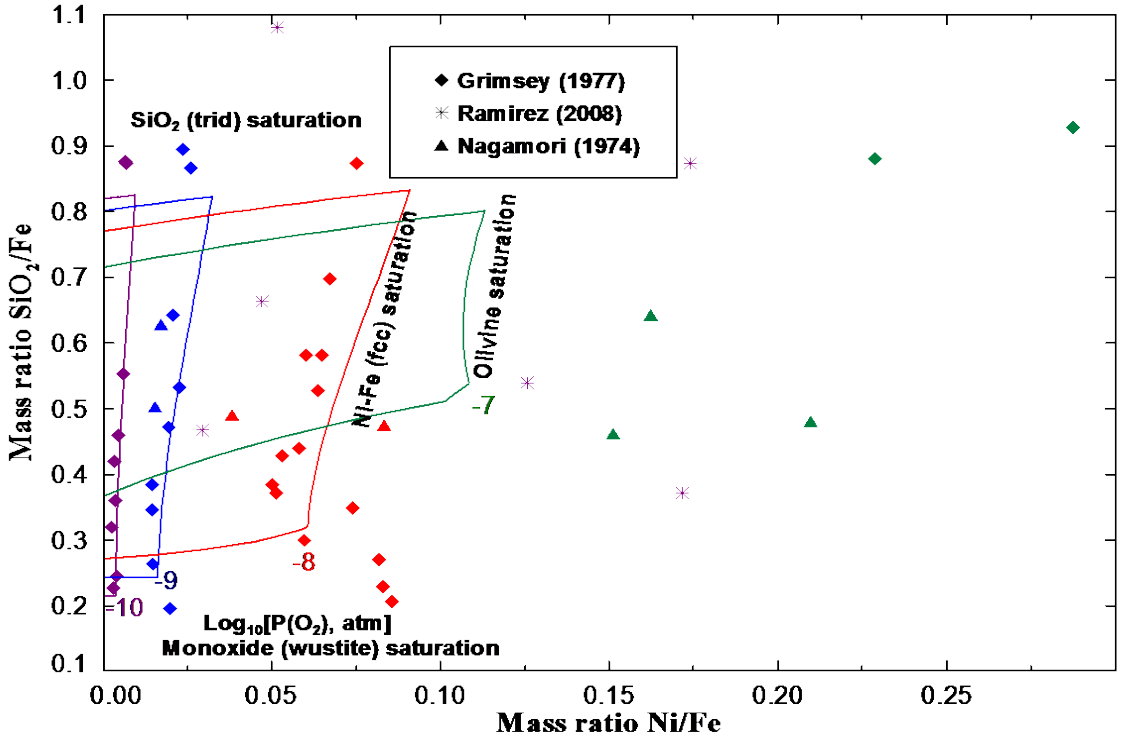

Figure 12.3. Liquid slag region of the Fe–Ni–O–Si system at 1300 °C and fixed partial pressure of oxygen. Experimental points [323, 340, 341] correspond to saturation with the Ni-Fe solid alloy.

Thus, in the Ni–Fe–O–Si system, the maximum solubility of nickel is limited by the saturation with the solid Ni-Fe alloy. This is not the case, however, for industrial smelting of Ni, where the liquid metallic Cu–Fe–Ni alloy or Cu_2S–FeS–NiS matte may be in equilibrium with slag. Under these conditions, more NiO may dissolve in slag. It is necessary to know γ(NiO) in the high-nickel slags. The equilibrium between slag and Cu-Ni alloy was studied by Wang et al. [342], by Taylor and Jeffes [343] and by Reddy and Acholonu [344]. However, copper itself readily dissolves in slags and may affect the activity coefficient of NiO. The equilibration with NiS-FeS mattes has similar problems: sulfur is soluble in slags, while mattes easily form suspensions in the slag phase. The effects of Cu and S on the solubility of Ni in slag will be discussed elsewhere.

The preferable technique is the equilibration of slag with the liquid Au-Fe-Ni alloy. It is applicable because the solubility of Au in slag is negligibly small, reportedly below <0.008 wt.% [345] under the conditions of interest. The system may still be considered to have four components Fe-Ni-O-Si, but instead of solid metal saturation, activity of liquid Ni is fixed as a

last degree of freedom. The assumption is made that $P(O_2)$ and SiO_2 have no effect on the thermodynamic properties of Au, Fe and Ni in liquid alloys. So, aNi(liq) may be calculated from the measured composition of the Au-Fe-Ni alloy using appropriate thermodynamic models. The accuracy of the applied thermodynamic model for liquid alloy is a potential source of error.

The equilibration with the Au-Fe-Ni alloy was used in the experiments of Grimsey and Biswas (1976) [339] and Wang et al. (1974) [346]. In both studies, one degree of freedom was set by silica saturation instead of the SiO_2/Fe ratio. The silica saturation was reached by conducting the experiments in SiO_2 crucibles. The oxygen partial pressure was controlled by the flow of CO/CO_2 gas mixture. Slag, alloy and gas phases were equilibrated, quenched and analyzed by wet chemical conventional methods. The drawback of the study of Wang et al (1974) [346] is that only the Ni content of the liquid alloy phase was measured. The iron solubility was neglected. The effect of iron on the activity of Ni in liquid Au-Fe-Ni alloy may be significant at low $P(O_2)$, where, according to Grimsey and Biswas [339], the iron content reaches 15 – 20 mol %.

The results of Grimsey and Biswas [339] and Wang et al. [346] were used to calculate aNiO according to the reaction (12.5). The standard Gibbs energy of reaction (12.5) was calculated to be -90.00, -86.59 and -83.19 $kJ \cdot mol^{-1}$ for 1250, 1300 and 1350 °C, respectively. The properties of NiO (liquid) were obtained previously in this study. The properties of Ni (liquid) were taken from the FSnobl database of the FactSage software [1]. aNi(liq) from the experimental studies [339, 346] were used. The results are plotted in Figure 12.4.

The experimental data of Grimsey and Biswas [339] and Wang et al [346] are in agreement up to the activity of NiO of about 0.09. At $P(O_2) = 10^{-7}$ atm, 1300 °C and above a(NiO) = 0.09, large discrepancies between the authors are observed, as well as contradiction with a previous trend. The calculations show that under these conditions the system reaches olivine saturation, so the experimental points correspond to some non-equilibrium conditions. At $P(O_2) = 10^{-6}$ atm, saturation with the spinel phase is predicted at even lower a(NiO).

Grimsey and Biswas [339] noticed that the activities of NiO as a function of wt.% Ni in slag have different slopes at $P(O_2) = 10^{-10}$ atm and at $P(O_2) = 10^{-8}$ atm. They pointed out that the activity coefficient γ(NiO) should then be different, which is contradictory to Henry's law. Grimsey and Biswas [339] suggested that some of the Ni should dissolve in the form of Ni^0 rather than Ni^{2+}. A more realistic explanation is that the change in $P(O_2)$ causes the variation of the Fe^{2+}/Fe^{3+} ratio in

slag. It is natural for $\gamma(\mathrm{NiO})$ to be slightly different if NiO is dissolved in different environment. The FeO/Fe_2O_3 ratio in slag as measured by Grimsey and Biswas [339] is presented in Figure 12.2. A small difference between the results of Grimsey and Biswas [339] and of Wang et al. [346] at $P(O_2) = 10^{-10}$ atm and very low nickel content most probably arises from the fact that Wang et al. [346] ignored the solubility of iron in liquid metal.

In this study, the properties of the Fe-O-Si slag were taken from the previous optimization [327]. The Fe-Ni-O and Ni-O-Si slags were modeled earlier in this study. The excess model parameters (in Joules) $q^{001}_{\mathrm{Ni,Si(Fe^{+2})}} = -25104$ and $q^{002}_{\mathrm{Fe^{+2},Si(Ni)}} = 125520$ were used for fine adjustment of $\gamma(\mathrm{NiO})$ in the Fe-Ni-O-Si slag. The calculated results are presented in Figure 12.3 and Figure 12.4. The agreement with the experimental data is very good.

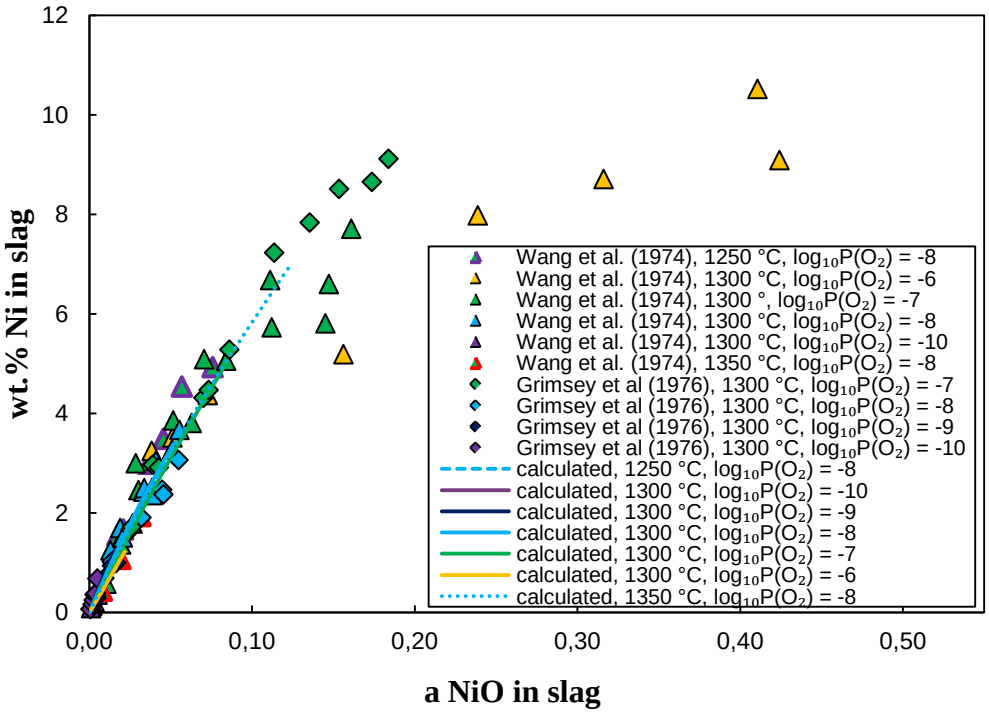

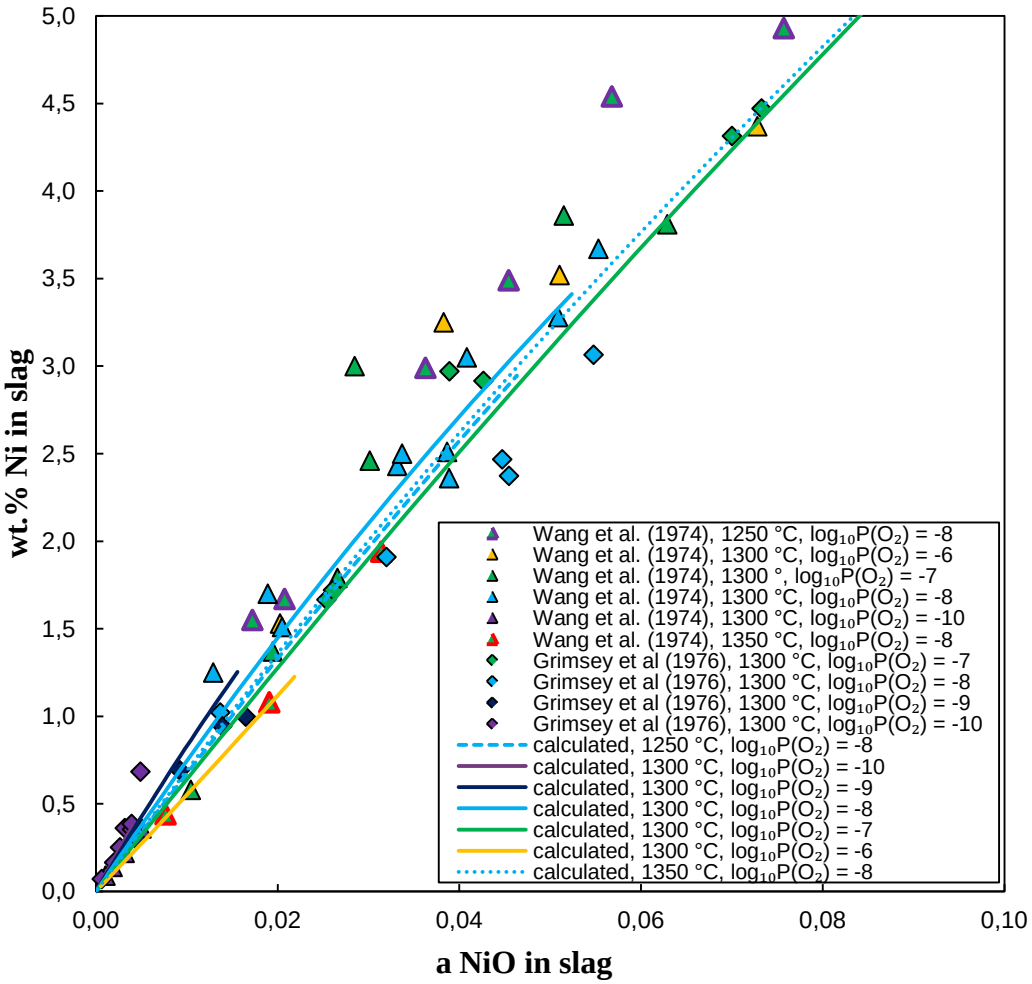
wt. % Ni in slag
a NiO in slag
5,0
4,5
4,0
3,5
3,0
2,5
2,0
1,5
1,0
0,5
0,0
0,00
0,02
0,04
0,06
0,08
0,10
Wang et al. (1974), 1250 °C, log10P(O2) = -8
Wang et al. (1974), 1300 °C, log10P(O2) = -6
Wang et al. (1974), 1300 °, log10P(O2) = -7
Wang et al. (1974), 1300 °C, log10P(O2) = -8
Wang et al. (1974), 1300 °C, log10P(O2) = -10
Wang et al. (1974), 1350 °C, log10P(O2) = -8
Grimsey et al (1976), 1300 °C, log10P(O2) = -7
Grimsey et al (1976), 1300 °C, log10P(O2) = -8
Grimsey et al (1976), 1300 °C, log10P(O2) = -9
Grimsey et al (1976), 1300 °C, log10P(O2) = -10
calculated, 1250 °C, log10P(O2) = -8
calculated, 1300 °C, log10P(O2) = -10
calculated, 1300 °C, log10P(O2) = -9
calculated, 1300 °C, log10P(O2) = -8
calculated, 1300 °C, log10P(O2) = -7
calculated, 1300 °C, log10P(O2) = -6
calculated, 1350 °C, log10P(O2) = -8

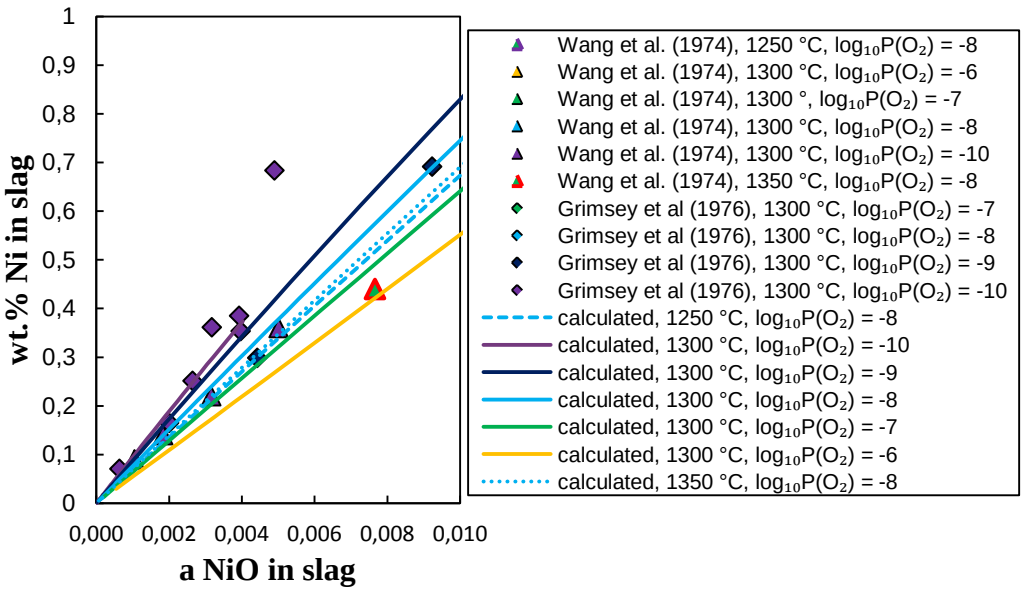

Figure 12.4. Activity of NiO in Fe-Ni-O-Si slag in equilibrium with Au-Fe-Ni alloys at SiO_2 saturation and fixed $P(O_2)$. Second and third figures are the magnifications of the first one. Calculated lines and experimental points [339, 346].

Grutzeck and Muan [302] investigated phase relations in the Fe–Ni–O–Si system in air ($P(O_2)$ = 0.21 atm) and at intermediate oxygen partial pressures in CO_2 atmosphere ($P(O_2) \approx 10^{-3}$ atm). Equilibrated samples were quenched into water or cooled in air and analyzed by conventional metallographic and polarizing microscopic techniques and X-ray diffraction analysis. A few experimental runs were made in sealed Pt tubes or SiO_2 capsules in order to determine the temperature of the liquidus invariant points, where cristobalite, olivine, spinel and monoxide phases coexist with liquid. In air, only one ternary eutectic point was determined at 1524 °C, with the following phase compositions: spinel (68 wt.% Fe_3O_4, 32 wt.% NiO), monoxide (33 wt.% Fe_3O_4, 67 wt.% NiO), cristobalite (SiO_2), liquid (33 wt.% Fe_3O_4, 39 wt.% NiO, 28 wt.% SiO_2). All the measured Fe was represented as Fe_3O_4. In CO_2 atmosphere, the ternary liquidus invariant point, at which spinel, monoxide, cristobalite, and liquid coexist in equilibrium, was lowered to 1433 °C and the composition of monoxide phase was substantially different from that in air: 38 wt.% Fe_3O_4, 62 wt.% NiO. However, it is not clear from the article how the compositions of phases in equilibrium were measured. Probably, they were estimated from the lattice parameters obtained by XRD.

The calculated liquidus projection of the Fe_3O_4–NiO–SiO_2 system in air is shown in Figure 12.5, along with the liquidus experimentally determined by Grutzeck and Muan [302]. The eutectic point is calculated to be at 1517 °C, with the following phase compositions: spinel (49.5 wt.% Fe_3O_4, 50.5 wt.% NiO), monoxide (41.3 wt.% Fe_3O_4, 58.7 wt.% NiO), cristobalite (SiO_2), and liquid (31.2 wt.% Fe_3O_4, 35.6 wt.% NiO, 33.1 wt.% SiO_2). The calculated compositions in the eutectic are different from those measured by Grutzeck and Muan [302], probably due to experimental error and low accuracy of the method applied to determine phase compositions.

The calculated eutectic temperature in CO_2 atmosphere is lowered to 1471 °C, with the following phase compositions: spinel (76.2 wt.% Fe_3O_4, 23.8 wt.% NiO), monoxide (49.5 wt.% Fe_3O_4, 50.5 wt.% NiO), cristobalite (SiO_2), and liquid (41.6 wt.% Fe_3O_4, 27.7 wt.% NiO, 30.7 wt.% SiO_2).

Temperature-composition diagrams of the Fe-Ni-O-Si system at constant silica contents in air along with the literature data of Grutzeck and Muan [302] are shown in Figure 12.6-Figure 12.11. Figure 12.12-Figure 12.17 show similar diagrams at $\log_{10}P(O_2) = -2.9$. This average partial pressure was chosen to represent the literature data of Grutzeck and Muan [302] in CO_2 atmosphere, where oxygen partial pressures mostly varied in the range $\log_{10}P(O_2) = -2.7...-3.0$.

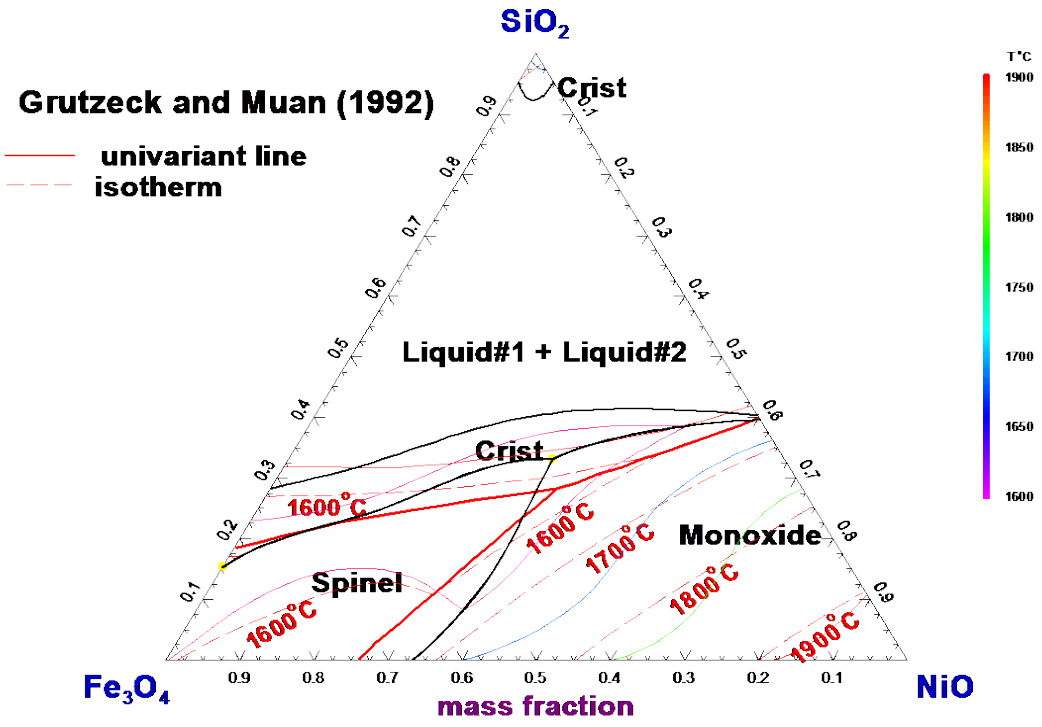

Figure 12.5 : Liquidus projection of the Fe_3O_4–NiO–SiO_2 system in air: smoothed literature data of Grutzeck and Muan [302] and calculated lines. See notations in Table 12.1

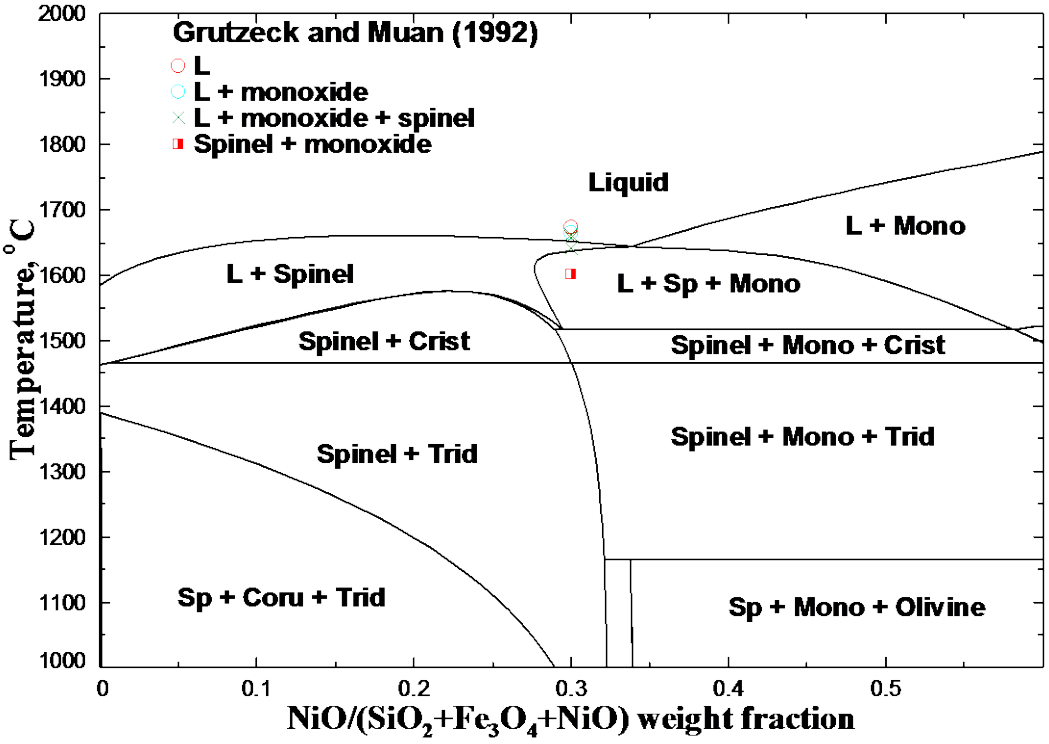

Figure 12.6 : Temperature-composition diagram of the Fe–Ni–O–Si system in air at 1 wt.% of SiO_2. See notations in Table 12.1

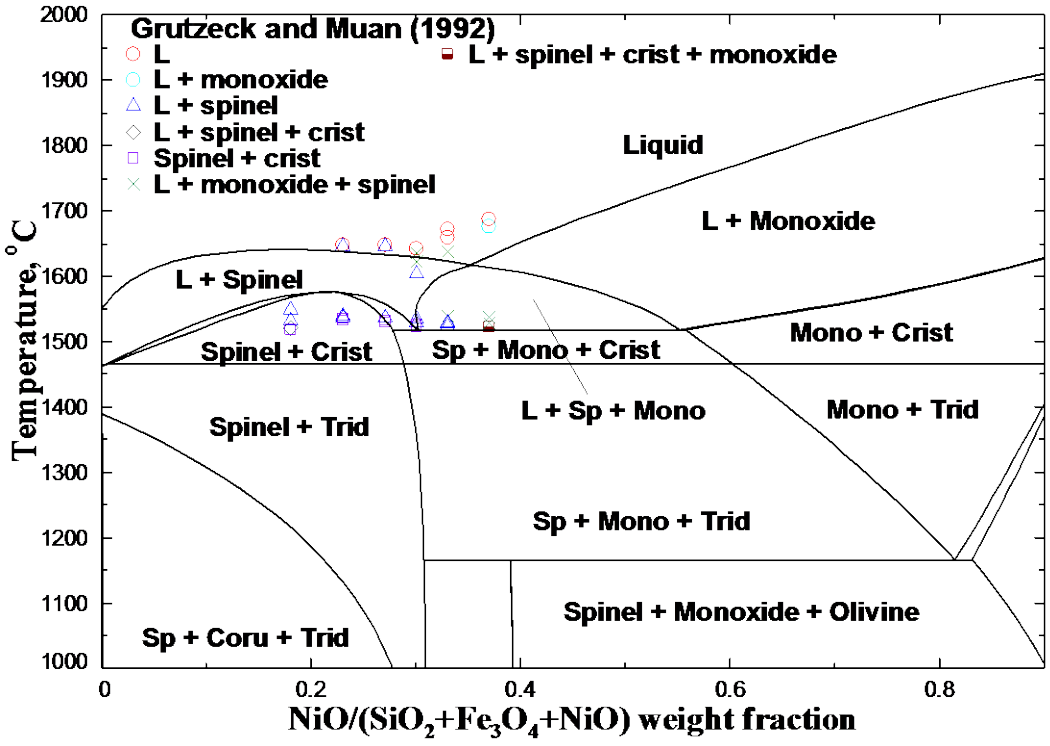

Figure 12.7 : Temperature-composition diagram of the Fe–Ni–O–Si system in air at 5 wt.% of SiO_2. See notations in Table 12.1

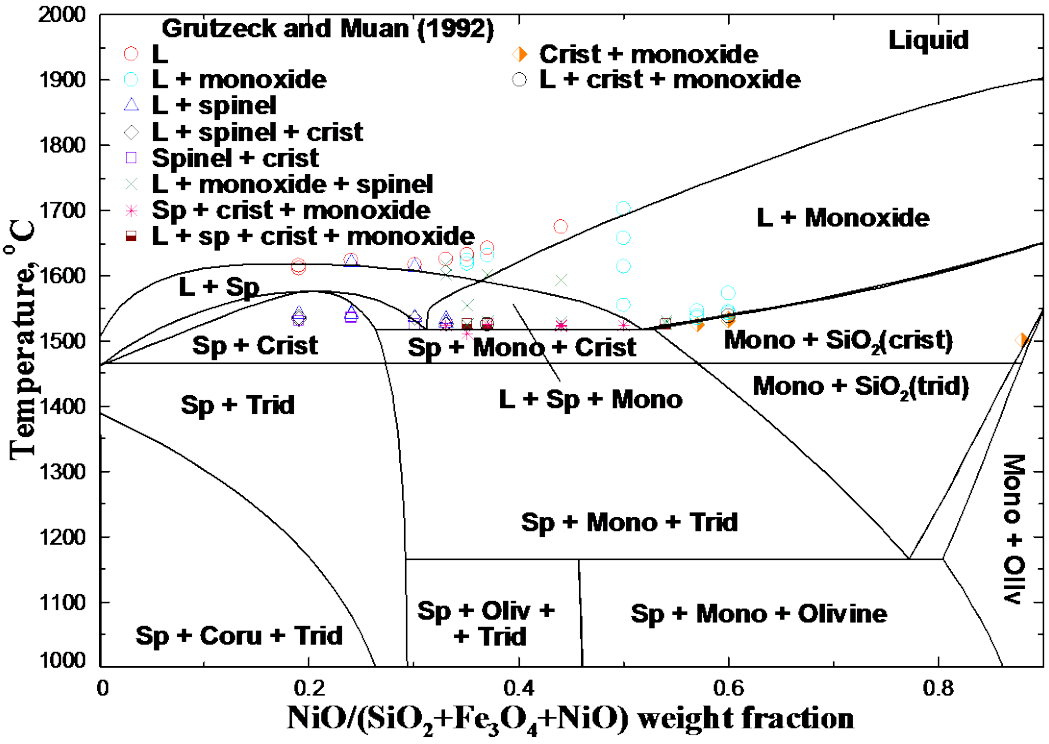

Figure 12.8 : Temperature-composition diagram of the Fe–Ni–O–Si system in air at 10 wt.% of SiO_2. See notations in Table 12.1

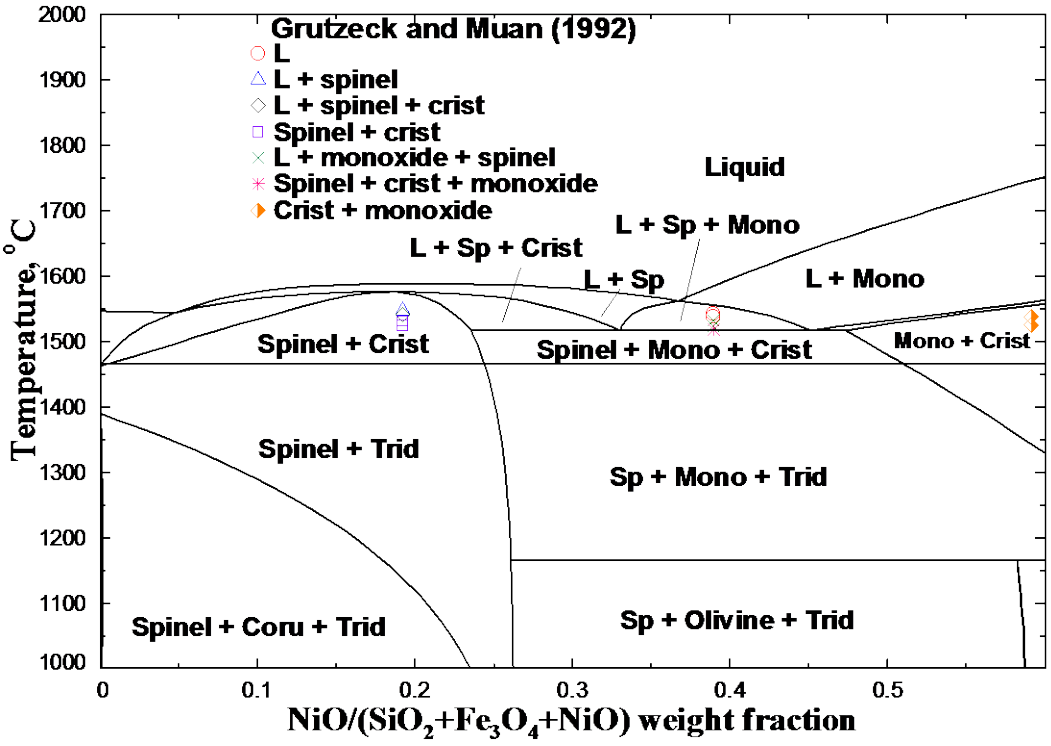

Figure 12.9 : Temperature-composition diagram of the Fe–Ni–O–Si system in air at 19.5 wt.% of SiO_2. See notations in Table 12.1

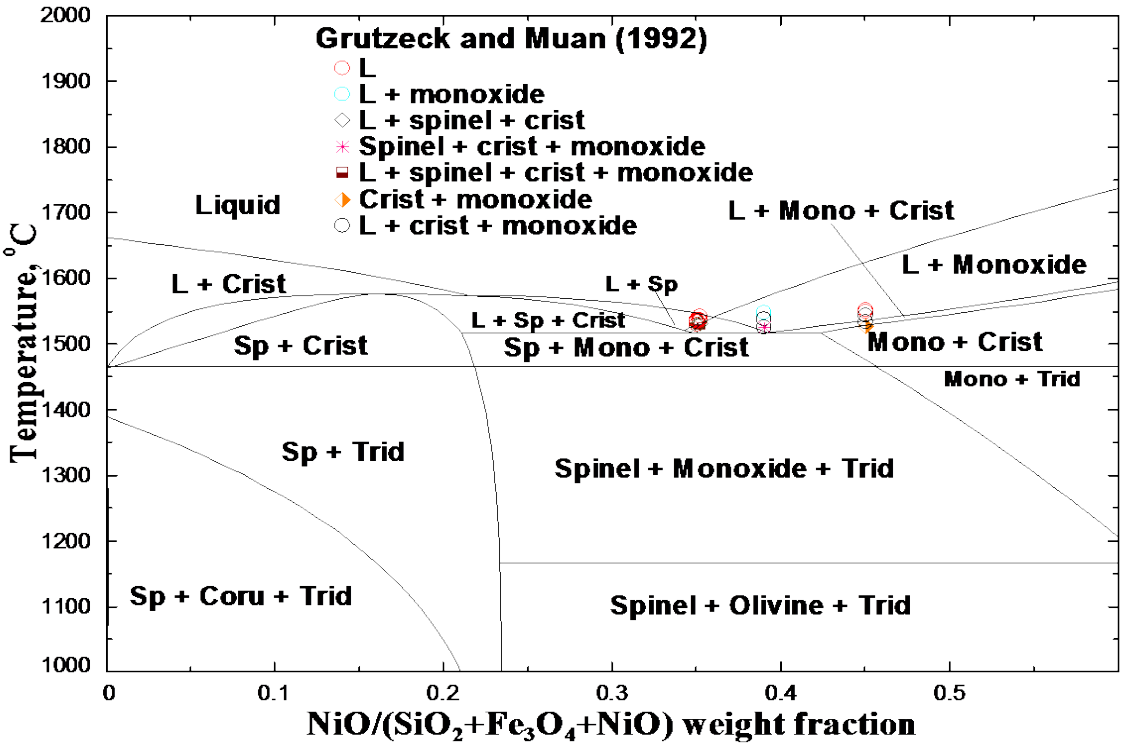

Figure 12.10 : Temperature-composition diagram of the Fe–Ni–O–Si system in air at 28 wt.% of SiO_2. See notations in Table 12.1

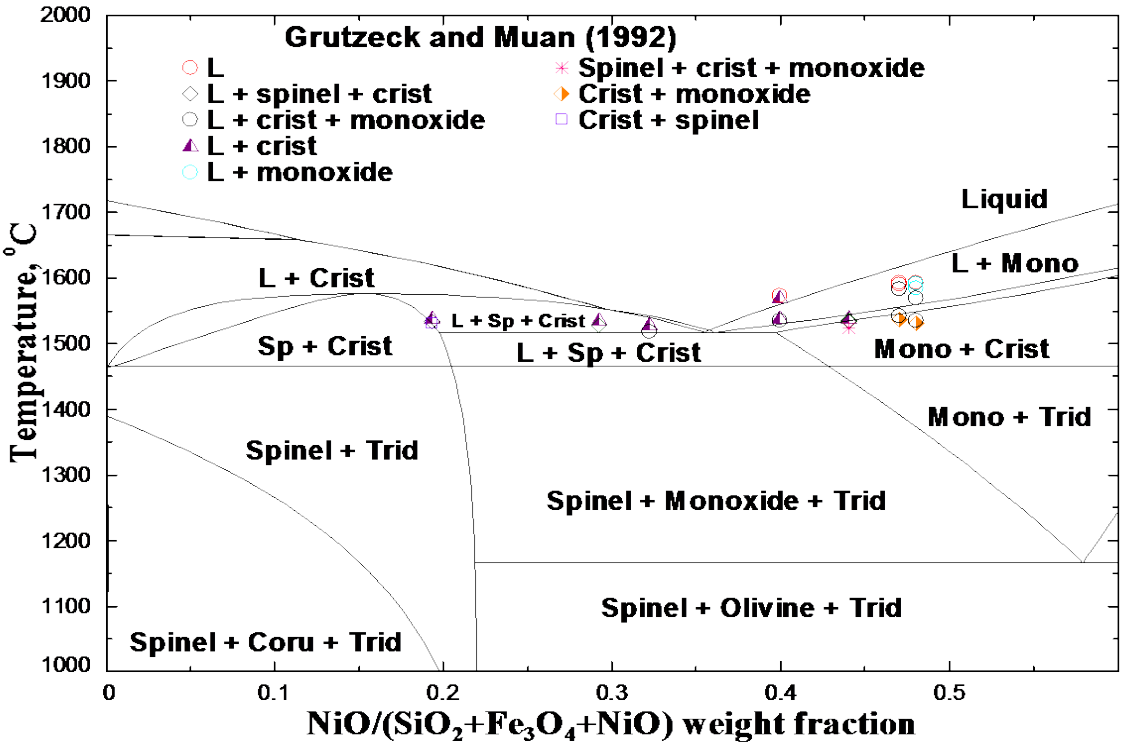

Figure 12.11 : Temperature-composition diagram of the Fe–Ni–O–Si system in air at 32.5 wt.% of silica. See notations in Table 12.1

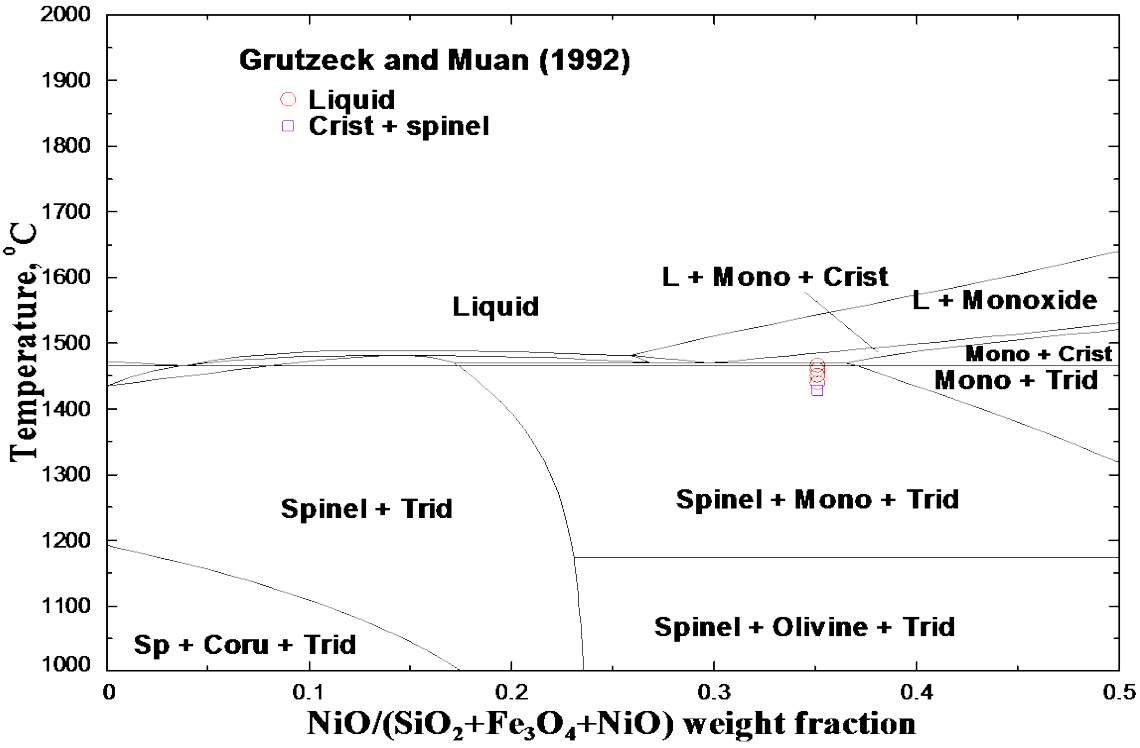

Figure 12.12: Temperature-composition diagram of the Fe–Ni–O–Si system at $\log_{10}P(O_2)$ = -2.9 and 27.3 wt.% of SiO_2. See notations in Table 12.1

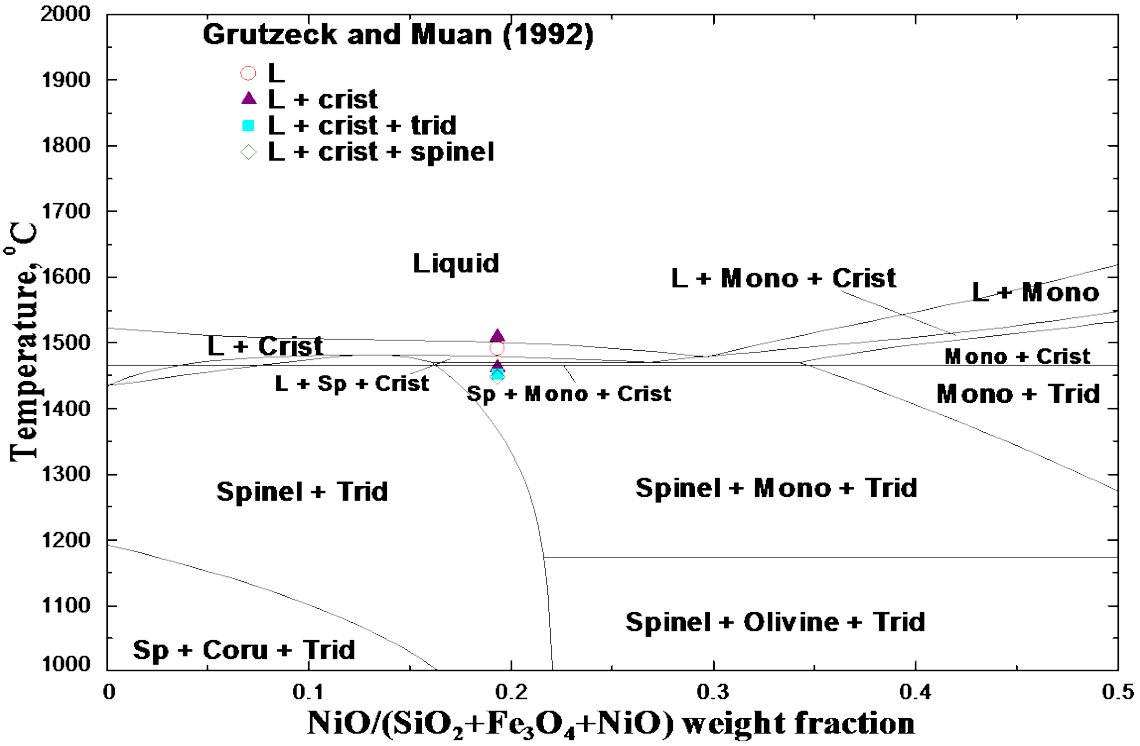

Figure 12.13: Temperature-composition diagram of the Fe–Ni–O–Si system at $\log_{10}P(O_2)$ = -2.9 and 31.9 wt.% of SiO_2. See notations in Table 12.1

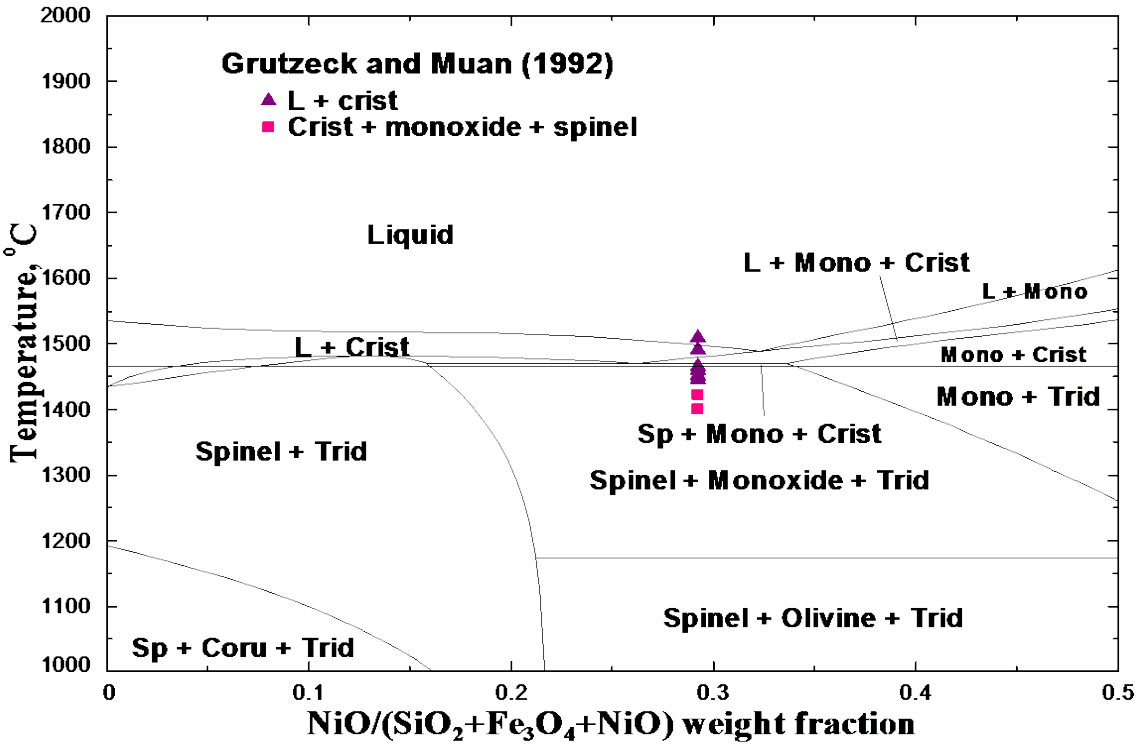

Figure 12.14: Temperature-composition diagram of the Fe–Ni–O–Si system at $\log_{10}P(O_2)$ = -2.9 and 33.1 wt.% of SiO_2. See notations in Table 12.1

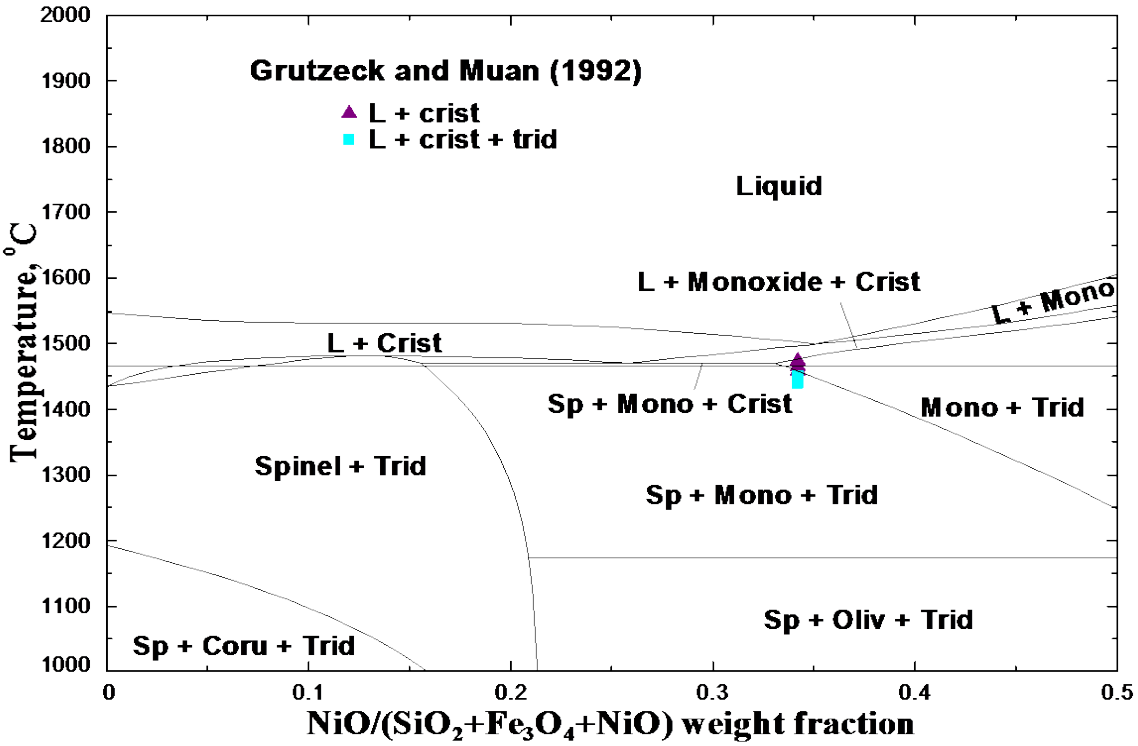

Figure 12.15: Temperature-composition diagram of the Fe–Ni–O–Si system at $\log_{10}P(O_2)$ = -2.9 and 34.2 wt.% of SiO_2. See notations in Table 12.1

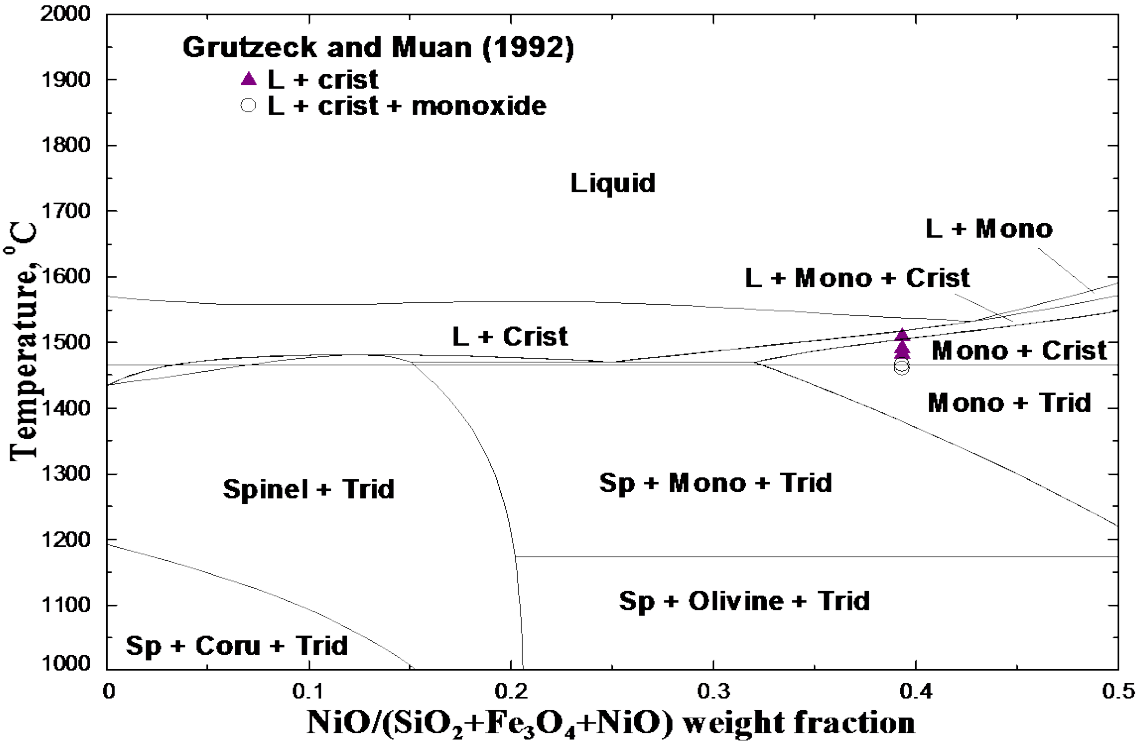

Figure 12.16: Temperature-composition diagram of the Fe–Ni–O–Si system at $\log_{10}P(O_2)$ = -2.9 and 36.4 wt.% of SiO_2. See notations in Table 12.1

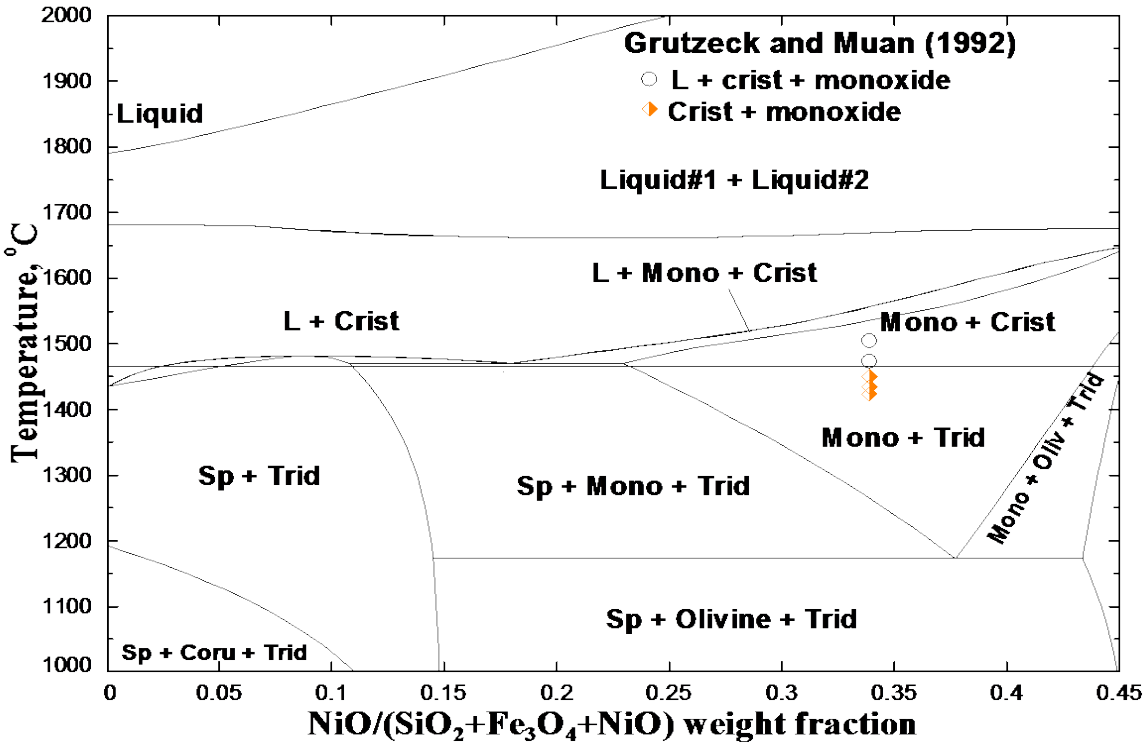

Figure 12.17: Temperature-composition diagram of the Fe–Ni–O–Si system at $\log_{10}P(O_2)$ = -2.9 and 54.4 wt.% of SiO_2. See notations in Table 12.1

Grutzeck and Muan [94] also investigated phase relations in the Fe–Ni–O–Si system under strongly reducing conditions obtained by CO_2/CO gas mixtures. Equilibrated samples were quenched and analyzed by transmitted and reflected light microscopy and X-ray diffraction analysis. Only one ternary peritectic point was determined at 1571 °C, with the following phase compositions: olivine (8 wt.% Fe_2SiO_4, 92 wt.% Ni_2SiO_4), monoxide (4.5 wt.% FeO, 95.5 wt.% NiO), cristobalite (SiO_2), liquid (19 wt.% FeO, 47 wt.% NiO, 34 wt.% SiO_2). However, the corresponding partial pressure of oxygen was not provided. Pyroxene was found to be not stable in the system.

Partial pressures of oxygen substantially varied unsystematically in the study of Grutzeck and Muan [94] from $\log_{10}P(O_2)$ = -4 up to -7 and, therefore, their data could not be represented by the temperature-composition diagrams, similar to those shown above. However, it should be mentioned that these data are described equally well.

12.3.2 Optimization

First, the model parameters for olivine solution were optimized to take into consideration the literature data on olivine. Then, two parameters of the Modified Quasichemical Model were optimized to describe the phase equilibria data involving liquid for the Fe–Ni–O–Si system. The optimized model parameters are given in Table 12.2.

The agreement between the calculated and experimental results is believed to be within experimental error limits. The disagreement with the experimental results of Grutzeck and Muan [302] is probably due to low accuracy of the experimental technique used to determine phase compositions.

Table 12.2: Optimized model parameters for the Al–Ni–O–Si and Fe–Ni–O–Si system ($J \cdot mol^{-1}$)

Slag (liquid oxide phase): Al_2O_3–FeO–NiO–SiO_2

$q^{001}_{Ni,Si(Fe^{+2})} = -25104$

$q^{002}_{Fe^{+2},Si(Ni)} = 125520$

$q^{001}_{Al,Si(Ni)} = -29288;$

$q^{002}_{Ni,Al(Si)} = -25104.$

The optimization of the $AlO_{1.5}$-NiO slag is described in Section 9.5.3 of this thesis;

Al_2O_3-SiO_2 was optimized within FToxide FactSage database [1];

NiO-SiO_2 and FeO-SiO_2 liquid oxides were optimized by Prostakova et al. [51] and Hidayat et al. [327], respectively;

The properties of the Al_2O_3–NiO–SiO_2, Fe_2O_3–NiO–SiO_2 and FeO–NiO–SiO_2 slags were calculated from the corresponding binary parameters using the asymmetric "Toop-like" model [28], with silica as the asymmetric component.

Olivine (orthosilicate solution) $(Fe^{2+}, Ni^{2+})^{M2}(Fe^{2+}, Ni^{2+})^{M1}SiO_4$

$G_{NiNi} = G(Ni_2SiO_4)$ [51];

$K_{FeNi} = G_{NiFe} - G_{FeNi} = 25104;$

$\Delta_{FeNi:NiFe} = G_{FeFe} + G_{NiNi} - G_{FeNi} - G_{NiFe} = -5439.2;$

$G_{FeFe} = G(Fe_2SiO_4)$ is taken from [327].

12.4 Al–Ni–O–Si system

12.4.1Literature review

Phase equilibria in the Al–Ni–O–Si system were investigated by Phillips et al. [90]. The Ni_2SiO_4–$NiAl_2O_4$, $NiAl_2O_4$–SiO_2 and $NiAl_2O_4$–$Al_6Si_2O_{13}$ sections of the system were studied by quenching and direct observational technique. The Ni_2SiO_4–$NiAl_2O_4$ join (see Figure 12.18) was found to be not binary in the sense that the compositions of crystalline phases could not be expressed in terms of the chosen components. The $NiAl_2O_4$–SiO_2 and $NiAl_2O_4$–$Al_6Si_2O_{13}$ sections shown in Figure 12.19 and Figure 12.20 were measured and the measurements indicate that this section is quasibinary. Some additional phases shown in brackets occur in small amounts on the calculated sections due to non-stoichiometry of $NiAl_2O_4$ spinel at high temperatures.

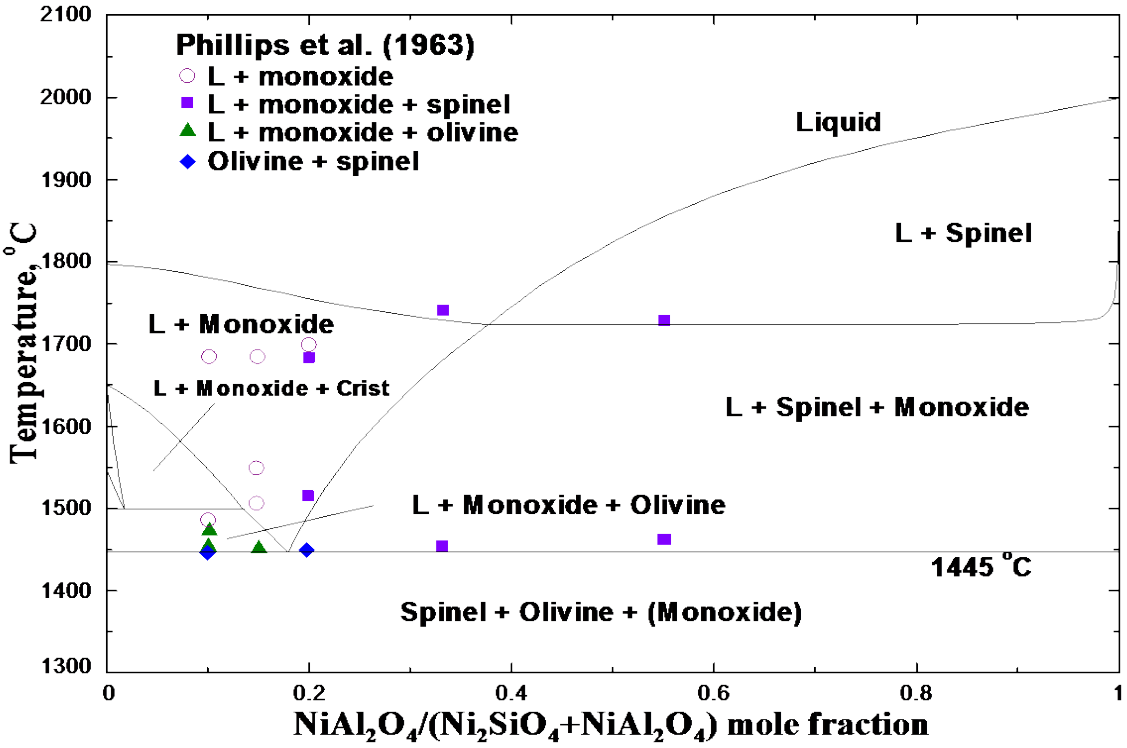

Figure 12.18: The Ni_2SiO_4–$NiAl_2O_4$ section of the Al–Ni–O–Si system: literature data of Phillips et al. [90] and calculated lines. See notations in Table 12.1

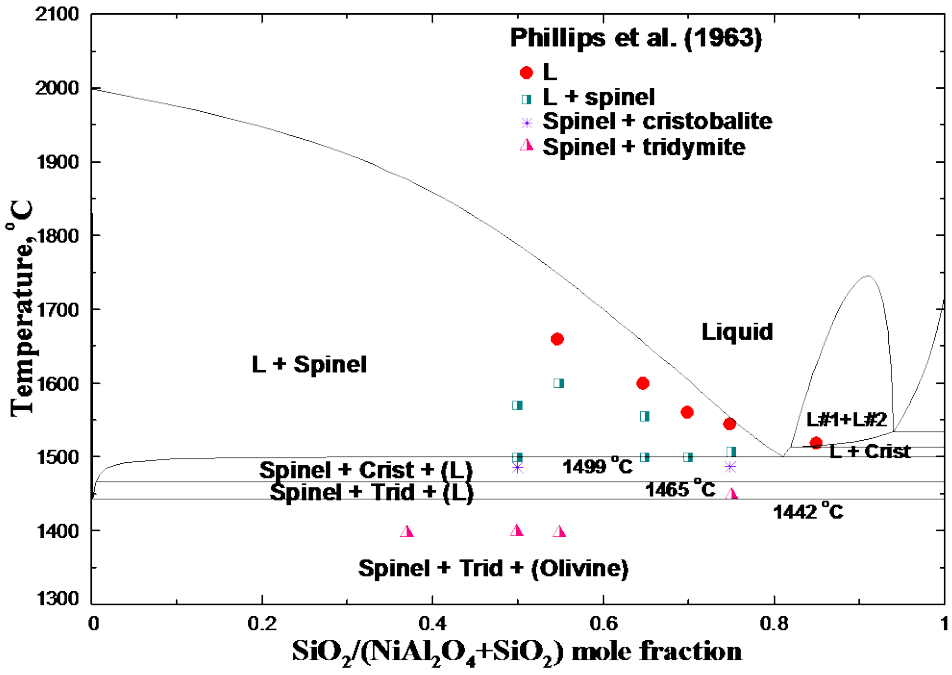

Figure 12.19: The $NiAl_2O_4$–SiO_2 section of the Al–Ni–O–Si system: literature data of Phillips et al. [90] and calculated lines. See notations in Table 12.1

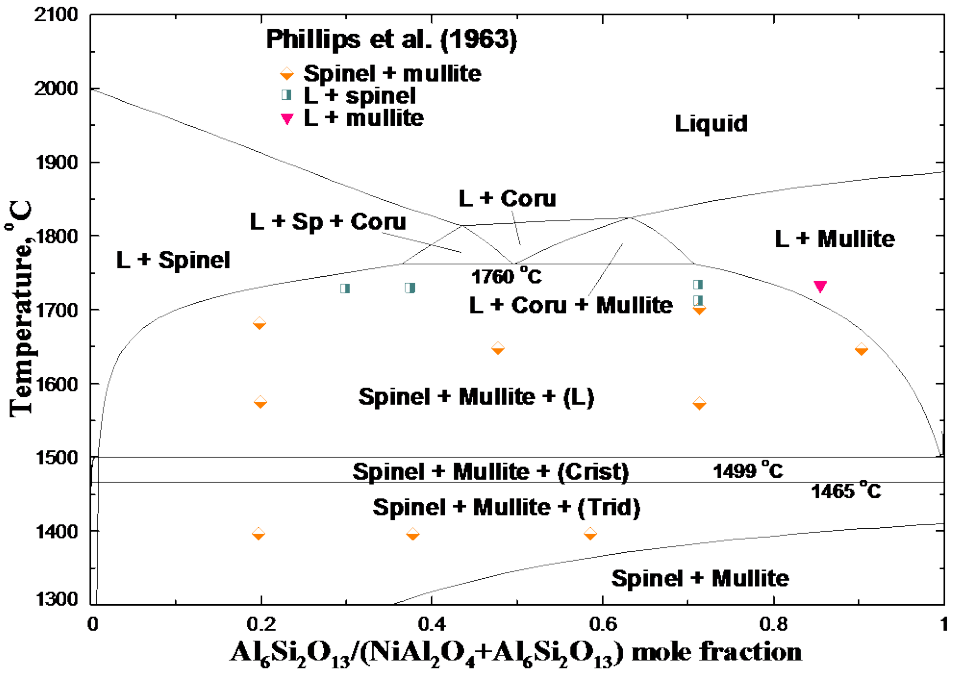

Figure 12.20: The $NiAl_2O_4$–$Al_6Si_2O_{13}$ section of the Al–Ni–O–Si system: literature data of Phillips et al. [90] and calculated lines. See notations in Table 12.1

12.4.2 Optimization

The only optimized phase in the Al–Ni–O–Si system was slag. The optimized model parameters are given in Table 12.2. The disagreement with the experimental results of Phillips et al. [90] is believed to be due to low accuracy of the experimental technique applied by these authors.

12.5 Summary of results

A simultaneous optimization of all available data over a wide range of temperatures and oxygen partial pressures (from air to metallic saturation) in the Al–Ni–O–Si and Fe–Ni–O–Si systems was performed at 1 atm total pressure. Optimized model equations for the thermodynamic properties of all phases reproduce all available thermodynamic and phase-equilibrium data within experimental error limits.

CHAPTER 13 PREDICTION OF PHASE EQUILIBRIA IN THE Fe–Mg–Ni–O–Si SYSTEM

Using the set of optimized model parameters, predictions of phase equilibria in the Fe–Mg–Ni–O–Si system were made and the parameters of the models were verified against available literature data.

The thermodynamic description of the Fe–Mg–Ni–O–Si chemical system applied in this study was based on previous optimizations of the Fe–Mg–Ni–O system (see Section 11.3.3), the Fe–Mg–O–Si system [347], the Fe–Ni–O–Si system (see Section 12.3) and the Mg–Ni–O–Si system (see CHAPTER 6).

Table 13.1 : Cation distribution in Fe-Mg-Ni olivine at 1000 °C : experimental data of Nord et al. [348] and calculated site occupancies

Sample	**Overall composition**		**Exp. M1 site occupancy**	**Exp. M2 site occupancy**	**Calc. M1 site occupancy**	**Calc. M2 site occupancy**
1	Si	1				
	Mg	1.14	0.43	0.71	0.47	0.67
	Fe	0.34	0.12	0.22	0.10	0.24
	Ni	0.52	0.45	0.07	0.43	0.09
2	Si	1				
	Mg	1.02	0.3	0.72	0.31	0.71
	Fe	0.08	0.02	0.06	0.02	0.06
	Ni	0.9	0.68	0.22	0.67	0.22

Table 13.1 shows the cation distribution in Fe-Mg-Ni olivine at 1000 °C. Nord et al. [348] measured it by a combination of Mössbauer spectroscopy and X-ray diffraction. As can be seen from the figure, the agreement between the experimental and calculated results is very good.

CHAPTER 14 PREDICTION OF PHASE EQUILIBRIA IN THE Ca–Fe–Ni–O AND Ca–Fe–Ni–O–Si SYSTEMS

Using the set of optimized model parameters, predictions of phase equilibria in the Ca–Fe–Ni–O and Ca–Fe–Ni–O–Si systems were performed and the parameters of the models were verified against available literature data.

14.1 Ca–Fe–Ni–O system

The thermodynamic description of the Ca–Fe–Ni–O system applied in this study was based on previous optimizations of the Ca–Fe–O chemical system [349], Fe–Ni–O (see CHAPTER 10) and Ca–Ni–O systems (see CHAPTER 5). The solubility of Ca in Fe-Ni spinel was modeled in this study by setting the $\Delta_{Fe^{+3}Ni^{+2}Ca^{+2}}$ model parameter, as described in Section 4.6.1, equal to zero.

The solubility limit of $CaFe_2O_4$ in $NiFe_2O_4$ in air was measured as 20 mol % at 1200 °C by Yamamura et al. [350] by means of X-ray diffraction and in the range of 15-30 mol % at 1300 °C by Vasiliu [351] using inductivity and magnetic permeability measurements. Projections of phase equilibria in the Ca–Fe–Ni–O system through the oxygen corner at 1200 and 1300 °C, along with these literature data, are shown in Figure 14.1 and Figure 14.2.

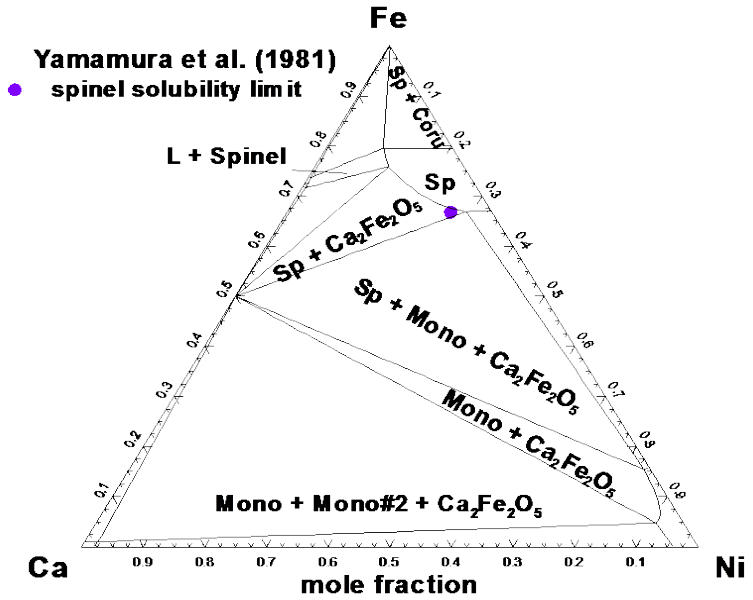

Figure 14.1 : Phase equilibria in the Ca–Fe–Ni–O system in air at 1200 °C : experimental data of Yamamura et al. [350] and calculated lines. See notations in Table 4.1

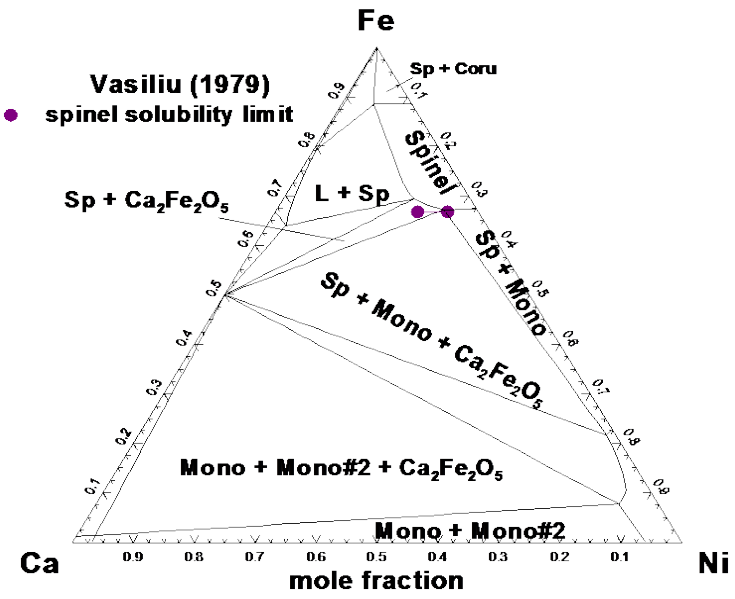

Figure 14.2 : Phase equilibria in the Ca–Fe–Ni–O system in air at 1300 °C: experimental data of Vasiliu [351] and calculated lines. See notations in Table 4.1

14.2 Ca–Fe–Ni–O–Si system

The thermodynamic description of the Ca–Fe–Ni–O–Si system applied in this study was based on previous optimizations of the Ca–Fe–Ni–O system (see Section 14.1), the Ca–Fe–O–Si system [47], the Ca–Ni–O–Si system (see Section 7.8.1) and the Fe–Ni–O–Si system (see Section 12.3).

Grimsey and Biswas [340] investigated the tendency of nickel to dissolve in iron silicate slags containing up to 25 wt.% of CaO and up to 4 wt.% Ni at 1300 °C in equilibrium with Fe-Ni foils and CO/CO_2 gas controlling the oxygen potential in the range of 10^{-8}-10^{-10} atm. In order to conduct the experimental study in the Ca–Fe–Ni–O–Si system, 7 degrees of freedom must be set. In addition to six degrees of freedom listed before for the Fe–Ni–O–Si system, it is preferable to fix the calcia content in slag. In the experiments of Grimsey and Biswas [340], the calcia content was set by mixing certain amounts of components in the initial slag before the equilibration. During the equilibration, the composition of slag changed and wt.% CaO in slag was measured after the equilibration. The calcia content for different points varied unsystematically. All results were divided into two groups – those with the CaO/Fe ratio in slag between 0 and 0.3 and those with the CaO/Fe ratio in slag between 0.3 and 0.8. They are plotted in Figure 14.3, along with the data for the Ca-free slag. It may be concluded that the Ni content of Ni-Fe saturated slags falls with the increase

of the CaO/Fe ratio in slag. Lines in Figure 14.3 were calculated with the fixed ratios CaO/Fe = 0.15 and 0.5. Calculated lines are in agreement with the experimental data.

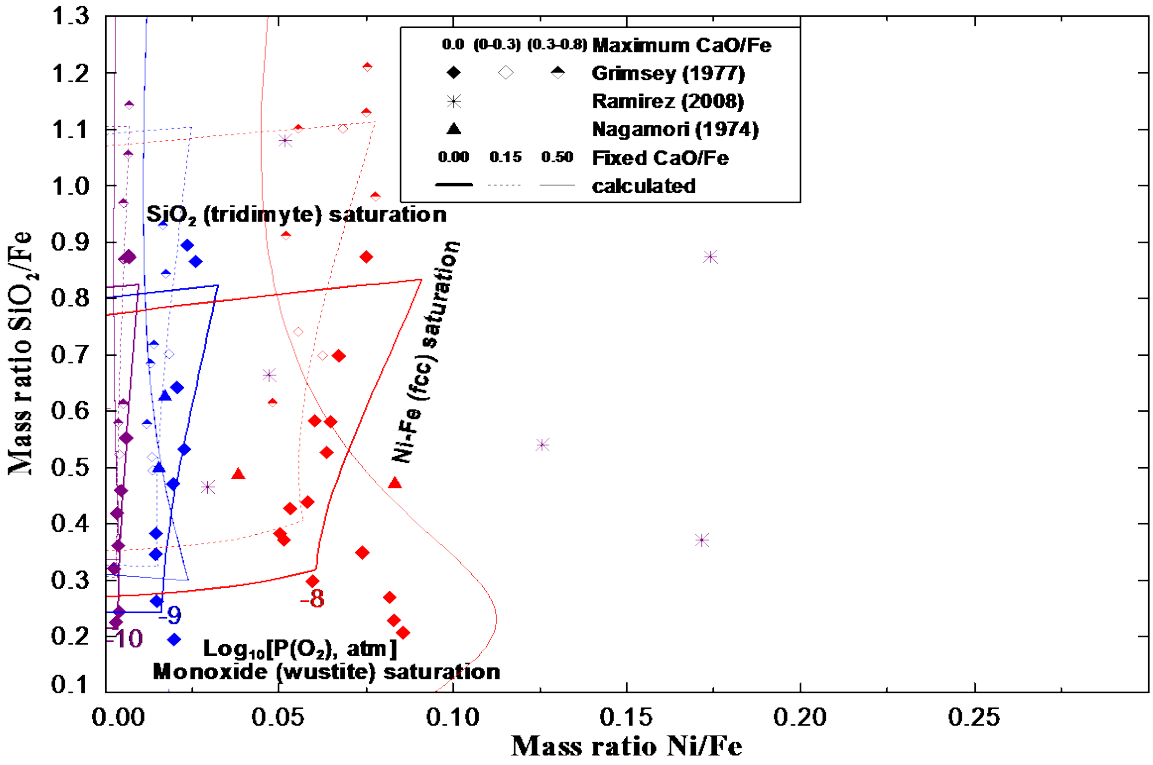

Figure 14.3. Liquid slag region of the Ca–Fe–Ni–O–Si system at 1300 °C, fixed partial pressure of oxygen and fixed CaO/Fe content in slag. Experimental points [323, 340, 341] correspond to saturation with the Ni-Fe solid alloy. The experimental data for Ca-containing slags [340] correspond to the ratios CaO/Fe = 0-0.3 and 0.3-0.8.

GENERAL DISCUSSION AND CONCLUSIONS

In order to develop a self-consistent multi-component thermodynamic database for nickel extraction from laterite ores, a large scale research program was undertaken, which naturally combined experimental investigation and computer-assisted thermodynamic modeling. Chemical systems relevant to nickel laterite ore processing were experimentally studied and optimized. The thermodynamic modeling part was performed using the FactSage thermochemical software and its databases [1] developed in the Centre for Research in Computational Thermochemistry at École Polytechnique de Montreal, Canada. The experimental program was carried out by our colleagues from the Pyrometallurgy Research Centre, Brisbane, Australia [2].

The experimental and thermodynamic modeling parts were closely integrated in order to enhance the effectiveness of the overall program in terms of quantity of the required experimental work and availability of specific data that are essential for thermodynamic modeling. This was achieved by applying thermodynamic assessments to identify priorities for experiments and planning experimental measurements to provide specific data for thermodynamic modeling. This approach increased the predictive ability of the applied thermodynamic models and enabled the characterization of phase relations over the wide range of compositions, temperatures and oxygen partial pressures of direct importance to metallurgical industries.

The whole set of experimental data, including the new experimental results and previously published data, was taken into consideration in the thermodynamic modeling of oxide phases in the Al_2O_3–CaO–FeO–Fe_2O_3–MgO–NiO–SiO_2 (Al–Ca–Fe–Mg–Ni–O–Si) multi-component system at a total pressure of 1 atm and a wide range of temperatures and oxygen partial pressures. All solid and liquid phases of 4 binary, 7 ternary, 5 quaternary and 2 quinary systems of the multi-component chemical system were optimized in the present study.

The optimizations are self-consistent and consistent with existing FToxid and FSstel metallic databases of the FactSage software. The applied models are based on the structure of the corresponding solution. The Modified Quasichemical Model, which takes into consideration second-nearest-neighbor cation ordering, was used for the slag (molten oxide) phase. The models based on the Compound Energy Formalism have been developed for the olivine, spinel and pyroxene solid solutions. A simple random mixing model with a polynomial expansion of the excess Gibbs energy was used for the monoxide and corundum solid solutions. A set of self-

consistent Gibbs energy functions was obtained that provides the best possible description of thermodynamic properties and phase equilibria in the chemical system. The literature data are reproduced within experimental error limits. Using optimized model parameters, valuable predictions of phase equilibria in the multicomponent systems have been made.

The detailed conclusions for the optimized systems are summarized as follows:

1. CaO–NiO, MgO–NiO and NiO–SiO_2 systems (CHAPTER 5)

The binary systems CaO–NiO, MgO–NiO and NiO–SiO_2 were optimized as well as the properties of pure solid and liquid NiO. The obtained thermodynamic functions are being used in optimizations of ternary and higher-order subsystems of the Al–Ca–Cr–Fe–Mg–Ni–O–Si system.

The approach employed in the present study is characterized by a combination of critical assessment of experimental data from the literature and thermodynamic modeling with experimental measurements of phase equilibria at a few selected compositions which, on the one hand, can be done most accurately and efficiently and, on the other hand, provide the most important data for thermodynamic modeling.

In particular, the CaO–NiO and MgO–NiO systems were studied by equilibration and quenching followed by electron probe X-ray microanalysis (EPMA) to resolve the discrepancies in the experimental data available in the literature. The miscibility gap in the CaO–NiO monoxide solid solution was measured from 1200 to 1600 °C. The phase equilibria between the MgO–NiO monoxide solution and Ni were studied at fixed oxygen partial pressures from $10^{-7.5}$ to $10^{-13.5}$ atm over the temperature range of 1000 to 1300 °C. These new measurements resolved the discrepancies in the earlier experimental data on phase diagrams, activities and heats of mixing.

The parameters of thermodynamic models for the oxide phases were optimized to reproduce simultaneously the experimental results from the present study and all thermodynamic and phase diagram data for the CaO–NiO, MgO–NiO and NiO–SiO_2 systems from the literature. A set of self-consistent Gibbs energy functions was obtained that provides the best possible description of thermodynamic properties and phase equilibria in these systems. All available data are reproduced within experimental error limits.

2. MgO–NiO–SiO_2 system (CHAPTER 6)

The $MgO–NiO–SiO_2$ system has been studied by a combination of critical assessment of the experimental data from the literature, thermodynamic modeling and experimental measurements of phase equilibria at selected compositions which, on the one hand, can be done most accurately and efficiently and, on the other hand, provide the most important data for thermodynamic modeling.

In particular, tie-lines olivine/monoxide, olivine/proto-pyroxene, liquid/olivine and liquid/cristobalite have been measured to complement the literature data and to resolve some contradictions. The experimental investigation has been carried out over the temperature range from 1400 to 1650 °C using an equilibration and quenching technique followed by EPMA.

The parameters of thermodynamic models for the oxide phases were optimized to reproduce simultaneously the experimental results from the present study and all thermodynamic and phase diagram data for the $MgO–NiO–SiO_2$ system from the literature. A set of self-consistent Gibbs energy functions was obtained that provides the best possible description of thermodynamic properties and phase equilibria in this system. All available data are reproduced within experimental uncertainties.

3. CaO–MgO–NiO–SiO_2 system and its ternary subsystems CaO–NiO–SiO_2 and CaO–MgO–NiO (CHAPTER 7)

The quaternary system $CaO–MgO–NiO–SiO_2$ and its ternary NiO-containing subsystems $CaO–NiO–SiO_2$ and CaO–MgO–NiO have been optimized at a total pressure of 1 atm.

Some discrepancies in the literature data for the $CaO–NiO–SiO_2$ system have been demonstrated. To resolve the conflicts in the literature data, new experimental investigation was carried out at Pyrosearch. The experimental procedure involved equilibration and ultra rapid quenching followed by electron probe X-ray microanalysis (EPMA) of the quenched samples.

The liquid oxide (slag) – solid oxide tie-lines were measured on the isothermal sections of the $CaO–NiO–SiO_2$ phase diagram at temperatures from 1330 to 1500 °C. The new experimental data were compared with the previously published results and discrepancies were clarified.

A simultaneous optimization of all available data in the quaternary $CaO–MgO–NiO–SiO_2$ system and its ternary subsystems $CaO–NiO–SiO_2$ and CaO–MgO–NiO has been performed. New experimental data and previously published experimental results were taken into consideration.

The optimized model parameters for oxide phases reproduce all available data within experimental error limits. A set of self-consistent Gibbs energy functions of the oxide phases in the chemical systems was derived.

4. Al–Fe–O system (CHAPTER 8)

A simultaneous optimization of all available data in the system Al–Fe–O at 1 atm total pressure has been performed. A set of self-consistent Gibbs energy functions of the oxide phases in the Al–Fe–O system was derived. The description of thermodynamic properties data and phase relations were obtained. The optimized model parameters for oxide phases reproduce all available data within experimental error limits.

5. Al–Ni–O system (CHAPTER 9)

Some discrepancies in the literature data for the Al_2O_3–NiO section of the Al–Ni–O system have been demonstrated. To help resolve the conflicts existing in the literature, a new experimental investigation was carried out in this study. The improved experimental technique included equilibration and quenching followed by electron probe X-ray microanalysis (EPMA). The Al_2O_3–NiO section of the Al–Ni–O phase diagram has been measured at 1500 and 1600 °C in air. The solubility of Al_2O_3 in $NiAl_2O_4$ as well as the solubilities of α-Al_2O_3 and NiO in each other have been measured. The experimental measurements provided additional data for a subsequent thermodynamic modeling.

A simultaneous optimization of all available data in the Ni-containing system Al–Ni–O at 1 atm total pressure was performed. New experimental data and previously published experimental results were taken into consideration. The best possible description of thermodynamic properties data and phase relations was obtained. The optimized model parameters for oxide phases reproduce all available data within experimental error limits. A set of self-consistent Gibbs energy functions of the oxide phases in the Al–Ni–O system was derived.

6. Fe–Ni–O system (CHAPTER 10)

Some discrepancies in the literature data for the Fe–Ni–O system were demonstrated. To help resolve the conflicts existing in the literature, a new experimental investigation has been carried out in this study. The compositions of wüstite/alloy and spinel/alloy in equilibrium have been measured at 1200 °C at partial pressures of oxygen $\log_{10}[P(O_2), \text{atm}] = -9$ and -10. The improved

experimental technique included equilibration and quenching followed by electron probe X-ray microanalysis (EPMA). The experimental measurements provided additional data for a subsequent thermodynamic modeling.

A simultaneous optimization of all available data in the Ni-containing system Fe–Ni–O at 1 atm total pressure has been performed. New experimental data and previously published experimental results were taken into consideration. The best possible description of thermodynamic properties data and phase relations has been obtained. The optimized model parameters for oxide phases reproduce all available data within experimental error limits. A set of self-consistent Gibbs energy functions of the oxide phases in the Fe–Ni–O system has been derived.

7. Al–Fe–Ni–O, Al–Mg–Ni–O and Fe–Mg–Ni–O systems (CHAPTER 11)

The thermodynamic database, combined from the Fe–Ni–O, Al–Ni–O, and Mg–Ni–O databases obtained earlier, proved to be capable of predicting thermodynamic properties and phase equilibria in the Al–Fe–Ni–O, Al–Mg–Ni–O and Fe–Mg–Ni–O chemical systems. The available experimental data are in good agreement with model predictions. The only optimized model parameter for the liquid phase reproduces available liquidus data for the Al–Fe–Ni–O system within experimental error limits.

8. Al–Ni–O–Si and Fe–Ni–O–Si systems (CHAPTER 12)

A simultaneous optimization of all available data over a wide range of temperatures and oxygen partial pressures (from air to metallic saturation) in the Al–Ni–O–Si and Fe–Ni–O–Si systems was performed at 1 atm total pressure. Optimized model equations for the thermodynamic properties of all phases reproduce all available thermodynamic and phase-equilibrium data within experimental error limits.

9. Fe–Mg–Ni–O–Si system (CHAPTER 13)

Using the set of optimized model parameters, predictions of phase equilibria in the Fe–Mg–Ni–O–Si system were made and the parameters of the models were verified against available literature data.

10. Ca–Fe–Ni–O and Ca–Fe–Ni–O–Si systems (CHAPTER 14)

Using the set of optimized model parameters, predictions of phase equilibria in the Ca–Fe–Ni–O and Ca–Fe–Ni–O–Si systems were made and the parameters of the models were verified against available literature data.

11.Database

The current database has been incorporated into the existing FactSage databases. By this means, the range of applications of FactSage databases has been expanded and the existing databases have been updated to describe the most recent and accurate experimental data of interest to industrial operations.

The obtained database along with software for Gibbs energy minimization allows the prediction of liquidus and solidus phase equilibria as well as the thermodynamic properties under conditions, such as range of compositions, temperatures and oxygen partial pressures, which are most useful for metallurgical operations and engineering practice.

As for future work, Cr and Co could be added to the database, Cr being one of the major components in laterite ores and Co being one of the impurities in the final product of ore processing. Also, the database could be extended to sulphide systems and used to calculate matte/slag/metal equilibria.

LIST OF REFERENCES

[1] C. W. Bale, *et al.*, "FactSage thermochemical software and databases - recent developments," *Calphad,* vol. 33, pp. 295-311, 2009.

[2] J. Chen, "Fundamental Studies on Reduction Roasting of Saprolite Ore in the Caron Process," Ph. D. Thesis, The University of Queensland, 2013.

[3] R. Sridhar, J. M. Toguri, and S. Simeonov, "Copper Losses and Thermodynamic Considerations in Copper Smelting," *Metall. Mater. Trans. B,* vol. 28B, pp. 191-200, 1997.

[4] R. A. Bergman, "Nickel production from low-iron laterite ores: Process descriptions," *CIM Bull.,* vol. 96, pp. 127-138, 2003.

[5] M. A. Rhamdhani, P. C. Hayes, and E. Jak, "Nickel laterite Part 1 - microstructure and phase characterizations during reduction roasting and leaching," *Trans. Inst. Min. Metall., Sect. C,* vol. 118, pp. 129-145, 2009.

[6] M. A. Rhamdhani, P. C. Hayes, and E. Jak, "Nickel laterite Part 2 - thermodynamic analysis of phase transformations occurring during reduction roasting," *Trans. Inst. Min. Metall., Sect. C,* vol. 118, pp. 146-155, 2009.

[7] A. D. Pelton, S. A. Decterov, G. Eriksson, C. Robelin, and Y. Dessureault, "The Modified Quasichemical Model. I - Binary Solutions," *Metall. Mater. Trans. B,* vol. 31B, pp. 651-659, 2000.

[8] A. D. Pelton and P. Chartrand, "The Modified Quasichemical Model. II - Multicomponent Solutions," *Metall. Mater. Trans. A,* vol. 32A, pp. 1355-1360, 2001.

[9] M. Hillert, B. Jansson, and B. Sundman, "Application of the Compound-Energy Model to Oxide Systems," *Z. Metallkd.,* vol. 79, pp. 81-87, 1988.

[10] *The observatory of economic complexity*: http://atlas.media.mit.edu/explore/stacked/export/show/all/7501/, 2013.

[11] J. Kyle, "Nickel laterite processing technologies – where to next?," in *ALTA Nickel/Cobalt/Copper Conference, Perth, Western Australia*, 2010, pp. 1-36.

[12] F. L. Prado, "Sixty years of Caron: current assessment," in *Int. Laterite Nickel Symp., Proc. Symp.*, 2004, pp. 593-598.

[13] A. R. Burkin, *Critical Reports on Applied Chemistry: Extractive Metallurgy of Nickel* vol. 17: John Wiley & Sons, Chichester, UK, 1987.

[14] M. G. King, "Nickel laterite technology - finally a new dawn?," *JOM,* vol. 57, pp. 35-39, 2005.

[15] A. D. Dalvi, W. G. Bacon, and R. C. Osborne, "The past and the future of nickel laterites," in *PDAC International Convention, Trade Show & Investors Exchange*, 2004, pp. 1-27.

[16] K. S. Rao, "Identifying some potential future hydrometallurgical processes in treatment of nickel laterites," in *Energy Technol., Proc. Symp.*, 2010, pp. 111-118.

[17] C. W. Bale, *et al.*, "FactSage Thermochemical Software and Databases," *Calphad,* vol. 26, pp. 189-228, 2002.

[18] E. Jak, P. C. Hayes, and H.-G. Lee, "Improved methodologies for the determination of high temperature phase equilibria," *Met. Mater. (Seoul),* vol. 1, pp. 1-8, 1995.

[19] E. Jak and P. C. Hayes, "Phase equilibria determination in complex slag systems," in *VII International Conference on Molten Slags Fluxes and Salts*, 2004, p. 85.

[20] S. Nikolic, P. C. Hayes, and E. Jak, "Phase Equilibria in Ferrous Calcium Silicate Slags: Part I. Intermediate Oxygen Partial Pressures in the Temperature Range 1200 °C to 1350 °C," *Metall. Trans. B,* vol. 39B, pp. 179-188, 2008.

[21] M. A. Rhamdhani, P. C. Hayes, and E. Jak, "Subsolidus Phase Equilibria of the Fe-Ni-O System," *Metall. Mater. Trans. B,* vol. 39B, pp. 690-701, 2008.

[22] E. Jak, H. G. Lee, P. Wu, A. D. Pelton, and P. C. Hayes, "Phase Equilibria in the System PbO-ZnO-SiO_2," in *6th AusImm Extractive Metallurgy Conference, Brisbane*, 1994, pp. 253-259.

[23] U. R. Kattner, "The Thermodynamic Modeling of Multicomponent Phase Equilibria," *JOM,* vol. 49, pp. 14-19, 1997.

[24] O. Redlich and A. T. Kister, "Thermodynamics of Nonelectrolytic Solutions. Algebraic Representation of Thermodynamic Properties and the Classification of Solutions," *Ind. Ing. Chem.,* vol. 40, pp. 345-348, 1948.

[25] L. Kaufman and H. Bernstein, *Computer Calculation of Phase Diagrams; With Special Reference to Refractory Metals (Refractory Materials, Vol. 4)*. New York: Academic, 1970.

[26] A. D. Pelton and M. Blander, "Computer-Assisted Analysis of the Thermodynamic Properties and Phase Diagrams of Slags," in *Proceedings of the Second International Symposium on Metallurgical Slags and Fluxes, TMS-AIME, Warrendale, PA*, 1984, pp. 281-294.

[27] A. D. Pelton and M. Blander, "Thermodynamic Analysis of Ordered Liquid Solutions by a Modified Quasi-Chemical Approach. Application to Silicate Slags," *Metall. Trans. B,* vol. 17B, pp. 805-815, 1986.

[28] A. D. Pelton, "A General "Geometric" Thermodynamic Model for Multicomponent Solutions," *Calphad,* vol. 25, pp. 319-328, 2001.

[29] W. G. I. Davenport, M. King, M. Schlesinger, and A. K. Biswas, *Extractive metallurgy of copper, 4th edition*: Pergamon Press, Oxford, United Kingdom, 2002.

[30] K. Mills, "The estimation of slag properties," 2011.

[31] T. I. Barry, A. T. Dinsdale, and J. A. Gisby, "Predictive Thermochemistry and Phase Equilibria of Slags," *JOM - J.Minerals, Metals & Materials Soc.,* vol. 45, pp. 32-38, 1993.

[32] *MTDATA*: Teddington, www.npl.co.uk/mtdata, 2013.

[33] *Thermo-calc*: Stockholm, www.thermocalc.com, 2013.

[34] *FactSage*: Ecole Polytechnique, Montréal, http://www.factsage.com/, 2008.

[35] M. Hillert, B. Jansson, B. Sundman, and J. Agren, "A two-sublattice model for molten solutions with different tendency for ionization," *Metall. Trans. A*, vol. 16A, pp. 261-266, 1985.

[36] F. Sommer, "Association model for the description of the thermodynamic functions of liquid alloys. I. Basic concepts," *Z. Metallkd.*, vol. 73, pp. 72-76, 1982.

[37] J. Lehmann, H. Gaye, and F. Bonnet, "Thermodynamics applied to ferro-alloys smelting," pp. 300-315.

[38] P. Chartrand and A. D. Pelton, "The Modified Quasichemical Model. III - Two Sublattices," *Metall. Mater. Trans. A*, vol. 32A, pp. 1397-1407, 2001.

[39] A. D. Pelton, P. Chartrand, and G. Eriksson, "The modified Quasichemical Model. IV - Two Sublattice Quadruplet Approximation," *Metall. Mater. Trans. A*, vol. 32A, pp. 1409-1415, 2001.

[40] C. M. B. Henderson, J. M. Charnock, and D. A. Plant, "Cation occupancies in Mg, Co, Ni, Zn, Al ferrite spinels: a multi-element EXAFS study," *J. Phys.: Condens. Matter*, vol. 19, pp. 076214/1-076214/25, 2007.

[41] S. A. Decterov, E. Jak, P. C. Hayes, and A. D. Pelton, "Experimental Study and Thermodynamic Optimization of the Fe-Zn-O System," *Metall. Mater. Trans. B*, vol. 32 B, pp. 643-657, 2001.

[42] I.-H. Jung, S. A. Decterov, and A. D. Pelton, "Critical Thermodynamic Evaluation and Optimization of the Fe-Mg-O System," *J. Phys. Chem. Solids*, vol. 65, pp. 1683-1695, 2004.

[43] I.-H. Jung, S. A. Decterov, and A. D. Pelton, "Critical Thermodynamic Evaluation and Optimization of the $MgO-Al_2O_3$, $CaO-MgO-Al_2O_3$ and $MgO-Al_2O_3-SiO_2$ Systems," *J. Phase Equilib.*, vol. 25, pp. 329-345, 2004.

[44] M. Hillert and M. Jarl, "A Model for Alloying Effects in Ferromagnetic Metals," *Calphad*, vol. 2, pp. 227-238, 1978.

[45] I.-H. Jung, S. A. Decterov, and A. D. Pelton, "Critical Thermodynamic Evaluation and Optimization of the $CaO-MgO-SiO_2$ System," *J. Eur. Ceram. Soc.*, vol. 25, pp. 313-333, 2005.

[46] I.-H. Jung, S. A. Decterov, and A. D. Pelton, "Critical Thermodynamic Evaluation and Optimization of the $FeO-Fe_2O_3-MgO-SiO_2$ System," *Metall. Mater. Trans. B*, vol. 38B, pp. 877-889, 2004.

[47] T. Hidayat, D. Shishin, S. A. Decterov, and E. Jak, "Critical thermodynamic evaluation and optimization of the $CaO-FeO-Fe_2O_3-SiO_2$ system," *submitted to Metall. Trans. B*, 2012.

[48] R. D. Shannon, "Revised effective ionic radii and systematic studies of interatomic distances in halides and chalcogenides," *Acta Crystallogr.*, vol. A32, pp. 751-767, 1976.

[49] P. Shi, S. K. Saxena, Z. Zang, and B. Sundman, "Thermodynamics of the Ca-Mg-Fe-Al-Si-O Pyroxenes: 1. Theoretical Model and Assessment of the Ca-Mg-Si-O System," *Calphad,* vol. 18, pp. 47-69, 1994.

[50] P. Wu, G. Eriksson, A. D. Pelton, and M. Blander, "Prediction of the Thermodynamic Properties and Phase Diagrams of Silicate Systems - Evaluation of the FeO-MgO-SiO_2 System," *ISIJ Int.,* vol. 33, pp. 26-35, 1993.

[51] V. Prostakova, J. Chen, E. Jak, and S. A. Decterov, "Experimental study and thermodynamic optimization of the CaO-NiO, MgO-NiO and NiO-SiO_2 systems," *CALPHAD: Comput. Coupling Phase Diagrams Thermochem.,* vol. 37, pp. 1-10, 2012.

[52] M. Valix, J. Y. Tang, and W. H. Cheung, "The effects of mineralogy on the biological leaching of nickel laterite ores," *Miner. Eng.,* vol. 14, pp. 1629-1635, 2001.

[53] M. H. Caron, "Fundamental and practical factors in ammonia leaching of nickel and cobalt ores," *J. Met.,* vol. 188, pp. 67-90, 1950.

[54] E. Jak, B. Zhao, S. Nikolic, and P. C. Hayes, "Experimental Measurement and Prediction of Complex Phase Equilibria in Industrial Non-ferrous Slag Systems," in *European Metallurgy Conference*, 2007, p. 1789.

[55] D.-H. Woo, H.-G. Lee, and I.-H. Jung, "Thermodynamic modeling of the NiO-SiO_2, MgO-NiO, CaO-NiO-SiO_2, MgO-NiO-SiO_2, CaO-MgO-NiO and CaO-MgO-NiO-SiO_2 systems," *J. Eur. Ceram. Soc.,* vol. 31, pp. 43-59, 2011.

[56] J. R. Taylor and A. T. Dinsdale, "A thermodynamic assessment of the Ni-O, Cr-O and Cr-Ni-O systems using the Ionic Liquid and Compound Energy models," *Z. Metallkd.,* vol. 81, pp. 354-366, 1990.

[57] I. Barin, *Thermodynamic Data for Pure Substances*: VCH, Weinheim, Germany, 1989.

[58] L. V. Gurvich, V. S. Yorish, and V. S. Yungman, "IVTANTERMO: Data bank on the thermodynamic properties of individual substances," *CODATA Bulletin,* vol. 58, pp. 12-13, 1985.

[59] L. V. Gurvich, V. S. Iorish, and I. V. Veitz, *IVTANTERMO: A Thermodynamic Database and Software System for the Personal Computer: User's Guide*: CRC, Boca Raton, FL, 1993.

[60] J. R. Tomlinson, L. Domash, R. G. Hay, and C. W. Montgomery, "The high-temperature heat content of nickel oxide," *J. Am. Chem. Soc.,* vol. 77, pp. 909-910, 1955.

[61] E. G. King, A. U. Christensen, and Jr., "Heat Contents above 298.15 K of Oxides of Cobalt and Nickel," *J. Am. Chem. Soc.,* vol. 80, pp. 1800-1801, 1958.

[62] A. F. Kapustinskii and K. A. Novosel'tsev, "Heat capacities of nickel suboxide. Free energy of formation of nickel suboxide," *Zh. Fiz. Khim.,* vol. 11, pp. 61-67, 1938.

[63] V. P. Zhuze, O. N. Novruzov, and A. I. Shelykh, "Thermal diffusivity in the region of continuous phase transitions," *Fiz. Tverd. Tela,* vol. 11, pp. 1287-1296, 1969.

[64] F. B. Lewis and N. H. Saunders, "Thermal conductivity of nickel(II) oxide and cobalt(II) oxide at the Neel temperature," *J. Phys. C,* vol. 6, pp. 2525-2532, 1973.

[65] M. Massot, *et al.*, "Critical behavior of CoO and NiO from specific heat, thermal conductivity, and thermal diffusivity measurements," *Phys. Rev. B,* vol. 77, p. 134438, 2008.

[66] H. Seltz, B. J. DeWitt, and H. J. McDonald, "The heat capacity of nickel oxide from 68 to 298 K and the thermodynamic properties of the oxide," *J. Am. Chem. Soc.,* vol. 62, pp. 88-89, 1940.

[67] E. G. King, "Heat Capacities at Low Temperatures and Entropies at 298.15 K of Nickelous Oxide, Cobaltous Oxide and Cobalt Spinel," *J. Am. Chem. Soc.,* vol. 79, pp. 2399-2400, 1957.

[68] H. Wartenberg and E. Prophet, "Melting-Point Diagrams of Highly Refractory Oxides. V. Systems with Magnesia," *Z. Anorg. Allgem. Chem.,* vol. 208, pp. 369-379, 1932.

[69] M. H. Tikkanen, *Private communication*.

[70] D. E. Smith, T. Y. Tien, and L. H. Van Vlack, "The System NiO-CaO," *J. Am. Ceram. Soc.,* vol. 52, pp. 459-460, 1969.

[71] S. Raghavan, "Terminal solid solubilities at 1313 K in the system calcium oxide-nickel oxide using a solid-state galvanic cell," *J. Mater. Sci. Lett.,* vol. 7, pp. 402-4, 1988.

[72] G. Rog, A. Kozlowska-Rog, and M. M. Bucko, "Determination of the activities in {xCaO + (1 - x)NiO} by solid-electrolyte galvanic cells in the temperature range 1123 K to 1313 K," *J. Chem. Thermodyn.,* vol. 30, pp. 43-47, 1998.

[73] E. M. Levin, C. R. Robbins, and H. F. McMurdie, *Phase Diagrams for Ceramists*: American Ceramic Society, 1964.

[74] S. Holgersson and A. Karlsson, "X-ray examination of a system of mixed crystals with monoxide components," *Z. Anorg. Allg. Chem.,* vol. 182, pp. 255-71, 1929.

[75] H. D. Nuessler and O. Kubaschewski, "Thermochemistry of the system magnesium oxide-nickel(II) oxide," *Z. Phys. Chem.,* vol. 121, pp. 187-191, 1980.

[76] P. K. Davies and A. Navrotsky, "Thermodynamics of Solid Solution Formation in NiO-MgO and NiO-ZnO," *J. Solid State Chem.,* vol. 38, pp. 264-276, 1981.

[77] W. C. J. Hahn and A. Muan, "Activity measurements in oxide solid solutions: the systems NiO-MgO and NiO-MnO in the temperature interval 1100-1300 °C," *J. Phys. Chem. Solids,* vol. 19, pp. 338-348, 1961.

[78] L. G. Evans and A. Muan, "Activity-composition relations in solid solutions and stabilities of end-member compounds in the system MgO-NiO-TiO_2 in contact with metallic nickel at 1400C," *Thermochim. Acta,* vol. 2, pp. 121-134, 1971.

[79] S. M. Ariya, N. V. Borisova, and M. P. Morozova, "Measurement of nickel monoxide activity in nickel monoxide-magnesium oxide solid solutions at 900 and 1000 ^{o}C," *Russ. J. Phys. Chem.,* vol. 46, pp. 123-124, 1972.

[80] S. Seetharaman and K. P. Abraham, "Thermodynamic activities of nickel oxide in nickel oxide-magnesium oxide solid solutions," *Indian J. Technol.,* vol. 6, pp. 123-124, 1968.

[81] C. Petot, G. Petot-Ervas, and M. Rigaud, "Thermodynamic properties of solid solutions of the oxide of magnesium and nickel," *Can. Metall. Q.,* vol. 10, pp. 203-205, 1971.

[82] H. Paulsson, "Activities of nickel(II) oxide in (nickel, magnesium) oxide (Ni, Mg)O solid solutions," *Chem. Scr.*, vol. 19, pp. 116-117, 1982.

[83] Y. Shirane, S. Nabika, S. Sakamoto, and I. Nakashima, "Activity measurements in the oxide solid solutions of nickel oxide-magnesia and nickel oxide-magnesia-silica systems in the temperature range between 1073 and 1273 K," *Int. J. Miner. Process.*, vol. 19, pp. 237-251, 1987.

[84] G. M. Kale, "Activity-composition relations in the nickel oxide-magnesium oxide system at 1300 K by the solid-state galvanic cell technique," *J. Am. Ceram. Soc.*, vol. 74, pp. 2209-2213, 1991.

[85] A. Jakobsson, S. Du, and S. Seetharaman, "Thermodynamic study of the nickel oxide-magnesia system in the temperature range 1073 to 1473 K by a galvanic cell techniques," *Metall. Trans. B*, vol. 24B, pp. 1023-1030, 1993.

[86] E. R. Kreidler and H. D. Park, "Activity of NiO in (Ni,Mg)O solid solutions," *J. Am. Ceram. Soc.*, vol. 77, pp. 2491-2493, 1994.

[87] S. Mukhopadhyay and K. T. Jacob, "Tie Lines and Activities in the System NiO-MgO-SiO_2 at 1373 K," *J. Phase Equilib.*, vol. 16, pp. 243-253, 1995.

[88] J. W. Greig, "Immiscibility in Silicate Melts. Part II," *Am. J. Sci., 5th Ser.*, vol. 13, pp. 133-154, 1927.

[89] A. E. Ringwood, "Melting relationships of nickel-magnesium olivines and some geochemical implications," *Geochim. Cosmochim. Acta*, vol. 10, pp. 297-303, 1956.

[90] B. Phillips, J. J. Hutta, and I. Warshaw, "Phase Equilibria in the System NiO-Al_2O_3-SiO_2," *J. Am. Ceram. Soc.*, vol. 46, pp. 579-83, 1963.

[91] S. A. Babayan, "Stable liquation in iron(II) oxide-silicon dioxide, cobalt(II) oxide-silicon dioxide, and nickel(II) oxide-silicon dioxide systems," *Arm. Khim. Zh.*, vol. 28, pp. 533-539, 1975.

[92] H. S. C. O'Neill, "Free Energies of Formation of NiO, CoO, Ni_2SiO_4, and Co_2SiO_4," *Am. Mineral.*, vol. 72, pp. 280-291, 1987.

[93] M. W. Grutzeck and A. Muan, "Phase Relations at Liquidus Temperatures in the System MgO-NiO-SiO_2," *J. Am. Ceram. Soc.*, vol. 71, pp. 638-643, 1988.

[94] M. W. Grutzeck and A. Muan, "Phase relations in the system iron oxide-NiO-SiO_2 under strongly reducing conditions," *J. Am. Ceram. Soc.*, vol. 75, pp. 1351-1356, 1992.

[95] H. Watanabe, "Thermochemical Properties of Synthetic High-Pressure Compounds Relevant to the Earth's Mantle," in *High-Pressure Res. Geophys.*, S. Akimoto and M. H. Manghnani, Eds., ed: Center for Academic Publications, Tokyo, 1982, pp. 441-464.

[96] R. A. Robie, B. S. Hemingway, J. Ito, and K. M. Krupka, "Heat Capacity and Entropy of Ni_2SiO_4-Olivine from 5 to 1000 K and Heat Capacity of Co_2SiO_4 from 360 to 1000 K," *Am. Mineral.*, vol. 69, pp. 1096-1101, 1984.

[97] M. Hirschmann, "Thermodynamics of multicomponent olivines and the solution properties of $(Ni,Mg,Fe)_2SiO_4$ and $(Ca,Mg,Fe)_2SiO_4$ olivines," *Am. Mineral.*, vol. 76, pp. 1232-1248, 1991.

[98] A. Navrotsky, "Nickel(II) silicate enthalphy of the olivine-spinel transition by solution calorimetry at 713 ^{o}C," *Earth Planet. Sci. Lett.,* vol. 19, pp. 471-475, 1973.

[99] T. Sugawara and M. Akaogi, "Calorimetric measurements of fusion enthalpies for Ni_2SiO_4 and Co_2SiO_4 olivines and application to olivine-liquid partitioning," *Geochim. Cosmochim. Acta,* vol. 67, pp. 2683-2693, 2003.

[100] A. Navrotsky, "Thermodynamics of Formation of the Silicates and Germanates of Some Divalent Transition Metals and of Magnesium," *J. Inorg. Nucl. Chem.,* vol. 33, pp. 4035-4050, 1971.

[101] R. W. Taylor and H. Schmalzried, "The Free Energy of Formation of Some Titanates, Silicates, and Magnesium Aluminate from Measurements Made with Galvanic Cells Involving Solid Electrolytes," *J. Phys. Chem.,* vol. 68, pp. 2444-2449, 1964.

[102] V. A. Levitskii, Y. G. Golovanova, S. G. Popov, and V. N. Chentsov, "Thermodynamics of binary oxide systems. Thermodynamic properties of nickel orthosilicate," *Russ. J. Phys. Chem.,* vol. 49, pp. 971-974, 1975.

[103] G. Rog and G. Borchardt, "Thermodynamocs of Nickel Orthosilicates," *J. Chem. Thermodyn.,* vol. 16, pp. 1103-1105, 1984.

[104] K. T. Jacob, G. M. Kale, A. Ramachandran, and A. K. Shukla, "Gibbs energy of formation of nickel orthosilicate (Ni_2SiO_4)," *High Temp. Mater. Processes,* vol. 7, pp. 141-148, 1986.

[105] G. Rog, A. Kozlowska-Rog, M. Bucko, and E. Glowacz, "Determination of the standard molar Gibbs free energies of formation of the silicates of cobalt and nickel by solid-state galvanic cells involving the CaF_2-based composite electrolyte," *J. Chem. Thermodyn.,* vol. 32, pp. 931-935, 2000.

[106] B. G. Lebedev and V. A. Levitskii, "Equilibrium of nickel orthosilicate with carbon monoxide at high temperatures," *Russ. J. Phys. Chem.,* vol. 35, pp. 1380-1382, 1961.

[107] A. Burdese, F. Abbattista, and R. Damiani, "Reduction equilibrium of iron, cobalt, and nickel silicate," *Metall. Ital.,* vol. 55, pp. 557-559, 1963.

[108] F. E. Campbell and P. L. Roeder, "Stability of olivine and pyroxene in the nickel-magnesium-silicon-oxygen system," *Am. Mineral.,* vol. 53, pp. 257-268, 1968.

[109] N. L. Dilaktorskii, "The solubility of nickel oxide in silicates and aluminosilicates," *Trudy Tret'ego Soveshchaniya Eksptl. Mineral i Petrog. Inst. Geol. Nauk,* pp. 79-82, 1940.

[110] Y. Shirane, "Phase Relations in the NiO-MgO-SiO_2 System at 1400 ^{o}C," *J. Japan Inst. Metals,* vol. 39, pp. 908-916, 1975.

[111] V. Rajamani, G. E. Brown, and C. T. Prewitt, "Cation Ordering in Ni-Mg Olivine," *Am. Mineral.,* vol. 60, pp. 292-299, 1975.

[112] D. L. Bish, "Cation Ordering in Synthetic and Natural Ni-Mg Olivine," *Am. Mineral.,* vol. 66, pp. 770-776, 1981.

[113] D. Bostroem, "Single-crystal x-ray diffraction studies of synthetic nickel-magnesium olivine solid solutions," *Am. Mineral.,* vol. 72, pp. 965-972, 1987.

[114] D. Bostroem, "Cation ordering at 1300 ^{o}C in the (nickel,magnesium)-olivine solid solution series," *Acta Chem. Scand.,* vol. 43, pp. 116-20, 1989.

[115] G. Ottonello, A. Della Giusta, and G. M. Molin, "Cation ordering in nickel-magnesium olivines," *Am. Mineral.,* vol. 74, pp. 411-21, 1989.

[116] X. Hu, K. Langer, and D. Bostroem, "Polarized electronic absorption spectra and nickel-magnesium partitioning in olivines $(Mg_{1-x}Ni_x)_2[SiO_4]$," *Eur. J. Mineral.,* vol. 2, pp. 29-41, 1990.

[117] J. Chen, R. Li, J. B. Parise, and D. J. Weidner, "Pressure-induced ordering in $(Ni,Mg)_2SiO_4$ olivine," *Am. Mineral.,* vol. 81, pp. 1519-1522, 1996.

[118] C. M. B. Henderson, S. A. T. Redfern, R. I. Smith, K. S. Knight, and J. M. Charnock, "Composition and temperature dependence of cation ordering in Ni-Mg olivine solid solutions: a time-of-flight neutron powder diffraction and EXAFS study," *Am. Mineral.,* vol. 86, pp. 1170-1187, 2001.

[119] M. M. Hirschmann, "Studies of nickel and minor elements in olivine and in silicate liquids," Univ. Washington, Seattle, WA, USA, 1992.

[120] G. Ottonello and R. Morlotti, "Thermodynamics of the (nickel+magnesium) olivine solid solution," *J. Chem. Thermodyn.,* vol. 19, pp. 809-818, 1987.

[121] D. Bostroem and E. Rosen, "Determination of activity -composition relations in nickel magnesium silicate ($(Ni,Mg)_2SiO_4$) solid solutions at 1200-1600 K by solid-state emf measurements," *Acta Chem. Scand., Ser. A,* vol. A42, pp. 149-55, 1988.

[122] S. Seifert and H. S. C. O'Neill, "Experimental determination of activity-composition relations in Ni_2SiO_4-Mg_2SiO_4 and Co_2SiO_4-Mg_2SiO_4 olivine solid solutions at 1200 K and 0.1 MPa and 1573 K and 0.5 GPa," *Geochim. Cosmochim. Acta,* vol. 51, pp. 97-104, 1987.

[123] V. Prostakova, J. Chen, E. Jak, and S. Decterov, "Experimental study and thermodynamic optimization of the MgO-NiO-SiO_2 system," *J. Chem. Thermodyn.,* vol. 62, pp. 43-55, 2013.

[124] E. B. Pretorius and A. Muan, "Stability of $CaNiSi_2O_6$(Niopside) and Activity-compostition relations of $CaMgSi_2O_6$-$CaNiSi_2O_6$ solid solutions at 1350 ^{o}C," *J. Am. Ceram. Soc.,* vol. 75, pp. 1458-1462, 1992.

[125] G. M. Biggar, "The System CaO-NiO-SiO_2," *J. Am. Ceram. Soc.,* vol. 52, pp. 316-317, 1969.

[126] P. Wu, G. Eriksson, and A. D. Pelton, "Critical Evaluation and Optimization of the Thermodynamic Properties and Phase Diagrams of the Calcia-Iron(II) Oxide, Calcia-Magnesia, Calcia-Manganese(II) Oxide, Iron(II) Oxide-Magnesia, Iron(II) Oxide-Manganese(II) Oxide, and Magnesia-Manganese(II) Oxide Systems," *J. Am. Ceram. Soc.,* vol. 76, pp. 2065-2075, 1993.

[127] G. Eriksson, P. Wu, M. Blander, and A. D. Pelton, "Critical Evaluation and Optimisation of the Thermodynamic Properties and Phase Diagrams of the MnO-SiO_2 and CaO-SiO_2 Systems," *Can. Metall. Q.,* vol. 33, pp. 13-21, 1994.

[128] L. Gjessing, "Crystal structure of metasilicates," *Nor. Geol. Tidsskr.*, vol. 20, pp. 265-267, 1941.

[129] A. Navrotsky and W. E. Coons, "Thermochemistry of some pyroxenes and related compounds," *Geochim. Cosmochim. Acta*, vol. 40, pp. 1281-1288, 1976.

[130] S. Mukhopadhyay and K. T. Jacob, "Phase equilibria in the system NiO-CaO-SiO_2 and Gibbs energy of formation of $CaNiSi_2O_6$," *Metall. Mater. Trans. A*, vol. 26A, pp. 2311-2315, 1995.

[131] E. B. Pretorius and A. Muan, "Activity of Nickel(II) Oxide in Silicate Melts," *J. Am. Ceram. Soc.*, vol. 75, pp. 1490-1496, 1992.

[132] W. B. White, G. J. McCarthy, and B. E. Scheetz, "Optical spectra of chromium, nickel, and cobalt-containing pyroxenes," *Am. Mineral.*, vol. 56, pp. 72-89, 1971.

[133] D. P. Wright and A. Navrotsky, "A thermochemical study of the distribution of cobalt and nickel between diopsidic pyroxene and melt," *Geochim. Cosmochim. Acta*, vol. 49, pp. 2385-2393, 1985.

[134] M. S. I. Team and W. Martienssen, *Ternary Alloy Systems. Phase Diagrams, Crystallographic and Thermodynamic Data. Part 3 Selected Systems from Al-B-Fe to C-Co-Fe* vol. 11D: Editors: Günter Effenberg, Svitlana Ilyenko, Springer, 2008.

[135] T. F. W. Barth and E. Posnjak, "Spinel structures: with and without variate atom equipoints," *Z. Kristallogr., Kristallgeom., Kristallphys., Kristallchem.*, vol. 82, pp. 325-341, 1932.

[136] F. C. Romeijn, "Physical and crystallographic properties of some spinels," *Philips Res. Rep.*, vol. 8, pp. 304-342, 1953.

[137] W. W. Roth, "Magnetic Properties of Normal Spinels with only A-A Interactions," *J. Phys.*, vol. 25, pp. 507-515, 1964.

[138] M. J. Rossiter, "The Mossbauer Spectra of Some Spinel Oxides Containing Iron," *J. Phys. Chem. Solids*, vol. 26, pp. 775-9, 1965.

[139] C. M. Yagnik and H. B. Mathur, "A Mossbauer and X-ray Diffraction Study on the Cation Distribution in $FeAl_2O_4$," *Journal of Physics C, Proceedings of the Physical Society (Solid State Physics)*, vol. 1, pp. 469-472, 1968.

[140] I. Gaballah, A. Courtois, F. Jeannot, and C. Gleitzer, "Distribution Cationique dans $FeAl_2O_4$ en Fonction de Divers Traitements," *C. R. Hebd. Seances Acad. Sci., Ser. C*, vol. 280, pp. 1367-1370, 1975.

[141] F. Chassagneux and A. Rousset, "Preparation et Etude Structurale des Spinelles $FeAl_{2-2z}Cr_{2z}O_4$," *J. Solid State Chem.*, vol. 16, pp. 161-166, 1976.

[142] B. L. Dickson and G. Smith, "Low-Temperature Optical Absorption and Mossbauer Spectra of Staurolite and Spinel," *Can. Mineral.*, vol. 14, Pt. 2, pp. 206-215, 1976.

[143] A. A. Karabtsov, V. O. Khurlolozhkin, and V. S. Urusov, "X-ray diffraction of cation distribution in positions depending on the composition of spinels (Mg,Fe) $(Fe,Al,Cr)_2O_4$," *Mineral. Zh.*, vol. 2, pp. 24-32, 1980.

[144] M. D. Osborn, M. E. Fleet, and G. M. Bancroft, "Fe^{2+}-Fe^{3+} Ordering in Chromite and Cr-Bearing Spinels," *Contrib. Mineral. Petrol.*, vol. 77, pp. 251-5, 1981.

[145] R. J. Hill, "X-Ray Powder Diffraction Profile Refinement of Synthetic Hercynite," *Am. Mineral.*, vol. 69, pp. 937-942, 1984.

[146] S. B. Bohlen, W. A. Dollase, and V. J. Wall, "Calibration and Applications of Spinel Equilibria in the System FeO-Al_2O_3-SiO_2," *J. Petrol.*, vol. 27, pp. 1143-1156, 1986.

[147] J. Nell, B. J. Wood, and T. O. Mason, "High Temperature Cation Distribution Fe_3O_4-$MgAl_2O_4$-$MgFe_2O_4$-$FeAl_2O_4$ Spinels from Thermopower and Conductivity Measurements," *Am. Mineral.*, vol. 74, pp. 339-351, 1989.

[148] J. Nell and B. J. Wood, "High-Temperature Electrical Measurements and Thermodynamic Properties of Fe_3O_4-$FeCr_2O_4$-$MgCr_2O_4$-$FeAl_2O_4$ Spinels," *Am. Mineral.*, vol. 76, pp. 405-426, 1991.

[149] L. Larsson, H. S. C. O'Neill, and H. Annersten, "Crystal Chemistry of Synthetic Hercynite ($FeAl_2O_4$) from XRD Structural Refinements and Moessbauer Spectroscopy," *Eur. J. Mineral.*, vol. 6, pp. 39-51, 1994.

[150] R. J. Harrison, S. A. T. Redfern, and H. S. C. O'Neill, "The Temperature Dependence of the Cation Distribution in Synthetic Hercynite ($FeAl_2O_4$ from In-Situ Neutron Structure Refinements," *Am. Mineral.*, vol. 83, pp. 1092-1099, 1998.

[151] A. C. Turnock and H. P. Eugster, "Fe-Al Oxides: Phase Relationsships below 1000 ^oC," *J. Petrol.*, vol. 3, pp. 533-565, 1962.

[152] G. Dehe, B. Seidel, C. Michalk, and K. Melzer, "Moessbauer Effect Study of Iron-Aluminum Oxide ($Fe_{3-x}Al_xO_4$)," in *Proc. - Int. Conf. Moessbauer Spectrosc., 5th*, Nucl. Inf. Cent.: Prague, Czech., 1975, pp. 106-113.

[153] J. M. Robertson and A. J. Pointon, "The Cation Distribution of Nickel Ferrite," *Solid State Commun.*, vol. 4, pp. 257-259, 1966.

[154] V. Raghavan, "Al-Fe-O (Aluminum-Iron-Oxygen)," *J. Phase Equilib. Diffus.*, vol. 31, p. 367, 2010.

[155] L. M. Atlas and W. K. Sumida, "Solidus, Subsolidus, and Subdissociation Phase Equilibria in the System Fe-Al-O," *J. Am. Ceram. Soc.*, vol. 41, pp. 150-160, 1958.

[156] E. G. King, "Heat Capacities at Low Temperatures and Entropies of Five Spinel Minerals," *J. Phys. Chem.*, vol. 60, pp. 410-412, 1956.

[157] S. Klemme and J. C. van Miltenburg, "Thermodynamic Properties of Hercynite ($FeAl_2O_4$) Based on Adiabatic Calorimetry at Low Temperatures," *Am. Mineral.*, vol. 88, pp. 68-72, 2003.

[158] B. G. Lebedev, "Thermodynamics of the Reaction of Hercynite with Carbon Monoxide," *Izv. Akad. Nauk SSSR, Otd. Tekh. Nauk, Met. Toplivo*, vol. 6, pp. 7-11, 1962.

[159] I. A. Novokhatskii and L. M. Lenev, "Thermodynamics of iron aluminate reduction with carbon monoxide," *Akad. nauk SSSR Isvest. Otd. Tekh. Met. i Gornoe Delo*, vol. 6, p. 47, 1963.

[160] V. Cirilli, "The reduction equilibrium of ferric oxides by carbon monoxide in the presence of alumina," *Gazzetta Chimica Italiana,* vol. 76, pp. 339-344, 1946.

[161] T. N. Rezukhina, V. A. Levitskii, and P. Ozhegov, "Thermodynamic Properties of Iron Aluminate," *Russ. J. Phys. Chem.,* vol. 37, p. 358, 1963.

[162] N. S. Zabeivorota, A. A. Lykasov, and G. G. Mikhailov, "Free Energy of Formation of Iron Aluminate," *Izv. Akad. Nauk SSSR, Neorg. Mater.,* vol. 16, pp. 551-552, 1980.

[163] L. M. Lenev, I. A. Novokhatskii, and A. V. Gorokh, "Thermodynamic Properties of Some Spinellides and Titanates," in *Eksp. Issled. Mineraloobrazov. Sukhikh Okisnykh Silikat. Sist.,* 1972, pp. 107-111.

[164] J. C. Chan, C. B. Alcock, and K. T. Jacob, "Electrochemical Measurement of the Oxygen Potential of the System Iron-Alumina-Hercynite in The Temperature Range 750 to 1600 C," *Can. Metall. Q.,* vol. 12, pp. 439-443, 1973.

[165] T. C. M. Pillay, J. D. D'Entremont, and J. Chipman, "Stability of Hercynite at High Temperatures," *J. Am. Ceram. Soc.,* vol. 43, pp. 583-585, 1960.

[166] R. O. Sack and M. S. Ghiorso, "An Internally Consistent Model for the Thermodynamic Properties of Fe-Mg-Titanomagnetite-Aluminate Spinels," *Contrib. Mineral. Petrol.,* vol. 106, pp. 474-505, 1991.

[167] G. Dehe, B. Seidel, K. Melzer, and C. Michalk, "Determination of Cation Distribution Model of the Spinel System $Fe_{3-x}Al_xO_4$," *Phys. Status Solidi A,* vol. 31, pp. 439-447, 1975.

[168] A. Muan and C. L. Gee, "Phase Equilibrium Studies in the System Iron Oxide-Al_2O_3 in Air and at 1 Atm O_2 Pressure," *J. Am. Ceram. Soc.,* vol. 39, pp. 207-214, 1956.

[169] A. Muan, "On the Stability of the Phase $Fe_2O_3{\cdot}Al_2O_3$," *Am. J. Sci.,* vol. 256, pp. 413-422, 1958.

[170] J. Majzlan, A. Navrotsky, and B. J. Evans, "Thermodynamics and Crystal Chemistry of the Hematite-Corundum Solid Solutions and the $FeAlO_3$ Phase," *Phys. Chem. Miner.,* vol. 29, pp. 515-526, 2002.

[171] J. C. Willshee and J. White, "Equilibrium relations in the systems FeO-Fe_2O_3-Al_2O_3 and FeO-Fe_2O_3-Cr_2O_3 up to 1750 ^oC in air," *Trans. J. Br. Ceram. Soc.,* vol. 67, pp. 271-284, 1968.

[172] R. G. Richards and J. White, "Phase Relationship of Iron-Oxide-Containing Spinels," *Trans. Brit. Ceram. Soc.,* vol. 53, p. 233, 1954.

[173] Z. Bojarski and Z. Isakow, "Study of aluminum(3+) and gallium(3+) solid solutions in α-iron(III) oxide," *Arch. Nauki Mater.,* vol. 4, pp. 3-19, 1983.

[174] A. Feenstra, S. Saemann, and B. Wunder, "An experimental study of Fe-Al solubility in the system corundum-hematite up to 40 kbar and 1300 °C," *J. Petrol.,* vol. 46, pp. 1881-1892, 2005.

[175] V. S. Escribano, J. M. G. Amores, E. Finocchio, M. Daturi, and B. G., "Characterization of α-$(Fe, Al)_2O_3$ Solid-solution Powders," *J. Mater. Chem.,* vol. 5, pp. 1943-1951, 1995.

[176] R. Hansson, P. C. Hayes, and E. Jak, "Experimental Study of Phase Equilibria in the Al-Fe-Zn-O System in Air," *Metall. Mater. Trans. B,* vol. 35B, pp. 633-642, 2004.

[177] M. A. Rhamdhani, T. Hidayat, P. C. Hayes, and E. Jak, "Subsolidus Phase Equilibria of Fe-Ni-X-O (X = Mg, Al) Systems in Air," *Metall. Mater. Trans. B,* vol. 40 B, pp. 25-38, 2009.

[178] V. Cremer, "Solid Solution Formation in the Chromite-Magnetite-Hercynite System at 500-1000 ^{o}C," *Neues Jahrb. Mineral., Abh.,* vol. 111, pp. 184-205, 1969.

[179] A. A. Lykasov and A. A. Kimyashev, "Activities of the components in a spinel solid solution of the Fe-Al-O system," *Russ. J. Phys. Chem. A,* vol. 85, pp. 1495-1498, 2011.

[180] J. Horn and H. J. Zacharias, "The Lines of Constant Vacancy Content in the Phase Diagram of The Aluminum Iron Ferrite System," *Phys. Status Solidi A,* vol. 113, pp. K103-K106, 1989.

[181] P. Vallet and P. Raccah, "Thermodynamic properties of solid iron(II) oxide," *Rev. Metall., Mem. Sci.,* vol. 62, pp. 1-29, 1965.

[182] T. O. Petric, K. T. Jacob, and C. B. Alcock, "Thermodynamic Properties of Fe_3O_4-$FeAl_2O_4$ Spinel Solid Solution," *J. Am. Ceram. Soc.,* vol. 64, pp. 632-639, 1981.

[183] V. W. A. Fischer and A. H. Hoffmann, "Das Zustandsschaubild Eisenoxydul-Aluminiumoxyd," *Arch. Eisenhuettenwes.,* vol. 27, pp. 343-346, 1956.

[184] I. A. Novokhatskii, B. F. Belov, A. V. Gorokh, and A. A. Savinskaya, "The Phase Diagram for The System Ferrous Oxide-Alumina," *Russ. J. Phys. Chem.,* vol. 39, pp. 1498-1500, 1965.

[185] F. Y. Galakhov, "Alumina region of ternary aluminosilicate systems. I. The FeO-Al_2O_3-SiO_2 and MnO-Al_2O_3-SiO_2 systems," *Izv. Akad. Nauk SSSR, Otdel Khim. Nauk,* vol. No 5, pp. 525-531, 1957.

[186] Y. P. Vorob'ev, M. P. Bogdanovich, A. N. Men, and G. I. Chufarov, "Solubility of aluminum oxide, vanadium(III) oxide, and chromium(III) oxide in wustite," *Izv. Akad. Nauk SSSR, Neorg. Mater.,* vol. 9, pp. 83-85, 1973.

[187] F. A. Elrefaie and W. W. Smeltzer, "Thermodynamics of the System Iron-Aluminium-Oxygen between 1073 and 1573 K," *Metall. Trans. B,* vol. 14B, pp. 85-92, 1983.

[188] K. Rosenbach and J. A. Schmitz, "Ternary System Iron(II) Oxide-Chromium(III) Oxide-Alumina," *Arch. Eisenhuettenwes.,* vol. 45, pp. 843-847, 1974.

[189] E. Schurmann and N. Bannenberg, "Metall-Schlackengleichgewichte im System Eisen-Aluminium-Sauerstoff als Grundlage der Aluminiumdesoxidation von Stahlschmelzen," *Arch. Eisenhuettenwes.,* vol. 55, pp. 409-414, 1984.

[190] W. Oelsen and G. Heynert, "Die Reaktionen zwischen Eisen-Mangan-Schmelzen und den Schmelzen ihrer Aluminate," *Arch. Eisenhuettenwes.,* vol. 26, pp. 567-575, 1955.

[191] B. D. Roiter, "Phase Equilibria in the Spinel Region of the System FeO-Fe_2O_3-Al_2O_3," *J. Am. Ceram. Soc.,* vol. 47, pp. 509-511, 1964.

[192] C. Meyers, T. O. Mason, W. T. Petuskey, J. W. Halloran, and J. K. Brown, "Phase Equilibria in the System Fe-Al-O," *J. Am. Ceram. Soc.,* vol. 63, pp. 659-663, 1980.

[193] S. Ban-Ya, A. Chiba , and A. Hikosaka, "Thermodynamics of FeO-M_xO_y (M_xO_y=CaO,SiO_2,TiO_2 and Al_2O_3)," *Binary melts in equilibrium with solid iron,* vol. 66, pp. 1484-1493, 1980.

[194] I. Ansara, N. Dupin, L. H. Leo, and B. Sundman, "Thermodynamic assessment of the Al-Ni system," *J. Alloys Compd.,* vol. 247, pp. 20-30, 1997.

[195] T. I. Barry*, et al.*, "The Compound Energy Model for Ionic Solutions with Applications to Solid Oxides," *J. Phase Equilib.,* vol. 13, pp. 459-475, 1992.

[196] F. A. Elrefaie and W. W. Smeltzer, "Phase equilibria in the subsolidus region of the NiO-α-Al_2O_3 system between 1000 and 1920 ^oC," *Oxid. Met.,* vol. 15, pp. 495-500, 1981.

[197] H. S. C. O'Neill, W. A. Dollase, and C. R. I. Ross, "Temperature dependence of the cation distribution in nickel aluminate ($NiAl_2O_4$) spinel: A powder XRD study," *Phys. Chem. Miner.,* vol. 18, pp. 302-319, 1991.

[198] S. Greenwald, S. J. Pickart, and F. H. Grannis, "Cation distribution and g factors of certain spinels containing Ni++, Mn++, Co++, Al+++, Ga+++. and Fe+++," *J. Chem. Phys.,* vol. 22, pp. 1597-1600, 1954.

[199] H. Schmalzried, "Radiographic investigation of the cation distribution in spinel phases," *Z. Phys. Chem. (Frankfurt),* vol. 28, pp. 203-219, 1961.

[200] R. K. Datta and R. Roy, "Equilibrium Order-disorder in Spinels," *J. Am. Ceram. Soc.,* vol. 50, pp. 578-583, 1967.

[201] W. Rogalla and H. Schmalzried, "Reactions between defects in ionic crystals," *Ber. Bunsen-Ges. Phys. Chem.,* vol. 72, pp. 12-19, 1968.

[202] R. F. Cooley and J. S. Reed, "Equilibrium Cation Distribution in Nickel Aluminate, Copper Aluminate, and Zinc Aluminate Spinels," *J. Am. Ceram. Soc.,* vol. 55, pp. 395-398, 1972.

[203] H. Furuhashi, M. Inagaki, and S. Naka, "Determination of cation distribution in spinels by x-ray diffraction method," *J. Inorg. Nucl. Chem.,* vol. 35, pp. 3009-3014, 1973.

[204] P. Porta, F. S. Stone, and R. G. Turner, "Distribution of nickel ions among octahedral and tetrahedral sites in nickel aluminum oxide-magnesium aluminum oxide ($NiAl_2O_4$-$MgAl_2O_4$)solid solutions," *J. Solid State Chem.,* vol. 11, pp. 135-147, 1974.

[205] F. Pepe, P. Porta, and M. Schiavello, "Cation Distribution in Spinel Solid Solutions and Correlations between Structural and Catalytic Properties," in *React. Solids, [Proc. Int. Symp.], 8th*, 1977, pp. 183-190.

[206] K. T. Jacob and C. B. Alcock, "Activities and Their Relation to Cation Distribution in Nickel Aluminate-Magnesium Aluminate ($NiAl_2O_4$-$MgAl_2O_4$)," *J. Solid State Chem.,* vol. 20, pp. 79-88, 1977.

[207] P. Porta, A. Anichini, and U. Bucciarelli, "Distribution of nickel ions among octahedral and tetrahedral sites in nickel zinc aluminate spinel solid solutions," *J. Chem. Soc., Faraday Trans. 1,* vol. 75, pp. 1876-1887, 1979.

[208] C. Otero Arean, M. L. Rodriguez Martinez, and A. Mata Arjona, "Structural study of cadmium nickel aluminate ($Cd_xNi_{1-x}Al_2O_4$) spinels," *Mater. Chem. Phys.*, vol. 8, pp. 443-450, 1983.

[209] C. O. Arean and J. S. Diez Vinuela, "Structural Study of Copper-Nickel Aluminate ($Cu_xNi_{1-x}Al_2O_4$) Spinels," *J. Solid State Chem.*, vol. 60, pp. 1-5, 1985.

[210] K. D. Becker and F. Rau, "High temperature ligand field spectra in spinels: cation disorder and cation kinetics in nickel aluminum oxide ($NiAl_2O_4$)," *Ber. Bunsen-Ges. Phys. Chem.*, vol. 91, pp. 1279-1282, 1987.

[211] K. Mocala and A. Navrotsky, "Structural and thermodynamic variation in nickel aluminate spinel," *J. Am. Ceram. Soc.*, vol. 72, pp. 826-832, 1989.

[212] T. Yao, O. Imafuji, and H. Jinno, "EXAFS study of cation distribution in nickel aluminate ferrites," *J. Am. Ceram. Soc.*, vol. 74, pp. 314-317, 1991.

[213] J. N. Roelofsen, R. C. Peterson, and M. Raudsepp, "Structural Variation in Nickel Aluminate Spinel ($NiAl_2O_4$)," *Am. Mineral.*, vol. 77, pp. 522-528, 1992.

[214] K. Shinoda, K. Sugiyama, K. Omote, and Y. Waseda, "Determination of cation distribution in $ZnFe_2O_4$, $NiFe_2O_4$ and $NiAl_2O_4$ spinels by an inhouse anomalous X-ray scattering method," *Int. J. Soc. Mater. Eng. Resour.*, vol. 4, pp. 20-29, 1996.

[215] Y. S. Jiong, L. Kou, P. Nash, and J. R. Selman, "Behavior of Nickel Aluminate Spinel under Reducing Conditions," *Proc. - Electrochem. Soc.*, vol. 97-94, pp. 456-468, 1997.

[216] Y. S. Han, J. B. Li, X. S. Ning, and B. Chi, "Temperature dependence of the cation distribution in nickel aluminate spinel from thermodynamics and x-rays," *J. Am. Ceram. Soc.*, vol. 88, pp. 3455-3457, 2005.

[217] M. A. Laguna-Bercero, M. L. Sanjuan, and R. I. Merino, "Raman spectroscopic study of cation disorder in poly- and single crystals of the nickel aluminate spinel," *J. Phys.: Condens. Matter*, vol. 19, pp. 186217/1-186217/10, 2007.

[218] M. Rotan, J. Tolchard, E. Rytter, M.-A. Einarsrud, and T. Grande, "On the solid solution of the spinel phase in the system $NiO\text{-}Al_2O_3$," *J. Solid State Chem.*, vol. 182, pp. 3412-3415, 2009.

[219] J. J. Bara, *et al.*, "Investigations of crystal and magnetic properties of nickel ferrite-aluminates," *Phys. Status Solidi A*, vol. 44, pp. 325-331, 1977.

[220] Q. Chen, *et al.*, "Investigation of the thermodynamic properties of $\gamma\text{-}Al_2O_3$," *Thermochim. Acta*, vol. 253, pp. 33-39, 1995.

[221] O. Kubaschewski, E. L. Evans, and C. B. Alcock, *Metallurgical Thermochemistry, 4th Ed.*: Pergamon Press, London, 1967.

[222] W. A. Roth, "Uber γ- und α-Aluminiumoxyd," *Angew. Chem.*, vol. 49, p. 198, 1936.

[223] V. Kostomaroff and M. Rey, "Measurement of heats of reaction by differential thermal analysis," *Silicates Ind.*, vol. 28, p. 9, 1963.

[224] T. Yokokawa and O. J. Kleppa, "A Calorimetric Study of the Transformation of Some Metastable Modifications of Alumina to α-Alumina," *J. Phys. Chem.*, vol. 68, pp. 3246-3249, 1964.

[225] M. S. J. Gani and R. McPherson, "The enthalpy of formation of aluminium titanate," *Thermochim. Acta*, vol. 7, p. 251, 1973.

[226] X. D. Phan, R. Castenet, and M. Laffitte, "Partial enthalpy of dissolution of γ-alumina in cryolite and transformation enthalpy between γ and α alumina," *Rev. Int. Hautes Temp. Refract.*, vol. 11, p. 285, 1974.

[227] A. Navrotsky, B. Wechsler, K. Geisinger, and F. Seifert, "Thermochemistry of $MgAl_2O_4$-$Al_{8/3}O_4$ Defect Spinels," *J. Am. Ceram. Soc.*, vol. 69, pp. 418-422, 1986.

[228] M. W. Chase, Jr., "JANAF Thermochemical Tables. Monograph No 9. Part I, aluminum-cobalt," *J. Phys. Chem. Ref. Data, Suppl.*, 1998.

[229] R. H. R. Castro, S. V. Ushakov, L. Gengembre, D. Gouvea, and A. Navrotsky, "Surface Energy and Thermodynamic Stability of γ-Alumina: Effect of Dopants and Water," *Chem. Mater.*, vol. 18, pp. 1867-1872, 2006.

[230] D. M. Chizhikov, B. S. Gol'dman, and E. K. Kazenas, "Heat Capacity of Nickel Aluminate, Titanate, and Chromite at Elevated Temperatures," *Zh. Fiz. Khim.*, vol. 49, pp. 492-493, 1975.

[231] N. S. Dzagnidze, N. G. Lezhava, T. A. Pavlenishvili, and G. D. Chachanidze, "High-temperature enthalpy and heat capacity of nickel aluminate ($NiAl_2O_4$)," *Izv. Akad. Nauk SSSR, Neorg. Mater.*, vol. 25, pp. 865-856, 1989.

[232] S. Klemme and J. C. van Miltenburg, "The heat capacities and thermodynamic properties of $NiAl_2O_4$ and $CoAl_2O_4$ measured by adiabatic calorimetry from T = (4 to 400)K," *J. Chem. Thermodyn.*, vol. 41, pp. 842-848, 2009.

[233] A. Navrotsky and O. J. Kleppa, "Thermodynamics of Formation of Simple Spinels," *J. Inorg. Nucl. Chem.*, vol. 30, pp. 479-498, 1968.

[234] M. Akaogi and A. Navrotsky, "Calorimetric Study of the Stability of Spinelloids in the System Nickel Aluminum Oxide ($NiAl_2O_4$)-Nickel(II) Silicate," *Phys. Chem. Miner.*, vol. 10, pp. 166-172, 1984.

[235] A. Navrotsky, "Cation Distribution Energies and Heats of Mixing in $MgFe_2O_4$-$MgAl_2O_4$-$ZnFe_2O_4$-$ZnAl_2O_4$, and $NiAl_2O_4$-$ZnAl_2O_4$ Spinels: Study by High-Temperature Calorimetry," *Am. Mineral.*, vol. 71, pp. 1160-1169, 1986.

[236] K. I. Lilova, K. Shih, C.-W. Pao, J.-F. Lee, and A. Navrotsky, "Thermodynamics of $NiAl_2O_4$-$NiFe_2O_4$ spinel solid solutions," *J. Am. Ceram. Soc.*, vol. 95, pp. 1-8, 2011.

[237] H. Schmalzried, "Measurement of the free enthalpy of reaction in the formation of spinel phases from the single oxides by aid of solid galvanic couples," *Z. Phys. Chem. (Muenchen, Ger.)*, vol. 25, pp. 178-192, 1960.

[238] J. D. Tretyakov and H. Schmalzried, "Thermodynamics of Spinel Phase (Chromite, Ferrite, Aluminate)," *Ber. Bunsen-Ges. Phys. Chem.*, vol. 69, pp. 396-402, 1965.

[239] V. A. Levitskii and T. N. Rezukhina, "Thermodynamic properties of cobalt and nickel aluminates from electromotive force data at elevated temperatures," *Izvt. Akad. Nauk SSSR, Neorg. Mater.*, vol. 2, pp. 145-150, 1966.

[240] G. Rog, "Thermodynamics of nickel ferrite and aluminate," *Rocz. Chem.*, vol. 50, pp. 147-149, 1976.

[241] F. A. Elrefaie and W. W. Smeltzer, "Thermodynamics of nickel-aluminum-oxygen system between 900 and 1400 K," *J. Electrochem. Soc.*, vol. 128, pp. 2237-2242, 1981.

[242] K. T. Jacob, "Solubility and Activity of Oxygen in Liquid Nickel in Equilibrium with α-Al_2O_3 and nickel aluminate $NiO \cdot (1 + x)Al_2O_3$," *Metall. Trans. B*, vol. 17B, pp. 763-770, 1986.

[243] A. Majumdar, A. McLean, H. B. Bell, and M. Iwase, "Thermodynamics of Nickel Aluminate Formation in Molten Nickel," *Can. Metall. Q.*, vol. 32, pp. 321-326, 1993.

[244] R. Fricke and G. Weitbrecht, "Active substances. LI. The equilibria of CO/CO_2 with Ni/NiO, and with (Ni + γ-Al_2O_3)/$NiAl_2O_4$, and their dependence on the physical state of the solid reactants," *Z. Elektrochem.*, vol. 48, pp. 87-106, 1942.

[245] L. M. Lenev and I. A. Novokhatski, "Thermodynamic characteristics of $NiAl_2O_4$," *Zh. Neorg. Khim.*, vol. 10, pp. 2400-2403, 1965.

[246] M. Timucin and A. Muan, "Activity-Composition Relations in $NiAl_2O_4$-$MnAl_2O_4$ Solid Solutions and Stabilities of $NiAl_2O_4$ and $MnAl_2O_4$ at 1300 and 1400 ^oC," *J. Am. Ceram. Soc.*, vol. 75, pp. 1399-1406, 1992.

[247] N. Kemori, I. Katayama, and Z. Kozuka, "Chemical potential and solubility of oxygen in nickel (s,l) equilibrated with both nickel(II) oxide (s) and NiX_2O_4(s) [X = Al, Ga]," *Trans. Jpn. Inst. Met.*, vol. 21, pp. 285-292, 1980.

[248] R. H. J. von Wartenberg H., "Melting diagrams of highly refractory oxides: IV, Aluminum oxide," *Z. Anorg. Allg. Chem.*, vol. 207, pp. 1-20, 1932.

[249] Y. Iida, "Formation of $NiAl_2O_4$ Spinel by Solid Reaction," *J. Jpn. Soc. Powder Powder Metall.*, vol. 6, pp. 55-68, 1959.

[250] A. M. Lejus and R. Collonongues, "Sur la Formation à Haute Température de Phases Type Alumine δ dans Plusieurs Systemes à Base d'Alumine," *Acad. Sci.*, vol. 254, pp. 2780-2781, 1962.

[251] K. Ando, "Solubility of NiO in Al_2O_3," *J. Am. Ceram. Soc.*, vol. 70, pp. C/309-C/311, 1987.

[252] A. Revcolevschi, "Nickel oxide-based aligned eutectics," *Mater. Sci. Res.*, vol. 20, pp. 115-130, 1986.

[253] R. Luoma, "A thermodynamic analysis of the system Fe-Ni-O," *Calphad*, vol. 19, pp. 279-295, 1995.

[254] L. Kjellqvist, M. Selleby, and B. Sundman, "Thermodynamic modelling of the Cr-Fe-Ni-O system," *Calphad*, vol. 32, pp. 577-592, 2008.

[255] A. Dinsdale, T.G.Chart, and M. NPL, *unpublished work*, 1986.

[256] S. I. Youssef, M. G. Natera, R. J. Begum, N. S. S. Murthy, and B. S. Srinivasan, "Polarized neutron study of the cation distribution and magnetic structure in nickel ferrite," in *Proc. Nucl. Phys. Solid State Phys. Symp., 13th*, 1969, pp. 173-177.

[257] G. A. Sawatzky, F. Van der Woude, and A. H. Morrish, "Moessbauer Study of Several Ferrimagnetic Spinels," *Phys. Rev.*, vol. 187, pp. 747-757, 1969.

[258] N. S. S. Murthy, M. G. Natera, S. I. Youssef, R. J. Begum, and C. M. Srivastava, "Yafet-Kittel Angles in Zinc-Nickel Ferrites," *Phys. Rev.*, vol. 181, pp. 969-977, 1969.

[259] J. G. Faller and C. E. Birchenall, "Temperature Dependence of Ordering in Magnesium Ferrite," *J. Appl. Crystallogr.*, vol. 3, pp. 496-503, 1970.

[260] E. H. Kuznetsov, V. D. Checherskii, and V. P. Romanov, "Nuclear gamma-resonance study of the degree of inversion in some simple spinel-ferrites at high temperatures," *Ukr. Fiz. Zh. (Russ. Ed.)*, vol. 20, pp. 1781-1786, 1975.

[261] H. V. Kiran, A. L. Shashimohan, D. K. Chakrabarty, and A. B. Biswas, "Structural and Magnetic Properties of Copper-Nickel Ferrites," *Phys. Status Solidi A*, vol. 66, pp. 743-747, 1981.

[262] K. Seshan, A. S. Bommannavar, and D. K. Chakrabarty, "Moessbauer Spectroscopic Studies of Magnesium-Nickel Ferrites," *J. Solid State Chem.*, vol. 47, pp. 107-112, 1983.

[263] M. Ahmad and T. Abbas, "Determination of Cation Distribution in Nickel Zinc Ferrites by X-ray Diffraction," *Turk. J. Phys.*, vol. 21, pp. 192-199, 1997.

[264] K. Tsukimura, S. Sasaki, and N. Kimizuka, "Cation Distributions in Nickel Ferrites," *Jpn. J. Appl. Phys., Part 1*, vol. 36, pp. 3609-3612, 1997.

[265] M. K. Fayek, S. S. Ata-Allah, and H. S. Refai, "On the cation distribution in $Ni_{1-x}Cu_xFe_{2-y}Al_yO_4$ spinels," *J. Appl. Phys.*, vol. 85, pp. 325-328, 1999.

[266] R. A. D. Pattrick, *et al.*, "Cation site occupancy in spinel ferrites studied by X-ray magnetic circular dichroism: Developing a method for mineralogists," *Eur. J. Mineral.*, vol. 14, pp. 1095-1102, 2002.

[267] K. Sugiyama, T. Okamoto, and Y. Waseda, "Anomalous x-ray scattering study for determining cation distribution in $ZnFe_2O_4$ and $NiFe_2O_4$," *High Temp. Mater. Processes (London, U. K.)*, vol. 23, pp. 357-364, 2004.

[268] M. A. F. Ramalho, *et al.*, "X-Ray diffraction and Moessbauer spectra of nickel ferrite prepared by combustion reaction," *J. Mater. Sci.*, vol. 42, pp. 3603-3606, 2007.

[269] S. Singhal and K. Chandra, "Cation distribution and magnetic properties in chromium-substituted nickel ferrites prepared using aerosol route," *J. Solid State Chem.*, vol. 180, pp. 296-300, 2007.

[270] F. Saito, *et al.*, "Site- and valence-selective study on the origin of Fe peaks in x-ray magnetic circular dichroism of Ni ferrites, $Fe[Ni_xFe_{2-x}]O_4$," *Physica B (Amsterdam)*, vol. 270, pp. 35-44, 1999.

[271] V. Raghavan, "The Fe-Ni-O (Iron-Nickel-Oxygen) System," in *Phase Diagrams of Ternary Alloys, Part 5. Ternary Systems Containing Iron and Oxygen*, ed: Indian Institute of Metals, Calcutta, 1989, pp. 222-231.

[272] V. Raghavan, "Fe-Ni-O (Iron-Nickel-Oxygen)," *J. Phase Equilib. Diffus.*, vol. 31, pp. 369-371, 2010.

[273] G. D. Chachanidze, "Thermodynamic properties of nickel and cobalt ferrites," *Izv. Akad. Nauk SSSR, Neorg. Mater.*, vol. 26, pp. 376-379, 1990.

[274] N. A. Landiya, *et al.*, "Determination of the High Temperature Enthalpies of Nickel and Cobalt Ferrites," *Izv. Akad. Nauk SSSR, Neorg. Mater.*, vol. 2, pp. 2050-2057, 1966.

[275] M. L. Bochirol, "Chaleur Specifique Vraie des Ferrites de Zinc, de Nickel et de Cobalt," *Compt. Rend.*, vol. 232, pp. 1474-1477, 1951.

[276] A. A. El-Sharkawy, A. Abousehly, E.-S. M. Higgy, and S. R. Atalla, "Specific heat capacity , thermal conductivity, and thermal diffusivity of spinel nickel antimonate ferrite ($Ni_{1+2x}Fe_{2-3x}Sb_xO_4$) in the temperature range 400-1000 K," *High Temp.-High Press.*, vol. 18, pp. 265-269, 1986.

[277] I. K. Kamilov, G. M. Shaknshaev, and K. K. Aliev, "Thermophysical properties of magnetic semiconductors," in *Teplofiz. Svoistva Tverd. Tel, Mater. Vses. Teplofiz. Konf. Svoistvam Veshchestv Vys. Temp., 3rd*, 1971, pp. 192-202.

[278] S. R. Pollack and K. R. Atkins, "Specific Heat of Ferrites at Liquid Helium Temperatures," *Phys. Rev.*, vol. 125, pp. 1248-1254, 1962.

[279] S. E. Ziemniak, L. M. Anovitz, R. A. Castelli, and W. D. Porter, "Magnetic contribution to heat capacity and entropy of nickel ferrite ($NiFe_2O_4$)," *J. Phys. Chem. Solids*, vol. 68, pp. 10-21, 2006.

[280] K. Terayama, M. Ikeda, and M. Taniguchi, "Study on phase equilibria in the nickel-iron-oxygen system at 1273 K," *Trans. Jpn. Inst. Met.*, vol. 27, pp. 176-179, 1986.

[281] M. C. Trinel-Dufour, "Etude thermodynamique des équilibres alliage-oxyde-spinelle dans le diagramme quaternaire Fe-Ni-Mg-O," Ph. D. Thesis, L'Université des sciences et techniques de Lille, 1977.

[282] E. G. King and K. K. Kelley, "Low-Temperature Heat Capacities of Copper Ferrites (With a Summary of Entropies at 298.15K of Spinel Minerals)," *Bureau of Mines Rept. of Investigations*, vol. 5502, p. 6, 1959.

[283] M. C. Trinel-Dufour, G. Pouillard, and P. Perrot, "The system iron-nickel-oxygen at 1273 K. Part 1. Phase equilibria," *J. Chem. Res. (S)*, p. 191, 1979.

[284] A. G. Zalazinskii, V. F. Balakirev, and G. I. Chufarov, "Oxygen pressure-composition diagram in the nickel-iron-oxygen system at 1000 ^{o}C," *Zh. Fiz. Khim.*, vol. 47, pp. 457-458, 1973.

[285] A. D. Dalvi and R. Sridhar, "Thermodynamics of the Fe-Ni-O and Fe-Ni systems at 1065 K to 1380 K," *Can. Metall. Q.*, vol. 15, pp. 349-357, 1976.

[286] F. Schneider and H. Schmalzried, "Thermodynamic Investigation of the System Ni-Fe-O," *Z. Phys. Chem.*, vol. 166, pp. 1-18, 1990.

[287] H. Davies and W. W. Smeltzer, "Oxygen and metal activities of the iron-nockel-oxygen system at 1000 C," *J. Electrochem. Soc.*, vol. 119, pp. 1362-1368, 1972.

[288] G. P. Popov and G. I. Chupharov, "Mechanism and conditions of equilibrium in reducing nickel ferrite with hydrogen," *Zh. Fiz. Khim.,* vol. 37, pp. 586-594, 1963.

[289] G. I. Chufarov, *et al.*, "Physical-chemical properties of ferrites having spinel structure," in *Fiz. Fiz.-Khim. Svoistva Ferritov, Mater. Dokl. Vses. Soveshch., 4th*, 1966, pp. 5-14.

[290] K. Ono, K. Yokogawa, A. Yamaguchi, and J. Nioriyama, "Thermodynamic study of the iron-nickel-oxygen system," *Nippon Kinzoku Gakkaishi,* vol. 35, pp. 750-756, 1971.

[291] G. S. Viktorovich and D. I. Lisovskii, "Equilibrium of the Solid Metal and Oxide in the Iron-Nickel-Oxygen System," *Tsvet. Metal.,* vol. 39, pp. 43-48, 1966.

[292] G. S. Viktorovich, V. A. Gutin, and D. I. Lisovskii, "The Wustite-Iron-Nickel Alloy Solid-Phase Equilibrium," *Tsvet. Met.,* vol. 39, pp. 47-49, 1966.

[293] G. A. Roeder and W. W. Smeltzer, "The dissociation pressures of iron-nickel oxides," *J. Electrochem. Soc.,* vol. 111, pp. 1074-1078, 1964.

[294] A. D. Dalvi and W. W. Smeltzer, "Thermodynamics of the Iron-Nickel-Oxygen System at 1000°C," *J. Electrochem. Soc.,* vol. 117, pp. 1431-1436, 1970.

[295] C. Gatellier, D. Henriet, and M. Olette, "Thermodynamic activity of the constituents of the solid-state iron-nickel system determined by an electrochemical method," *C. R. Acad. Sci., Paris, Ser. C,* vol. 271, pp. 453-456, 1970.

[296] H. Schmalzried and J. D. Tretjakow, "Fehlordnung in Ferriten," *Ber. Bunsen-Ges. Phys. Chem.,* vol. 70, pp. 180-188, 1966.

[297] I. Katayama, Y. Watanabe, and Z. Kozuka, "Thermodynamic study of spinel type solid solutions of the iron oxide (Fe_3O_4)-nickel ferrite ($NiFe_2O_4$) system by the E.M.F. method," *Trans. Jpn. Inst. Met.,* vol. 20, pp. 593-596, 1979.

[298] R. V. S. M. H. S. Rajendran S., "Phase Analysis in the Fe2O3-NiO Mixed Oxides Prepared by Co-Precipitation," *J. Solid State Chem.,* vol. 53, pp. 227-235, 1984.

[299] K. Ono, Y. Ueda, A. Yamaguchi, and J. Moriyama, "Thermodynamic study of Fe-Ni solid solutions," *Nippon Kinzoku Gakkaishi,* vol. 36, pp. 188-194, 1972.

[300] H. M. O'Bryan, F. R. Monforte, and R. Blair, "Oxygen Content of Nickel Ferrites at 1300 C," *J. Am. Ceram. Soc.,* vol. 48, pp. 577-580, 1965.

[301] M. W. Shafer, "High Temperature Phase Relations in the Ferrite Region of the Ni-Fe-O System," *J. Phys. Chem.,* vol. 65, pp. 2055-2062, 1961.

[302] M. W. Grutzeck and A. Muan, "Liquid-Solid equilibria in the system FeO-NiO-Fe_2O_3-SiO_2," *J. Am. Ceram. Soc.,* vol. 75, pp. 1342-1350, 1992.

[303] N. I. Gran' and A. A. Tseidler, "Reactions between alloy and slag in systems Fe-Co-O and Fe-Ni-O," *Tsvetnye Metal.,* vol. 30, pp. 44-49, 1957.

[304] L. S. Tsemekhman and S. E. Vaisburd, "Variation of the Ratio Fe(III)/Fe(II) with the Composition of the Equilibrium Metallic Phase in the Systems Iron-Nickel-Oxygen and Iron-Cobalt-Oxygen and the Activity of the Components," *Russ. J. Phys. Chem.,* vol. 43, pp. 1777-1780, 1969.

[305] C. von Bohlen Halbach and W. Leitgebel, "Uber die Einwirkung von Sauerstoff auf Eisen-Nickel-und Kupfer-Nickel-Schmelzen1941," vol. 4, pp. 37-44.

[306] U. Kuxmann and F. Koch, "Die Gleichwichte zwischen Eisen und Sauerstoff in Nickelschmelzen unter eisenoxidhaltigen Schlacken," *Metall (Berlin),* vol. 40, pp. 479-485, 1986.

[307] H. Schenck, E. Steinmetz, and R. Grundmann, "Iron oxide-nickel oxide phase diagram and the equilibrums between iron oxide-nickel oxide-alumina slags and iron-nickel melts at steelmaking temperatures," *Arch. Eisenhuettenwes.,* vol. 39, pp. 895-901, 1968.

[308] V. F. Belov, *et al.*, "Moessbauer effect study of nickel and magnesium-manganese ferrites containing scandium sesquioxide additives," *Porosh. Met.,* vol. 11, pp. 46-50, 1971.

[309] S. Niziol, "Investigation of the influence of the aluminum content on the crystallographic and magnetic structures of the ($NiFe_{2-x}Al_xO_4$) ferrite by the neutron diffraction method," *Phys. Status Solidi A,* vol. 17, pp. 555-560, 1973.

[310] N. M. Chebotaev, *et al.*, "X-ray structural studies of solid solutions of nickel ferrite and aluminate," *Izv. Vyssh. Uchebn. Zaved., Khim. Khim. Tekhnol.,* vol. 19, pp. 516-517, 1976.

[311] S. K. Kulshreshtha, "Cation distribution and canted spin alignment in nickel iron aluminum oxide ($NiFeAlO_4$)," *J. Mater. Sci. Lett.,* vol. 5, pp. 638-640, 1986.

[312] K. T. Jacob and S. S. Pandit, "Characterization of alloy-spinel-corundum equilibrium in the system iron-nickel-aluminum-oxygen," *Trans. Iron Steel Inst. Jpn.,* vol. 28, pp. 91-96, 1988.

[313] A. Kozlowska-Rog and G. Rog, "Thermodynamic properties of solid solutions of magnesium nickel aluminate ($Ni_xMg_{1-x}Al_2O_4$)," *Pol. J. Chem.,* vol. 54, pp. 2115-2118, 1980.

[314] K. Seshan, A. L. Shashimohan, D. K. Chakrabarty, and A. B. Biswas, "Effect of cation distribution on the properties of some magnesium-nickel ferrites," *Phys. Status Solidi A,* vol. 68, pp. 97-101, 1981.

[315] K. Seshan, M. J. Patni, and D. K. Chakrabarty, "Ferromagnetic Resonance Studies in Some Polycrystalline Magnesium Nickel Ferrites," *J. Solid State Chem.,* vol. 42, pp. 206-211, 1982.

[316] M. A. Amer, "57Fe Mossbauer, Infrared and X-ray Studies of the System $Zn_{1-x}Cu_xCr_{0.8}Fe_{1.2}O_4$," *Phys. Status Solidi A,* vol. 181, pp. 539-550, 2000.

[317] V. K. Mittal, *et al.*, "Solid state synthesis of Mg-Ni ferrite and characterization by XRD and XPS," *J. Nucl. Mater.,* vol. 335, pp. 302-310, 2004.

[318] V. K. Mittal, *et al.*, "Cation distribution in $Ni_xMg_{1-x}Fe_2O_4$ studied by XPS and Moessbauer spectroscopy," *Solid State Commun.,* vol. 137, pp. 6-10, 2005.

[319] K. Sheshan, A. L. Shashimohan, D. K. Chakrabarty, and A. B. Biswas, "Cation distribution and magnetic properties of a (nickel magnesium) iron oxide $(NiMg)Fe_2O_4$ system," in *Proc. Nucl. Phys. Solid State Phys. Symp.,* 1976, pp. 298-300.

[320] M. A. Amer and M. El Hiti, "Mossbauer and X-ray Studies for $Ni_{0.2}Zn_xMg_{0.8-x}Fe_2O_4$ Ferrites," *J. Magn. Magn. Mater.*, vol. 234, pp. 118-125, 2001.

[321] L. A. Bashkirov and M. G. Bashkirova, "Phase Equilibria in the System NiO-MgO-Fe_2O_3 in the Region of Compositions with Less than 50 mole % Ferric Oxide," *Inorg. Mater.*, vol. 7, pp. 1245-1248, 1971.

[322] M. C. Trinel-Dufour, G. Pouillard, and P. Perrot, "Activity-composition relations in the solid spinel solution nickel ferrite ($NiFe_2O_{14}$)-magnesium ferrite ($MgFe_2O_4$) at 1273 K," *Rev. Chim. Miner.*, vol. 15, pp. 513-520, 1978.

[323] A. C. Ramirez, A. R. Serrano, E. R. Salinas, A. R. Lopez, and M. V. Ramirez, "The solubility and activity determination of NiO in the SiO_2-NiO-FeO system," *J. Non-Cryst. Solids*, vol. 354, pp. 3533-3539, 2008.

[324] P. L. Lin and A. D. Pelton, "A Structural Model for Binary Silicate Systems," *Metall. Trans. B*, vol. 10B, pp. 667-675, 1979.

[325] J. Grobner, H. L. Lukas, and F. Aldinger, "Thermodynamic Calculation of the Ternary System Al-Si-C," *Calphad*, vol. 20, pp. 247-254, 1996.

[326] J. Lacaze and B. Sundman, "An Assessment of the Iron-Carbon-Silicon System," *Metall. Trans. A*, vol. 22A, pp. 2211-2223, 1991.

[327] T. Hidayat, D. Shishin, S. A. Decterov, and E. Jak, "Experimental Study and Thermodynamic Re-evaluation of the FeO-Fe_2O_3-SiO_2 System," *submitted to Metall. Trans. B*, 2012.

[328] P. V. Riboud and A. Muan, "Phase Equilibria in a Part of the System "FeO"-MnO-SiO_2," *Trans. Met. Soc. AIME*, vol. 224, pp. 27-33, 1962.

[329] H. Annersten, T. Ericsson, and A. Filippidis, "Cation Ordering in Ni-Fe Olivines," *Am. Mineral.*, vol. 67, pp. 1212-1217, 1982.

[330] N. O. Ovchinnikov, L. P. Nikitina, and E. Y. Khiltova, "The real structure and thermodynamic properties of olivine solid solutions $(Fe_{1-x}Ni_x)_2SiO_4$," *Zap. Vseross. Mineral. O-va.*, vol. 121, pp. 15-28, 1992.

[331] S. Wissmann, D. Niemeier, and K. D. Becker, "High-temperature Studies of Cation Distribution and Iron Diffusion in Olivines," *Conf. Proc. - Ital. Phys. Soc.*, vol. 50, pp. 797-800, 1996.

[332] R. Schuhmann and P. J. Ensio, "Thermodynamics of Iron-Silicate Slags: Slags Saturated with Gamma Iron," *Trans. AIME, J. Met.*, vol. 3, pp. 401-411, 1951.

[333] E. J. Michal and R. Schuhmann, "Thermodynamics of Iron-Silicate Slags: Slags Saturated with Solid Silica," *Transactions AIME (vol. 194,) J. of Metals*, vol. 4, pp. 723-728, 1952.

[334] R. Schuhmann, R. G. Powell, and E. J. Michal, "Constitution of the FeO-Fe_2O_3-SiO_2 System at Slag-Making Temperatures," *Trans AIME, J. Met.*, vol. 197, pp. 1097-1104, 1953.

[335] W. C. Allen and R. B. Snow, "The Orthosilicate-Iron Oxide Portion of the System CaO-"FeO"-SiO_2," *J. Am. Ceram. Soc.*, vol. 38, pp. 264-280, 1955.

[336] C. Bodsworth, "The Activity of Ferrous Oxide in Silicate Melts," *J. Iron Steel Inst.*, vol. 193, pp. 13-24, 1959.

[337] T. Oishi, T. Goto, Y. Kayahara, K. Ono, and J. Moriyama, "Oxygen Pressure Measurements of Silica Saturated Fe-O-SiO_2 Melts by EMF Method Using Zircohia Solid Electrolite," *Metall. Trans. B,* vol. 13B, pp. 423-427, 1982.

[338] A. Muan, "Phase Equilibria in the System FeO-Fe_2O_3-SiO_2," *Trans. Metall. Soc. AIME,* vol. 203, p. 965, 1955.

[339] E. J. Grimsey and A. K. Biswas, "Solubility of Nickel in Silica-Saturated Iron Silicate Slags at 1573 K," *Trans. Instn Min. Metall. (Section C: Mineral processing & Extractive Metallurgy),* vol. 85, pp. C200-207, 1976.

[340] E. J. Grimsey and A. K. Biswas, "Solubility of Nickel in Iron-Silicate Slags both Lime-Free and with Lime at 1573 K," *Trans. Instn. Min. Metall. (Section C: Mineral processing & Extractive Metallurgy),* vol. 86, pp. C1-8, 1977.

[341] M. Nagamori, "Metal Loss to Slag. II. Oxidic Dissolution of Nickel in Fayalite Slag and Thermodynamics of Continuous Converting of Nickel-Copper Matte," *Metall. Trans. B,* vol. 5B, pp. 539-548, 1974.

[342] S. S. Wang, A. J. Kurtis, and J. M. Toguri, "Distribution of Copper-Nickel and Copper-Cobalt between Copper-Nickel and Copper-Cobalt Alloys and Silica Saturated Fayalite Slags," *Can. Metall. Q.*, vol. 12, pp. 383-390, 1973.

[343] J. R. Taylor and J. H. E. Jeffes, "Slag-Metal Equilibriums between Liquid Nickel-Copper Alloys and Iron Silicate Slags of Varying Composition," *Inst. Min. Metall., Trans., Sect. C,* vol. 84, pp. C136-C148, 1975.

[344] R. G. Reddy and C. C. Acholonu, "Distribution of nickel between copper-nickel and alumina saturated iron silicate slags," *Metall. Trans. B,* vol. 15B, pp. 33-37, 1984.

[345] J. M. Toguri and N. H. Santander, "Distribution of Copper between Copper-Gold Alloys and Silica-Saturated Fayalite Slags," *Metall. Trans.*, vol. 3, pp. 586-588, 1972.

[346] S. S. Wang, N. H. Santander, and J. M. Toguri, "The Solubility of Nickel and Cobalt in Iron Silicate Slags," *Metall. Trans.*, vol. 5, pp. 261-265, 1974.

[347] S. A. Decterov, I.-H. Jung, and A. D. Pelton, "Thermodynamic Modeling of the FeO-Fe_2O_3-MgO-SiO_2 System," *J. Am. Ceram. Soc.*, vol. 85, pp. 2903-2910, 2002.

[348] A. G. Nord, H. Annersten, and A. Filippidis, "The Cation Distribution in Synthetic Mg-Fe-Ni Olivines," *Am. Mineral.*, vol. 67, pp. 1206-1211, 1982.

[349] T. Hidayat, D. Shishin, S. A. Decterov, and E. Jak, "Thermodynamic Optimization of the CaO-FeO-Fe_2O_3 System," *submitted to Metall. Trans. B,* 2012.

[350] H. Yamamura, H. Haneda, A. Watanabe, Y. Moriyoshi, and S. Shirasaki, "Magnetic Properties in the System Iron Nickel Oxide-Calcium Iron Oxide ($NiFe_2O_4$-$CaFe_2O_4$)," *Yogyo Kyokaishi,* vol. 89, pp. 595-598, 1981.

[351] A. Vasiliu, "Initial Permeability and Curie Temperature in the Compounds of the Calcium Nickel Ferrite ($Ca_xNi_{1-x}Fe_2O_4$) System," *Bul. Inst. Politeh. Iasi, Sect. 1,* vol. 25, pp. 103-108, 1979.